NASA CR-134499
R73AEG443

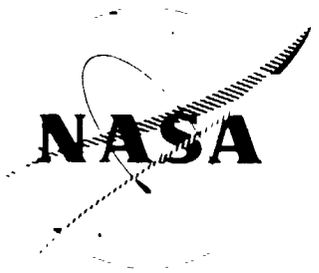

QUIET ENGINE PROGRAM
TURBINE NOISE SUPPRESSION

VOLUME I
General Treatment Evaluation and Measurement Techniques

by

A. Clemons
H. Hehmann
K. Radecki

GENERAL ELECTRIC COMPANY

Prepared For

National Aeronautics and Space Administration

NASA Lewis Research Center
Contract NASA3-12430

1. Report No.	2. Government Accession No.	3. Recipient's Catalog No.
NASA CR-134499		

4. Title and Subtitle	5. Report Date
QUIET ENGINE PROGRAM TURBINE NOISE SUPPRESSION Volume I - General Treatment Evaluation and Measurement Techniques	December 1973 6. Performing Organization Code
7. Author(s) A. Clemons, H. Hehmann, and K. Radecki	8. Performing Organization Report No. R73AEG443
9. Performing Organization Name and Address General Electric Aircraft Engine Group Cincinnati, Ohio 45215	10. Work Unit No. 11. Contract or Grant No. NASA 3-12430
12. Sponsoring Agency Name and Address National Aeronautics and Space Administration Washington, D.C. 20546	13. Type of Report and Period Covered Contractor Report 14. Sponsoring Agency Code

15. Supplementary Notes

Project Manager, E.W. Conrad, V/STOL & Noise Division
NASA Lewis Research Center, Cleveland, Ohio 44135

16. Abstract

Acoustic treatment was developed for jet engine turbine noise suppression. Acoustic impedance and duct transmission loss measurements were made for various suppression systems. An environmental compatibility study on several material types having suppression characteristics is presented. Two sets of engine hardware were designed and are described along with engine test results which include probe, farfield, near field, and acoustic directional array data. Comparisons of the expected and the measured suppression levels are given as well as a discussion of test results and design techniques.

17. Key Words (Suggested by Author(s))	18. Distribution Statement
Acoustic Treatment, High Temperature Turbine Noise	Unclassified - Unlimited

19. Security Classif. (of this report)	20. Security Classif. (of this page)	21. No. of Pages	22. Price*
Unclassified	Unclassified	258	$3.00

* For sale by the National Technical Information Service, Springfield, Virginia 22151

TABLE OF CONTENTS

VOLUME I

LIST OF ILLUSTRATIONS

LIST OF ILLUSTRATIONS - CONTINUED

LIST OF ILLUSTRATIONS - CONTINUED

LIST OF ILLUSTRATIONS - CONTINUED

LIST OF ILLUSTRATIONS - CONTINUED

LIST OF ILLUSTRATIONS - CONTINUED

LIST OF ILLUSTRATIONS - CONTINUED

LIST OF ILLUSTRATIONS -- CONTINUED

LIST OF ILLUSTRATIONS - CONTINUED

LIST OF ILLUSTRATIONS - CONTINUED

LIST OF ILLUSTRATIONS - CONTINUED

LIST OF TABLES

SUMMARY

Acoustic treatment was developed for the NASA QEP engines A and C for suppression of turbine generated noise. The design study required turbine noise spectra predictions and a definition of the turbine exhaust environment based on predicted engine cycle data. An evaluation of the various suppression systems including single-degree-of-freedom; multiple-degree-of-freedom and bulk-type absorbers was conducted. Acoustic impedance and duct transmission loss measurements were made for approximately 30 different proposed suppression configurations. A materials environmental compatibility study was undertaken to determine which materials were capable of functioning in the turbine exhaust environment, and these were then rated on the basis of manufacturing difficulty, weight, and cost requirements. The configurations were rated acoustically by applying measured duct transmission loss values to the predicted turbine noise spectra and calculating the potential PNL reduction. The recommended treatment configurations for both engines were based on these results.

Engine tests were perfor ..l on both engines, with emphasis placed on evaluating the treatment suppression of the low pressure turbine blade passing frequencies. Engine A contained a four-stage low pressure turbine and was tested both at approach and takeoff speeds for a hardwall baseline and two treated configurations. Engine C contained a two-stage low pressure turbine and was tested in an untreated and in one treated configuration at approach and takeoff speeds. Data were recorded using acoustic probes, near field and far-field microphones, and a directional microphone array located in the farfield.

Probe data presented the most satisfactory means of evaluating the treatment suppression of the blade passing frequencies. The power level of the fundamental frequencies on engine A was suppressed as much as 16.5 dB and harmonics up to 19.5 dB at approach. At takeoff suppression ranged from 3.2 to 9.8 dB. Engine C tone power level suppression reached 11.1 dB at approach and 9.5 dB at takeoff.

The directional microphone array measurements were the most satisfactory means of evaluating broadband data. On engine A the aft sound pressure level suppression peaked at 6.5 dB and 4.5 db at approach and takeoff respectively. Engine C broadband noise SPL suppression reached 10 dB at approach power and 5.5 dB at takeoff.

INTRODUCTION

During the past few years much emphasis has been placed on jet engine noise reduction with almost all the effort concentrated on fan and jet noise suppression. As the technology has advanced in these areas, turbine radiated noise has become an important contributor to the effective perceived noise level (EPNL) of jet engine aircraft. Therefore, in order for most future aircraft to meet the required EPNL limits as established by the FAA, turbine noise suppression has become necessary.

Both NASA and the General Electric Company recognized this problem and under the NASA Quiet Engine Program, a program providing for the development of acoustic treatment for turbine noise suppression was initiated by NASA and the General Electric Company's Aircraft Engine Group.

The primary objective of this program was to first investigate potential suppression materials and to then identify the treatment configuration design for optimum suppression of turbine radiated noise. This is contained in Volume I. The second phase of the program, contained in Volume II, was to measure the reduction in the engine perceived noise level (PNL) resulting from the turbine treatment on the fully suppressed fan configurations of Quiet Engines A and C.

SECTION I

ACOUSTIC TREATMENT EVALUATION

A. Treatment Configurations

The three different types of systems evaluated for turbine noise suppression are referred to as follows:

- Single-degree-of-freedom (SDOF)
- Multiple-degree-of-freedom (MDOF)
- Bulk absorbers

A generalized comparison of transmission loss capabilities for each system based on initial duct test results is given in Figure 1. Although these trends were recorded in a cold flow duct facility the same trend exists at elevated temperatures. From these initial suppression shapes it was believed that the MDOF and bulk absorber systems offered a wider suppression bandwidth than SDOF systems.

1. SDOF System

An analytical study, using the procedure as given in Ingard and Ising[1], was made to identify the parameters of SCOF resonators that control the absorption bandwidth, and how these parameters may be changed such that the most effective SDOF resonator design could be produced. The goal was to make SDOF systems (which are more desirable in respect to weight, manufacturing techniques, and cost requirements than the MDOF systems) equivalent acoustically to MDOF systems. A comparison of acoustic reactance values for a 2.54-cm (1.0 in.) thick SDOF system and for a bulk-type absorber of the same thickness is given in Figure 2. The slope, dx/df, of the reactance curve for the bulk absorber is less than that of the SDOF system in the region of zero (optimum) reactance. That is, the reactance is more nearly zero for the bulk absorber over a greater frequency range and this results in increased suppression bandwidth. Thus the objective is to design a SDOF system with the slope of the reactance minimized.

The acoustical impedance is defined as $Z_A = P/U$ where P is the acoustic pressure and U is the volume velocity through a surface.

The acoustical reactance of a single opening into a cavity (Helmholtz resonator) is given by:

$$X = \omega M - 1/\omega C_A$$

where

$M = \text{mass}/S^2$ = acoustical mass (mass within opening)

$C_A = V/\rho c^2$ = acoustical capacitance

then:

$$X = \frac{2\pi f \rho \ell}{\Sigma} - \frac{\rho c^2}{2\pi f V}$$

where ρ = density of air

ℓ = plate thickness + 0.85 x hole diameter

S = hole area

c = velocity of sound in air

V = cavity volume

f = frequency

In the case of a single hole or of an array of holes in a perforated plate over a cavity, the volume velocity and therefore reactance is defined over the face plate area rather than just the hole area, then

$$X = \frac{2\pi f \rho \ell}{\sigma} - \frac{\rho c^2 A}{2\pi f V} = \frac{2\pi f \rho \ell}{\sigma} - \frac{\rho c^2}{2\pi f B}$$

where σ = porosity

σA = hole area, S

B = core thickness

The reactance of a system consisting of an array of holes is dependent on the face plate porosity, the core thickness, the hole diameter and the face plate thickness. The slope of the reactance is seen to decrease with increasing core thickness and increasing porosity as shown in Figure 3. The reactance change as a function of core thickness is shown in Figure 4. The slope is also seen to be a function of the face plate thickness and hole diameter. Decreasing the slope calls for thinner panels and smaller hole sizes. In the selection of panel configurations to be evaluated in the high temperature duct facility, an effort was made to include designs in which some of the parameters would be included in the experimental results. A description of the SDOF systems evaluated is given in Figures 5 through 7.

2. MDOF System

An analytical model, which is described by Kazin, et al.,[2] developed for predicting acoustic reactance for MDOF systems, was used in a study to optimize the tuning and bandwidth of MDOF systems. Resistance damping coefficients were a required program input. These values were based on dc flow resistance measurements for perforated sheets. MDOF systems differ from SDOF systems in respect to the parameters that influence the acoustic reactance behavior. The cavities are coupled to each other such that damping for any one element affects the total system. Shown in Figure 8 are results of a typical MDOF system with

low damping coefficients. As an example of the effect of adding damping, the same configuration with damping is given in Figure 9. The measurements were taken using a standard standing wave impedance tube. This apparatus and the procedures in taking measurements are discussed in Smith, et al[3]. The reactance here has only one resonance (zero reactance value) as compared to three in the case without damping, the zero reactance value is shifted to a higher frequency with the slope decreased, thereby producing a wide suppression bandwidth.

Two types of MDOF configurations were evaluated: the double sandwich resonator which is two SDOF configurations stacked together and the triangular core MDOF system. Descriptions of both these systems as evaluated are given in Figures 10 and 11.

3. Bulk Absorbers

The bulk-type absorbers are described in Figures 12 and 13. Two types of bulk systems, "Cerafelt" and "Cer-vit", were acoustically evaluated. A complete description of these materials is given in the Environmental Compatibility section (Vol. II). The bulk absorbers are characterized by their wide suppression bandwidth due to the relatively small rate of change in reactance as a function of frequency.

B. ACOUSTIC TREATMENT CHARACTERISTICS

1. Normal Incidence Impedance

a. Predictions

The acoustic impedance was predicted or measured for all the configurations that were selected to be evaluated in the transmission loss duct facility. A total of 30 configurations were selected to be tested of which 20 were single-degree-of-freedom, 5 were multiple-degree-of-freedom, and 5 were bulk-type absorbers (nonmetallic) such as Cer-vit and Cerafelt. Shown in Table I is a matrix that includes nine of the SDOF configurations. These nine configurations were the first SDOF configurations to be fabricated and tested in the transmission loss duct facility. This matrix illustrates the wide range of porosity and panel thickness represented in this selection of designs. Presented in Table II is an even larger matrix of SDOF designs that were later fabricated and tested in the duct facility. However, data from only the original nine SDOF selections, as given in Table I, were available at the time engine treatment recommendations were made for both engines A and C.

Measured acoustic reactance and resistance, and calculated reactance, for configurations at ambient and at engine environment temperatures are presented in Figures 14 to 73. The data were recorded at 130 dB in the high intensity impedance tube except for Figures 69-73 which were recorded on the B&K apparatus at 100 dB. The included predictions are a result of analytical models (developed for SDOF and for MDOF systems described in References 1 and 2) and have the capability of calculating the acoustic reactance only in the presence of air flow. Predictions were made both for flow and no flow conditions. The acoustic reactance with flow is calculated by decreasing the end correction factor,

B. Phillips,[4] on the acoustic mass of the system as the air flow velocity is increased. This has a definite effect on resonator systems, causing the peak attenuation frequency to be shifted to higher frequencies as the flow is increased. No acoustic resistance predictions were made for the resonator systems at the engine environment temperature. This decision was based on the fact that no data had been obtained to substantiate the analytical model being employed for predictions at increased temperature. The behavior of the resistance at higher temperatures was not clearly understood at this time. Flow resistance tests were undertaken for increased temperature and are discussed later in this report.

Table I. Single Degree of Freedom Panels for Transmission Loss Duct Facility.

	CORE THICKNESS			
FACE PLATE POROSITY	.0063m (1/4")	.0095m (3/8")	.0127m (1/2")	.0190m (3/4")
2.5%	X			
4.0%	X	X		
7.0%	X	X	X	X
10.0%			X	
14.5%				X

ALL PANELS HAVE THE FOLLOWING DIMENSIONS:

- FACE PLATE HOLE DIAMETER .159cm (.0625")
- FACE PLATE THICKNESS .076cm (.03")
- HONEYCOMB CORE CELL SIZE 1.270cm (.5")

Table II. SDOF Panel Selections.

Porosity	CORE THICKNESS						
	.318cm (1/8)"	.635cm (1/4")	.953cm (3/8")	1.27cm (1/2")	1.91cm (3/4")	2.54cm (1.0")	3.81cm (1/5")
2.5%		X					
4%	X	X	X	X			
7%		X	X	X	X	X	
10%				X		X	
14%				X	X	X	X
22.5%				X		X	

b. Measurements

Impedance measurements were made using a standing wave apparatus. A sketch of the facility is shown in Figure 74. All measurements were taken at ambient temperatures in the absence of air flow. Two Altec acoustic drivers were used to produce a high intensity environment equivalent to that expected in the engine turbine exhaust area. The standing wave pattern was measured by means of a translating waveguide probe.

All the SDOF test samples were approximately 2.54 cm (1.0 in.) in diameter. However, the triangular-core MDOF configurations were tested in a modified impedance facility capable of accepting a 9.9 cm (3.89 in.) square sample. This was necessary since a 2.54 cm (1.0 in.) sample from the triangular core was too small to give a true representation of the configuration. With this increase in specimen size and the increased impedance tube dimensions, data is limited to frequency measurements $\leq$ 4000 Hz. The test specimen holder allowed variation in the backing depth such that any core thickness could be accomodated in the impedance tube. The face plates were removable so that plates with different porosities could be tested. This variation in both porosity and panel depth enabled all configurations to be represented in the impedance facility.

2. DC Flow Resistance

The effect of high temperatures, as encountered in the core nozzle region of an engine, on the dc flow resistance of a perforated plate was investigated. It was thought that the increased temperature may have resulted in nonlinear viscous losses in the perforated face plate. A dc flow resistance facility was constructed to permit testing up to 578° K (580° F). A sketch of the facility is shown in Figure 75. Two vacuum pumps in series were used to generate the flow which was measured using a Merriam flow meter in combination with a micromanometer. A thermocouple was required since an accurate temperature through the flow meter is needed to determine the flow rate. The rate of flow through the system was controlled by a valve located upstream of the flow meter The air was heated by a Chromalox circulation heater and was passed into a plenum of approximately 3.5×10^{-3} cubic meters (216 cubic inches). Plenum air exited through a 5.1-cm (2 in.) diameter test sample. The test samples were 9% open and 22% open with 0.16 cm (1/16 in.) hole diameter. The temperature of the plenum air was also recorded using a thermocouple.

The dc flow resistance is given by $R = \Delta P/u$, where ΔP is the pressure drop across the test sample and u is the linear velocity, which is obtained by dividing the volume velocity by the total sample area. The pressure drop across the sample is given by

$$\Delta P_T = (1/2\ \rho\ v^2 + P)_{plenum} - (1/2\ \rho\ v^2 + P)_{atmosphere} \qquad (2)$$

This can be simplified to

$$\Delta P_T = P_{plenum} - P_{atmosphere} \qquad (3)$$

since $1/2\ \rho\ v^2$ for the plenum and for the downstream side of the sample are typically less than 0.25 cm (0.1 inch) H_2O at a linear velocity of 5 m/sec.

The velocity through the sample was determined by calculating the flow using the flow meter calibration curves, and correcting for barometric pressure and temperature. This value is the volume velocity, i.e., cubic meters per second. The linear velocity was computed by dividing this value by the total sample area and multiplying by the term $\frac{P_o\sqrt{T}}{P\sqrt{T_o}}$ which corrects for the change in density of air in the plenum, and therefore the velocity. Here, P_o and T_o are the absolute pressure and temperature in the flow meter and P and T are the absolute pressure and temperature in the plenum. The absolute pressures are less than 0.51 meters (20 inches) H_2O above atmospheric so that the pressure terms can be neglected.

Results of these tests are presented in Figure 76. They show the flow resistance versus temperature at a flow velocity of 5 m/sec. These values were derived from the measurement at each temperature by (1) plotting resistance as a function of flow velocity, (2) constructing a best fit curve, and (3) noting the resistance value at this desired velocity. A solid line is drawn in the figure to represent the inverse relationship between resistance and temperature. That is, the data show the flow resistance to be inversely proportional to the temperature. The resistance can also be said to be directly proportional to the density of the air. Data scatter are greater than expected with several data points as much as $\pm$ 15% from the average value. The scatter is attributed to temperature monitoring problems, difficulty in holding the heater output constant, problems occurring in measuring these small pressure differentials, and unsteady flow output from the vacuum pumps. There were, therefore, no increased viscous losses at higher temperatures.

C. TRANSMISSION LOSS EVALUATION

1. Facility Description

The acoustic duct test facility is shown in Figures 77 and 78. This facility was used in performing transmission loss measurements for all the treatment configurations. Referring to Figure 79, it is seen that air to the test section enters through a gate valve located in the 20.2-cm (8 in.) diameter supply line. The airflow is controlled by a pressure regulating valve downstream of a flow measuring orifice. A preburner and burner are situated downstream of the valves. Aviation fuel can be supplied to the burner in controlled amounts. A schematic showing the fuel supply is given in Figure 80. A transition section aft of the burners converts the circular pipe to a rectangular cross section with internal dimensions of 10.1 cm (4 in.) x 20.2 cm (8 in.).

To reduce upstream piping and valve noise and thus improve the signal-to-noise ratio of the test facility, a muffler was installed in the test section walls downstream of the burner. The muffler system consists of a perforated plate with a wire screen backing over a bulk-type sound-absorbing material.

A thermocouple and a pitot-static pressure probe were located immediately upstream of the test section. Swagelock fittings were provided in this section to enable acoustic probes (for the measurement of acoustic pressure level) to be inserted into the duct.

The two 45.7-cm (18.0 in.) long rectangular test sections were each capable of receiving acoustic test panels of 6.35 cm (2.5 in.) maximum depth, this is shown in Figure 81. Swagelock fittings were also provided downstream of the treatment for the installation of acoustic probes. The duct was terminated in a diffuser section exhausting into the atmosphere.

The noise source used in all tests was a Hartmann noise generator and is shown in Figure 82. A tone is generated by directing a supersonic flow of air into a cylindrical cavity. By varying the cavity depth, different frequencies could be generated. A schematic of all the instrumentation required in the acoustic data acquisition is shown in Figure 83.

The calibration of the cavity was performed by removing the exhaust diffuser and positioning a calibration rake, Figure 84, at the end of the test section. The rake was attached to the stem of a 25.4 cm (10 in.) actuator and was thus able to traverse the duct cross section. The rake consisted of a vertical row of seven thermocouples and a row of seven total pressure probes equally spaced over 8.9 cm (3.5 in.). The rake was initially positioned 0.63 cm (0.25 in.) from the side duct wall. Additional readings were taken 2.5 cm (1.0 in.), 5.1 cm (2.0 in.), 7.68 cm (3.0 in.), 10.15 cm (4.0 in.), 12.70 cm (5.0 in.), 15.2 cm (6.0 in.), 17.8 cm (7.0 in.), and 19.7 cm (7.75 in.) from this wall. These locations were set by the actuator control dial readout. The calibration was performed with the air supply to the Hartmann Generator turned on. Although this airflow was small 0.079 kg/sec (0.175 lb/sec) it was sufficient to affect the temperature distribution in the duct.

A required test point was set, approximately, by referring to the plot of the mass flow parametric equation and to the carpet plot relating the air mass flow to orifice pressure drop and upstream pressure.

The mass flow parametric equation is presented below:

$$\frac{W\sqrt{T}}{AP_S} = M\sqrt{\frac{\gamma g}{R}\left[1 + \left(\frac{\gamma-1}{2}\right) M_N^2\right]} \qquad (4)$$

where
- W = required mass flow in test section
- T = temperature in test section, °R
- A = effective area of test section
- P_S = static pressure in test section
- M = required Mach number in test section
- γ = ratio of specific heat at constant pressure to specific heat at constant volume = $\frac{c_p}{c_v}$
- g = acceleration of gravity
- R = universal gas constant

This relationship has been plotted in graphical form in Figure 85. Thus for a required Mach No. (M), the mass flow rate can be found if T, A, and P_s are known (for ambient conditions assume $\gamma = 1.4$, for high temperature conditions assume $\gamma = 1.35$).

Assume that P_s is 10.3×10^3 kg/m^2 atmospheric (14.7 lb/in.^{2} atmospheric), since the duct exhausts to atmosphere, and also that the effective area of the duct is 187 sq cm (29 sq in.). The required air mass flow rate can be equated to actual Mach number at various test section temperatures by using Figure 86.

Note: The "effective" area of the duct can be found accurately by using true Mach No.'s found from the calibration and true mass flows measured by the orifice and substituting these values into the mass flow parametric equations and solving for A. This calculation was repeated for several test conditions and resulted in an average value of 187 sq. cm (29 sq in.).

The equation for rate of flow through the facility orifice is

$$W_a = 1.4067\ Y \sqrt{\frac{P_1 \Delta P}{T_1}} \qquad (5)$$

where W_a = mass flow rate kg/sec, (lb/sec)

Y = expansion factor = $1.0 - 0.01174\ \frac{\Delta P}{P_1} \simeq 1$

P = pressure downstream of orifice absolute, kg/m^2 (lb/in.^{2})

ΔP = pressure drop across orifice, cm of water (in. water)

T_1 = incoming air temp °R

This equation is shown as a carpet plot in Figure 87. The mass flow parametric equation enables an approximate mass flow to be established for the facility at various test section temperatures and Mach numbers. The carpet plot assists in obtaining the required mass flow. In practice, it has been found more suitable to keep the pressure downstream of the gate valve (P_1) constant at 703×10^2 kg/m^2 absolute $\simeq$ 597×10^2 gauge (100 psia, $\simeq$ 85 psig) and adjust the pressure drop (ΔP) across the orifice by means of the regulator valve in order to meet the various flow requirements.

The equation is now reduced to:

$$W_a \simeq 14\sqrt{\frac{\Delta P}{T_1}} \qquad (6)$$

In Figure 88, W_a is plotted against ΔP for an air inlet temperature of 540° R (300° K).

The burner was ignited and fuel was supplied at increasing flow rates until the upstream thermocouple indicated the desired temperature (corrected for radiation effect, Figure 89). When conditions were steady, readings were taken of upstream total pressure, upstream temperature, and the seven rake total pressures and temperatures. The ambient conditions were also noted. The rake was then moved to a new position and these data were recorded. The upstream static pressure was also recorded.

The relationship between the single upstream thermocouple reading and the true average value of the rake temperatures over the Mach number range is shown in Figures 90-94. It can be seen from the summary plot, Figure 95, that as the Mach number is increased, the single thermocouple reading agrees more closely with the actual average temperature across the duct area. This may in part be due to the reduced effect of the Hartmann air flow. The data, as shown in Figure 96, have been arranged so that the temperature distributions over the duct cross section can be easily observed.

The relationship between the Mach number calculated from the upstream probe pressure reading and that calculated from the average values measured by the rake are shown in Figures 97-100. There is no variation due to temperature as can be seen by the summary plot of Figure 101.

The total pressure reading, in inches of water, obtained from the total and static probes is converted to Mach number by the following process:

1. Ensure pressure readings are absolute by correcting for initial manometer settings.

2. Multiply barometric pressure reading in cm (inches) of mercury by 13.6 to convert to cm (inches) of water.

3. Add barometer reading from No. 2 to values of total (P_T) and static (P_S) pressure obtained from No. 1.

4. Calculate ratio $\frac{P_S}{P_T}$ for each case.

5. Use carpet plot of M vs. P_S/P_T (Figure 102) to obtain Mach number. Assume $\gamma = 1.4$ for ambient conditions and $\gamma = 1.35$ for high temperature conditions).

Alternatively, direct readouts of Mach number vs. total gage pressure, P_T, in cm (inches) of water, for a range of static pressures, P_S, in cm (inches) of water, are given in Figures 103 and 104 for $\gamma = 1.4$ and $\gamma = 1.35$.

The relationship between true Mach Number and fuel flow (which was measured by frequency in Hz proportional to weight flow by the flow meter) for the range of test temperatures is shown in Figure 105. The amount of fuel used at a given test temperature and Mach number is dependent on the inlet air temperature. Thus some variation above and below the lines is to be expected.

2. Panel Fabrication

The single-degree-of-freedom (SDOF) resonator panels consisted of a core, facing, and back sheet with side and end plates. The overall dimensions were 45.7 cm (18 in.) by 11.2 cm (4.4 in.) for each panel. A sample panel and the components of the panel are shown in Figures 106 and 107, respectively. The face plates were 0.076-cm (0.03 in.) thick sheet, perforated with 0.159-cm (1/16 in.) diameter holes in a staggered pattern and varied in density to give the different porosities. The back and side plates were 0.127 cm (0.05 in.) thick. The core material used for the SDOF configurations was honeycomb having 1.27 cm (1/2 in.) square cell size with 0.0152 cm (0.006 in.) ribbon. All panel components were 321SS. The brazing alloy used "Coast metal 50 Powder".

Joining of the face plate and back plate to the core material was accomplished by brazing in a high vacuum furnace. The brazing alloy (CM-50 of Ni-Si-B) operates at temperatures up to 1033° K to 1089° K (1400-1500° F) with good oxidation resistance. The powder was applied to the panel face and back plates by both flame spraying techniques and broadcasting onto an acrylic base cementing agent. Both methods proved to be satisfactory on a laboratory scale and the method most practical was used in panel production. Stopoff was applied at the face and back plate edges and to the low carbon steel plates used to separate the panels during the brazing process.

The panels were assembled on the vacuum furnace hearth plate with separator plates on top, bottom, and sandwiched between the panel assemblies. Flat weights were applied to the top of the stock, and sheet metal heat shields were located along the side to prevent warpage normally caused by nonuniform heating and cooling. The panels were brazed at 1380° K (2025° F) 10 minutes under vacuum equal to better than 5.0×10^{-4} torr. Furnace leak outgassing rates were less that 4 microns per hour total prior to applying heat to the furnace. A slow heating rate of 266° K (20° F) per minute was used to reach the brazing temperature. After brazing, the parts were vacuum cooled to 1033° K (1400° F) and helium quenched to room temperature. For most of the panel, the braze was 100% effective. Capillary action drew brazing allowance up the nodes strengthening the honeycomb. However, some panels had voids at points near the outer edge probably caused by honeycomb deflection and warpage of the plate. When necessary, defective panels were rebrazed with extra alloy applied as a slurry. All of the side plates were TIG tack welded to the face and back plates and the end plates were completely TIG welded to the face, back, and side plates.

The two-degree-of-freedom double-sandwich-type panels were fabricated the same as described above. The only difference being in the addition of the inner perforated sheet. The two-degree-of-freedom configurations having a triangular core were also fabricated the same as previously described. The triangular-core material was 321SS with a wall thickness of 0.0635 cm (0.02 in.). The required shape of the core material was formed by a bending process. Alternate walls were perforated with slots using an electronic drill.

3. Test Results

The corrected transmission loss values for all the acoustic test panels as listed in Table III are given in Figures 108 through 222. Almost all of the test panel configurations were evaluated at the following test conditions.

- Average duct temperature 589° K (600° F)
- Duct Mach numbers of 0.21, 0.25, 0.30, and 0.45
- Treated length to duct height ratio (L/H) of 4.5 or 2.25

The acoustic duct facility has already been described. The instrumentation for the acoustic measurements was given in Figure 83. The upstream duct (forward of the acoustic treatment section) sound pressure level profile measurements were made with the five-element acoustic probe rake as indicated in the schematic. A multiplex average sound pressure level was then used to represent the upstream sound pressure level. A similar acoustic probe rake was located downstream of the acoustic treatment section of the duct. The multiplex average of the five probes was used to represent the downstream sound pressure level. The transmission loss (difference between the two sound pressure values) was then found.

The values were corrected for the noise level difference between the upstream and downstream probes with a hardwall configuration in the treatment section of the duct. Thus, all the results as given are suppression values resulting directly from the insertion of treatment within the treatment section (corrected transmission loss).

Most of the treatment configurations were tested for a L/H value of 4.5 and at a temperature as predicted for the turbine exhaust environment. Each configuration was tested at four different gas stream Mach numbers. The results of these tests were used in the evaluation and the selection of the engine treatment configurations for both engines A and C. The frequency range from 2,000 Hz to 10,000 Hz was investigated. The specific frequencies at which data were recorded corresponded to the frequencies at which the Hartmann generator gave maximum acoustic power. In some of the figures the test results are plotted with an open circle symbol rather than the dark circle. The open symbols are used to indicate that the total suppression at that frequency could not be measured due to the noise floor existing within the acoustic duct. For many of the treatment configurations there appears to be one or more inconsistent data points. These for the most part are attributed to data scatter. A limited number of probe immersions were used. Therefore, at certain frequencies the full power level may not have been recorded. For these reasons a best fit curve was drawn through the data thus giving the suppression for each configuration at each set of conditions.

These test results were examined on a basis of peak suppression, peak suppression frequency, and suppression bandwidth as an initial selection method. These configurations were then evaluated on the basis of their potential to suppress the turbine spectrum in terms of PNL.

Table III. Listing of High Temperature Duct Transmission Loss Test Results.

FIGURE	PANEL DESCRIPTION	FIGURE	PANEL DESCRIPTION
108 - 111	SDOF No. 1	164 - 167	SDOF No. 21
112 - 115	SDOF No. 2	168 - 170	SDOF No. 22
116 - 119	SDOF No. 3	171 - 174	SDOF No. 23
120 - 123	SDOF No. 4	175 - 177	SDOF No. 24
124 - 127	SDOF No. 5	178 - 181	MDOF I
128 - 131	SDOF No. 8	182 - 185	MDOF II
132 - 135	SDOF No. 10	186 - 189	MDOF III
136 - 139	SDOF No. 12	190 - 198	Double Sandwich II
140 - 143	SDOF No. 14	199 - 202	Double Sandwich III
144 - 147	SDOF No. 16	203 - 206	CER-VIT No. 1
148 - 151	SDOF No. 17	207 - 210	CER-VIT No. 2
152 - 155	SDOF No. 18	211 - 214	CER-VIT No. 3
156 - 159	SDOF No. 19	215 - 218	CER-VIT No. 4
160 - 163	SDOF No. 20	219 - 222	Cerafelt (1.5 inch) (3.8cm)

Data from the double sandwich II configuration, which was recommended to be installed on engine A, are shown in Figures 193-198. These results correspond to an L/H value of 3.0 and were obtained at somewhat different temperatures and Mach numbers than were used for the majority of the tests. These conditions more closely approximate the measured values within the engine A turbine treatment section.

The effects of panel depth, porosity, and Mach number on suppression amplitude and peak frequency were investigated. These results were also used in developing the procedure for turbine treatment design as presented in the section on Treatment Design contained in the Discussion of Results.

SECTION II

TEST INSTRUMENTATION

A. ACOUSTIC PROBES

The acoustic probes, Figure 223, consisted of a stainless steel waveguide with a streamlined tip containing four rows of nine holes each such that their total area approximated that of the waveguide's internal cross sectional area. A microphone was located at the opposite end of the probe, which was also attached to an "infinite" termination (coil of tubing which was long enough so that reflections from its end would be negligible) at the microphone position. The total length of the probes from sensing tip to microphone was approximately 1.0 meter.

It was suspected that airflow at elevated temperatures over the tip of a waveguide acoustic probe might alter the acoustic impedance of the probe opening and thereby change the effective probe loss relative to a no flow condition. It was already known from Olson[5], that an increased temperature in the probe tube would result in increased viscous losses. An example of this effect is shown in Figure 224 for 533° K (500° F) and 811° K (1000° F). Up to a 3 dB increase in probe loss at 10 kHz is predicted. Of course, in both the test facility and engine tests, the internal temperature of the probe will not be constant but will vary from the gas temperature at the tip of the probe to a much lower value at the microphone. The latter temperature will depend on the ambient temperature, the probe length, and the cooling effect of flow over the external probe stem. For these reasons, the high temperature application was not expected to produce additional viscous losses in excess of 1 dB. To investigate the effects of high temperature airflow over the probe tip, an acoustic probe calibration facility, Figure 225, was constructed.

The facility consisted of a 0.305-m (12 in.) long, 0.0254-m (1 in.) diameter cylindrical test section inserted between muffler sections. The upstream muffler section was connected to a plenum containing wire mesh screens as flow straighteners. This in turn was connected to a hydrogen burner and a shop air supply. The test section contained provisions for inserting a probe so that the tip could be positioned along the axis of the test section. In addition, a 0.64 cm (1/4 in.) microphone could be mounted at the plane of the openings of the probe tip. The external portion of the microphone was water cooled. The test section was modified after completion of the first series of tests to reduce the background noise and thereby increase the signal/noise ratio. This modification consisted of welding a hollow water-cooled plate lengthwise to the test section so that the cross section presented a flat surface on which the microphone could be mounted. The plate also contained provision for mounting the test probe while maintaining a smooth internal surface.

An Altec 290D acoustic driver was located upstream of the test section and was used to generate a sine wave acoustic signal. The difference between the signal amplitude measured at the flush-mounted microphone and at the probe-mounted microphone, after correcting for microphone sensitivity, is defined as probe loss.

Velocity profiles, turbulence measurements, and temperature profiles were made in the test section. Shown in Figure 226 are the normalized velocity and turbulence measurements at midstream for M = 0.39. Normalized temperature profiles are shown in Figure 227 at midstream temperatures of 533° K (500° F) and 811° K (1000° F). The normalized temperatures are plotted in degrees Rankine. All the above mentioned measurements were made with the acoustic probe removed from the test section. These measurements were not repeated using the modified test section. The only change anticipated would be reduced turbulence intensity.

Calibration tests were conducted in the facility using the original test section with no airflow and T = 288° K (60° F); with M = 0.40, 0.30, and 0.20, T = 288° K (60°); M = 0.40, T = 533° K (500° F); and M = 0.40, T = 811° K (1000° F).

Shown in Figure 228 is the SPL measured in the test section by the reference microphone with a probe present. Measurements were made on-line with a B&K 6% analyzer which was used to analyze individual frequency bands. It can be shown that the noise peaks are not due to vortex shedding since they are independent of Mach number. At Mach = 0.40, the vortex shedding frequency should be 4.35 kHz. The second peak appears to be a phenomena of transverse duct resonance which occurs at f = nc/2D = 6.78 kHz. Here, n is an integer, c is the velocity of sound, and D is the diameter of the test section. The calibration signal was at least 6 dB above these background levels.

The measured probe response at M = 0.0 - 0.40 is shown in Figure 229. Probe losses appear to increase slightly with increasing frequency due to the presence of airflow. These results, however, were not verified in modified test section calibrations (Figure 230) which shows no effect due to airflow.

The effect of increasing temperature at M = 0.40 is seen in Figure 231. Data at 533° K (500° F) and 811° K (1000° F), recorded in the original facility, is plotted relative to results found with no flow. No distinct trend is seen. These curves were derived from the average of two test runs. Repeatability was approximately $\pm$ 1 dB up to 4 kHz and $\pm$ 1.5 dB at 6 kHz. Data were taken only at 500 Hz intervals due to time limitations imposed for temperature stabilization while using individual bottles of hydrogen as a fuel.

The repeatability problem of the flow data is at least in part due to the unsteadiness of both the reference microphone and probe microphone outputs. Even with a 6% bandwidth filter tuned to the signal frequency and a signal to noise ratio in excess of 6 dB, each microphone output typically fluctuated $\pm$ 1.5 dB. Evidently, turbulence in the flow changed the impedance seen by the acoustic driver, thereby affecting its output. An attempt was made to equalize pressure on the driver diaphragm to increase its efficiency by installing a short section of tubing from the back of the driver diaphragm to the section of pipe ahead of the driver. This, however, resulted in diaphragm failure due to water condensing on the diaphragm and coil.

An electronic counter was used to set each frequency for comparison between repeat runs. However, temperature variations between runs had

the effect of altering the signal wavelength. As can be seen in Figure 229, there is an oscillation superimposed on the frequency response curves. This is a function of the length of the probe between tip and microphone block and also the wavelength, and is a result of the discontinuity at the microphone block. The tubing had a circular cross section whereas the block had a square internal cross section to permit installation of a microphone on the flat wall. Any temperature change, therefore, will result in a frequency shift of the oscillation pattern. The effect on probe loss computations would be small at low frequencies; at high frequencies, however, the accuracy of the calibration is limited to the peak-to-peak amplitude of this oscillation.

The test data show that the airflow does not significantly affect the value of probe loss and that temperatures at the probe tip have no effect greater than the internal reflection effect. Therefore, probe calibrations at ambient pressure and temperature in the absence of airflow can be assumed to apply at duct conditions up to M = 0.40 and T = 811° K (1000° F). The probe loss values used in the engine data reduction are shown in Figure 232. This was based on calibration runs for each of the five probes and was fitted to the data to minimize the oscillation amplitude since this is temperature dependent.

The power level is calculated from probe data by logarithmically summing the levels at each immersion (after correcting for probe losses and applying a power factor correction based on the duct area).

$$PWL = \left(\log \sum_{i=1}^{n}\right)\left[SPL_i + \text{Probe Loss} + 10 \log A_i\right] \qquad (7)$$

where n = number of immersions

A_i = area of each annular area in meters^2

B. DIRECTIONAL ACOUSTIC ARRAY

The directional acoustic broadside microphone array, Figure 233, consists of a rigid beam containing 14 equally spaced Hewlett-Packard microphones, Model 14109B, and associated shading and summing elctronics.

It operates on the principle of unequal path length between the source and each microphone element. Microphones and electronics were therefore phase matched. In designing the broadside microphone array several objectives needed to be satisfied. These included frequency range, beam width, and the ability to operate at a specific distance from the source. The number of elements and the spacing between them are the principle design parameters, and these in turn are limited by economic and size limitations. The physical size of the array was the first constraint imposed. This in turn sets the lowest frequency, whereas the number of elements (an economic constraint) sets the upper

frequency limit. It was found based on Albers,[6] that an array of 14 elements with a spacing of 0.35-m (12 in.) between them would result in a beamwidth of approximately ± 1-1/2° at 2000 Hz for a source-receiver distance of 30.48-m (100 ft) with the second major lobe occuring at approximately 33 degrees from the array axis.

The off-axis rejection offered by a uniform array is not adequate, due to the anticipated presence of interferring noise sources of similar or greater amplitude than the source on which the array is trained. The sensitivity of the side lobes was, therefore, controlled by a process called "shading". In the shaded broadside (source direction normal to the line of the microphone elements) array all the microphones are operated in phase, but their sensitivities are varied. The Dolph-Chebyscheff shading technique was used. This method described by Albers[6] and Dolph[7] optimizes the array directivity pattern so that for any minor lobe level relative to the major lobe level the minimum beam width is obtained. This system requires adjusting the gains of the individual array elements before summation. The physical placement of the elements in an unshaded array will yield the same major lobe pattern in a Dolph-Chebyscheff array with only slightly increased beam width.

The electronic amplifier assembly was designed to sum the outputs of the 14 array elements both uniformly and with Dolph-Chebyscheff gain weighting (with side lobe suppression of 40 dB). This unit also contained the 200-volt supply for the condenser microphones. Gain weighting is accomplished by switchable voltage dividers at the input of each channel. The cannels are then summed by four Analog Devices No. 144A Operational Amplifiers. The outputs of these summing amplifiers are then combined to provide a single summed output for all 14 channels.

This resulted in a highly directional microphone system emcompassing a frequency range from 1.25 kHz to 6.3 kHz, and a narrow beam width and sufficient included angle between on-axis and off-axis lobes to be able to separate closely spaced sources. The array characteristics (based on an outdoor calibration with a single acoustic driver as a source) extended from 1.25 kHz to 6.3 kHz are shown in Figure 234. The peak at zero degrees represents the on-axis sensitivity of the array. This falls off to the horizontal line which represents the effective side lobe suppression. Additional peaks represents off-axis major lobe sensitivity. The off-axis sensitivity is the undesirable result of an array design exhibiting large side lobe suppression and a narrow beam pattern. The side lobe sensitivity, as measured, is greater than the design goal of -40 dB relative to the on-axis sensitivity. This increased sensitivity arises from atmospheric conditions which cause the acoustic signal to arrive at each microphone element at a less than optimum phase relationship. The side lobes, off-axis major lobes, atmospheric disturbances, ground reflection, large source size (as opposed to the optimum point source), the tolerance involved in placing the microphone elements on the proper radius of curvature, and the tolerance of each microphone sensitivity, each provide for potential system inaccuracy.

C. NEAR FIELD MICROPHONES

An array of microphones mounted in close to the sources can be used to help pinpoint the source of an acoustic signal. It will be of no help in calculating power level due to the close proximity to the source.

D. FARFIELD MICROPHONES

An array of farfield microphones is the accepted procedure for determining the sound pressure level and power level of a source. The array was comprised of 16 B&K Model 4133 microphones located at angles measured from the inlet of 10 degrees through 160 degrees in 10 degree increments on a 45.8m (150 ft) arc. A height of 12.2 in. (40 ft) was chosen in order to reduce the effect of ground reflections in the frequency range of interest.

The ground surface consists of crushed gravel with approximately 5 cm (2 in.) being the largest dimension. It extended well beyond the microphone arc and up to the concrete engine pad.

REFERENCES

1. Ingard, Uno and Ising, Hartnut, "Acoustic Nonlinearity of an Orifice," The Journal of the Acoustic Society of America, Feb. 1967.

2. Kazin, S.B., Smith, E.B., and Huber T.R., "A Linear Dynamical Acoustic Liner Model," Technical Memorandum No. 68-331 GF Class 2 (Can be obtained upon request from GE Evendale Technical Information Center).

3. Smith E.B., Benzakein M.J., and Radecki K.P., "Study and Tests to Reduce Compressor Sounds of Jet Aircraft," FAA Technical Report No. FAA DS-68-7.

4. Phillips, B., "Effects of High-Wave Amplitude and Mean Flow," NASA TM X-1582, February 15, 1968.

5. Olson, H.F., "Acoustical Engineering," D. Van Nostrand Company Inc., 1957.

6. Albers, V.M., "Underwater Acoustics Handbook," The Pennsylvania State University Press, University Park, Pennsylvania, 1965, pp. 189-190.

7. Dolph, C.L., "A Current Distribution of Broadside Arrays which Optimizes the Relationship Between Beam Width and Side-Lobe Level," Proceedings of the Institure of Radio Engineers, June, 1946, pp. 335-348; Dolph, C.L., "Discussion on 'A Current Distribution of Broadside Arrays...," Proceedings of the Institute of Radio Engineers, May 1947, p. 492; Krauss, J.D., Antennas, McGraw-Hill Book Co., New York, 1950; and Albers, V.M., "Underwater Acoustics Handbook," The Pennsylvania State University Press, University Park, Pennsylvania, 1965, pp. 188-199.

8. Rice, Edward J., "Attenuation of Sound in Soft Walled Circular Ducts" - NASA TM X 52442, Lewis Research Center, May 20-21, 1968.

9. Wirt, L.S., "Gas Turbine Exhaust Noise and its Attenuation," SAE Paper 1002B, International Automotive Engineering Congress, Detroit, Michigan, Jan. 11-15, 1965.

10. McMillan, P.W., Glass Ceramics, Academic Press, New York, 1964.

11. Kolom, A.L., and Ackley, J.M., "Soundwich - The Sound Attenuating Structure," 1969 Southern Metals Conference, ASM, Noise Abatement Symposium, Grand Bahamas, April, 1969.

12. Benzakein, M.J., Smith, E.B., "Turbine Noise Generation and Suppression," ASME Publication 73 WA/GT-7, November 11-15, 1973.

13. Military Handbook 23.

14. Sullins, R.T., "Manual for Structural Stability Analysis of Sandwich Plates and Shells," NASA Report CR1457, December 1969.

15. Ffowcs Williams, J.F., "The Acoustics of Turbulence Near Sound Absorbing Liners," J. Fluid Mech., Vol. 51, Part 4, February 1972.

16. Kazin, S.B., and Paas, J.E., "NASA/GE Quiet Engine "A" Acoustic Test Results," NASA CR121175, Lewis Research Center, 1973.

17. Hayden, R., "Bolt Beranek and Newman Report," NAS1-9559-14.

18. Kazin, S.B., and Paas, J.E., "NASA/GE Quiet Engine "C" Acoustic Test Results," NASA CR 121176 Lewis Research Center, 1973.

19. Cremer, Lothar. "Theorie der Luftschall - Dämpfung im Rechteckkanal mit Schluckender Wand und das sich Dabei ergebende höchste Dämpfungsmass," Akustische Beihefte, Acustica Vol. 3 Heft 2, 1953.

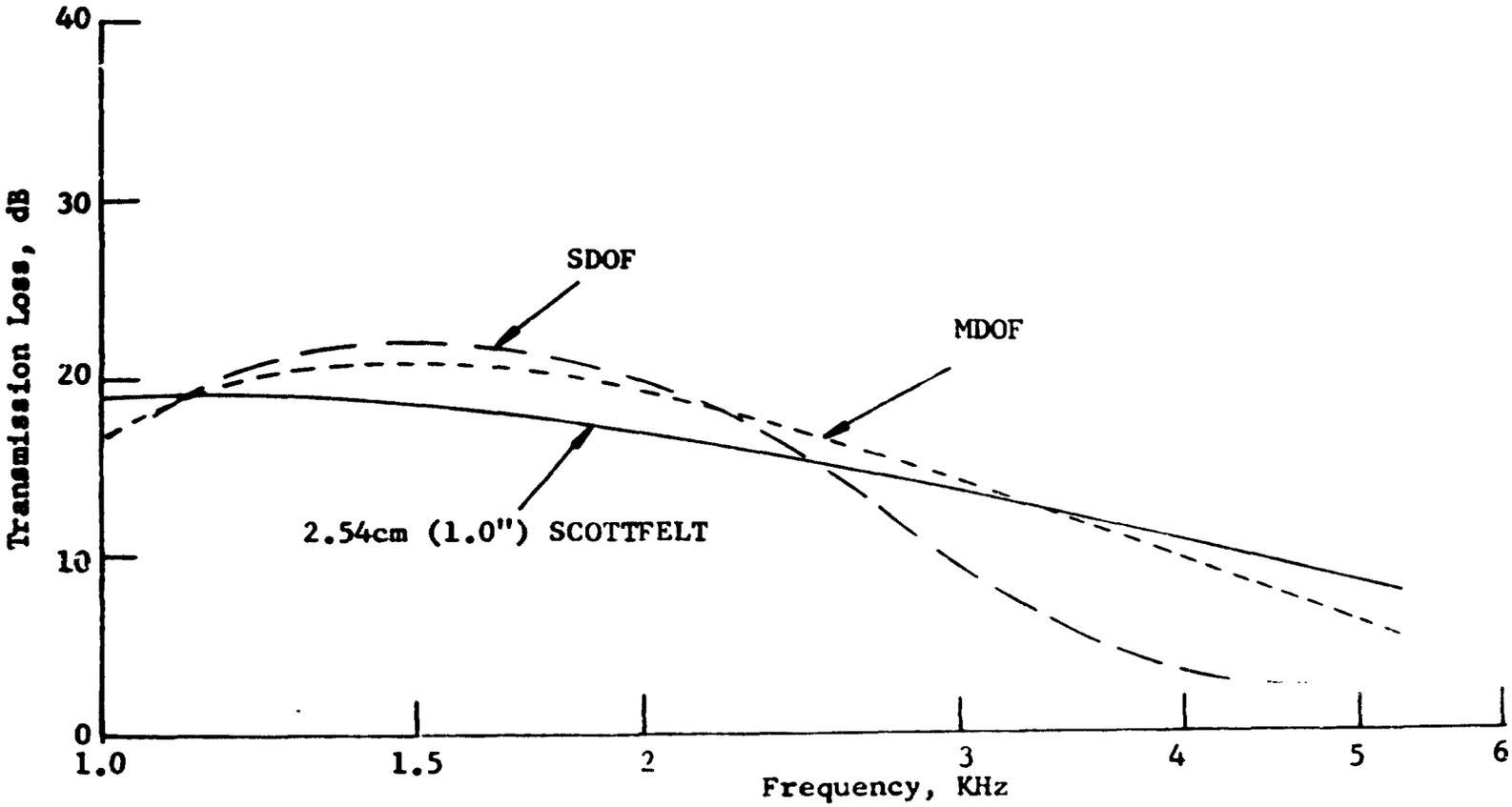

Figure 1. Generalized Comparison of Single- and Multiple-Degree-of-Freedom Panels with SCOTTFELT in the 4.45 cm (17.5") Duct, Mn = 0.4.

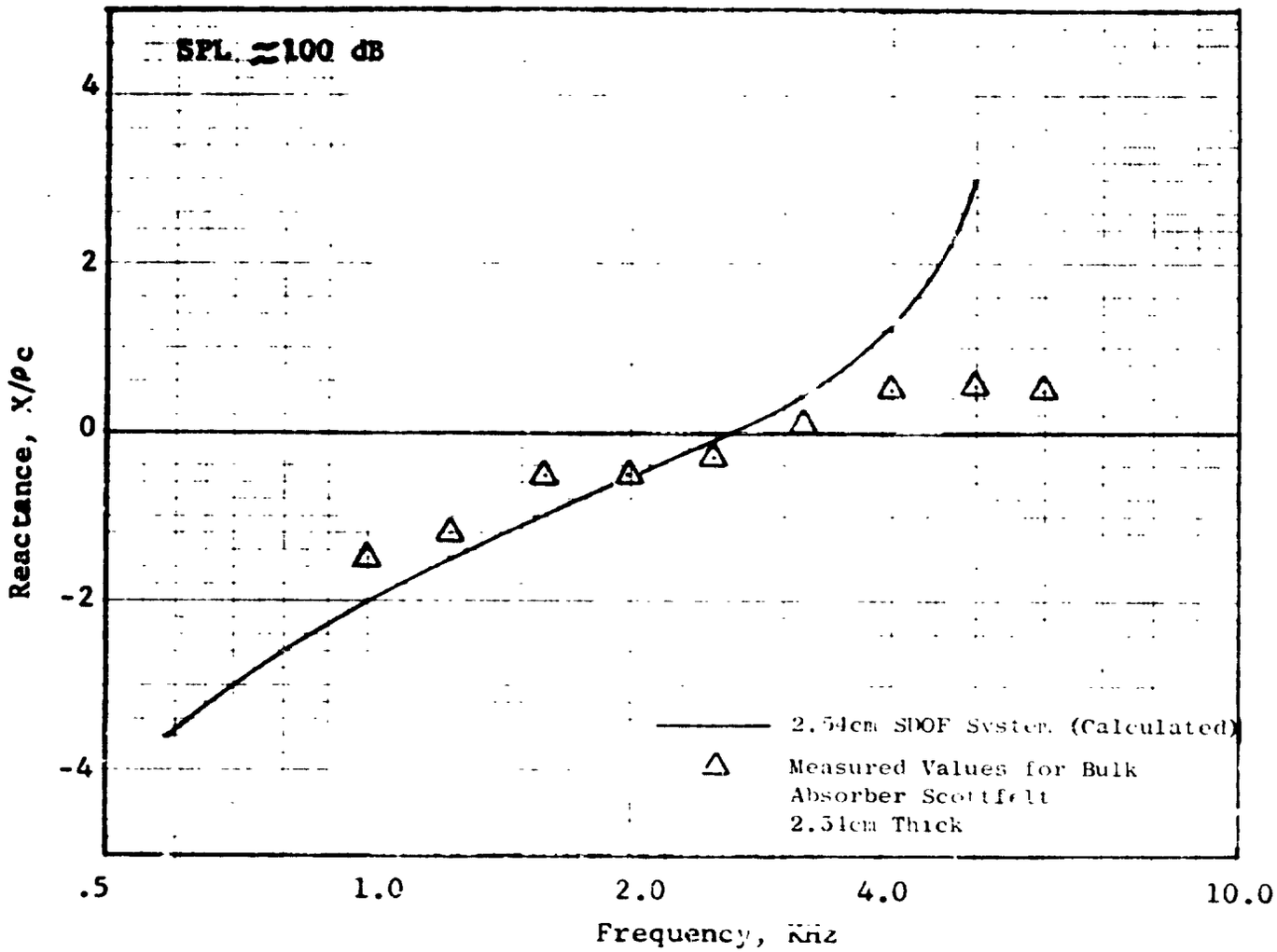

Figure 2. Acoustic Reactance for SDOF Vs. Bulk Absorber.

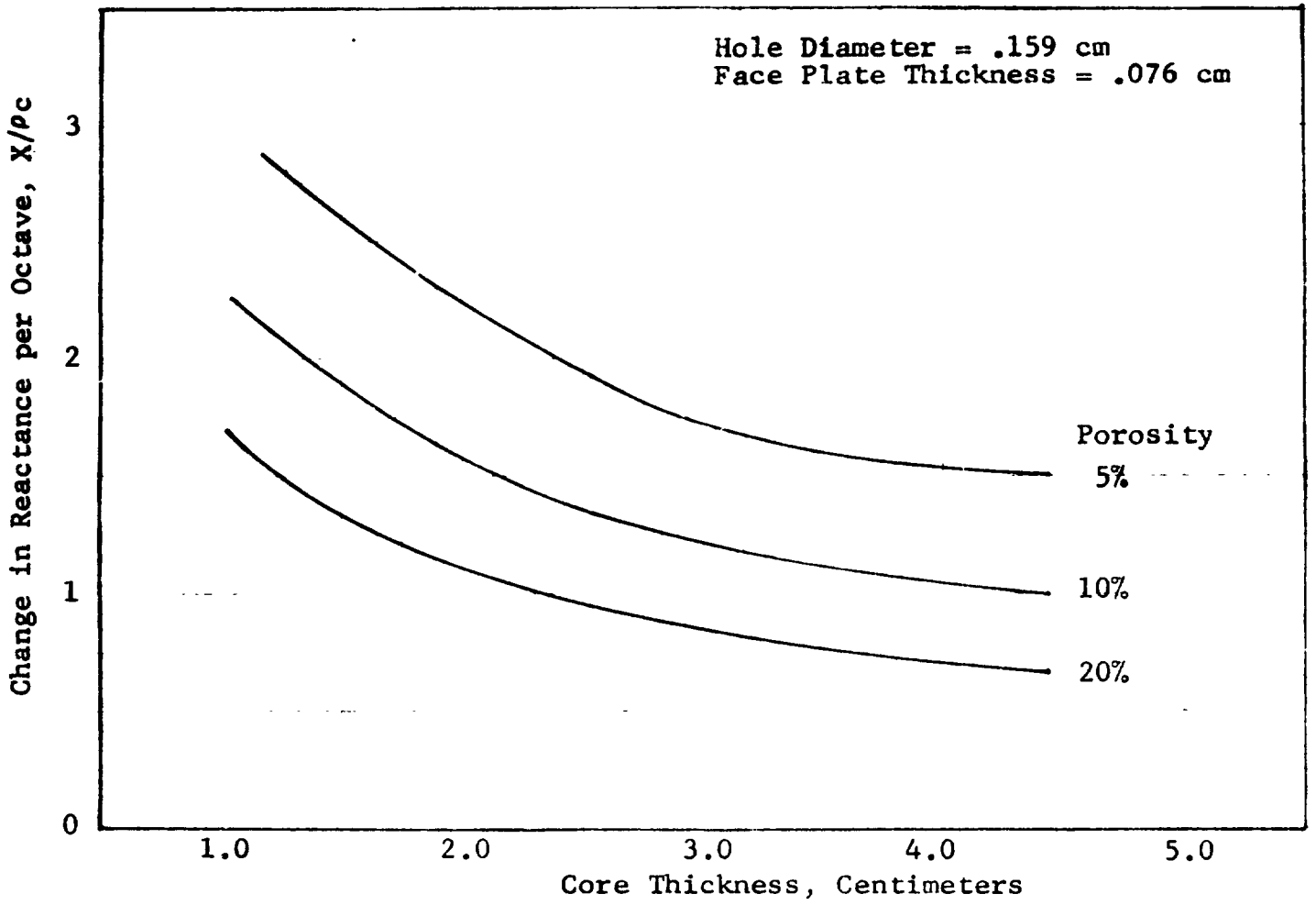

Figure 3. Change in Acoustic Reactance Versus Core Thickness for Different Porosities.

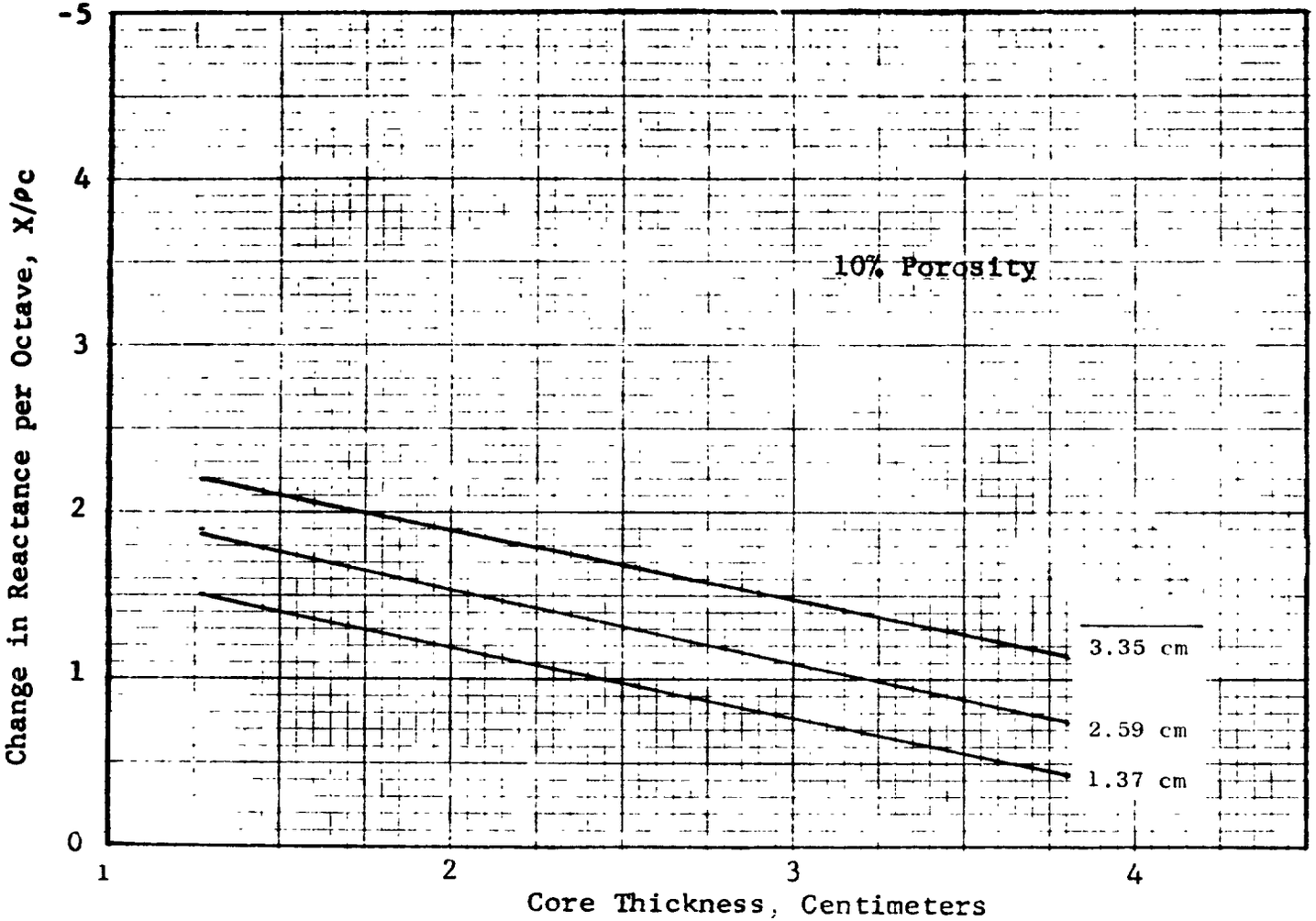

Figure 4. Change in Reactance Vs. Core Thickness for Various Combinations of Face Plate Thickness and Hole Diameters.

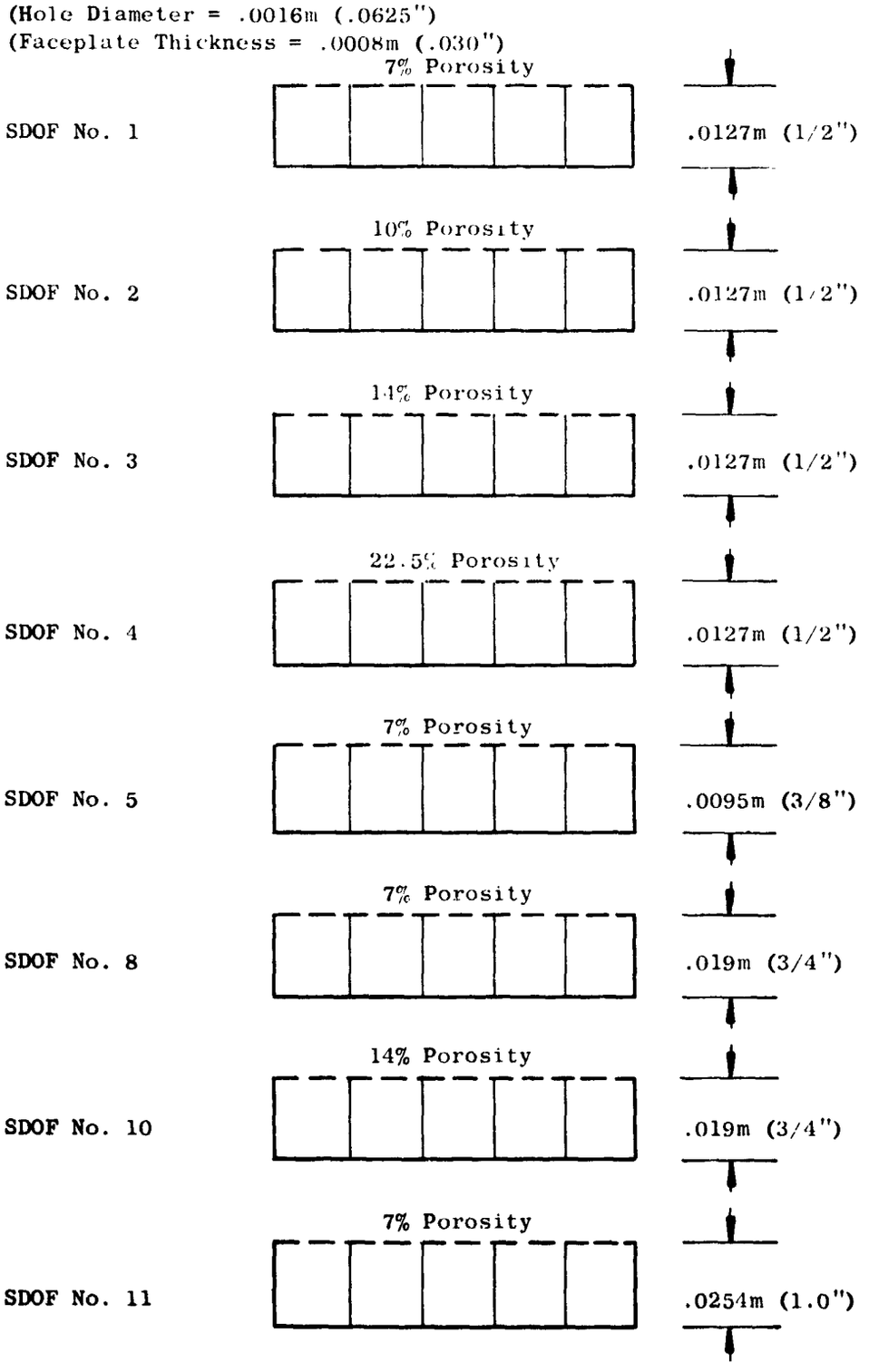

Figure 5. High Temperature Test Panels, Single-Degree-of-Freedom Resonators, .0127m (1/2") Square Cell Honeycomb Core.

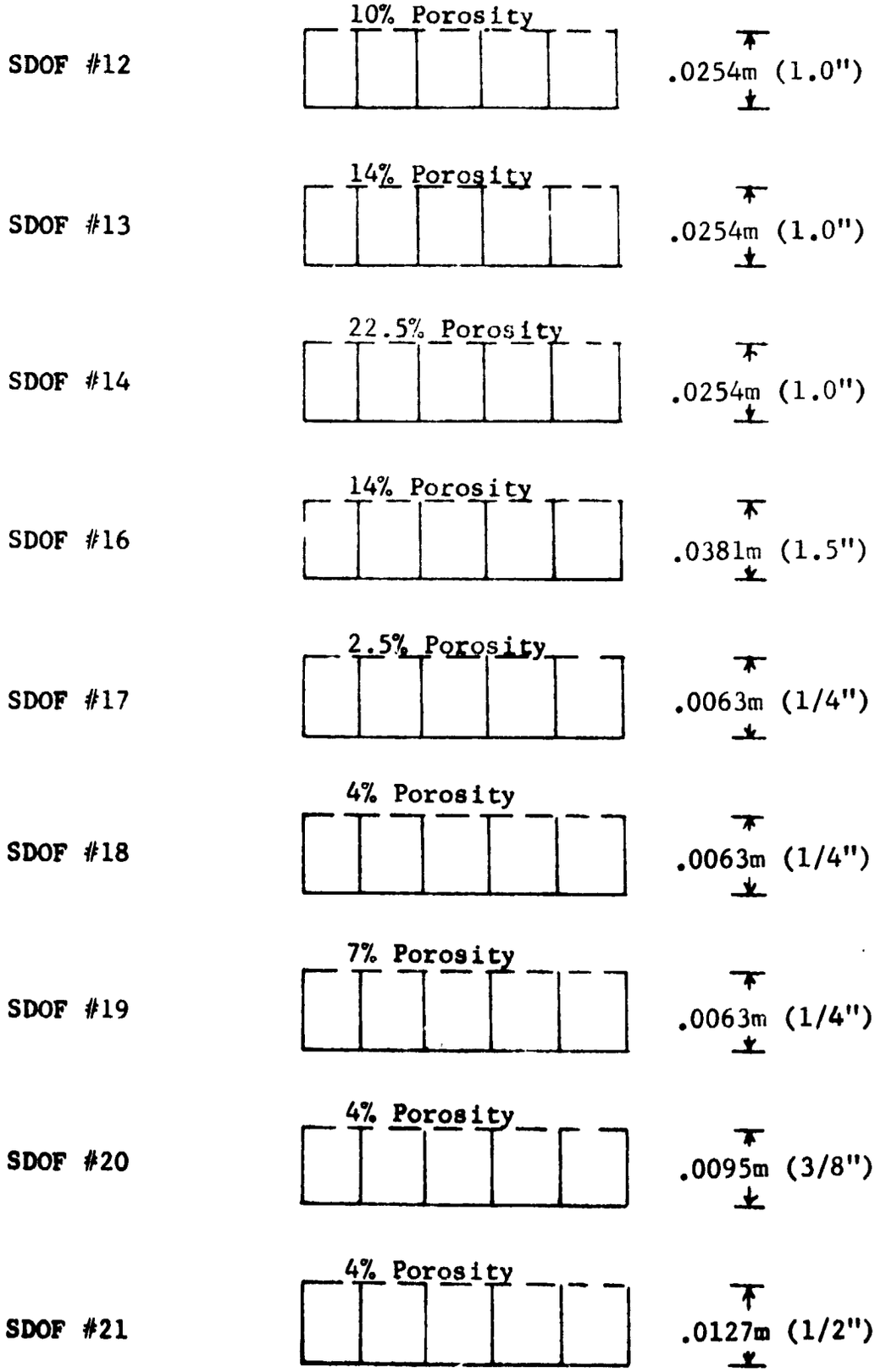

Figure 6. High Temperature Test Panels.

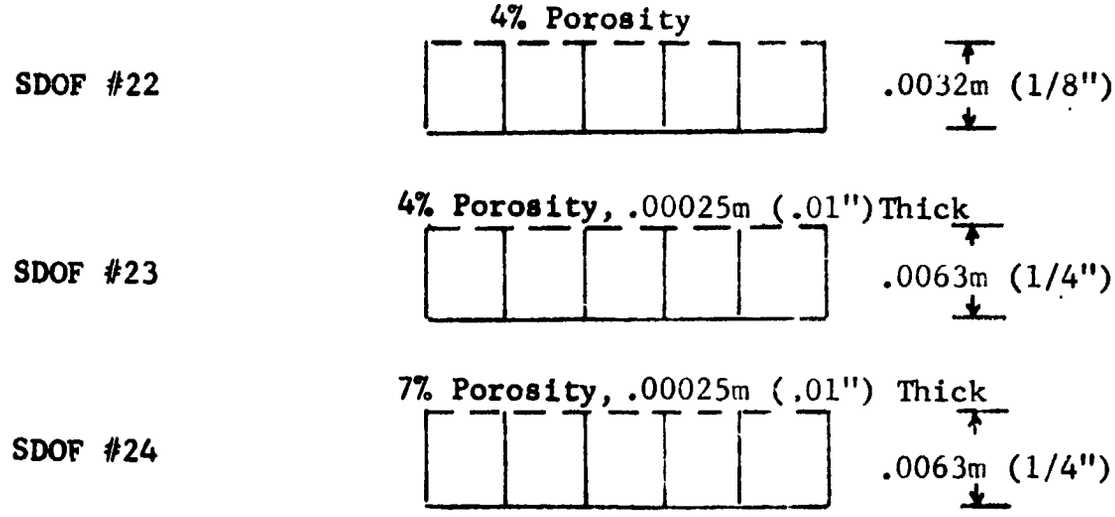

Figure 7. High Temperature Test Panels.

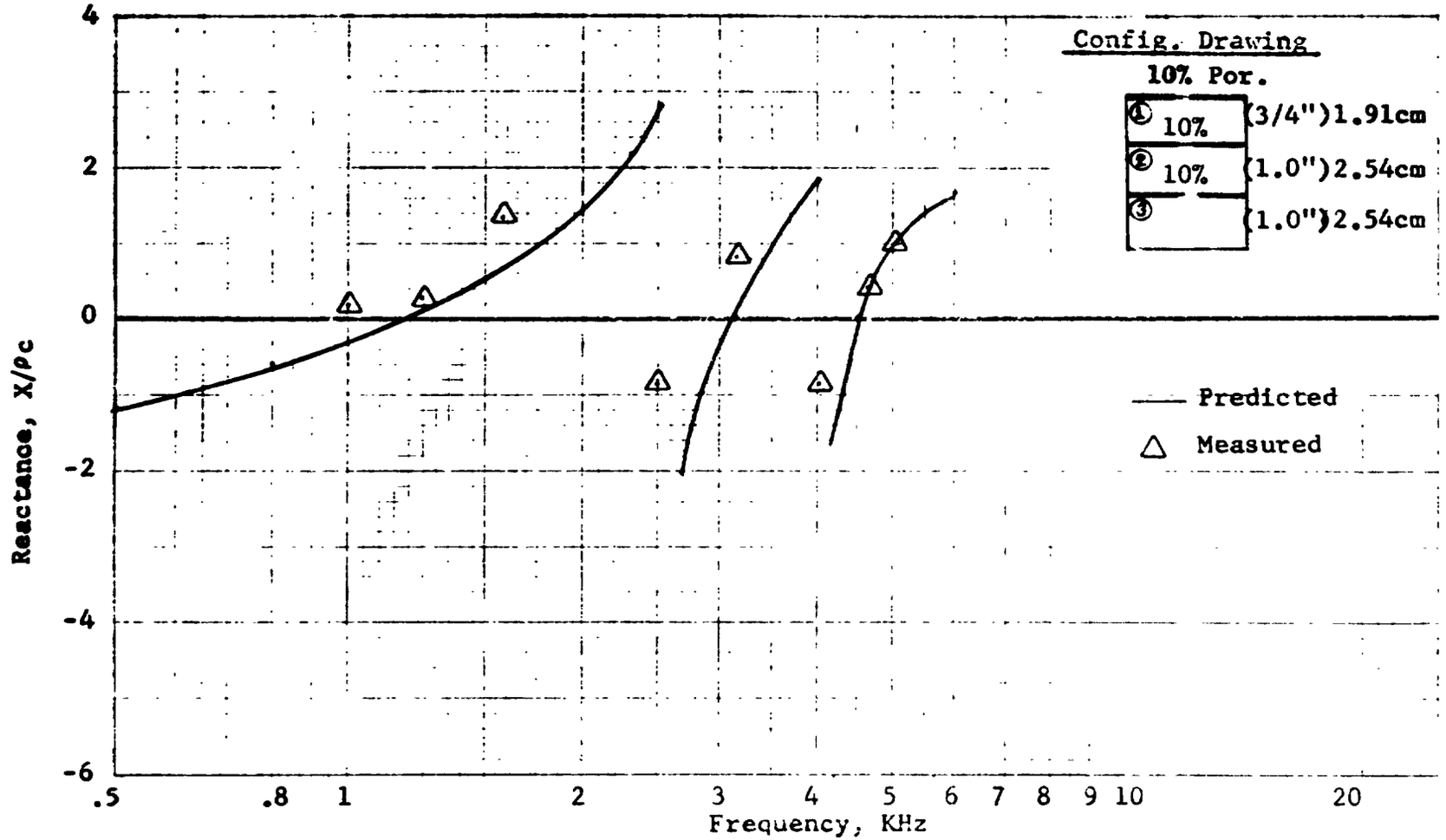

Figure 8. Reactance of Three-Degree-of-Freedom System with Low Damping.

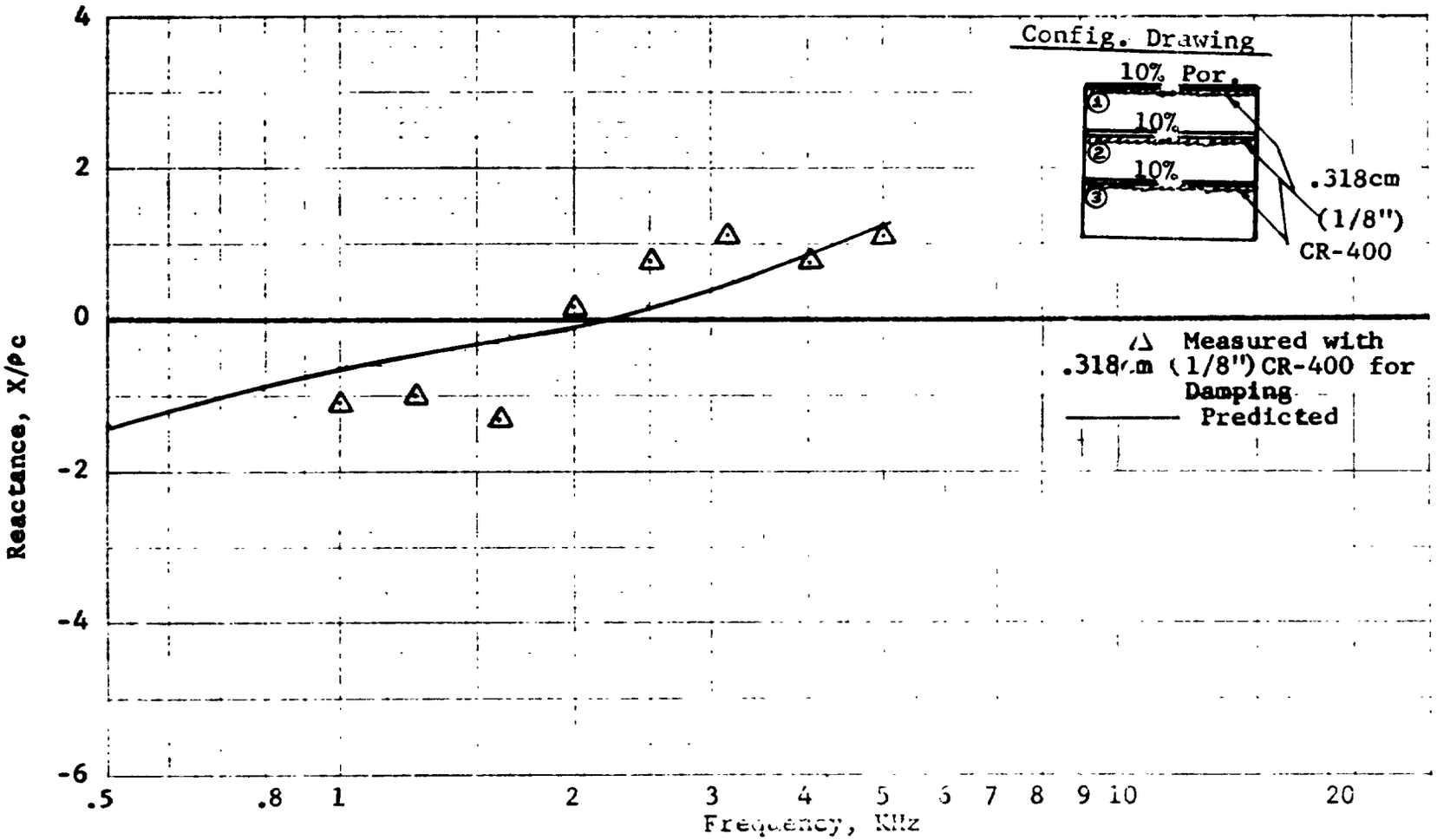

Figure 9. Reactance of Three-Degree-of-Freedom System with Damping.

(Hole Diameter .0016m (.0625")
(Faceplate Thickness .0008m (.030")
(Core Wall Thickness .0005m (.020")

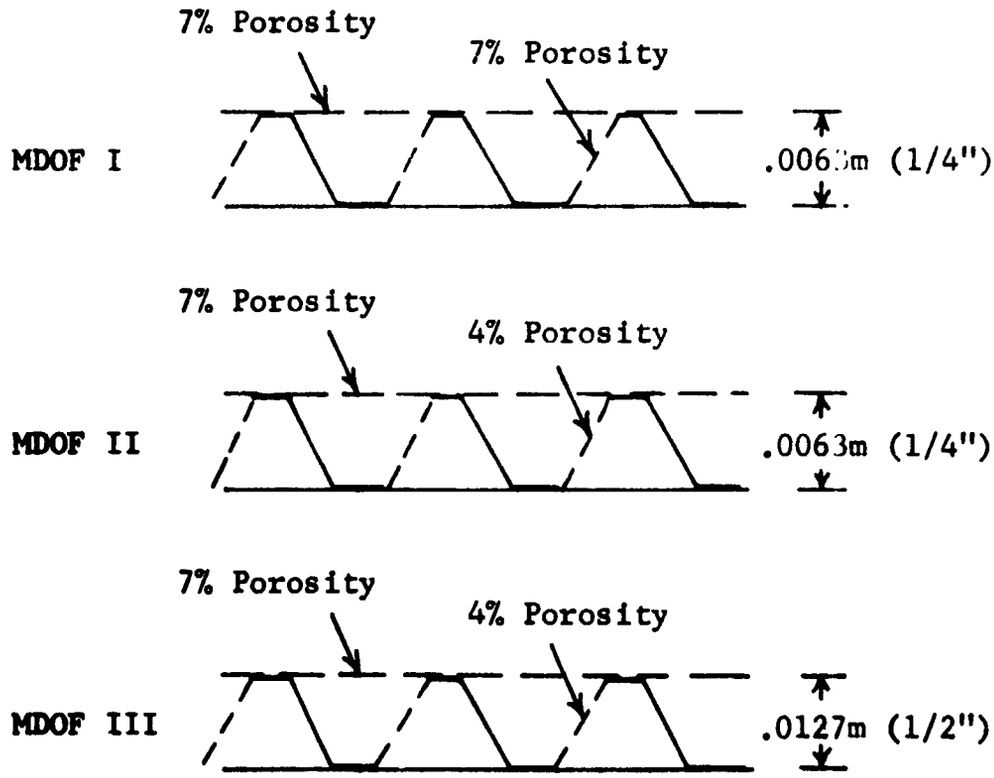

Figure 10. High Temperature Test Panels Multiple Degree of Freedom Resonators.

(Hole Diameter .0016m (.0625")
(Faceplate & Core Plate Thickness .008m (.03")

DOUBLE SANDWICH II

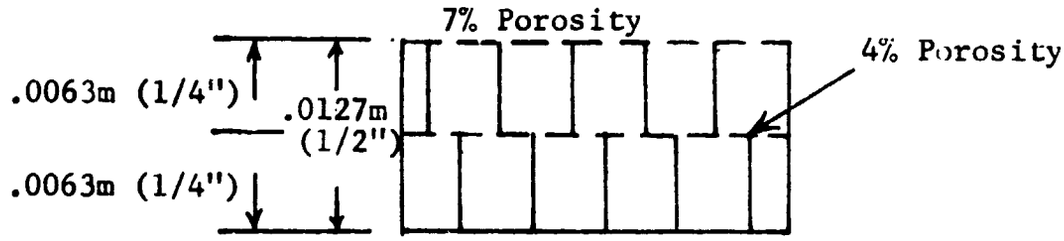

DOUBLE SANDWICH III

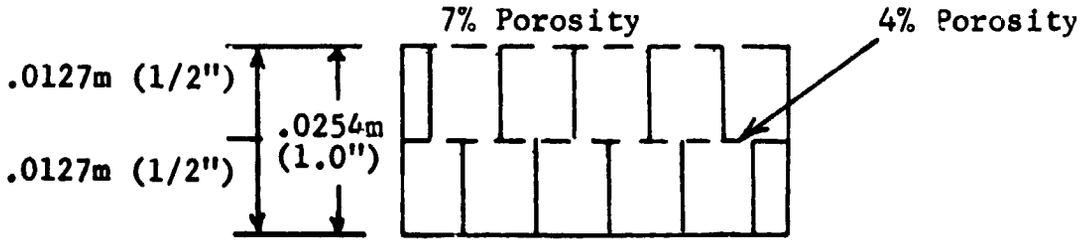

Figure 11. High Temperature Test Panels Double Layer Honeycomb Resonators.

(Molten Homogenous Glass)

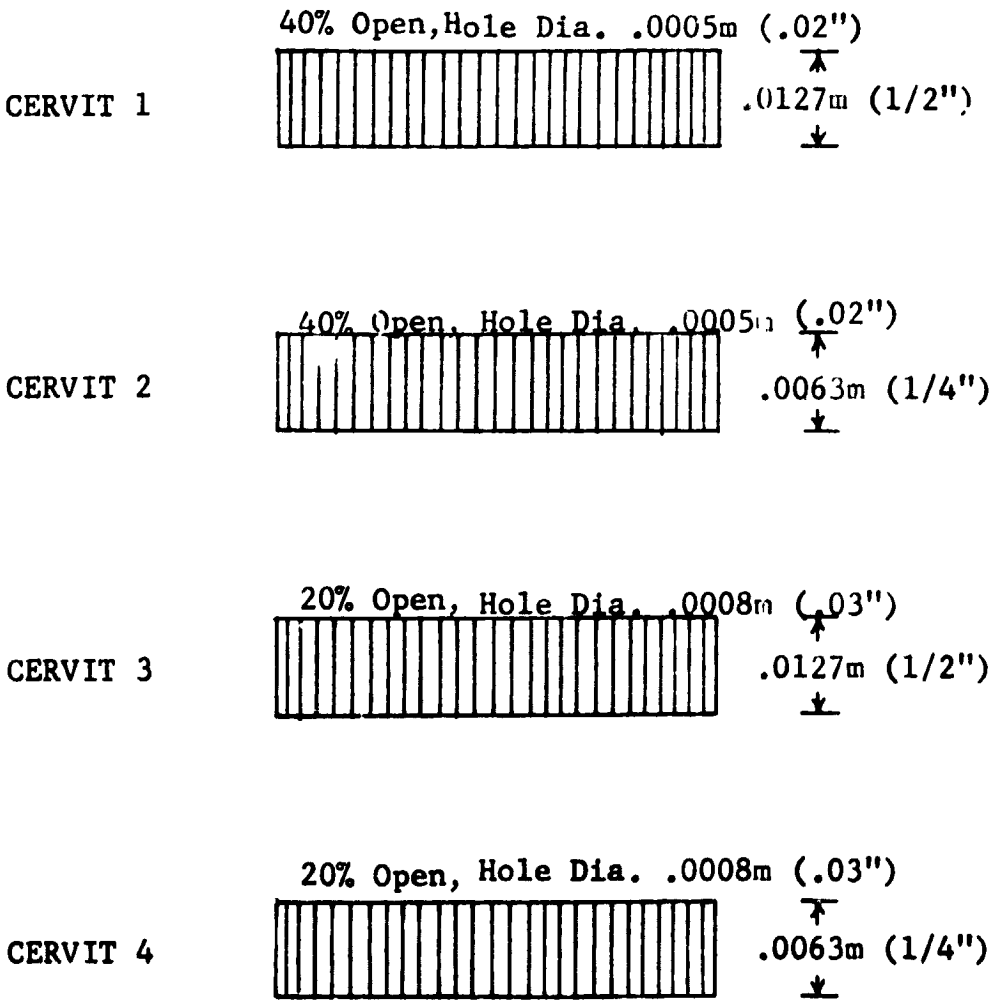

Figure 12. High Temperature Test Panels Non-Metallic Configurations Cervit 126.

Figure 13. High Temperature Cerafelt Test Panel.

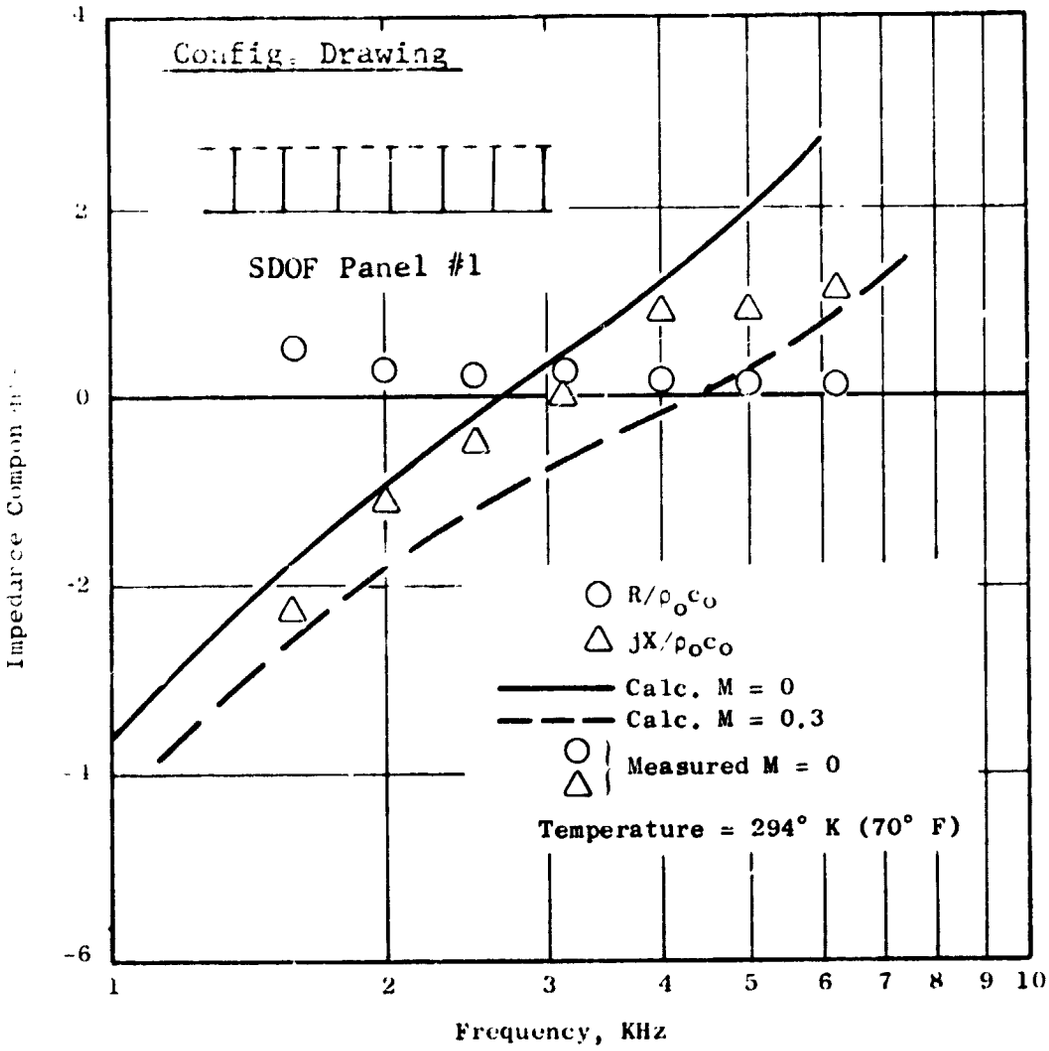

Figure 14. Impedance Components of SDOF Panel No. 1 at Ambient Conditions.

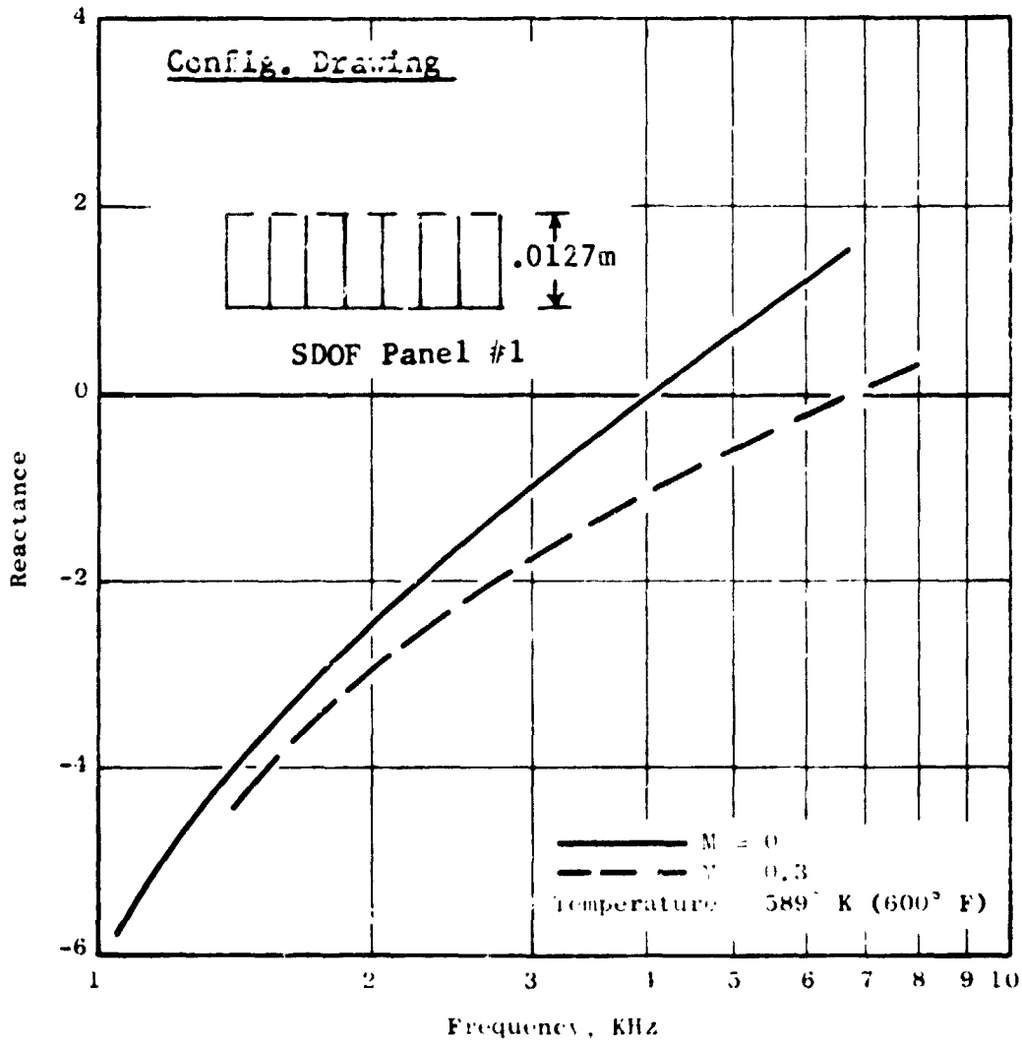

Figure 15. Calculated Reactance of SDOF Panel No. 1 at Turbine Temperatures.

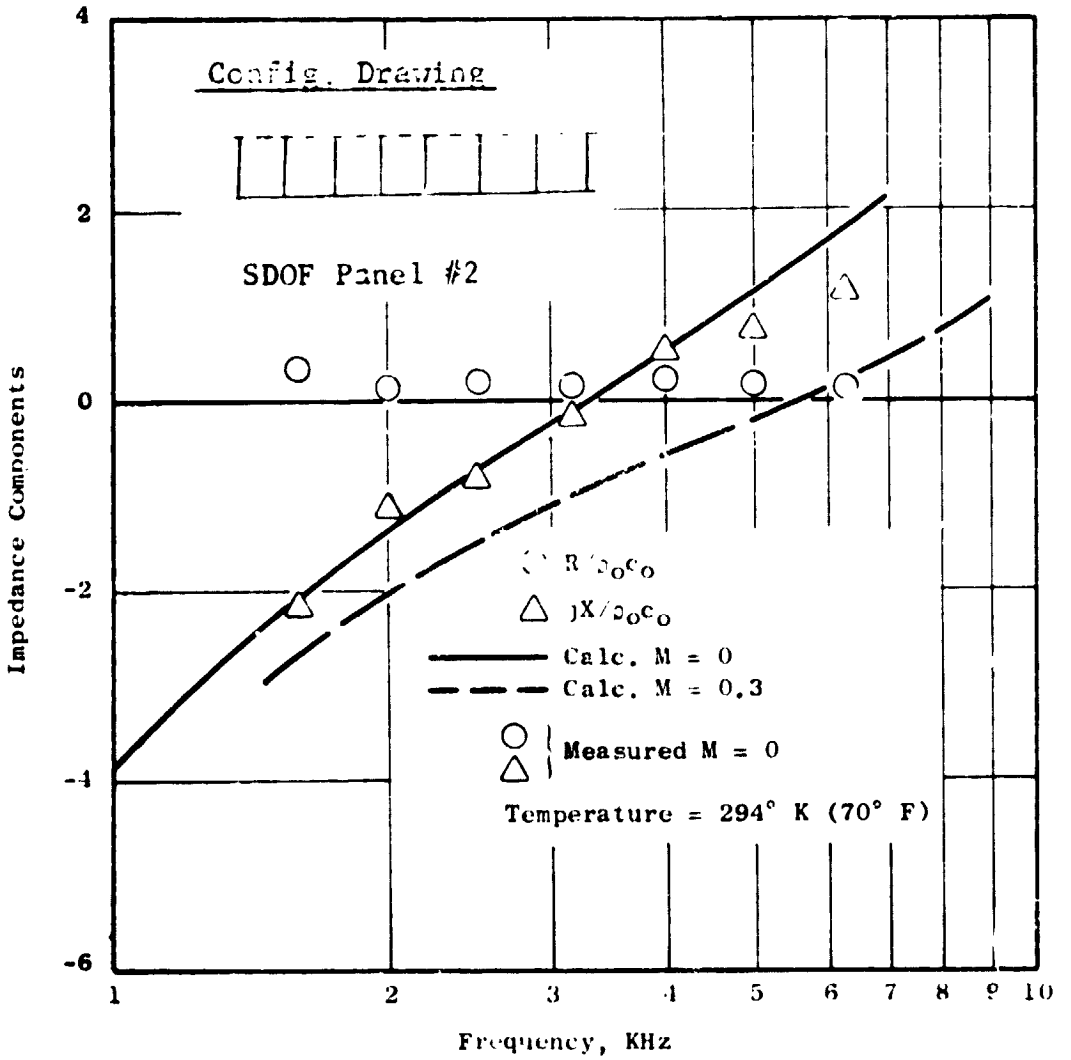

Figure 16. Impedance Components of SDOF Panel No. 2 at Ambient Conditions.

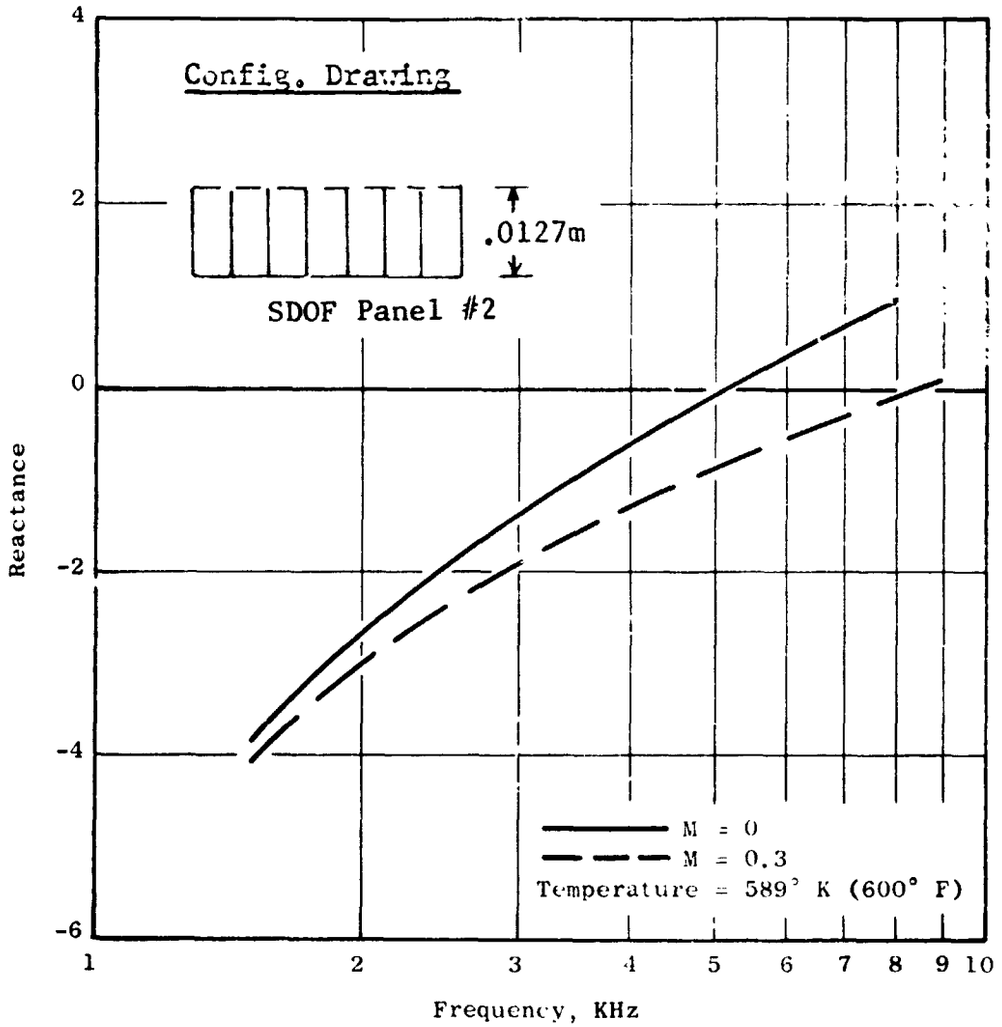

Figure 17. Calculated Reactance of SDOF Panel No. 2 at Turbine Temperatures.

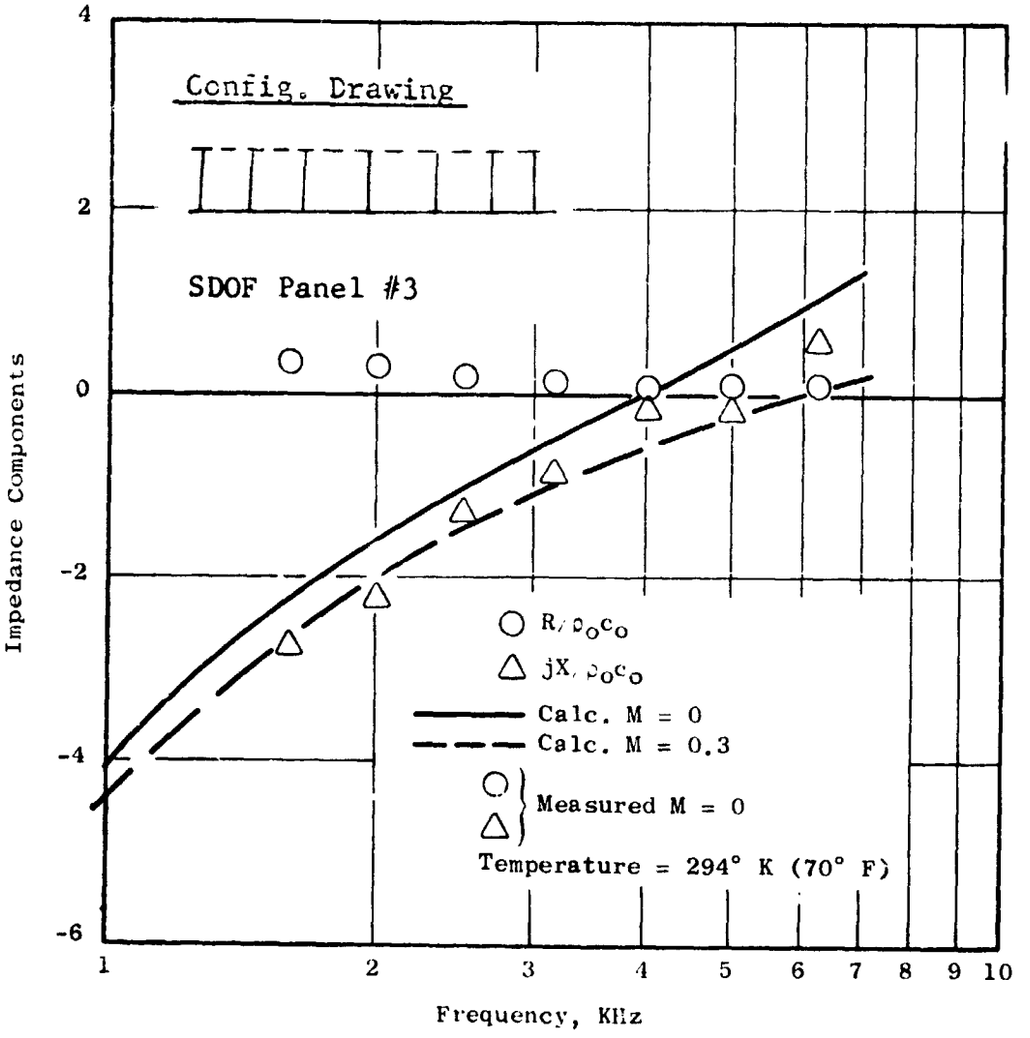

Figure 18. Impedance Components of SDOF Panel No. 3 at Ambient Conditions.

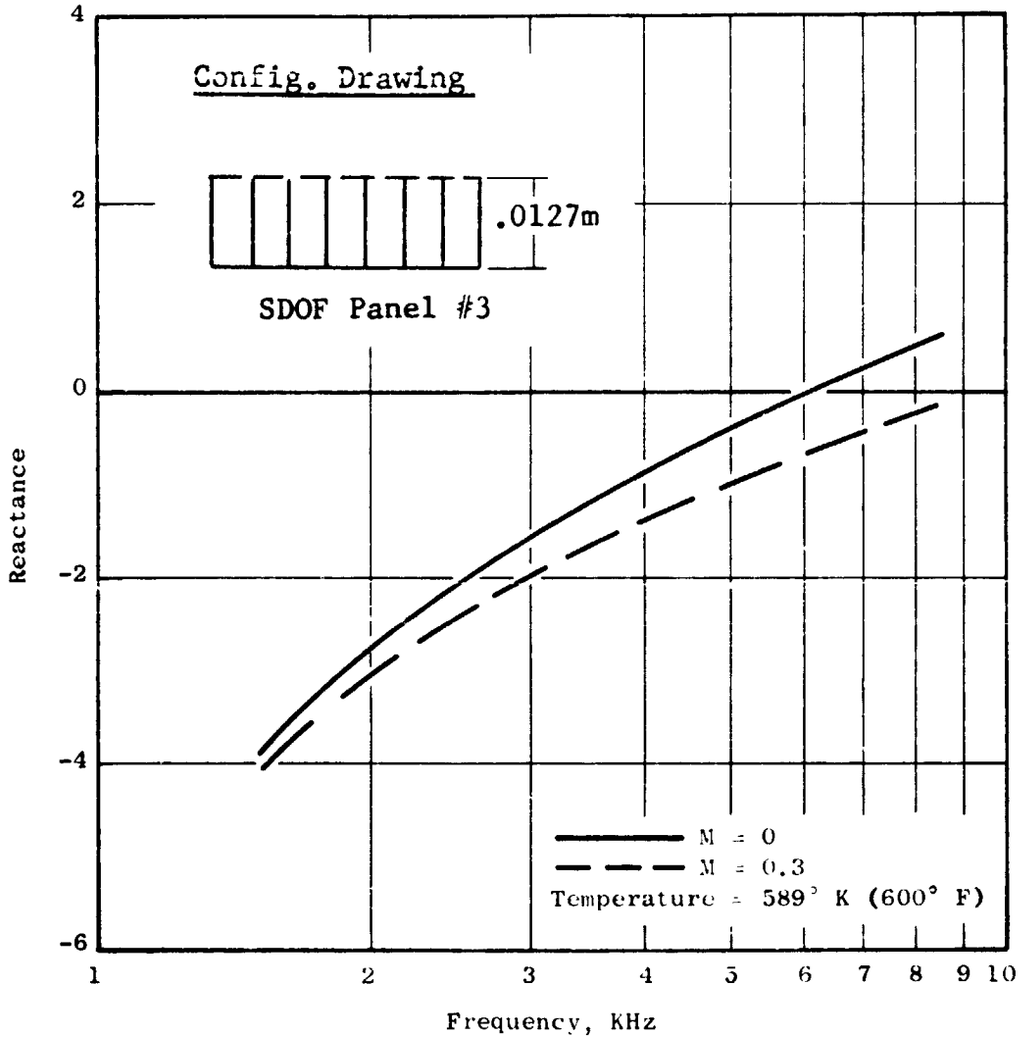

Figure 19. Calculated Reactance of SDOF Panel No. 3 at Turbine Temperatures.

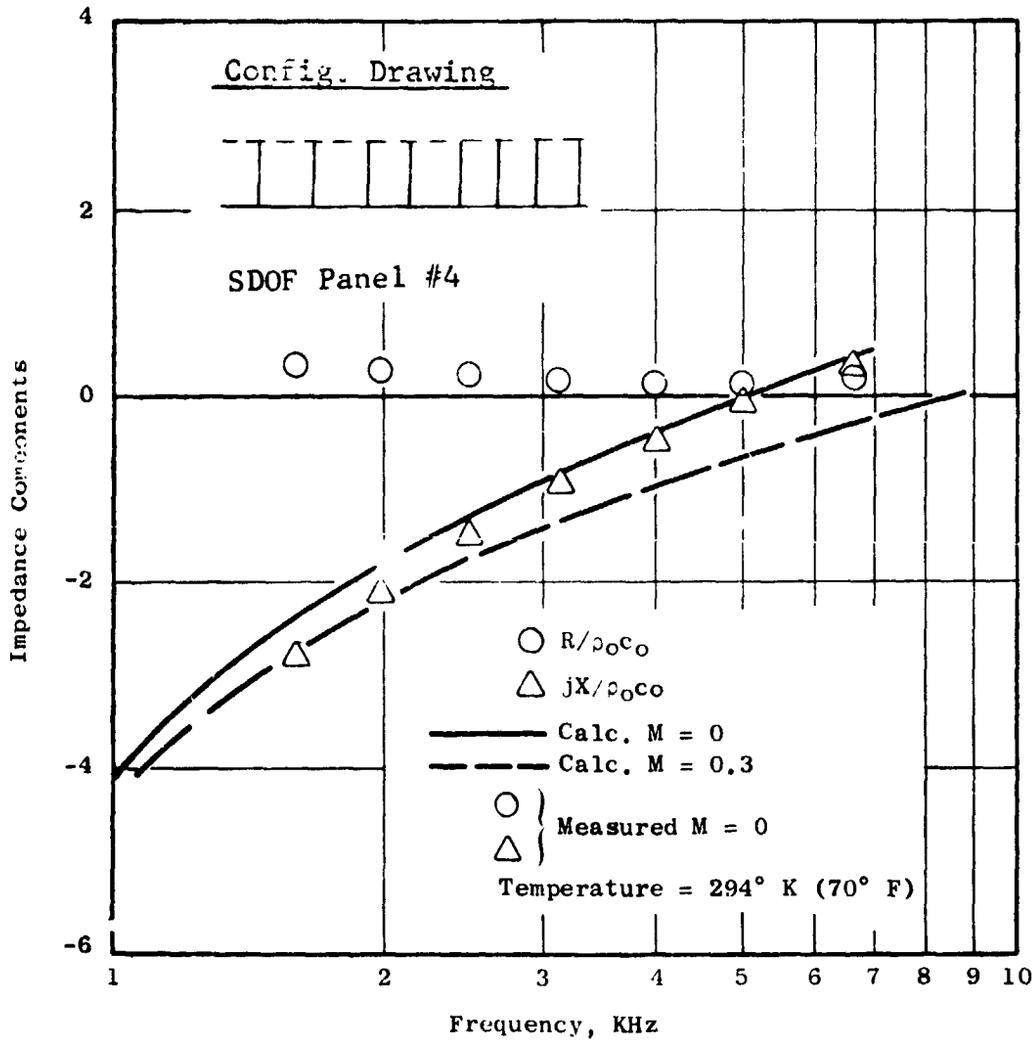

Figure 20. Impedance Components of SDOF Panel No. 4 at Ambient Conditions.

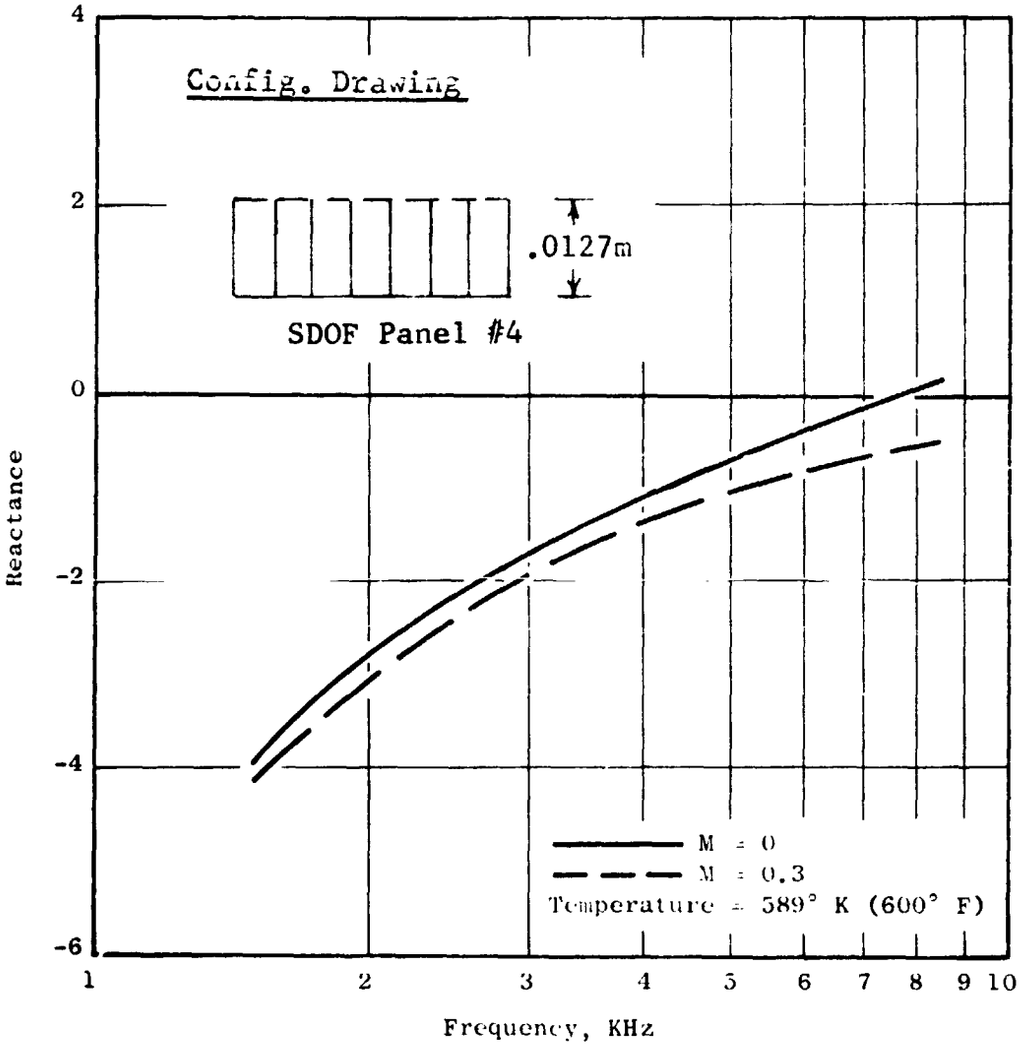

Figure 21. Calculated Reactance of SDOF Panel No. 4 at Turbine Temperatures.

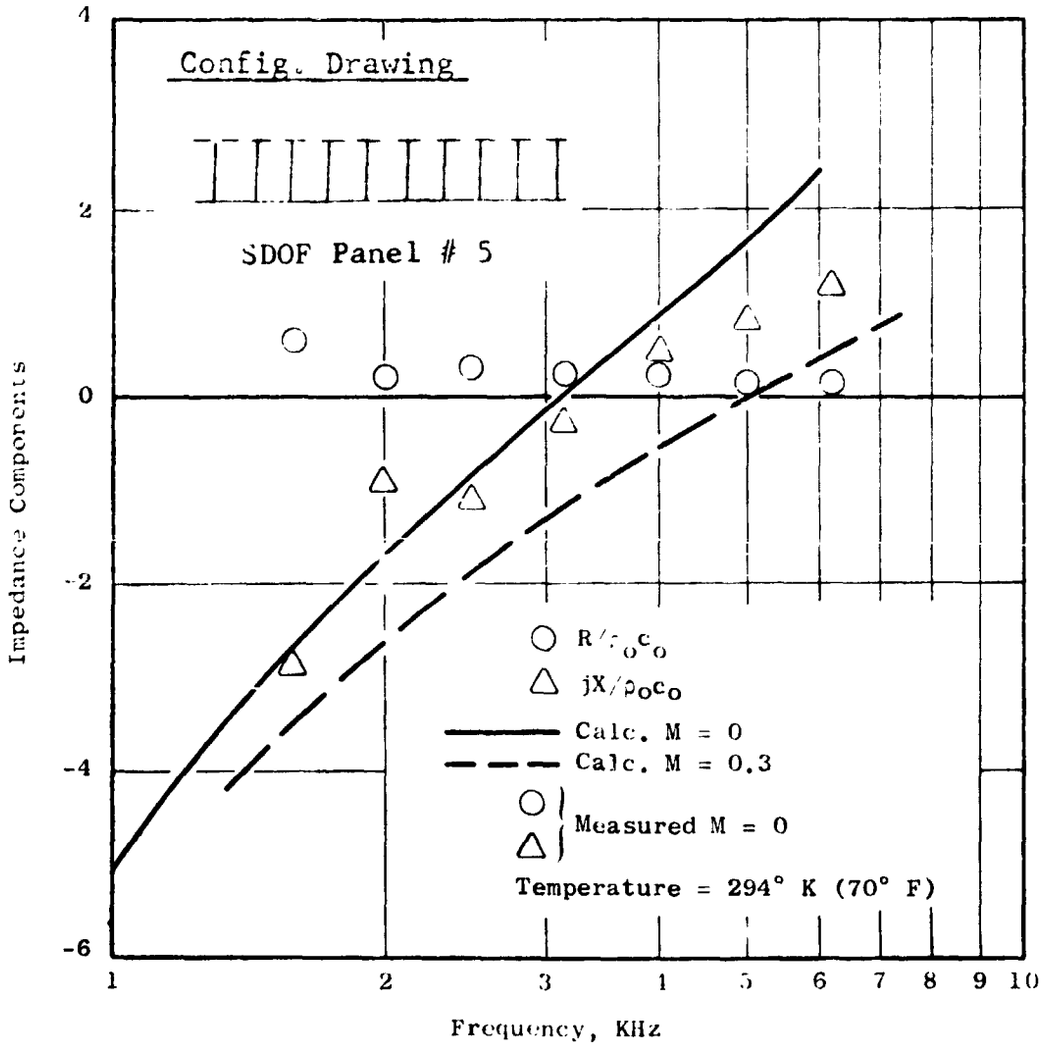

Figure 22. Impedance Components of SDOF Panel No. 5 at Ambient Conditions.

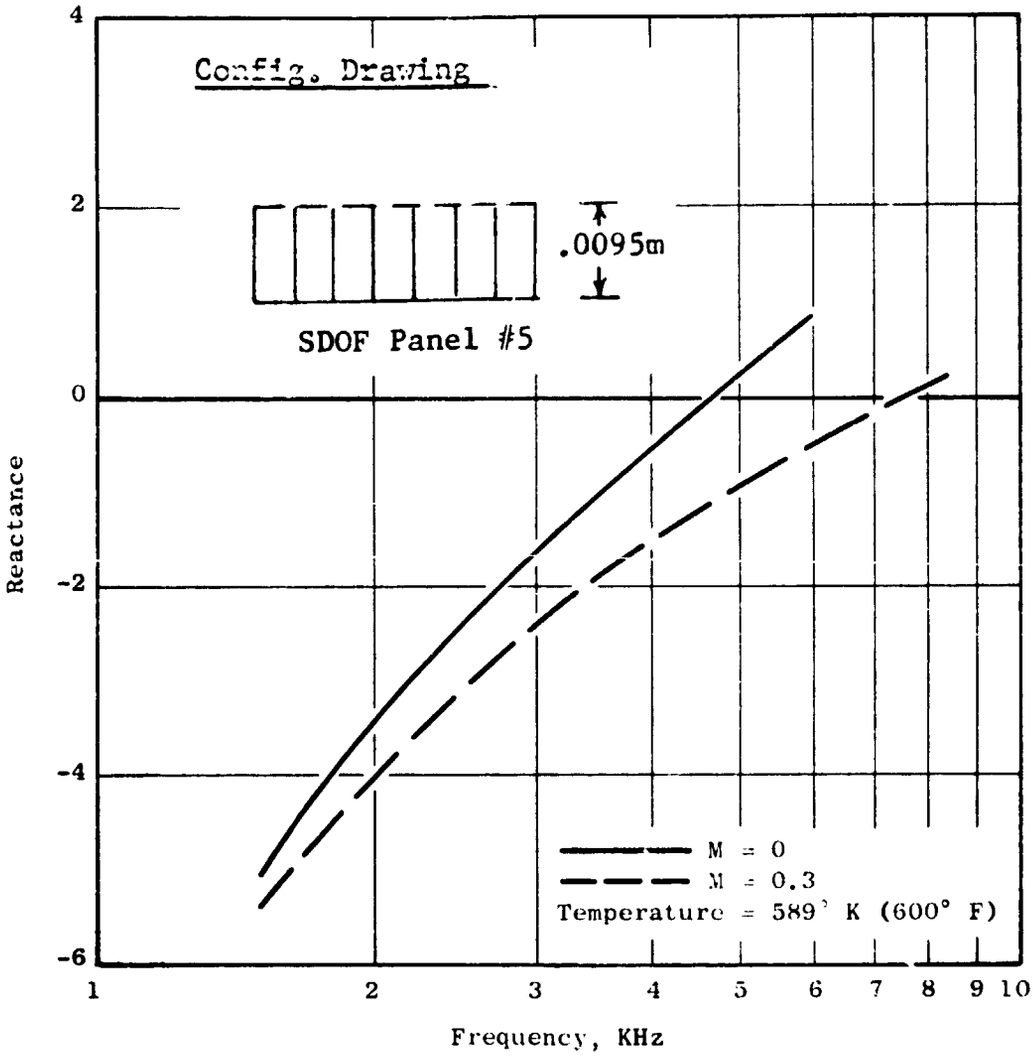

Figure 23. Calculated Reactance of SDOF Panel No. 5 at Turbine Temperatures.

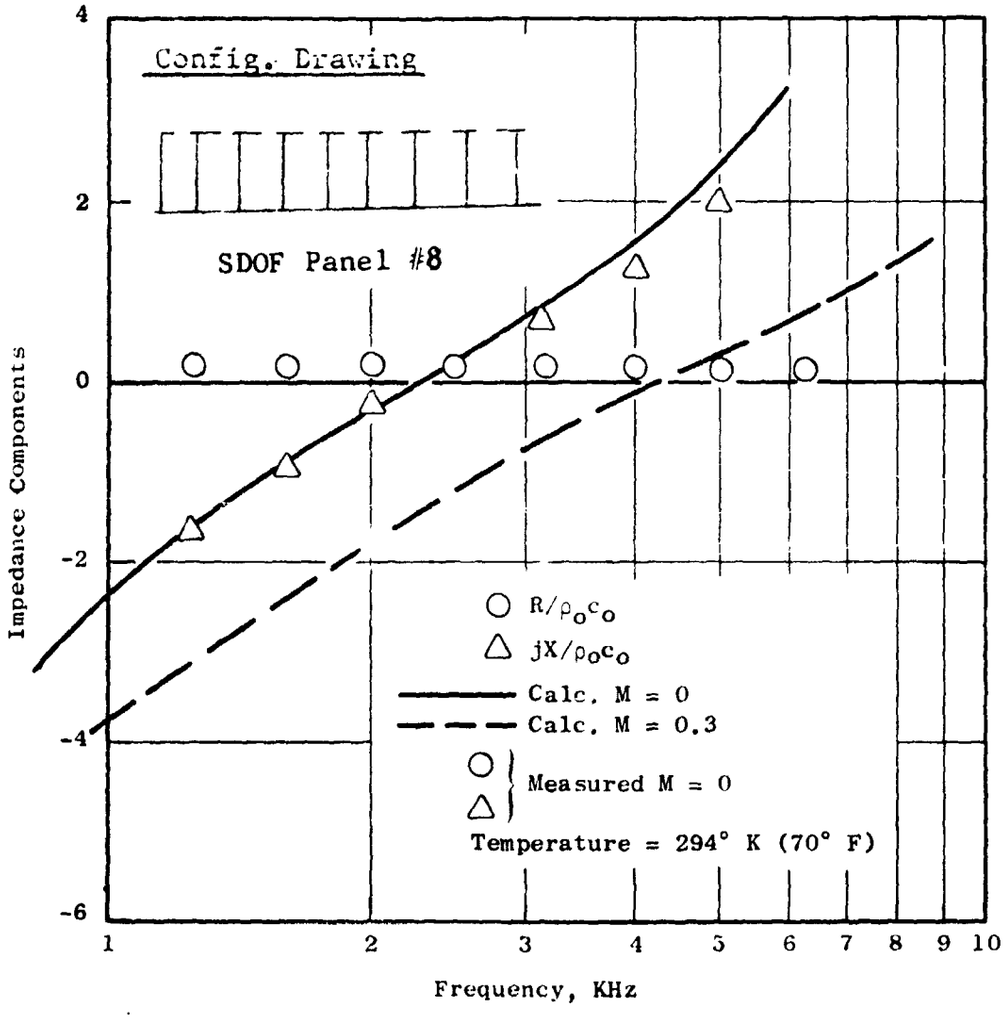

Figure 24. Impedance Components of SDOF Panel No. 8 at Ambient Conditions.

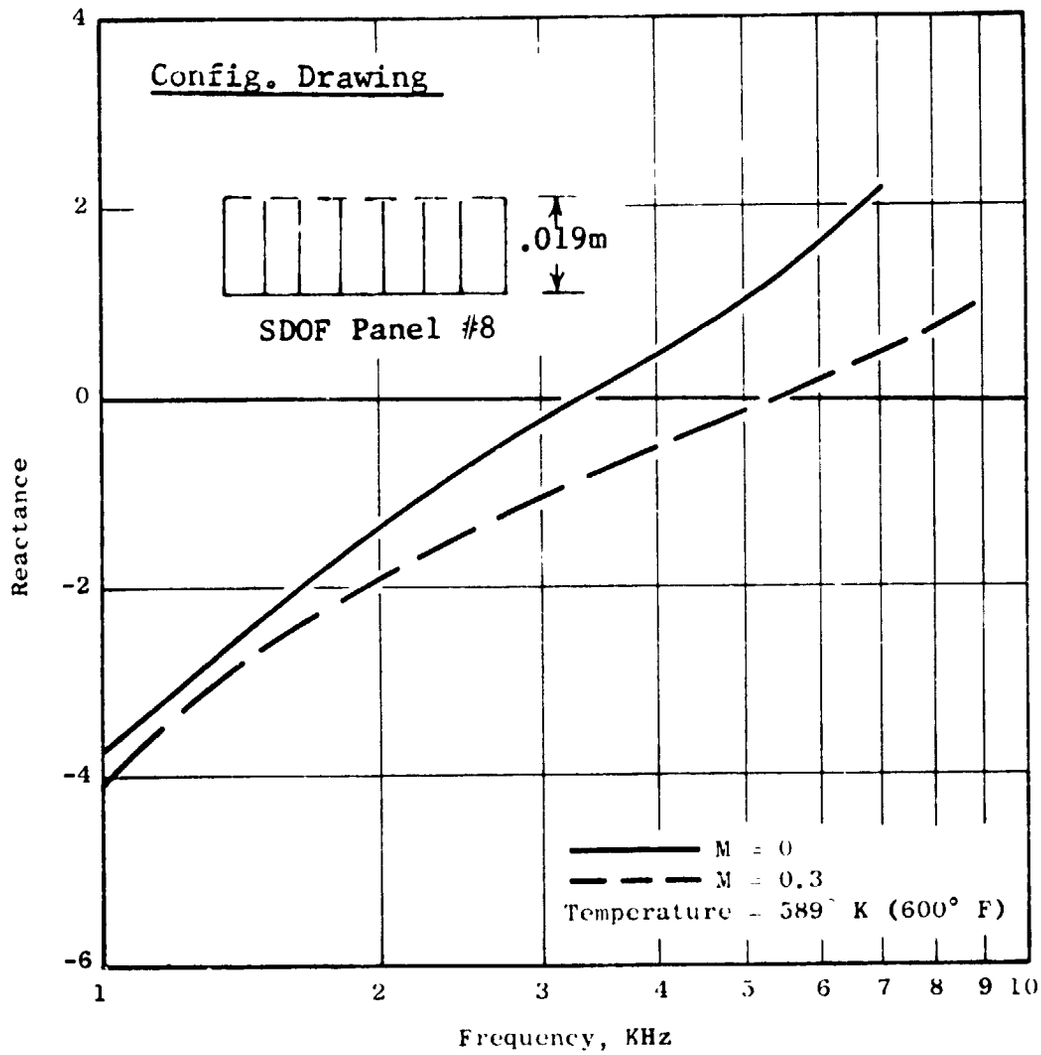

Figure 25. Calculated Reactance of SDOF Panel No. 8 at Turbine Temperatures.

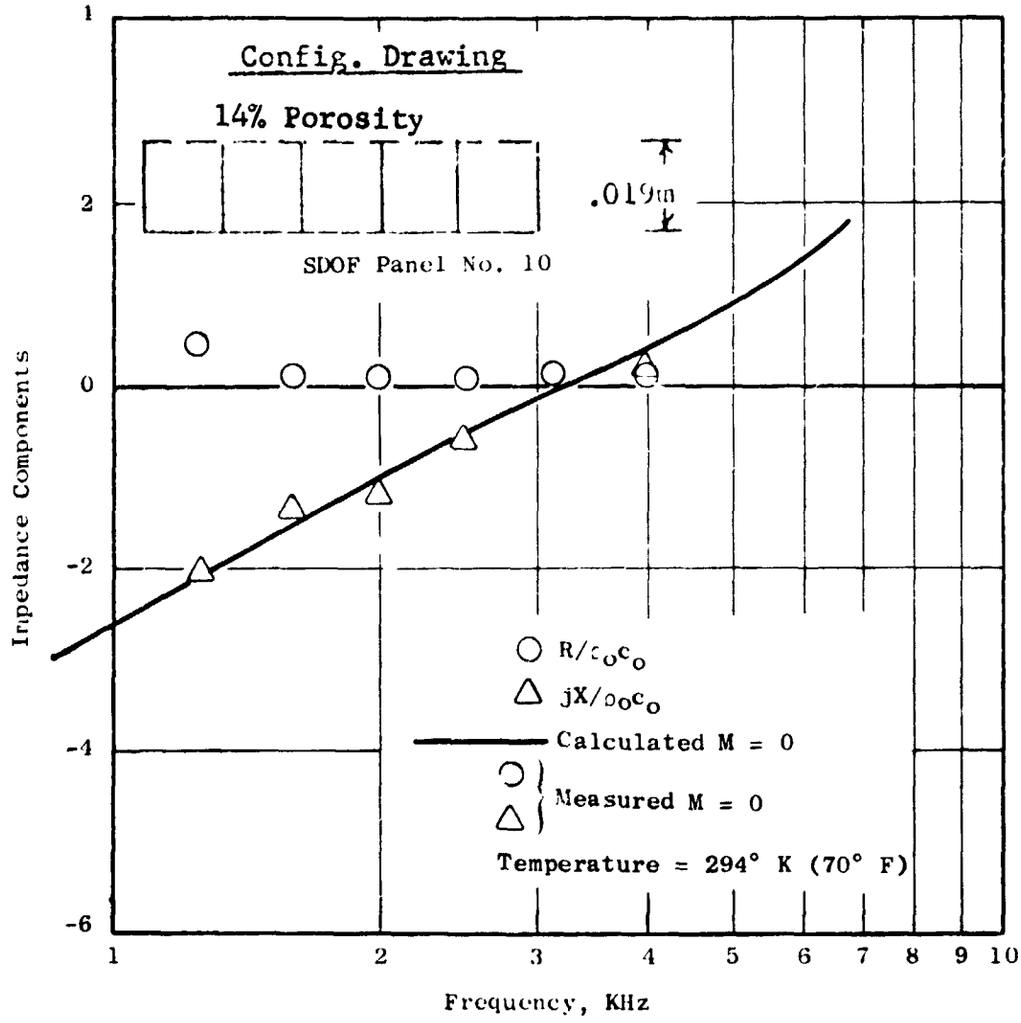

Figure 26. Impedance Components of SDOF Panel No. 10 at Ambient Conditions.

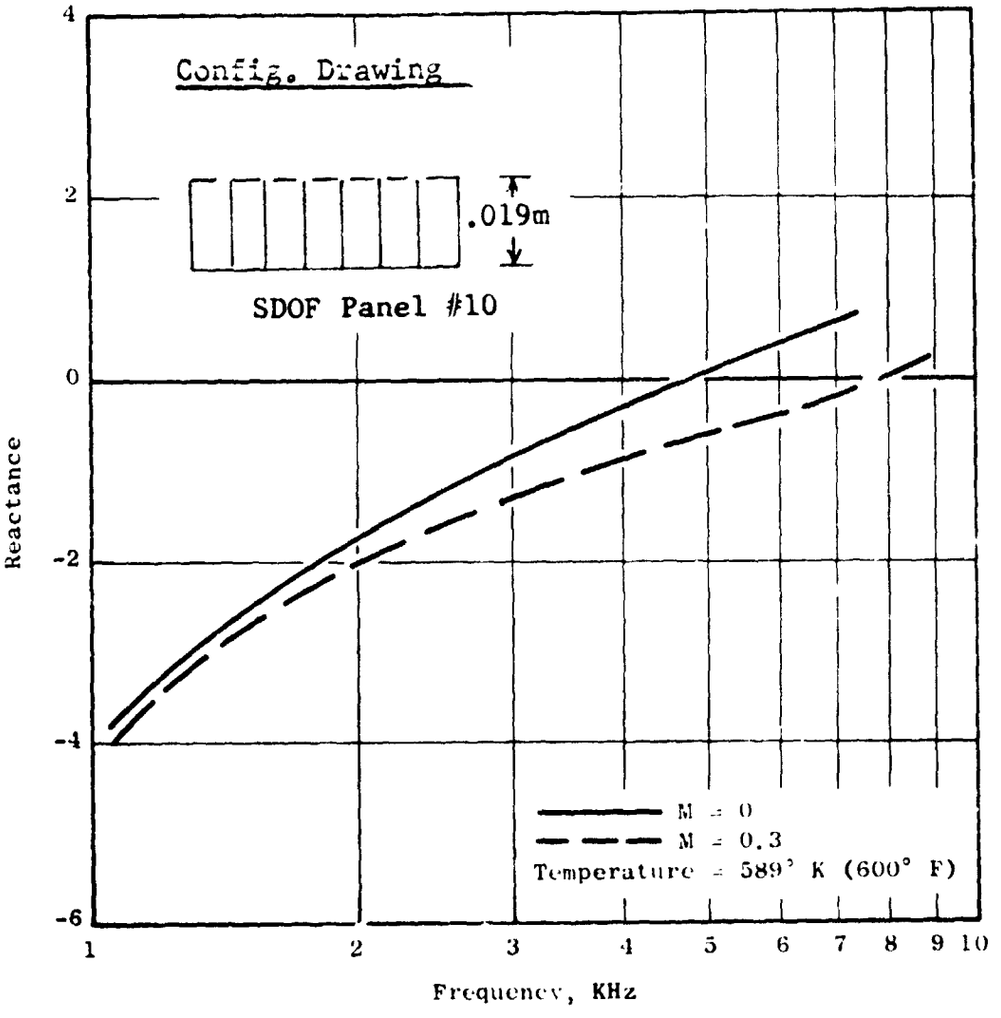

Figure 27. Calculated Reactance of SDOF Panel No. 10 at Turbine Temperatures.

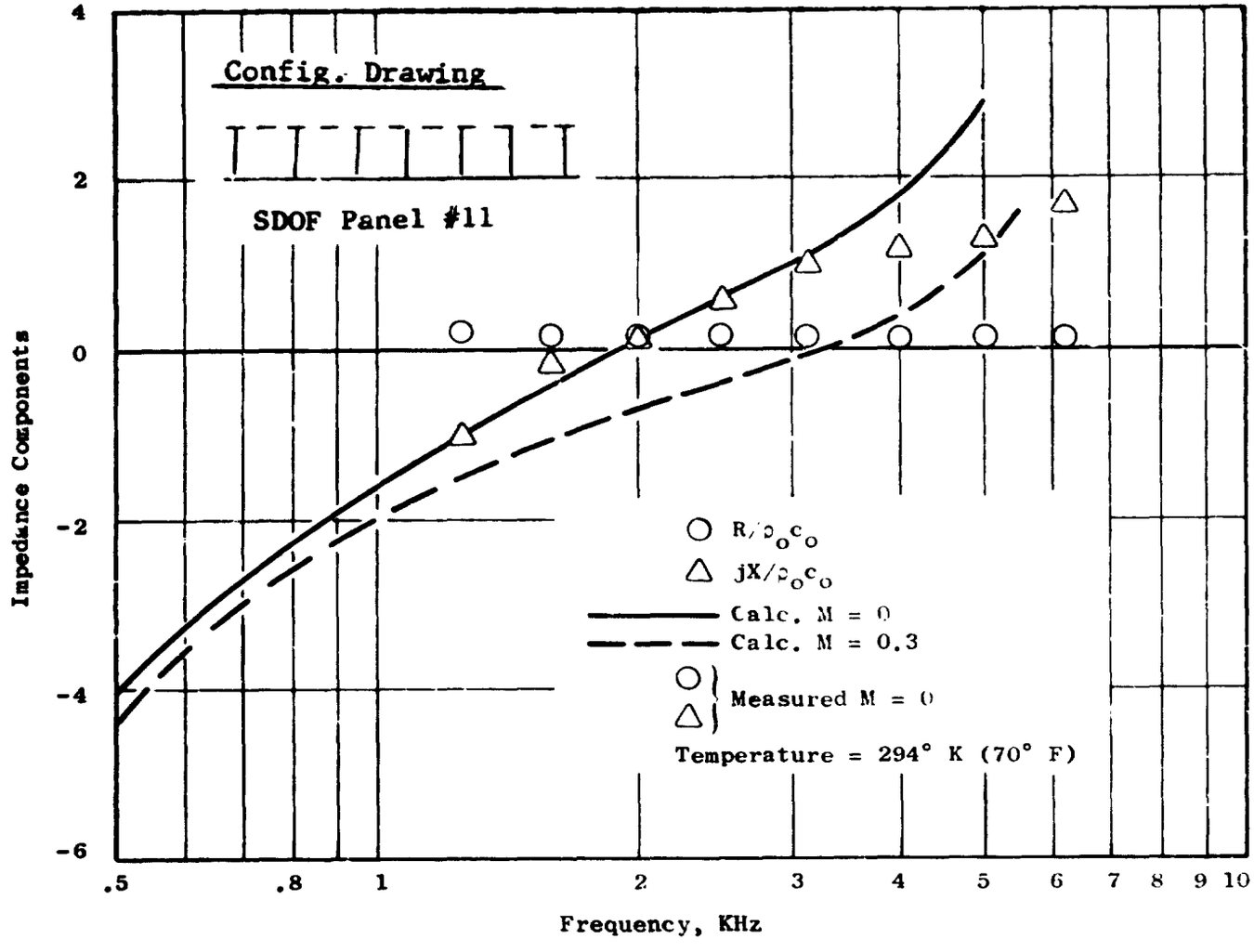

Figure 28. Impedance Components of SDOF Panel No. 11 at Ambient Conditions.

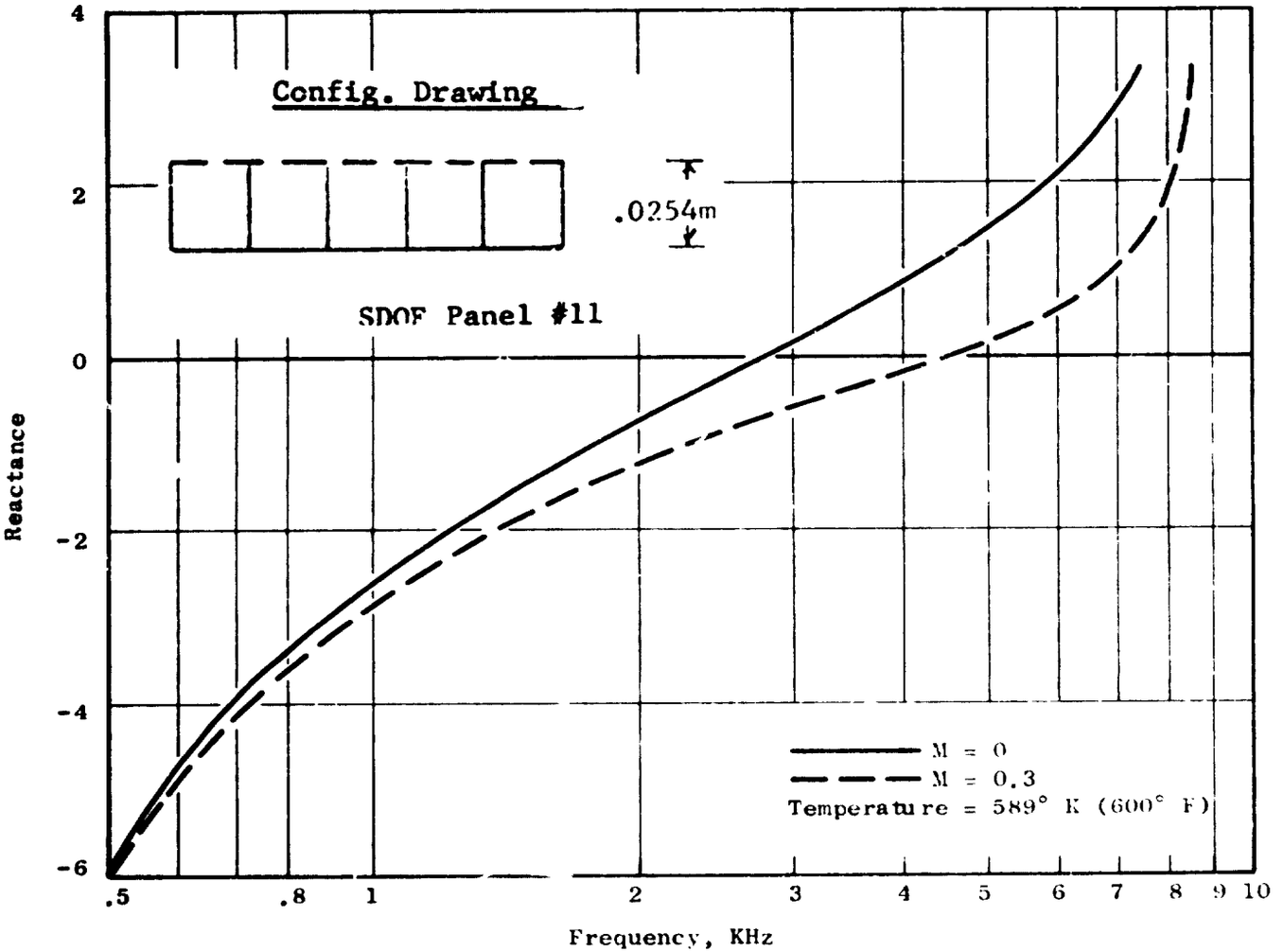

Figure 29. Calculated Reactance of SDOF Panel No. 11 at Turbine Temperatures.

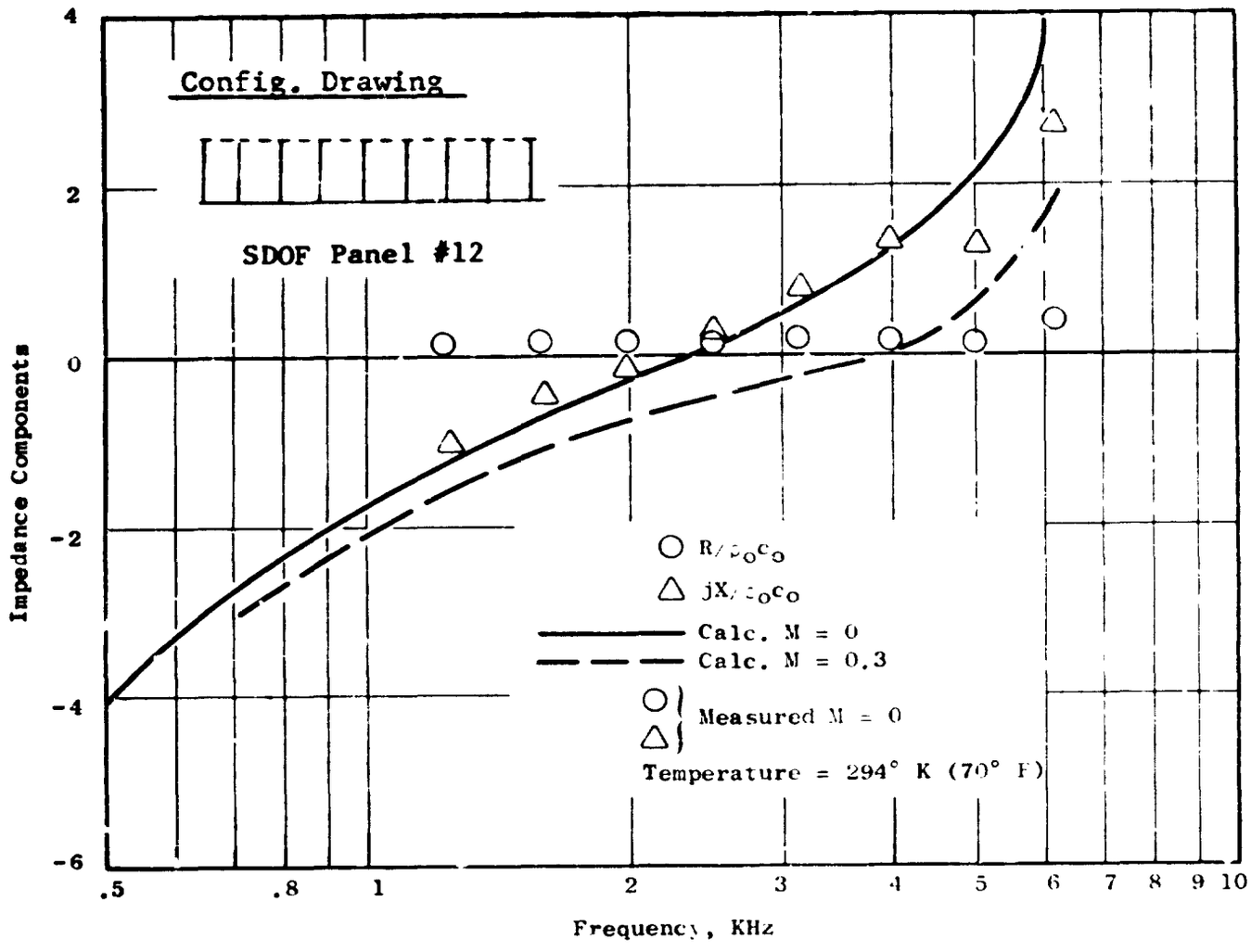

Figure 30. Impedance Components of SDOF Panel No. 12 at Ambient Conditions.

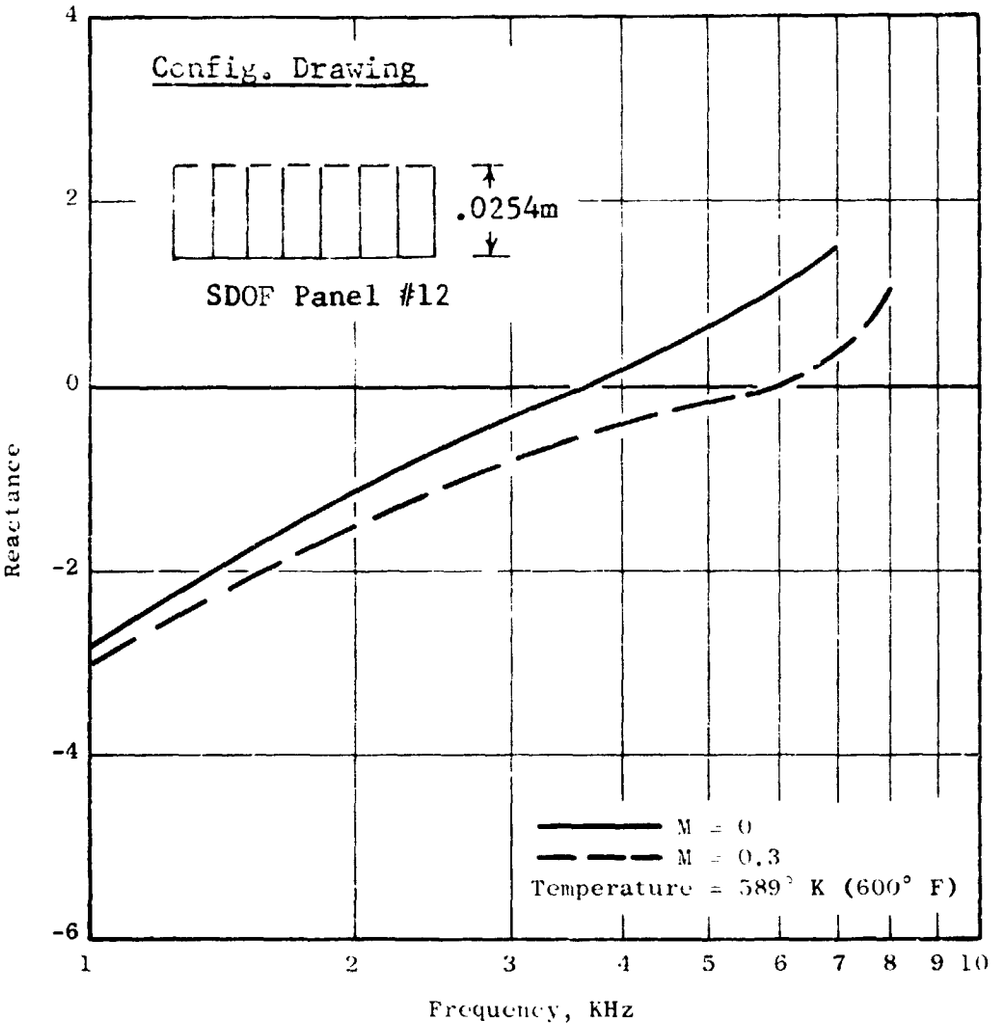

Figure 31. Calculated Reactance of SDOF Panel No. 12 at Turbine Temperatures.

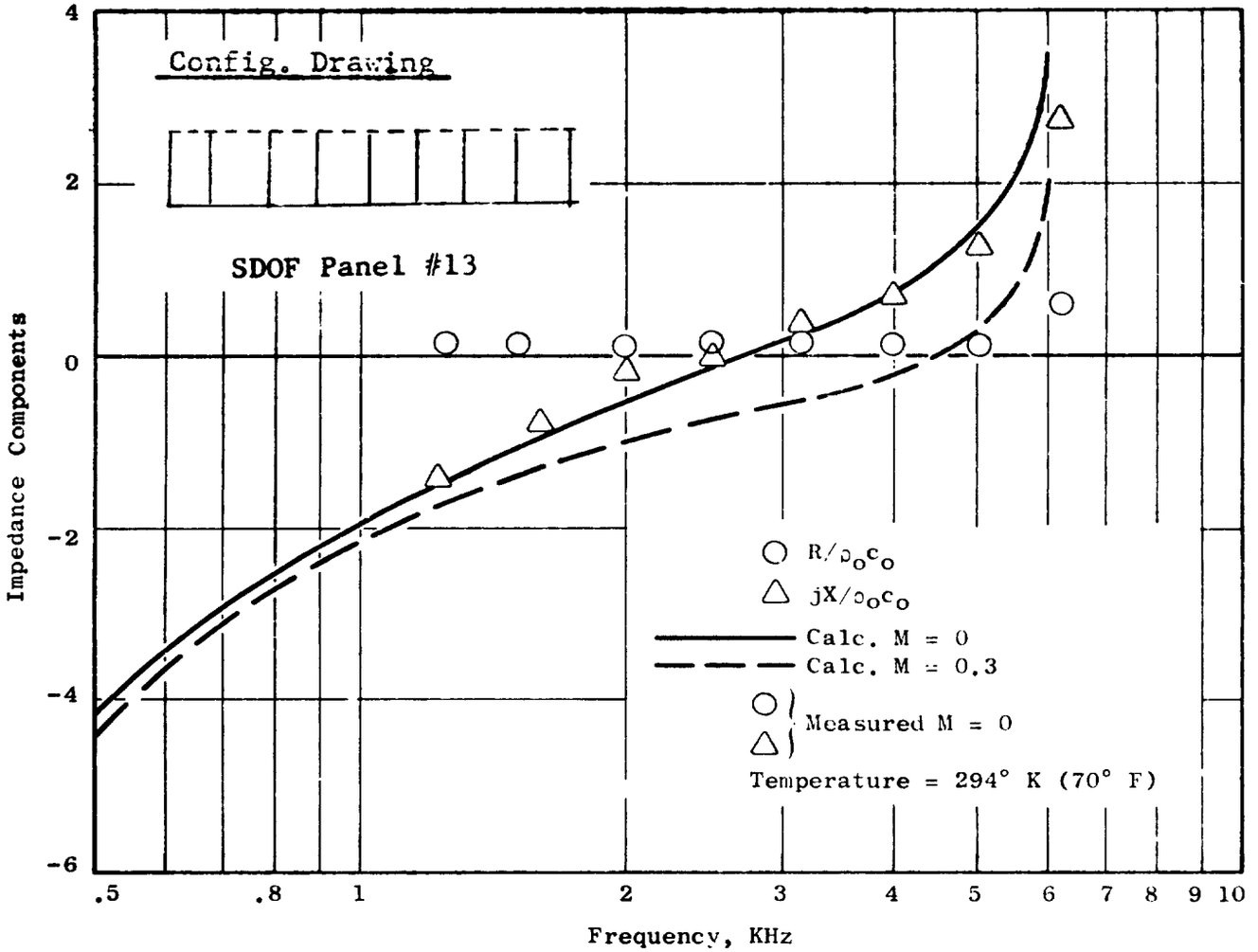

Figure 32. Impedance Components of SDOF Panel No. 13 at Ambient Conditions.

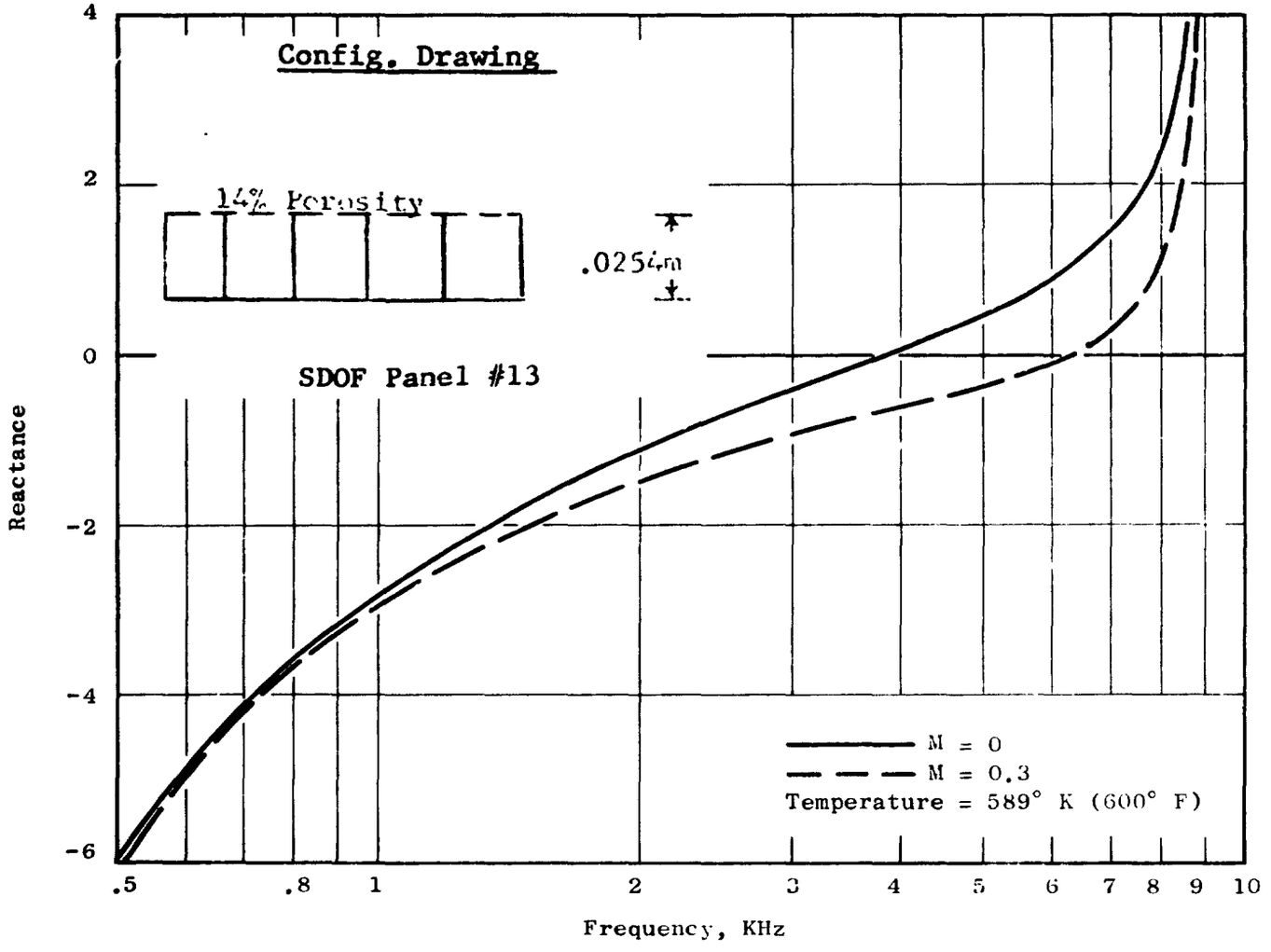

Figure 33. Calculated Reactance of SDOF Panel No. 13 at Turbine Temperatures.

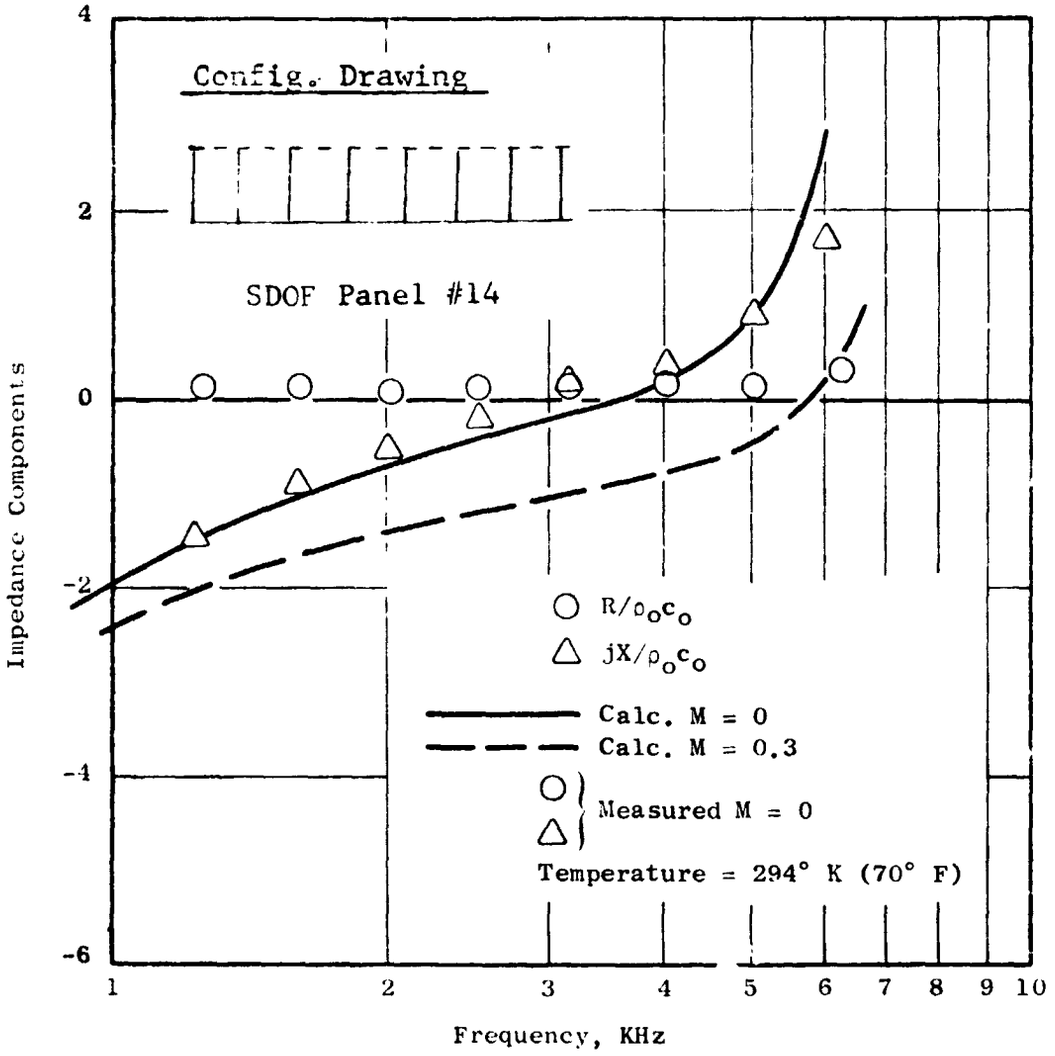

Figure 34. Impedance Components of SDOF Panel No. 14 at Ambient Conditions.

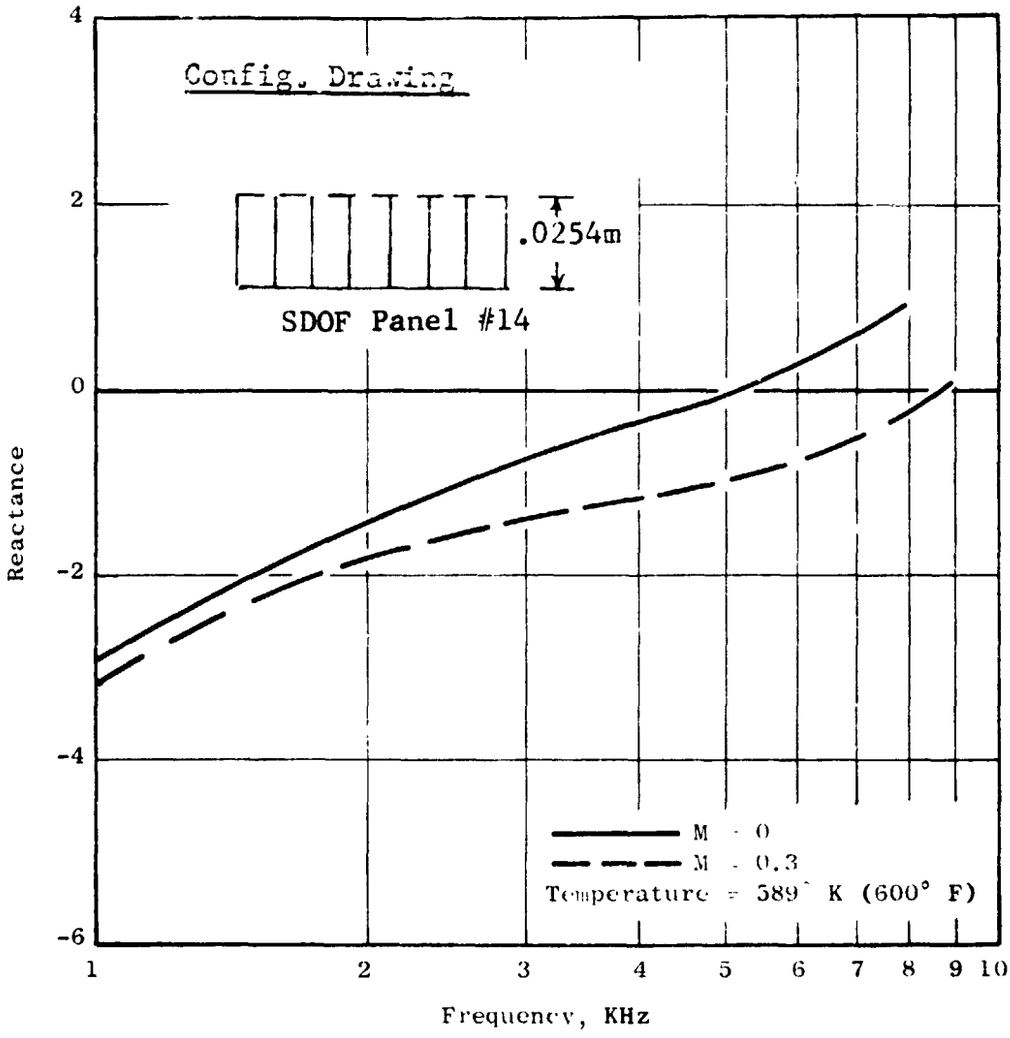

Figure 35. Calculated Reactance of SDOF Panel No. 14 at Turbine Temperatures.

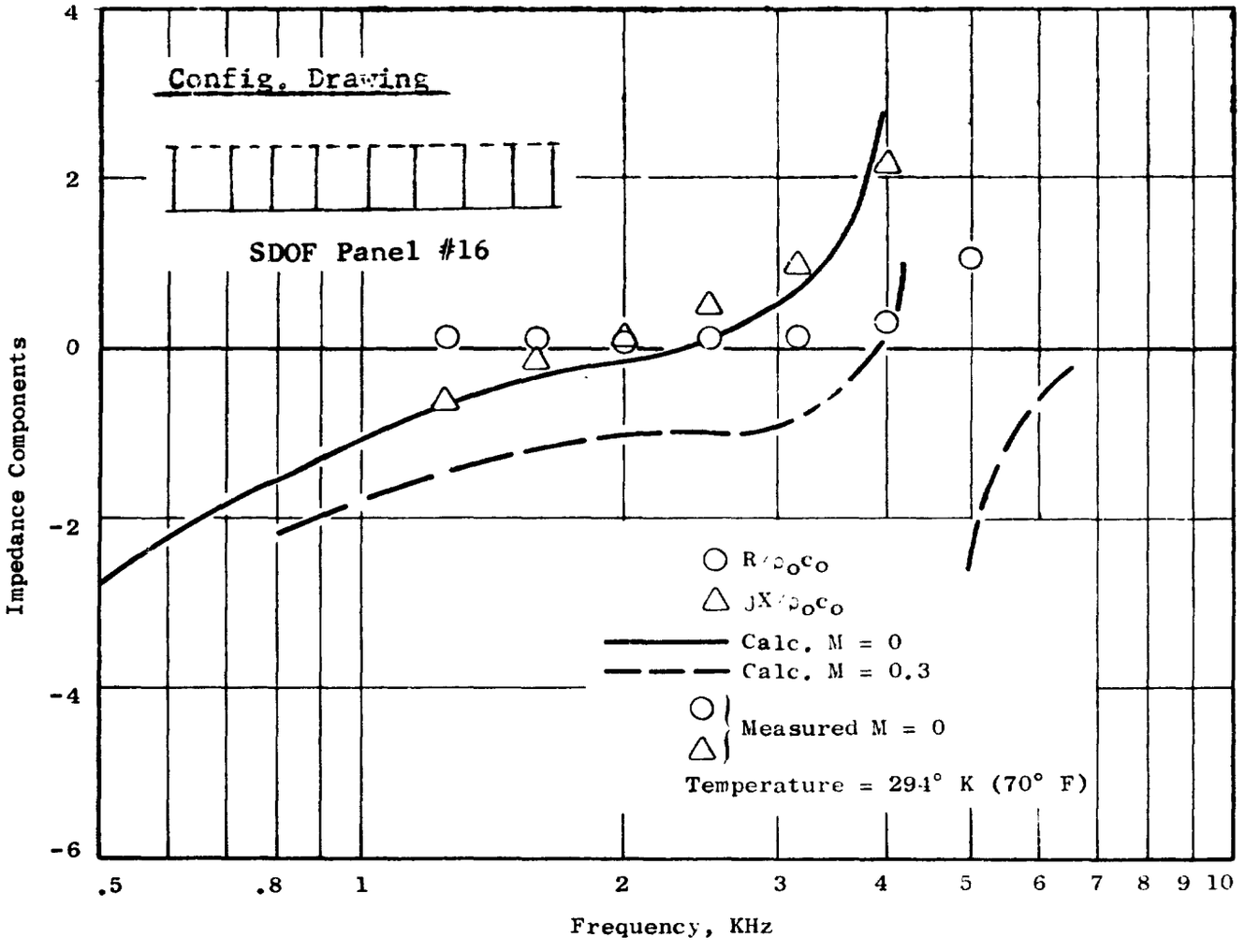

Figure 36. Impedance Components of SDOF Panel No. 16 at Ambient Conditions.

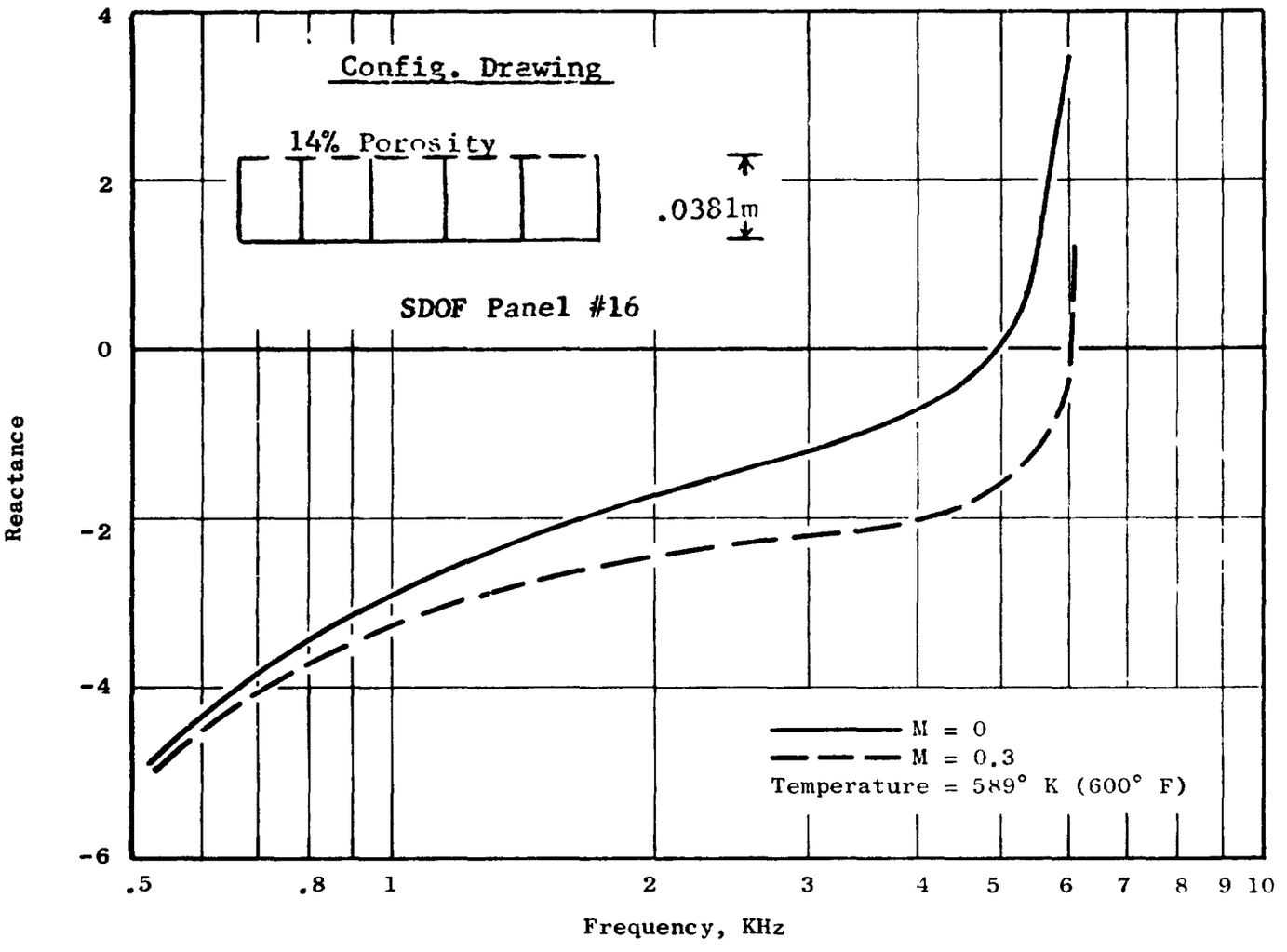

Figure 37. Calculated Reactance of SDOF Panel No. 16 at Turbine Temperatures.

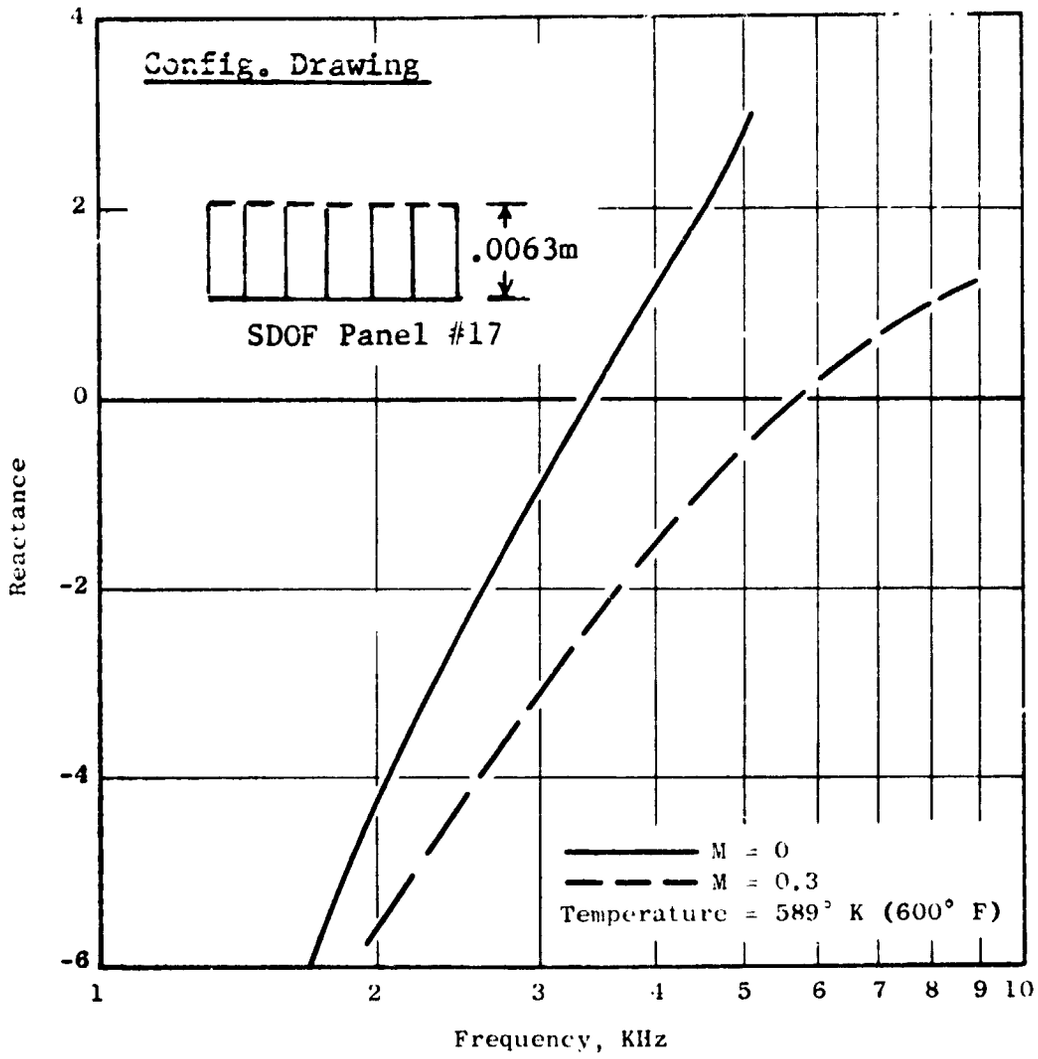

Figure 38. Reactance of SDOF Panel No. 17 at Ambient Conditions.

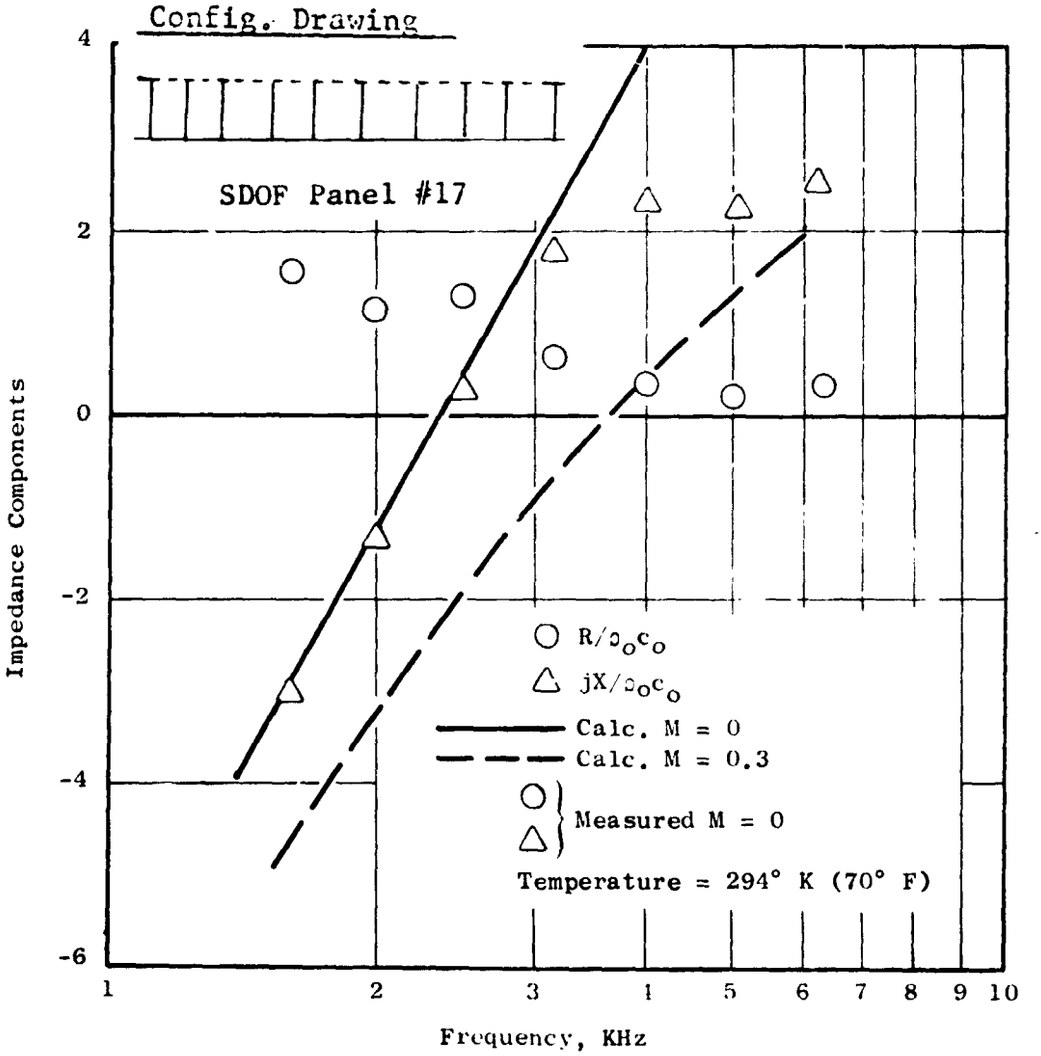

Figure 39. Calculated Impedance Components of SDOF Panel No. 17 at Turbine Temperatures.

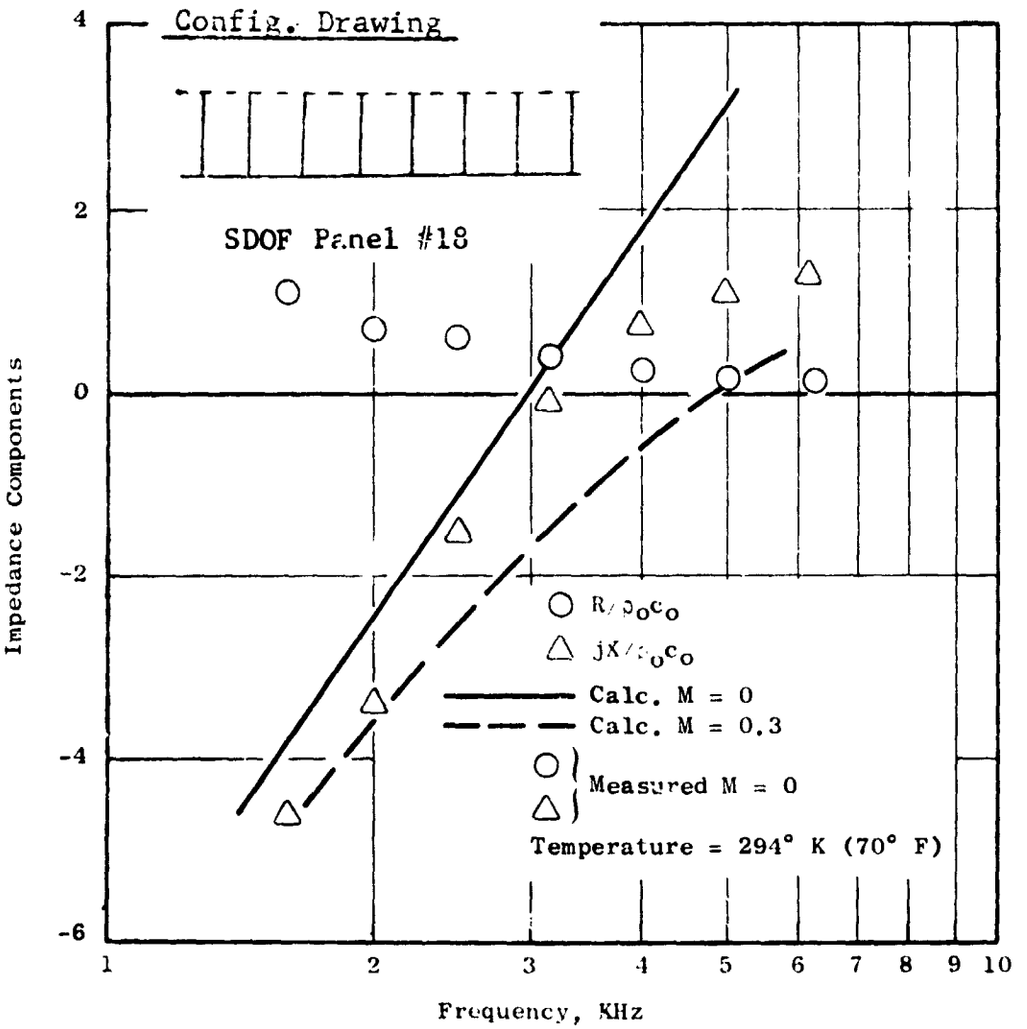

Figure 40. Impedance Components of SDOF Panel No. 18 at Ambient Conditions.

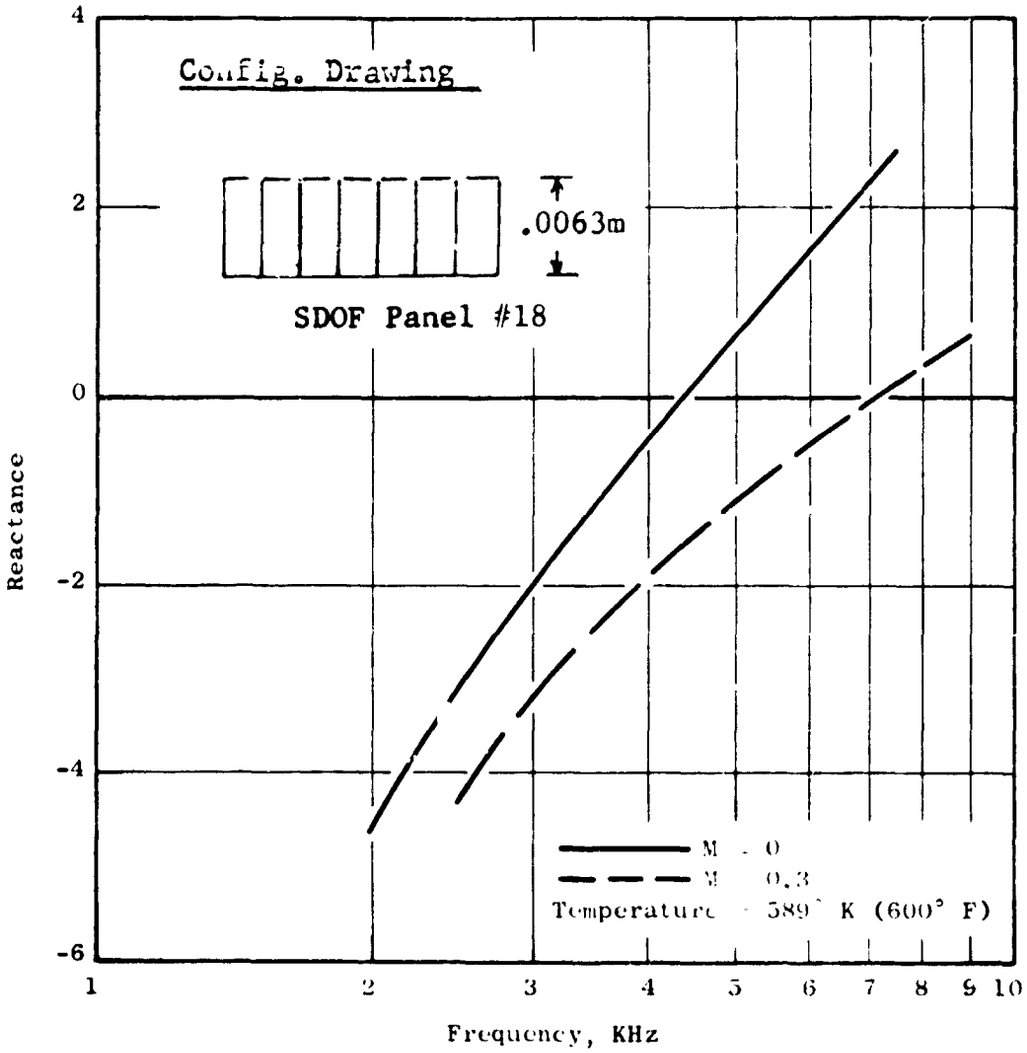

Figure 41. Calculated Reactance of SDOF Panel No. 18 at Turbine Temperatures.

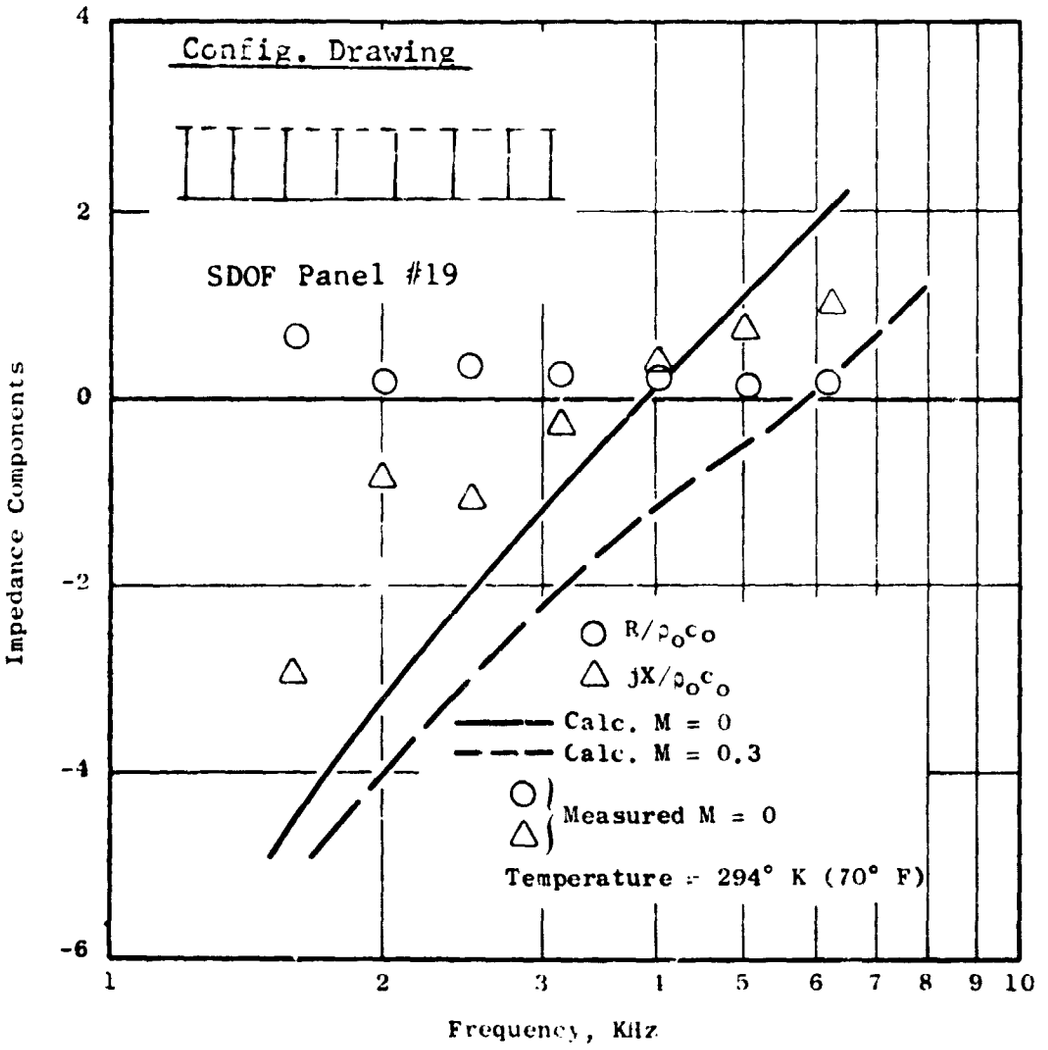

Figure 42. Impedance Components of SDOF Panel No. 19 at Ambient Conditions.

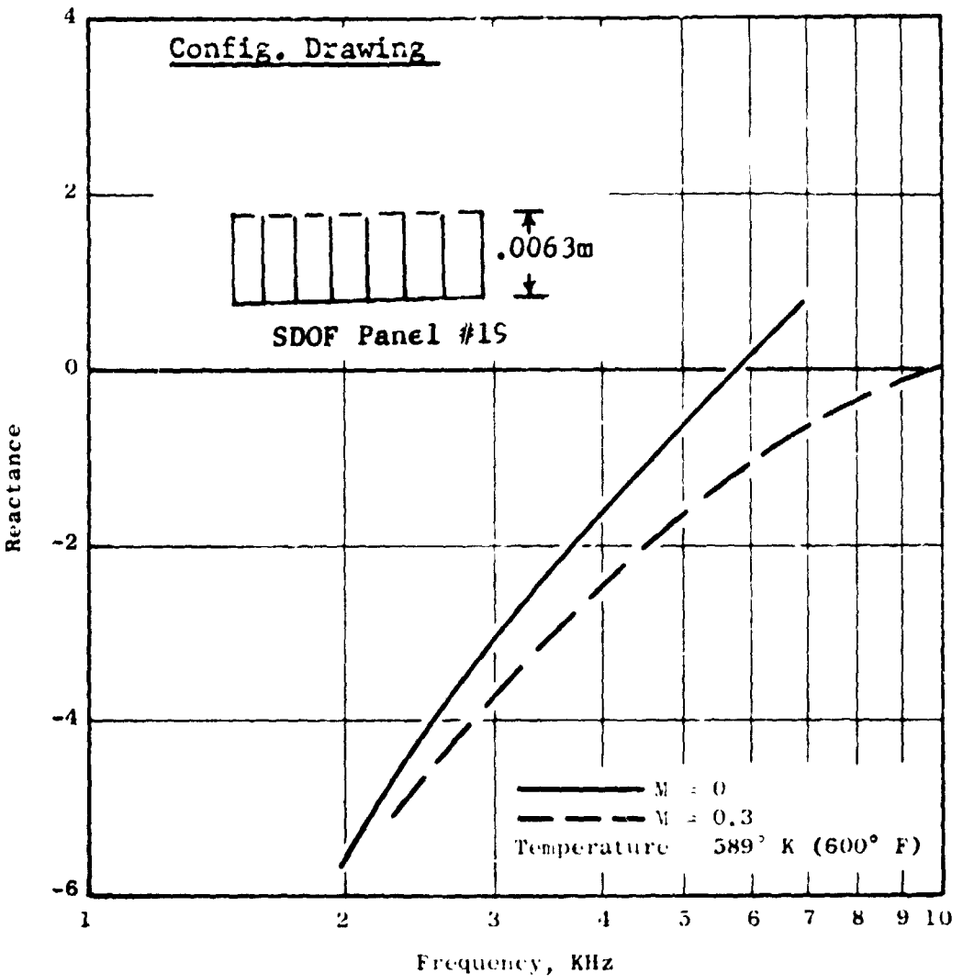

Figure 43. Calculated Reactance of SDOF Panel No. 19 at Turbine Temperatures.

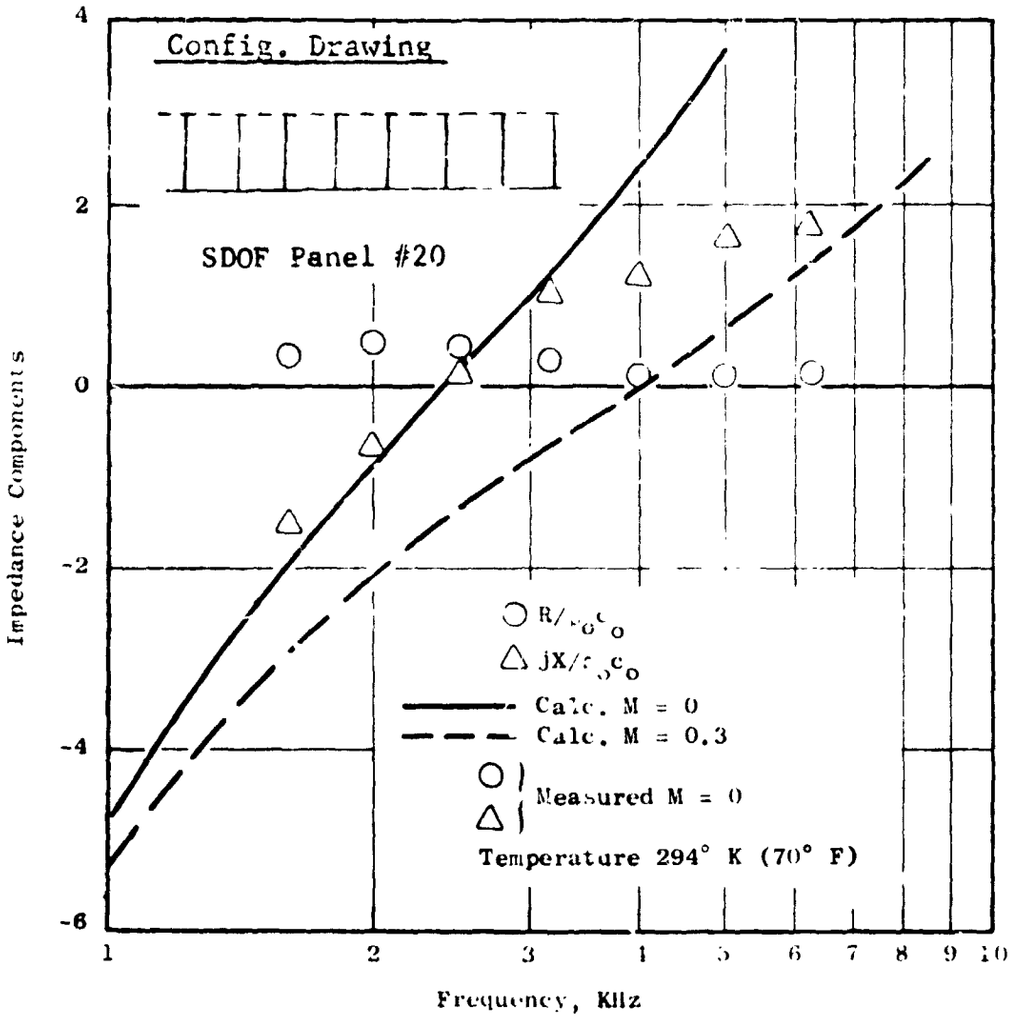

Figure 44. Impedance Components of SDOF Panel No. 20 at Ambient Conditions.

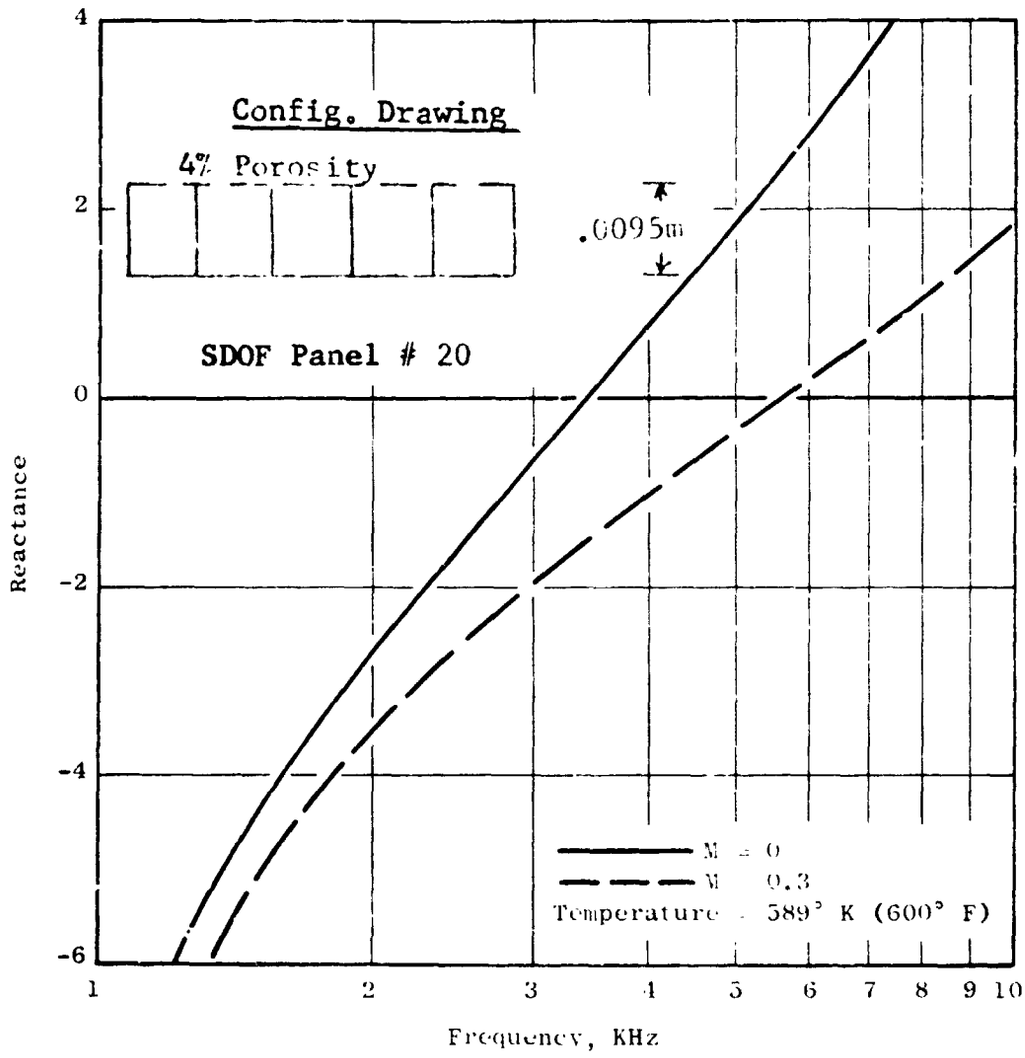

Figure 45. Calculated Reactance of SDOF Panel No. 20 at Turbine Temperatures.

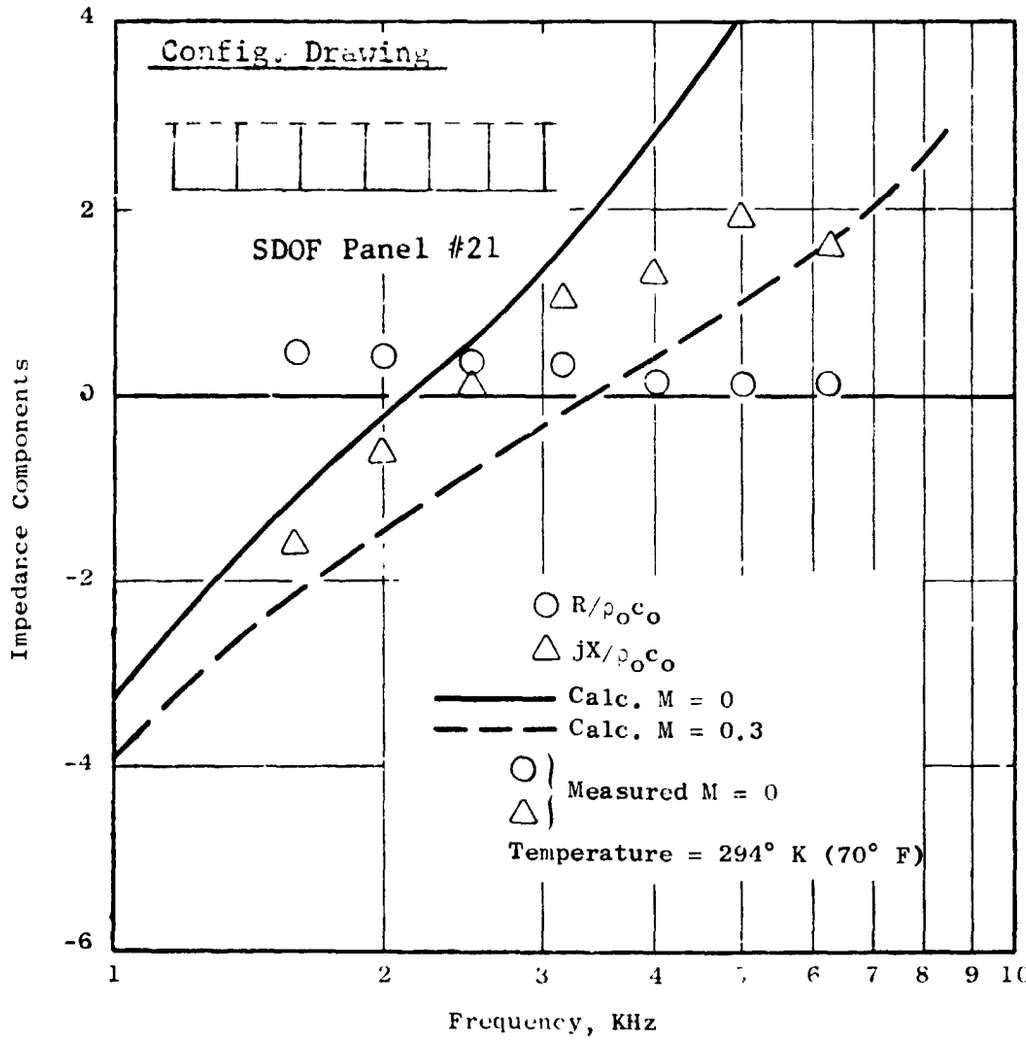

Figure 46. Impedance Components of SDOF Panel No. 21 at Ambient Conditions.

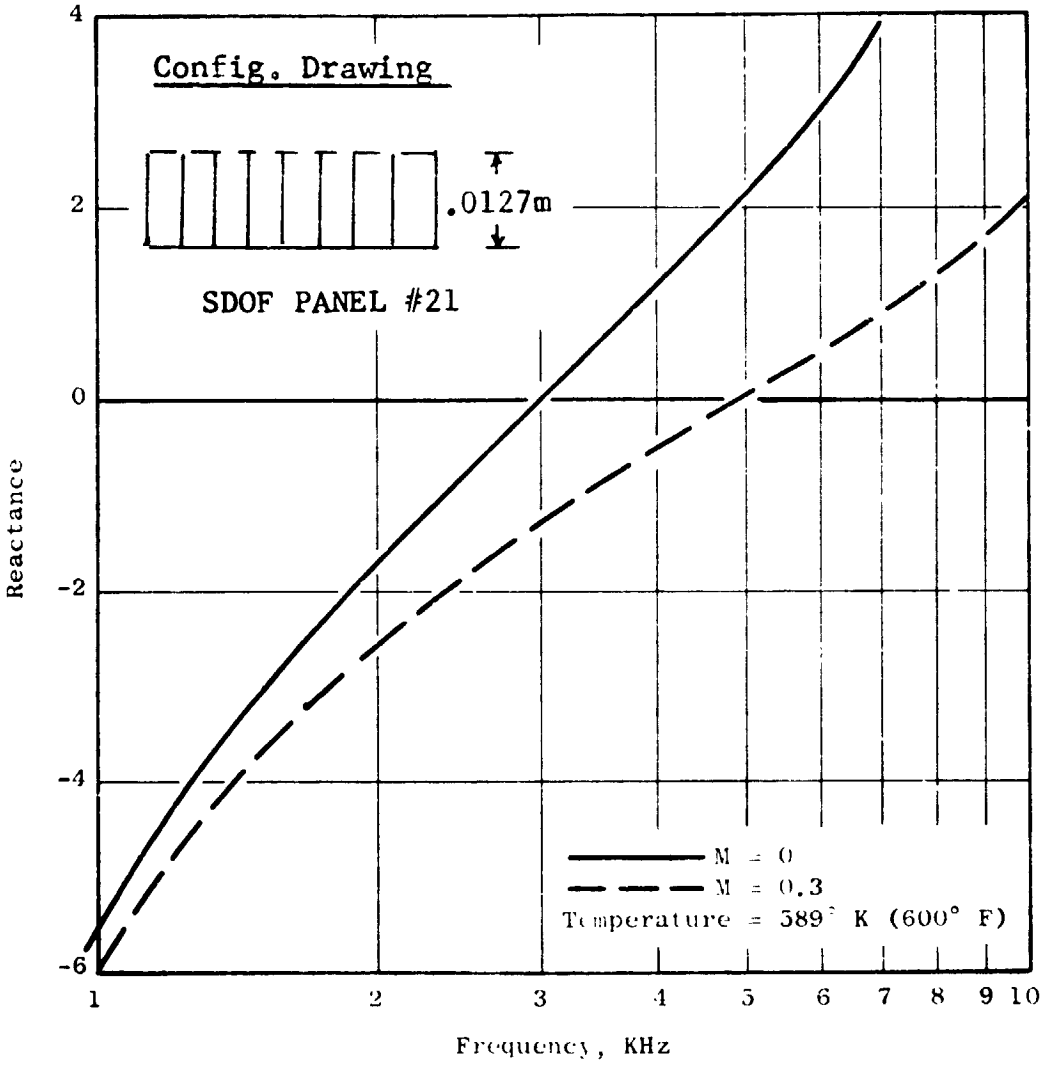

Figure 47. Calculated Reactance of SDOF Panel No. 21 at Turbine Temperatures.

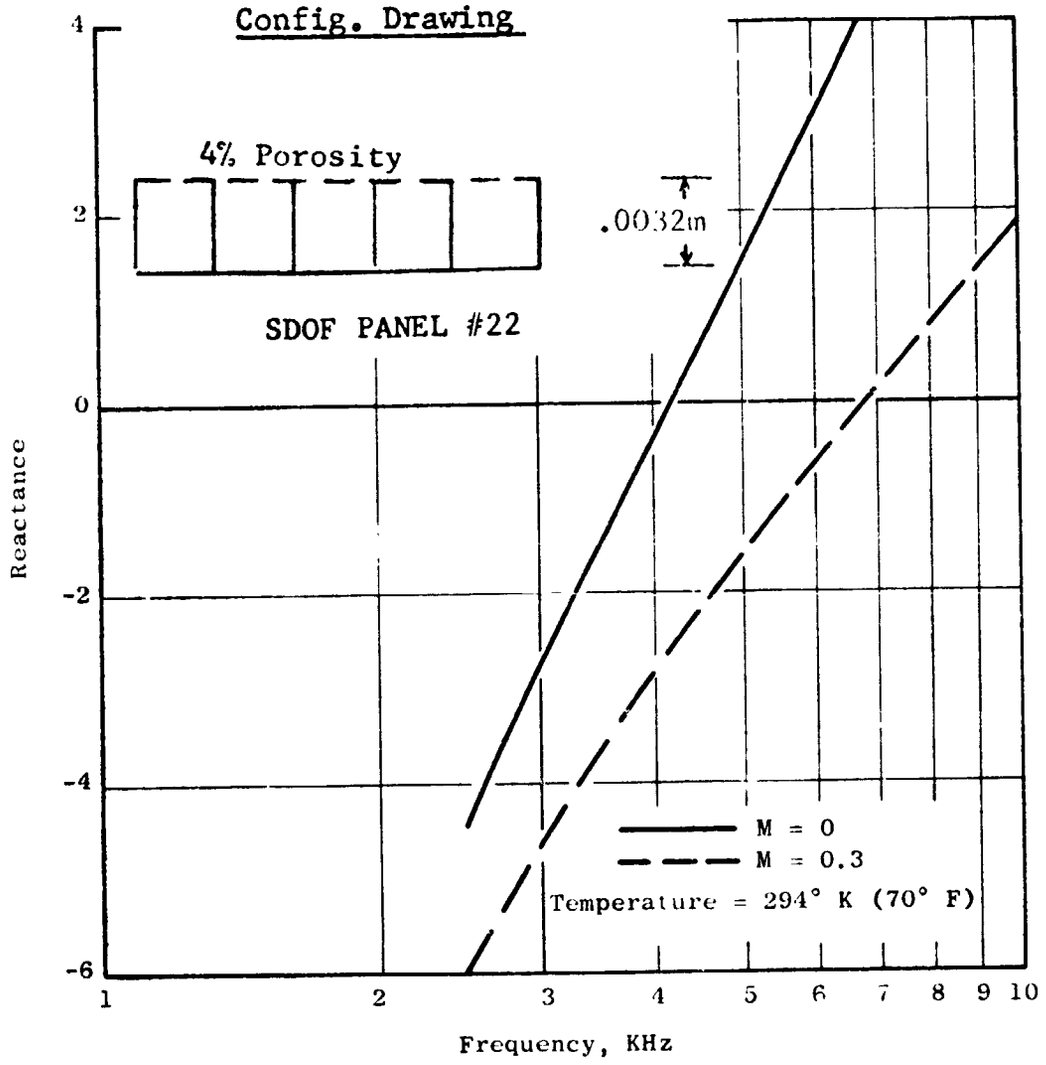

Figure 48. Calculated Reactance of SDOF Panel No. 22 at Ambient Conditions.

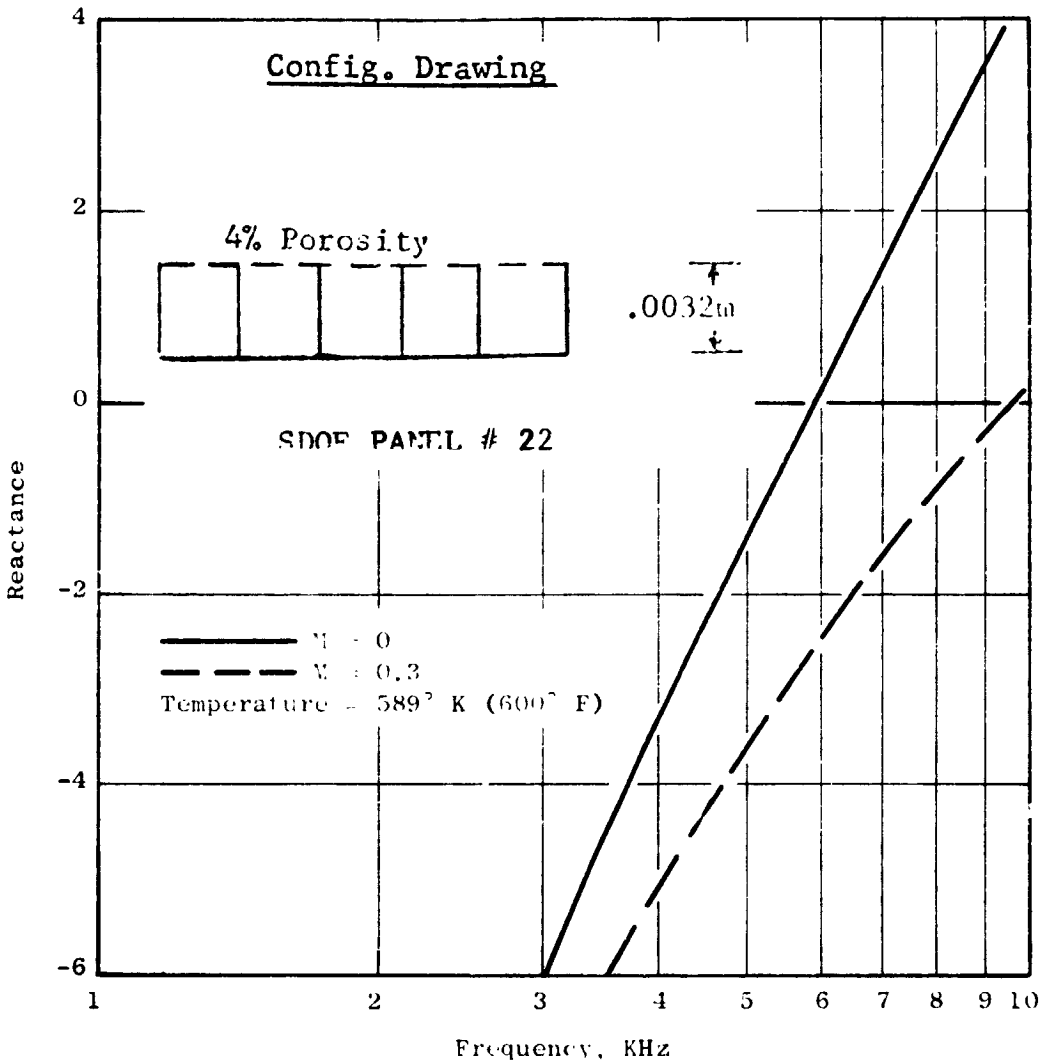

Figure 49. Calculated Reactance of SDOF Panel No. 22 at Turbine Temperatures.

Config. Drawing

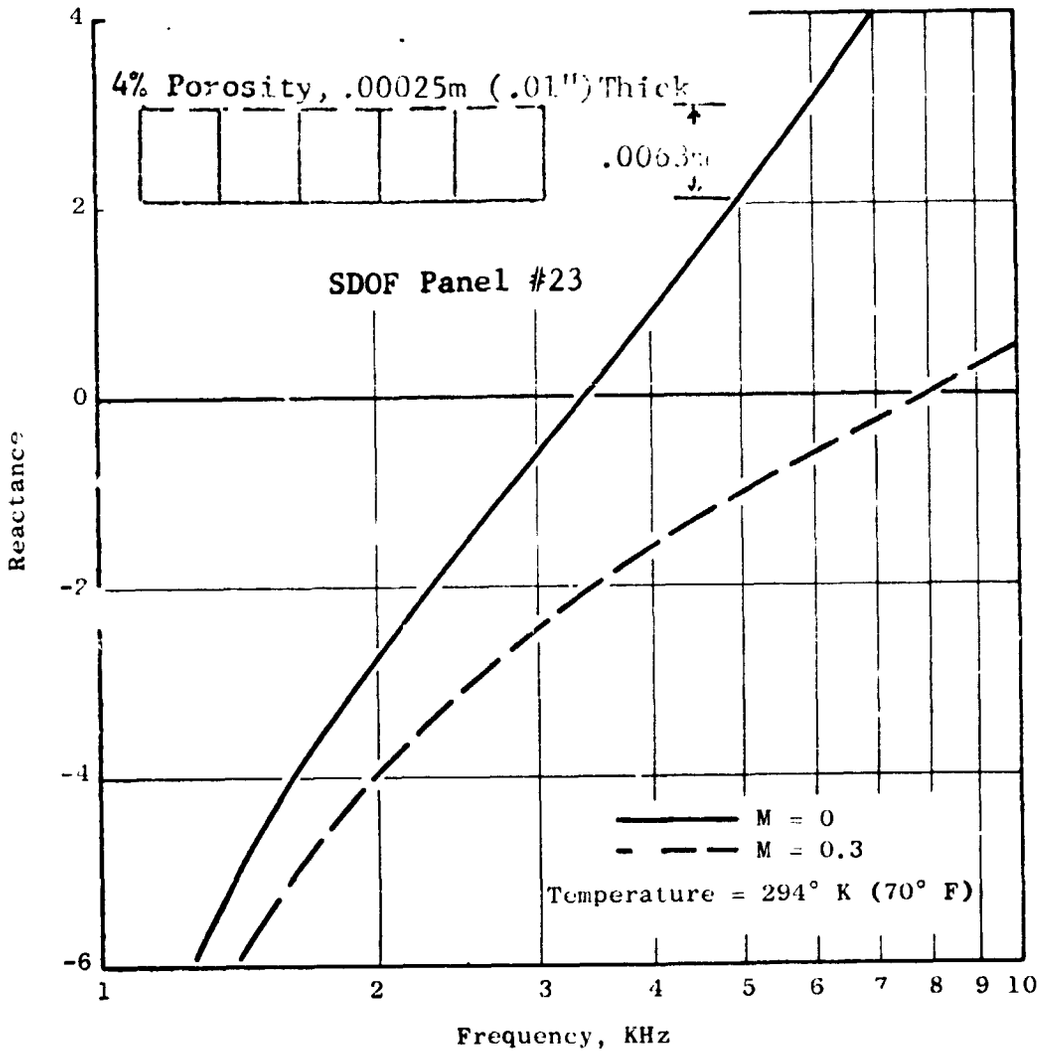

Figure 50. Calculated Reactance of SDOF Panel No. 23 at Ambient Conditions.

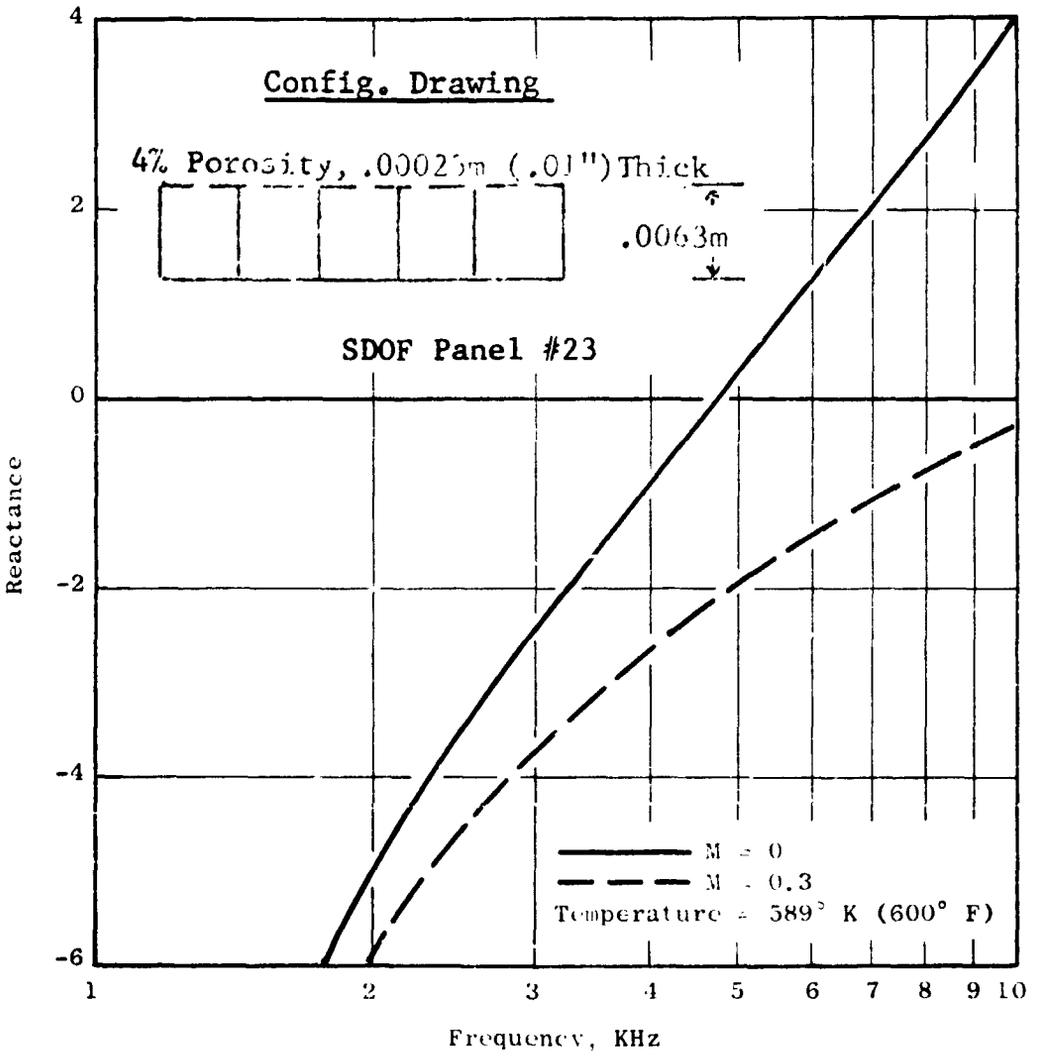

Figure 51. Calculated Reactance of SDOF Panel No. 23 at Turbine Temperatures.

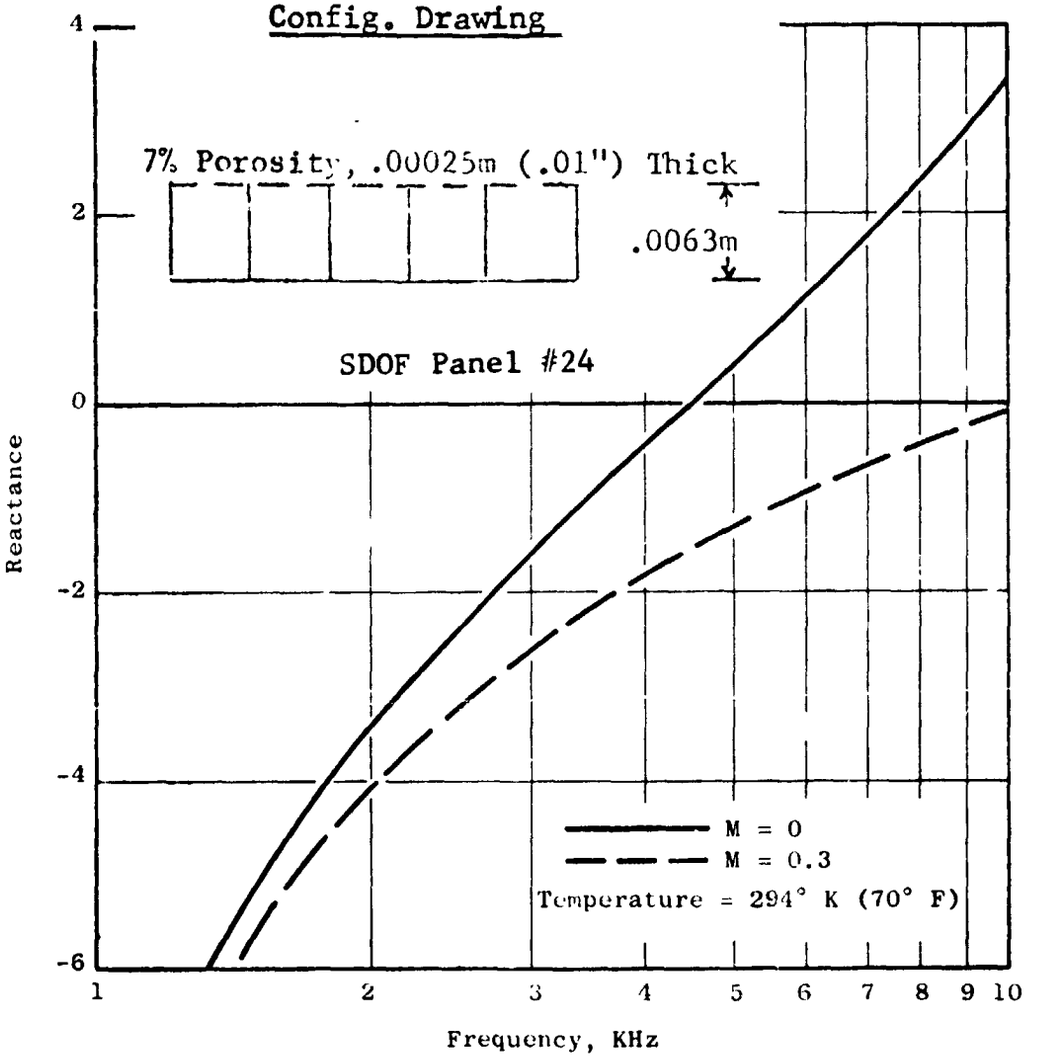

Figure 52. Calculated Reactance of SDOF Panel No. 24 at Ambient Conditions.

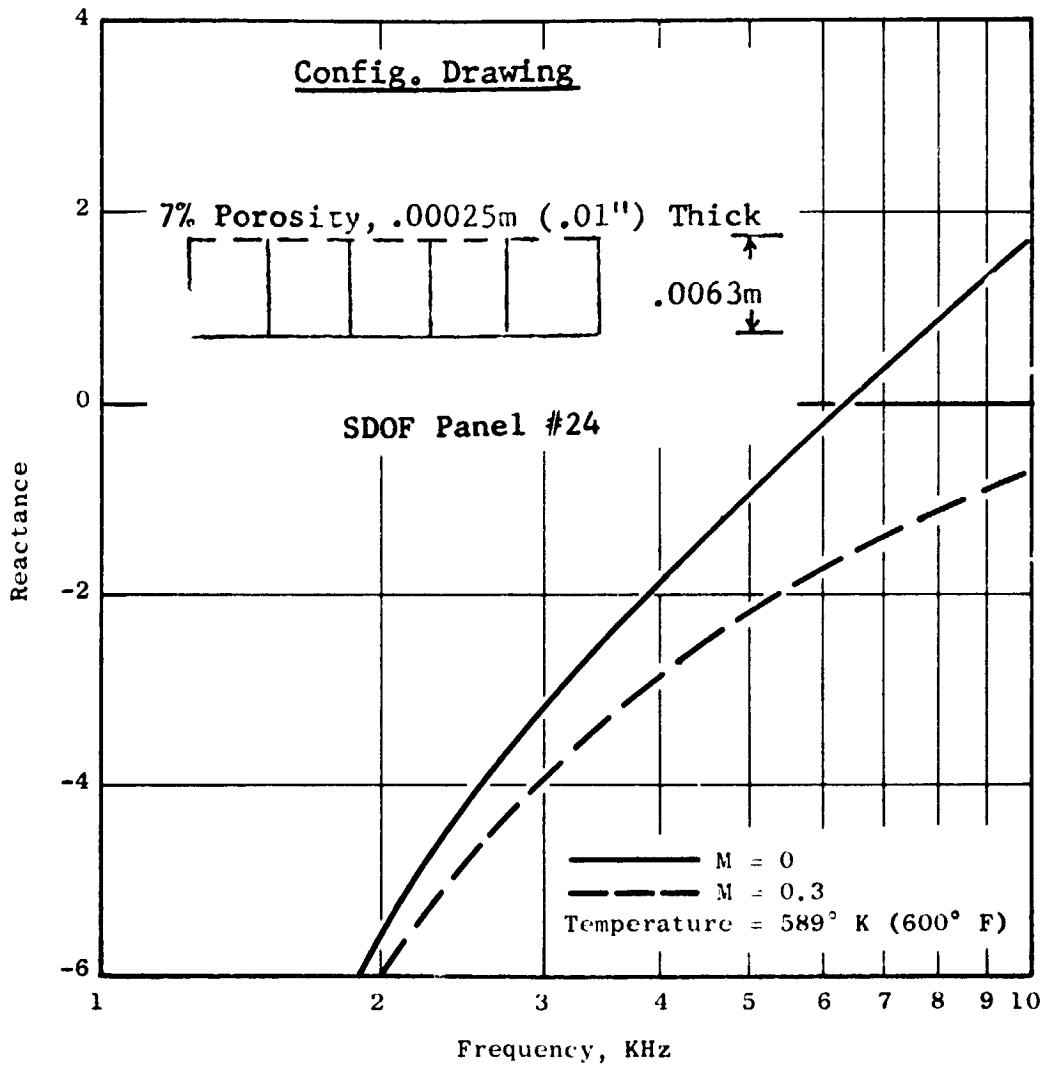

Figure 53. Calculated Reactance of SDOF Panel No. 24 at Turbine Temperatures.

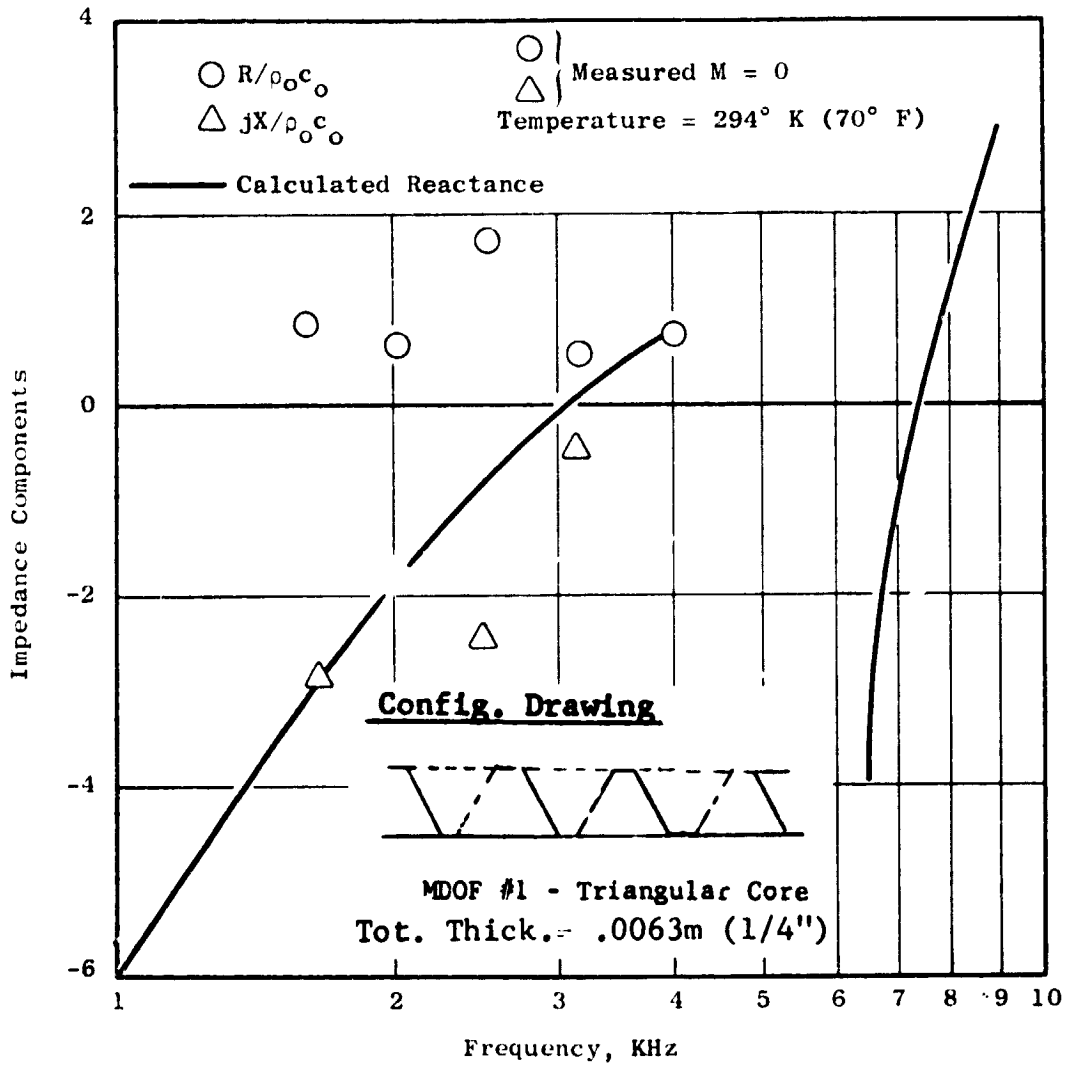

Figure 54. Impedance Components of Panel MDOF I at Ambient Conditions.

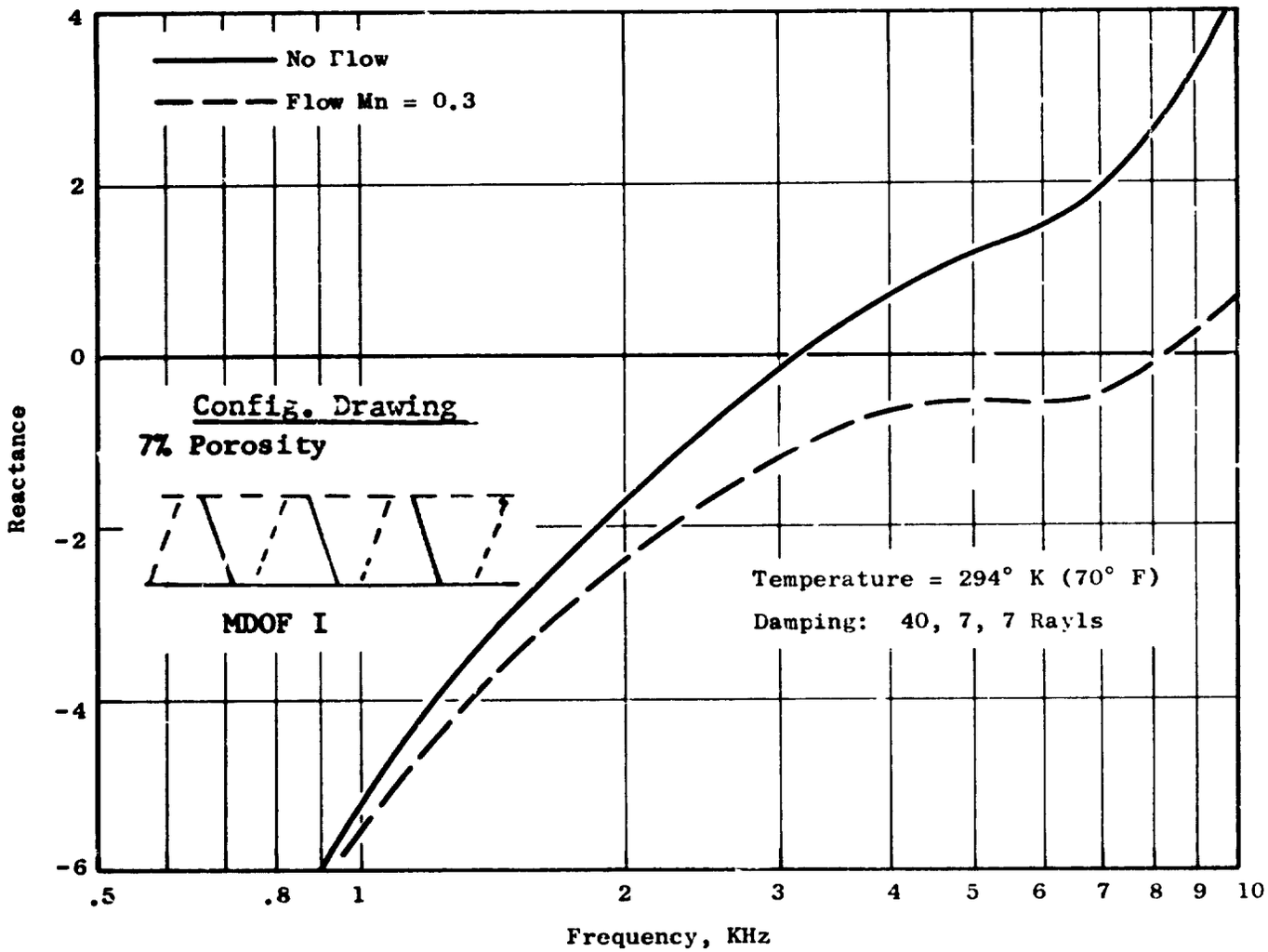

Figure 55. Calculated Reactance of Panel MDOF I at Turbine Temperatures.

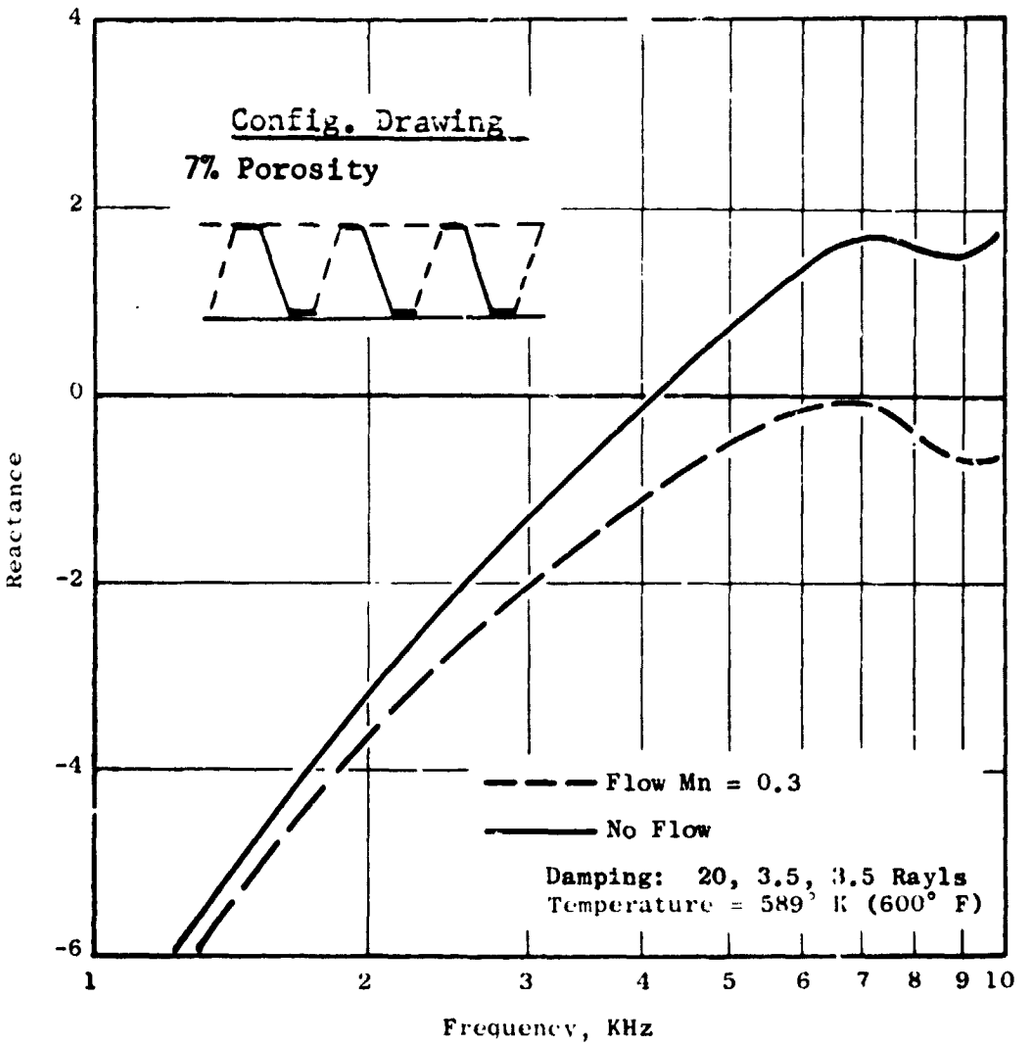

Figure 56. Calculated Reactance of Panel MDOF I with Damping at Turbine Temperatures.

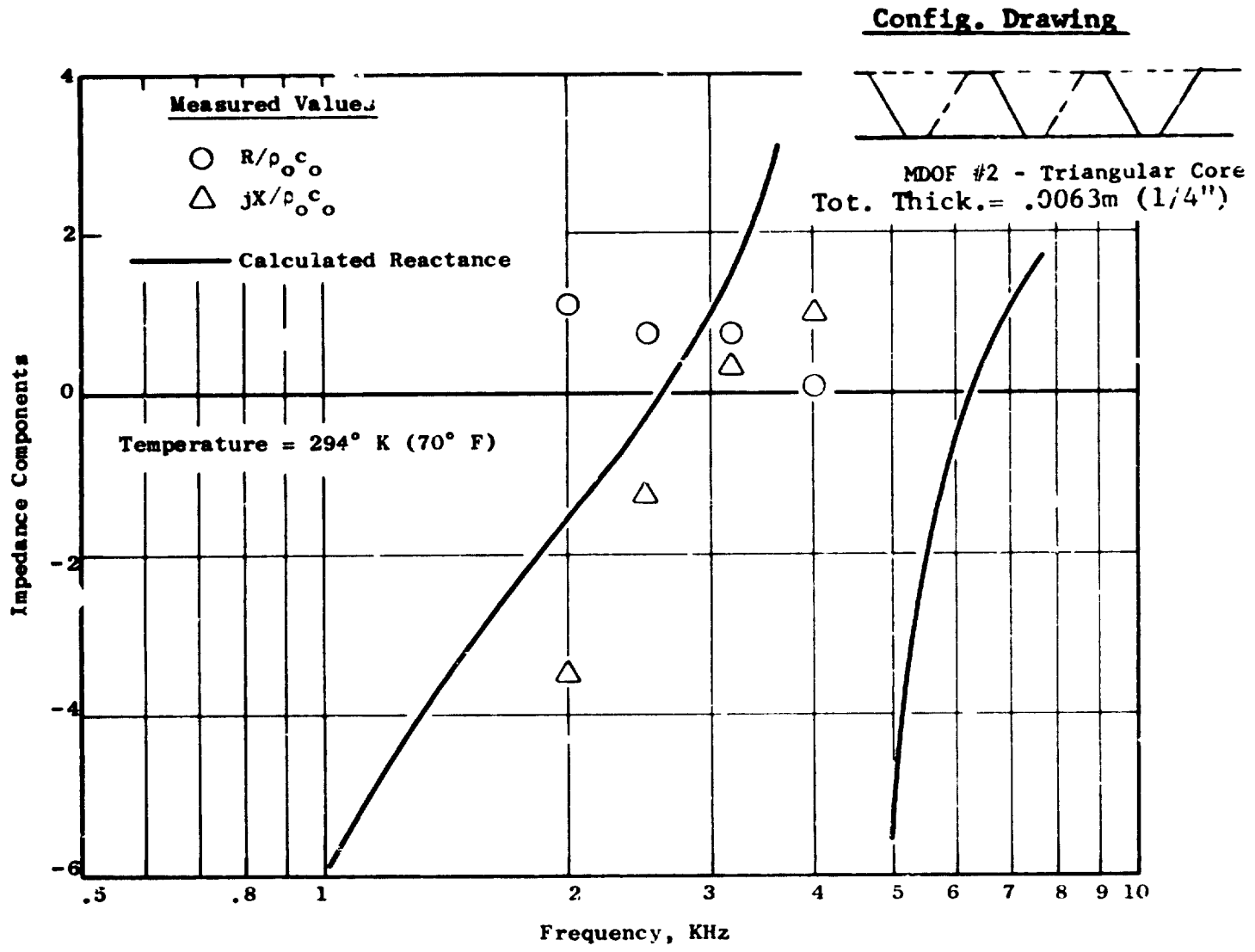

Figure 57. Impedance Components of Panel MDOF II at Ambient Conditions.

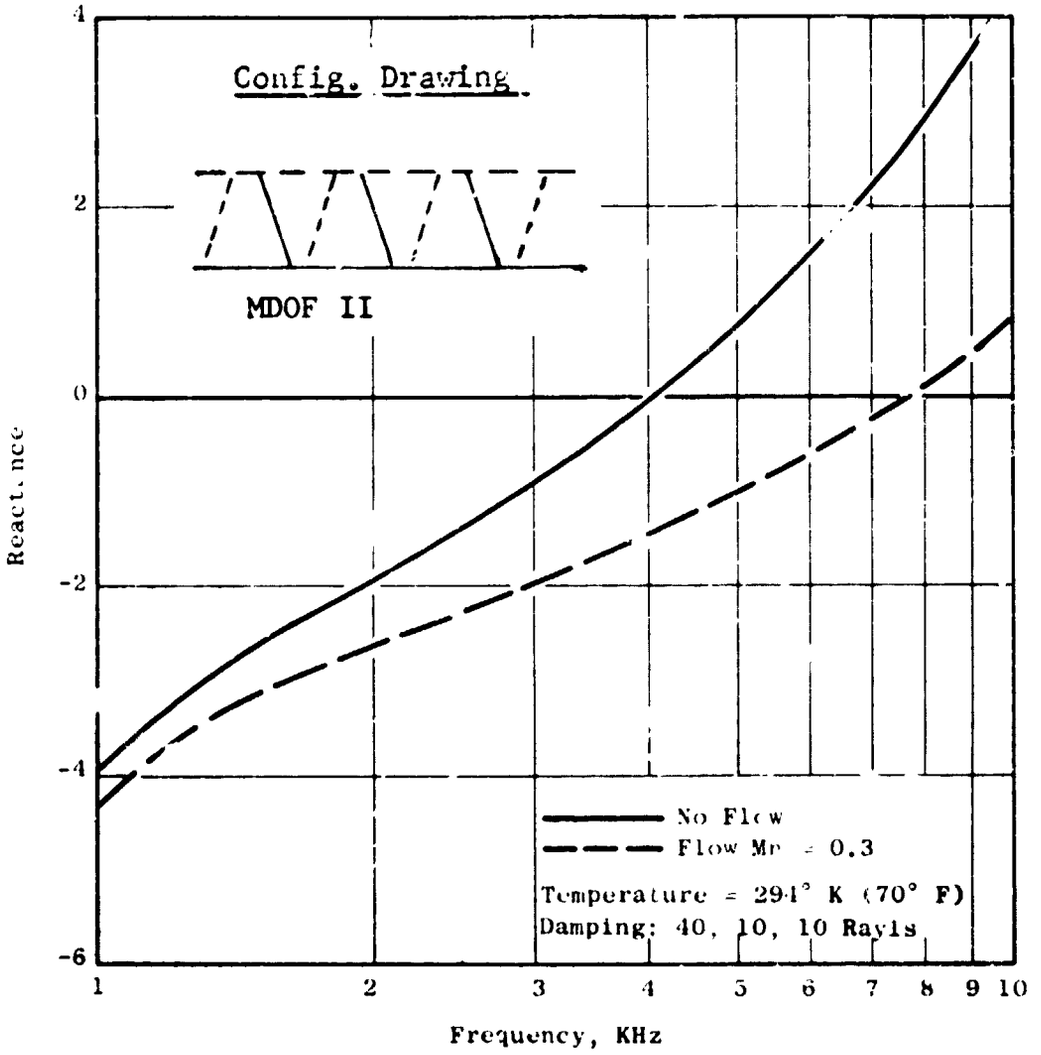

Figure 58. Calculated Reactance of Panel MDOF II at Turbine Temperatures.

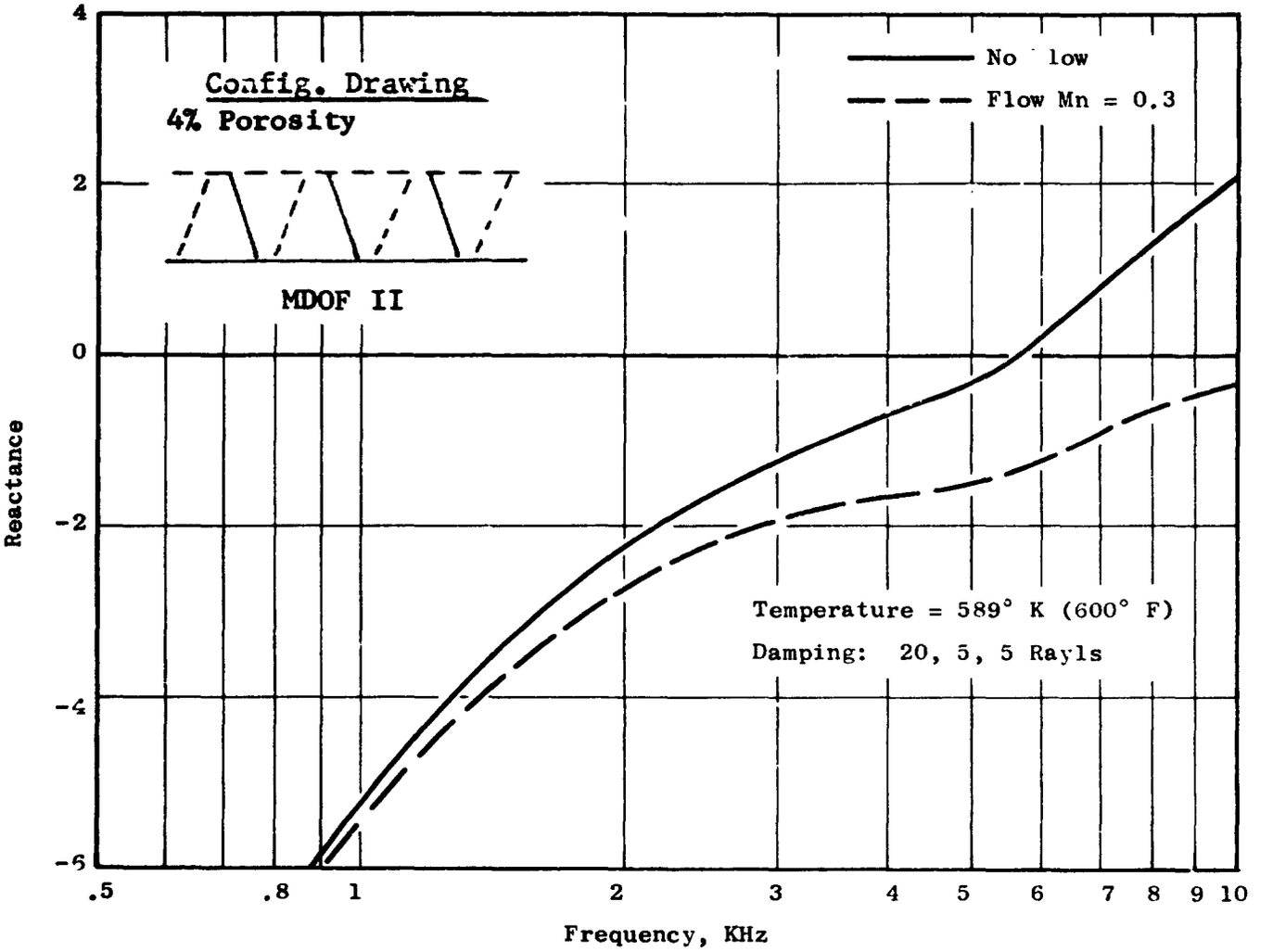

Figure 59. Calculated Reactance of Panel MDOF II with Damping at Turbine Temperatures.

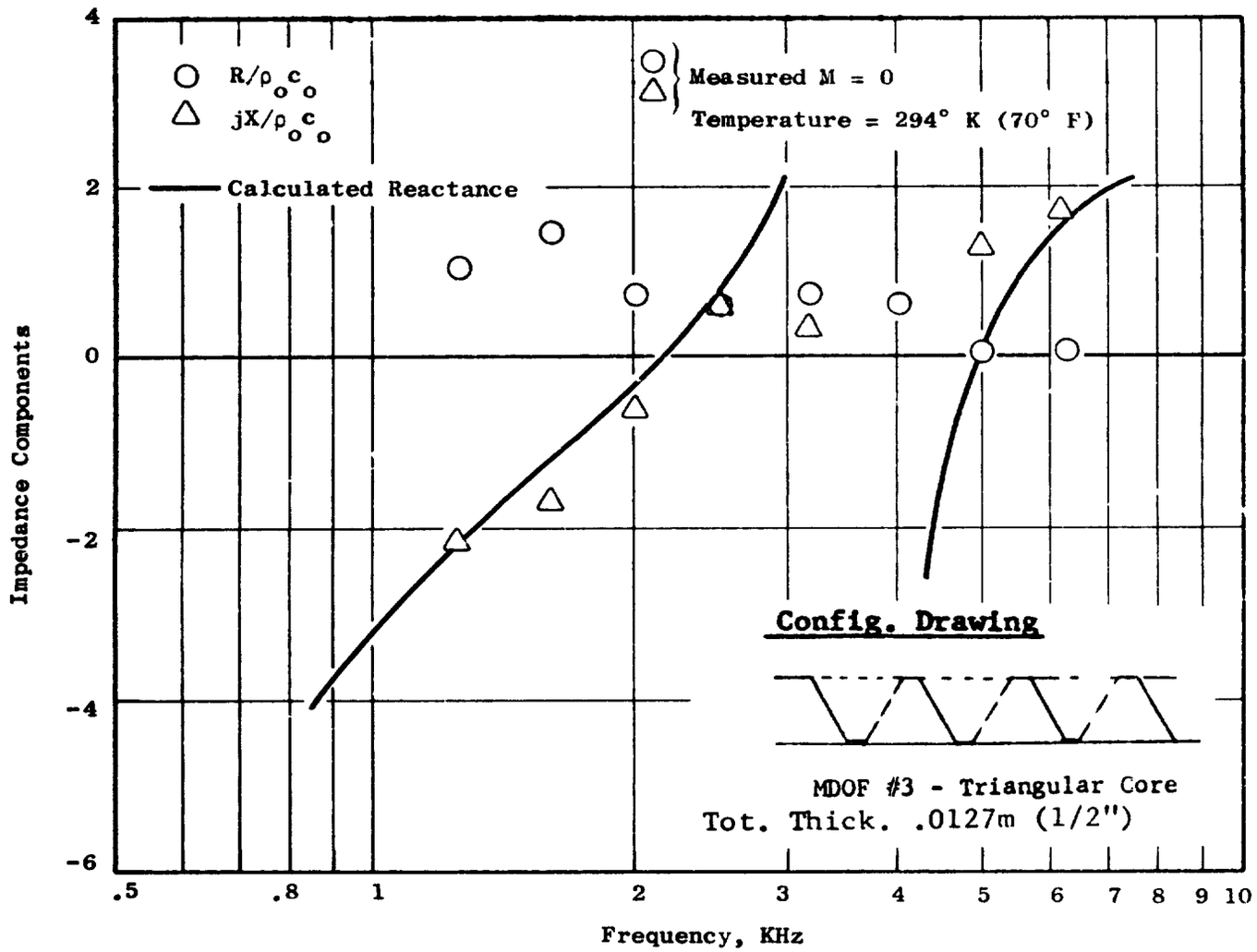

Figure 60. Impedance Components of Panel MDOF III at Ambient Conditions.

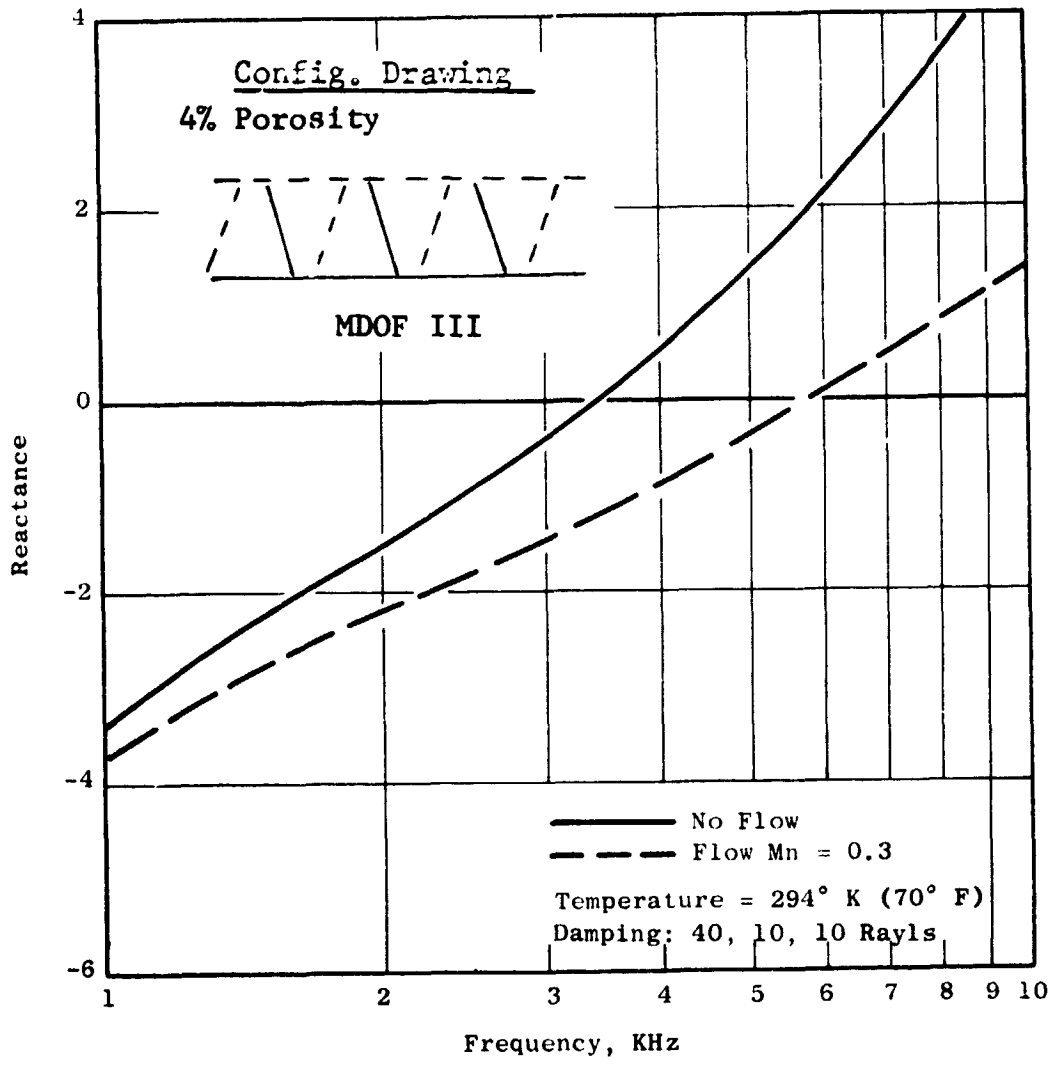

Figure 61. Calculated Reactance of Panel MDOF III with High Damping at Ambient Conditions.

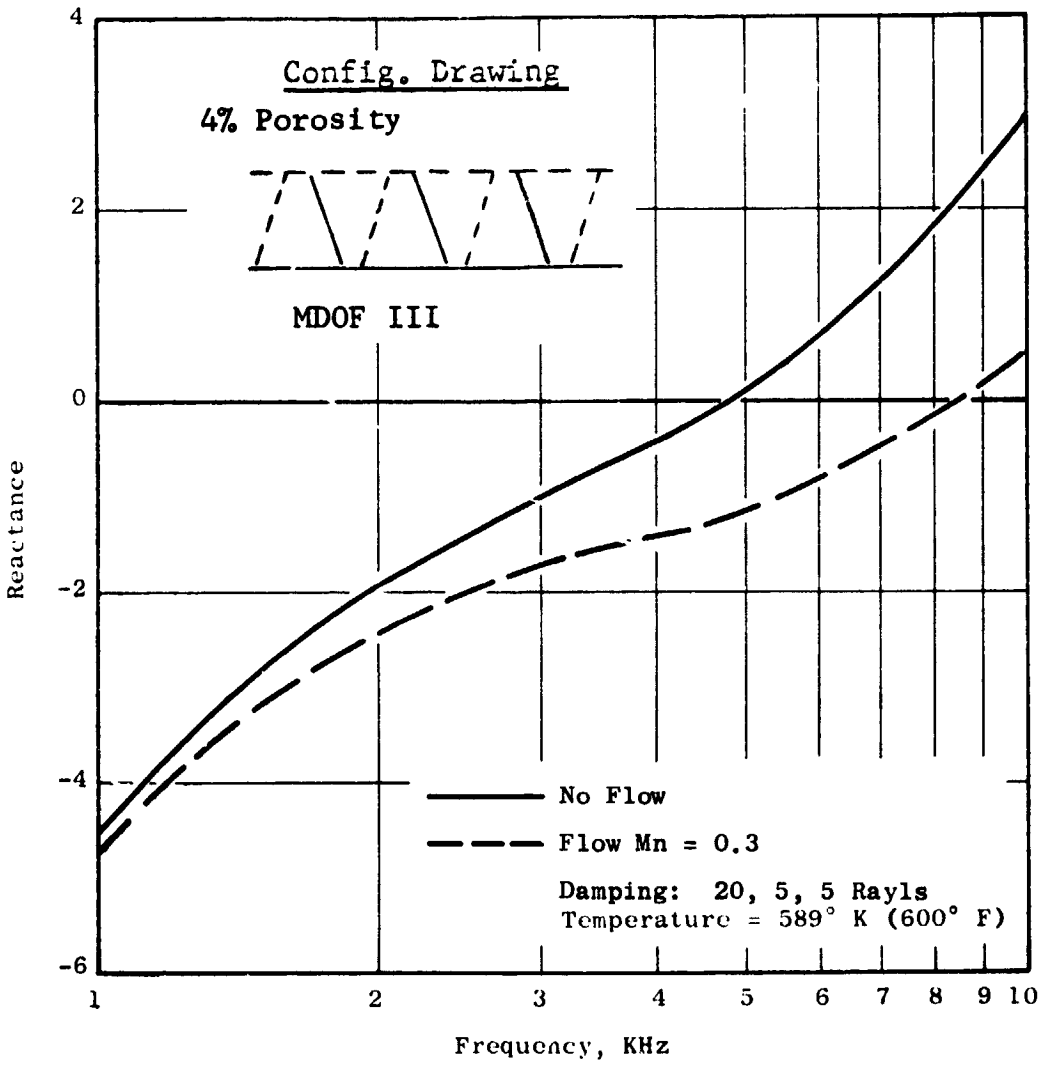

Figure 62. Calculated Reactance of Panel MDOF III with Low Damping at Turbine Temperatures.

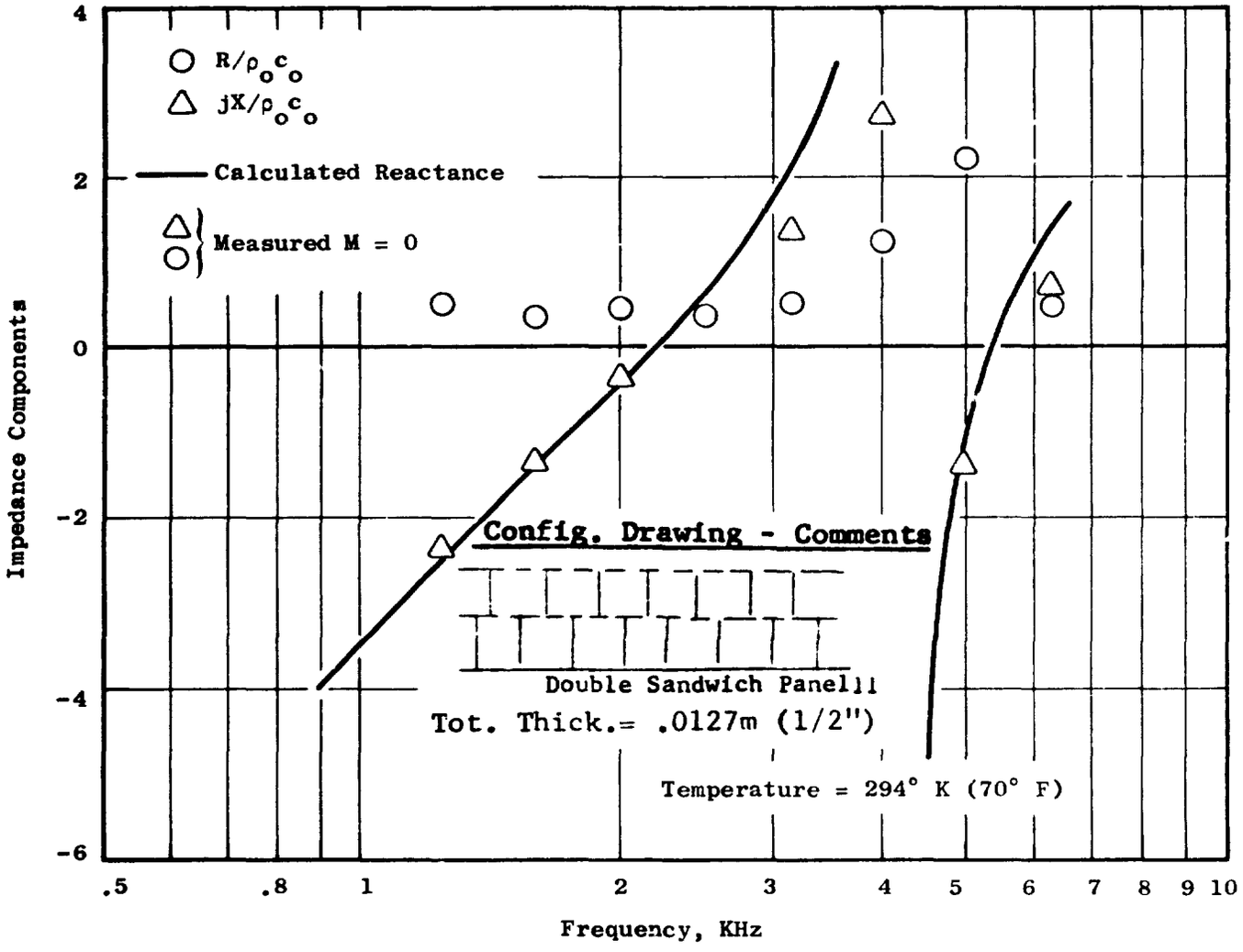

Figure 63. Impedance Components of Double Sandwich II at Ambient Conditions.

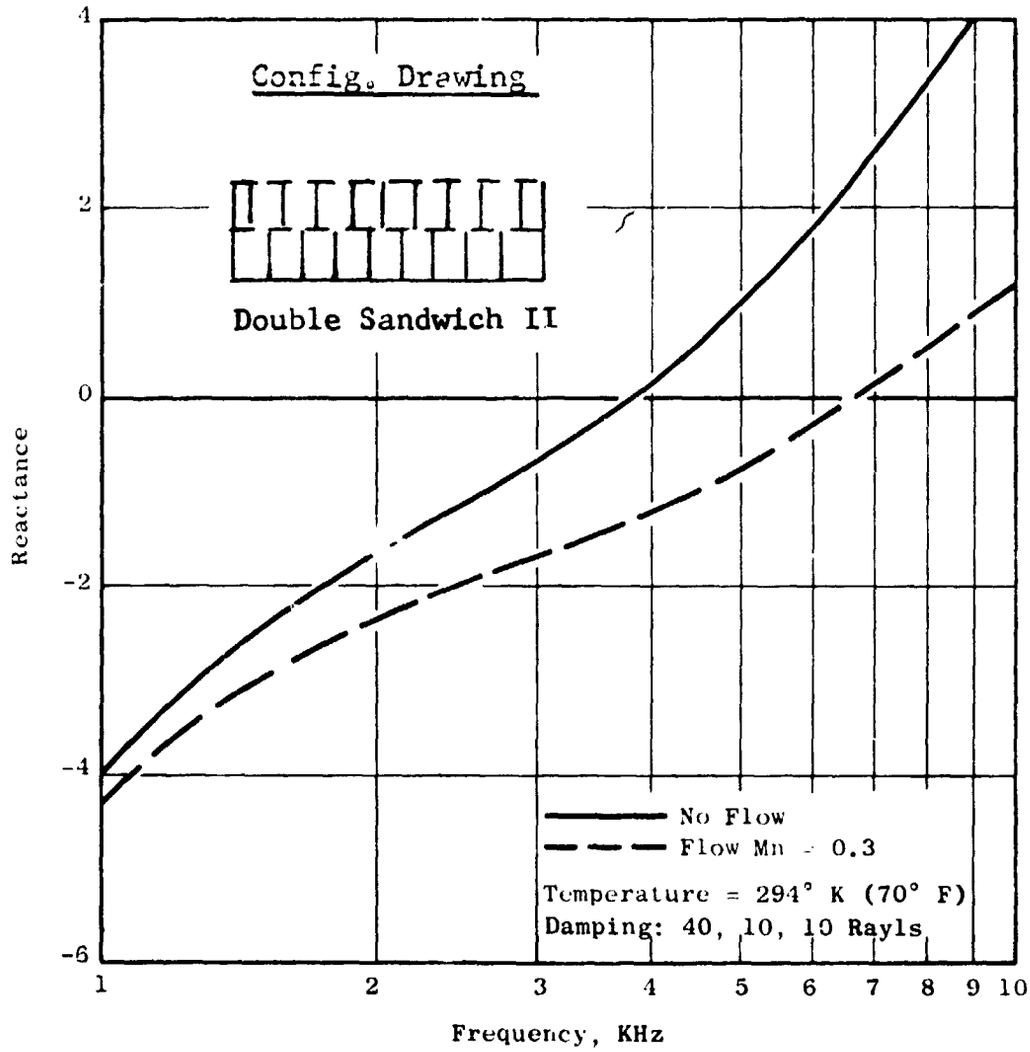

Figure 64. Calculated Reactance of Double Sandwich II with High Damping at Turbine Temperatures.

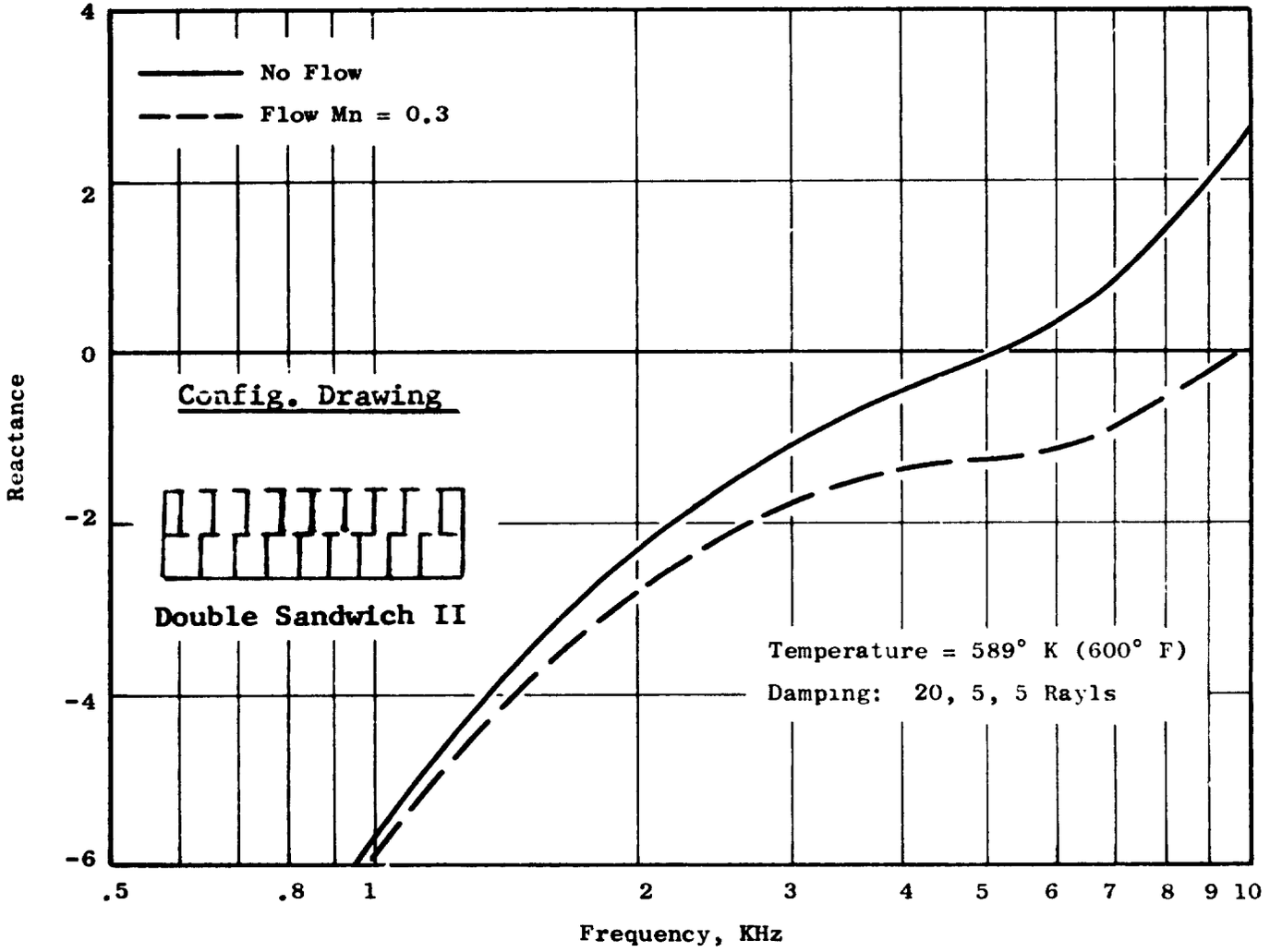

Figure 65. Calculated Reactance of Double Sandwich II with Low Damping at Turbine Temperatures.

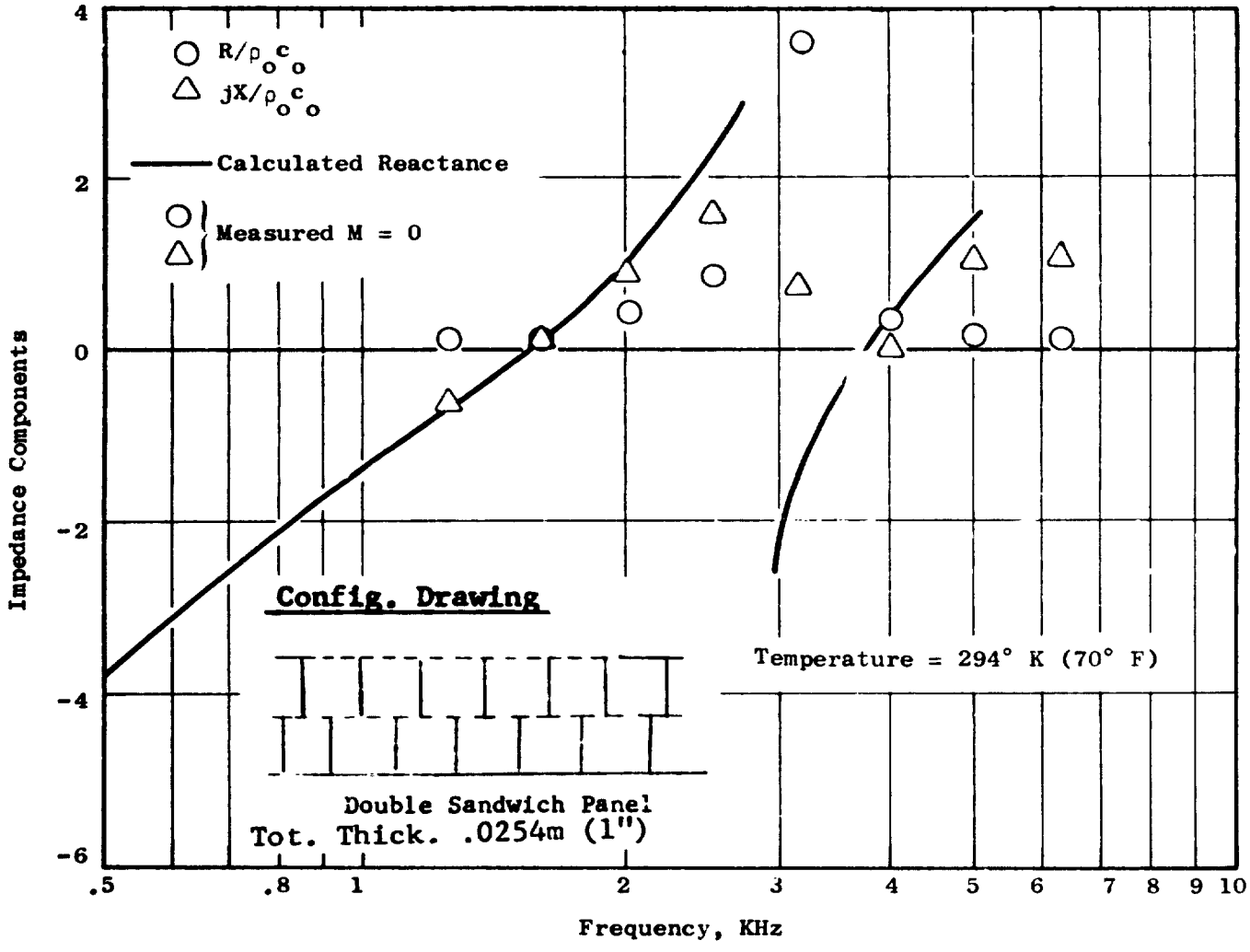

Figure 66. Impedance Components of Double Sandwich III at Ambient Conditions.

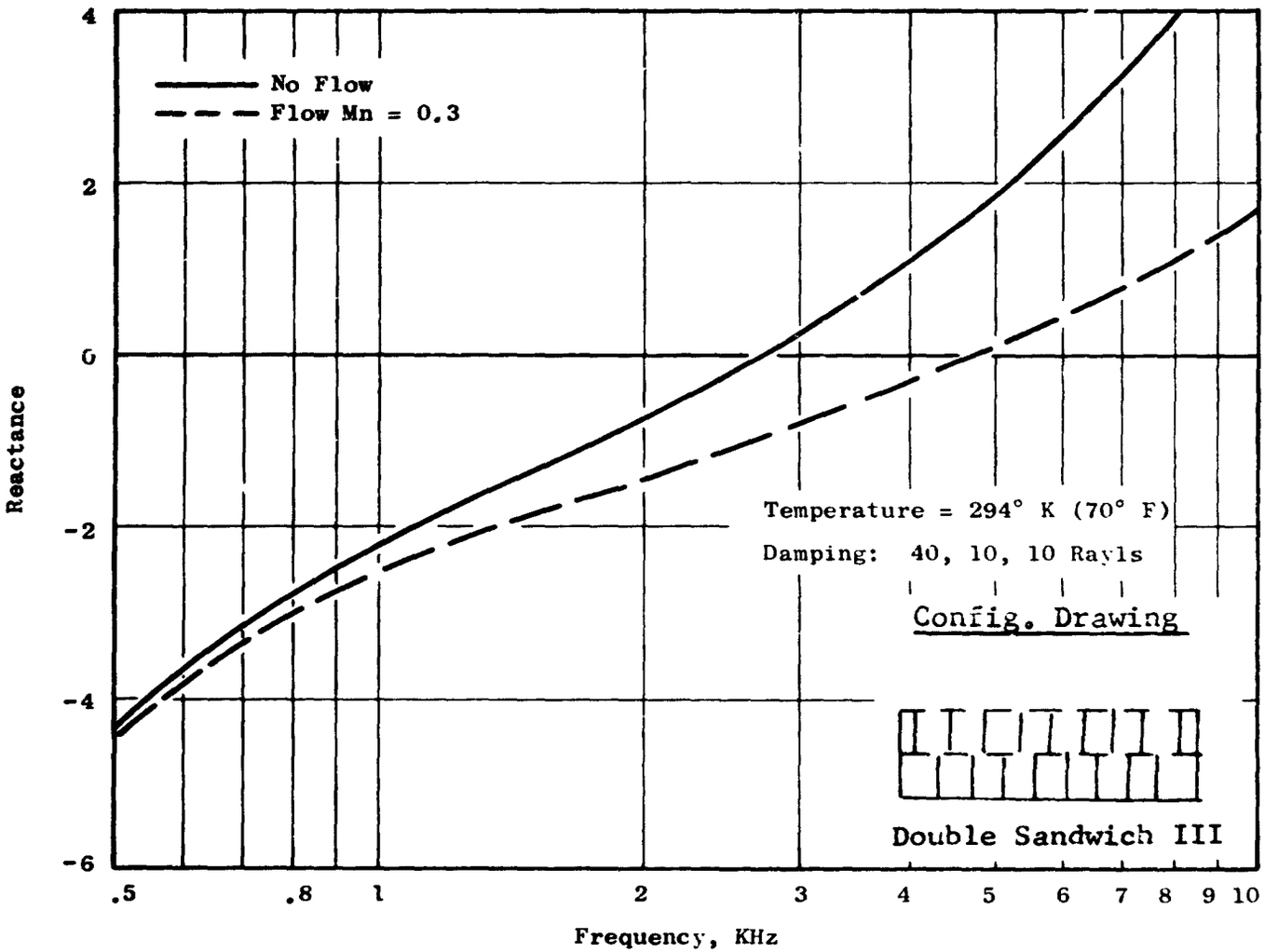

Figure 67. Calculated Reactance of Double Sandwich III with High Damping at Turbine Temperatures.

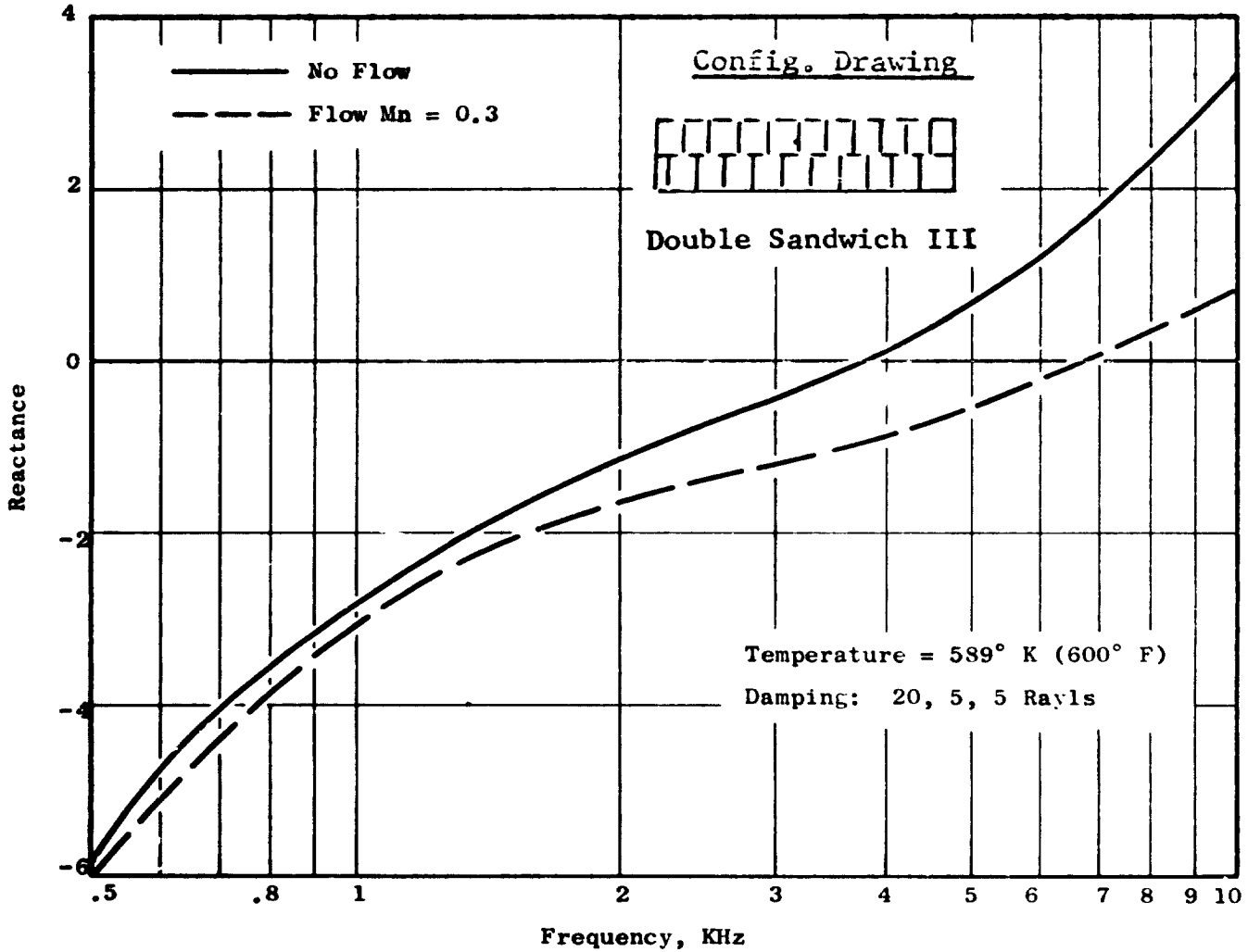

Figure 68. Calculated Reactance of Double Sandwich III with Low Damping at Turbine Temperatures.

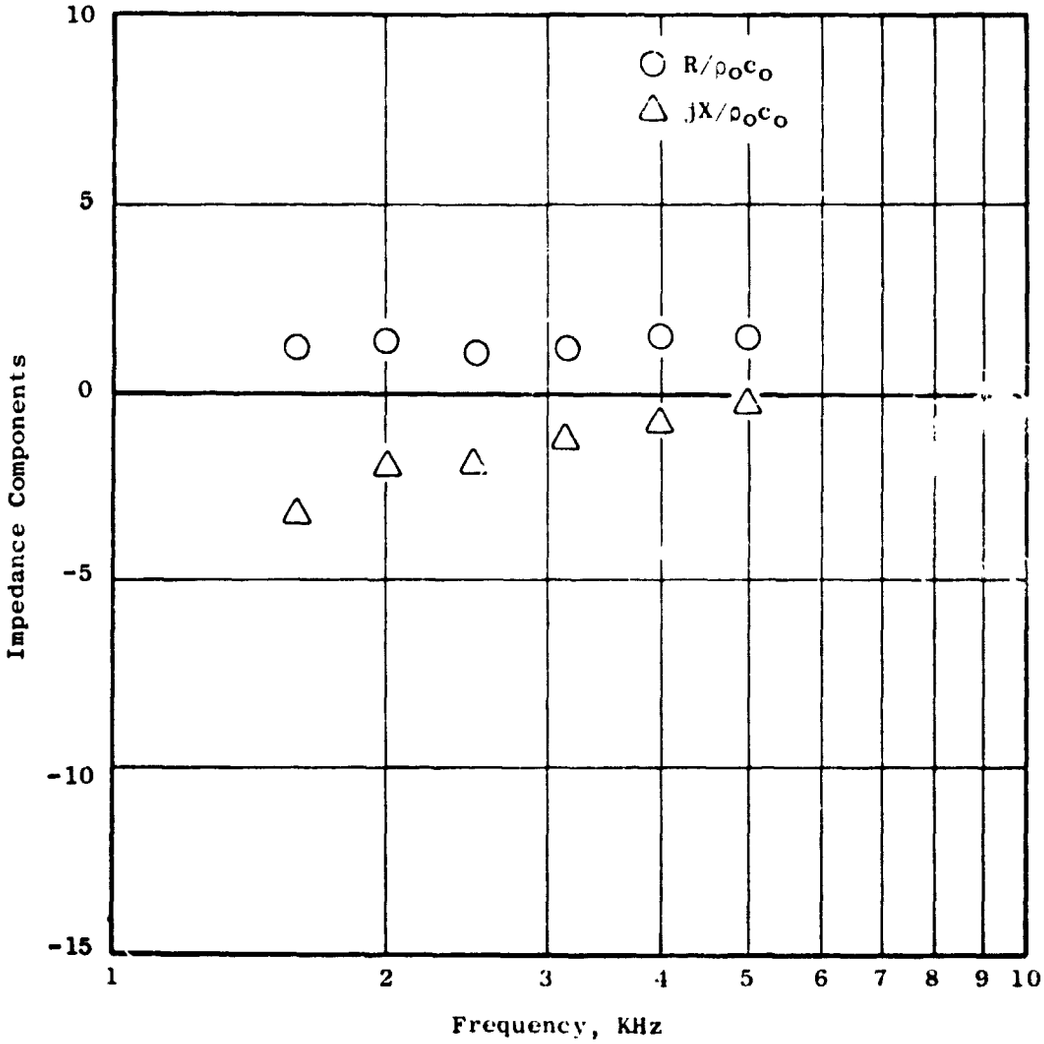

Figure 69. Impedance Components of CER-VIT No. 1 (40% Porosity Facing, 0.127m (1/2 inch) Thick).

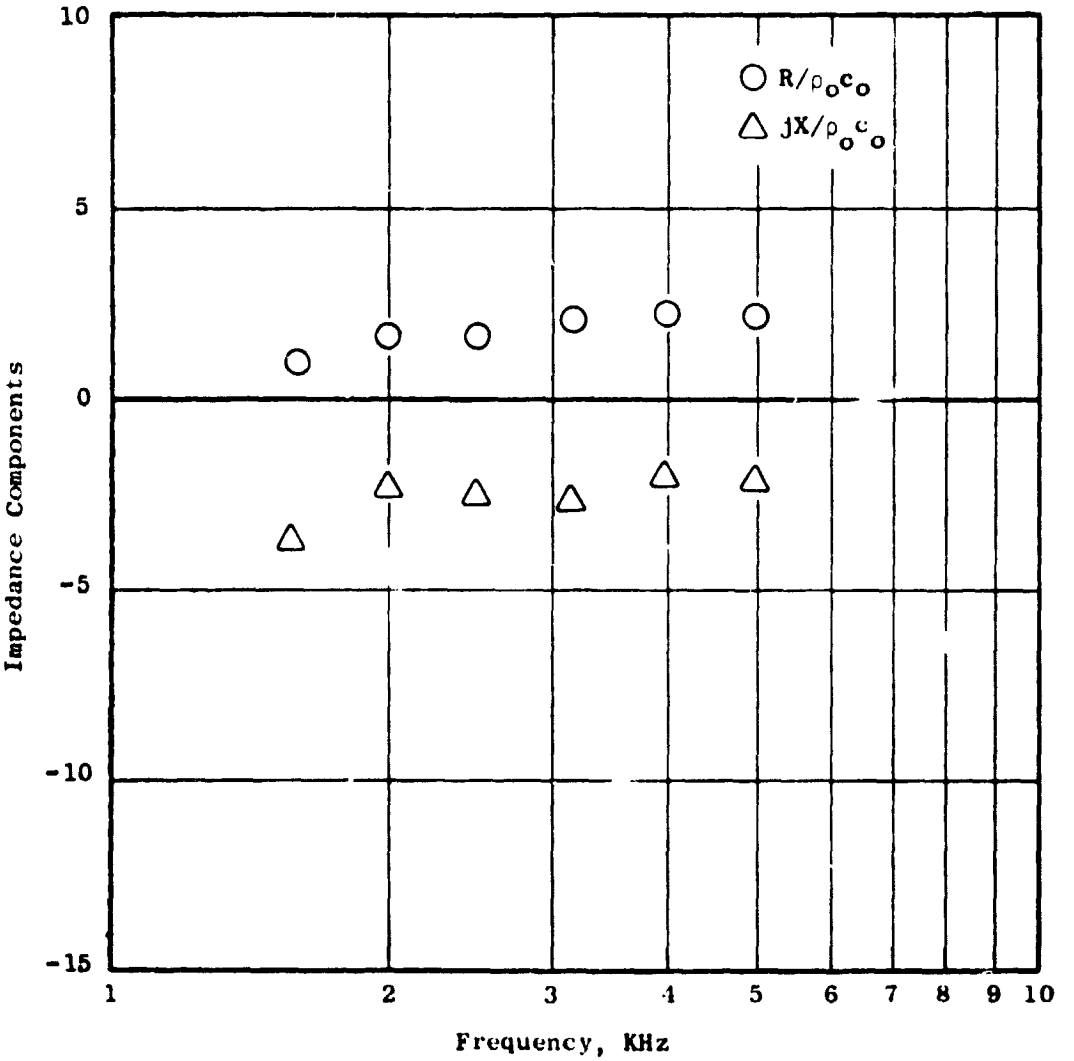

Figure 70. Impedance Components of CER-VIT No. 2 (40% Porosity Facing, .0063m (1/4 inch) Thick).

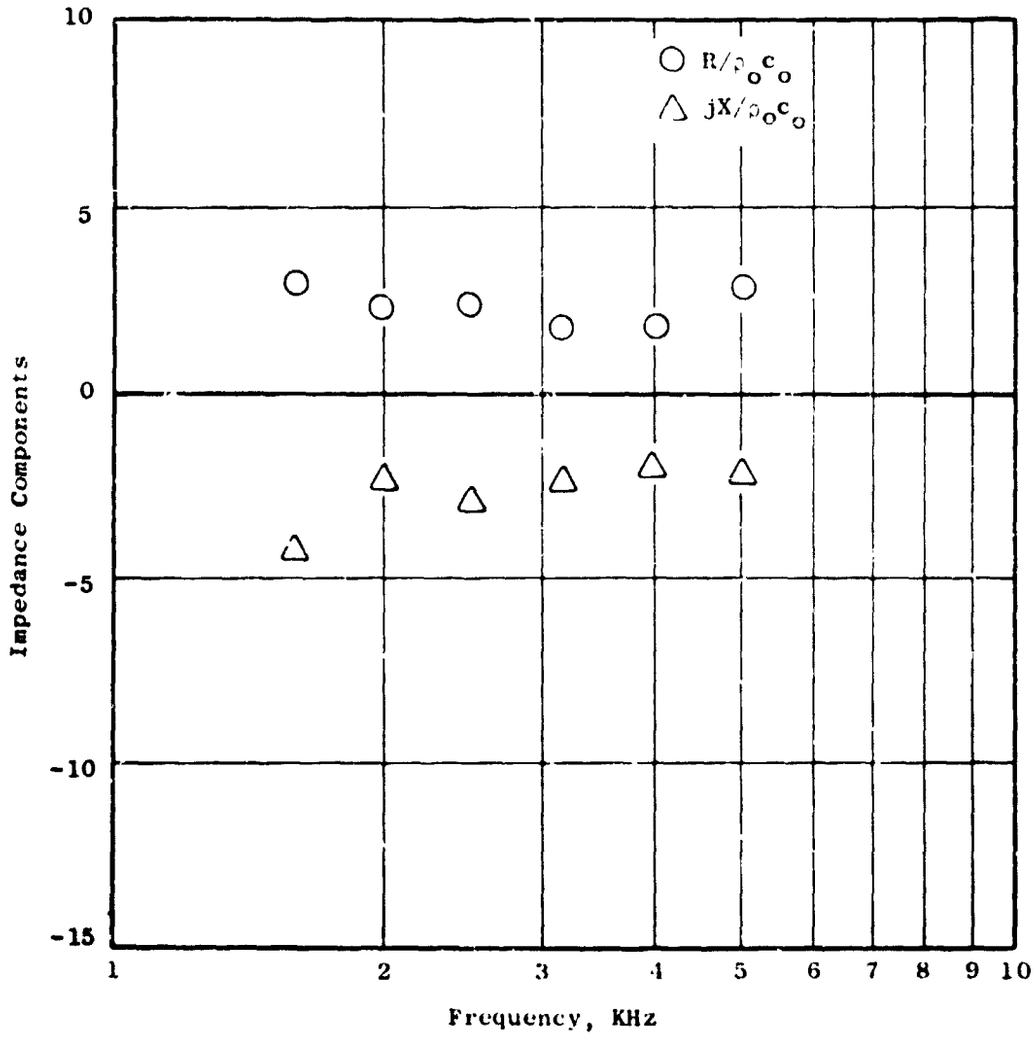

Figure 71. Impedance Components of CER-VIT No. 3 (20% Porosity Facing, .127m (1/2 inch) Thick).

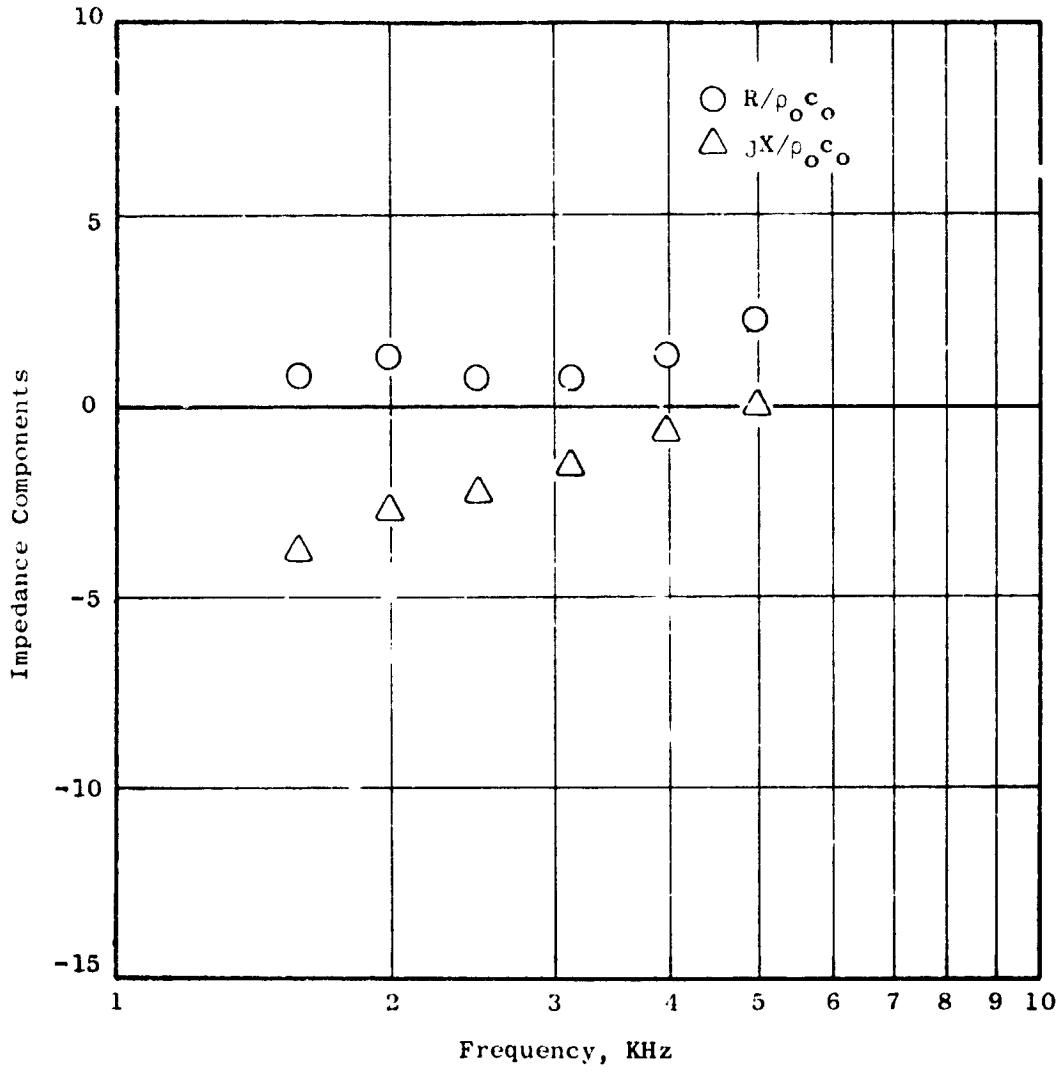

Figure 72. Impedance Components of CER-VIT No. 4 (20% Porosity Facing, .0063m (1/4 inch) Thick).

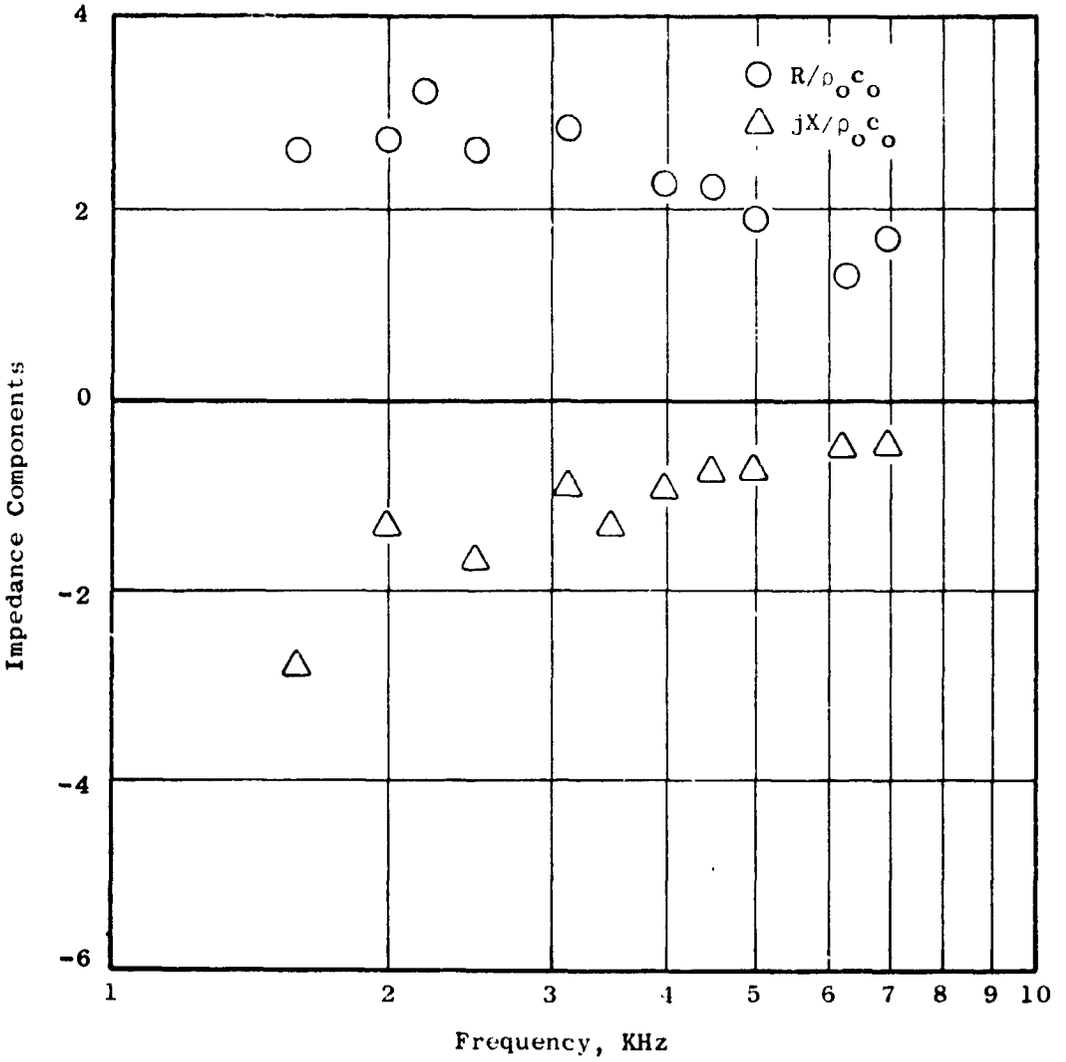

Figure 73. Impedance Components of Cerafelt (22.5% Porosity Facing, .038m (1.5 inch) Thick).

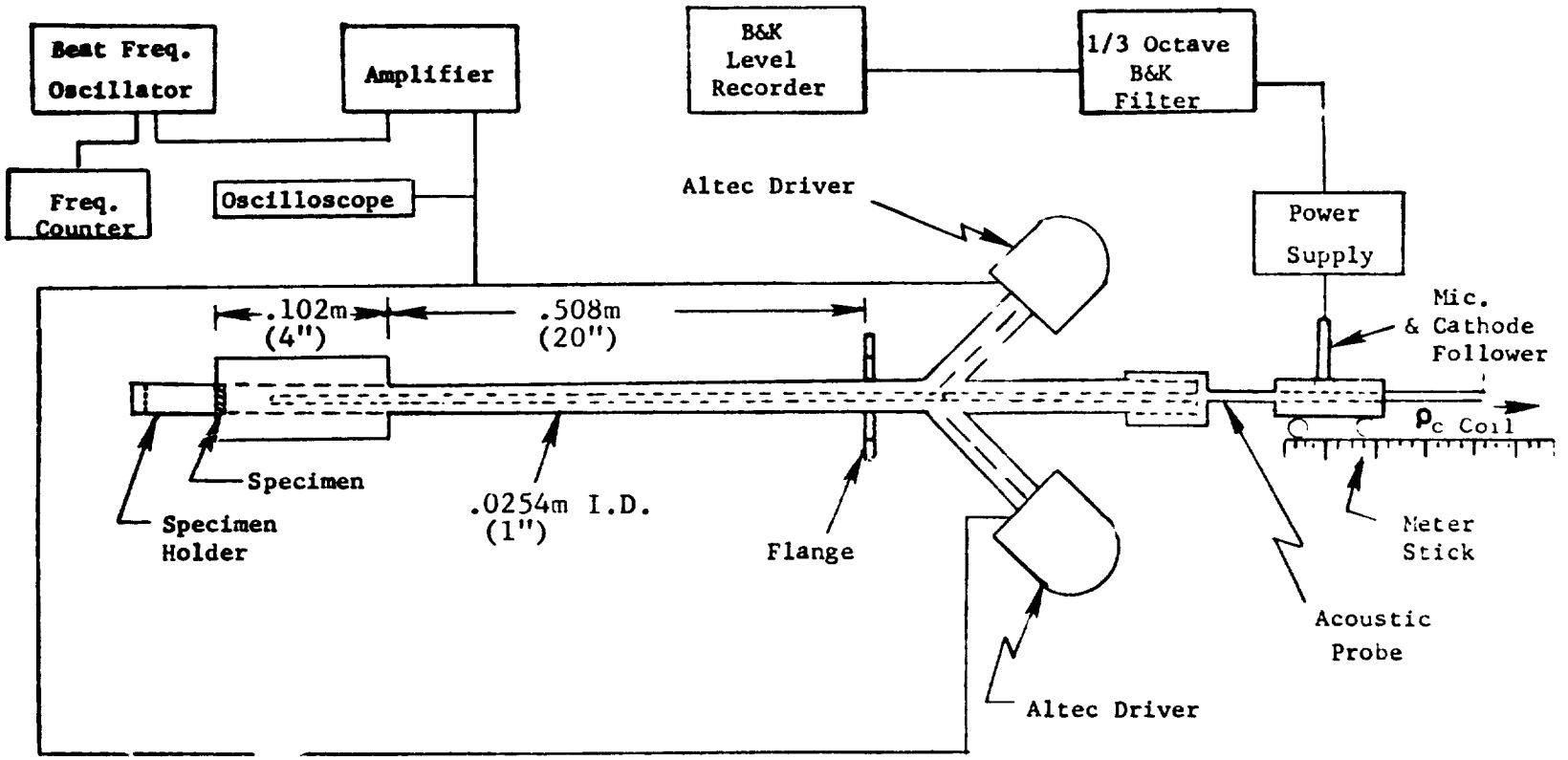

Figure 74. High Intensity Impedance Tube Facility.

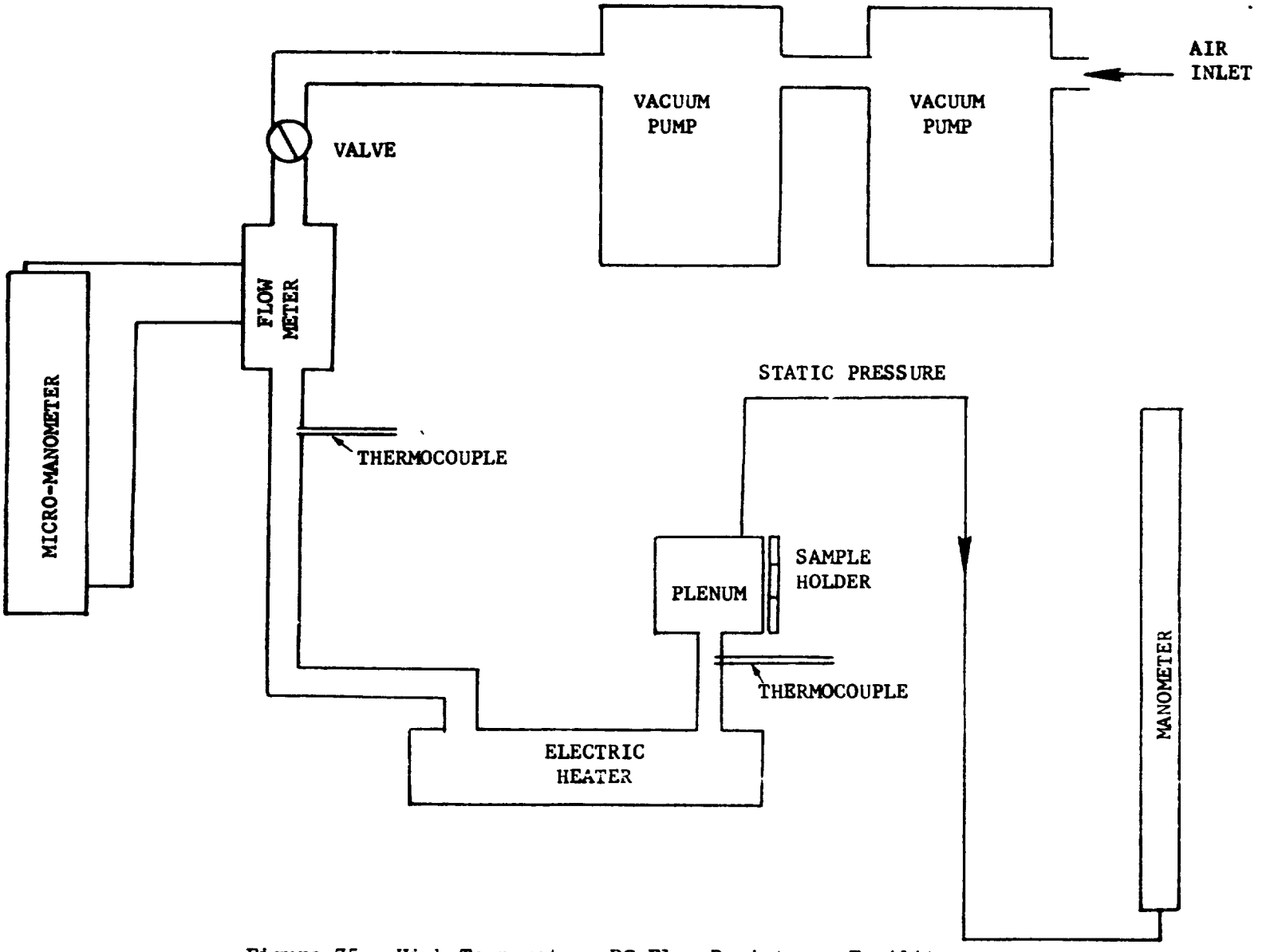

Figure 75. High Temperature DC Flow Resistance Facility.

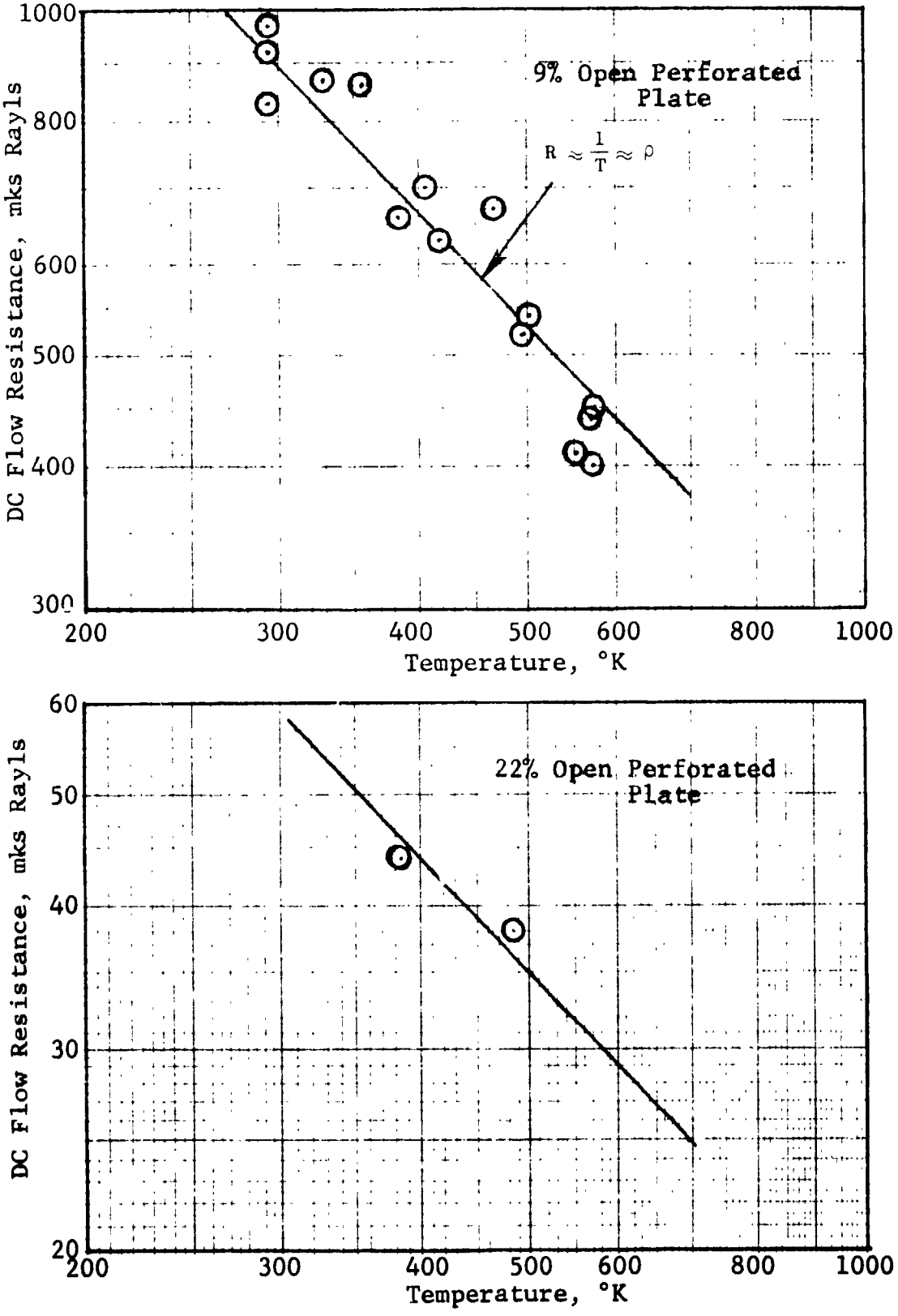

Figure 76. DC Flow Resistance Vs. Temperature for Perforated Plates.

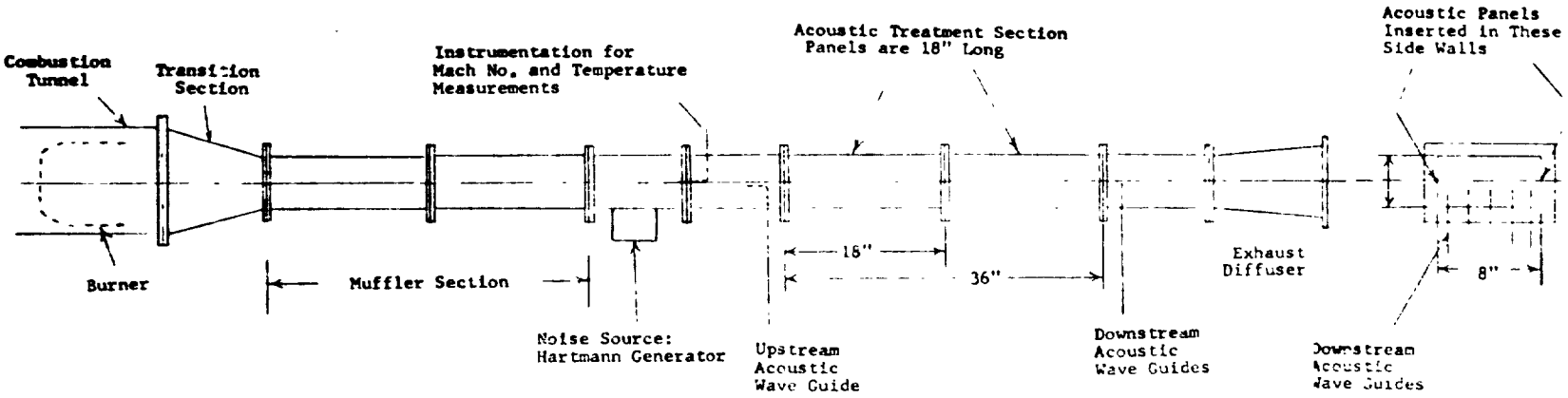

Figure 77. Schematic of High Temperature Acoustic Duct Facility In-Duct Measurements with Acoustic Wave Guides.

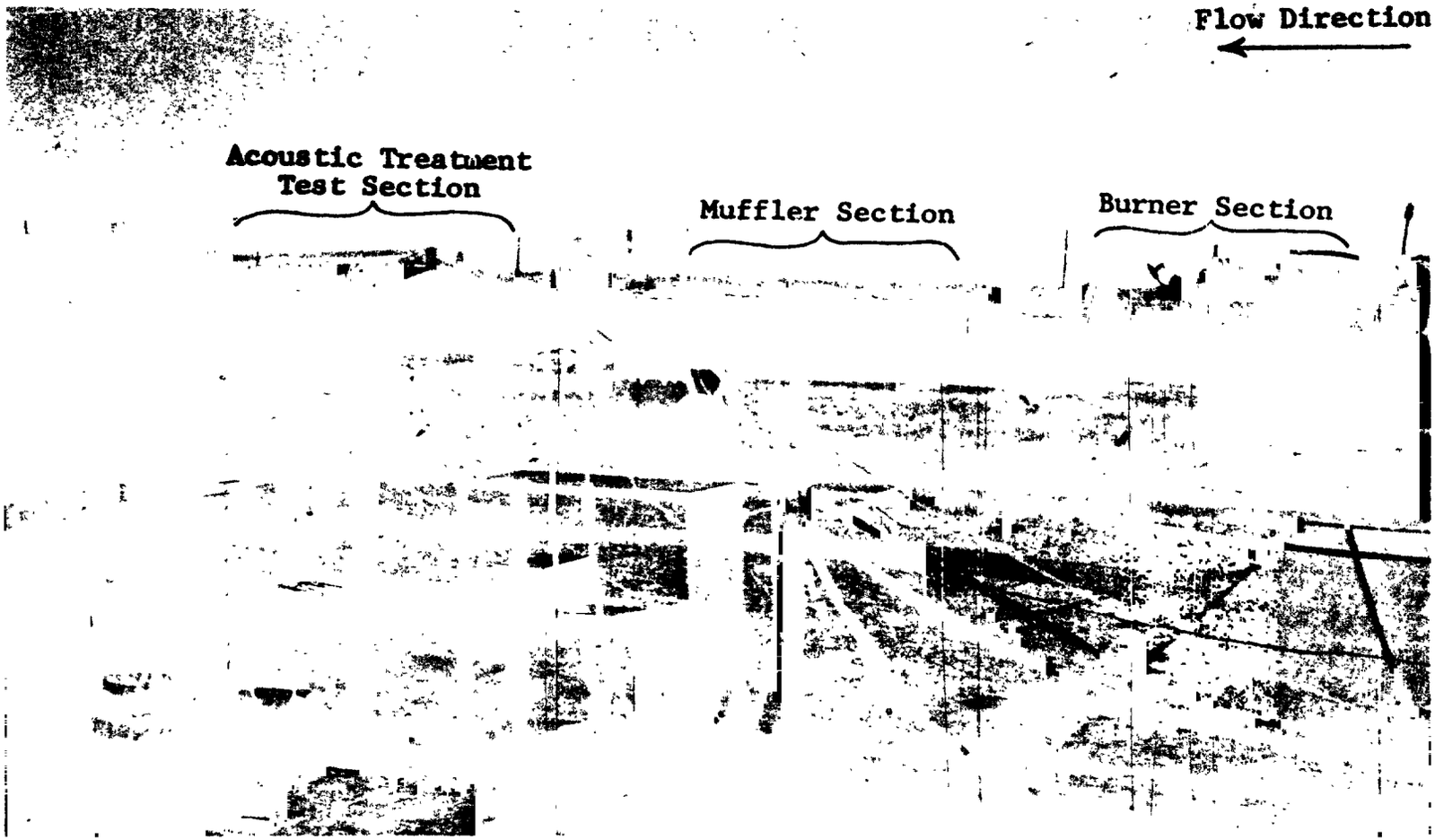

Figure 78. High Temperature Acoustic Duct Facility Component Details.

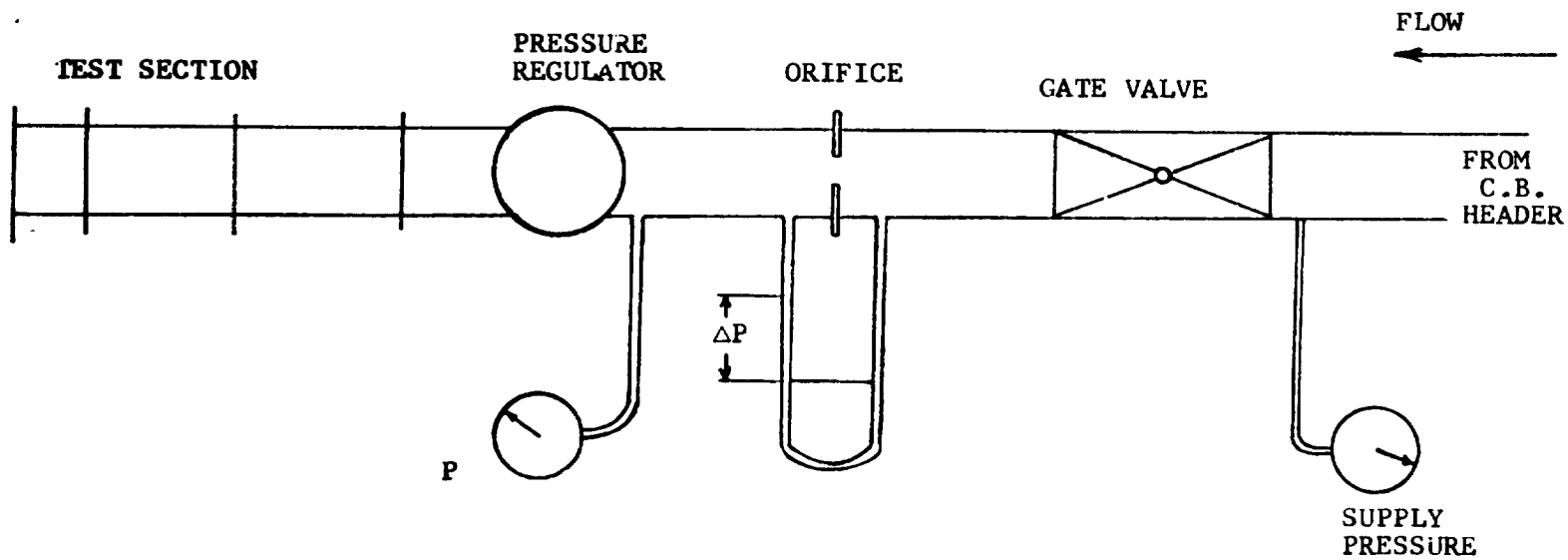

Figure 79. Air Supply Schematic.

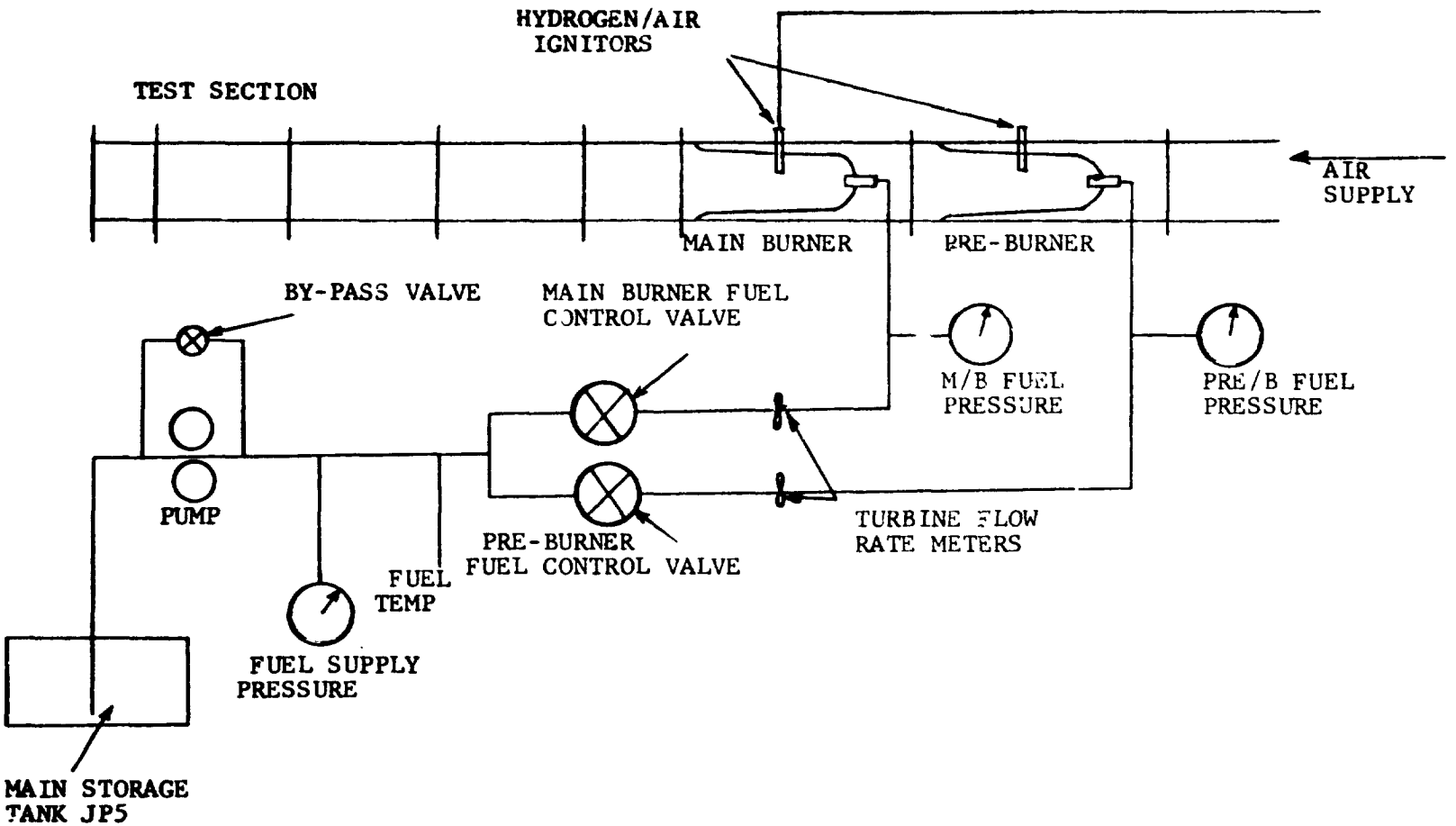

Figure 80. Fuel Supply Schematic.

Figure 81. High Temperature Acoustic Duct View of Test Section Looking Downstream of Flow.

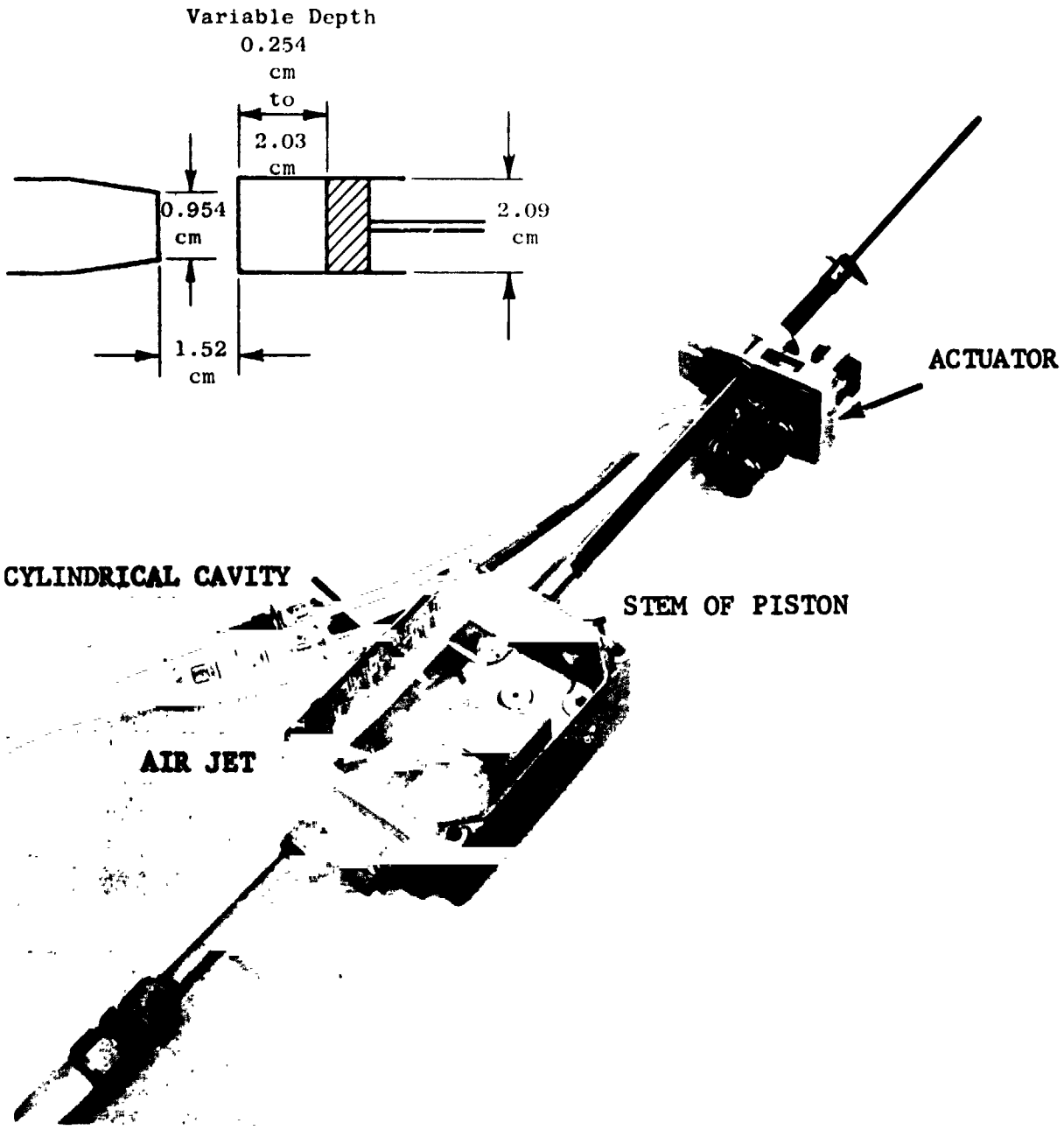

Figure 82. Hartmann Noise Generator.

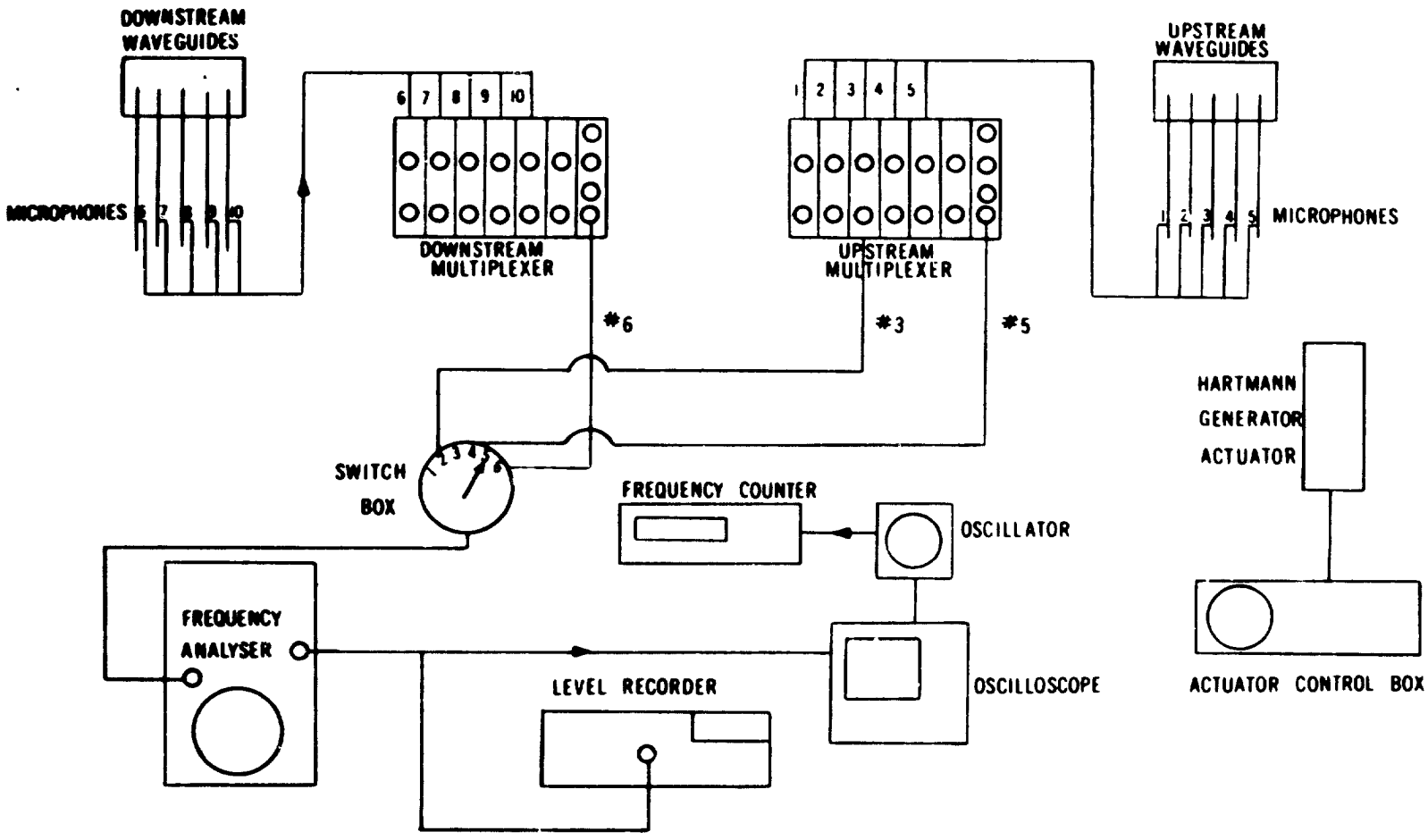

Figure 83. Schematic of High Temperature Acoustic Duct Instrumentation.

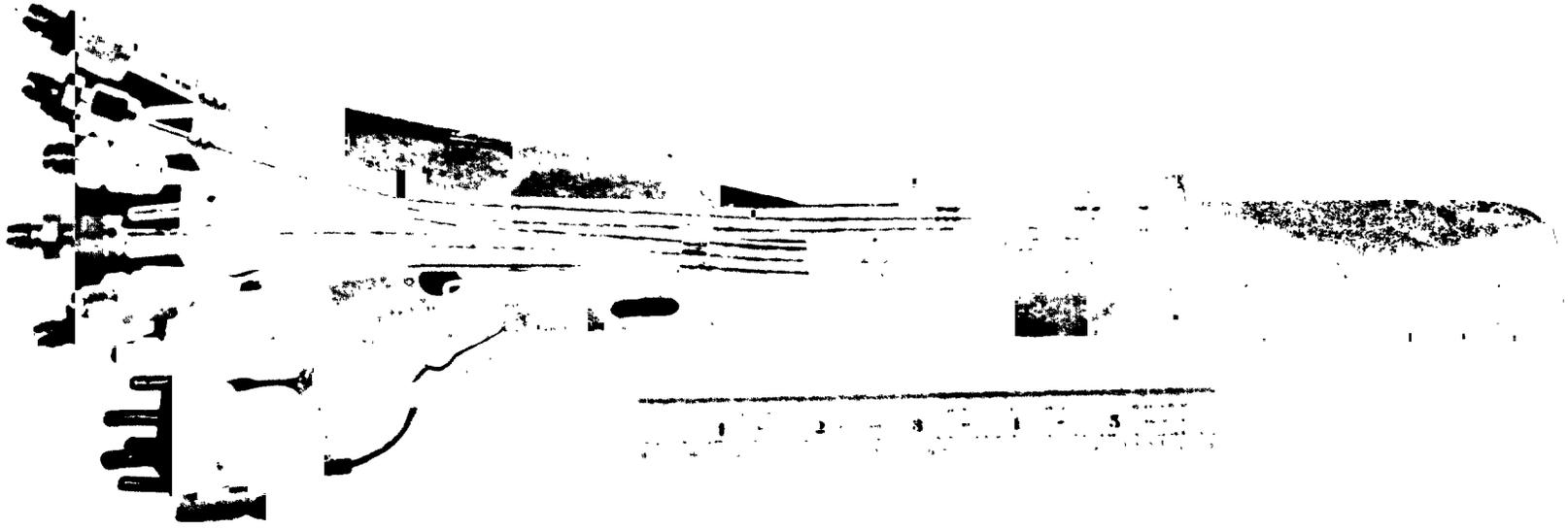

Figure 84. High Temperature Acoustic Duct Facility Calibration Rake.

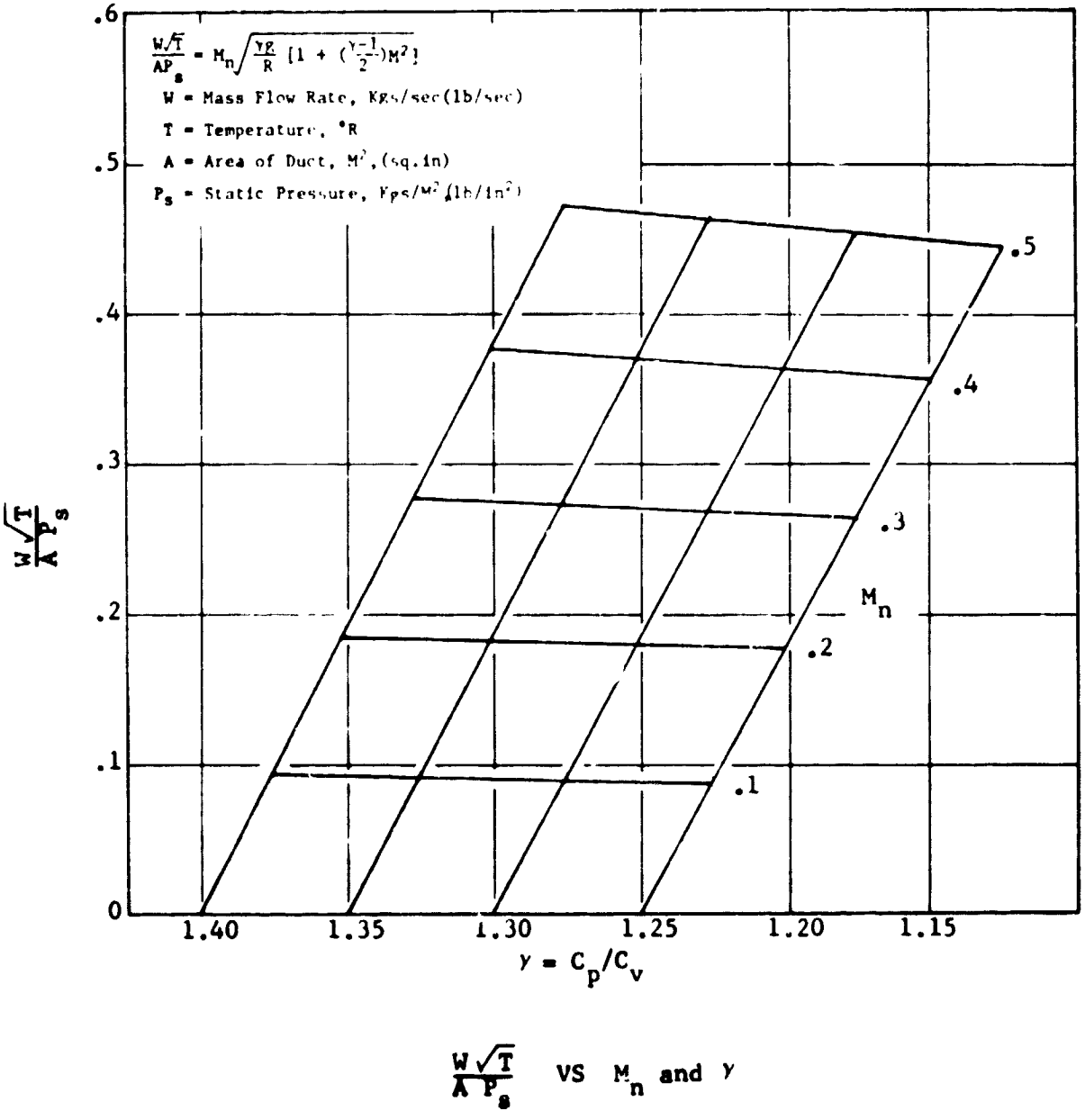

$\frac{W\sqrt{T}}{A P_s}$ VS M_n and γ

Figure 85. Mass Flow Parametric Equation.

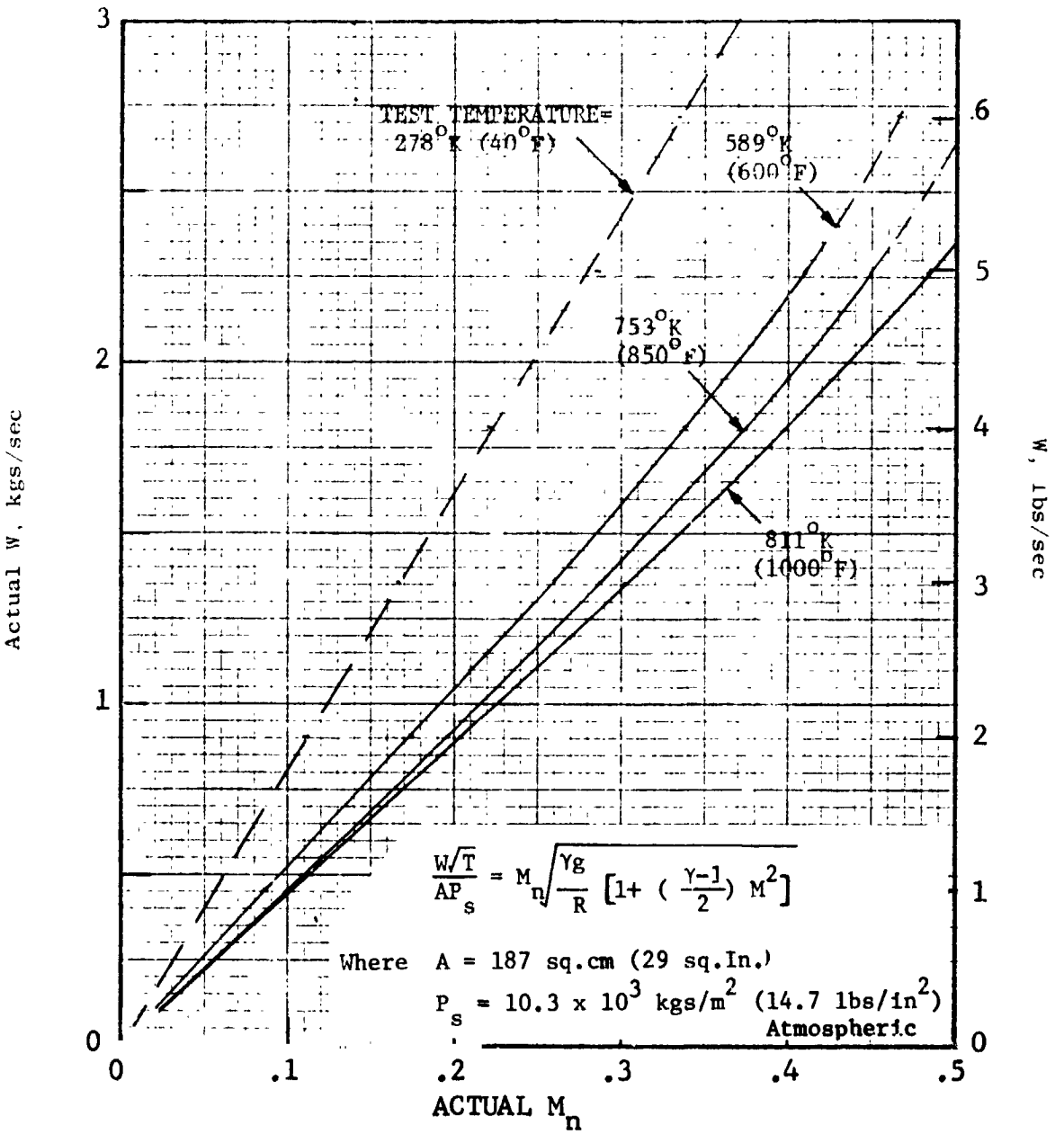

Figure 86. Summary of Required Air Mass Flow Rate Vs. Actual Mach Number.

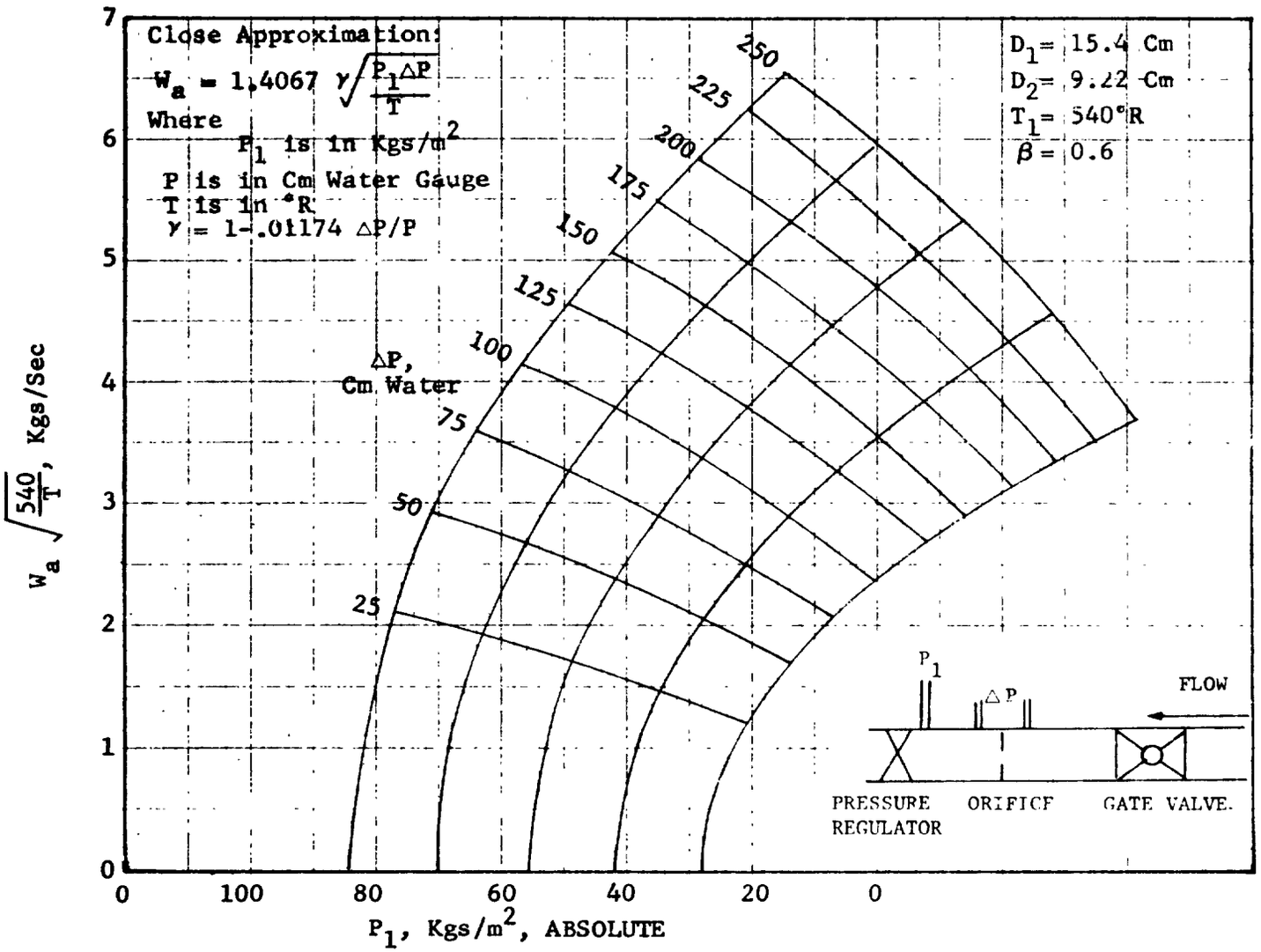

Figure 87. Carpet Plot of W_a Vs. P1 and ΔP.

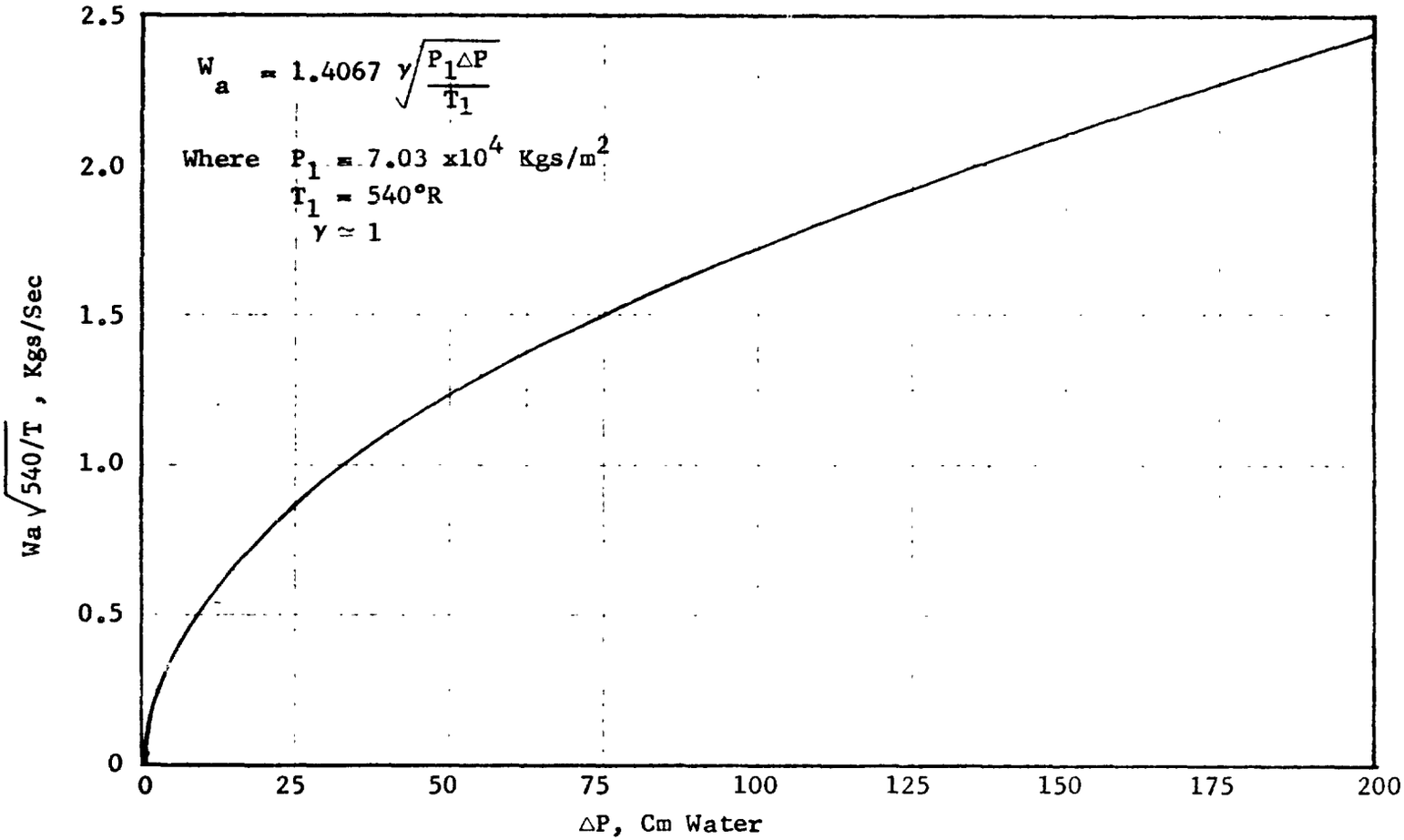

Figure 88. Flow Thru Orifice when $P_1 = 7.03 \times 10^4$ Kgs/m^2.

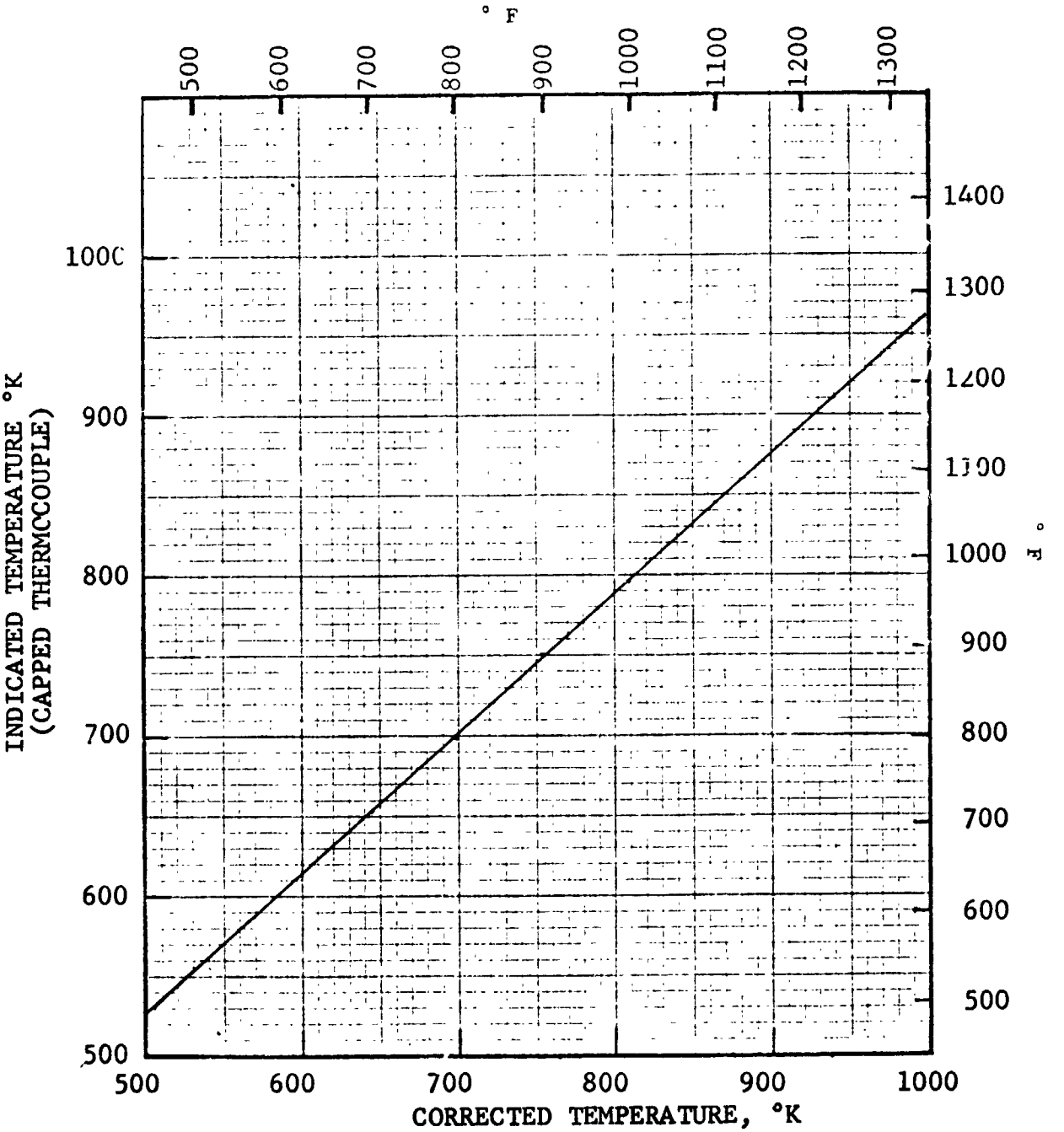

Figure 89. Thermocouple Radiation Correction.

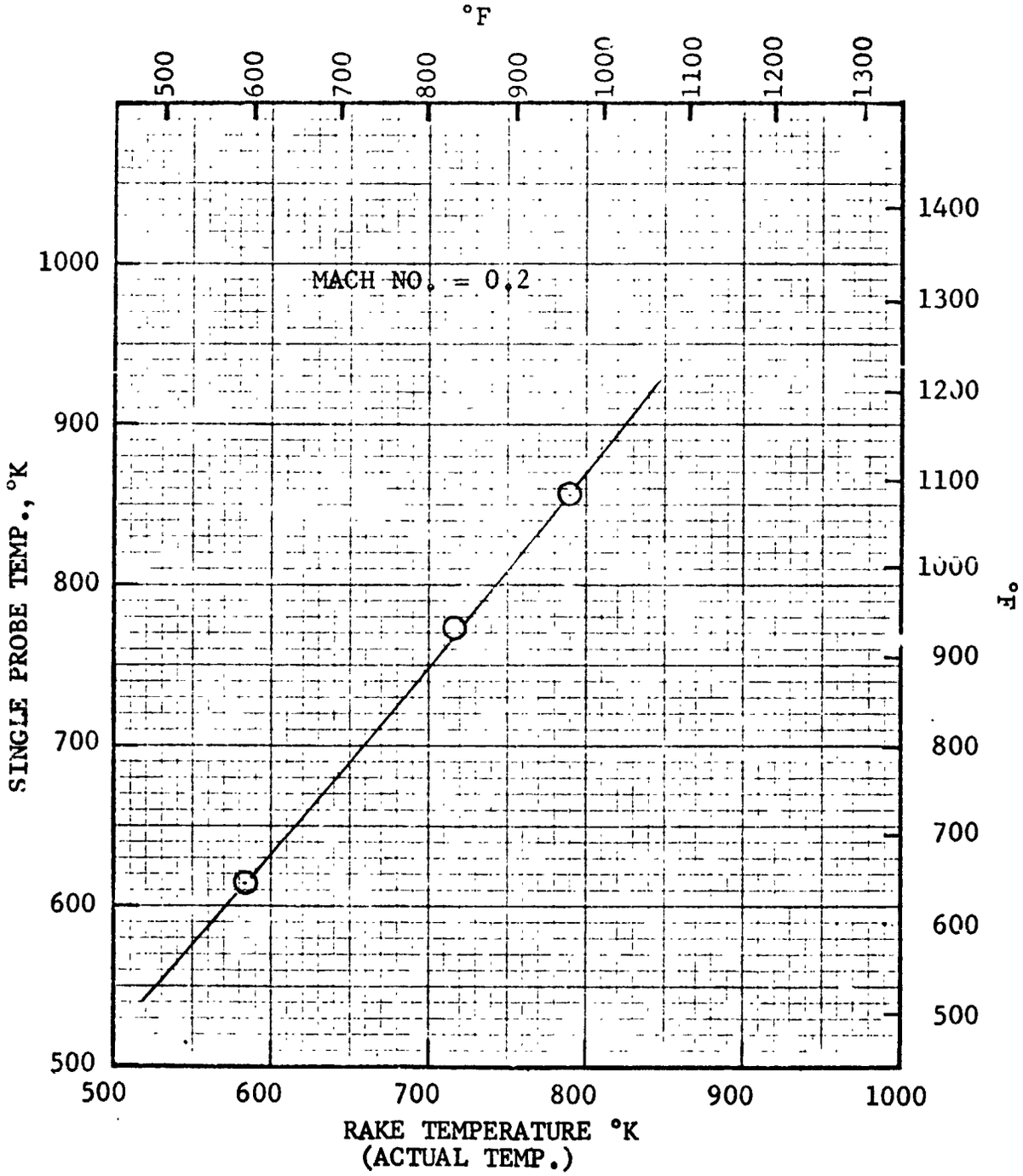

Figure 90. Temperature Relationship of Probes at Mach No. = 0.20.

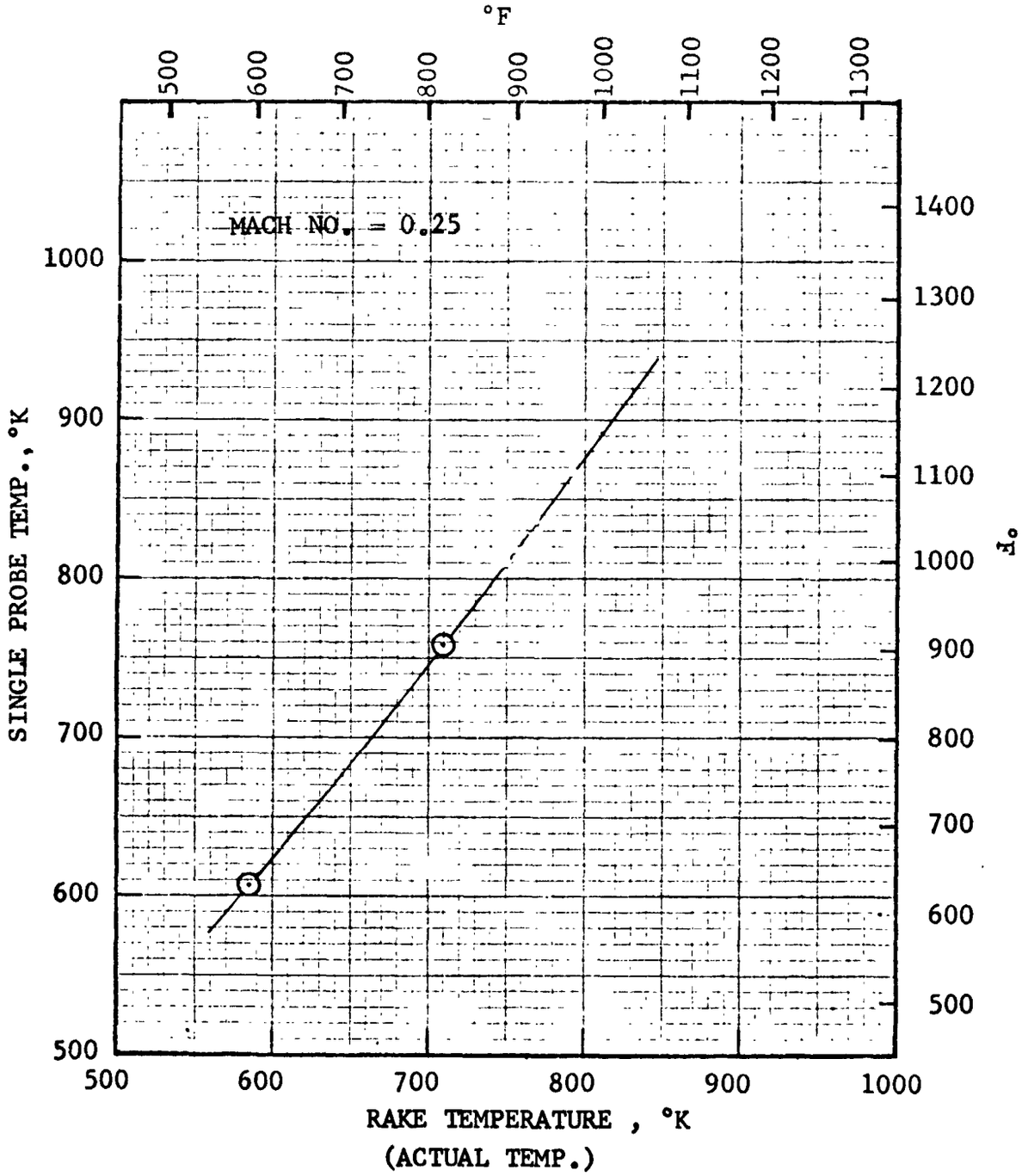

Figure 91. Temperature Relationship of Probes at Mach No. = 0.25.

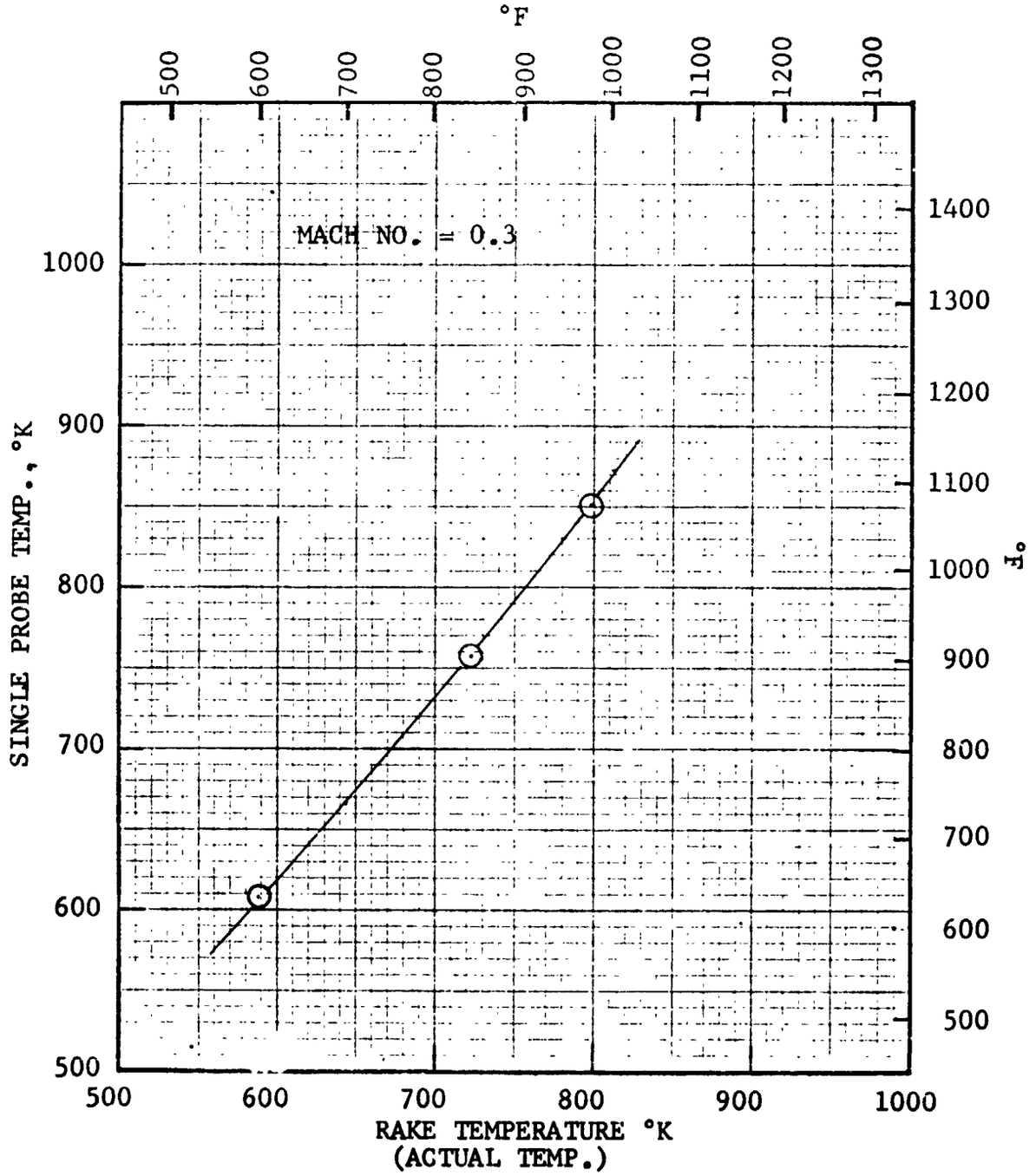

Figure 92. Temperature Relationship of Probes at Mach No. = 0.30.

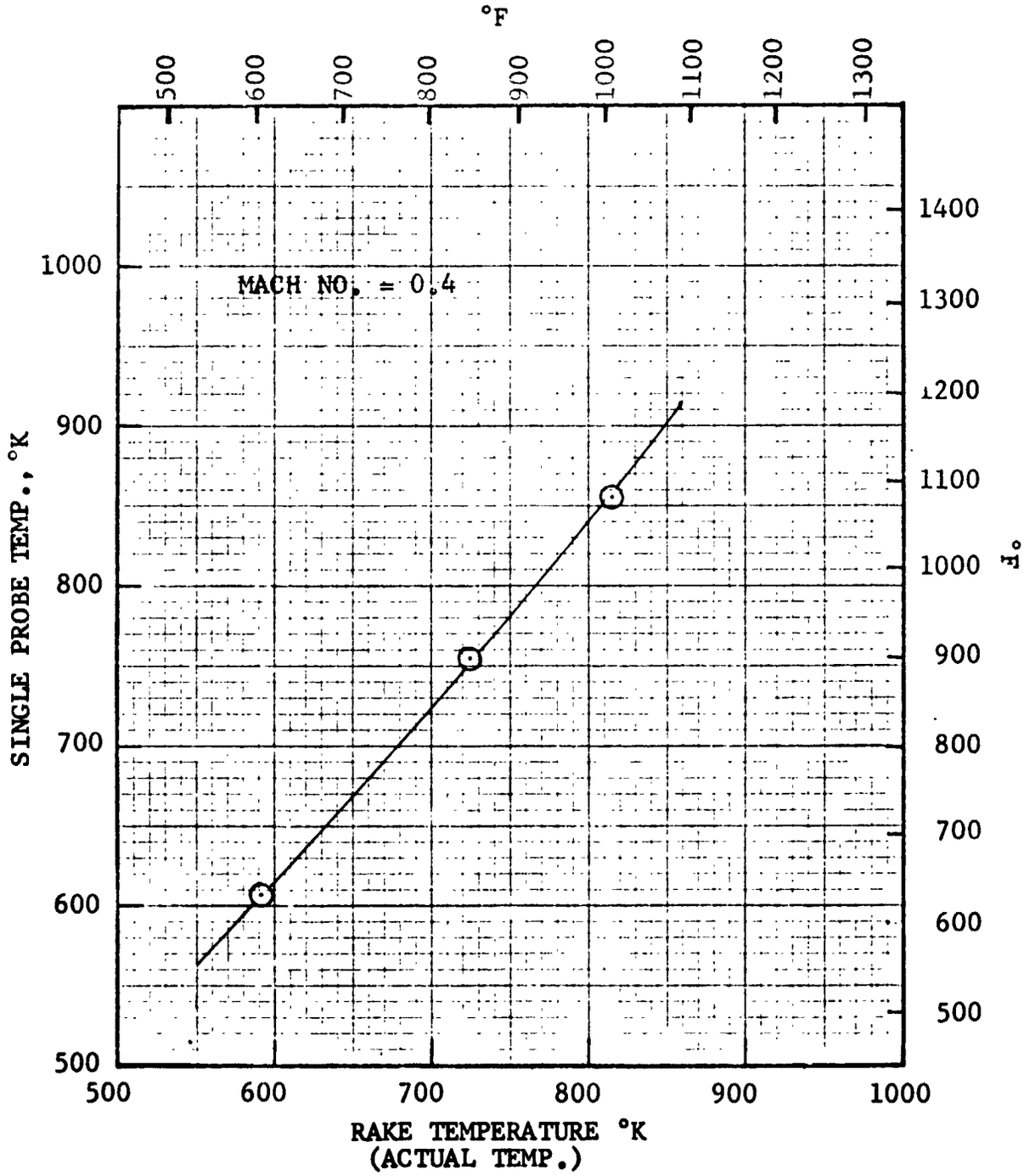

Figure 93. Temperature Relationship of Probes at Mach No. = 0.40.

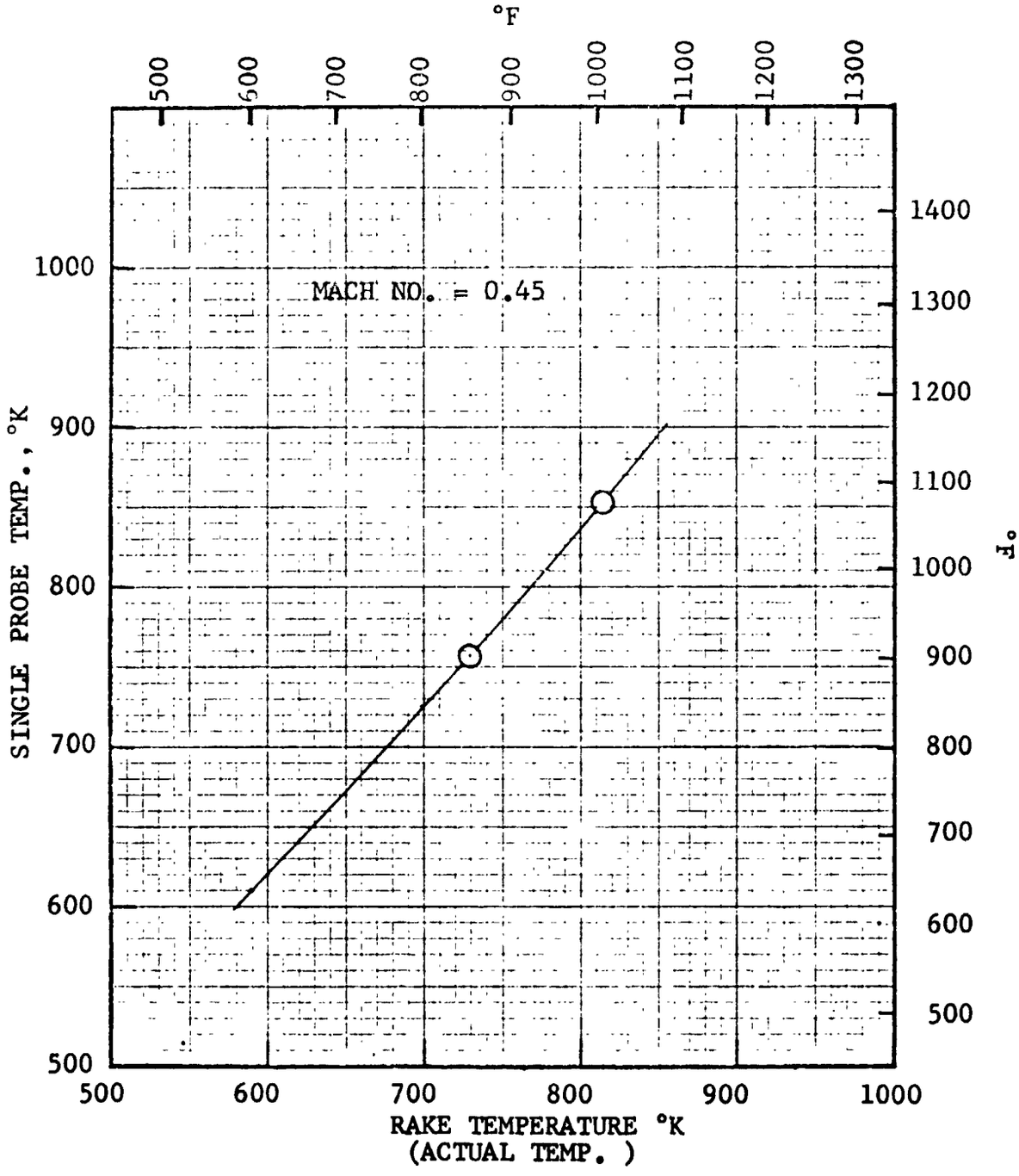

Figure 94. Temperature Relationship of Probes at Mach No. = 0.45.

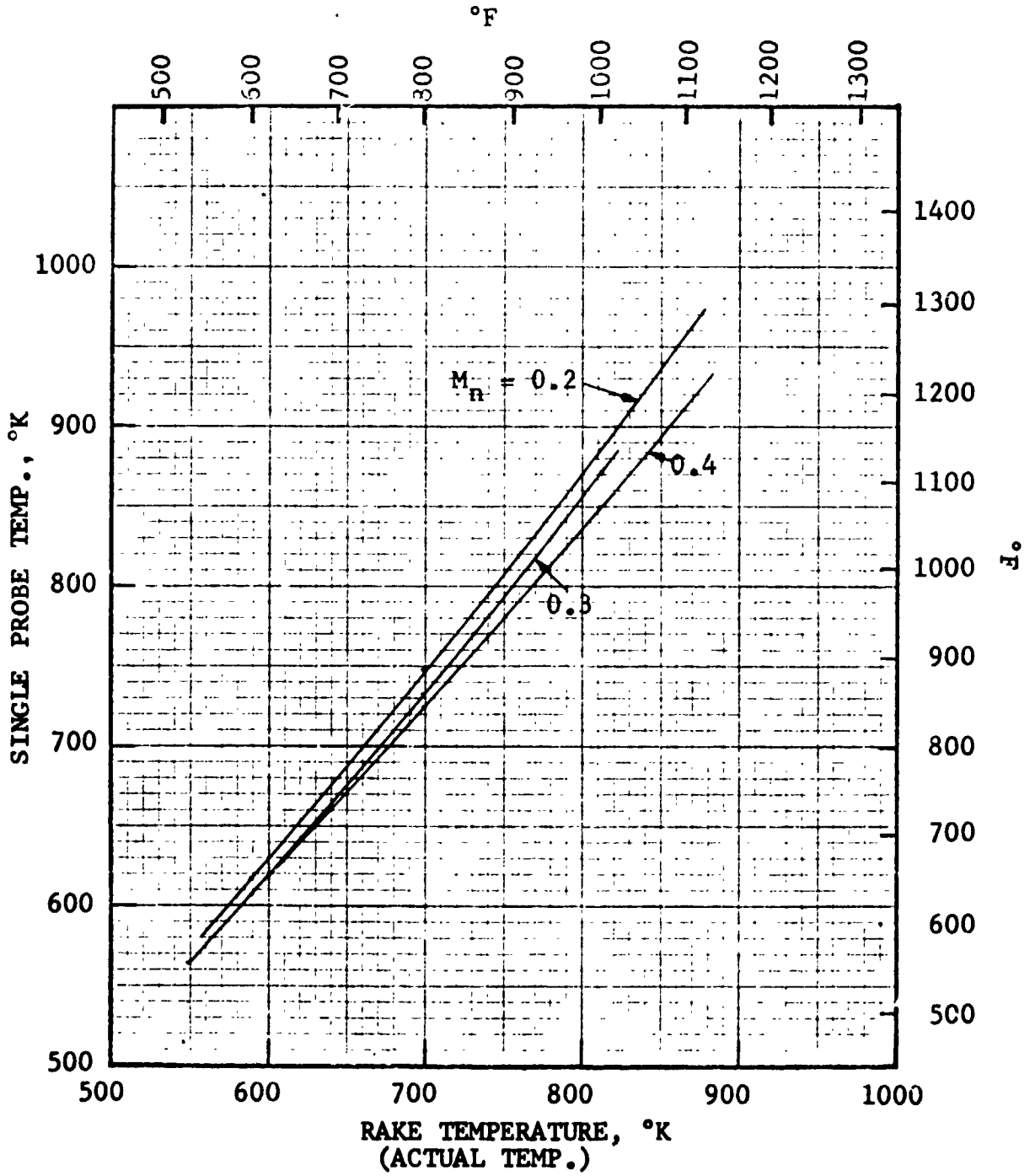

Figure 95. Summary of Probe Temperature Relationships.

REQUIRED TEMPERATURE = 589°K (600°F)

DISTANCE FROM WEST WALL		UPSTREAM PROBE TEMPERATURE		DOWNSTREAM RAKE TEMPERATURES							
Cm	Inches	°K	°F								
1.27	.25	610	635	°K	558	555	555	548	548	510	520
				°F	545	542	542	540	540	460	475
2.54	1.00	610	635	°K	581	574	574	576	576	573	564
				°F	587	582	582	578	578	572	555
5.10	2.00	612	638	°K	587	586	587	580	577	576	566
				°F	598	596	597	585	580	578	560
7.63	3.00	607	632	°K	589	586	587	580	577	576	566
				°F	600	596	594	585	580	577	560
10.15	4.00	612	638	°K	586	595	592	589	585	583	582
				°F	595	612	606	600	594	590	588
12.70	5.00	610	635	°K	600	600	597	594	589	587	576
				°F	620	619	616	610	600	598	577
15.20	6.00	610	635	°K	607	607	606	602	597	594	582
				°F	634	632	631	624	615	610	588
17.80	7.00	609	634	°K	614	614	616	612	605	602	590
				°F	645	647	650	642	630	624	602
19.70	7.75	609	634	°K	611	610	609	606	604	602	591
				°F	640	635	637	632	628	625	604
AVERAGE VALUE		610	635	°K	585						
				°F	596						
DISTANCE FROM TOP OF DUCT				Cm	1.27	2.54	3.81	5.10	6.35	7.63	8.90
				In.	0.50	1.00	1.50	2.00	2.50	3.00	3.50

Figure 96. Duct Temp ature Profile.

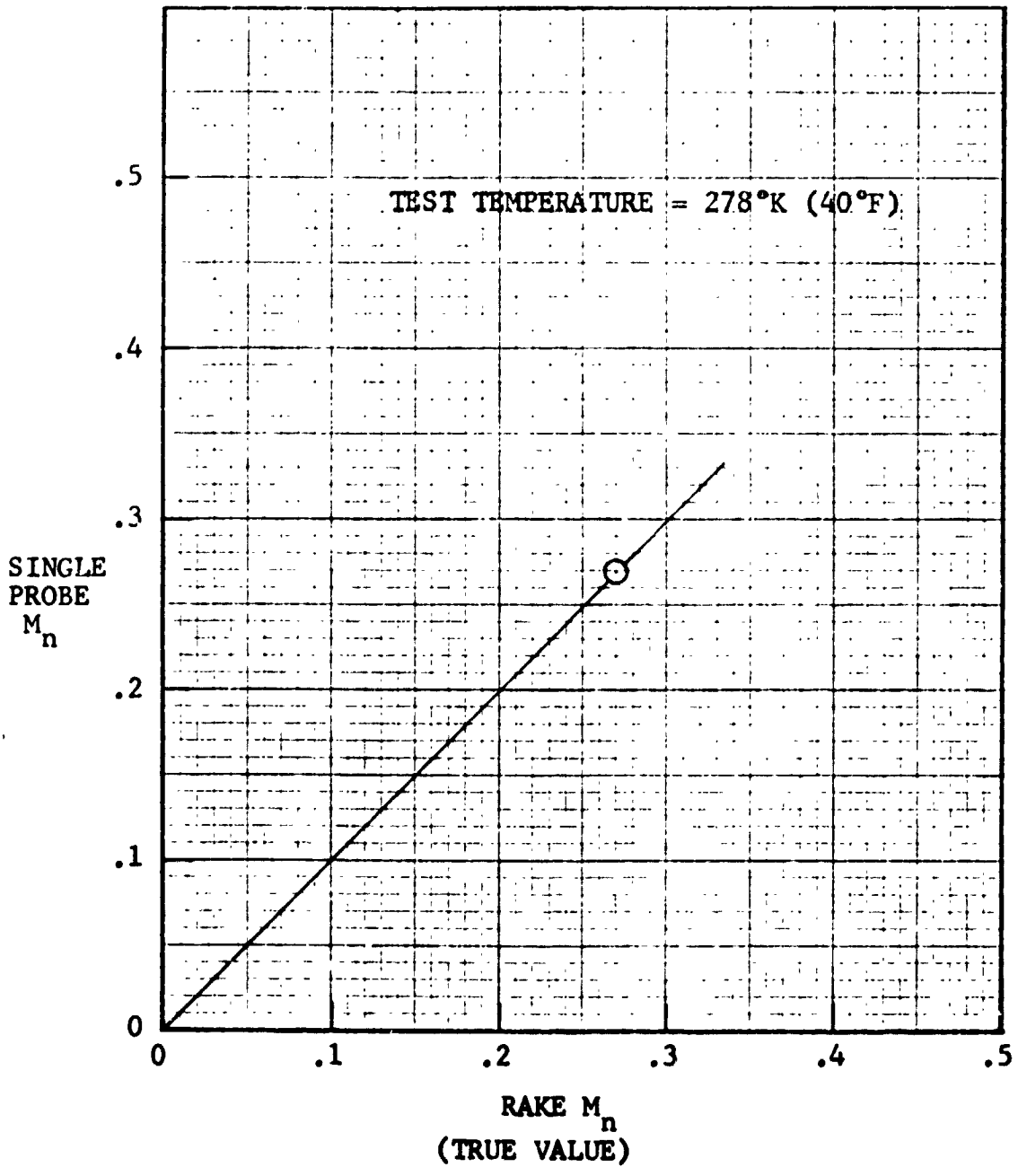

Figure 97. Mach No. Relationship at 278° K (40° F).

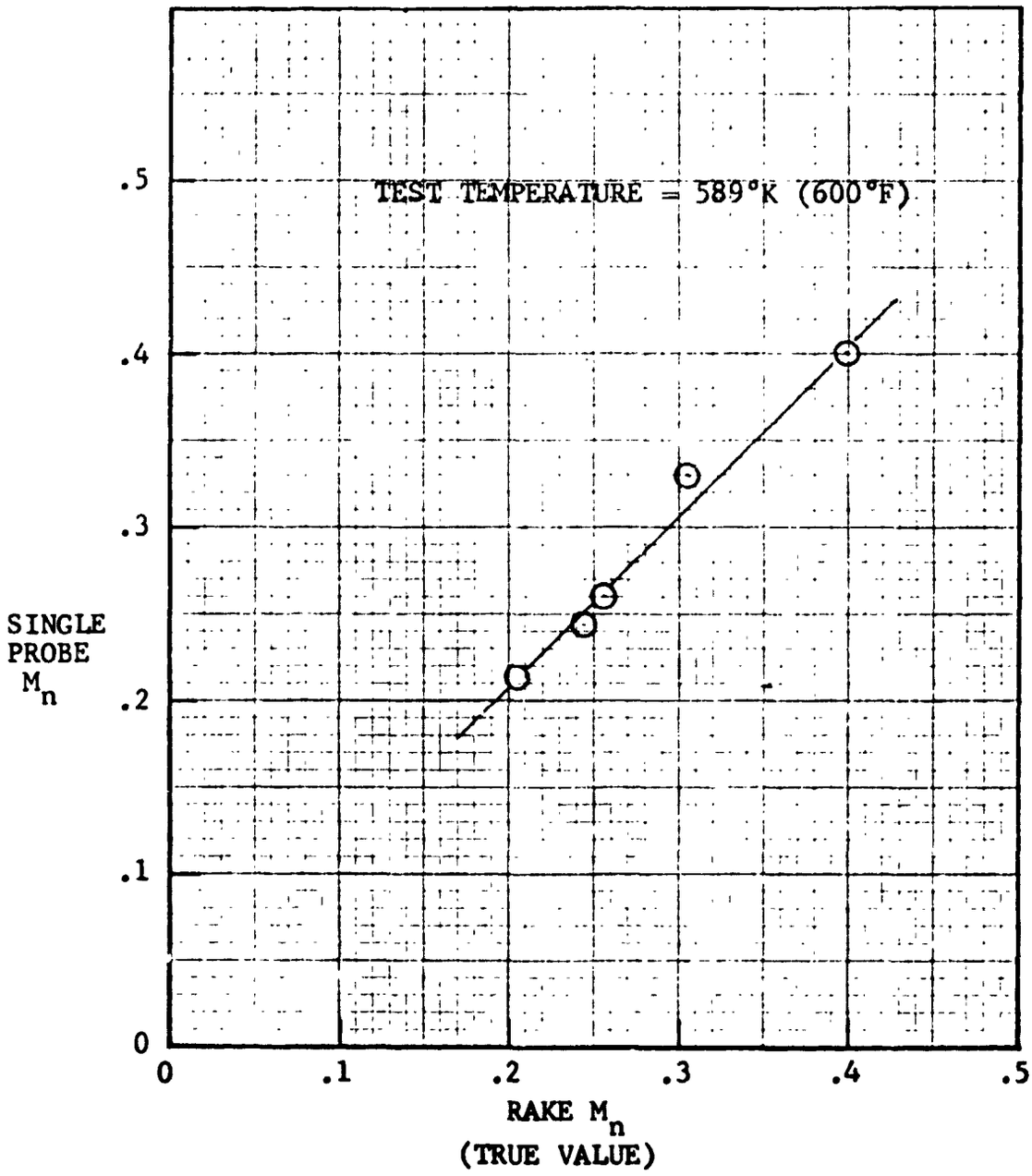

Figure 98. Mach No. Relationship at 589° K (600° F).

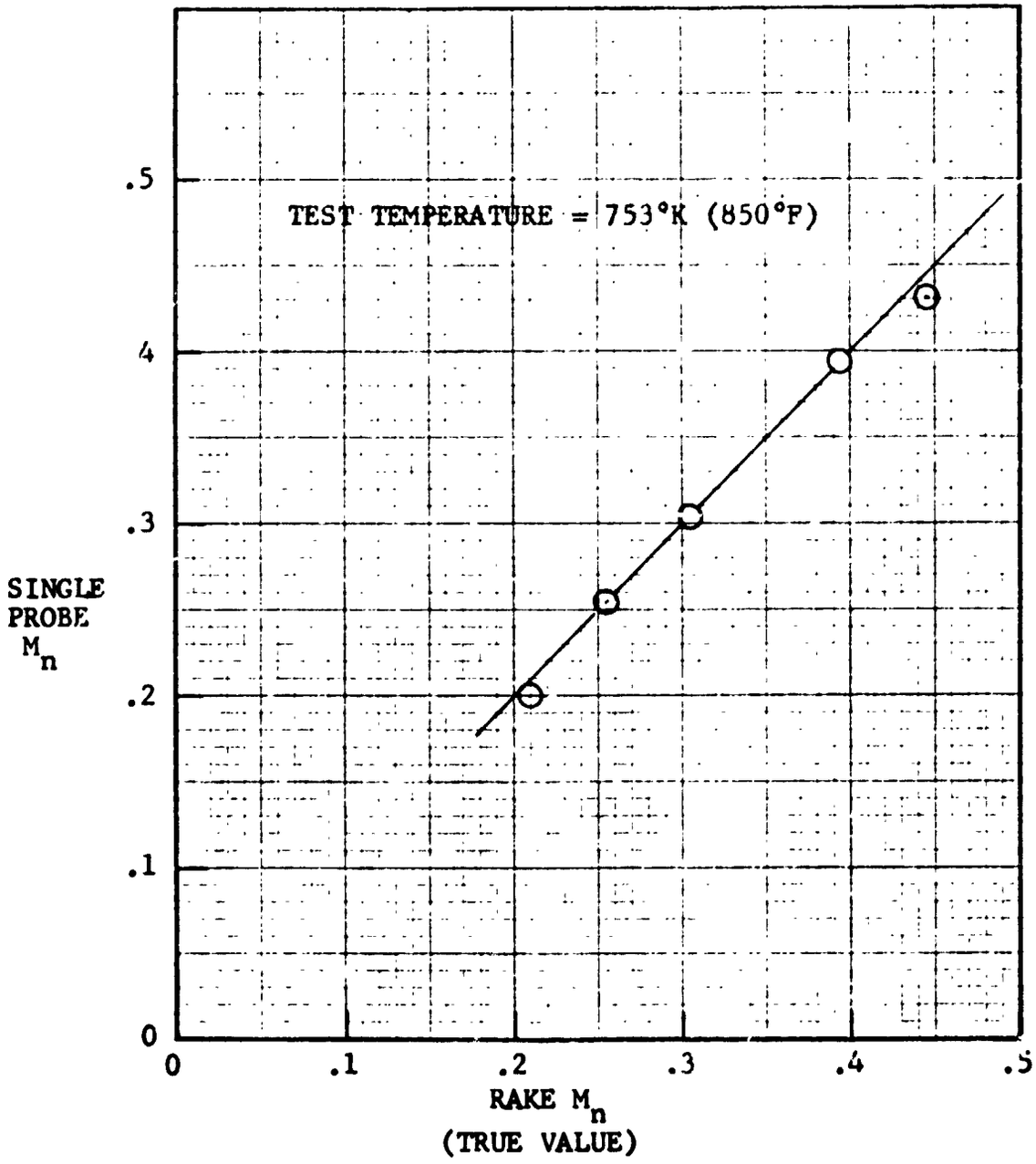

Figure 99. Mach No. Relationship at 753° K (850° F).

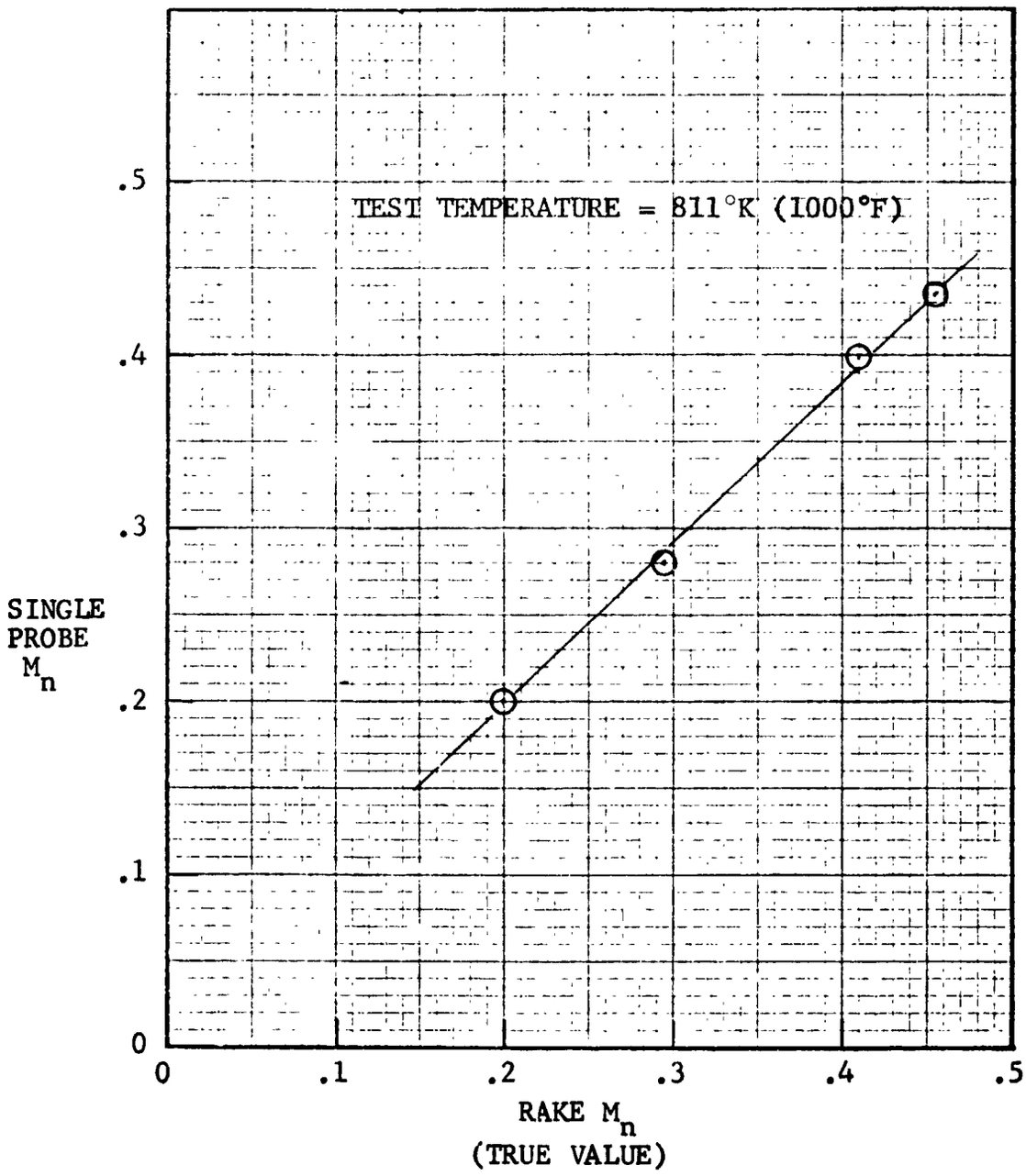

Figure 100. Mach No. Relationship at 811° K (1000° F).

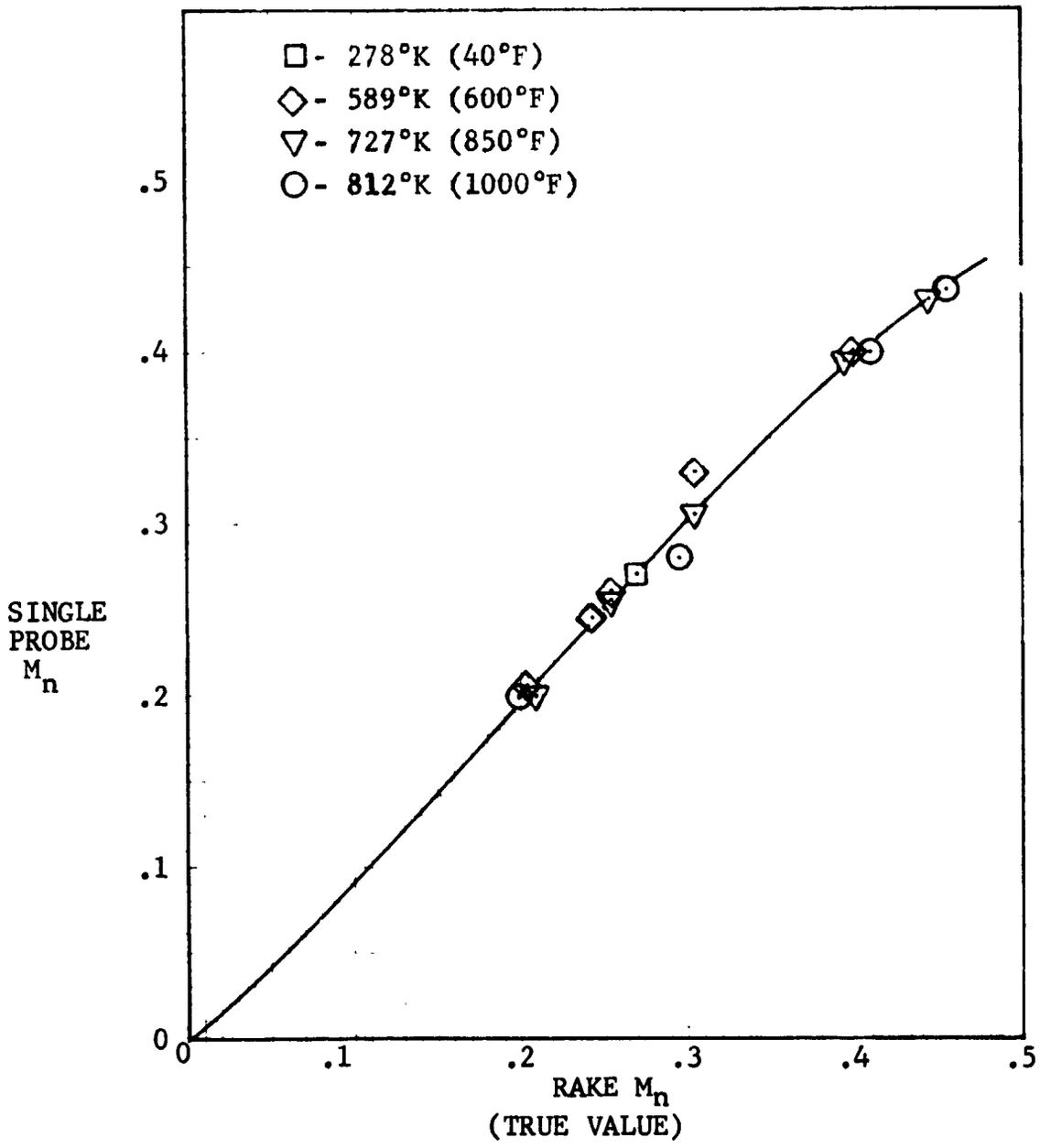

Figure 101. High Temperature Duct Calibration.

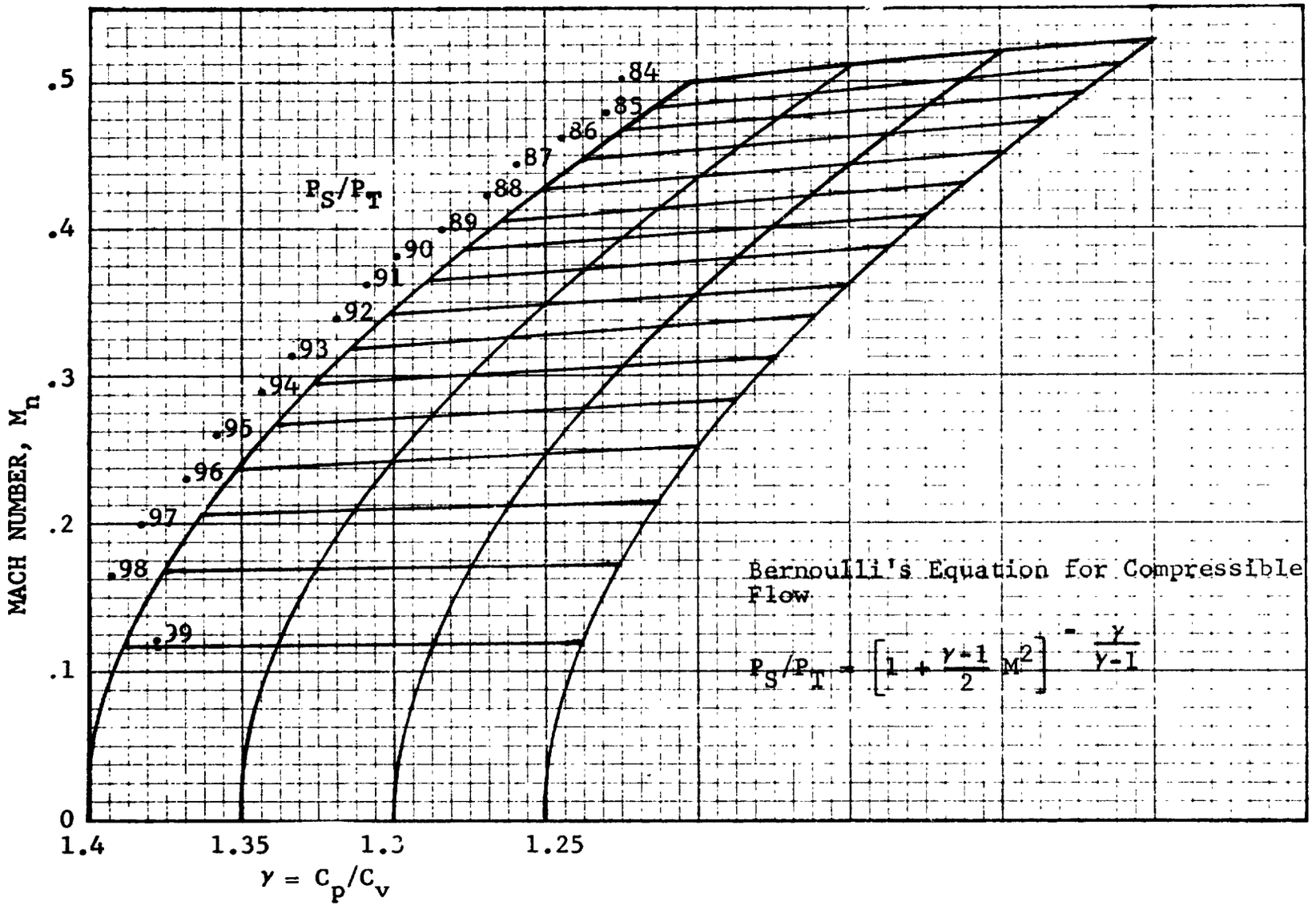

Figure 102. Carpet Plot of Mach Number Vs. Pressure Ratio and γ.

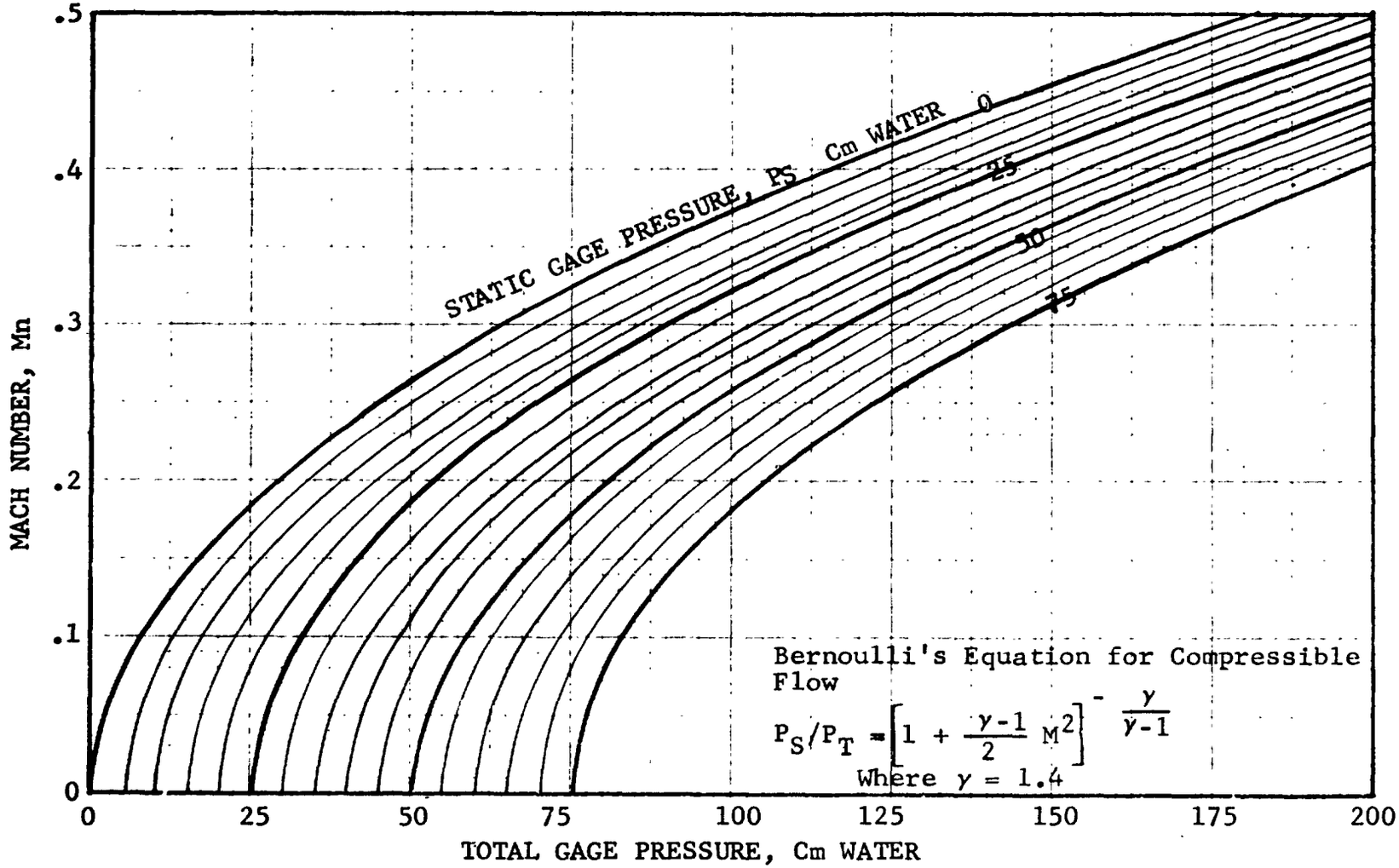

Figure 103. Mach Number Vs. P_T and P_S, $\gamma = 1.4$.

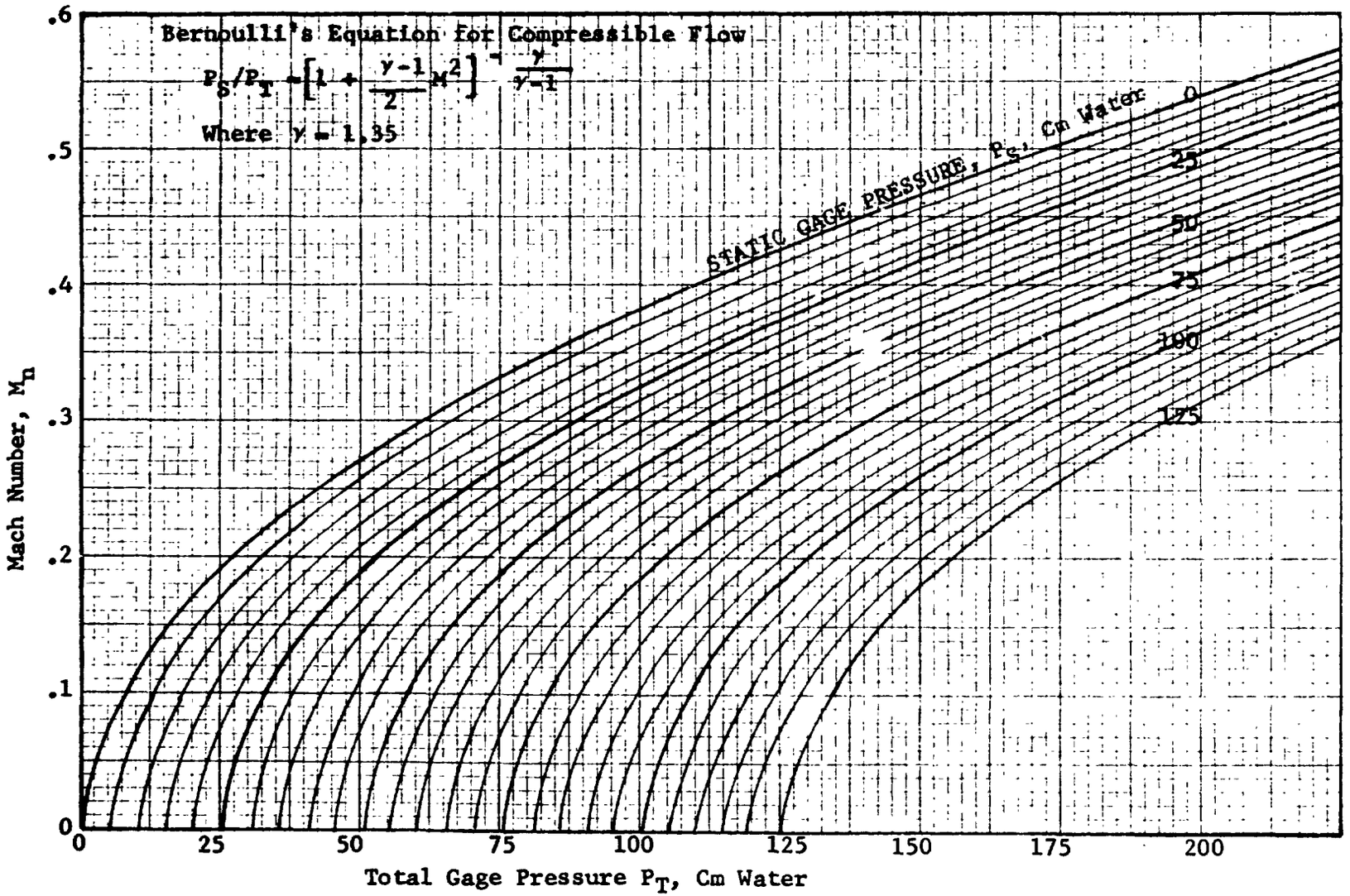

Figure 104. Mach Number Vs. P_T and P_S, γ = 1.35.

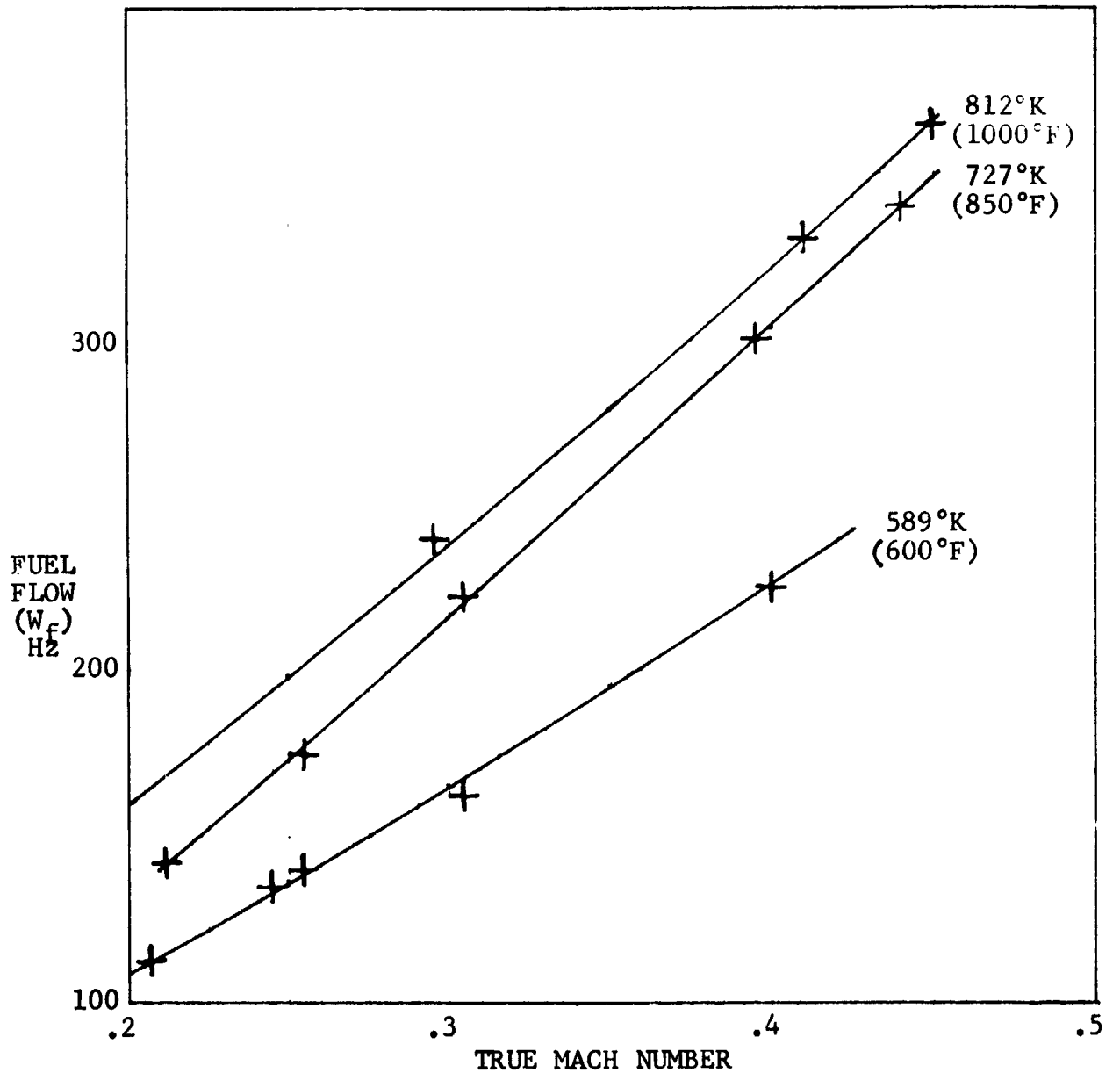

Figure 105. True Mach Number Vs. Fuel Flow.

Figure 106. Typical SDOF Panel with Side Plates Unattached.

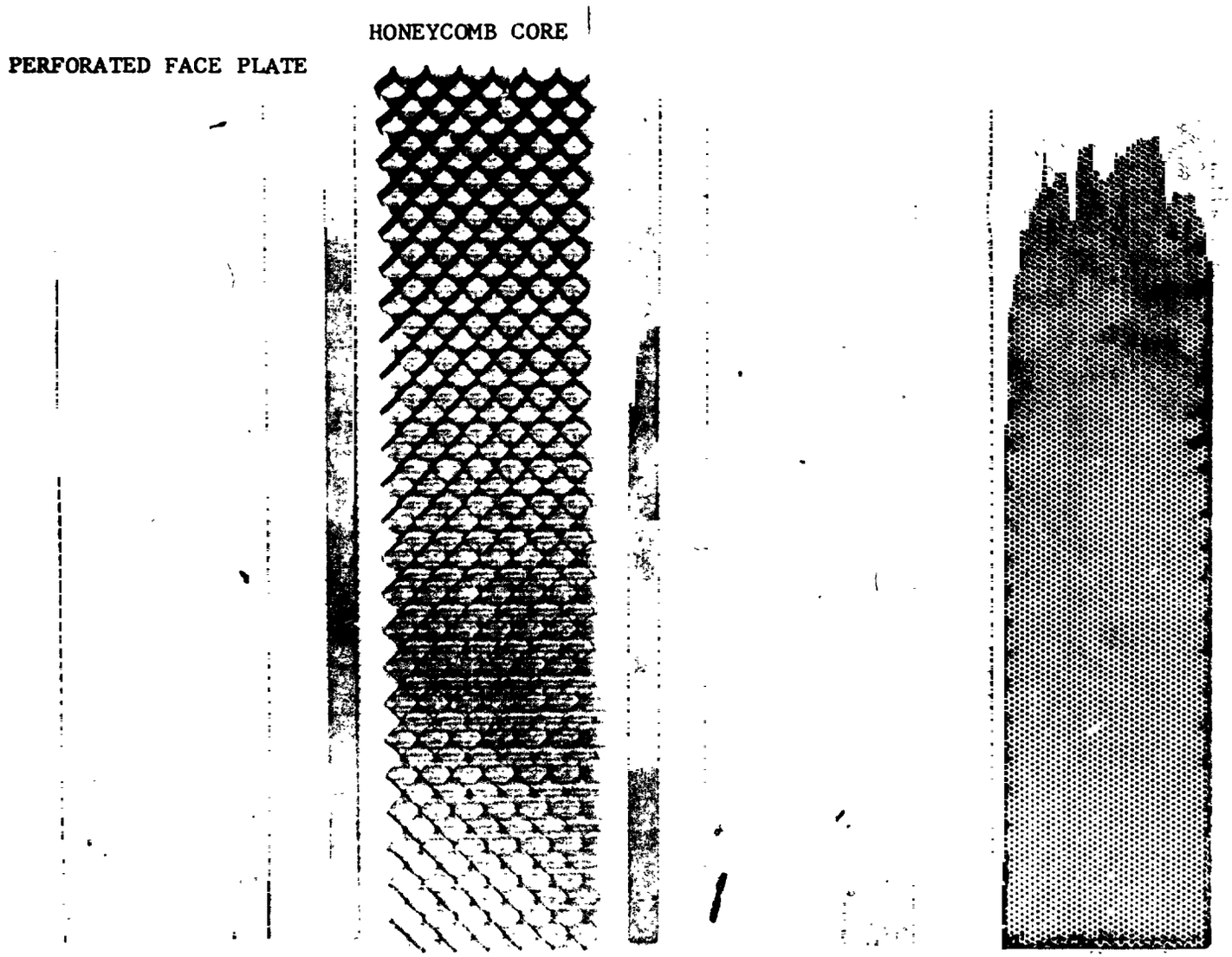

Figure 107. Assembly Details of Typical SDOF Panel.

HIGH TEMPERATURE ACOUSTIC DUCT .102m x .203m (4"x8")
TREATED ON TWO SIDES IN EXHAUST CONFIGURATION
L/H 4.5 TEMP. 589 °K 600 °F Mn 0.21

MATERIAL SDOF #1

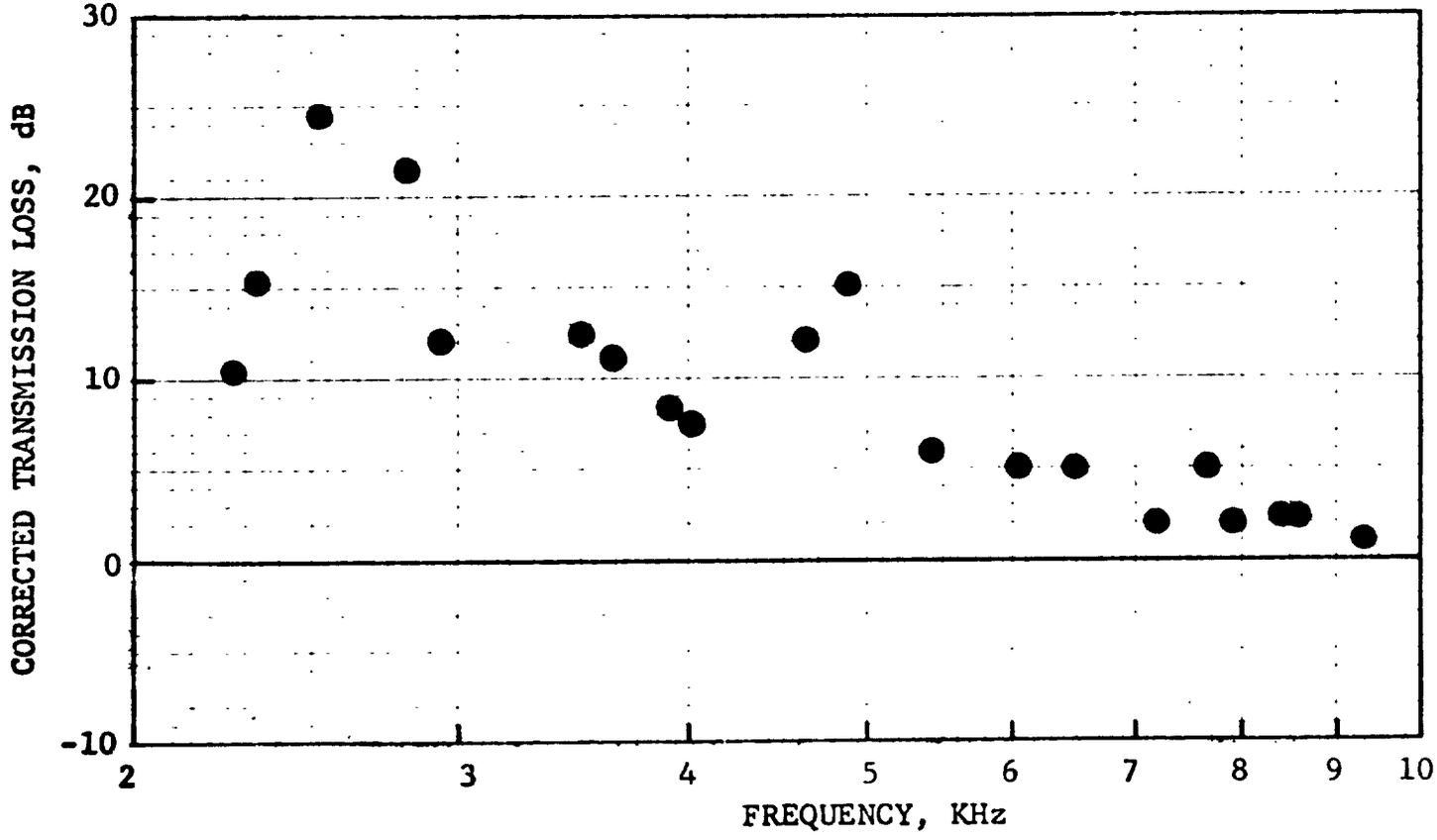

Figure 108. Corrected Transmission Loss Vs. Frequency.

HIGH TEMPERATURE ACOUSTIC DUCT .102m x .203m (4"x8")
TREATED ON TWO SIDES IN EXHAUST CONFIGURATION
L/H 4.5 TEMP. 589 °K 600 °F Mn 0.25

MATERIAL SDOF #1

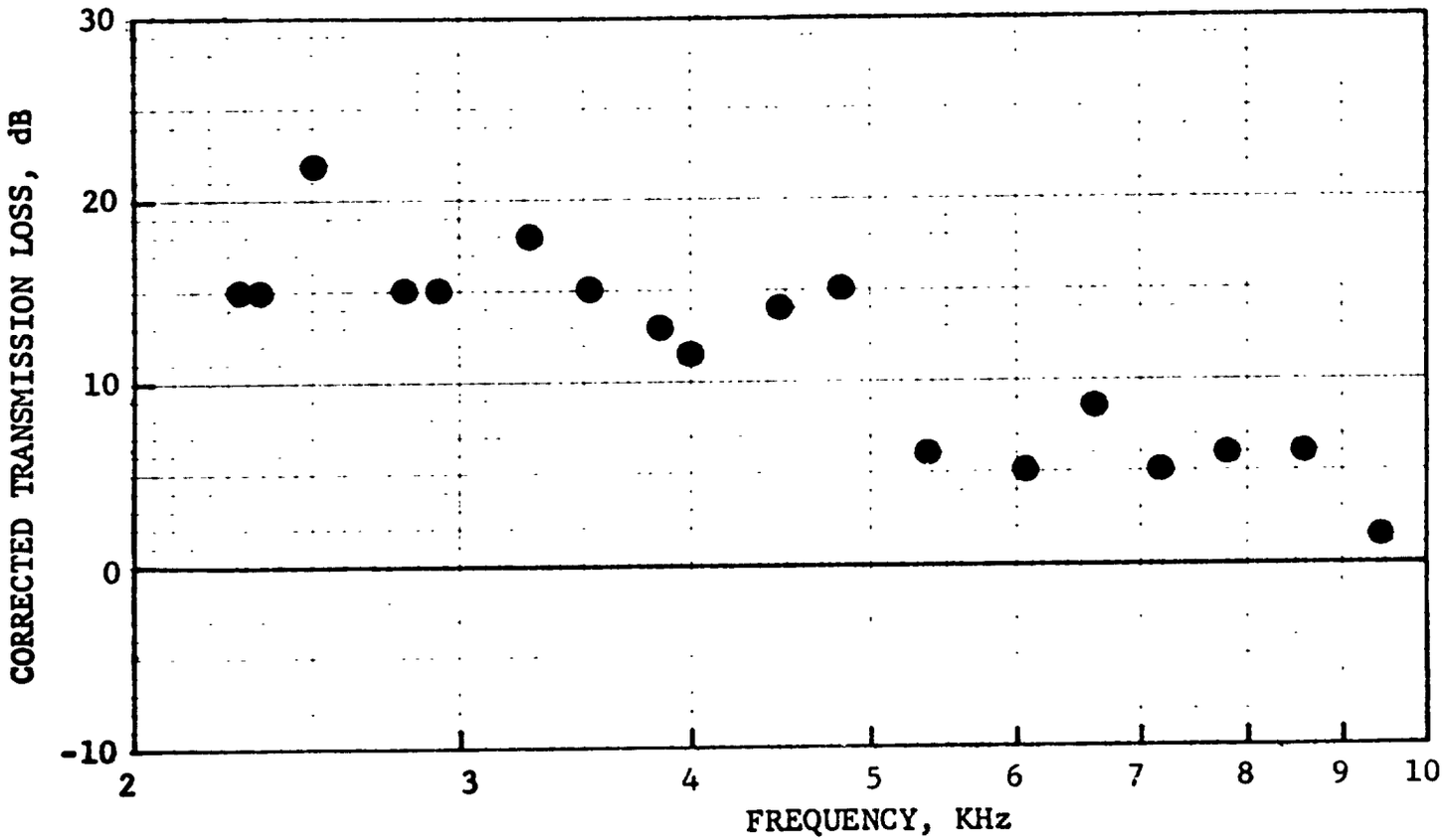

Figure 109. Corrected Transmission Loss Vs. Frequency.

HIGH TEMPERATURE ACOUSTIC DUCT .102m x .203m (4"x8")
TREATED ON TWO SIDES IN EXHAUST CONFIGURATION
L/H 4.5 TEMP. 589 °K 600 °F Mn 0.3

MATERIAL SDOF #1

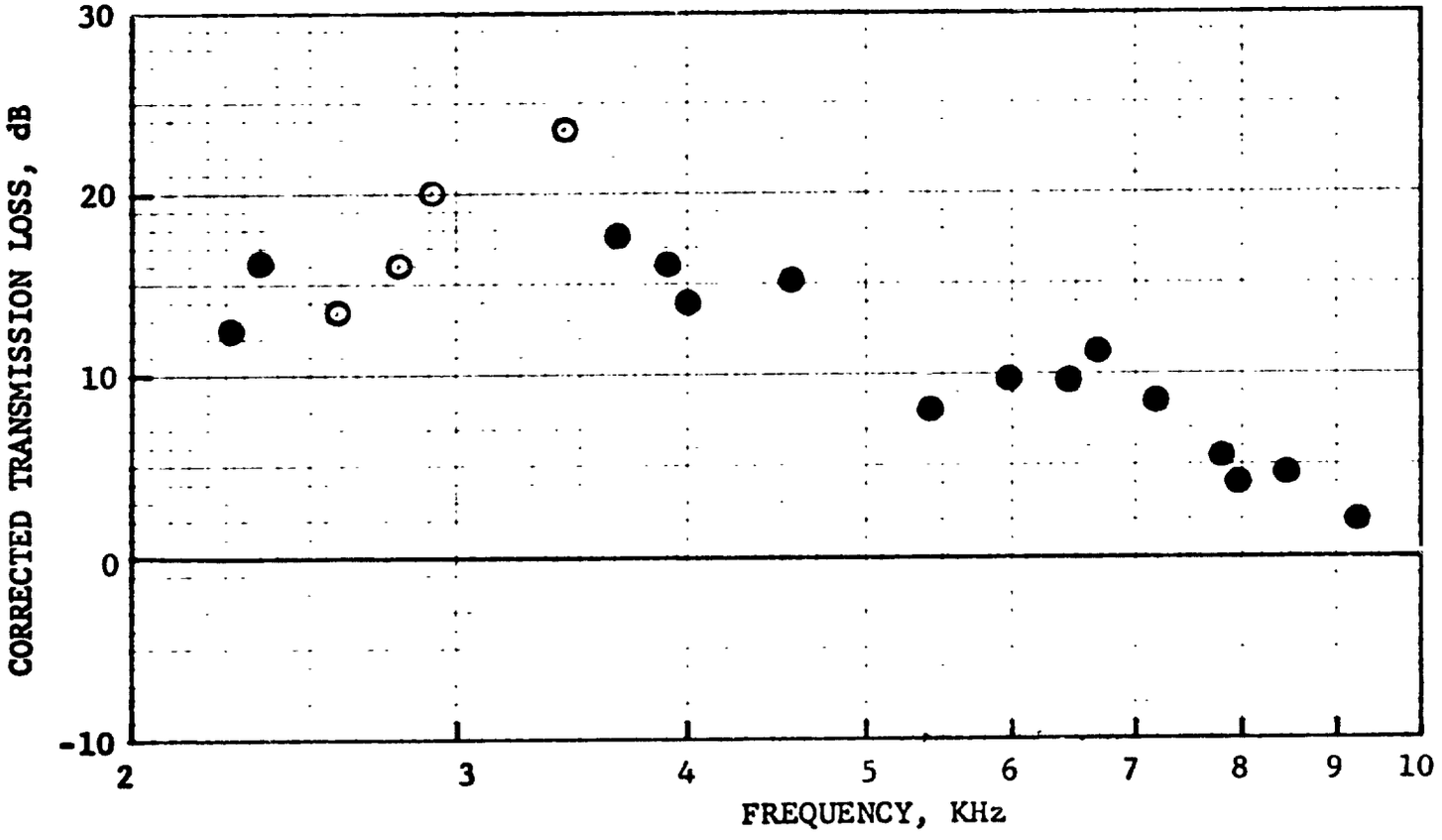

Figure 110. Corrected Transmission Loss Vs. Frequency.

HIGH TEMPERATURE ACOUSTIC DUCT .102m x .203m (4" x 8")
TREATED ON TWO SIDES IN EXHAUST CONFIGURATION
L/H 4.5 TEMP. 589 °K 600 °F Mn 0.4

MATERIAL SDOF #1

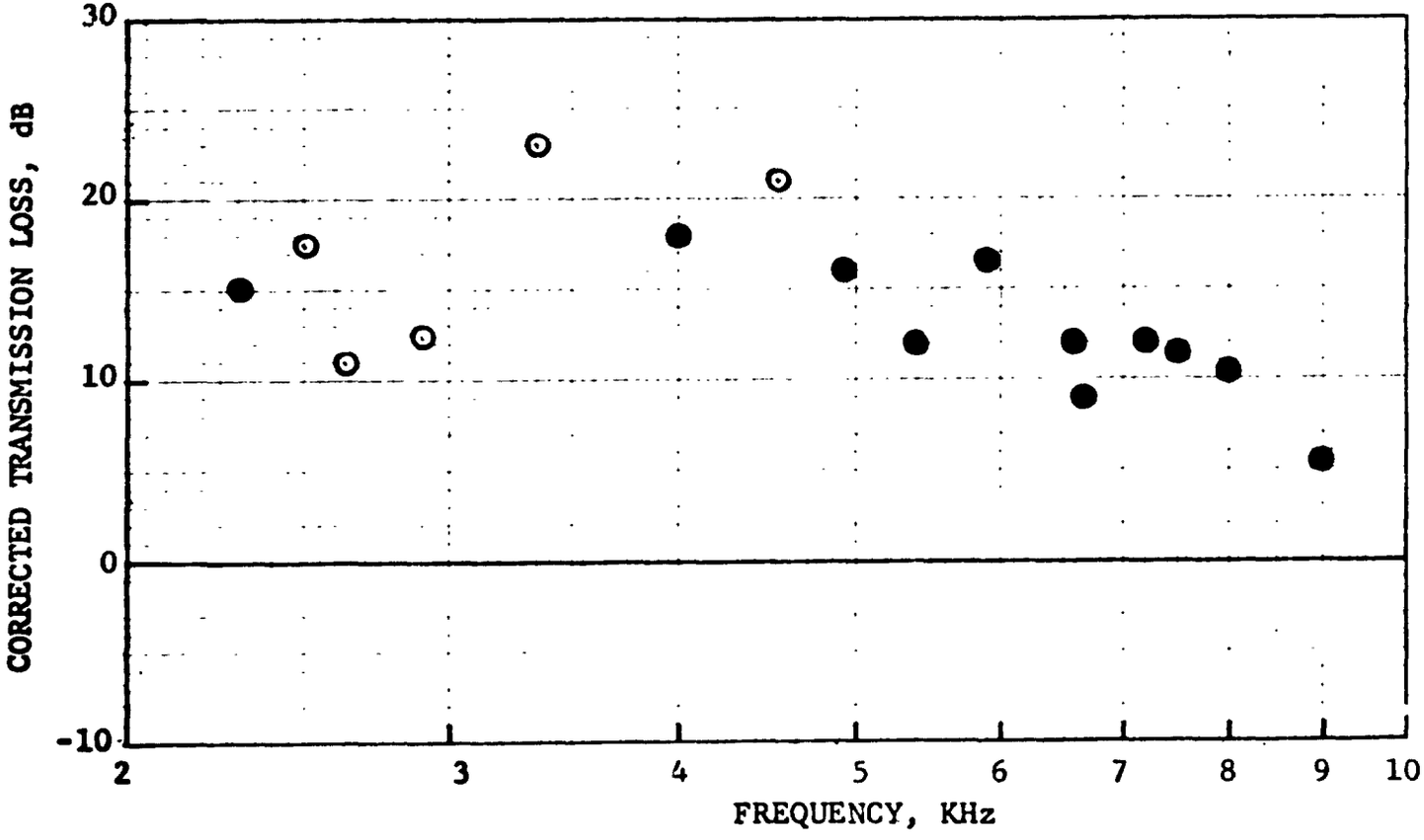

Figure 111. Corrected Transmission Loss Vs. Frequency.

HIGH TEMPERATURE ACOUSTIC DUCT .102m x .203m (4"x8")
TREATED ON TWO SIDES IN EXHAUST CONFIGURATION
L/H 4.5 TEMP. 589 °K 600 °F Mn 0.21

MATERIAL SDOF #2

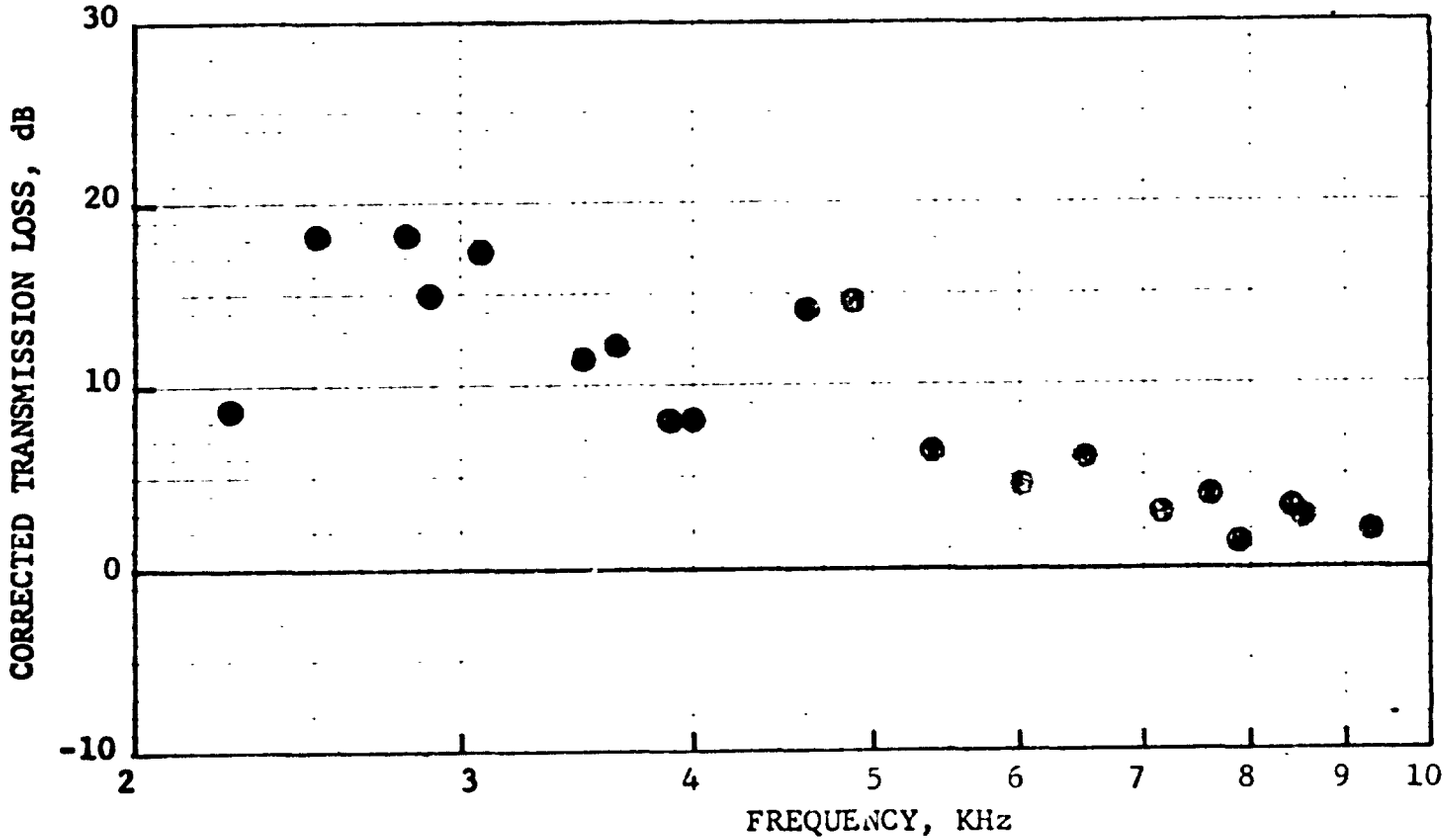

Figure 112. Corrected Transmission Loss Vs. Frequency.

HIGH TEMPERATURE ACOUSTIC DUCT .102m x .203m (4"x8")
TREATED ON TWO SIDES IN EXHAUST CONFIGURATION
L/H 4.5 TEMP. 589 °K 600 °F Mn 0.25

MATERIAL SDOF #2

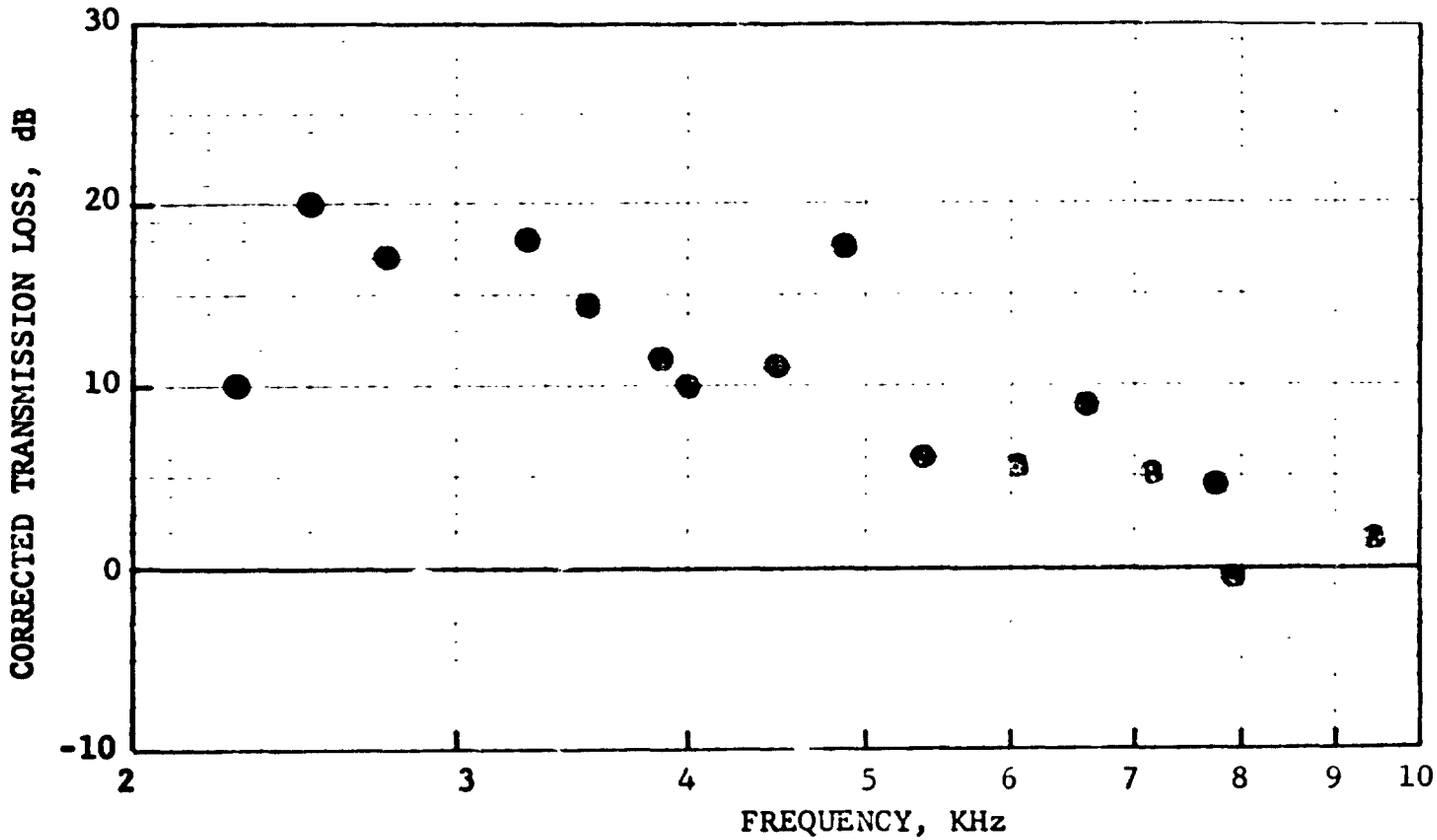

Figure 113. Corrected Transmission Loss Vs. Frequency.

HIGH TEMPERATURE ACOUSTIC DUCT .102m x .203m (4"x8")
TREATED ON TWO SIDES IN EXHAUST CONFIGURATION
L/H 4.5 TEMP. 589 °K 600 °F Mn 0.3

MATERIAL SDOF #2

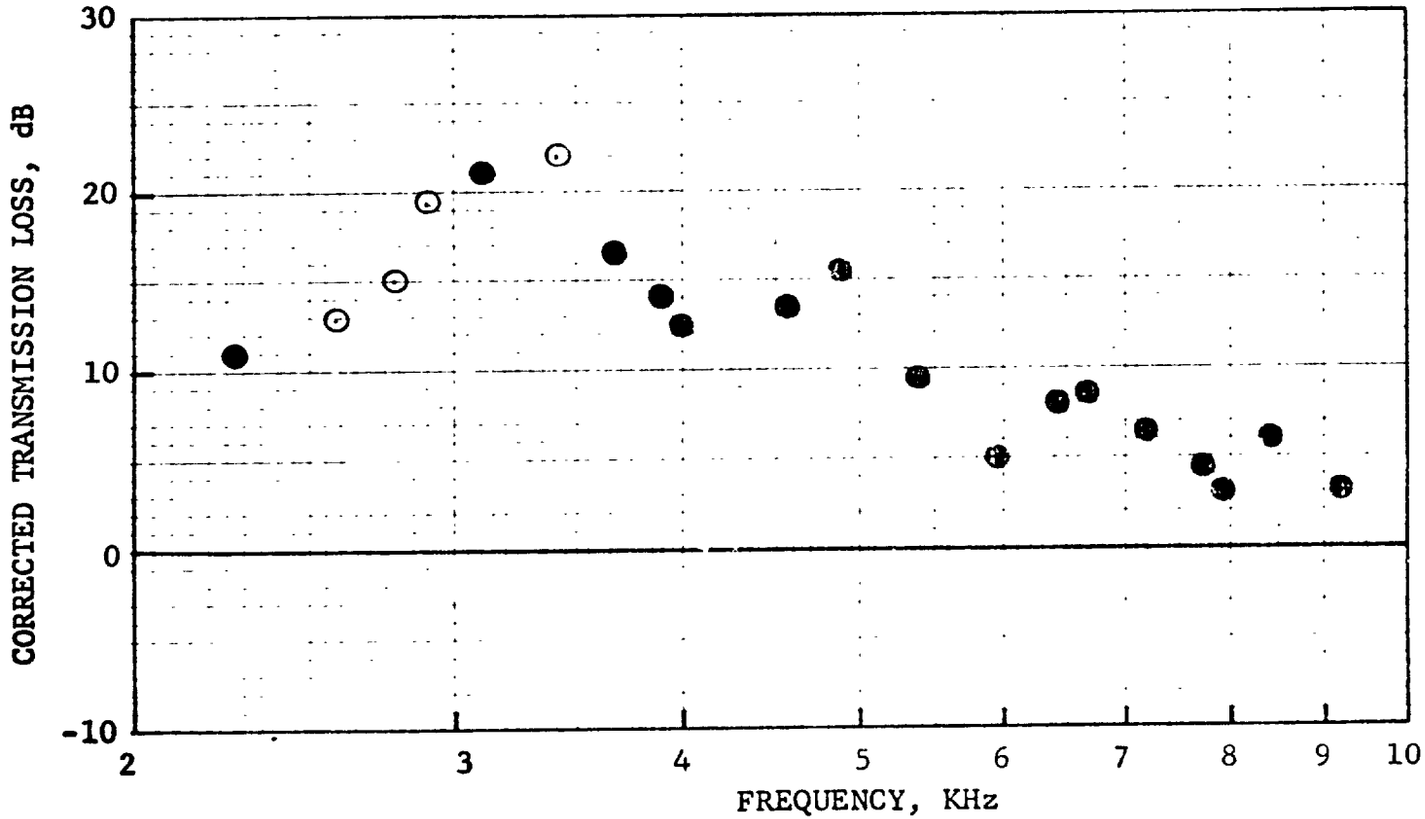

Figure 114. Corrected Transmission Loss Vs. Frequency.

HIGH TEMPERATURE ACOUSTIC DUCT .102m x .203m (4"x8")
TREATED ON TWO SIDES IN EXHAUST CONFIGURATION
L/H 4.5 TEMP. 589 °K 600 °F Mn 0.4

MATERIAL SDOF#2

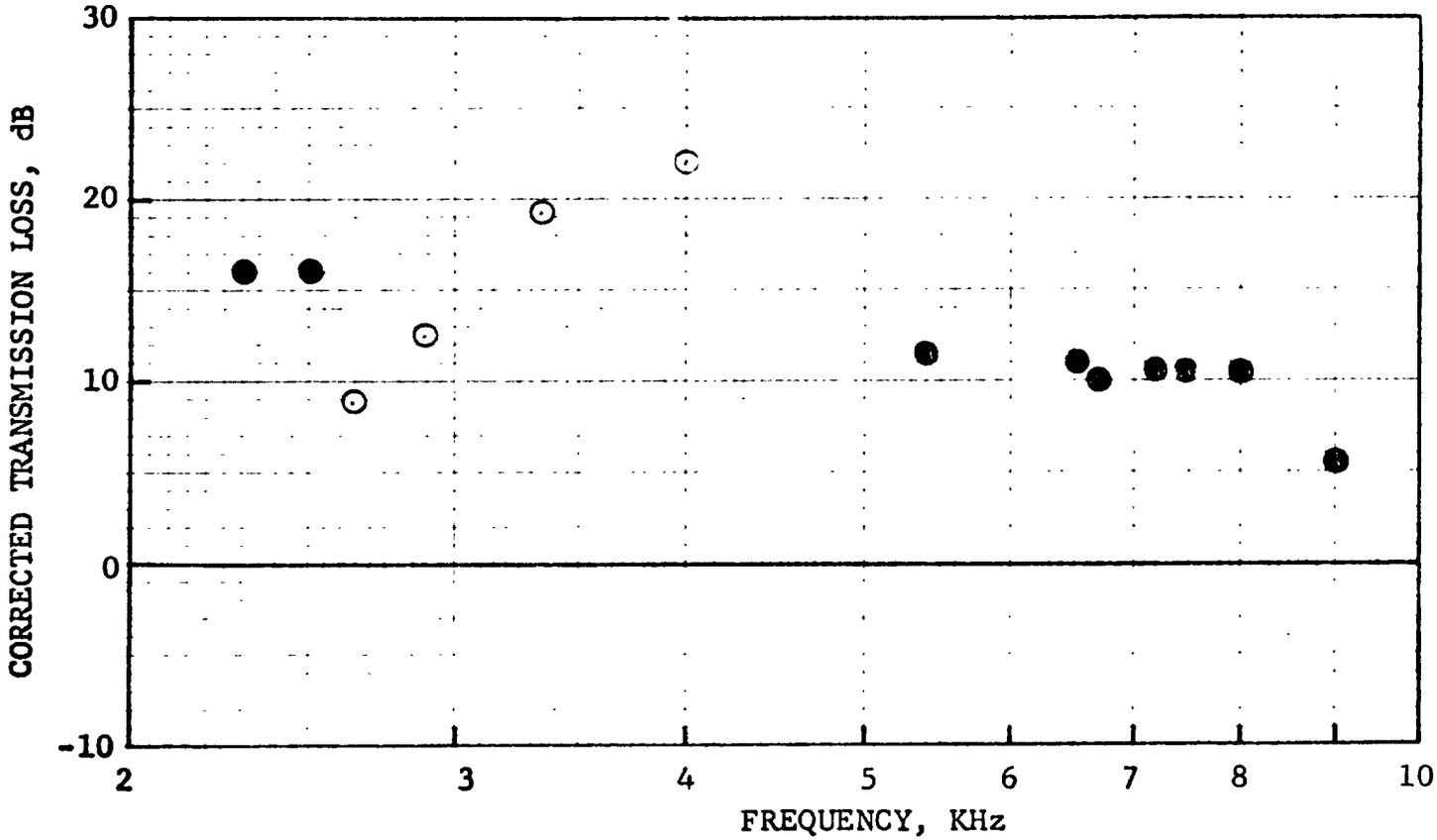

Figure 115. Corrected Transmission Loss Vs. Frequency.

HIGH TEMPERATURE ACOUSTIC DUCT .102m x .203m (4"x8")
TREATED ON TWO SIDES IN EXHAUST CONFIGURATION
L/H 4.5 TEMP. 589 °K 600 °F Mn 0.21

MATERIAL SDOF #3

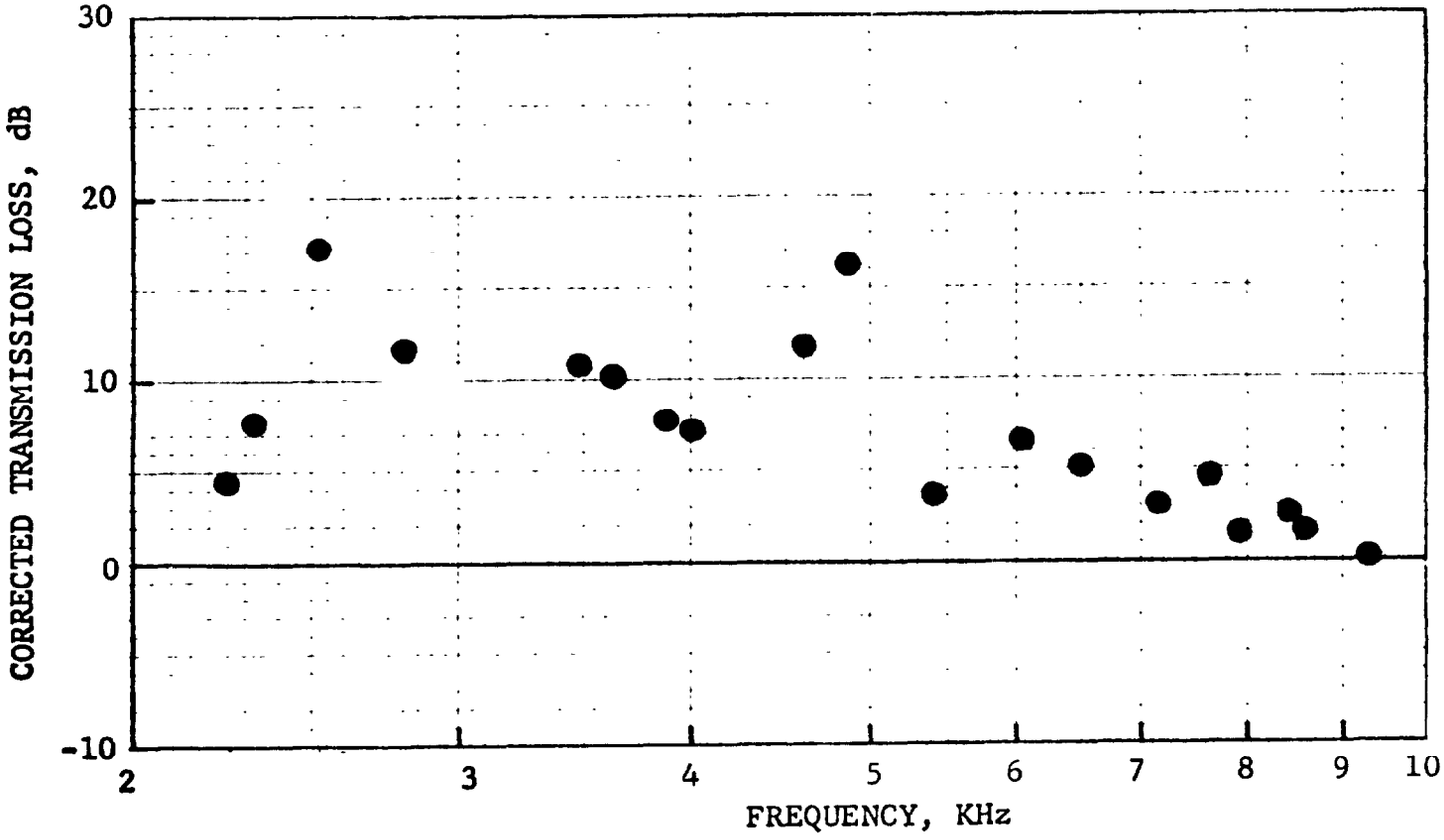

Figure 116. Corrected Transmission Loss Vs. Frequency.

HIGH TEMPERATURE ACOUSTIC DUCT .102m x .203m (4"x8")
TREATED ON TWO SIDES IN EXHAUST CONFIGURATION
L/H 4.5 TEMP. 589 °K 600 °F Mn 0.25

MATERIAL SDOF #3

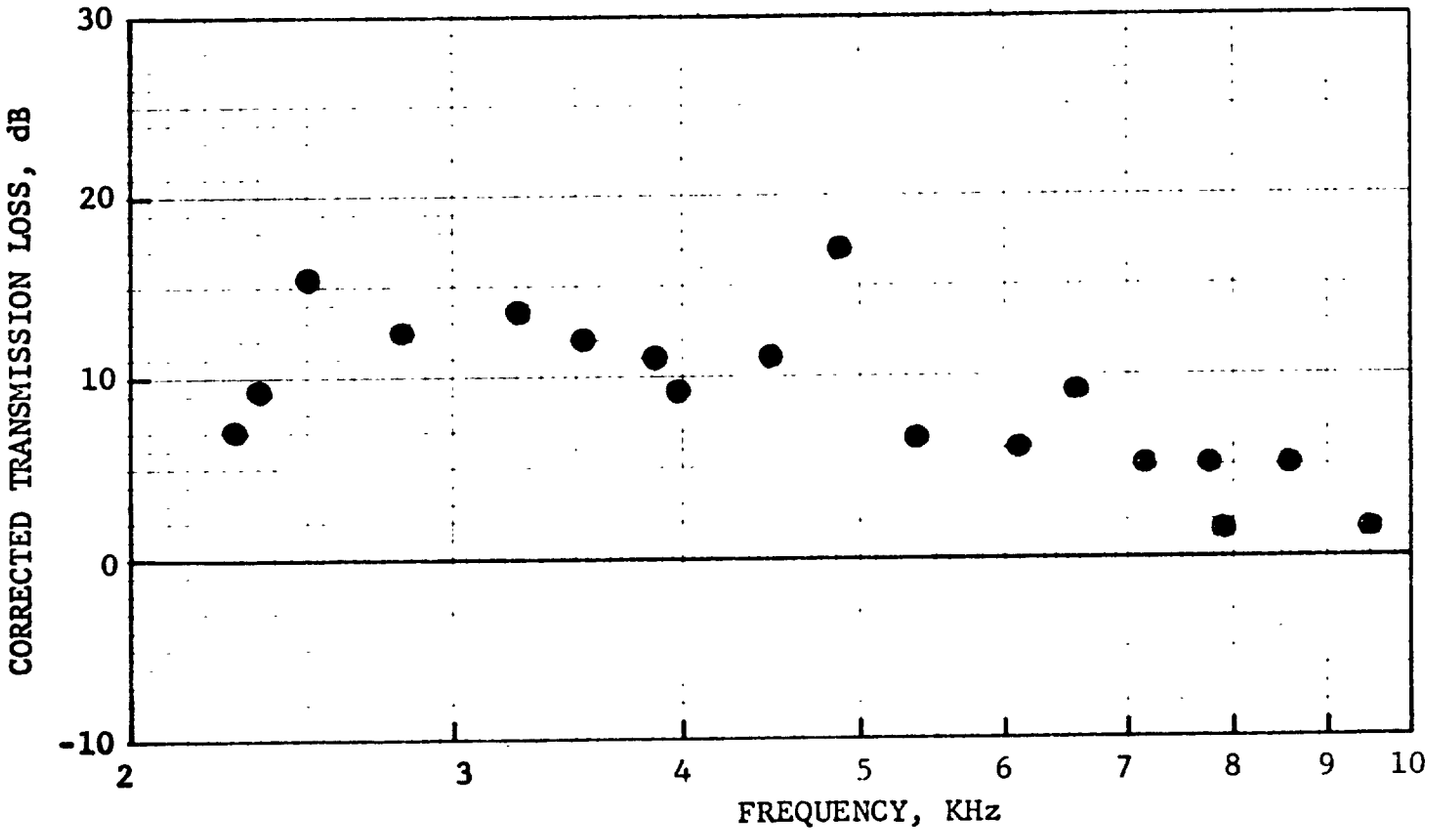

Figure 117. Corrected Transmission Loss Vs. Frequency.

HIGH TEMPERATURE ACOUSTIC DUCT .102m x .203m (4"x8")
TREATED ON TWO SIDES IN EXHAUST CONFIGURATION
L/H 4.5 TEMP. 589 °K 699 °F Mn 0.3

MATERIAL SDOF #3

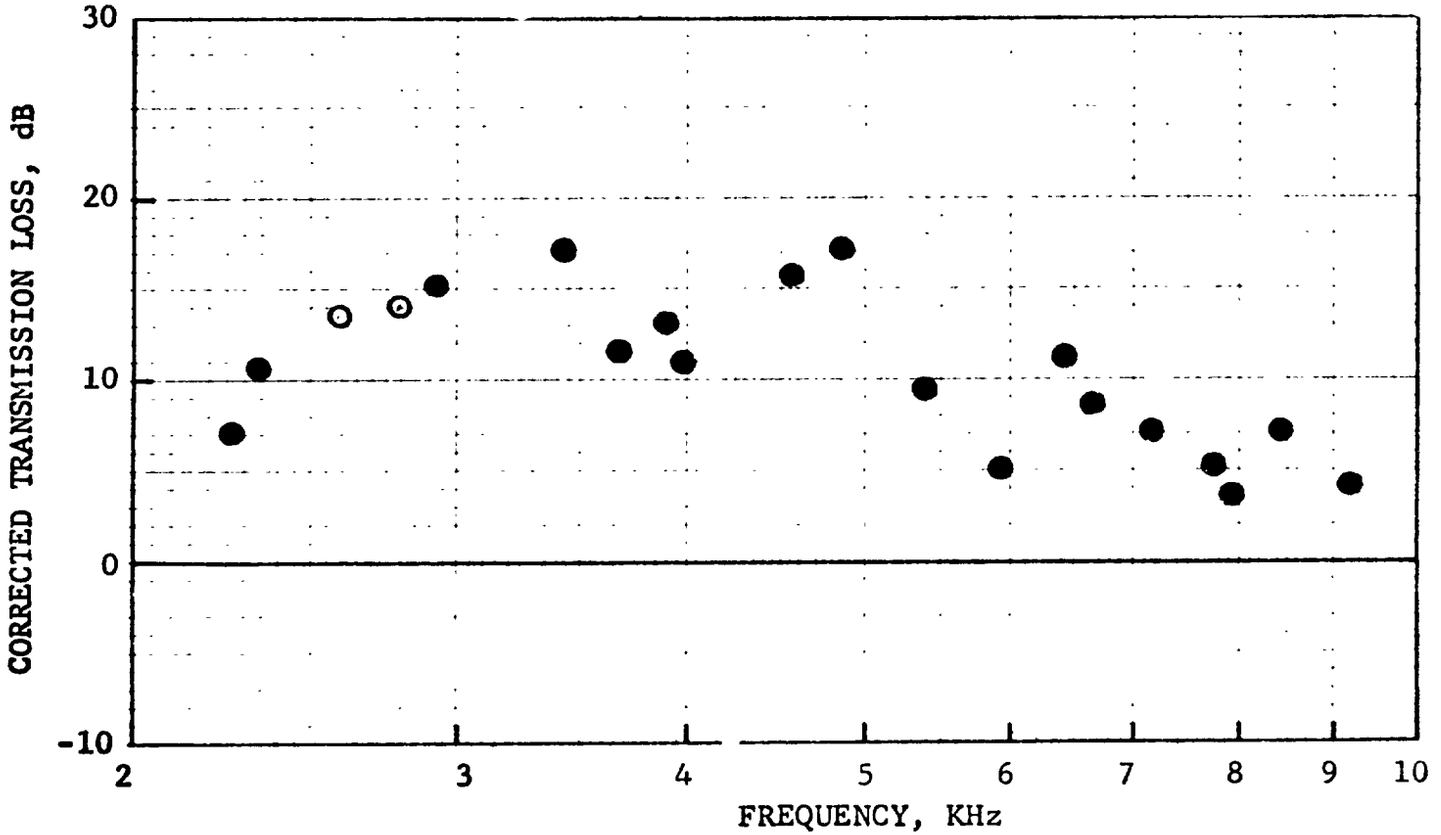

Figure 118. Corrected Transmission Loss Vs. Frequency.

HIGH TEMPERATURE ACOUSTIC DUCT .102m x .203m (4"x8")
TREATED ON TWO SIDES IN EXHAUST CONFIGURATION
L/H 4.5 TEMP. 589 °K 600 °F Mn 0.4

MATERIAL SDOF #3

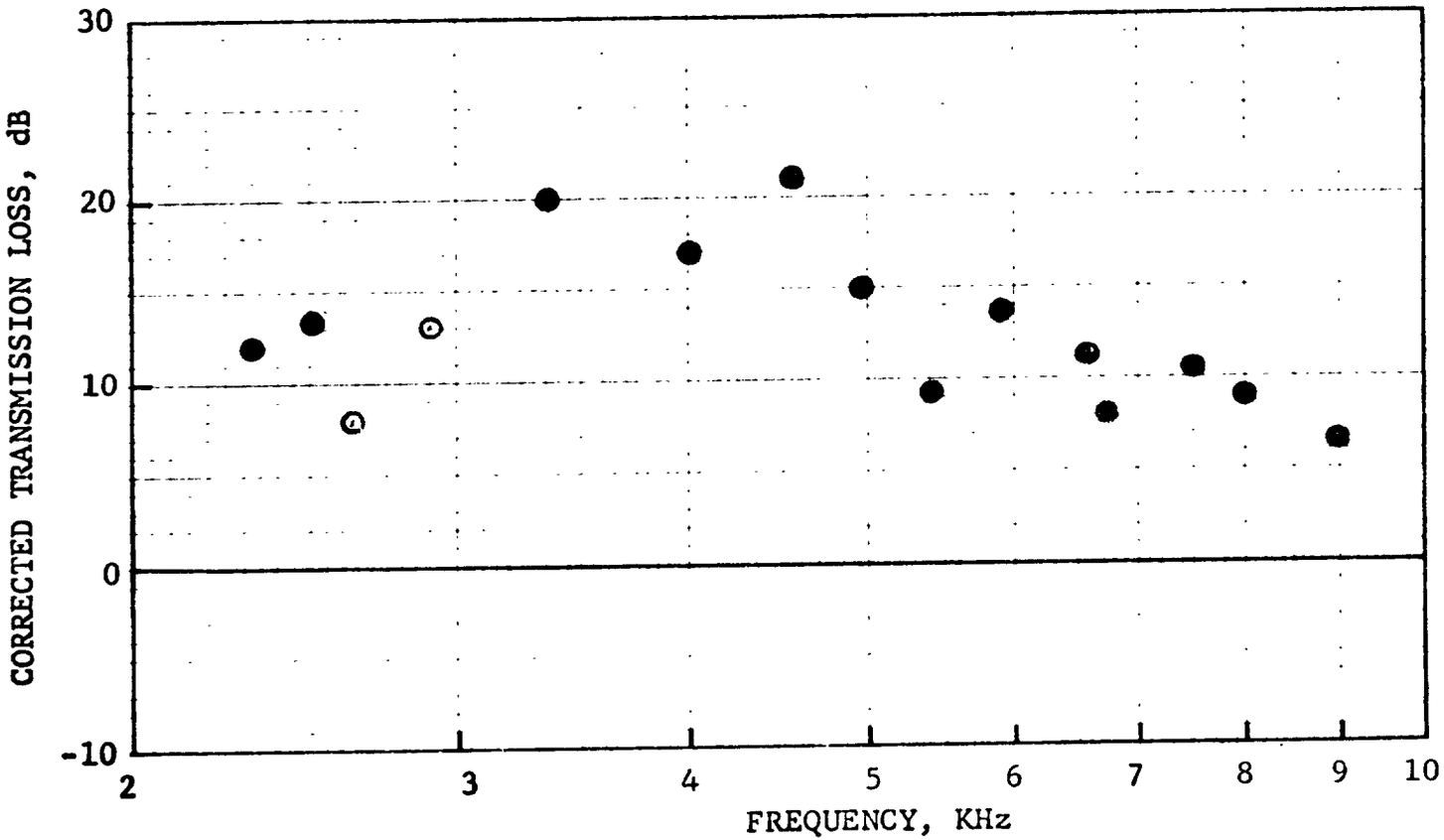

Figure 119. Corrected Transmission Loss Vs. Frequency.

HIGH TEMPERATURE ACOUSTIC DUCT .102m x .203m (4"x8")
TREATED ON TWO SIDES IN EXHAUST CONFIGURATION
L/H 4.5 TEMP. 589 °K 600 °F Mn 0.21

MATERIAL SDOF #4

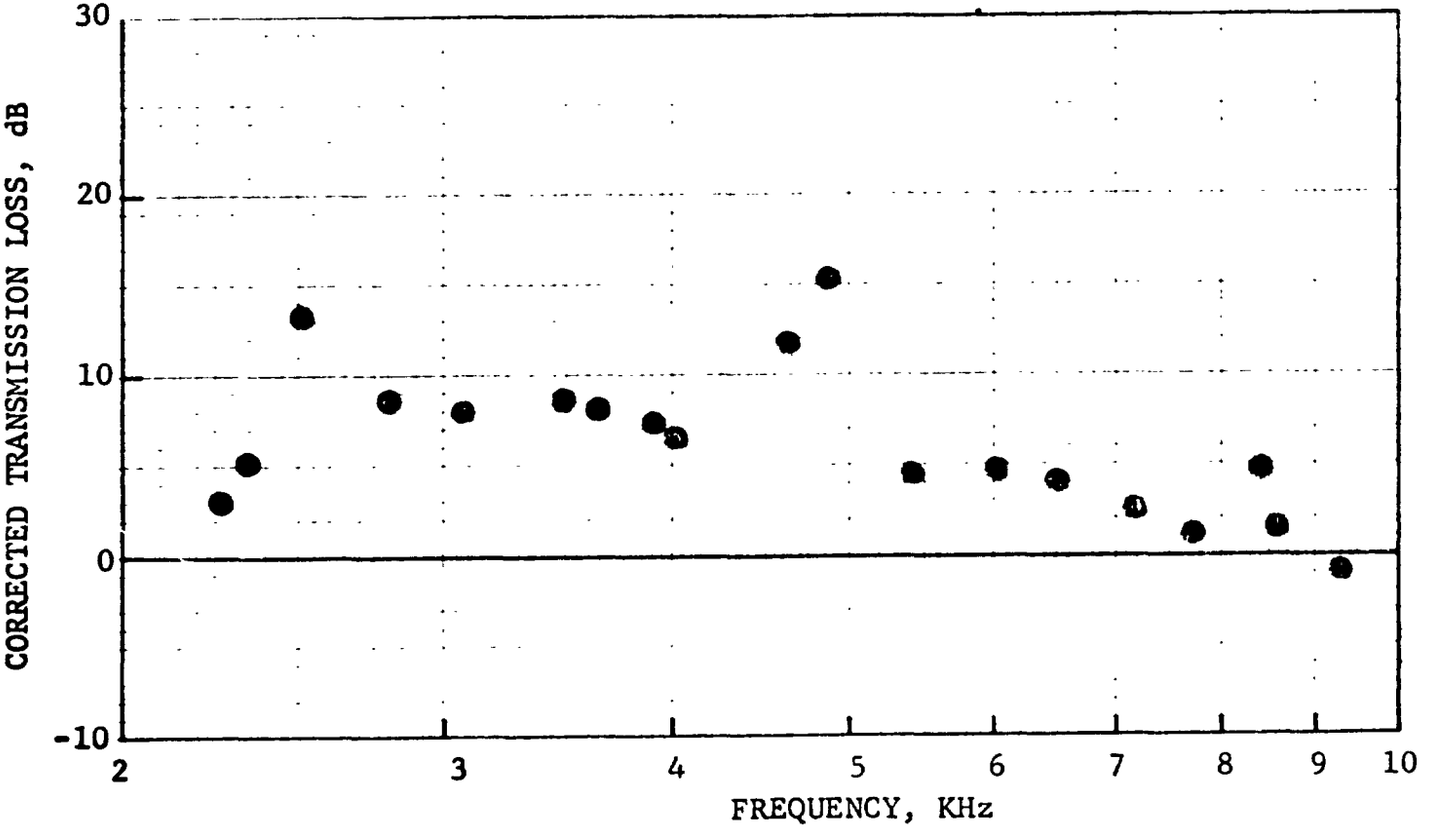

Figure 120. Corrected Transmission Loss Vs. Frequency.

HIGH TEMPERATURE ACOUSTIC DUCT .102m x .203m (4"x8")
TREATED ON TWO SIDES IN EXHAUST CONFIGURATION
L/H 4.5 TEMP. 589 °K 600 °F Mn 0.25

MATERIAL SDOF #4

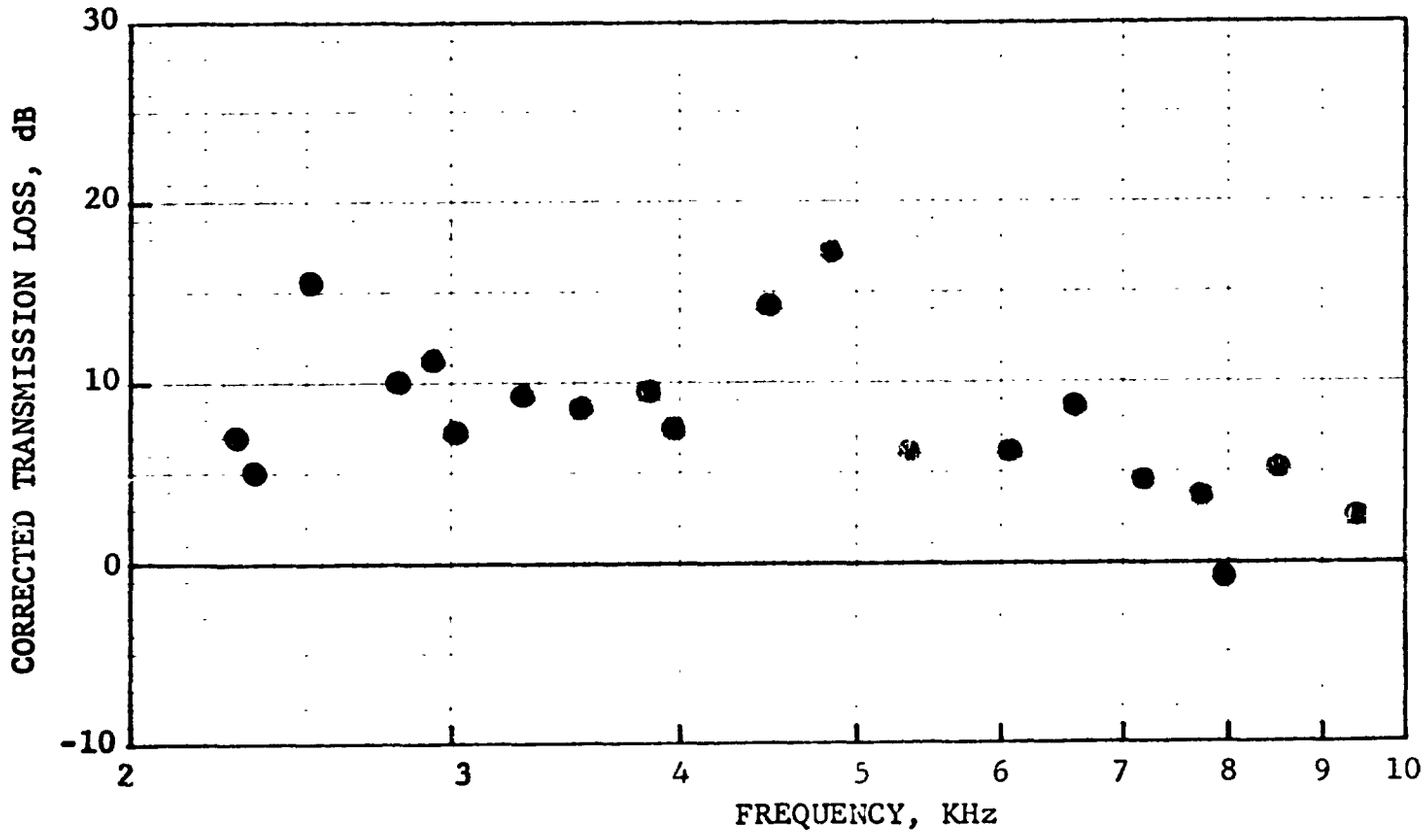

Figure 121. Corrected Transmission Loss Vs. Frequency.

HIGH TEMPERATURE ACOUSTIC DUCT .102m x .203m (4"x8")
TREATED ON TWO SIDES IN EXHAUST CONFIGURATION
L/H 4.5 TEMP. 589 °K 600 °F Mn 0.3

MATERIAL SDOF #4

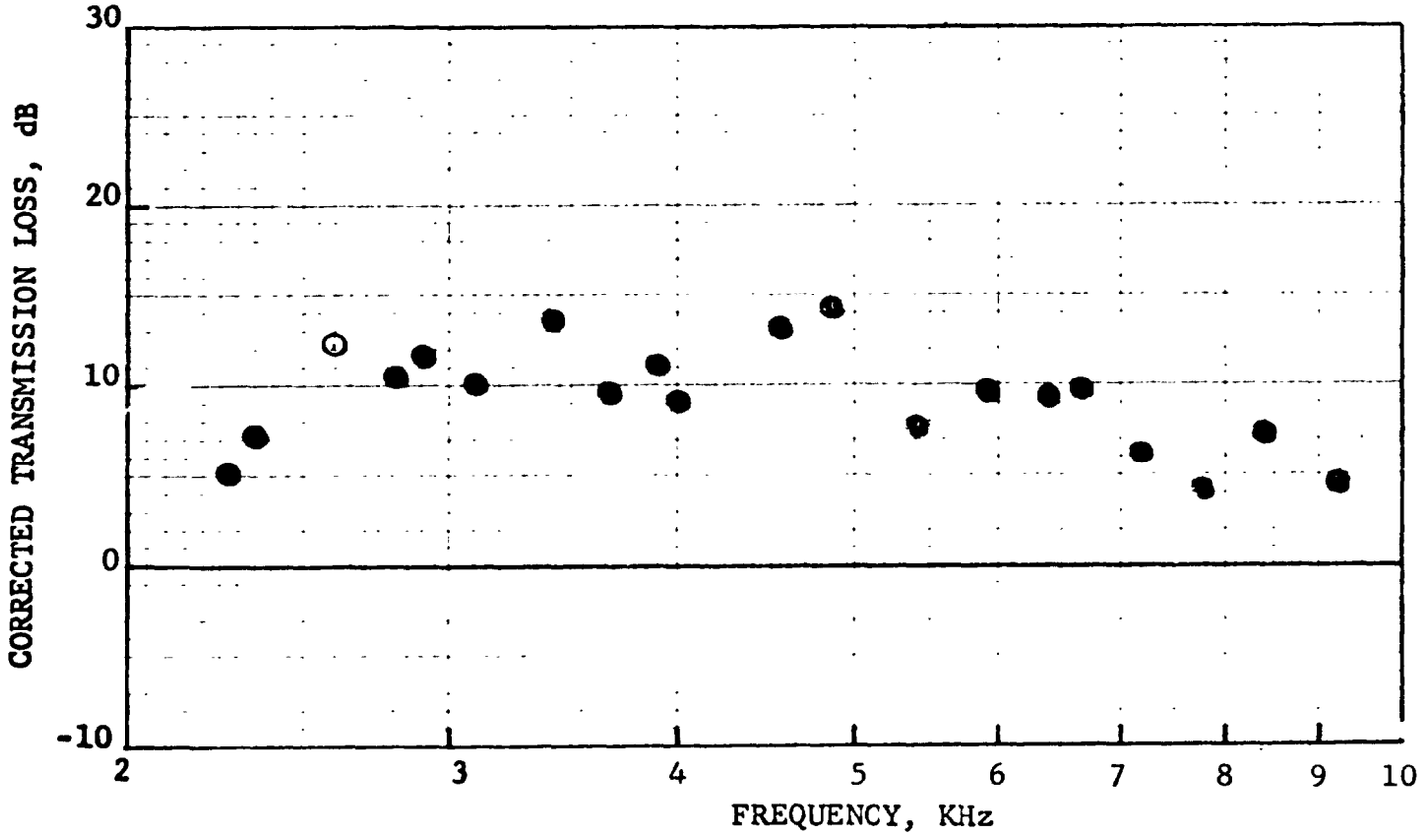

Figure 122. Corrected Transmission Loss Vs. Frequency.

HIGH TEMPERATURE ACOUSTIC DUCT .102m x .203m (4"x8")
TREATED ON TWO SIDES IN EXHAUST CONFIGURATION
L/H 4.5 TEMP. 589 °K 600 °F Mn 0.4

MATERIAL SDOF #4

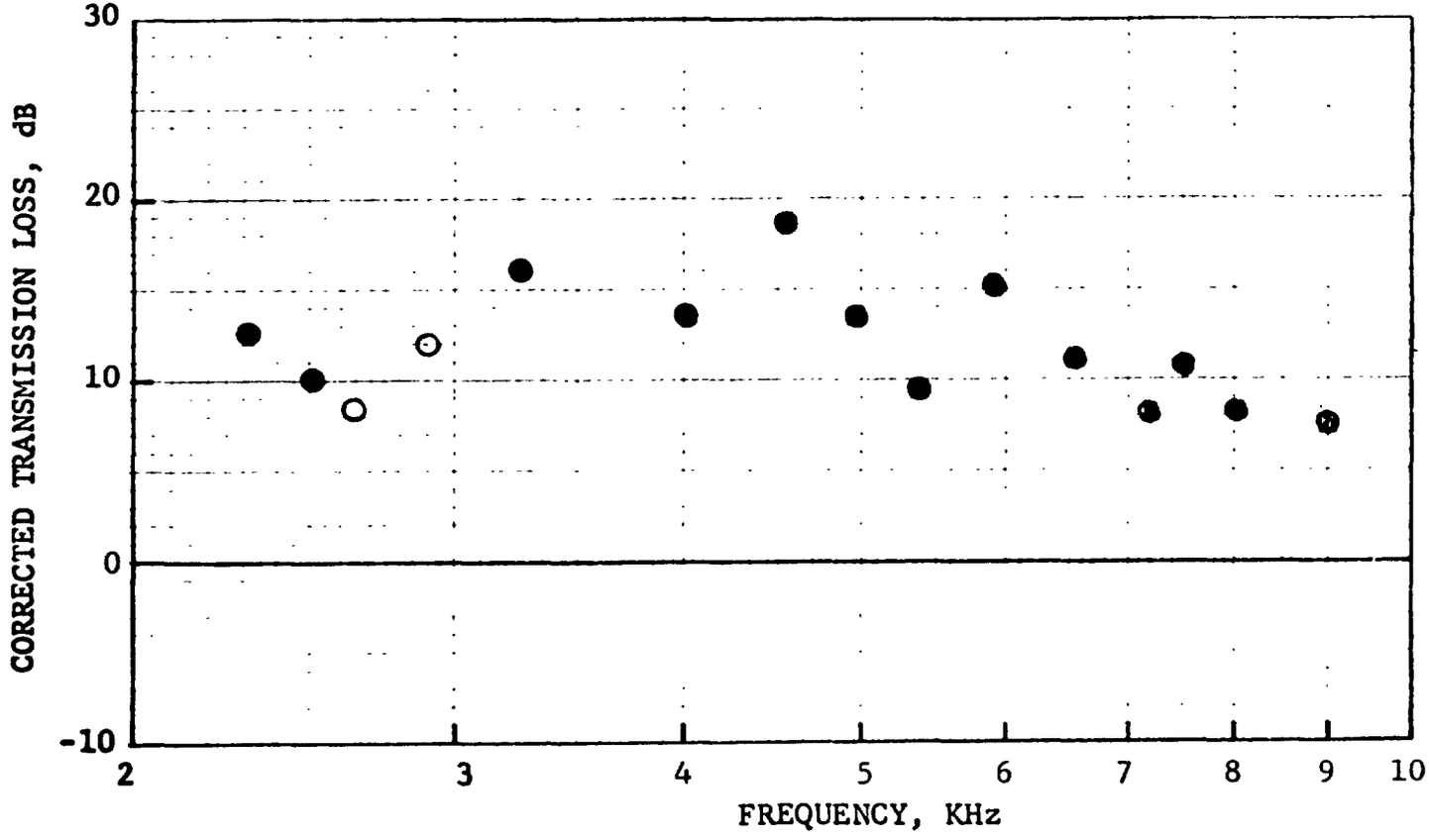

Figure 123. Corrected Transmission Loss Vs. Frequency.

HIGH TEMPERATURE ACOUSTIC DUCT .102m x .203m (4"x8")
TREATED ON TWO SIDES IN EXHAUST CONFIGURATION
L/H 4.5 TEMP. 589 °K 600 °F Mn 0.21

MATERIAL SDOF #5

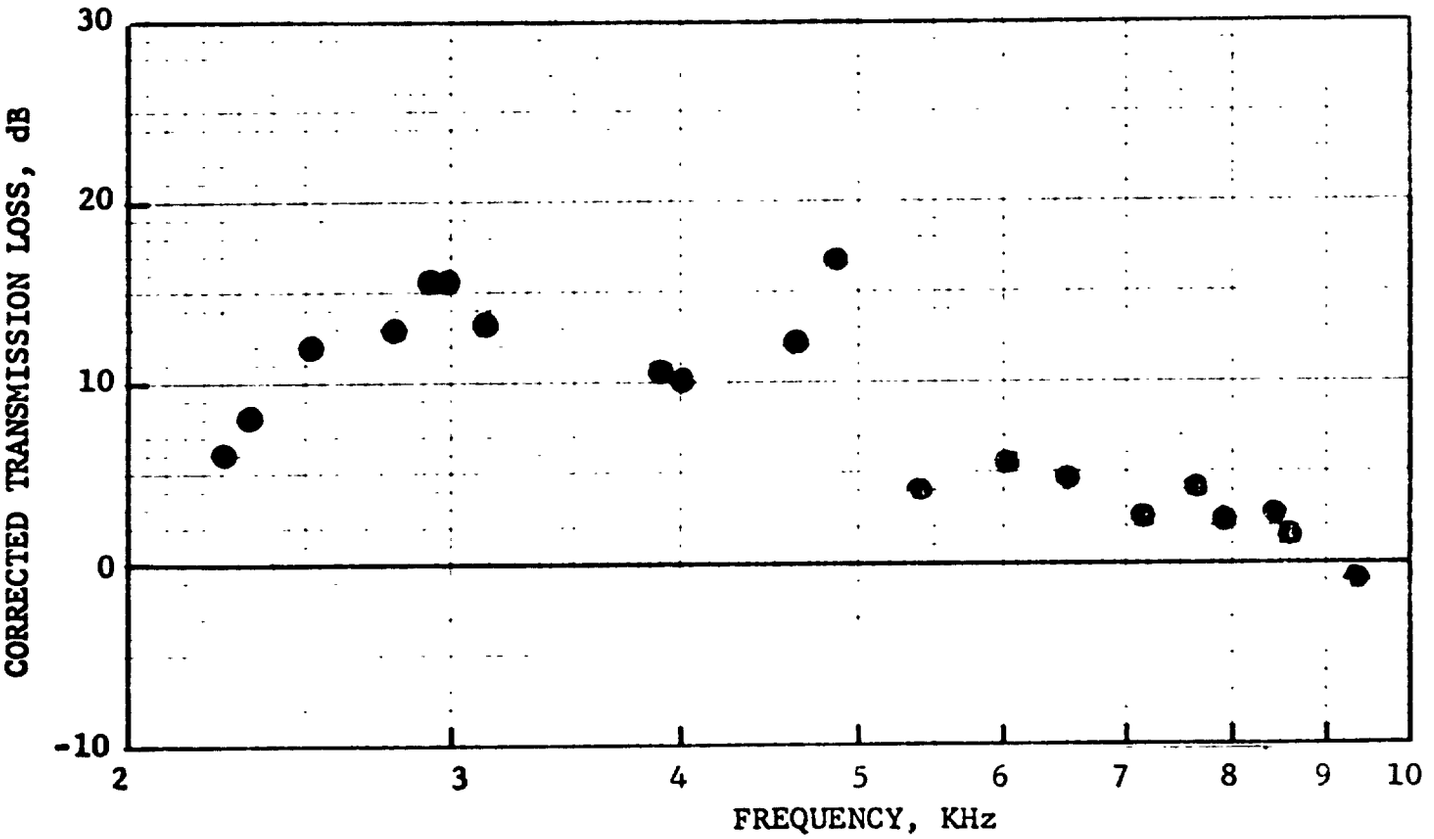

Figure 124. Corrected Transmission Loss Vs. Frequency.

HIGH TEMPERATURE ACOUSTIC DUCT .102m x .203m (4"x8")
TREATED ON TWO SIDES IN EXHAUST CONFIGURATION
L/H 4.5 TEMP. 589 °K 600 °F Mn 0.25

MATERIAL SDOF #5

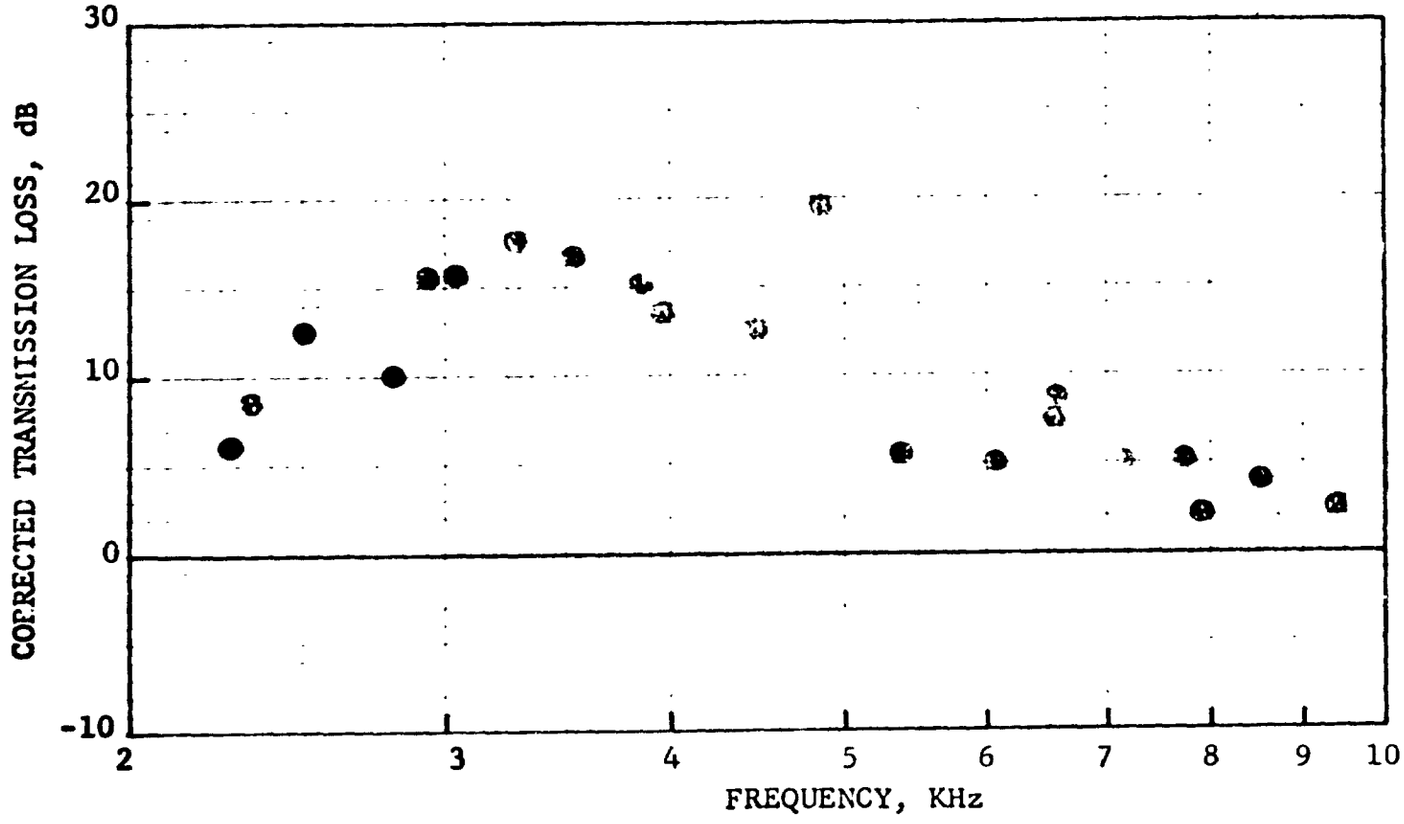

Figure 125. Corrected Transmission Loss Vs. Frequency.

HIGH TEMPERATURE ACOUSTIC DUCT .102m x .203m (4"x8")
TREATED ON TWO SIDES IN EXHAUST CONFIGURATION
L/H 4.5 TEMP. 589 °K 600 °F Mn 0.3

MATERIAL SDOF #5

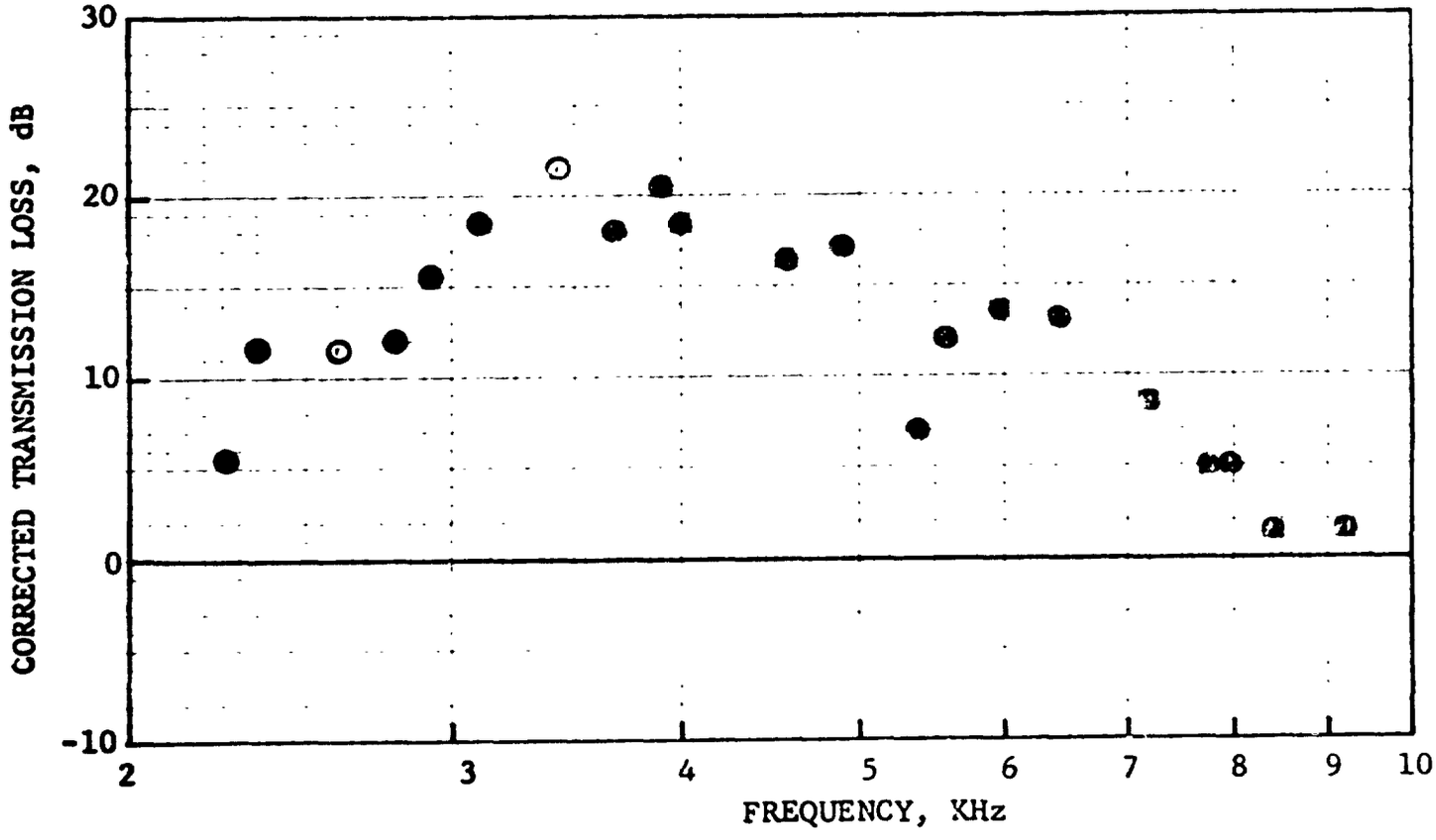

Figure 126. Corrected Transmission Loss Vs. Frequency.

HIGH TEMPERATURE ACOUSTIC DUCT .102m x .203m (4"x8")
TREATED ON TWO SIDES IN EXHAUST CONFIGURATION
L/H 4.5 TEMP. 589 °K 600 °F Mn 0.4

MATERIAL SDOF #5

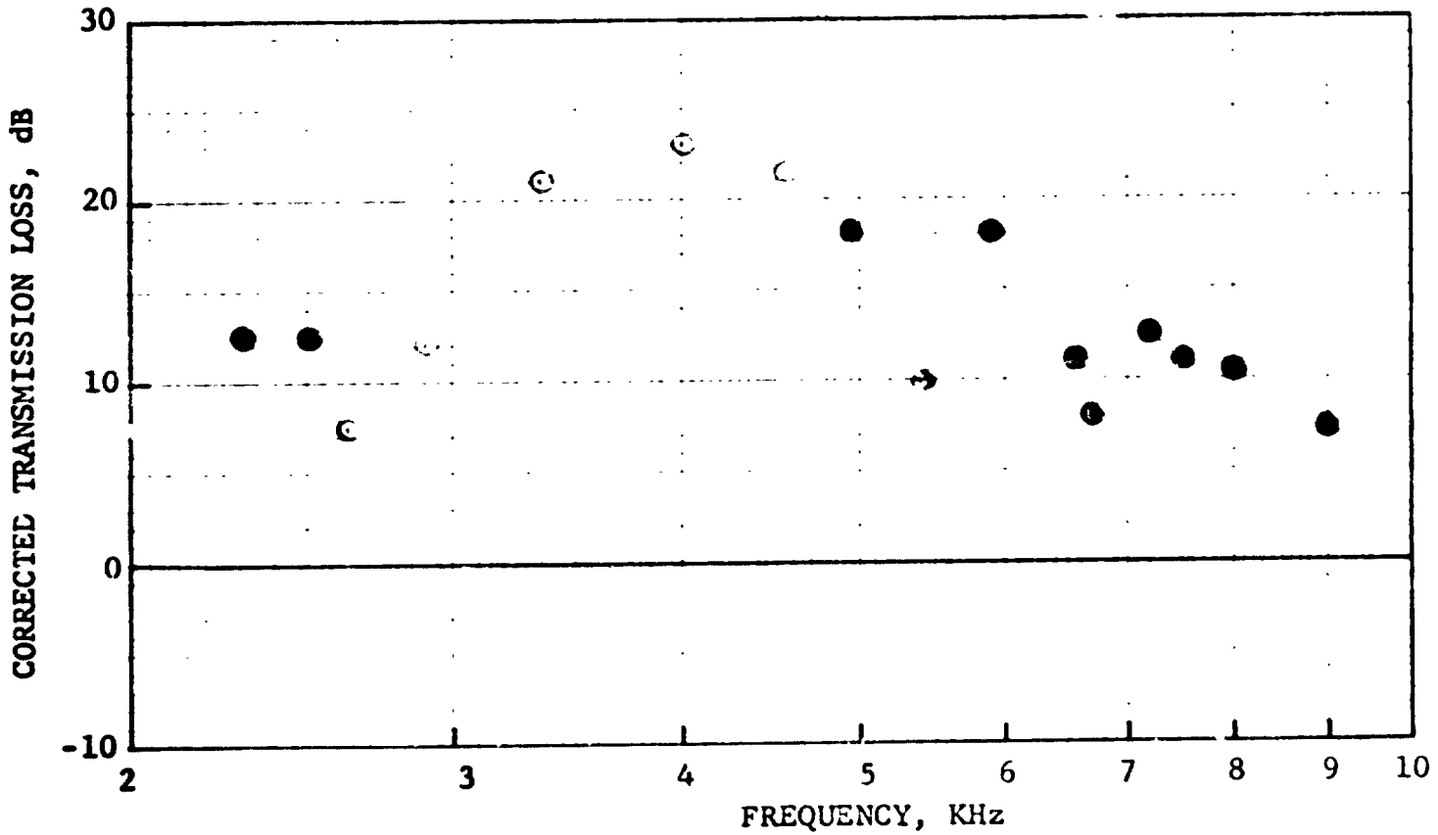

Figure 127. Corrected Transmission Loss Vs. Frequency.

HIGH TEMPERATURE ACOUSTIC DUCT .102m x .203m (4"x8")
TREATED ON TWO SIDES IN EXHAUST CONFIGURATION
L/H 4.5 TEMP. 589 °K 600 °F Min 0.21

MATERIAL SDOF #8

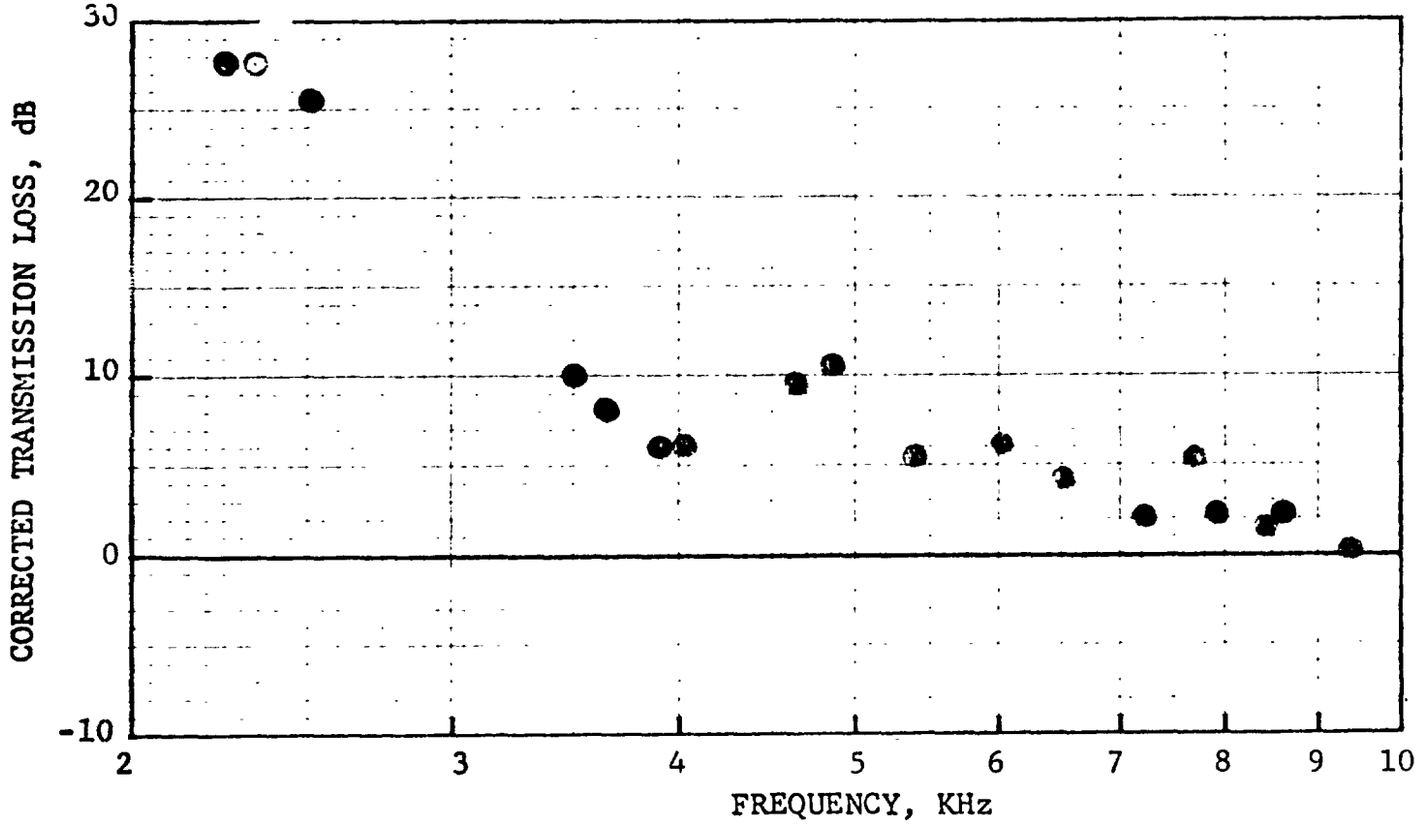

Figure 128. Corrected Transmission Loss Vs. Frequency.

HIGH TEMPERATURE ACOUSTIC DUCT .102m x .203m (4"x8")
TREATED ON TWO SIDES IN EXHAUST CONFIGURATION
L/H 4.5 TEMP. 589 °K 600 °F Mn 0.25
MATERIAL SDOF #8

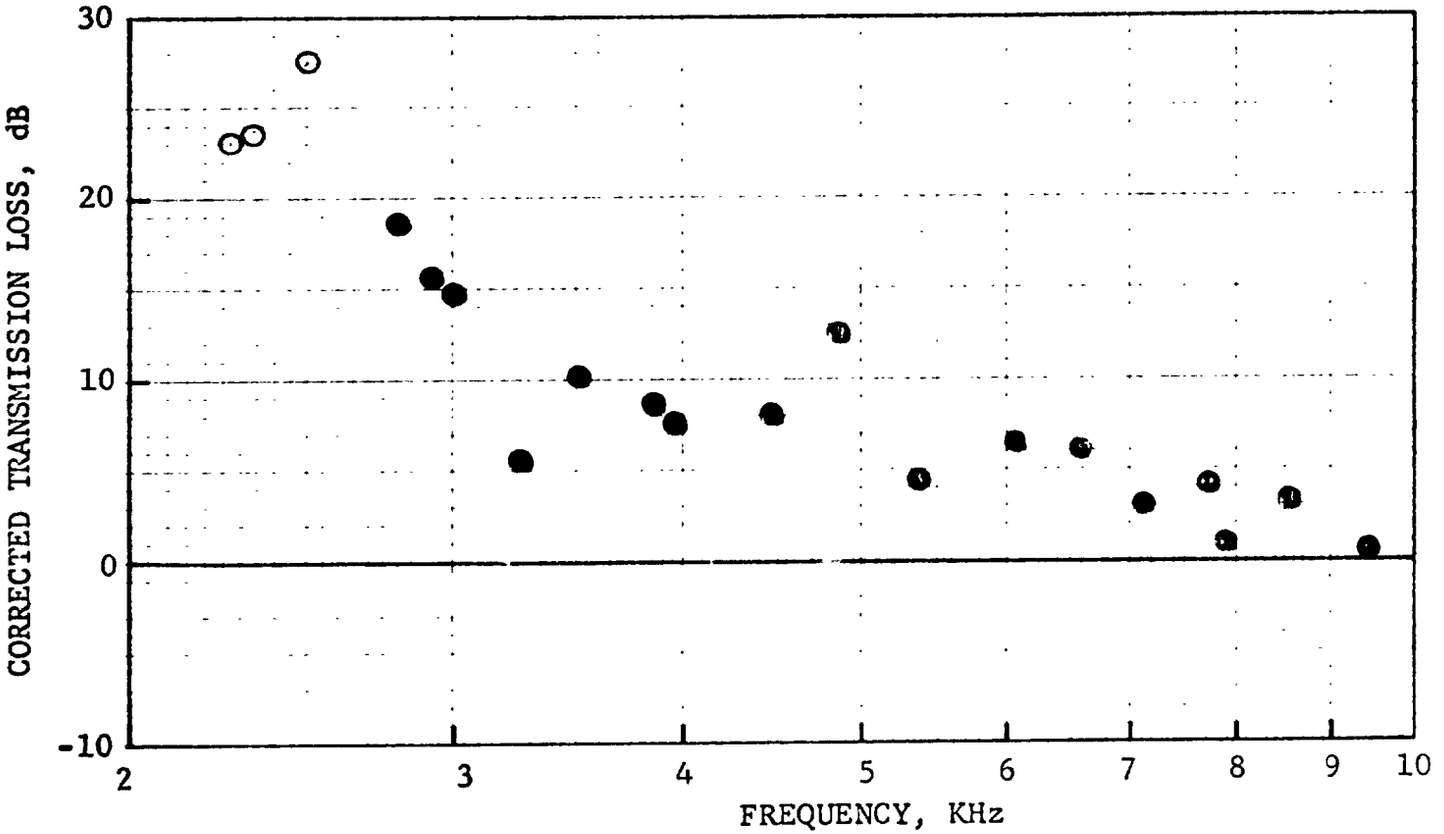

Figure 129. Corrected Transmission Loss Vs. Frequency.

HIGH TEMPERATURE ACOUSTIC DUCT .102m x .203m (4"x8")
TREATED ON TWO SIDES IN EXHAUST CONFIGURATION
L/H 4.5 TEMP. 589 °K 600 °F Mn 0.3

MATERIAL SDOF #8

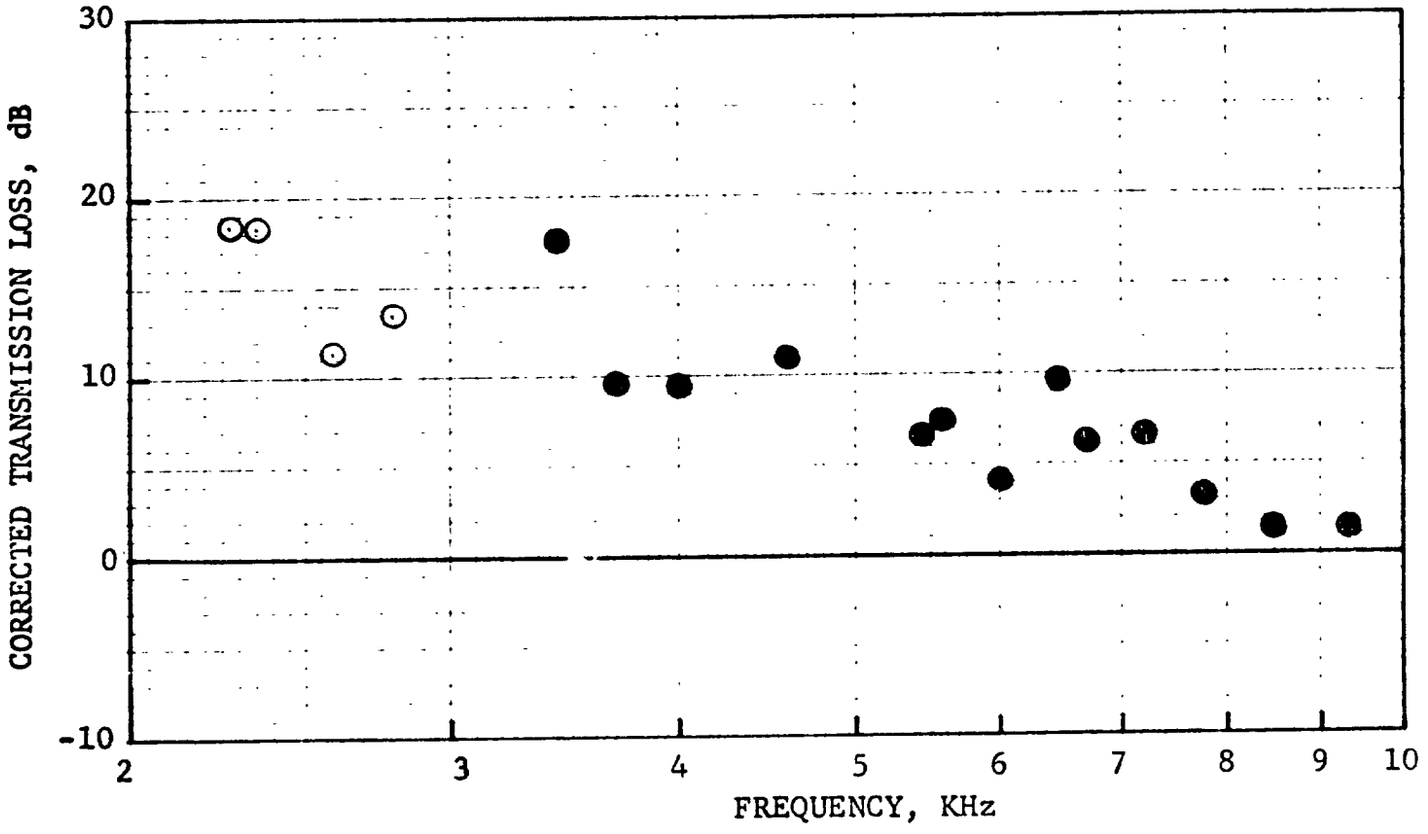

Figure 130. Corrected Transmission Loss Vs. Frequency.

HIGH TEMPERATURE ACOUSTIC DUCT .102m x .203m (4"x8")
TREATED ON TWO SIDES IN EXHAUST CONFIGURATION
L/H 4.5 TEMP. 589 °K 600 °F Mn 0.4

MATERIAL SDOF #8

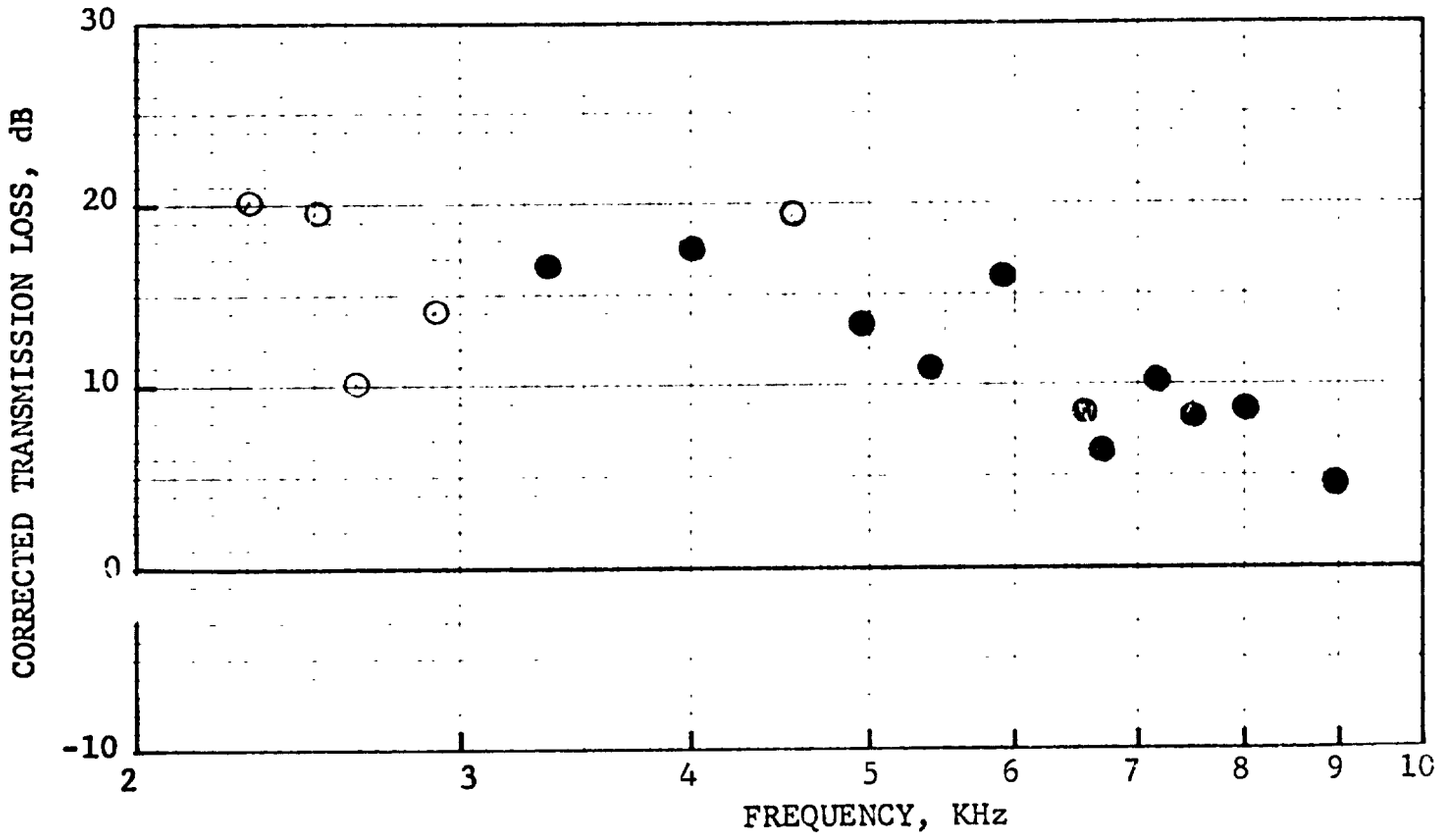

Figure 131. Corrected Transmission Loss Vs. Frequency.

HIGH TEMPERATURE ACOUSTIC DUCT .102m x .203m (4"x8")
TREATED ON TWO SIDES IN EXHAUST CONFIGURATION
L/H 4.5 TEMP. 589 °K 600 °F Mn 0.21

MATERIAL SDOR #10

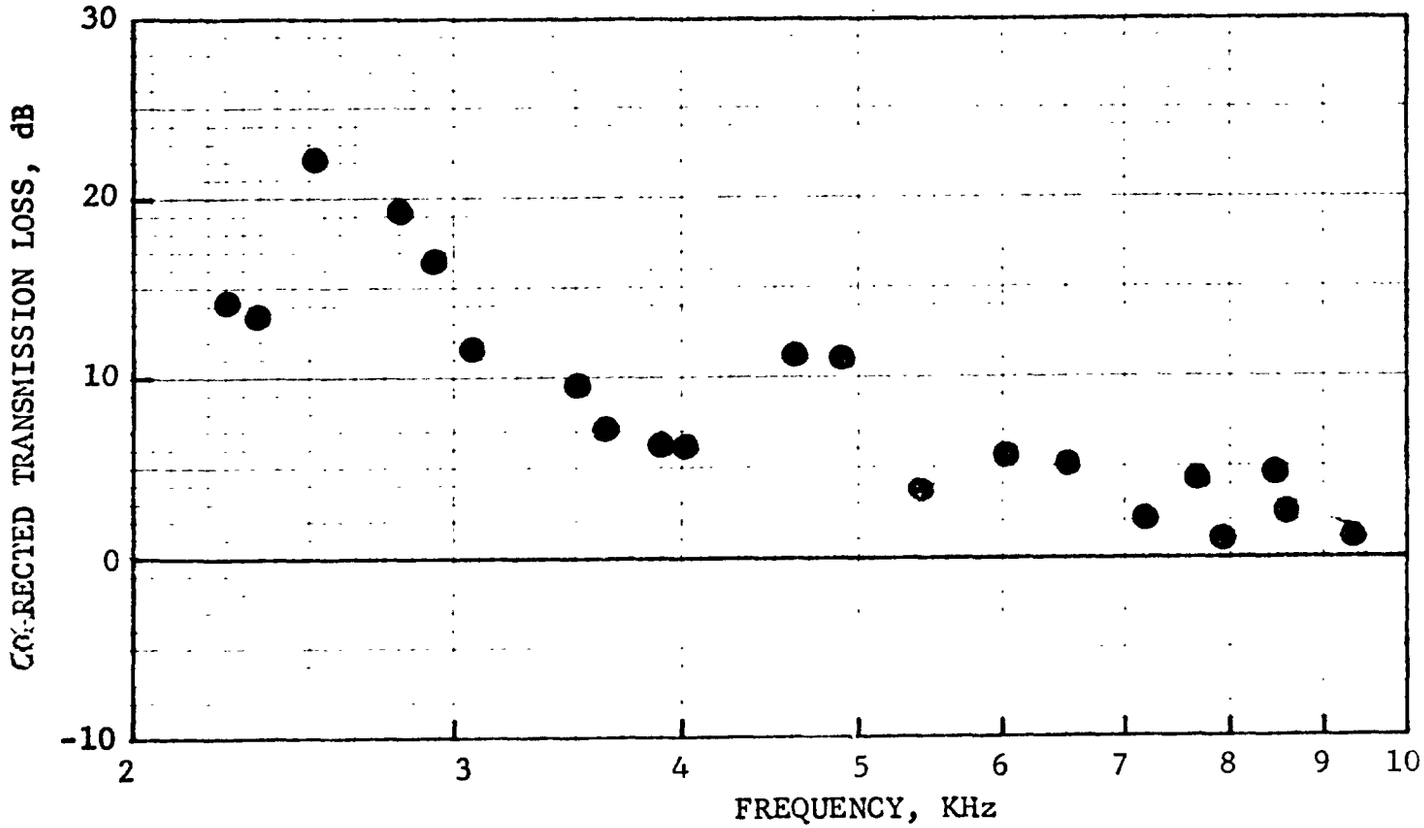

Figure 132. Corrected Transmission Loss Vs. Frequency.

HIGH TEMPERATURE ACOUSTIC DUCT .102m x .203m (4"x8")
TREATED ON TWO SIDES IN EXHAUST CONFIGURATION
L/H 4.5 TEMP. 589 °K 600 °F Mn 0.25

MATERIAL SDOF #10

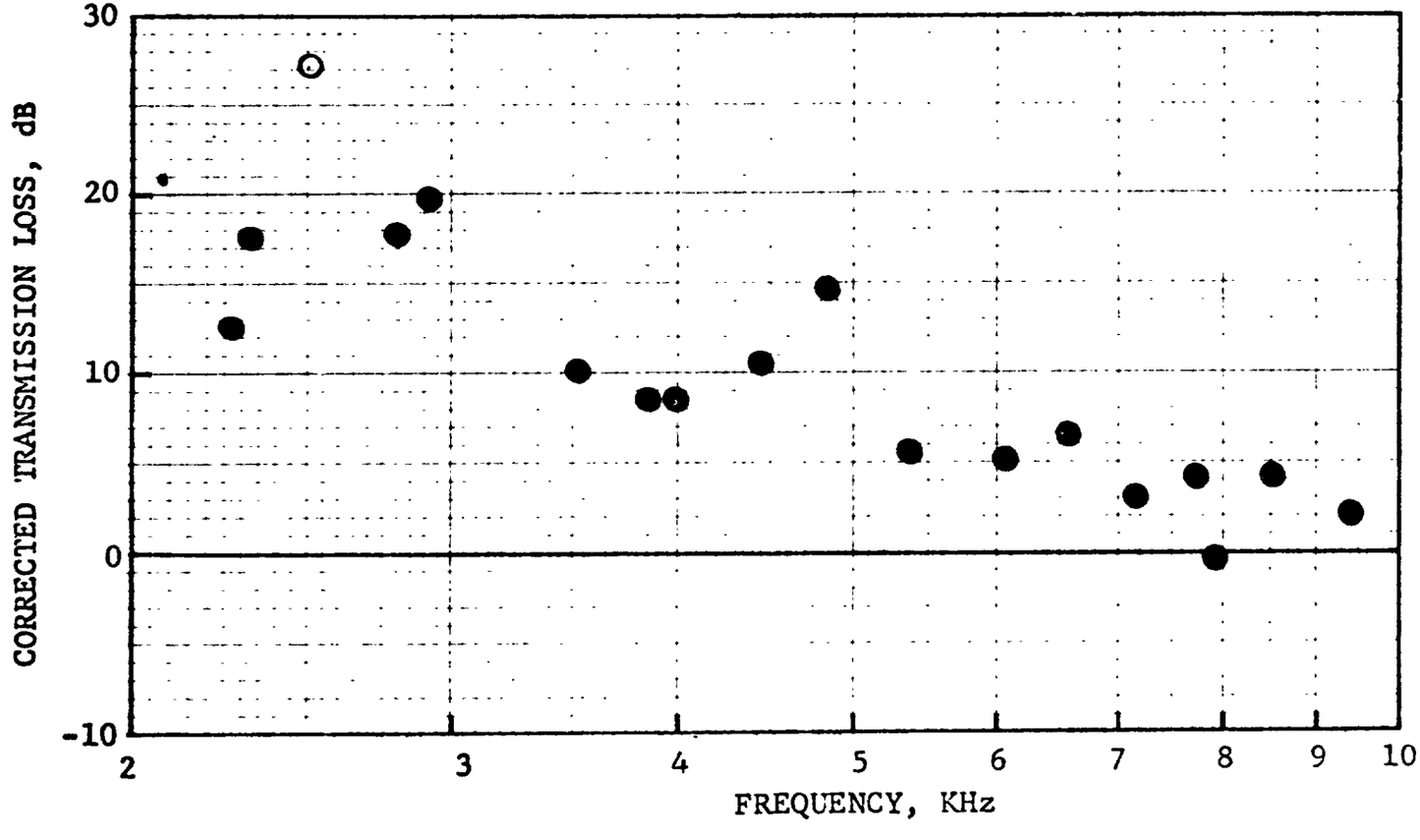

Figure 133. Corrected Transmission Loss Vs. Frequency.

HIGH TEMPERATURE ACOUSTIC DUCT .102m x .203m (4"x8")
TREATED ON TWO SIDES IN EXHAUST CONFIGURATION
L/H 4.5 TEMP. 589 °K 600 °F Mn 0.3

MATERIAL SDOF #10

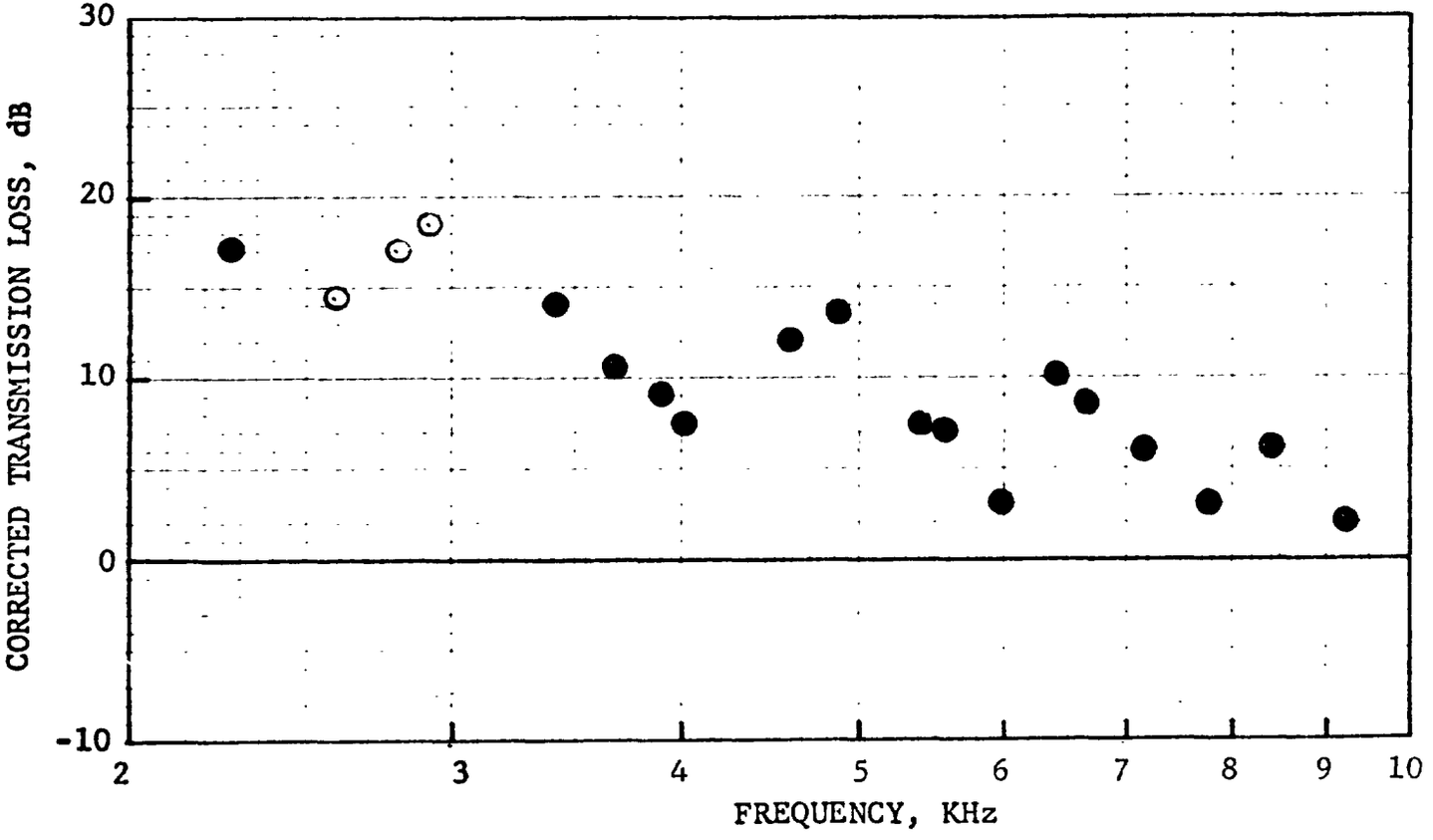

Figure 134. Corrected Transmission Loss Vs. Frequency.

HIGH TEMPERATURE ACOUSTIC DUCT .102m x .203m (4"x8")
TREATED ON TWO SIDES IN EXHAUST CONFIGURATION
L/H 4.5 TEMP. 589 °K 600 °F Mn 0.4

MATERIAL SDOF #10

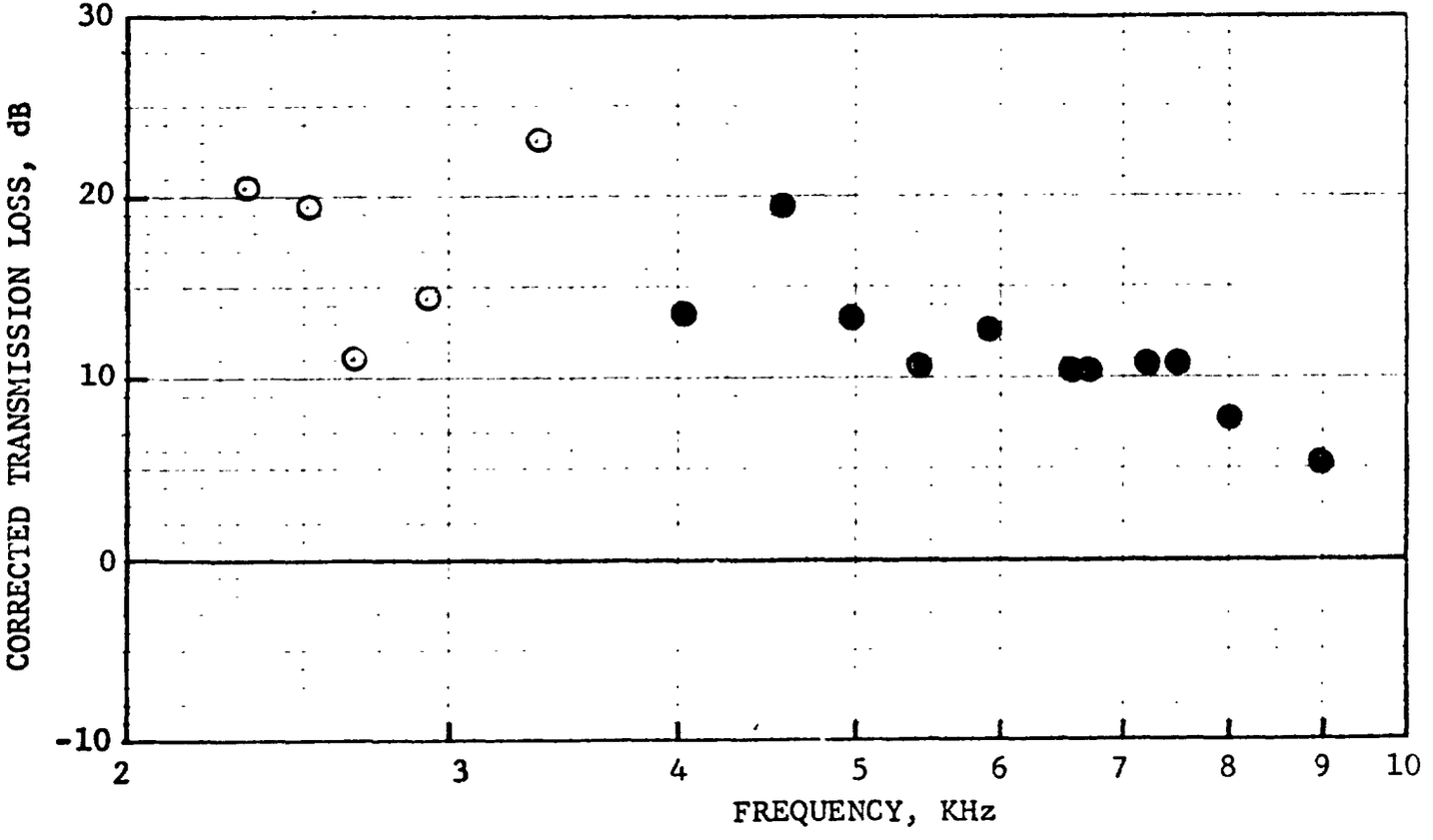

Figure 135. Corrected Transmission Loss Vs. Frequency.

HIGH TEMPERATURE ACOUSTIC DUCT .102m x .203m (4"x8")
TREATED ON TWO SIDES IN EXHAUST CONFIGURATION
L/H 4.5 TEMP. 589 °K 600 °F Mn 0.21

MATERIAL SDOF #12

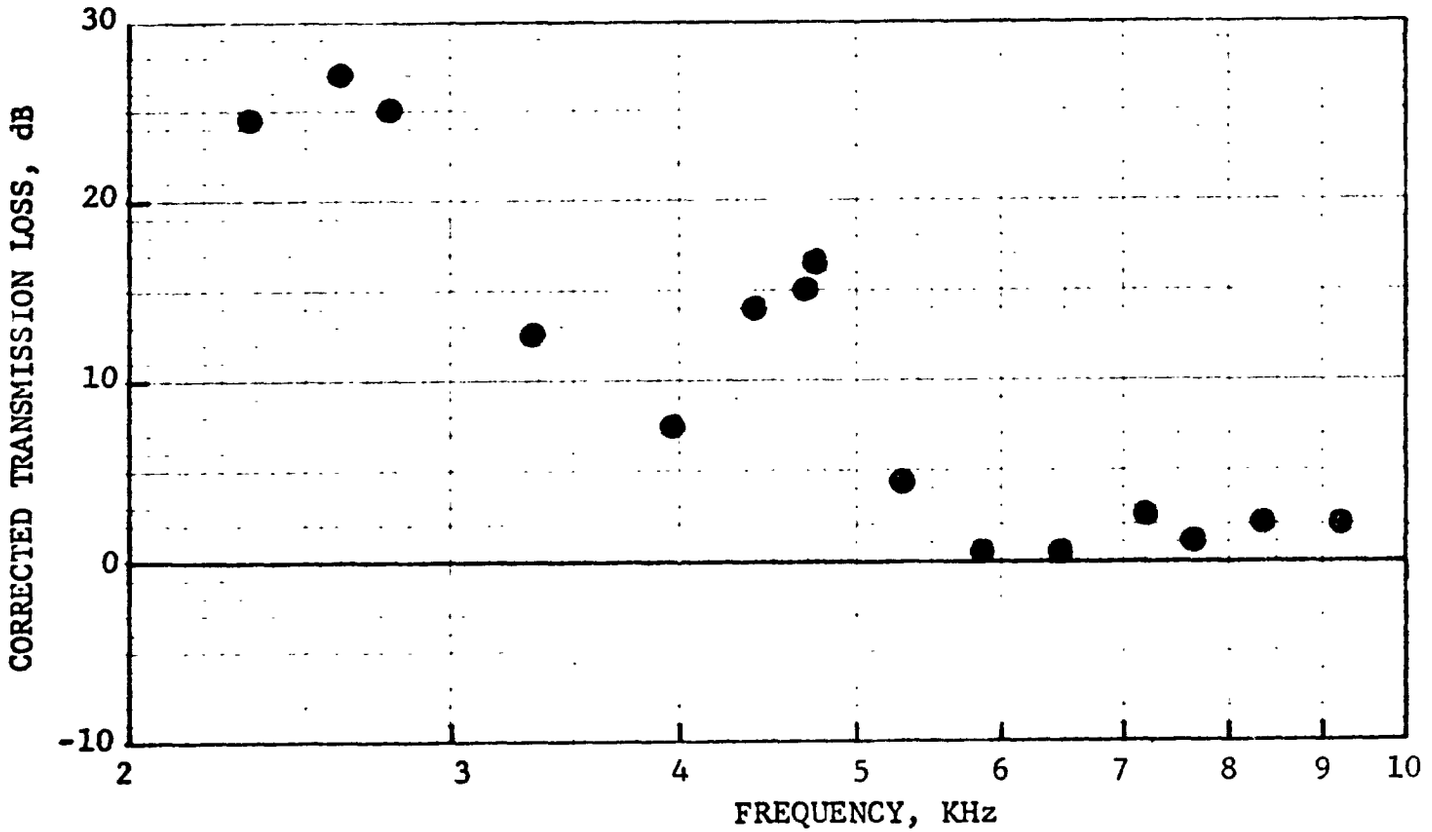

Figure 136. Corrected Transmission Loss Vs. Frequency.

HIGH TEMPERATURE ACOUSTIC DUCT .102m x .203m (4"x8")
TREATED ON TWO SIDES IN EXHAUST CONFIGURATION
L/H 4.5 TEMP. 589 °K 600 °F Mn 0.25

MATERIAL SDOF #12

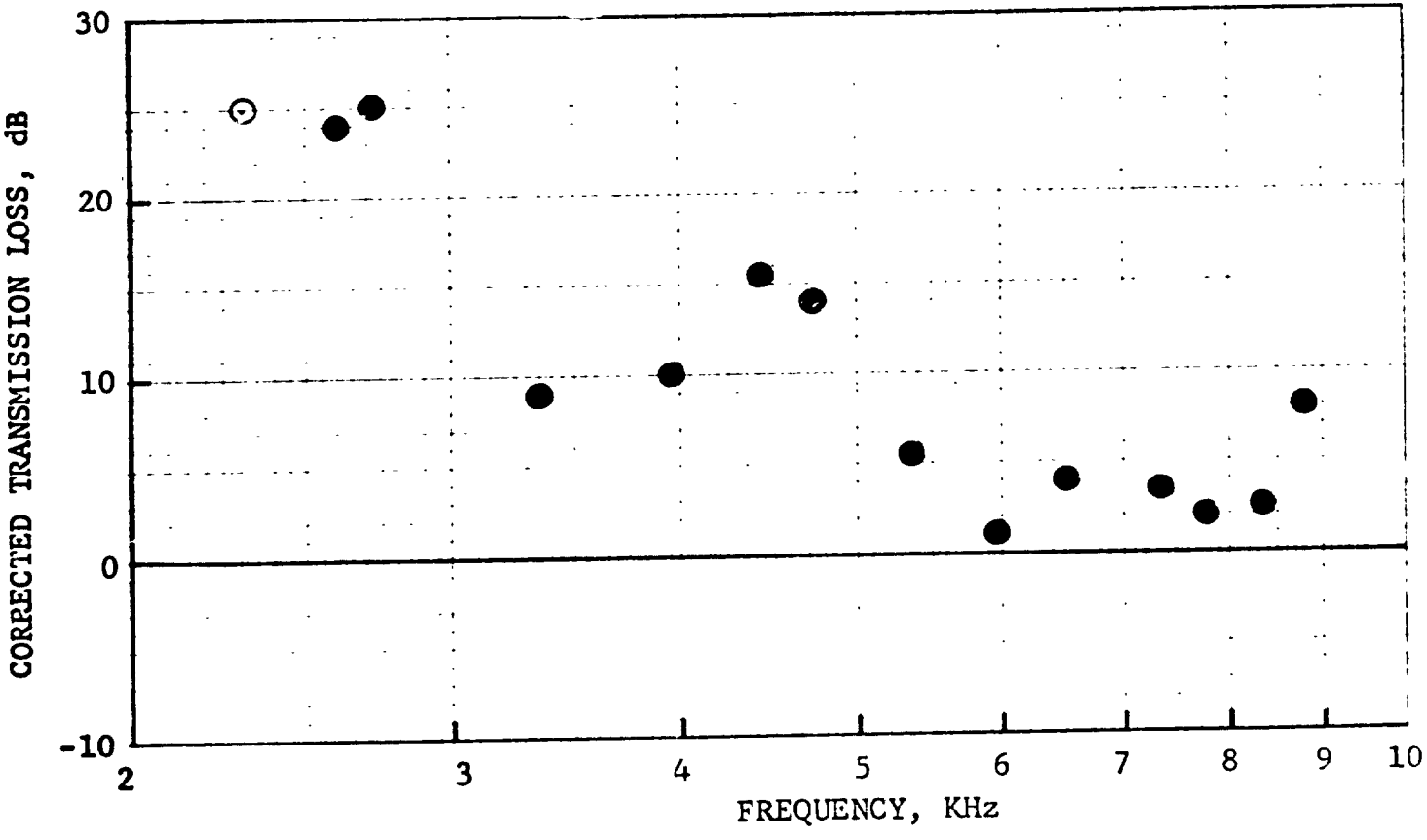

Figure 137. Corrected Transmission Loss Vs. Frequency.

HIGH TEMPERATURE ACOUSTIC DUCT .102m x .203m (4"x8")
TREATED ON TWO SIDES IN E.HAUST CONFIGURATION
L/H 4.5 TEMP. 589 °K 600 °F Mn 0.3

MATERIAL SDOF #12

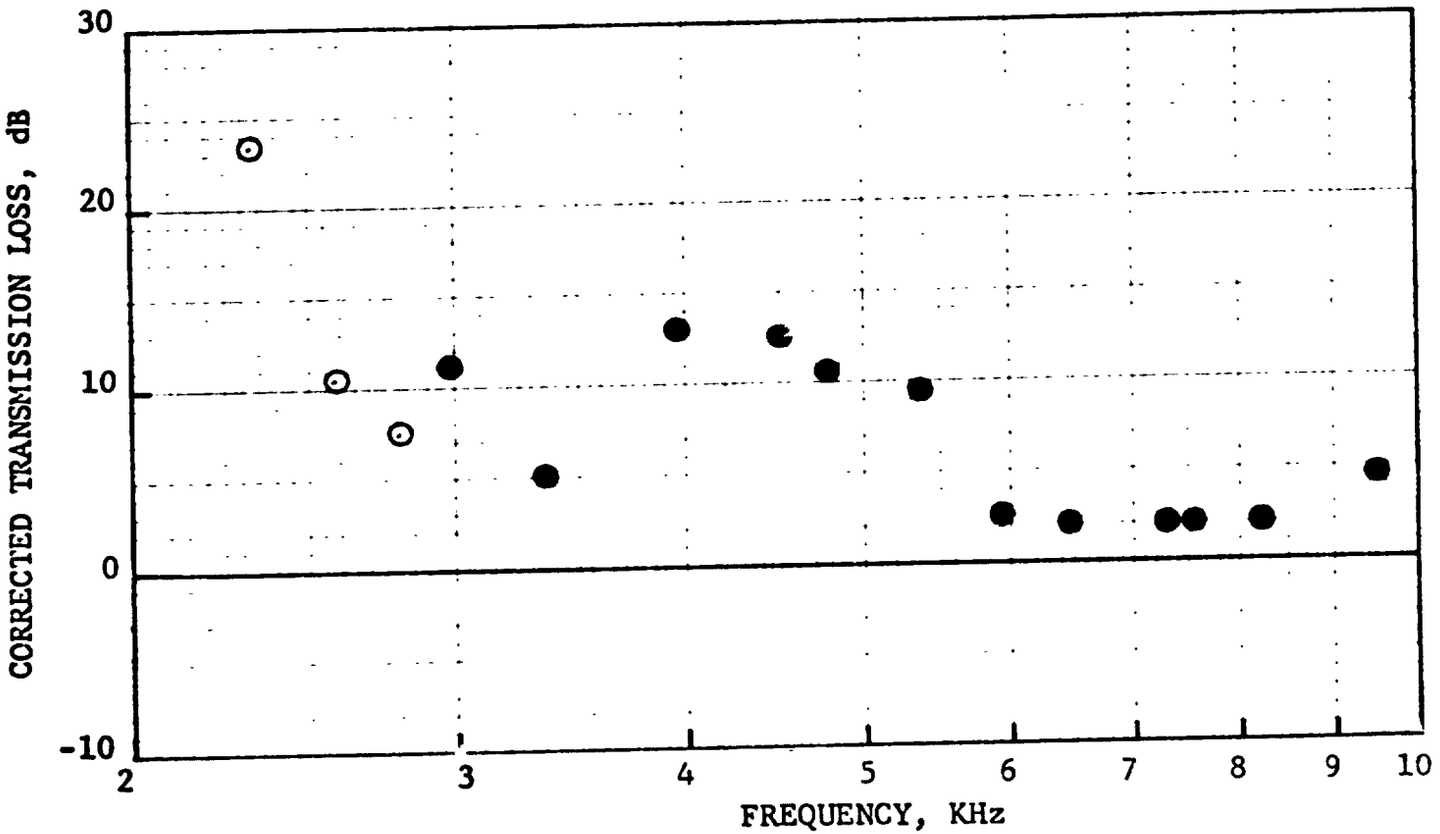

Figure 138. Corrected Transmission Loss Vs. Frequency.

HIGH TEMPERATURE ACOUSTIC DUCT .102m x .203m (4"x8")
TREATED ON TWO SIDES IN EXHAUST CONFIGURATION
L/H 4.5 TEMP. 589 °K 600 °F Mn 0.4

MATERIAL SDOF #12

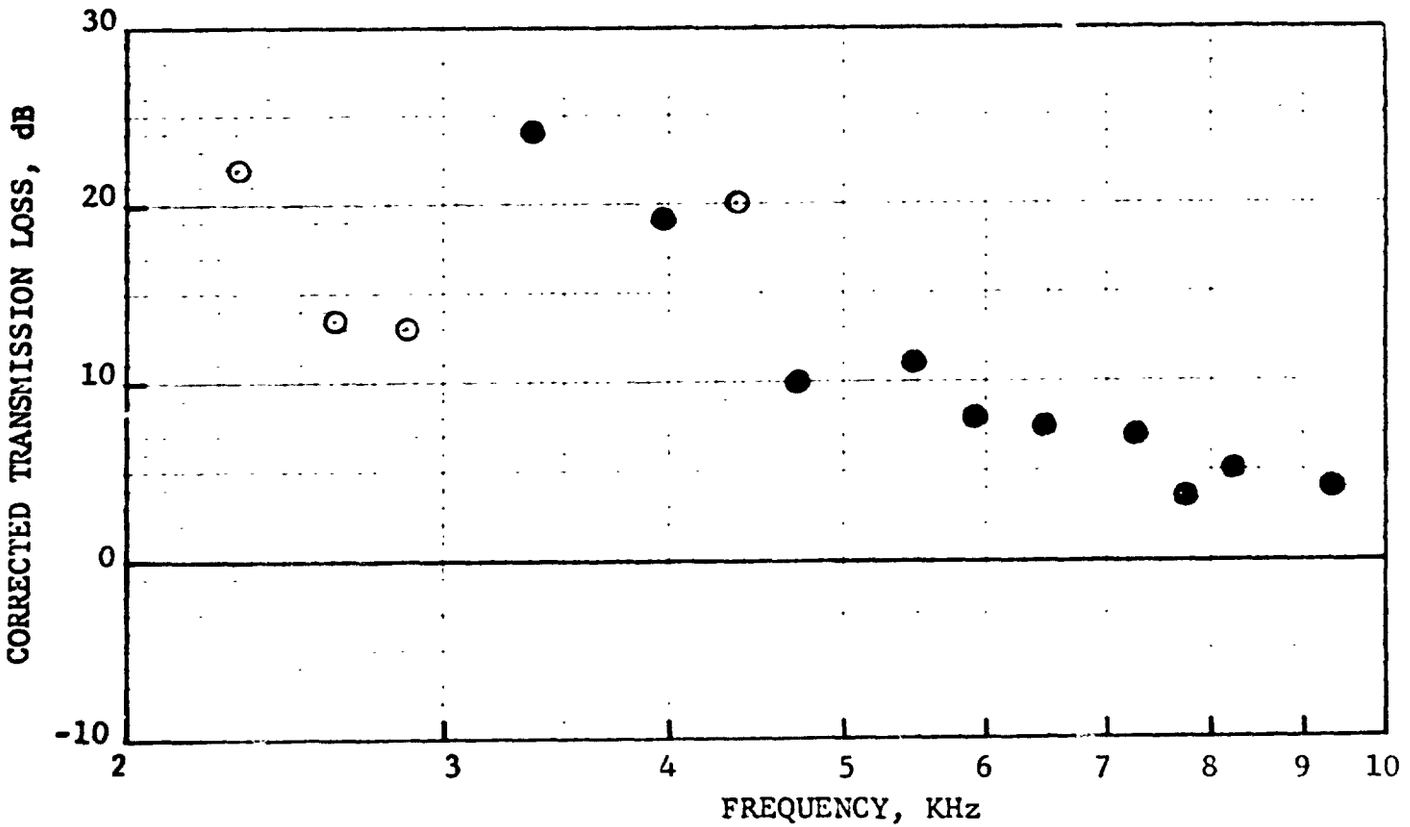

Figure 139. Corrected Transmission Loss Vs. Frequency.

HIGH TEMPERATURE ACOUSTIC DUCT .102m x .203m (4"x8")
TREATED ON TWO SIDES IN EXHAUST CONFIGURATION
L/H 4.5 TEMP. 589 °K 600 °F Mn 0.21

MATERIAL SDOF #14

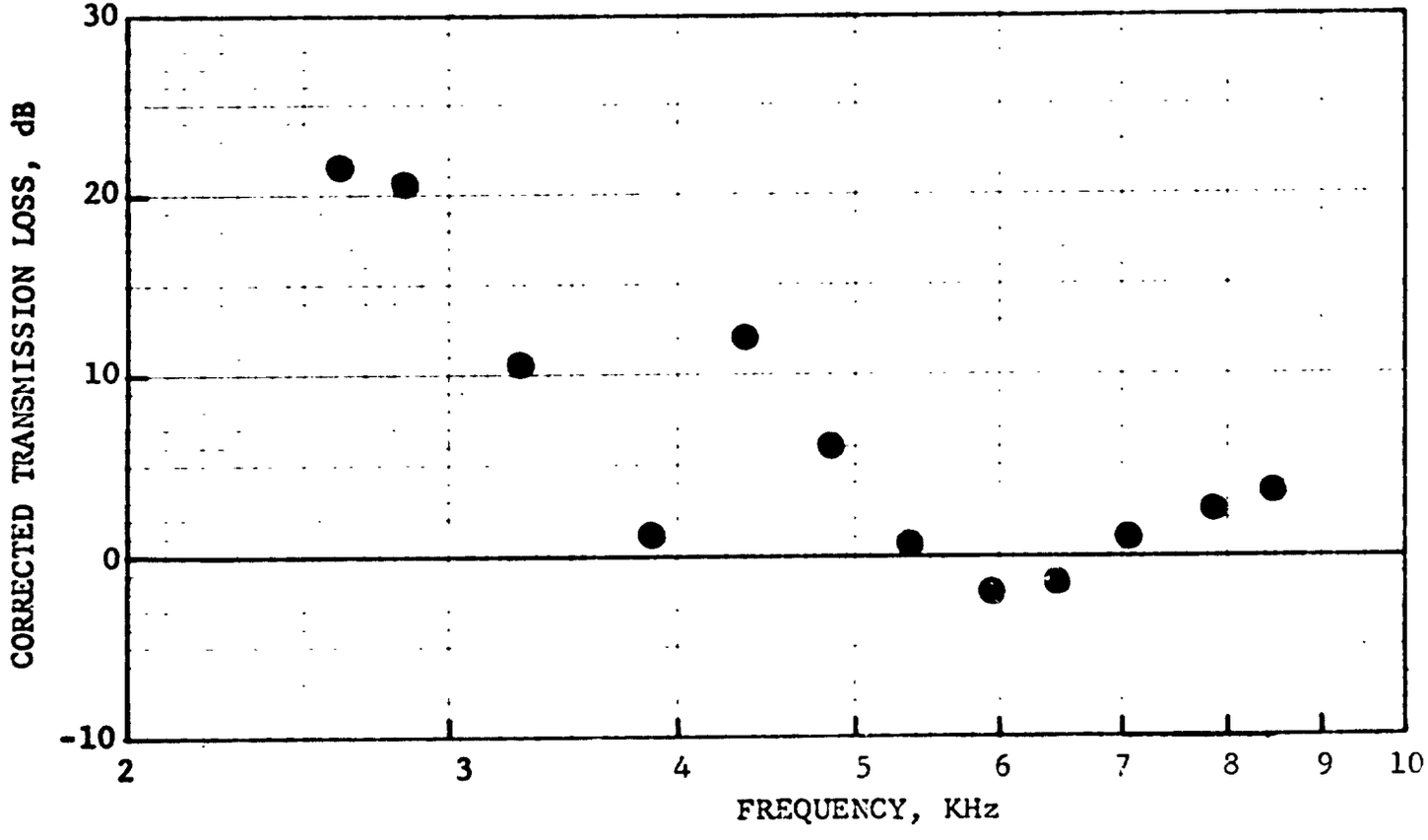

Figure 140. Corrected Transmission Loss Vs. Frequency.

HIGH TEMPERATURE ACOUSTIC DUCT .102m x .203m (4"x8")
TREATED ON TWO SIDES IN EXHAUST CONFIGURATION
L/H 4.5 TEMP. 589 °K 600 °F Mn 0.25

MATERIAL SDOF #14

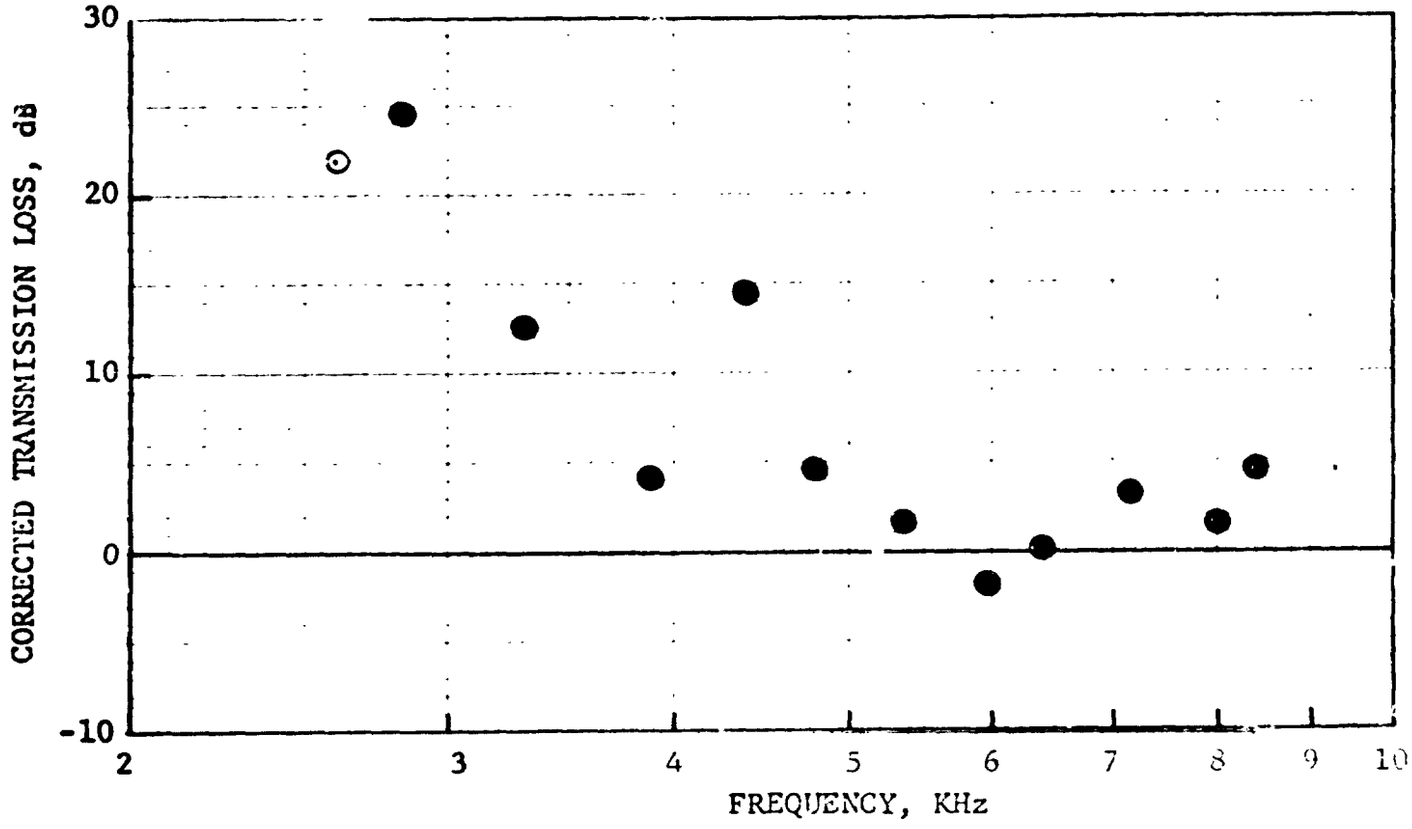

Figure 141. Corrected Transmission Loss Vs. Frequency.

HIGH TEMPERATURE ACOUSTIC DUCT .102m x .203m (4"x8")
TREATED ON TWO SIDES IN EXHAUST CONFIGURATION
L/H 4.5 TEMP. 589 °K 600 °F Mn 0.3

MATERIAL SDOF #14

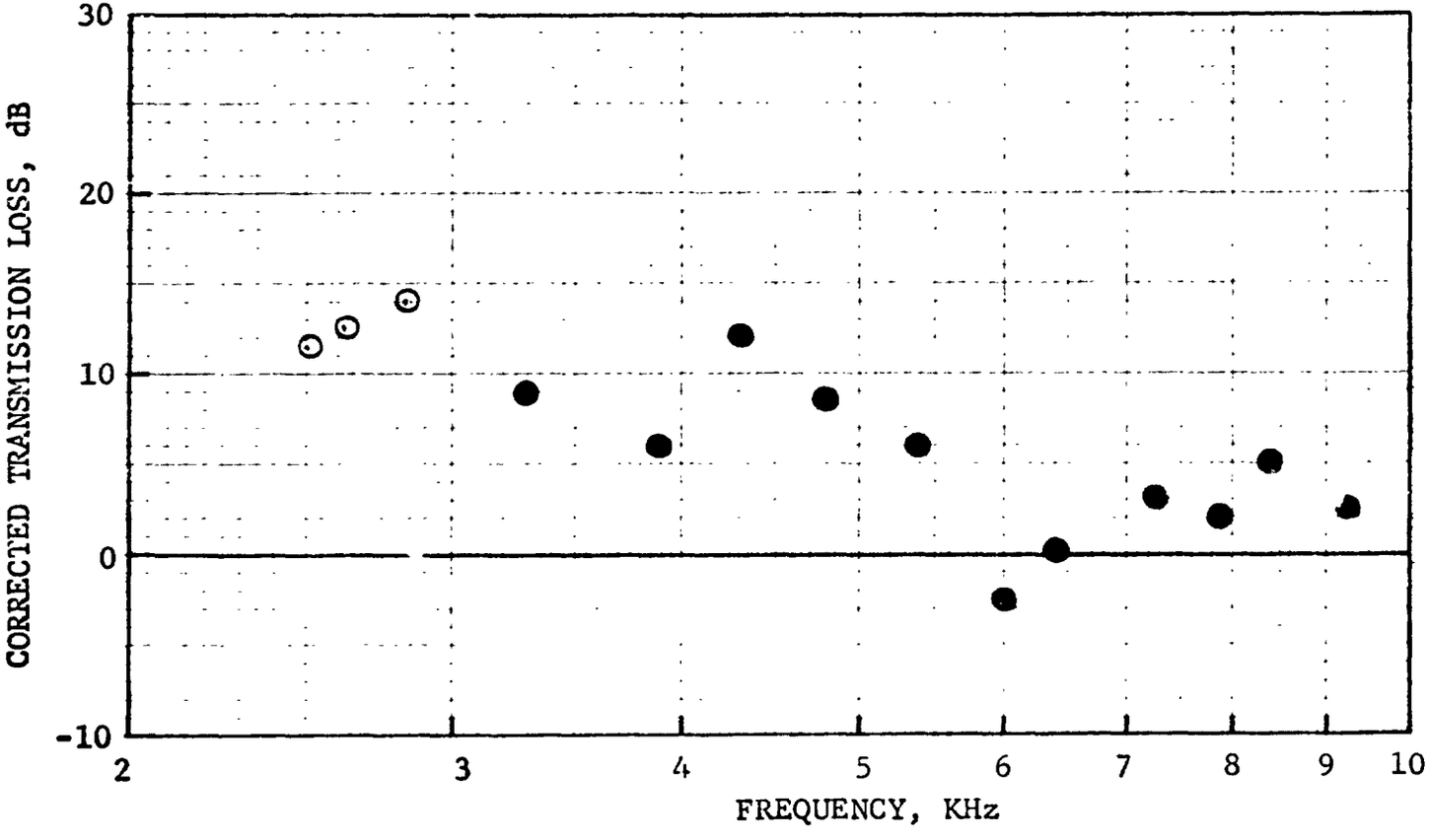

Figure 142. Corrected Transmission Loss Vs. Frequency.

HIGH TEMPERATURE ACOUSTIC DUCT .102m x .203m (4"x8")
TREATED ON TWO SIDES IN EXHAUST CONFIGURATION
L/H 4.5 TEMP. 589 °K 600 °F Mn 0.4

MATERIAL SDOF #14

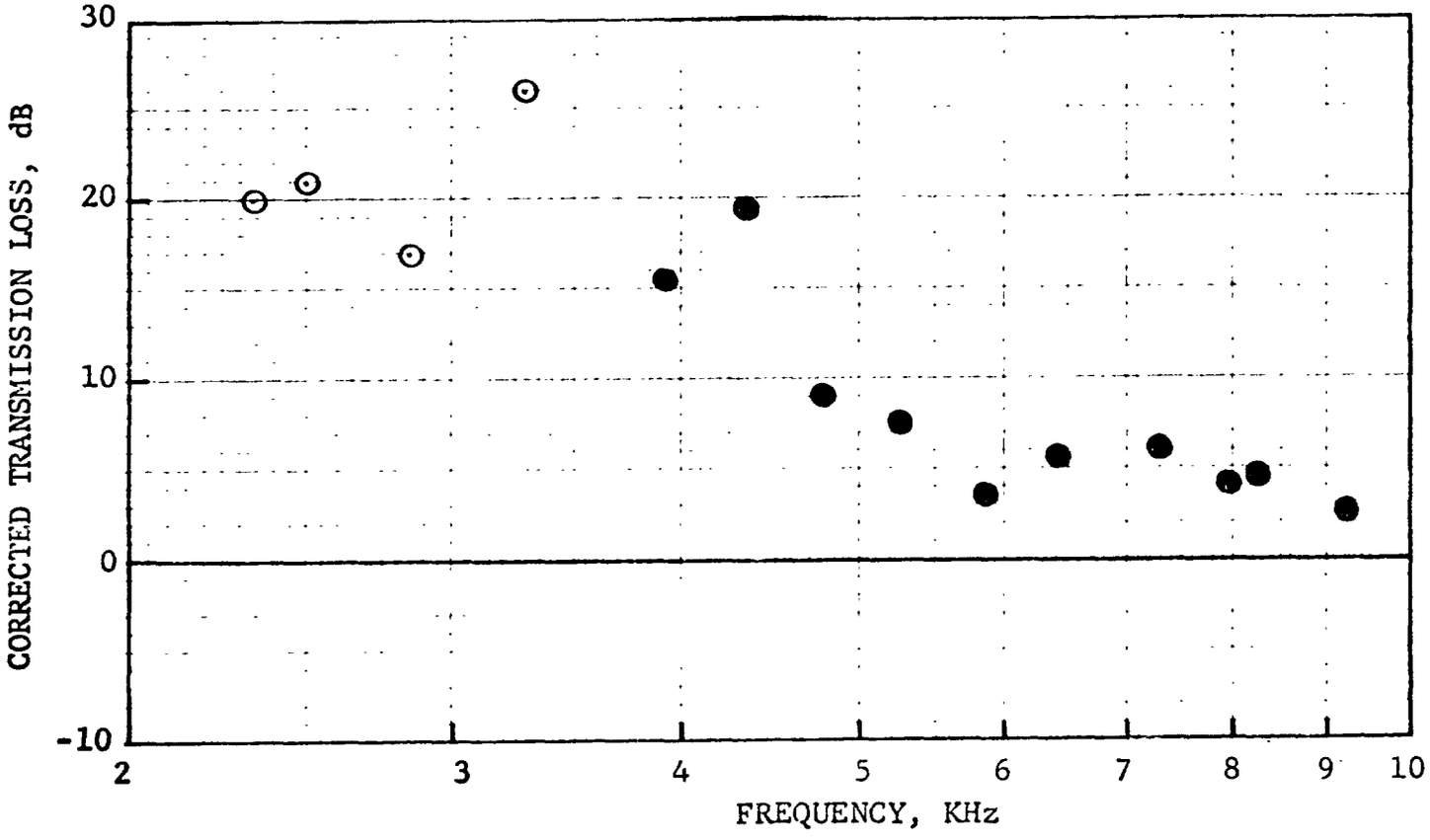

Figure 143. Corrected Transmission Loss Vs. Frequency.

HIGH TEMPERATURE ACOUSTIC DUCT .102m x .203m (4"x8")
TREATED ON TWO SIDES IN EXHAUST CONFIGURATION
L/H 4.5 TEMP. 589 °K 600 °F Mn 0.21

MATERIAL SDOF #16

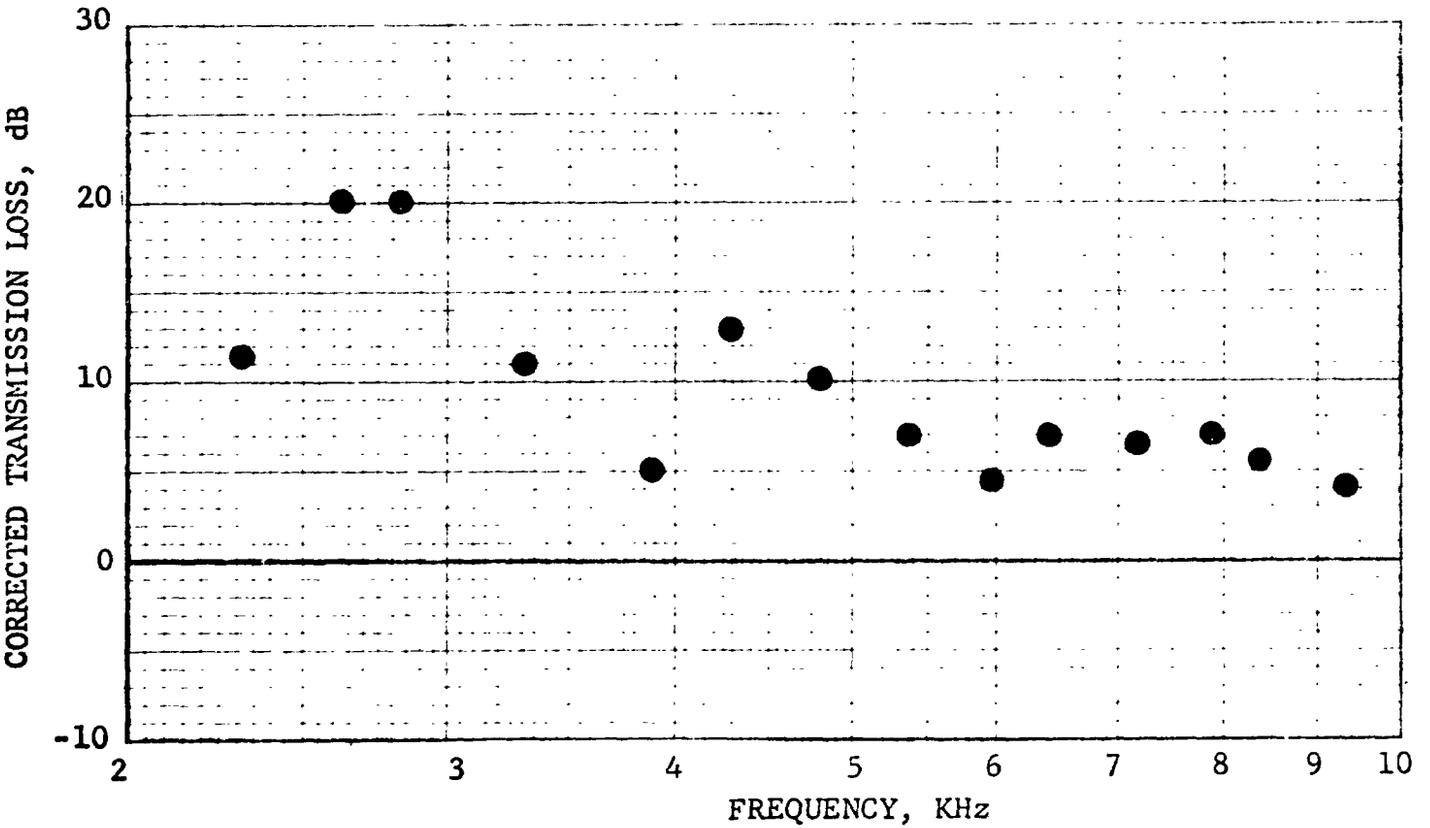

Figure 144. Corrected Transmission Loss Vs. Frequency.

HIGH TEMPERATURE ACOUSTIC DUCT .102m x .203m (4"x8")
TREATED ON TWO SIDES IN EXHAUST CONFIGURATION
L/H 4.5 TEMP. 589 °K 600 °F Mn 0.25

MATERIAL SDOF #16

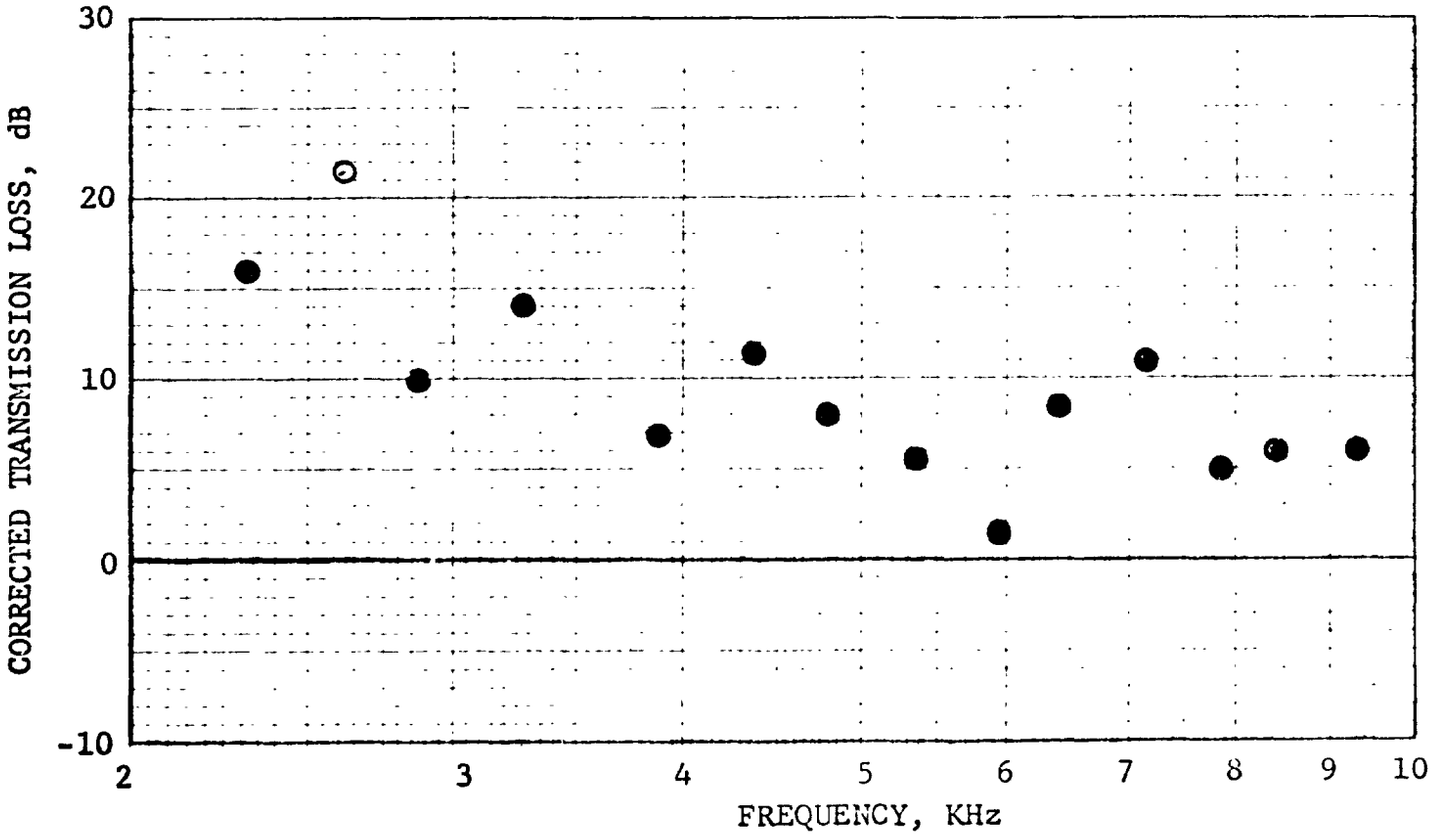

Figure 145. Corrected Transmission Loss Vs. Frequency.

HIGH TEMPERATURE ACOUSTIC DUCT .102m x .203m (4"x8")
TREATED ON TWO SIDES IN EXHAUST CONFIGURATION
L/H 4.5 TEMP. 589 °K 600 °F Mn 0.3

MATERIAL SDOF #16

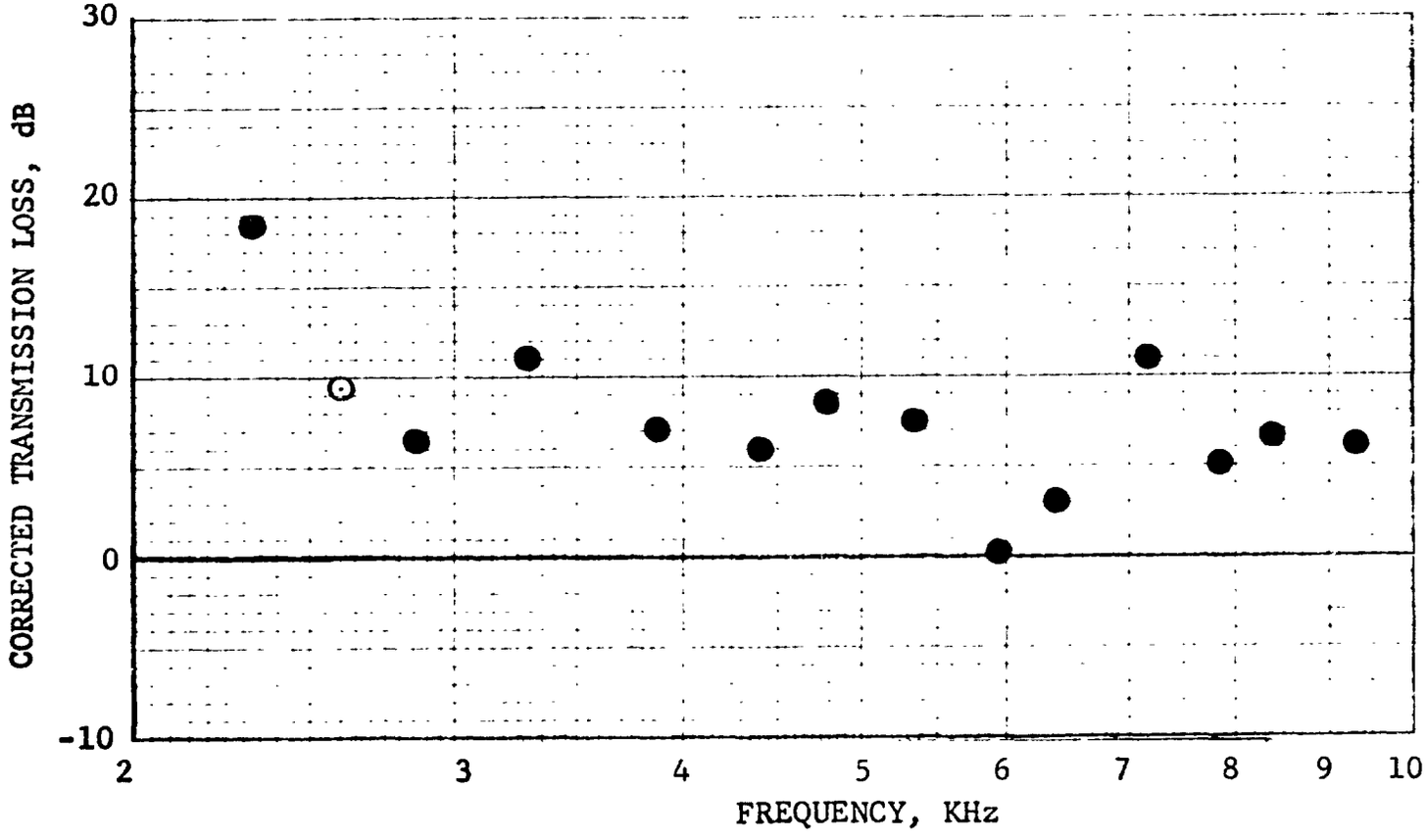

Figure 146. Corrected Transmission Loss Vs. Frequency.

HIGH TEMPERATURE ACOUSTIC DUCT .102m x .203m (4"x8")
TREATED ON TWO SIDES IN EXHAUST CONFIGURATION
L/H 4.5 TEMP. 589 °K ( ) °F Mn 0.4

MATERIAL SDOF #16

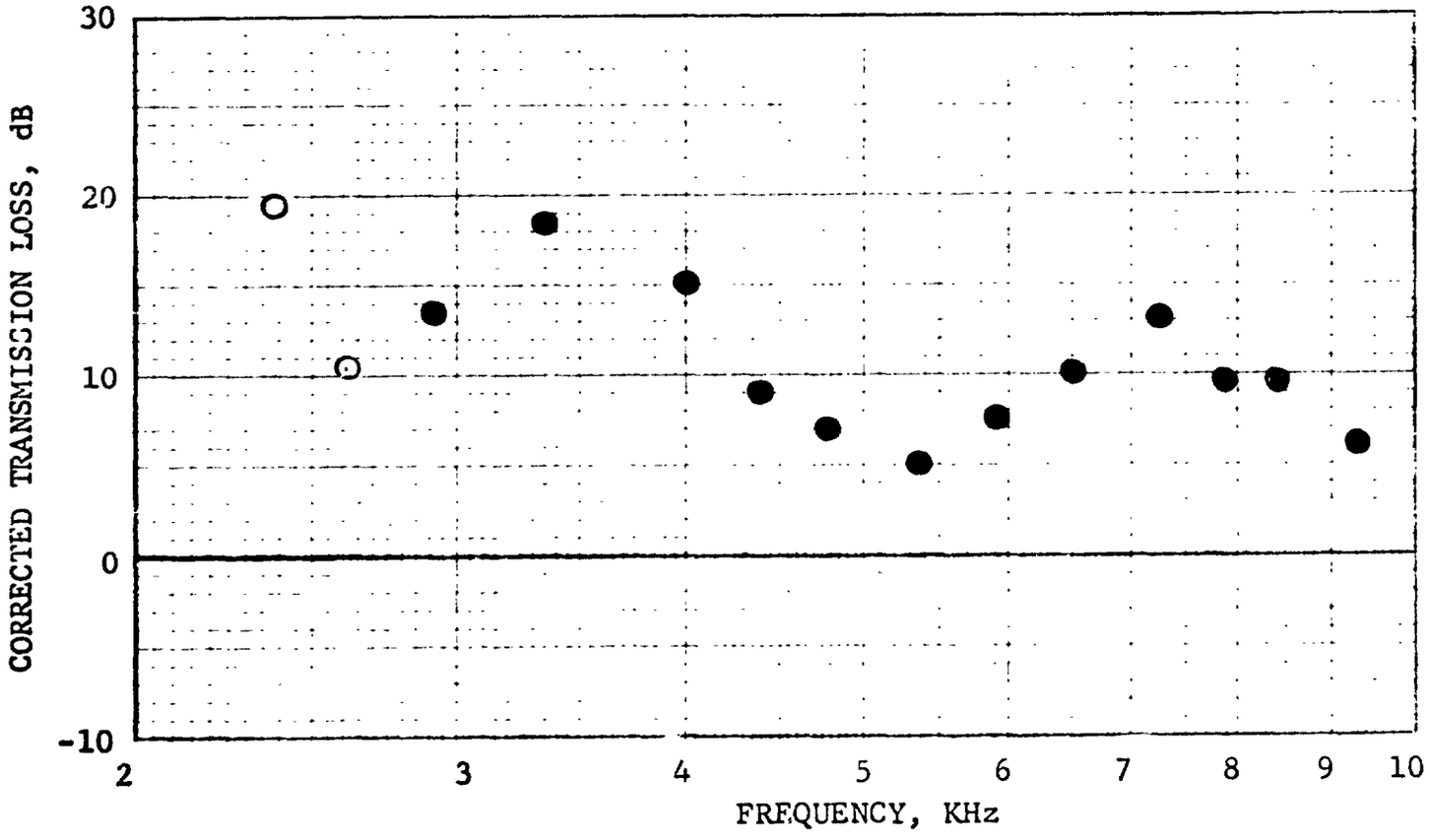

Figure 147. Corrected Transmission Loss Vs. Frequency.

HIGH TEMPERATURE ACOUSTIC DUCT .102m x .203m (4"x8")
TREATED ON TWO SIDES IN EXHAUST CONFIGURATION
L/H 4.5 TEMP. 589 °K 600 °F Mn 0.21

MATERIAL SDOF #17

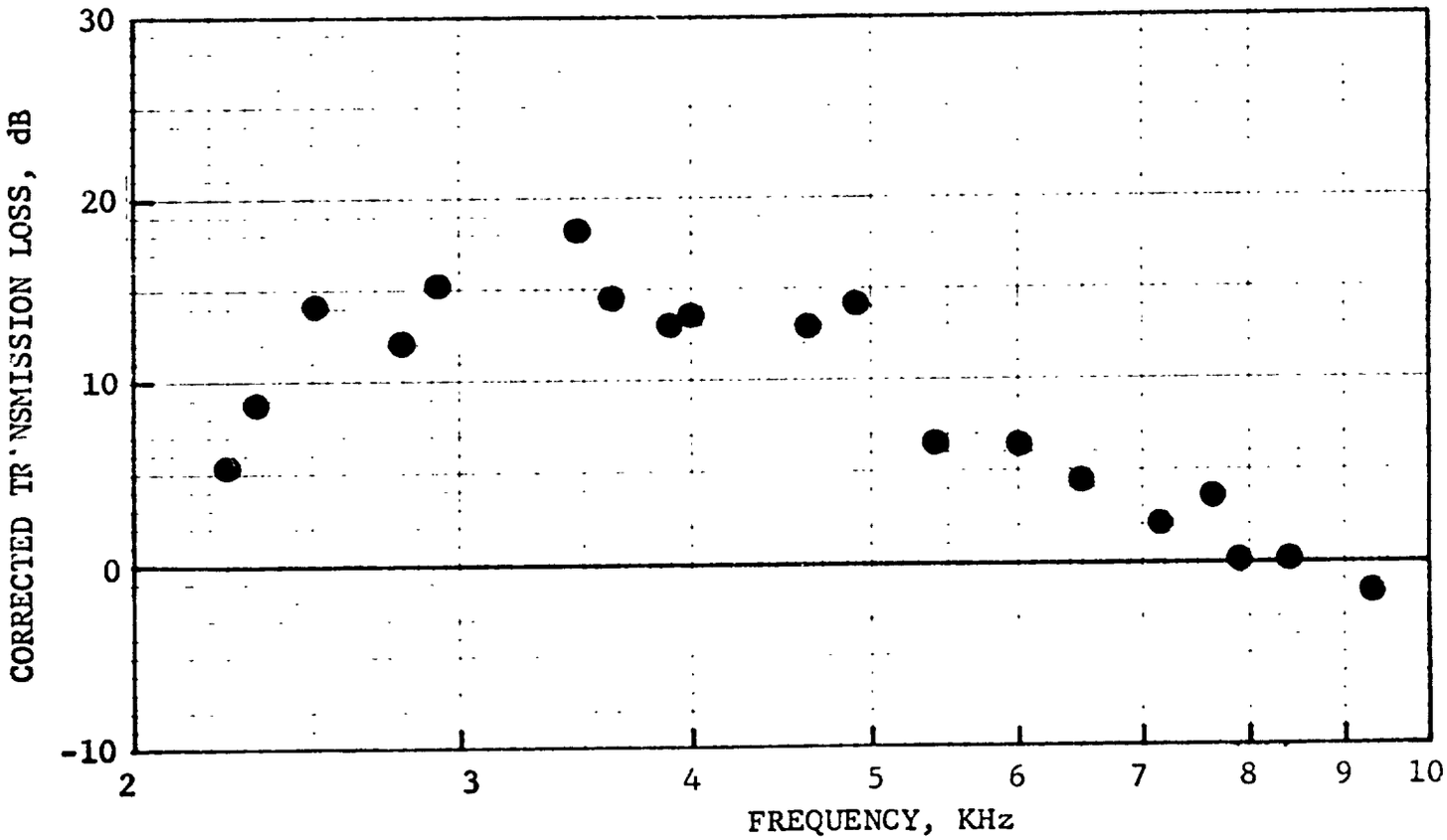

Figure 148. Corrected Transmission Loss Vs. Frequency.

HIGH TEMPERATURE ACOUSTIC DUCT .102m x .203m (4"x8")
TREATED ON TWO SIDES IN EXHAUST CONFIGURATION
L/H 4.5 TEMP. 589 °K 600 °F Mn 0.25

MATERIAL SDOF #17

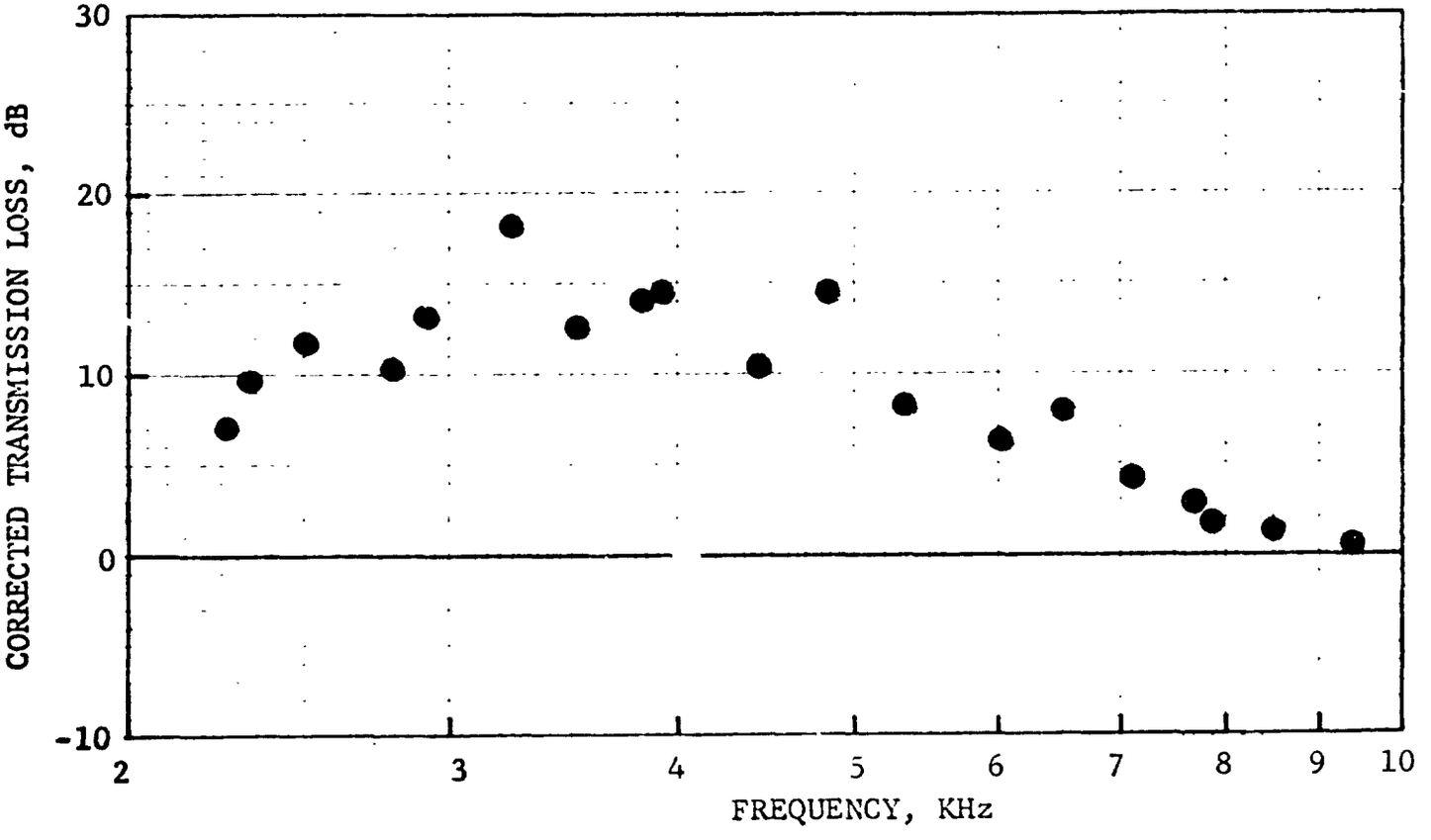

Figure 149. Corrected Transmission Loss Vs. Frequency.

HIGH TEMPERATURE ACOUSTIC DUCT .102m x .203m (4"x8")
TREATED ON TWO SIDES IN EXHAUST CONFIGURATION
L/H 4.5 TEMP. 589 °K 600 °F Mn 0.3

MATERIAL SDOF #17

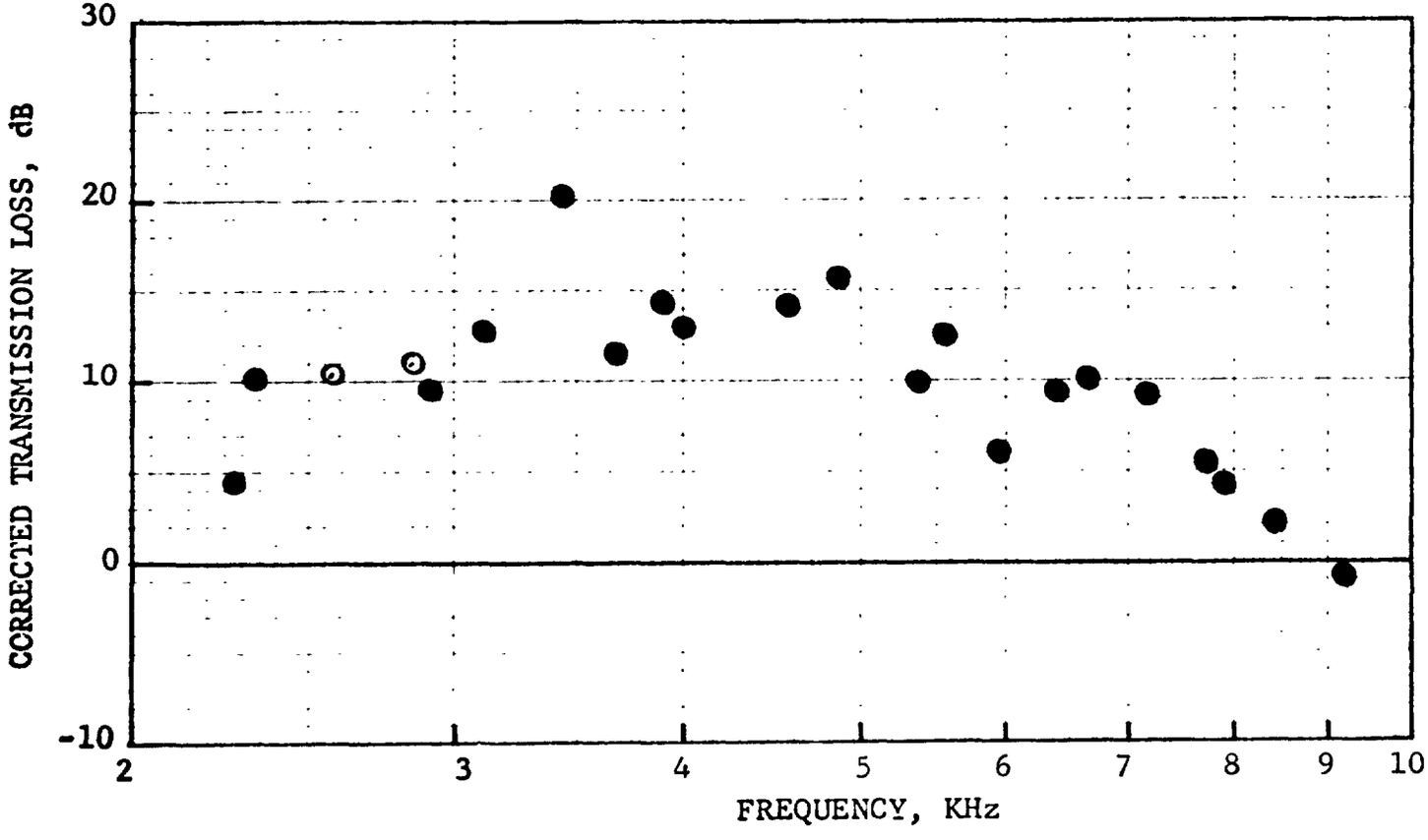

Figure 150. Corrected Transmission Loss Vs. Frequency.

HIGH TEMPERATURE ACOUSTIC DUCT .102m x .203m (4"x8")
TREATED ON TWO SIDES IN EXHAUST CONFIGURATION
L/H 4.5 TEMP. 589 °K 600 °F Mn 0.4

MATERIAL SDOF #17

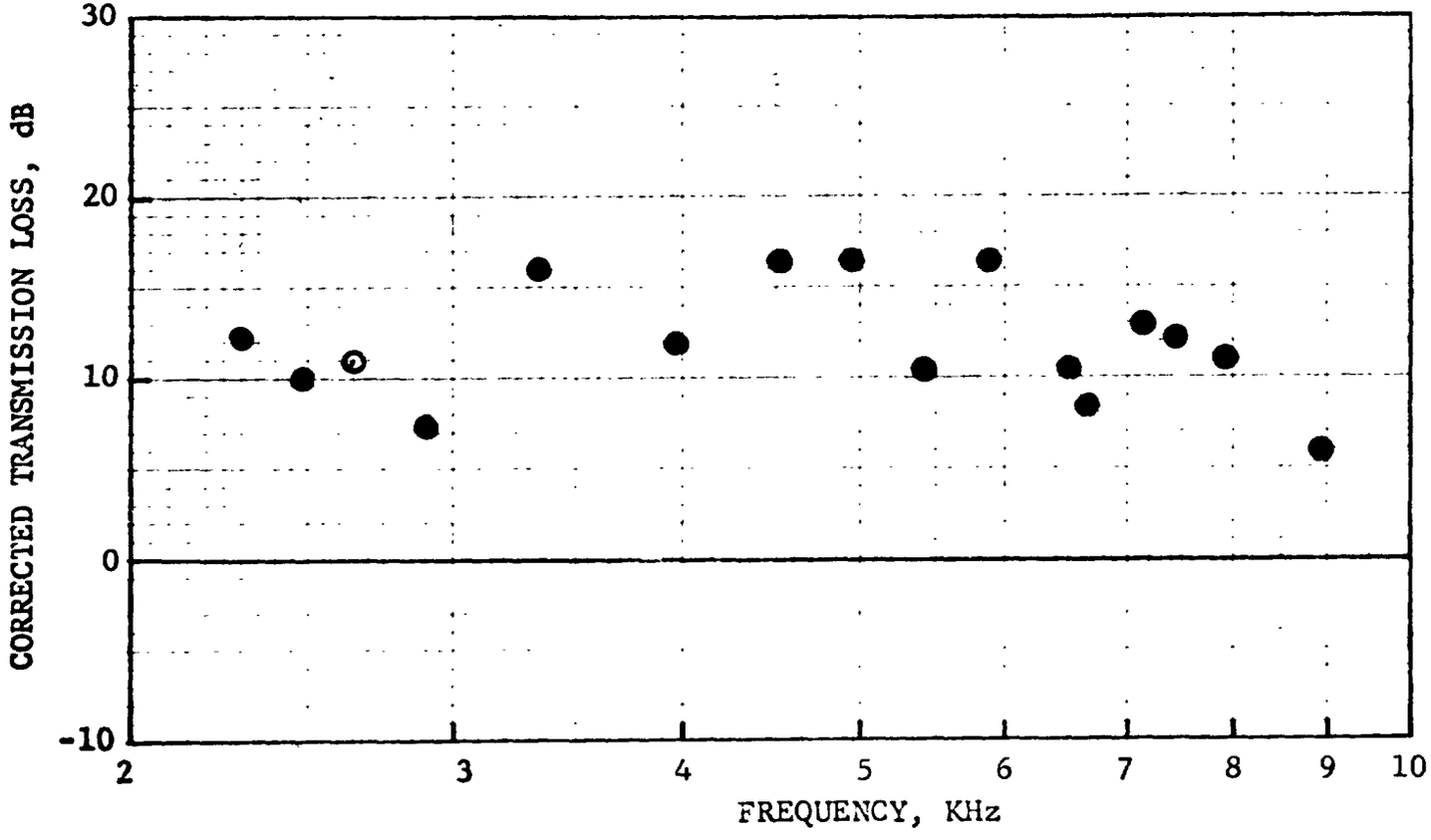

Figure 151. Corrected Transmission Loss Vs. Frequency.

HIGH TEMPERATURE ACOUSTIC DUCT .102m x .203m (4"x8")
TREATED ON TWO SIDES IN EXHAUST CONFIGURATION
L/H 4.5 TEMP. 589 °K 600 °F Mn 0.21

MATERIAL SDOF #18

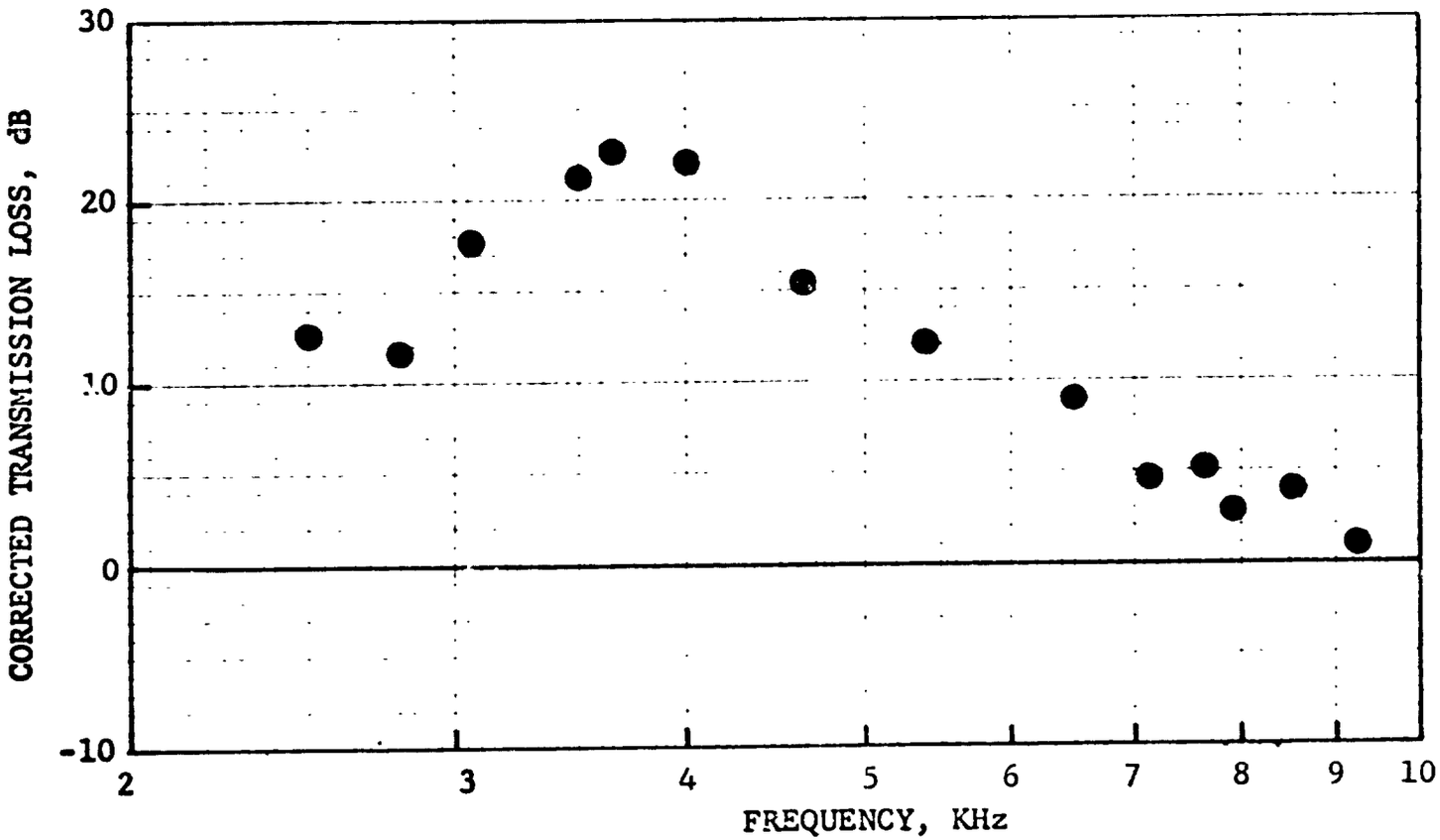

Figure 152. Corrected Transmission Loss Vs. Frequency.

HIGH TEMPERATURE ACOUSTIC DUCT .102m x .203m (4"x8")
TREATED ON TWO SIDES IN EXHAUST CONFIGURATION
L/H 4.5 TEMP. 589 °K 600 °F Mn 0.25

MATERIAL SDOF #18

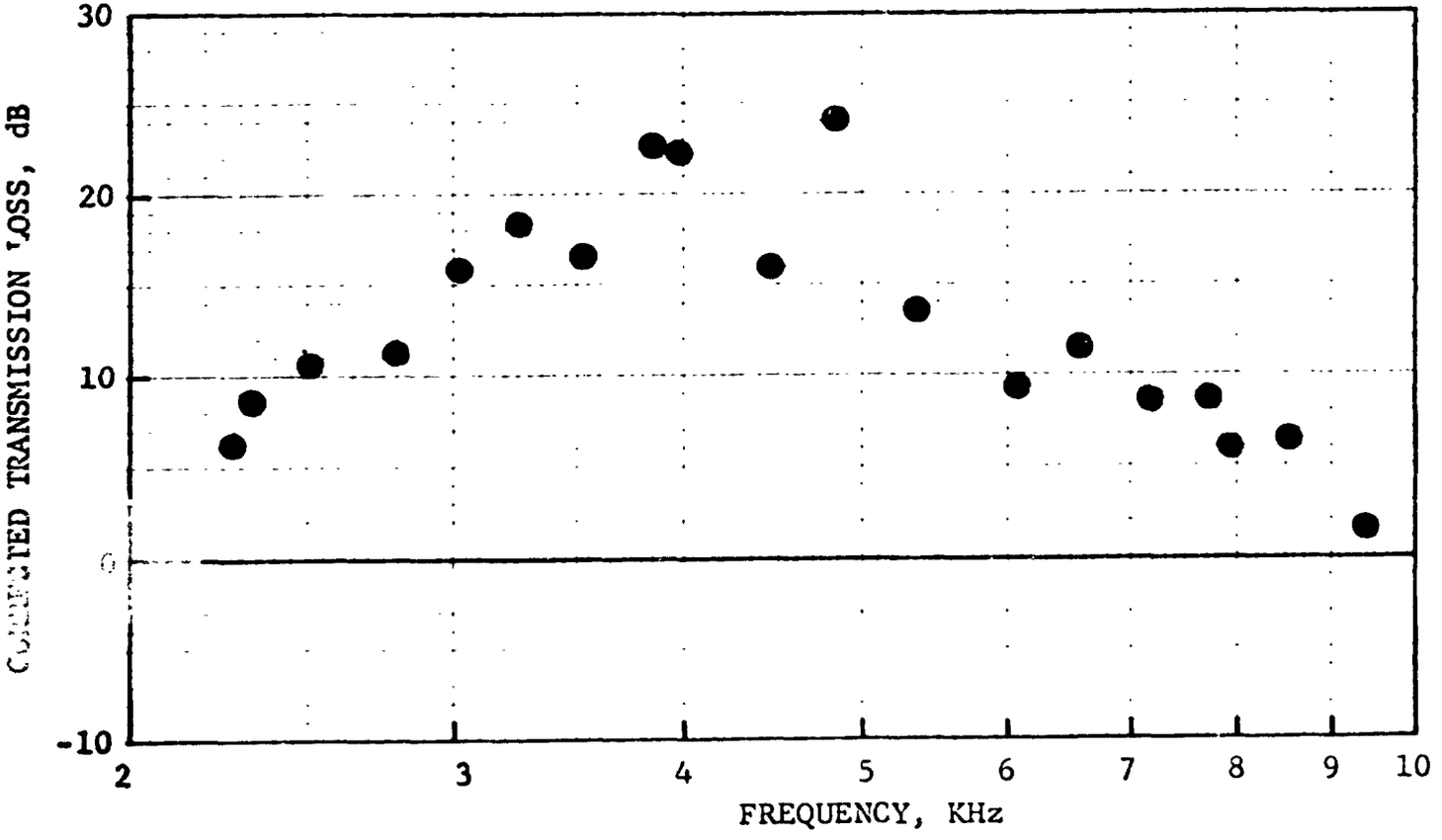

Figure 153. Corrected Transmission Loss Vs. Frequency.

HIGH TEMPERATURE ACOUSTIC DUCT .102m x .203m (4"x8")
TREATED ON TWO SIDES IN EXHAUST CONFIGURATION
L/H 4.5 TEMP. 589 °K 600 °F Mn 0.3

MATERIAL SDOF #18

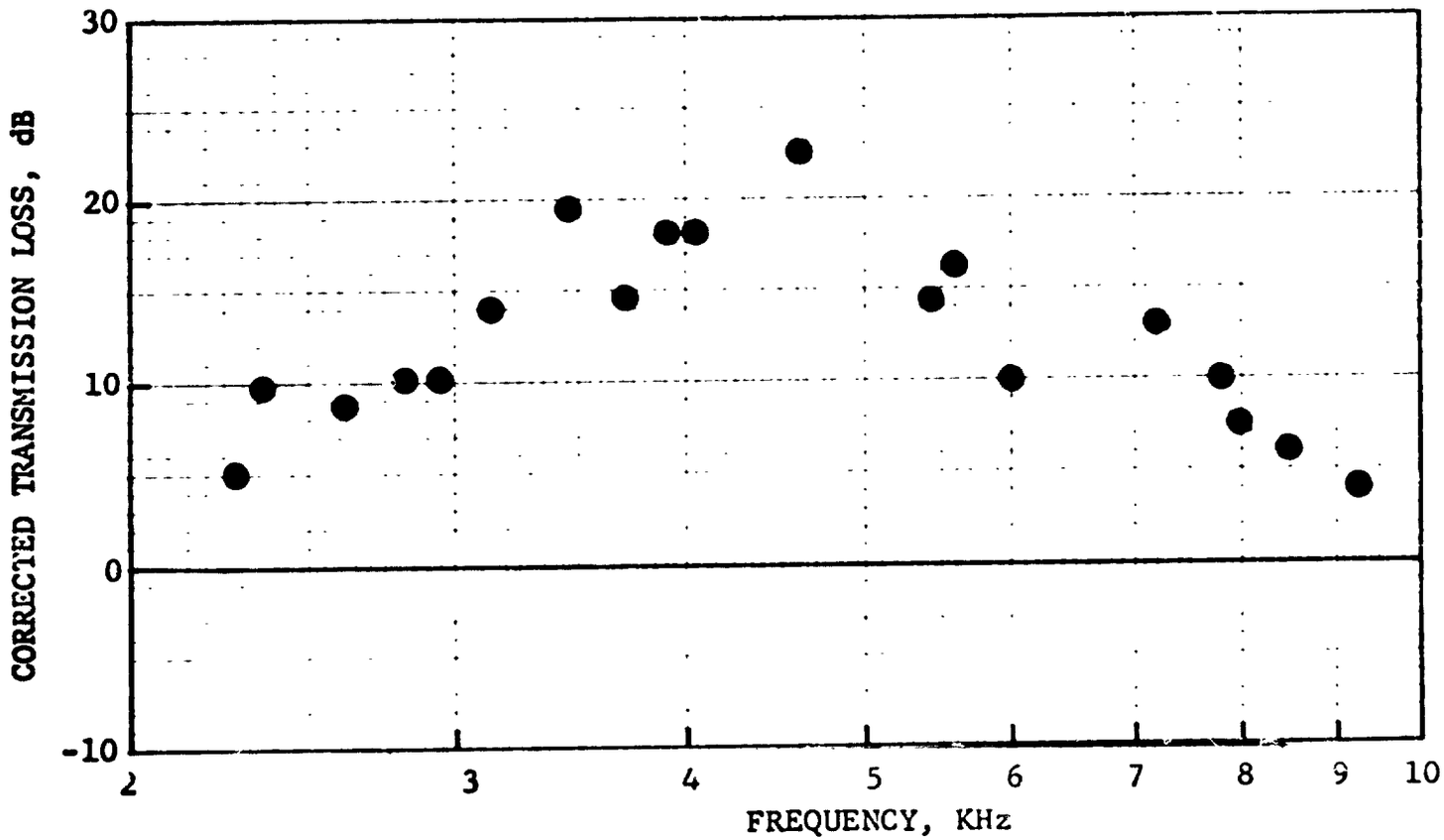

Figure 154. Corrected Transmission Loss Vs. Frequency.

HIGH TEMPERATURE ACOUSTIC DUCT .102m x .203m (4"x8")
TREATED ON TWO SIDES IN EXHAUST CONFIGURATION
L/H 4.5 TEMP. 589 °K 600 °F Δn 0.4

MATERIAL SDOF 18

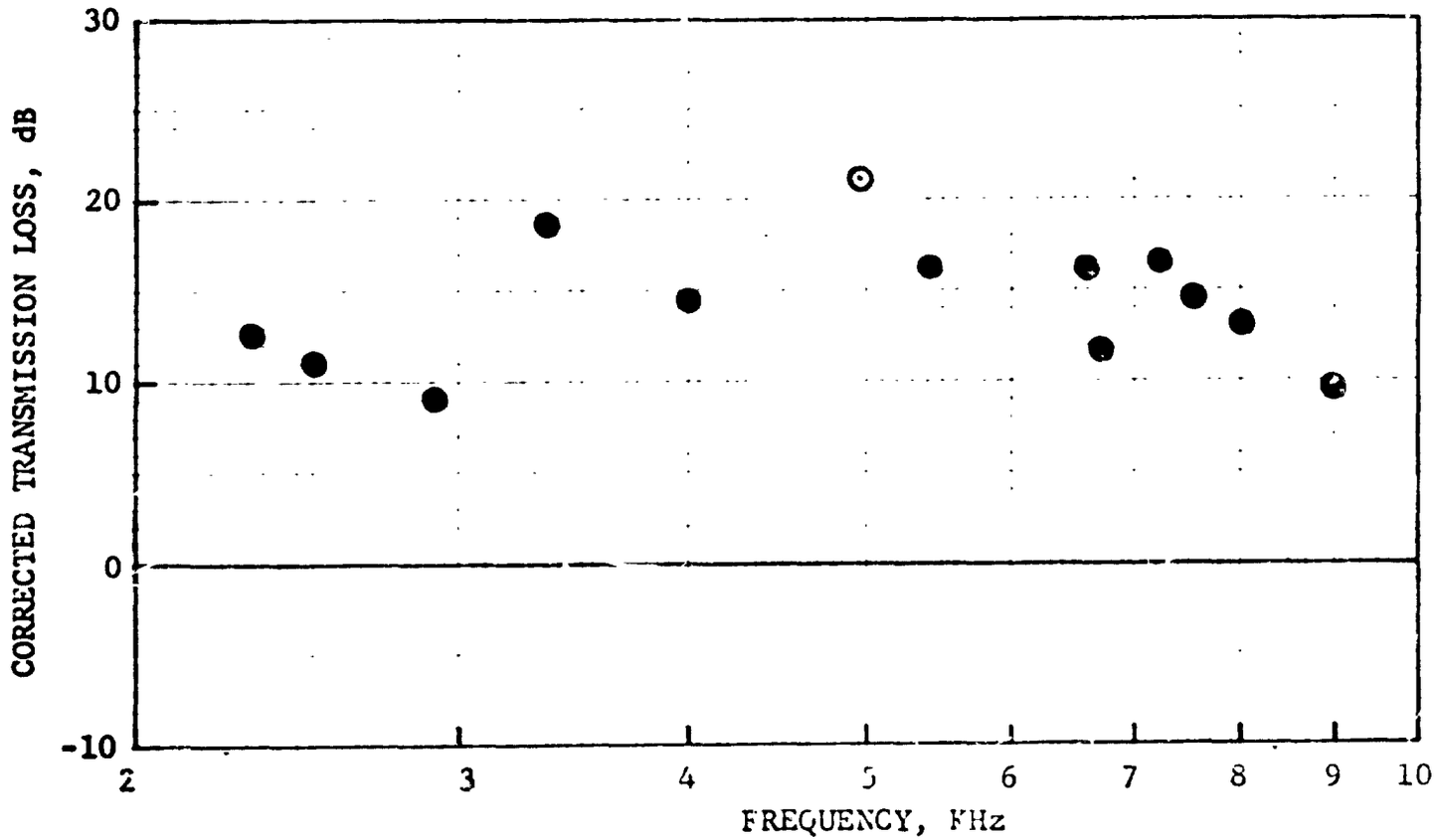

Figure 155. Corrected Transmission Loss Vs. Frequency.

HIGH TEMPERATURE ACOUSTIC DUCT .102m x .203m (4"x8")
TREATED ON TWO SIDES IN EXHAUST CONFIGURATION
L/H 4.5 TEMP. 589 °K 600 °F Mn 0.21

MATERIAL SDOF #19

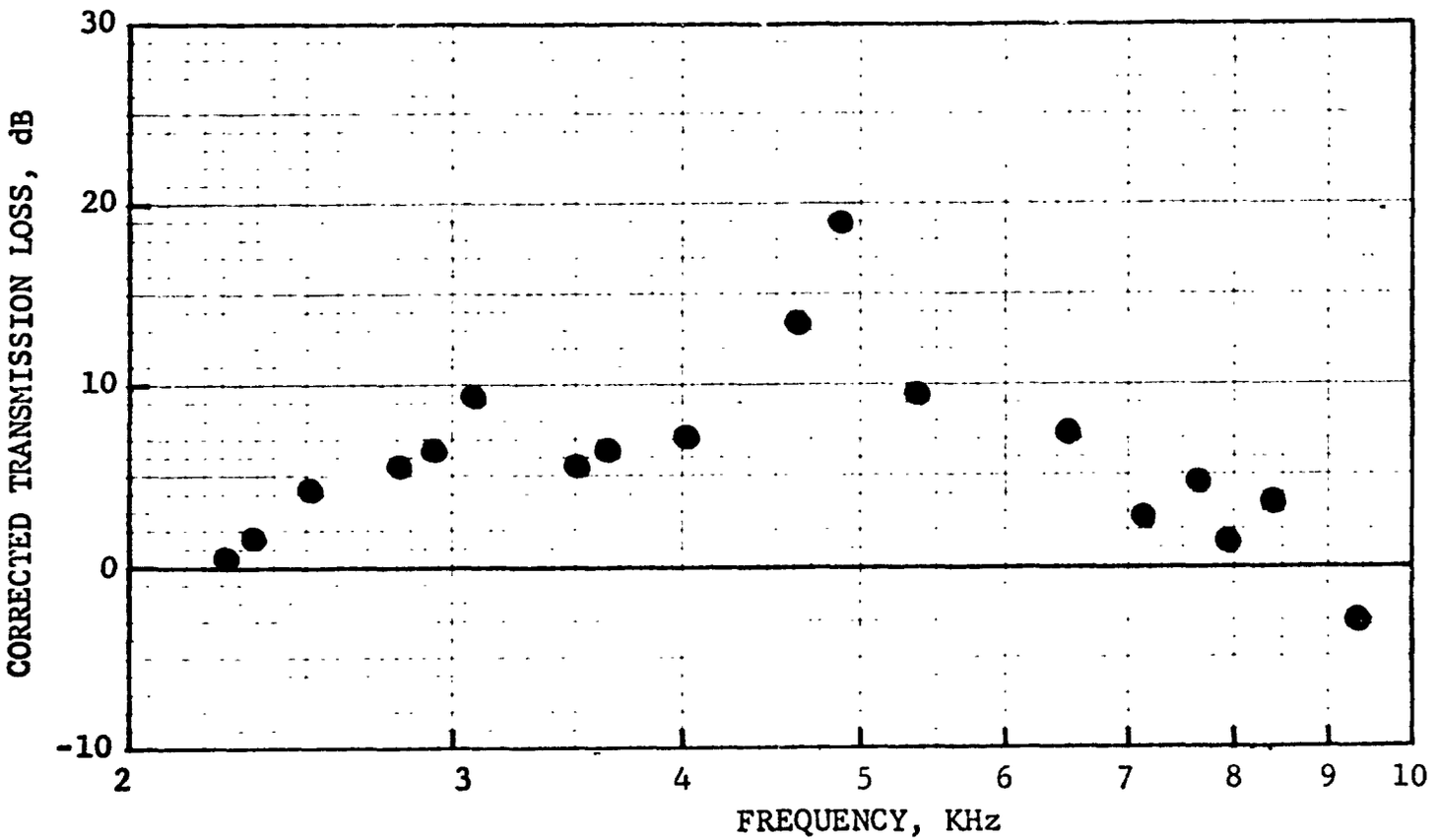

Figure 156. Corrected Transmission Loss Vs. Frequency.

HIGH TEMPERATURE ACOUSTIC DUCT .102m x .203m (4"x8")
TREATED ON TWO SIDES IN EXHAUST CONFIGURATION
L/H 4.5 TEMP. 589 °K 600 °F Mn 0.25

MATERIAL SDOF #19

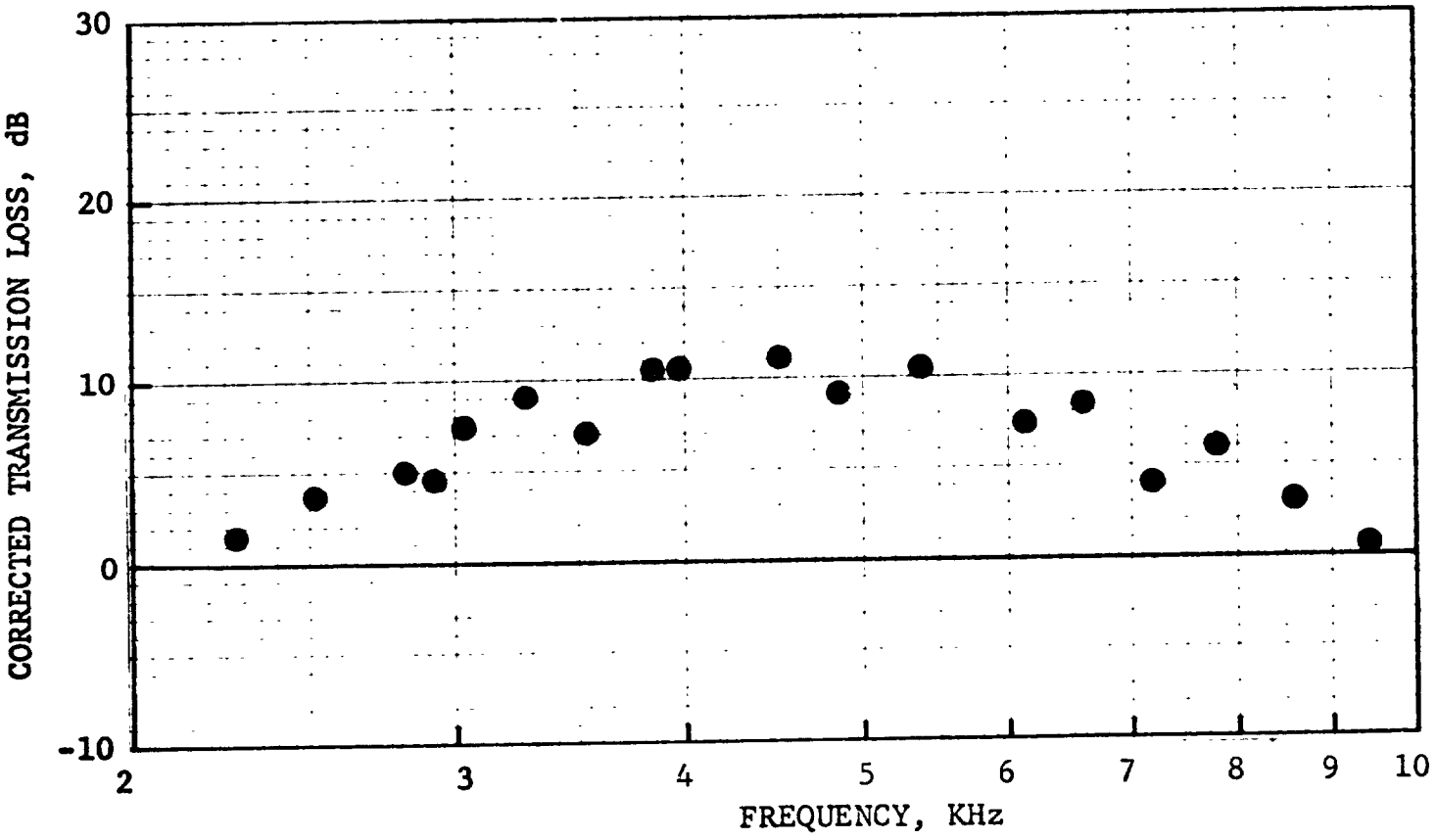

Figure 157. Corrected Transmission Loss Vs. Frequency.

HIGH TEMPERATURE ACOUSTIC DUCT .102m x .203m (4"x8")
TREATED ON TWO SIDES IN EXHAUST CONFIGURATION
L/H 4.5 TEMP. 589 °K 600 °F Mn 0.3

MATERIAL SDOF #19

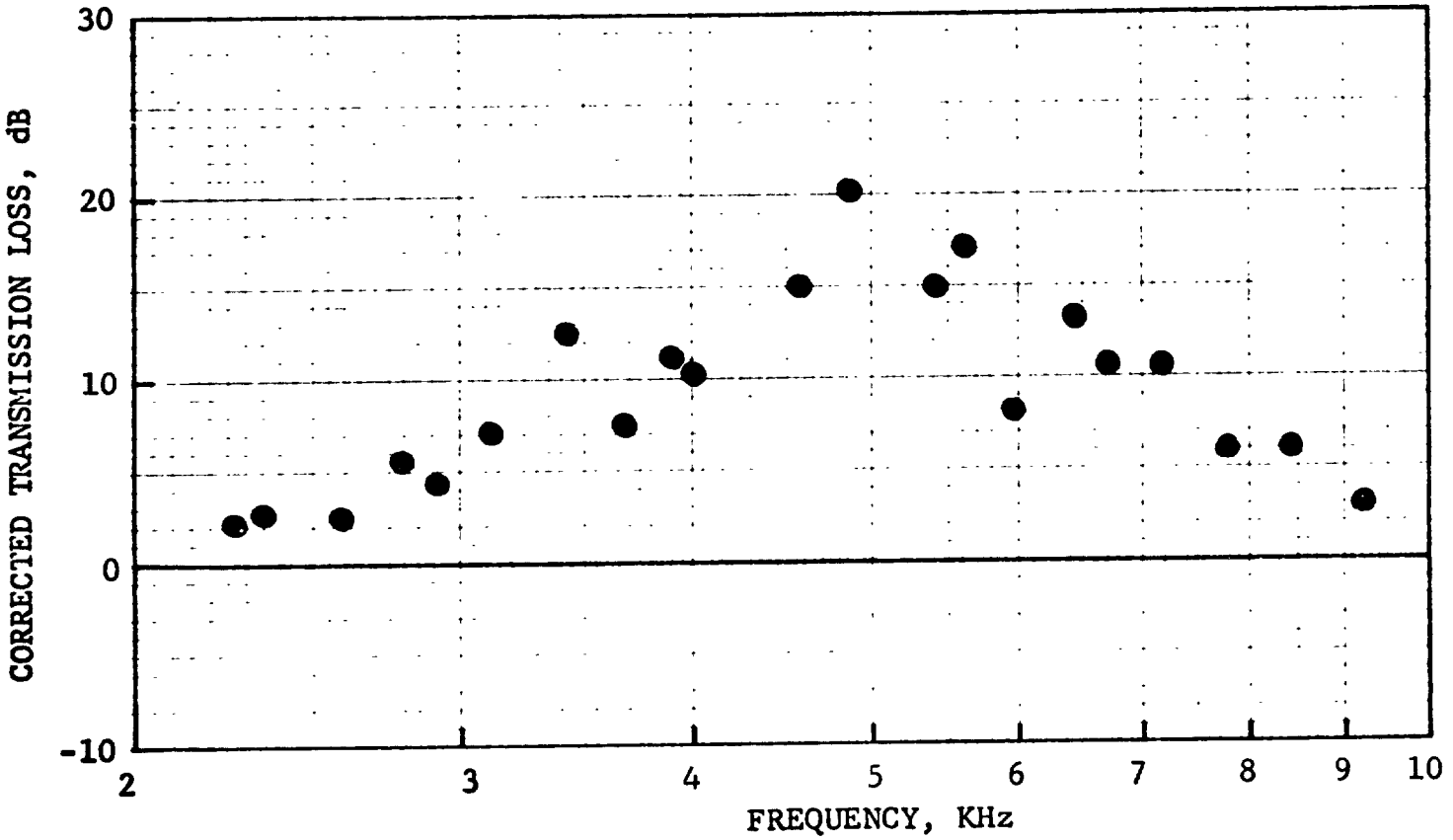

Figure 158. Corrected Transmission Loss Vs. Frequency.

HIGH TEMPERATURE ACOUSTIC DUCT .102m x .203m (4"x8")
TREATED ON TWO SIDES IN EXHAUST CONFIGURATION
L/H 4.5 TEMP. 589 °K 600 °F Mn 0.4

MATERIAL SDOF #19

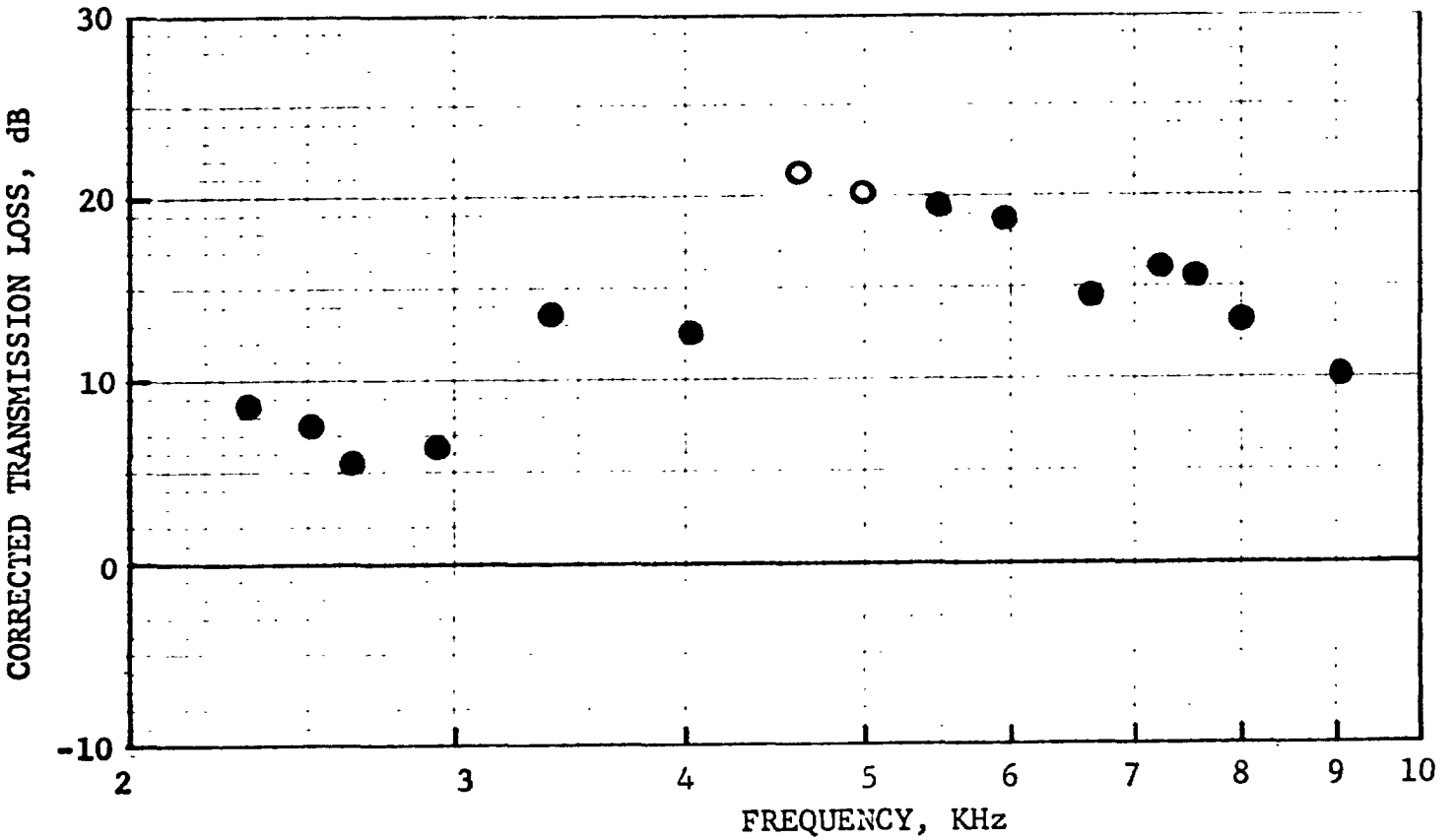

Figure 159. Corrected Transmission Loss Vs. Frequency.

HIGH TEMPERATURE ACOUSTIC DUCT .102m x .203m (4"x8")
TREATED ON TWO SIDES IN EXHAUST CONFIGURATION
L/H 4.5 TEMP. 589 °K 600 °F Mn 0.21

MATERIAL SDOF #20

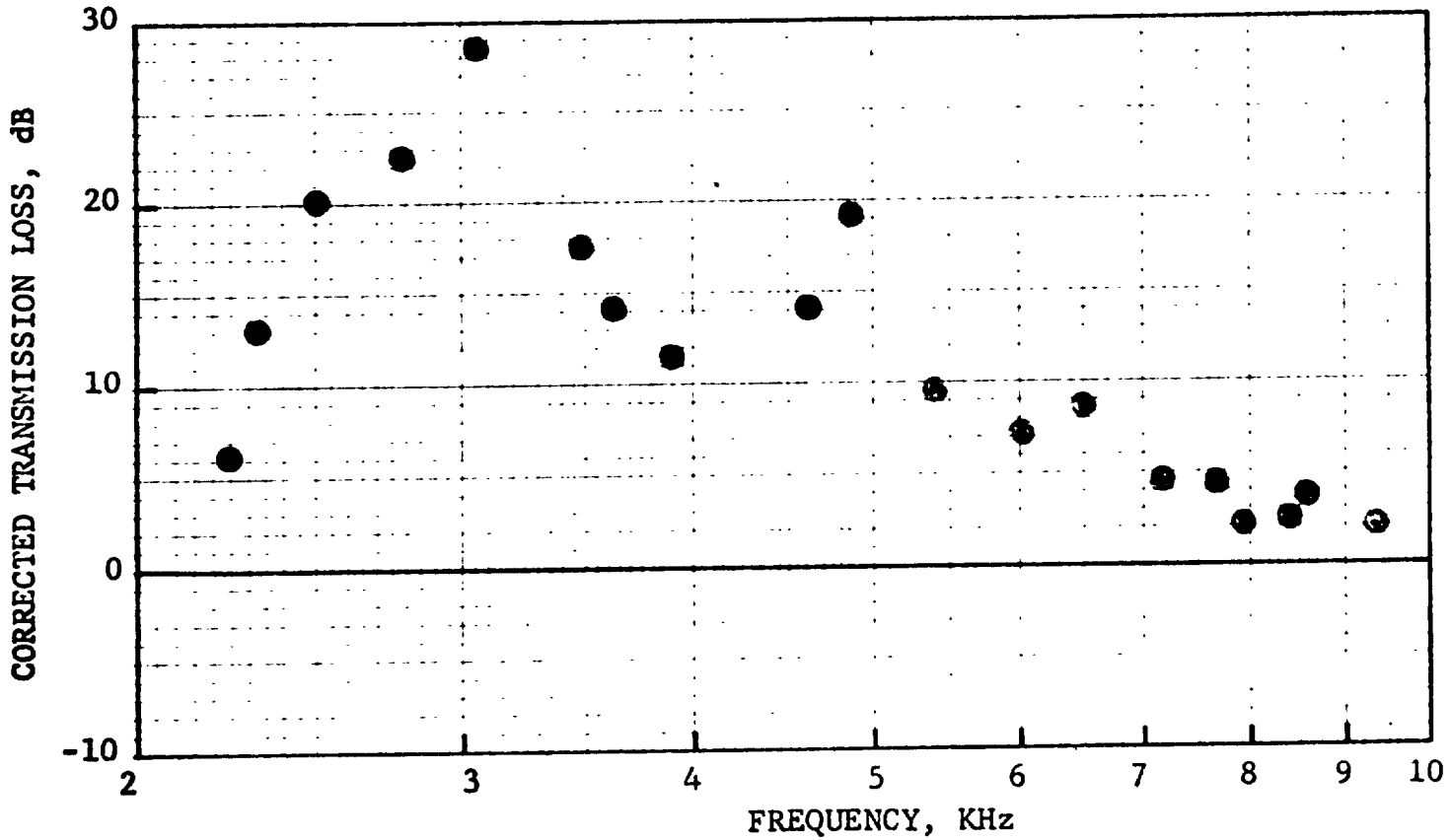

Figure 160. Corrected Transmission Loss Vs. Frequency.

HIGH TEMPERATURE ACOUSTIC DUCT .102m x .203m (4"x8")
TREATED ON TWO SIDES IN EXHAUST CONFIGURATION
L/H 4.5 TEMP. 589 °K 600 °F Mn 0.25

MATERIAL SDOF #20

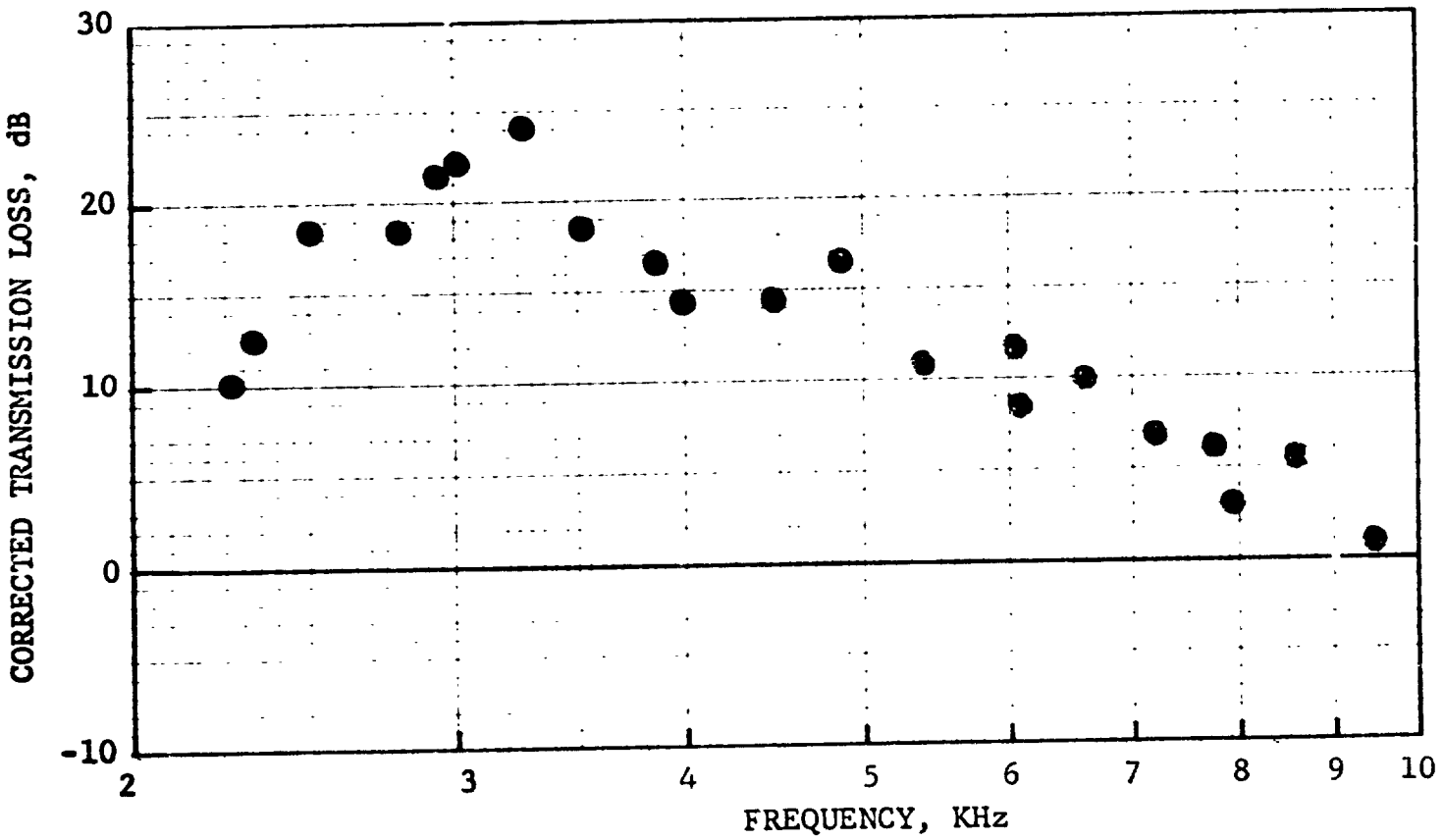

Figure 161. Corrected Transmission Loss Vs. Frequency.

HIGH TEMPERATURE ACOUSTIC DUCT .102m x .203m (4"x8")
TREATED ON TWO SIDES IN EXHAUST CONFIGURATION
L/H 4.5 TEMP. 589 °K 600 °F Mn 0.3

MATERIAL SDOF #20

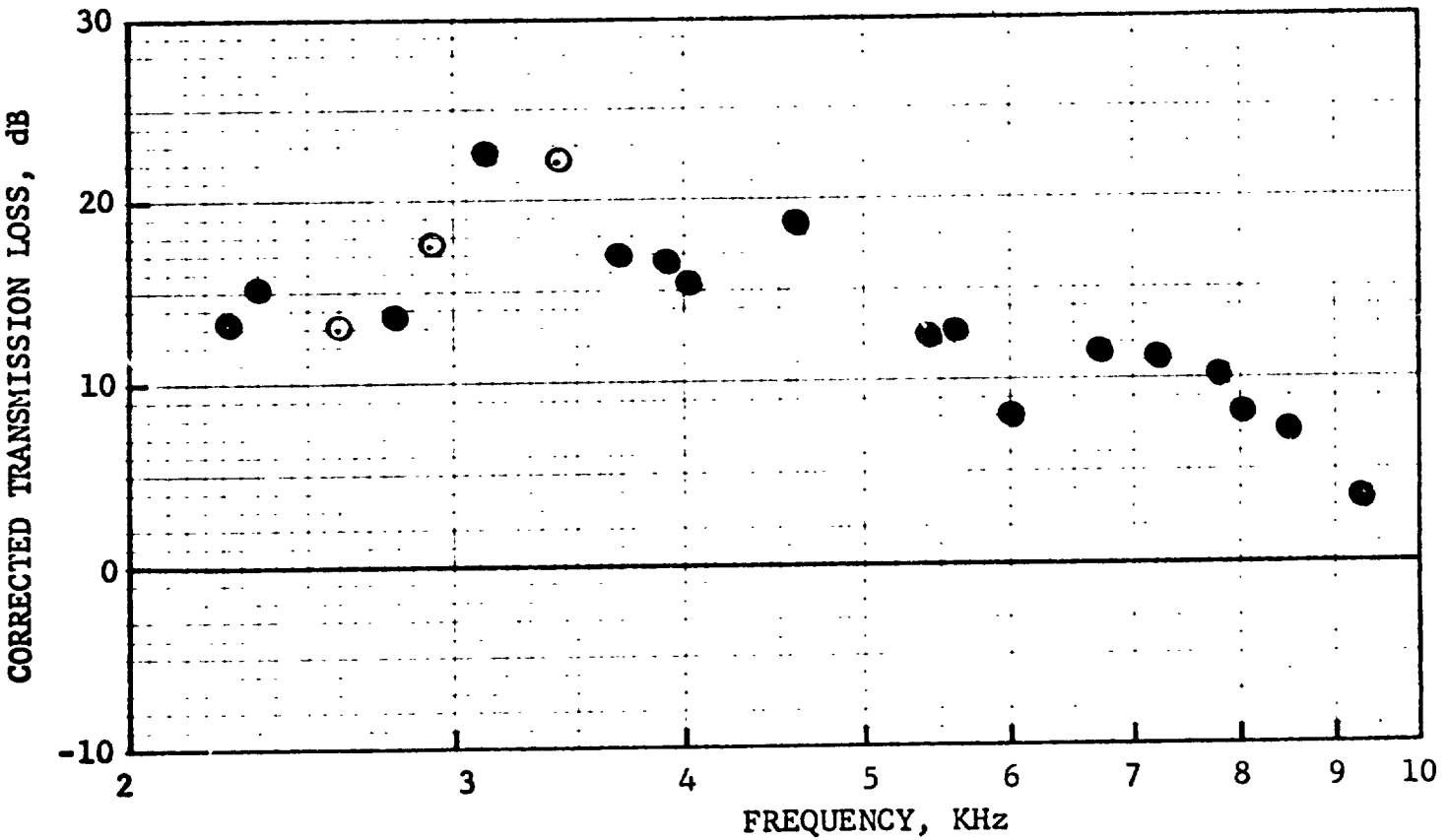

Figure 162. Corrected Transmission Loss Vs. Frequency.

HIGH TEMPERATURE ACOUSTIC DUCT .102m x .203m (4"x8")
TREATED ON TWO SIDES IN EXHAUST CONFIGURATION
L/H 4.5 TEMP. 589 °K 600 °F Mn 0.4

MATERIAL SDOF #20

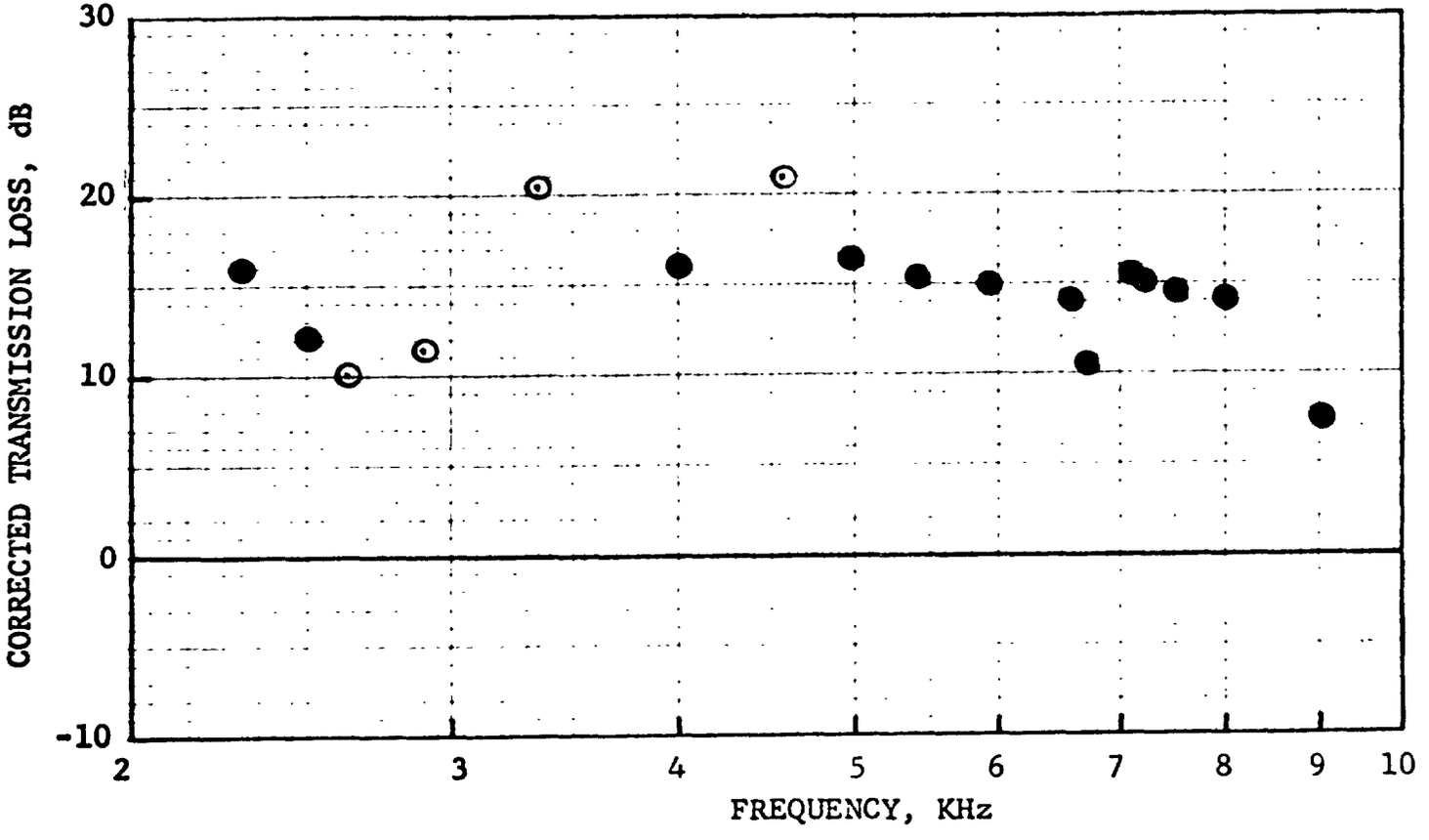

Figure 163. Corrected Transmission Loss Vs. Frequency.

HIGH TEMPERATURE ACOUSTIC DUCT .102m x .203m (4"x8")
TREATED ON TWO SIDES IN EXHAUST CONFIGURATION
L/H 4.5 TEMP. 589 °K 600 °F Mn 0.21

MATERIAL SDOF #21

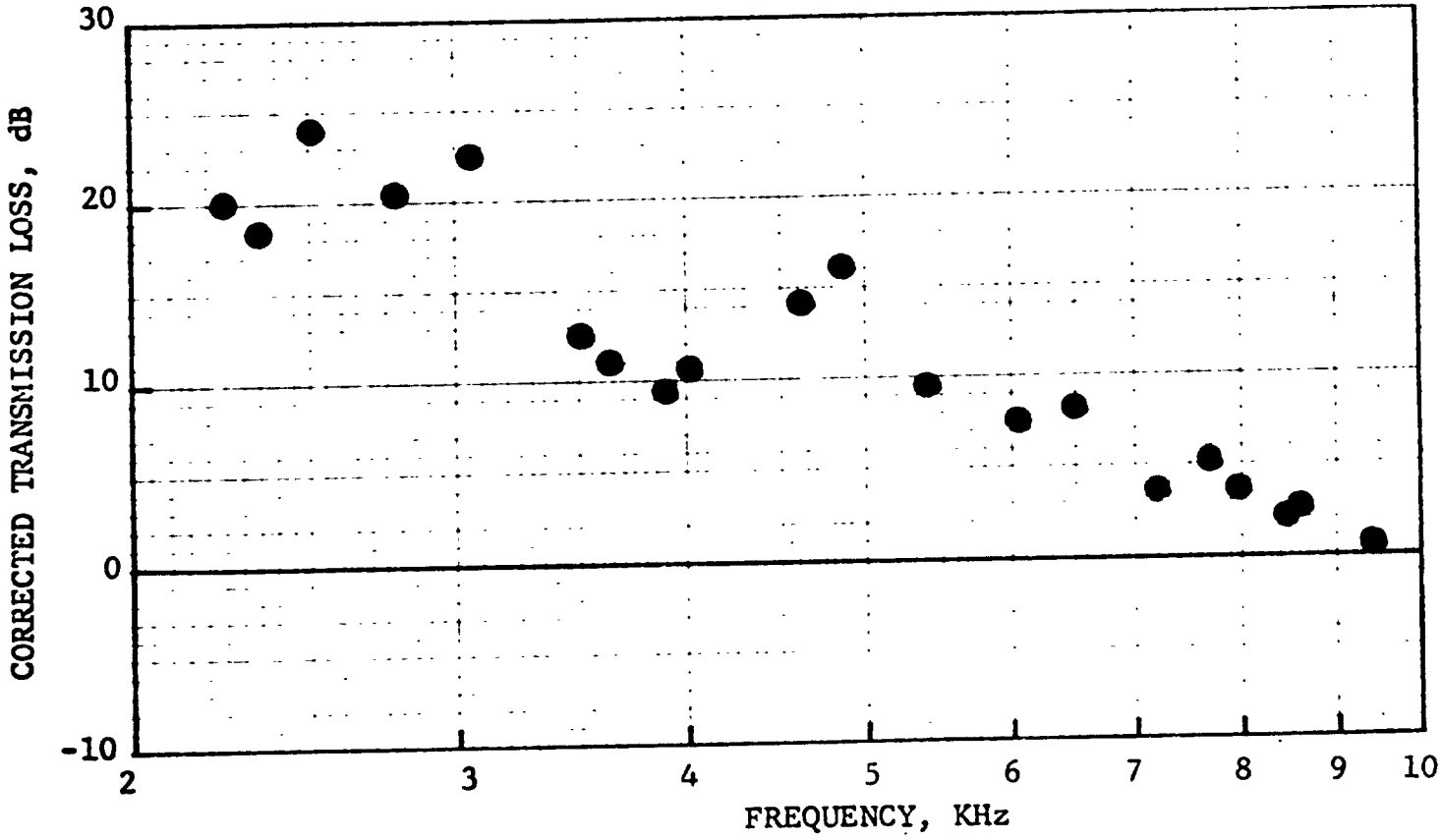

Figure 164. Corrected Transmission Loss Vs. Frequency.

HIGH TEMPERATURE ACOUSTIC DUCT .102m x .203m (4"x8")
TREATED ON TWO SIDES IN EXHAUST CONFIGURATION
L/H 4.5 TEMP. 589 °K 600 °F Mn 0.25

MATERIAL SDOF #21

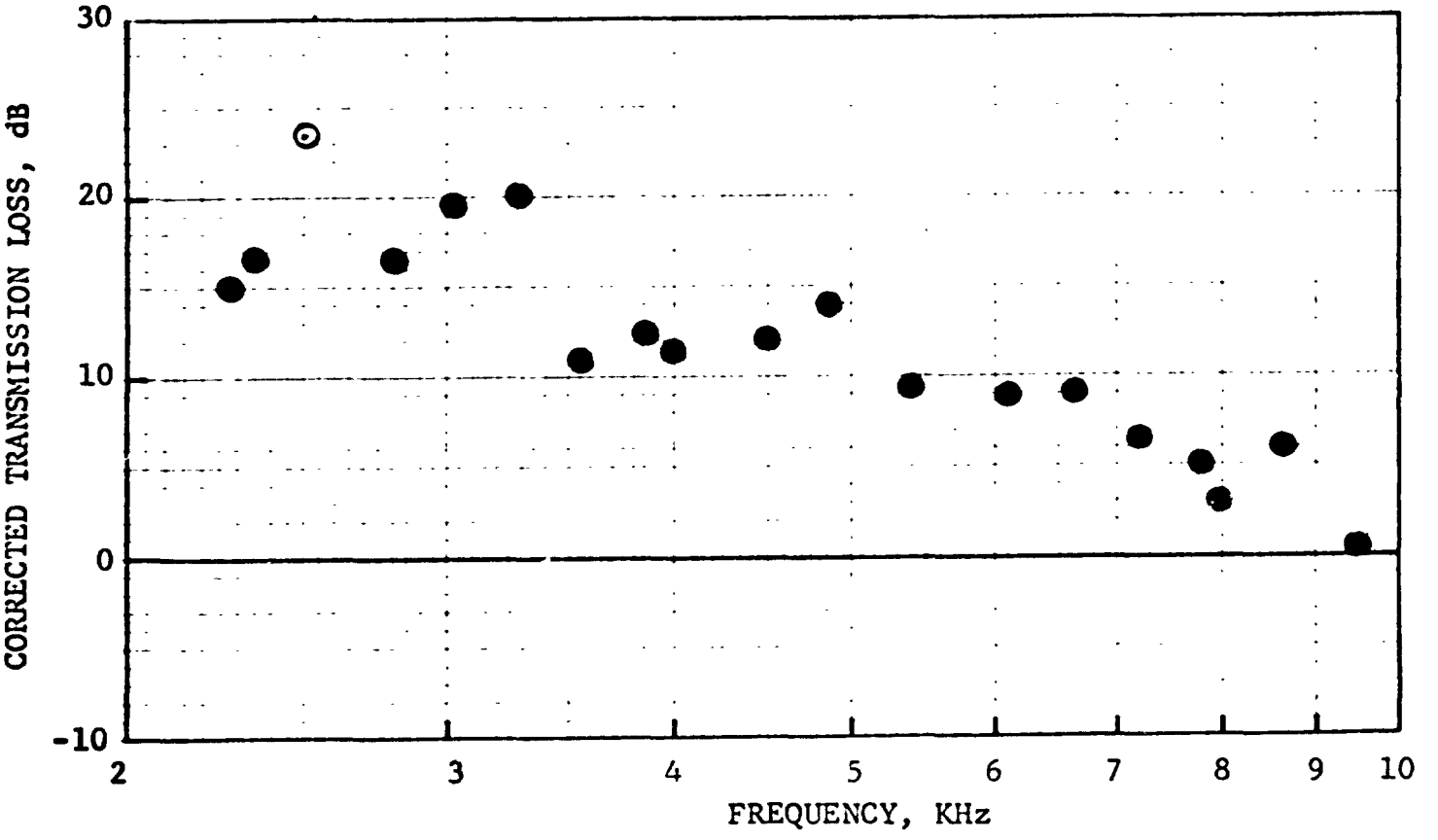

Figure 165. Corrected Transmission Loss Vs. Frequency.

HIGH TEMPERATURE ACOUSTIC DUCT .102m x .203m (4"x8")
TREATED ON TWO SIDES IN EXHAUST CONFIGURATION
L/H 4.5 TEMP. 589 °K 600 °F Mn 0.3

MATERIAL SDOF #21

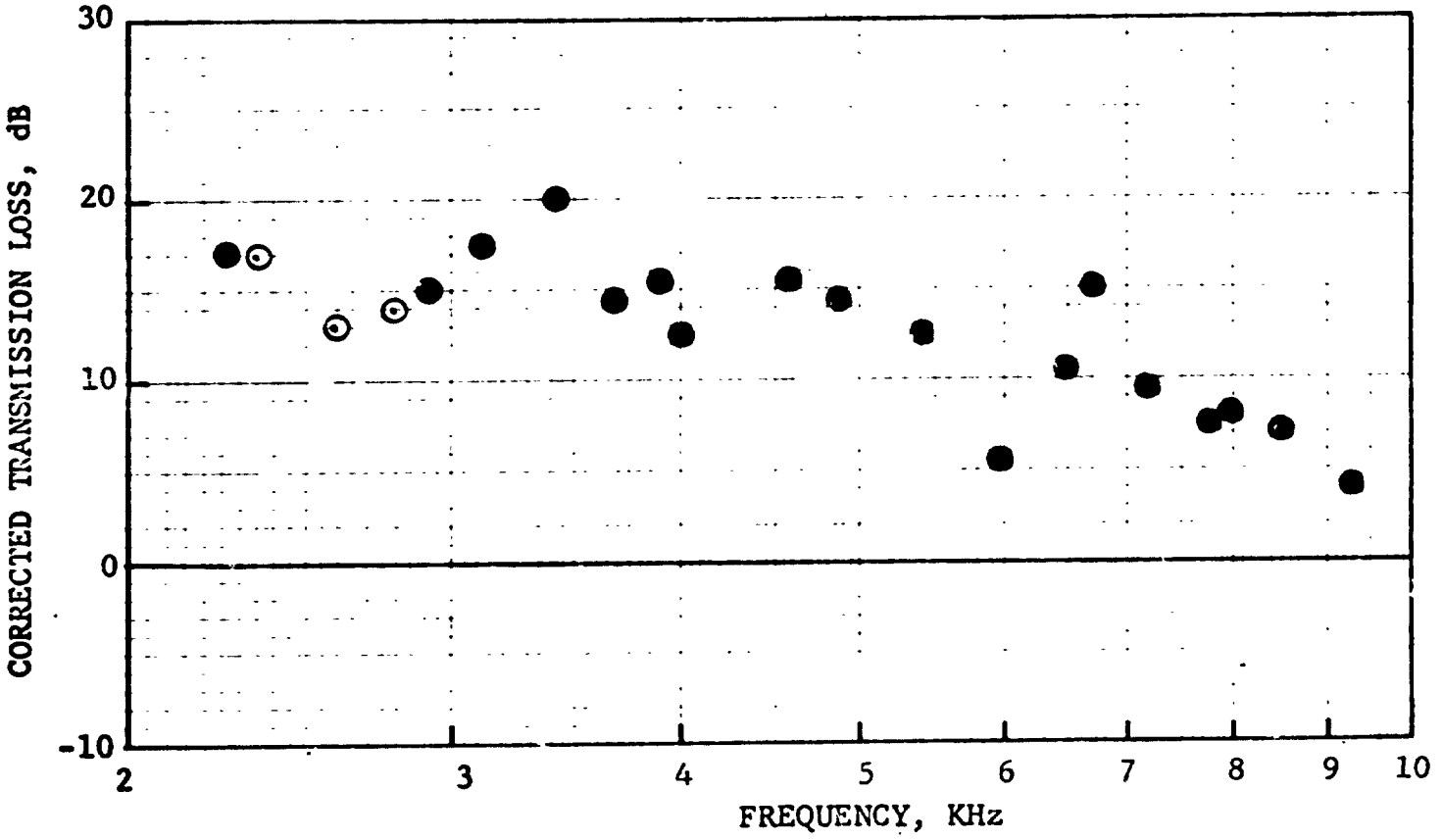

Figure 166. Corrected Transmission Loss Vs. Frequency.

HIGH TEMPERATURE ACOUSTIC DUCT .102m x .203m (4"x8")
TREATED ON TWO SIDES IN EXHAUST CONFIGURATION
L/H 4.5 TEMP. 589 °K 600 °F Mn 0.4

MATERIAL SDOF #21

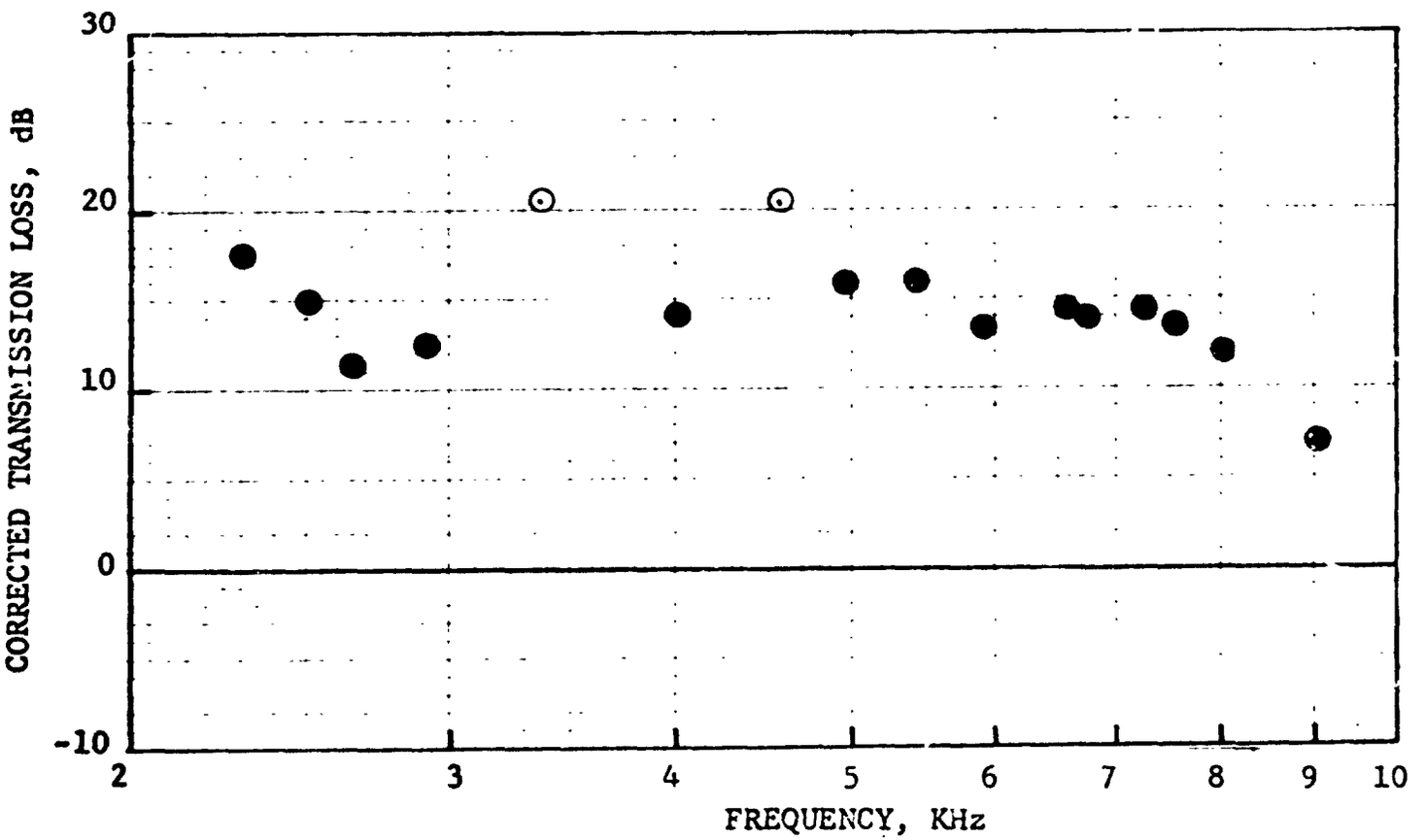

Figure 167. Corrected Transmission Loss Vs. Frequency.

HIGH TEMPERATURE ACOUSTIC DUCT .102m x .203m (4"x8")
TREATED ON TWO SIDES IN EXHAUST CONFIGURATION
L/H 4.5 TEMP. 589 °K 600 °F Mn 0.21

MATERIAL SDOF #22

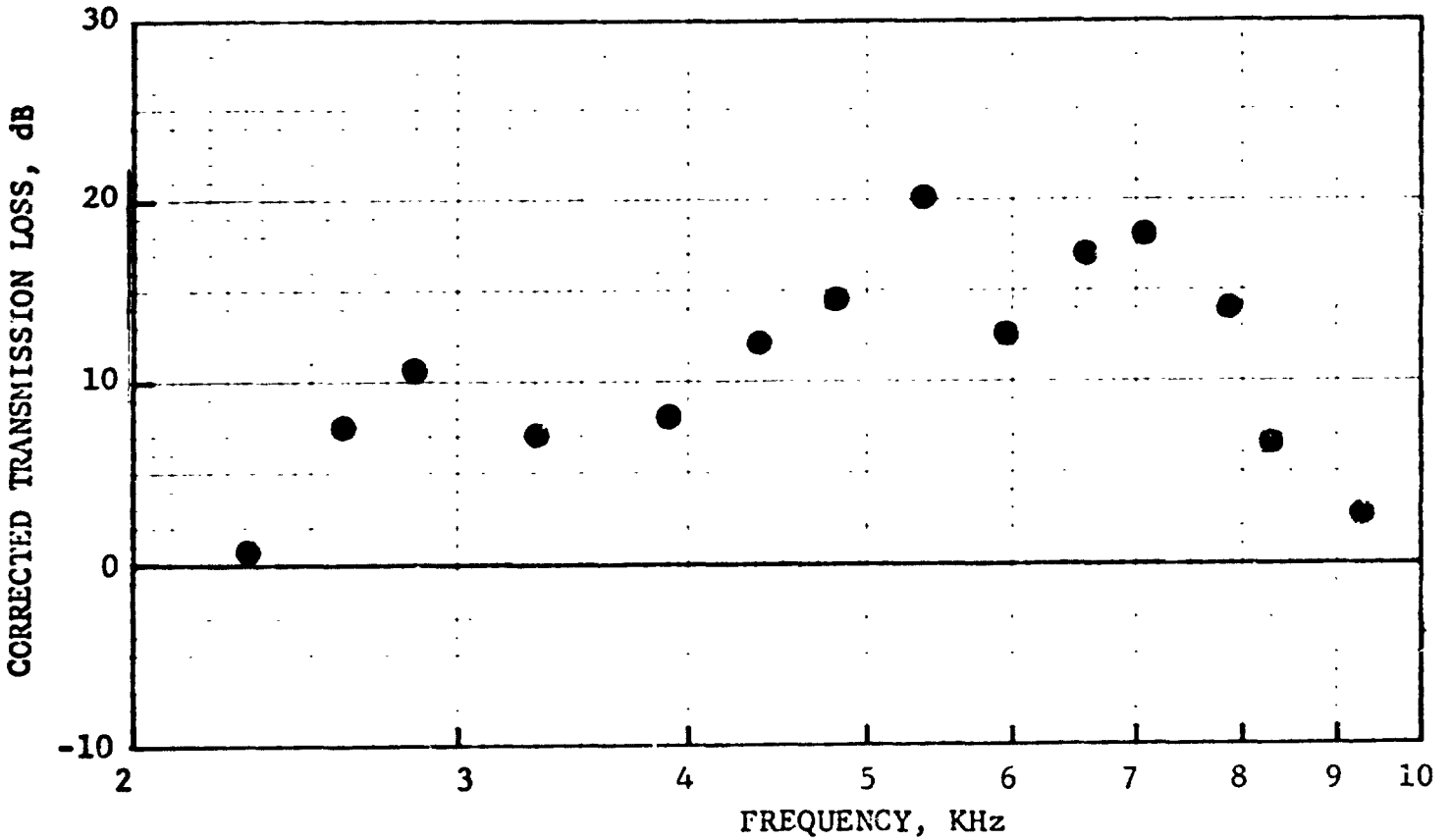

Figure 168. Corrected Transmission Loss Vs. Frequency.

HIGH TEMPERATURE ACOUSTIC DUCT .102m x .203m (4"x8")
TREATED ON TWO SIDES IN EXHAUST CONFIGURATION
L/H 4.5 TEMP. 589 °K 600 °F Mn 0.25

MATERIAL SDOF #22

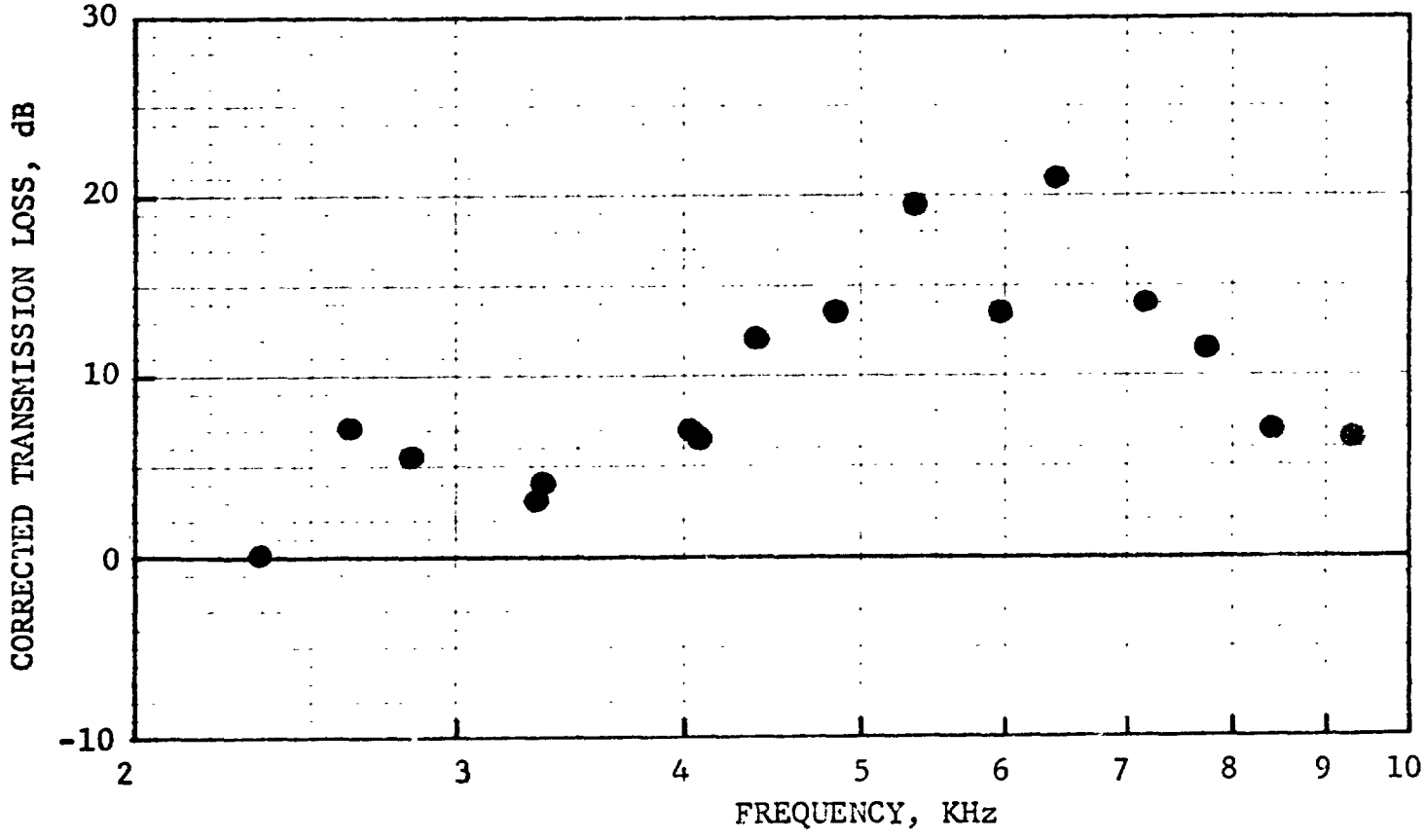

Figure 169. Corrected Transmission Loss Vs. Frequency.

HIGH TEMPERATURE ACOUSTIC DUCT .102m x .203m (4"x8")
TREATED ON TWO SIDES IN EXHAUST CONFIGURATION
L/H 4.5 TEMP. 589 °K 600 °F Mn 0.3

MATERIAL SDOF #22

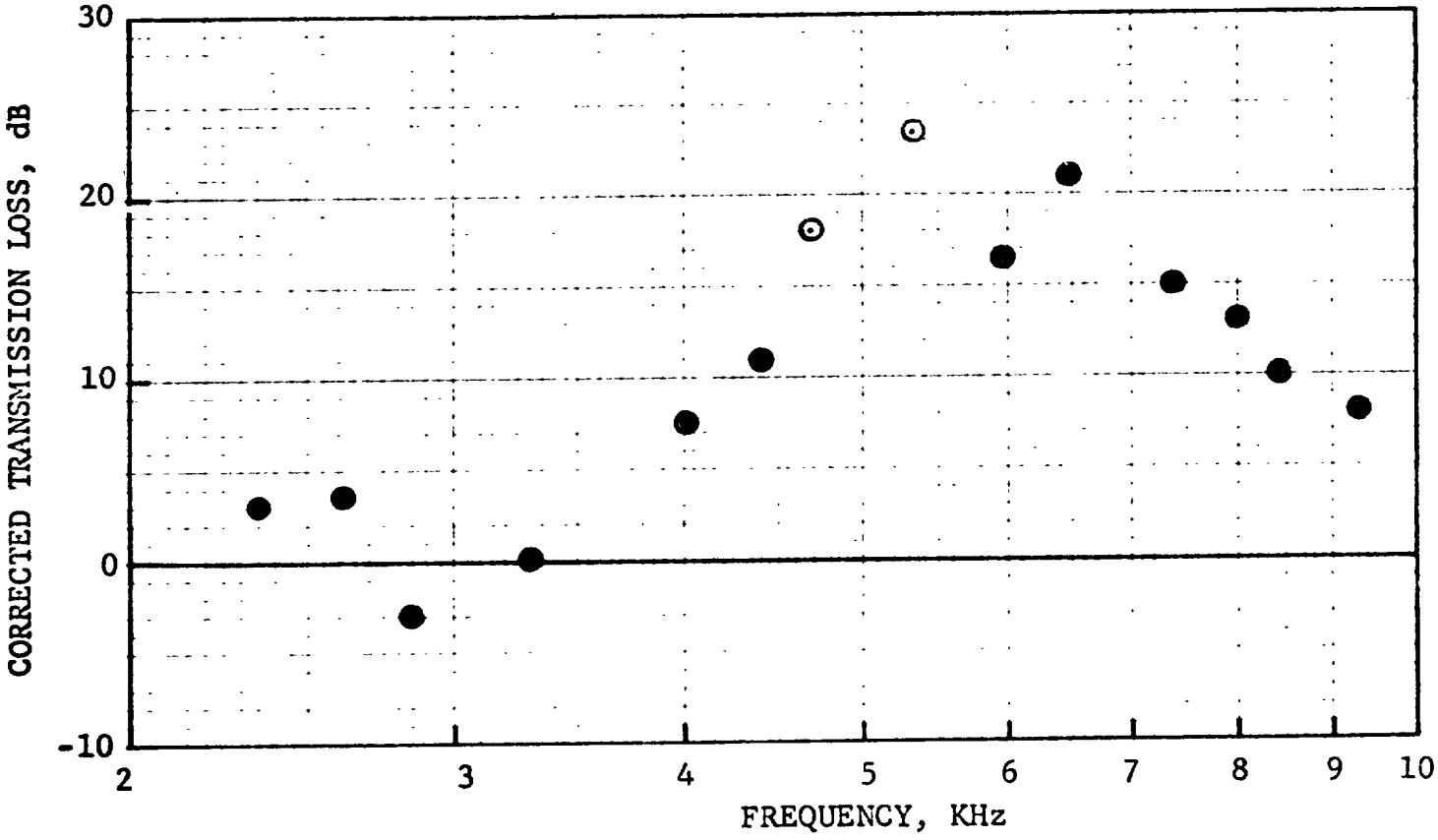

Figure 170. Corrected Transmission Loss Vs. Frequency.

HIGH TEMPERATURE ACOUSTIC DUCT .102m x .203m (4"x8")
TREATED ON TWO SIDES IN EXHAUST CONFIGURATION
L/H 4.5 TEMP. 589 °K 600 °F Mn 0.21

MATERIAL SDOF #23

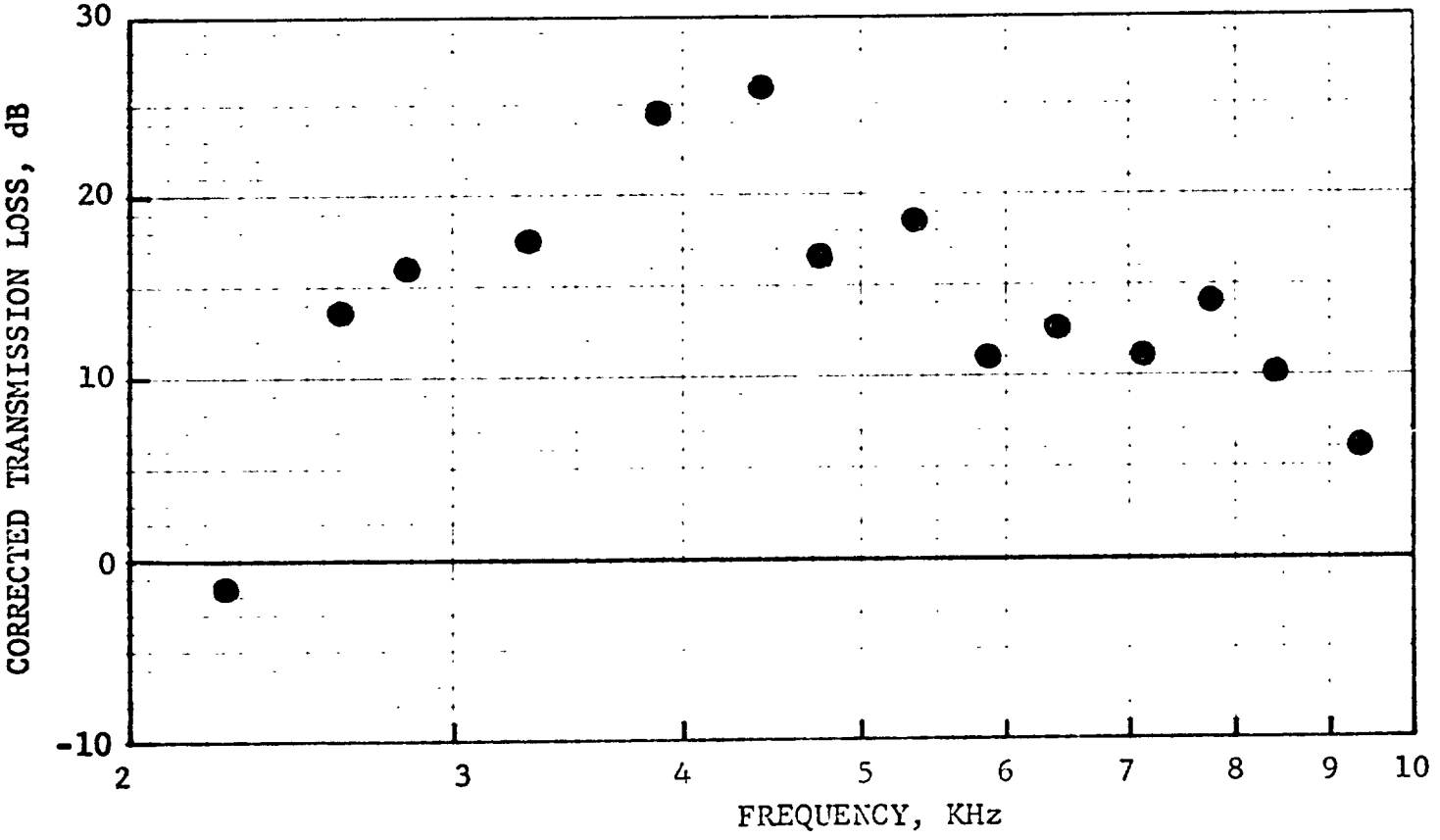

Figure 171. Corrected Transmission Loss Vs. Frequency.

HIGH TEMPERATURE ACOUSTIC DUCT .102m x .203m (4"x8")
TREATED ON TWO SIDES IN EXHAUST CONFIGURATION
L/H 4.5 TEMP. 589 °K 600 °F Mn 0.25

MATERIAL SDOF #23

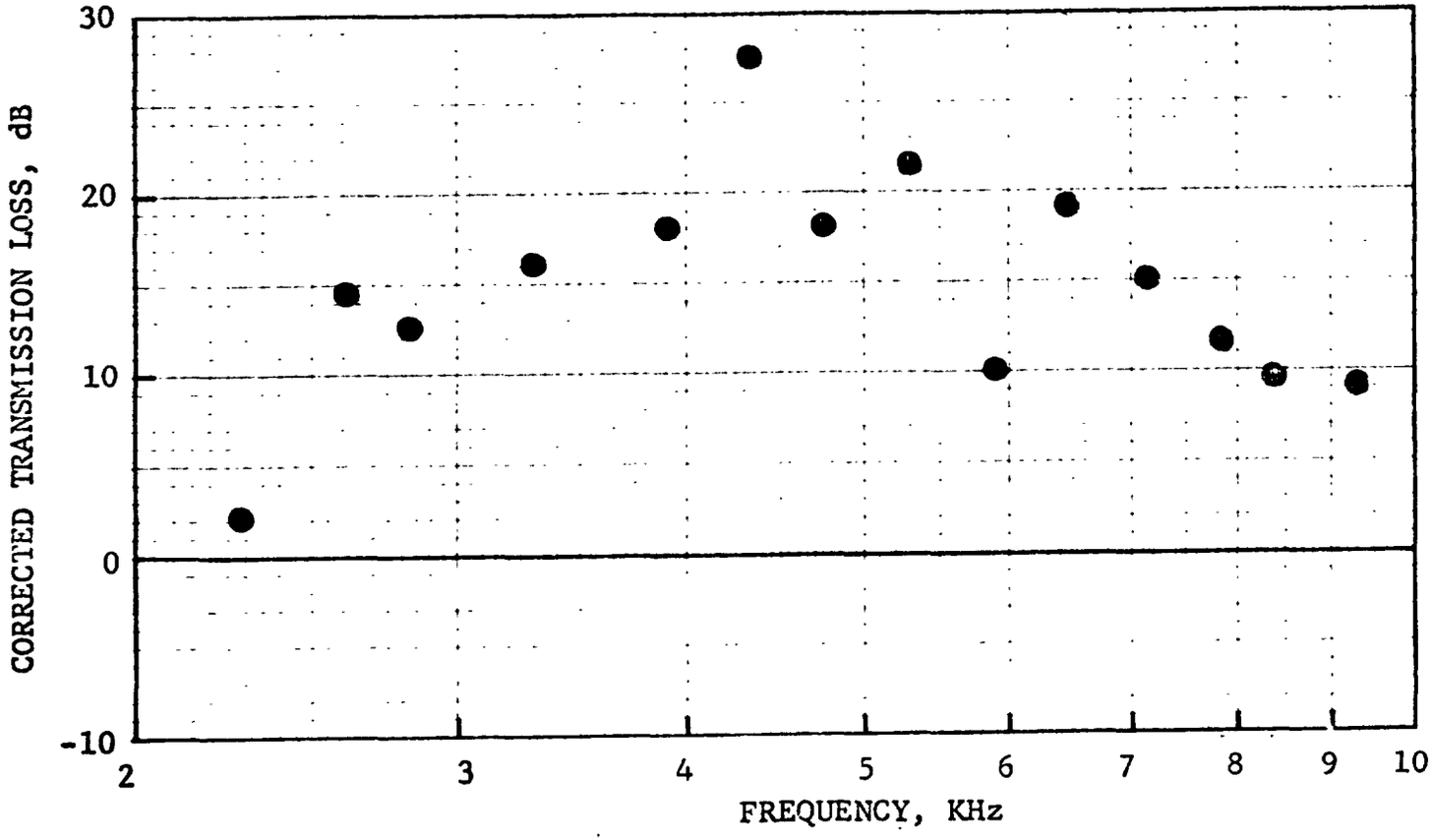

Figure 172. Corrected Transmission Loss Vs. Frequency.

HIGH TEMPERATURE ACOUSTIC DUCT .102m x .203m (4"x8")
TREATED ON TWO SIDES IN EXHAUST CONFIGURATION
L/H 4.5 TEMP. 589 °K 600 °F Mn 0.3

MATERIAL SDOF #23

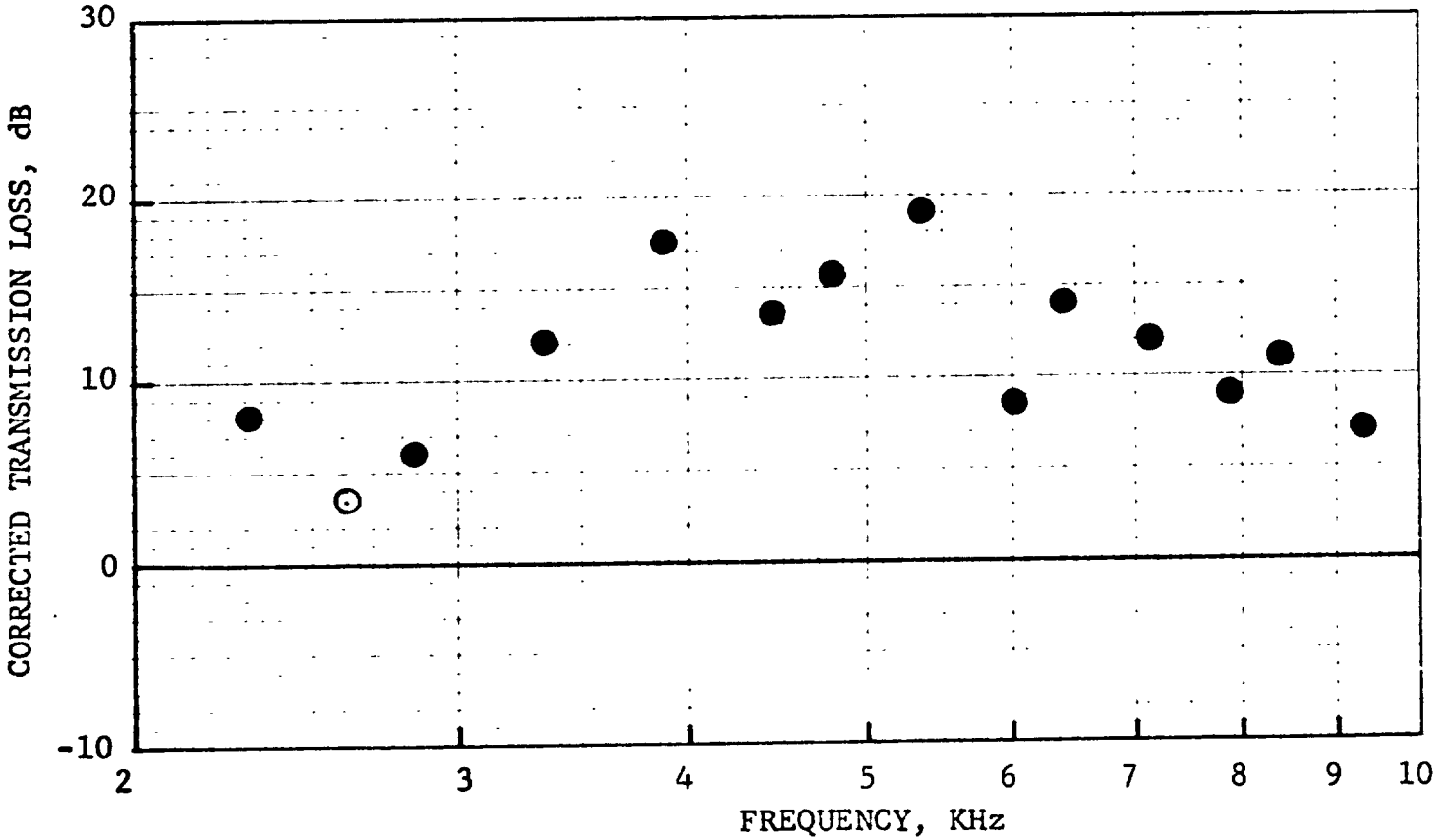

Figure 173. Corrected Transmission Loss Vs. Frequency.

HIGH TEMPERATURE ACOUSTIC DUCT .102m x .203m (4"x8")
TREATED ON TWO SIDES IN EXHAUST CONFIGURATION
L/H 4.5 TEMP. 589 °K 600 °F Mn 0.4

MATERIAL SDOF #23

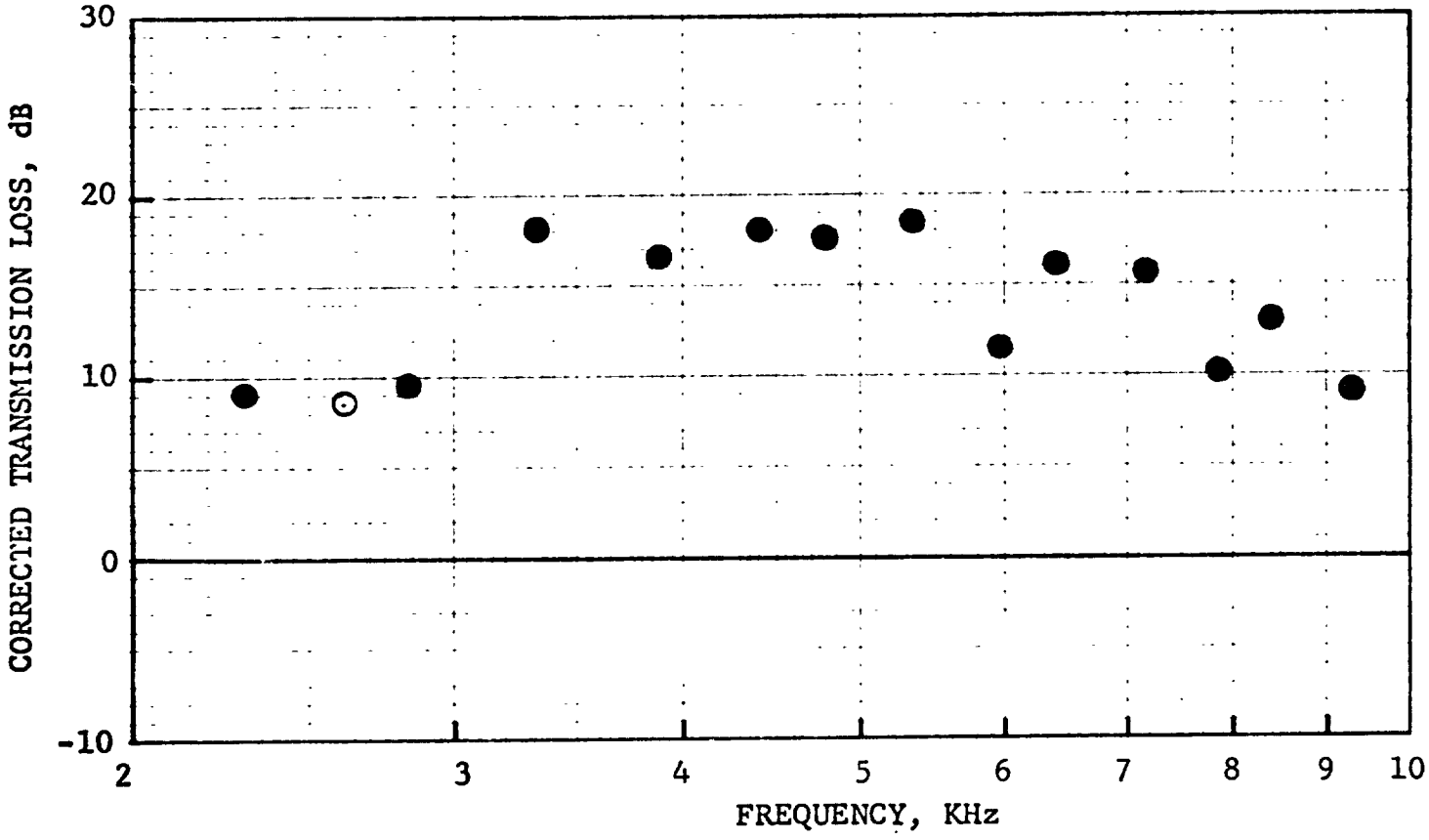

Figure 174. Corrected Transmission Loss Vs. Frequency.

HIGH TEMPERATURE ACOUSTIC DUCT .102m x .203m (4"x8")
TREATED ON TWO SIDES IN EXHAUST CONFIGURATION
L/H 4.5 TEMP. 589 °K 600 °F Mn 0.25

MATERIAL SDOF #24

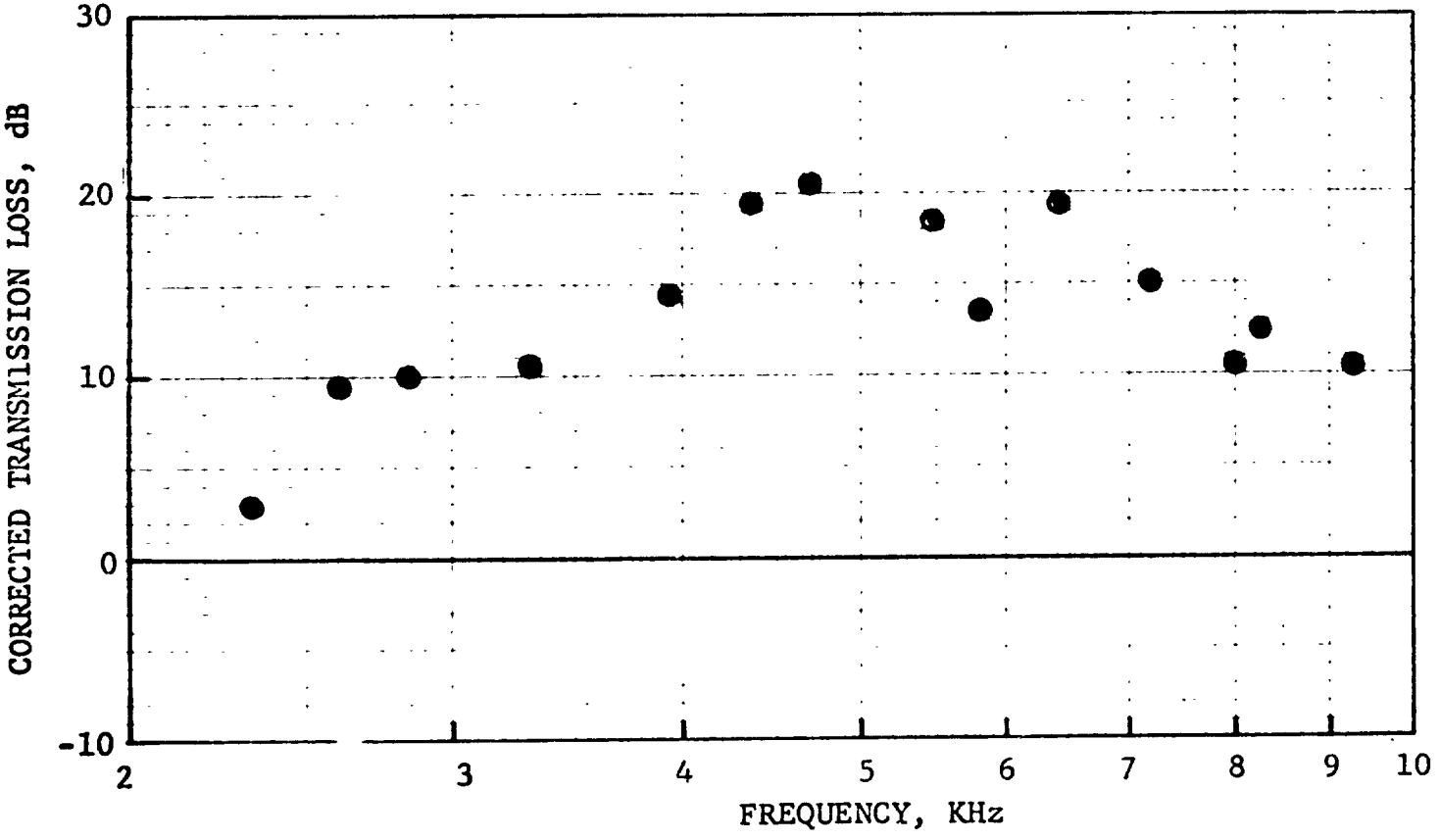

Figure 175. Corrected Transmission Loss Vs. Frequency.

HIGH TEMPERATURE ACOUSTIC DUCT .102m x .203m (4"x8")
TREATED ON TWO SIDES IN EXHAUST CONFIGURATION
L/H 4.5 TEMP. 589 °K 600 °F Mn 0.3

MATERIAL SDOF #24

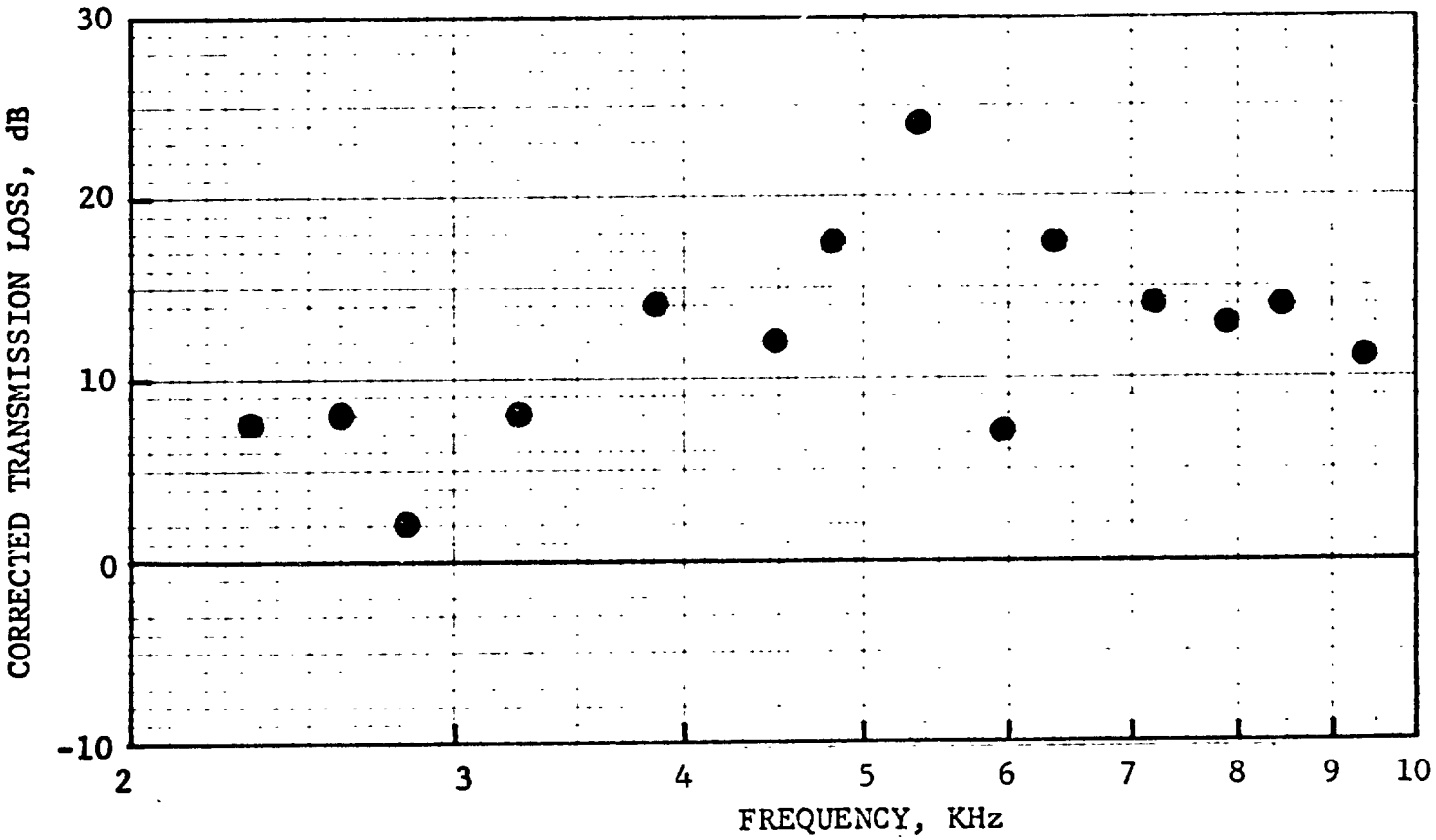

Figure 176. Corrected Transmission Loss Vs. Frequency.

HIGH TEMPERATURE ACOUSTIC DUCT .102m x .203m (4"x8")
TREATED ON TWO SIDES IN EXHAUST CONFIGURATION
L/H 4.5 TEMP. 589 °K 600 °F Mn 0.4

MATERIAL SDOF #24

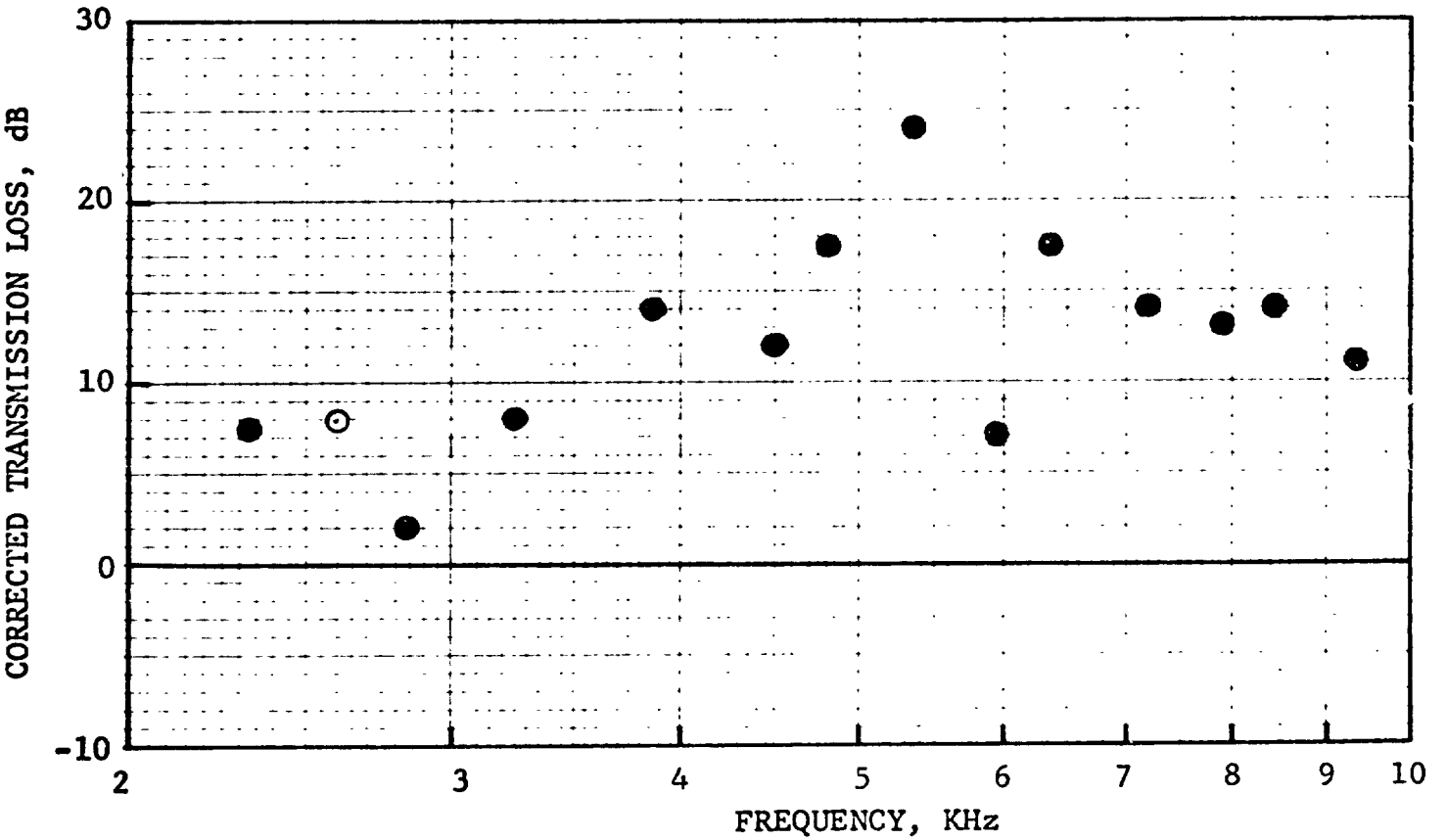

Figure 177. Corrected Transmission Loss Vs. Frequency.

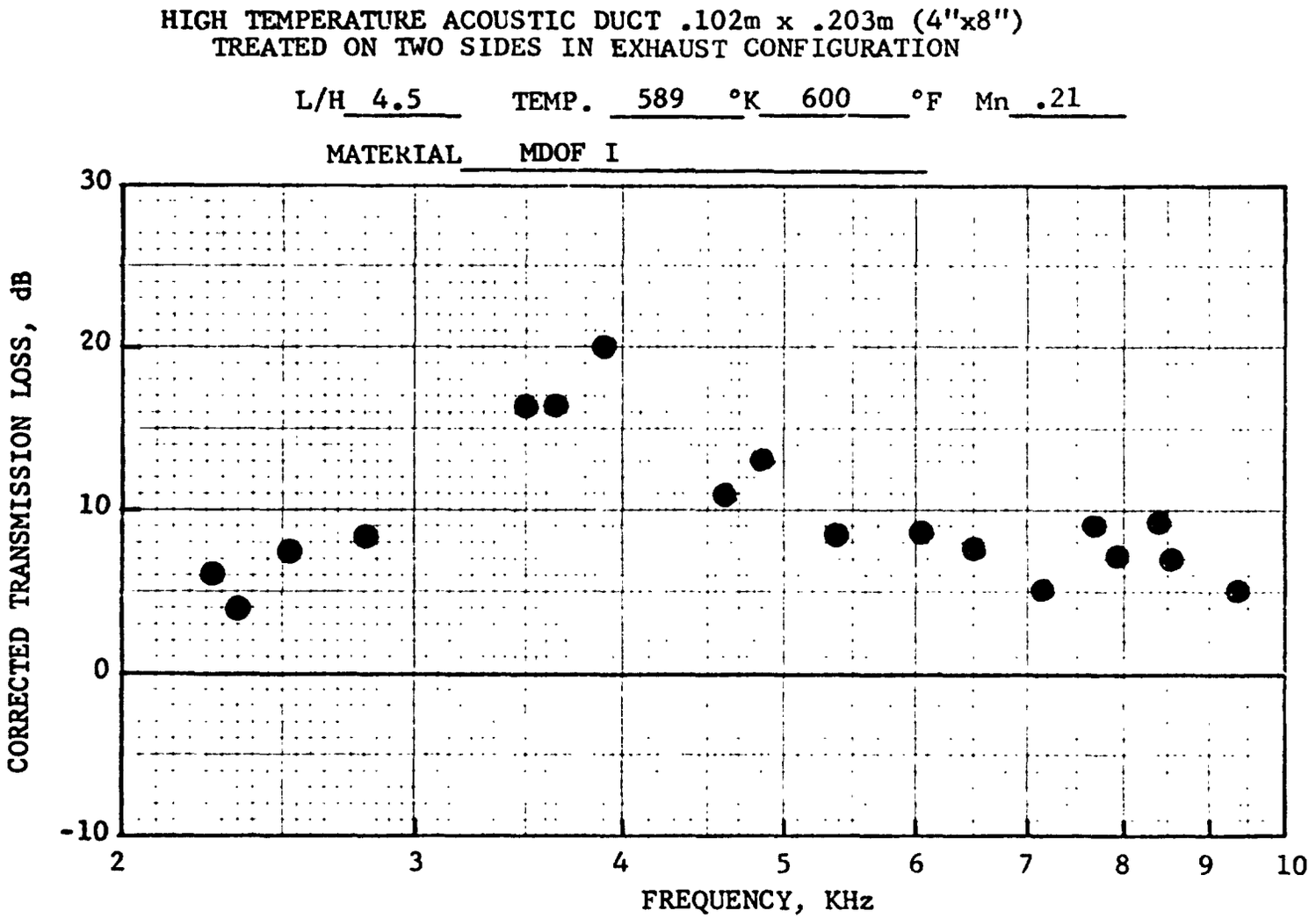

Figure 178. Corrected Transmission Loss Vs. Frequency.

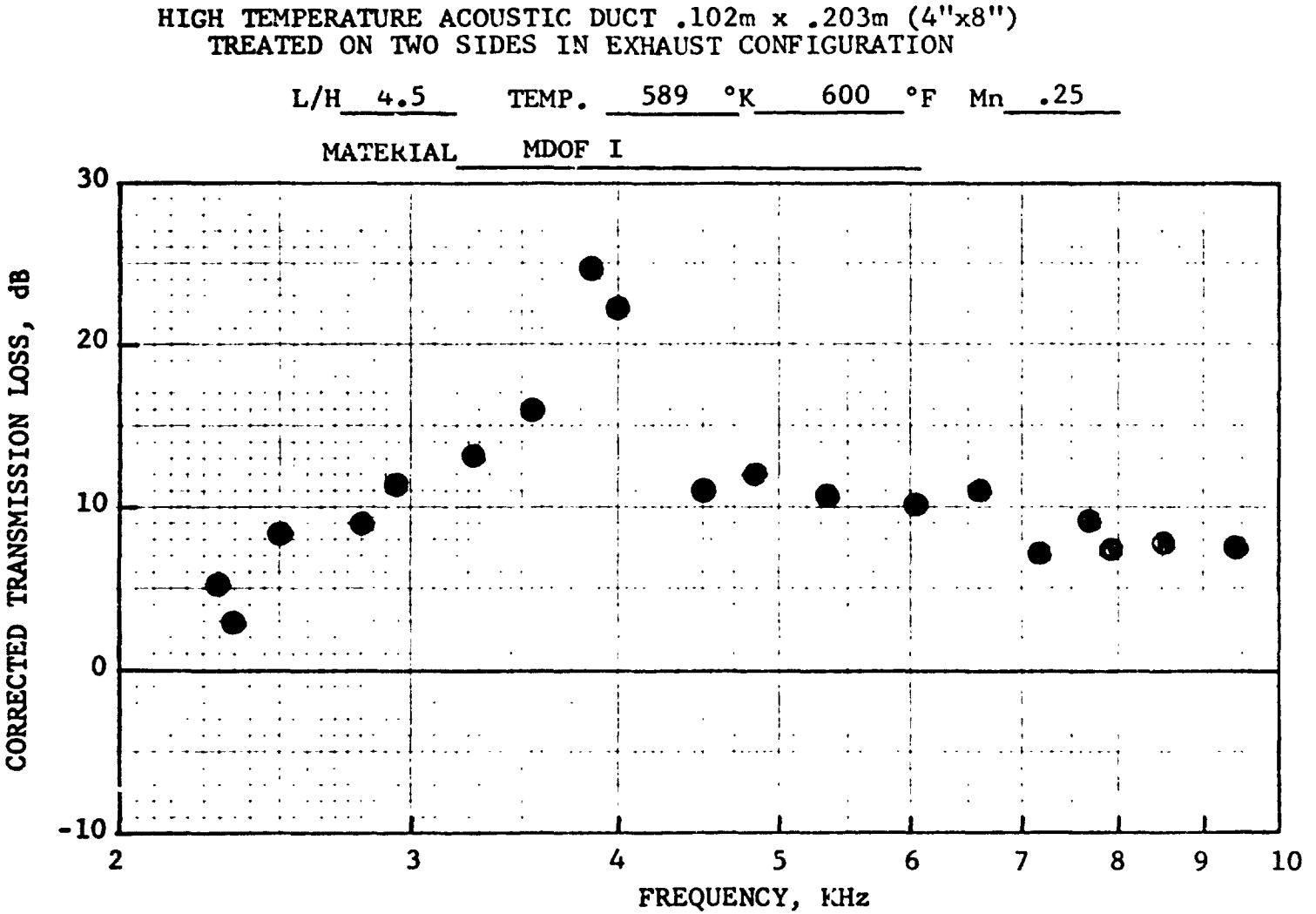

Figure 179. Corrected Transmission Loss Vs. Frequency.

HIGH TEMPERATURE ACOUSTIC DUCT .102m x .203m (4"x8")
TREATED ON TWO SIDES IN EXHAUST CONFIGURATION

L/H 4.5 TEMP. 589 °K 600 °F Mn .3

MATERIAL MDOF I

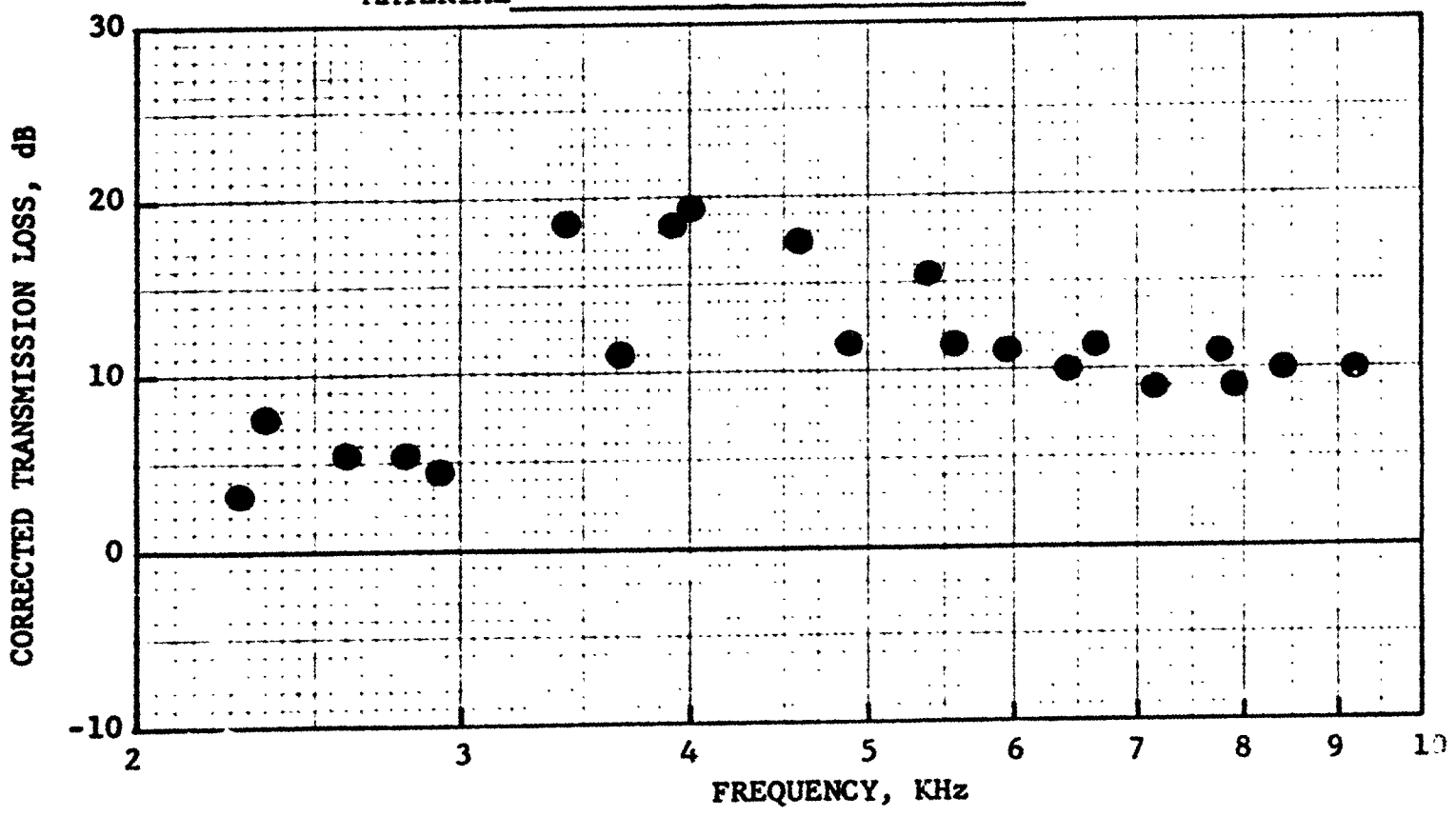

Figure 180. Corrected Transmission Loss Vs. Frequency.

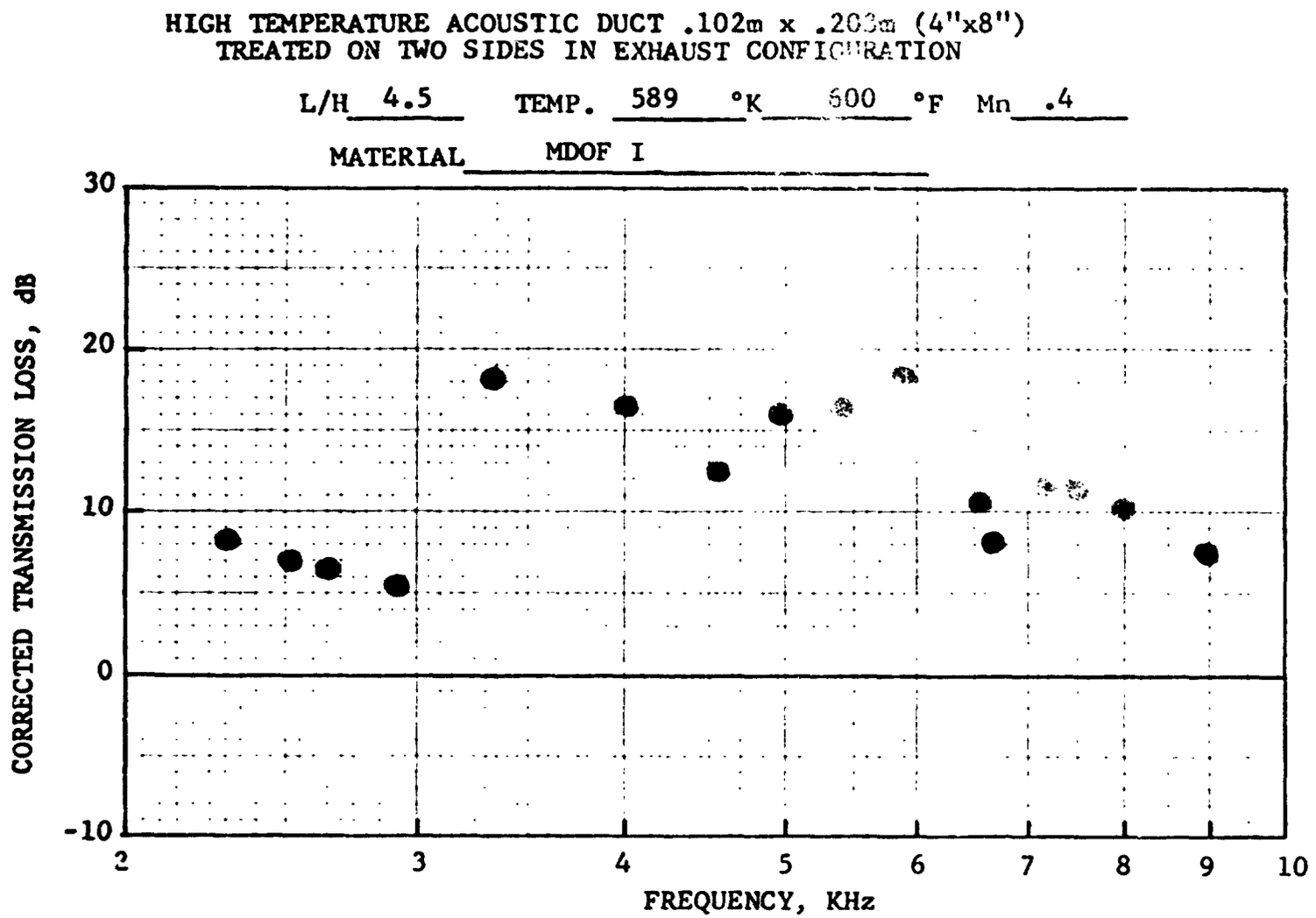

Figure 181. Corrected Transmission Loss Vs. Frequency.

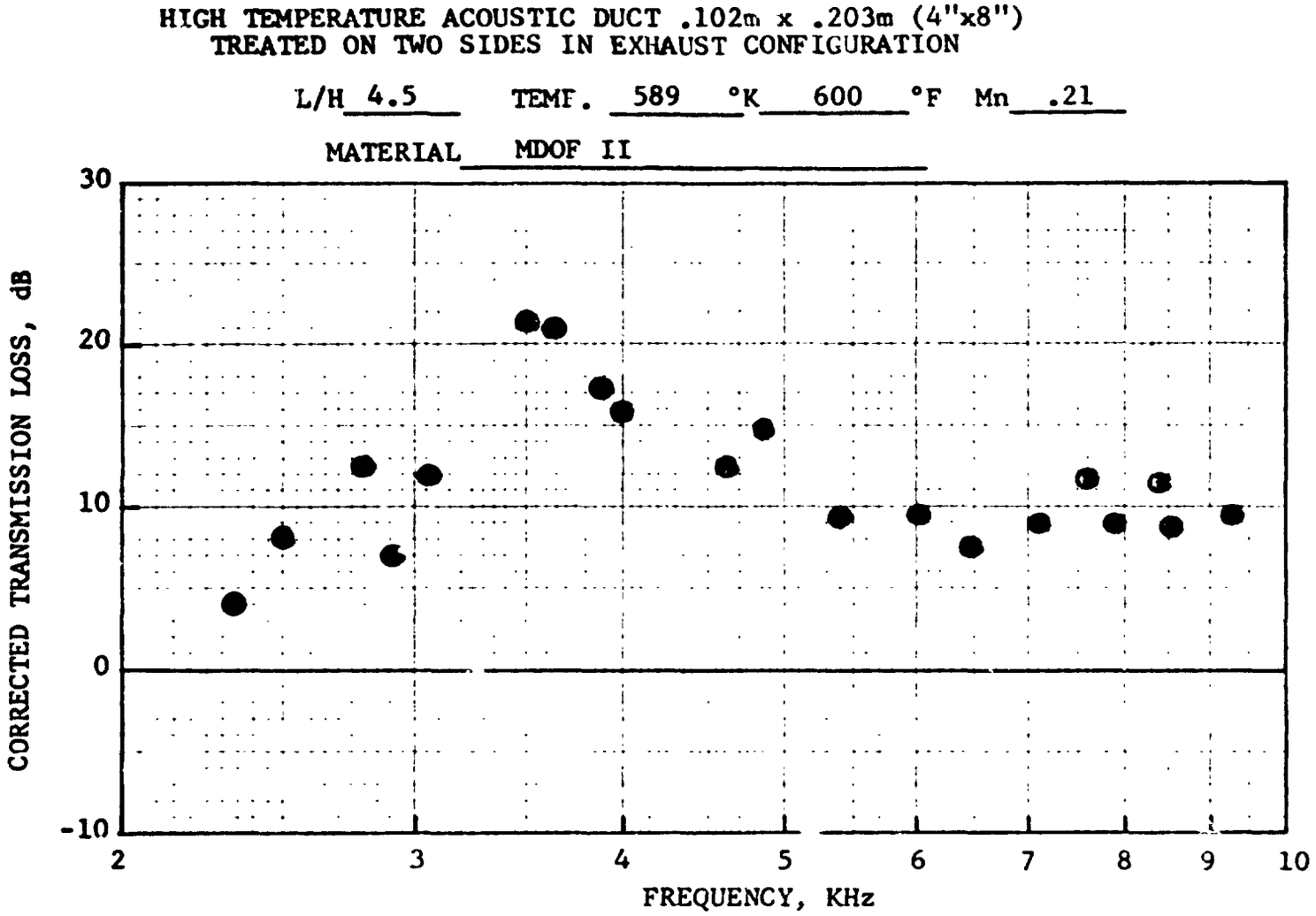

Figure 182. Corrected Transmission Loss Vs. Frequency.

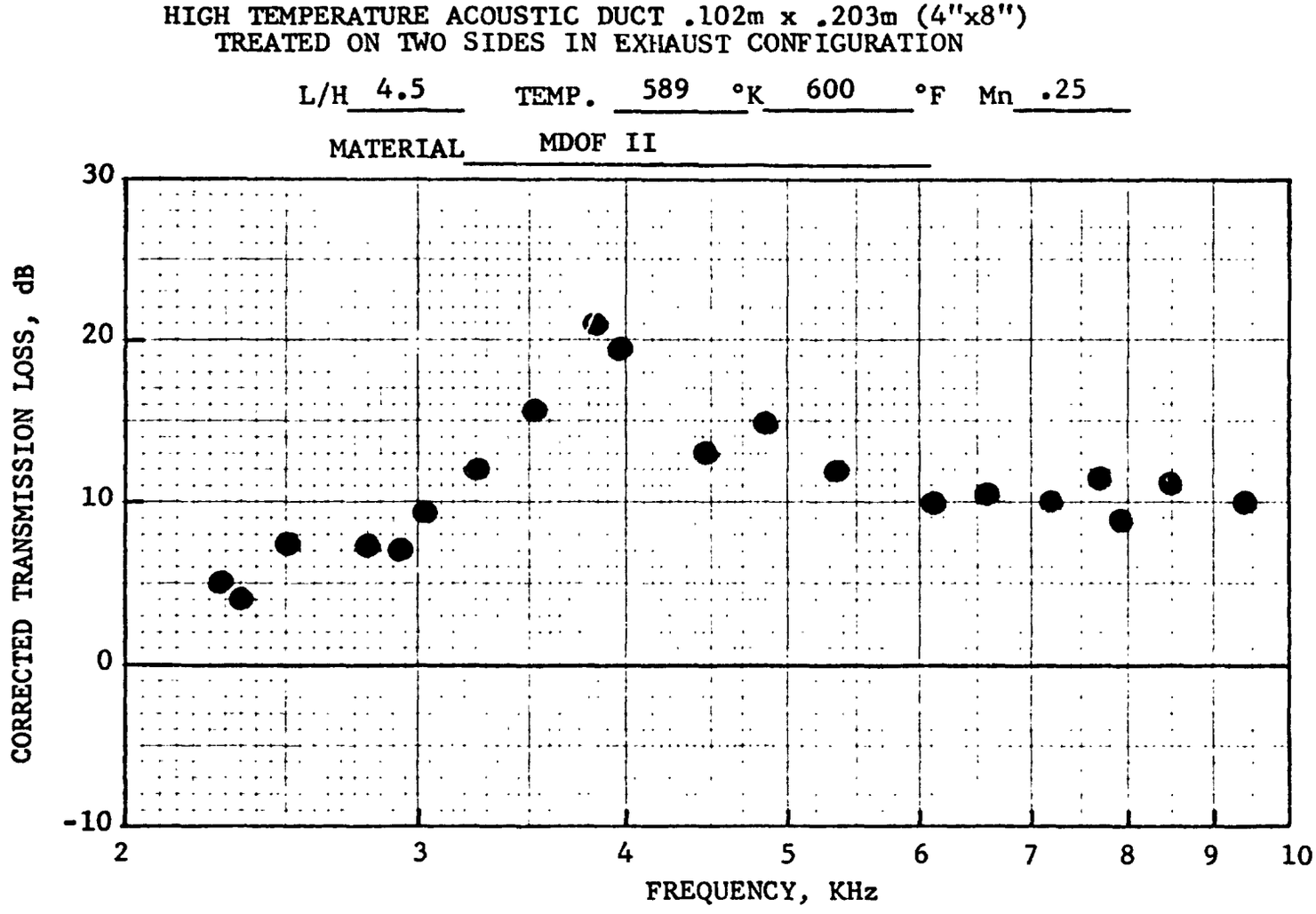

Figure 183. Corrected Transmission Loss Vs. Frequency.

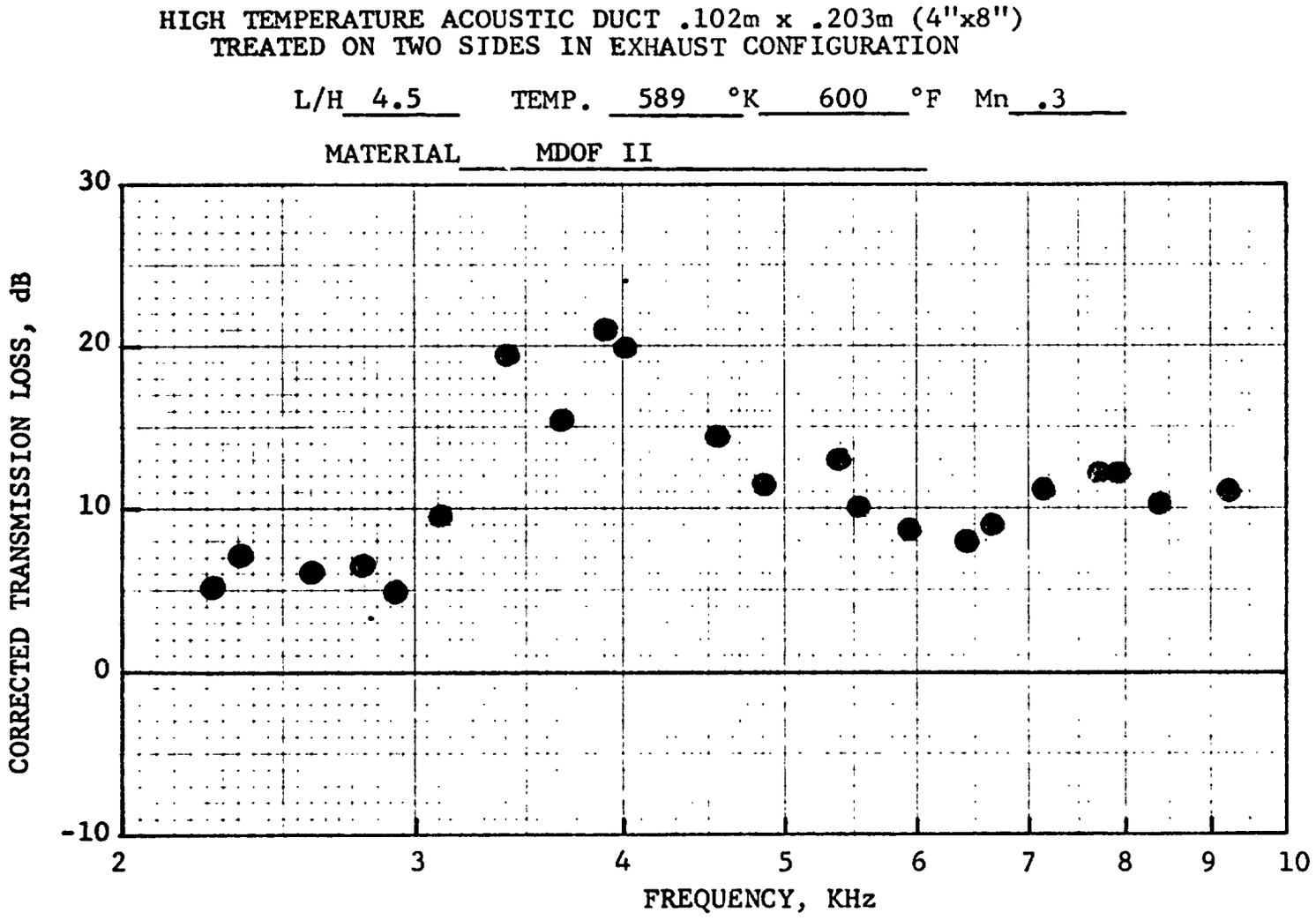

Figure 184. Corrected Transmission Loss Vs. Frequency.

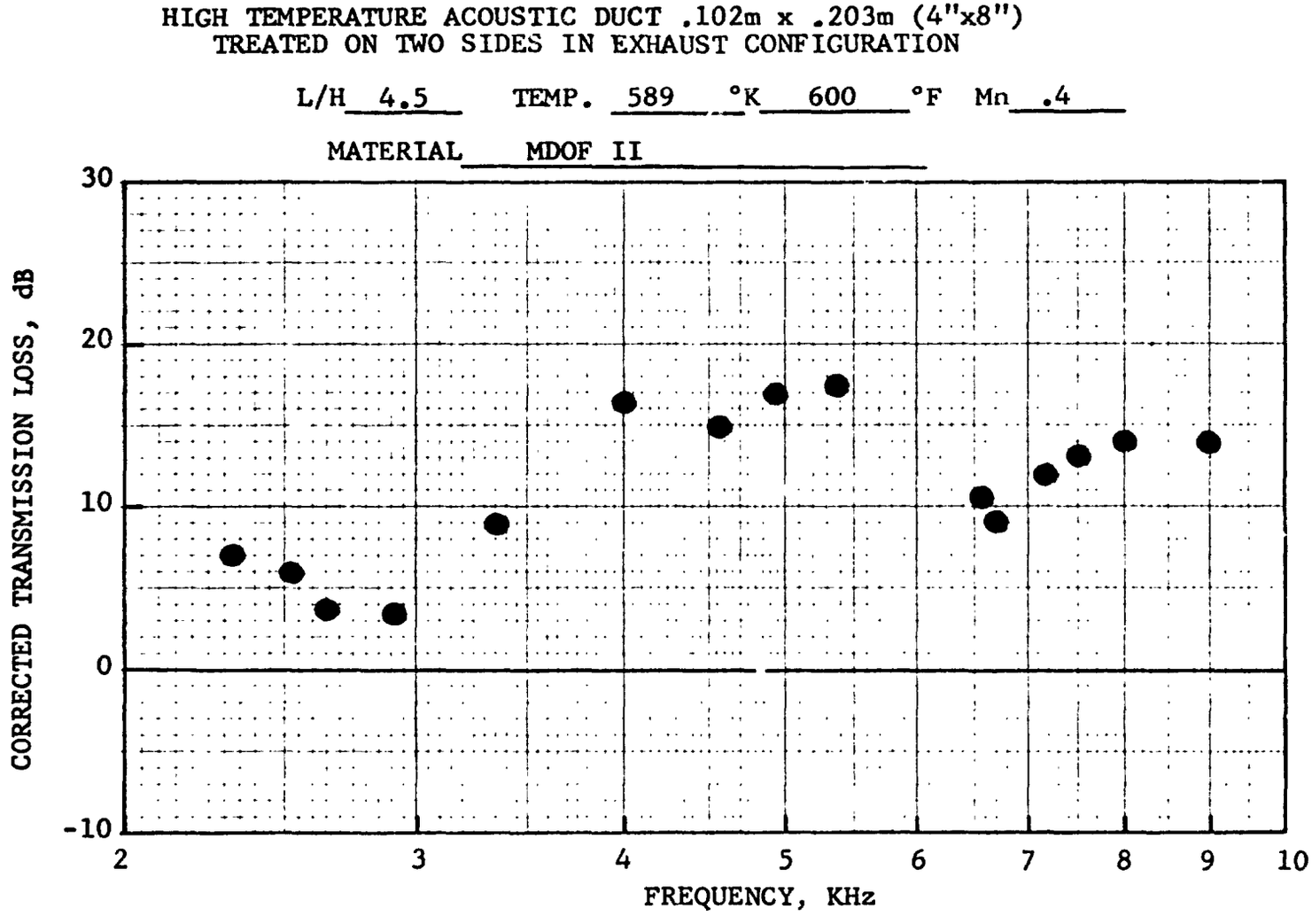

Figure 185. Corrected Transmission Loss Vs. Frequency.

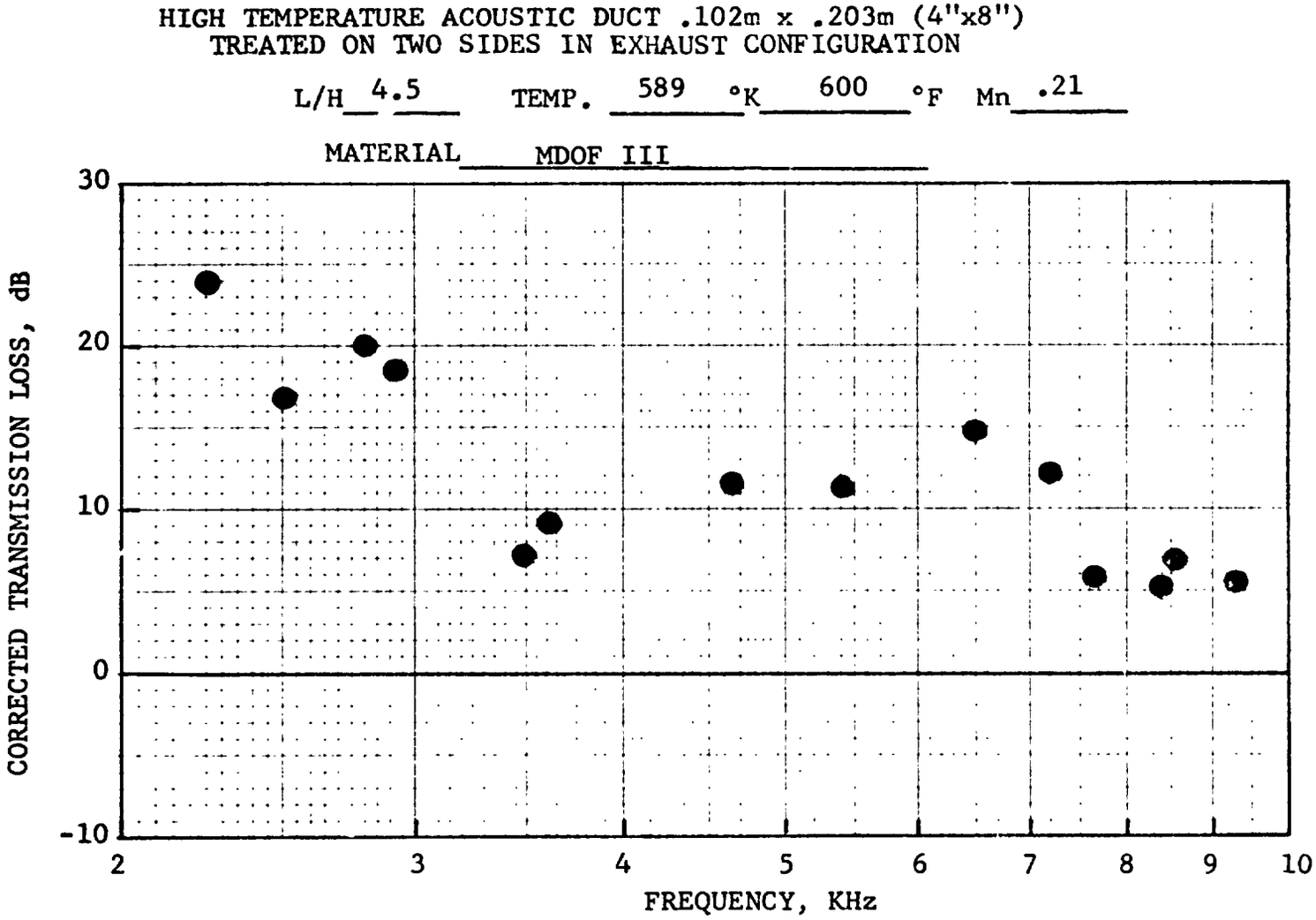

Figure 186. Corrected Transmission Loss Vs. Frequency.

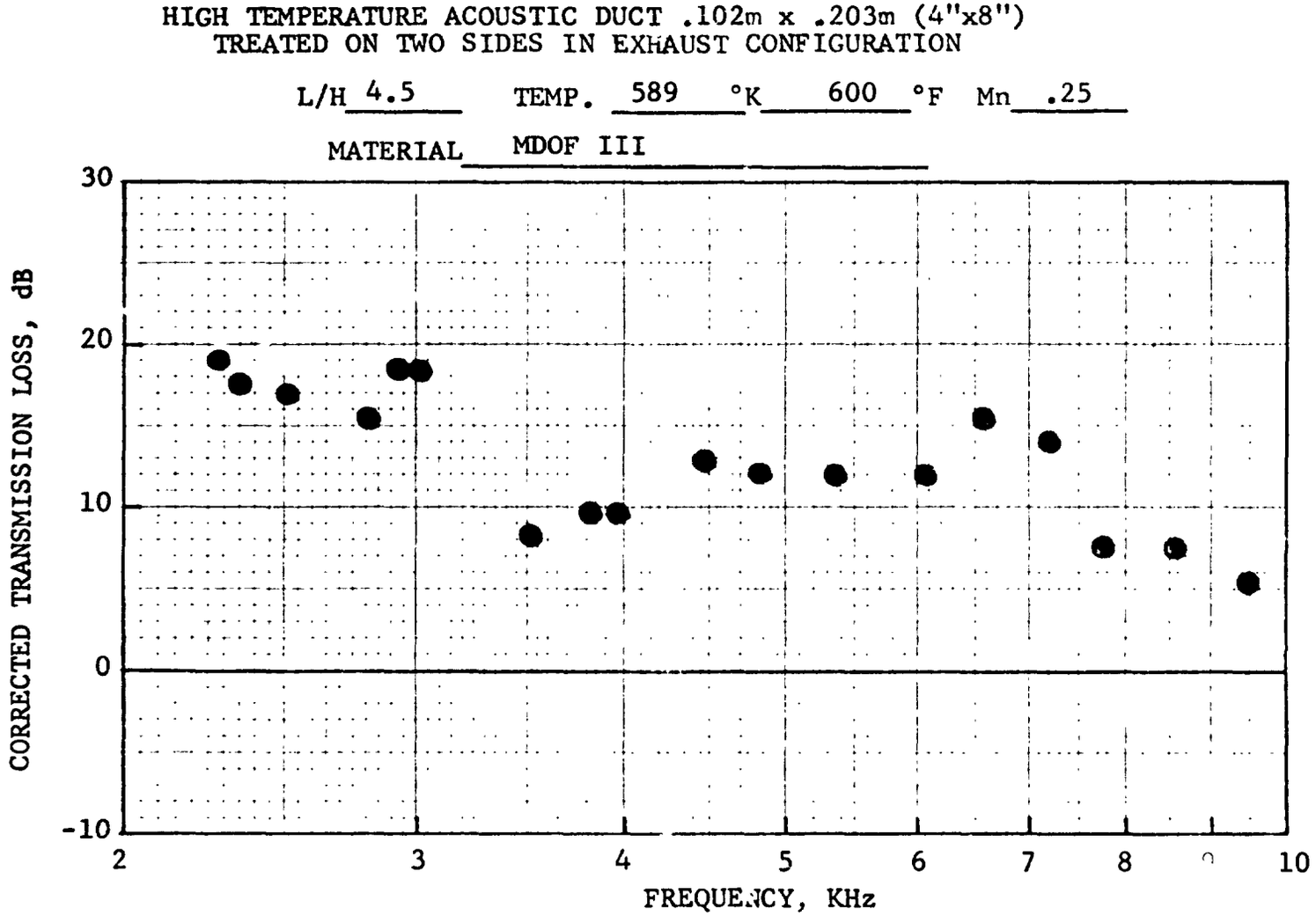

Figure 187. Corrected Transmission Lo s Vs. Frequency.

HIGH TEMPERATURE ACOUSTIC DUCT .102m x .203m (4"x8")
TREATED ON TWO SIDES IN EXHAUST CONFIGURATION

L/H 4.5 TEMP. 589 °K 600 °F Mn .3

MATERIAL MDOF III

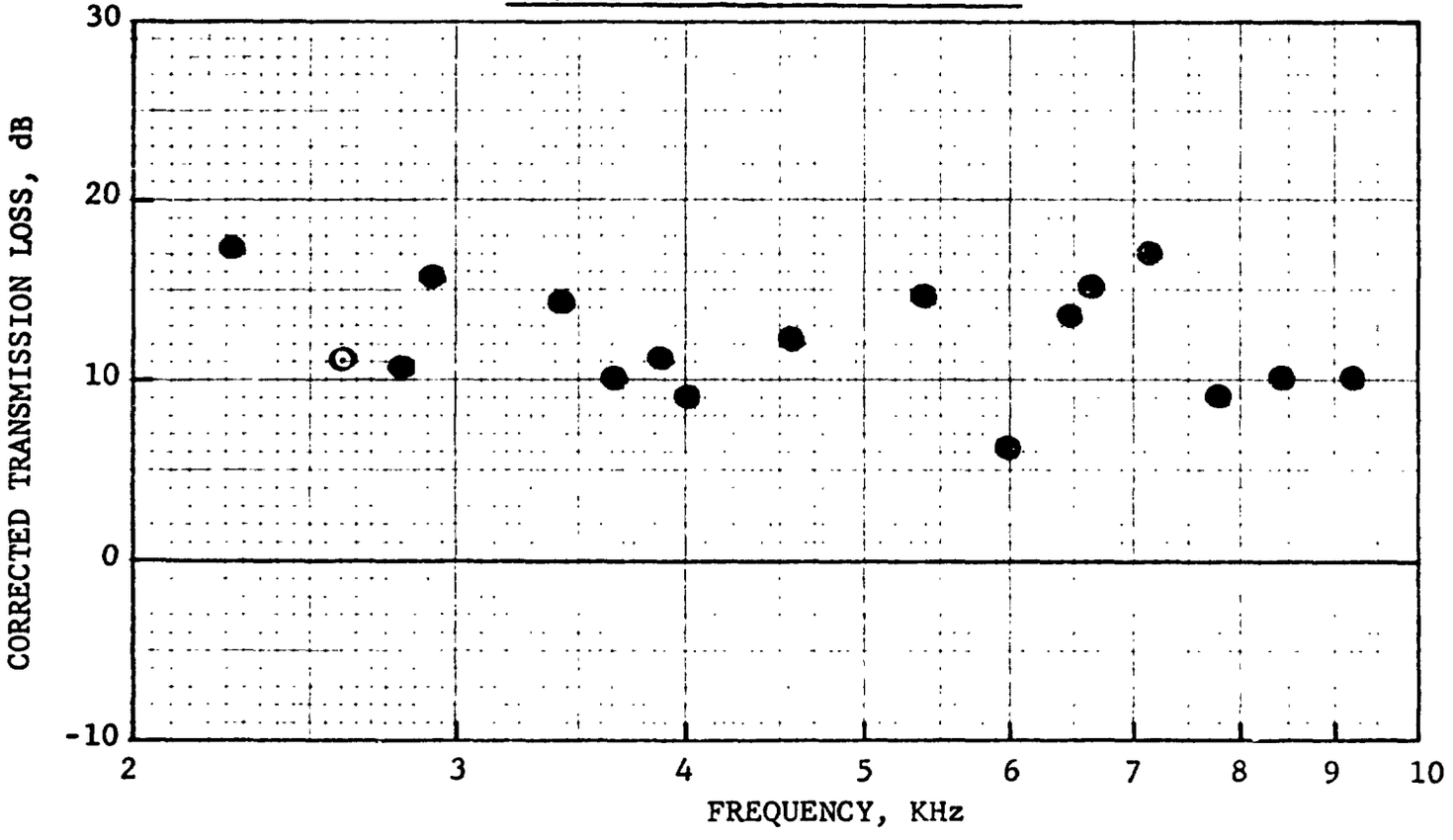

Figure 188. Corrected Transmission Loss Vs. Frequency.

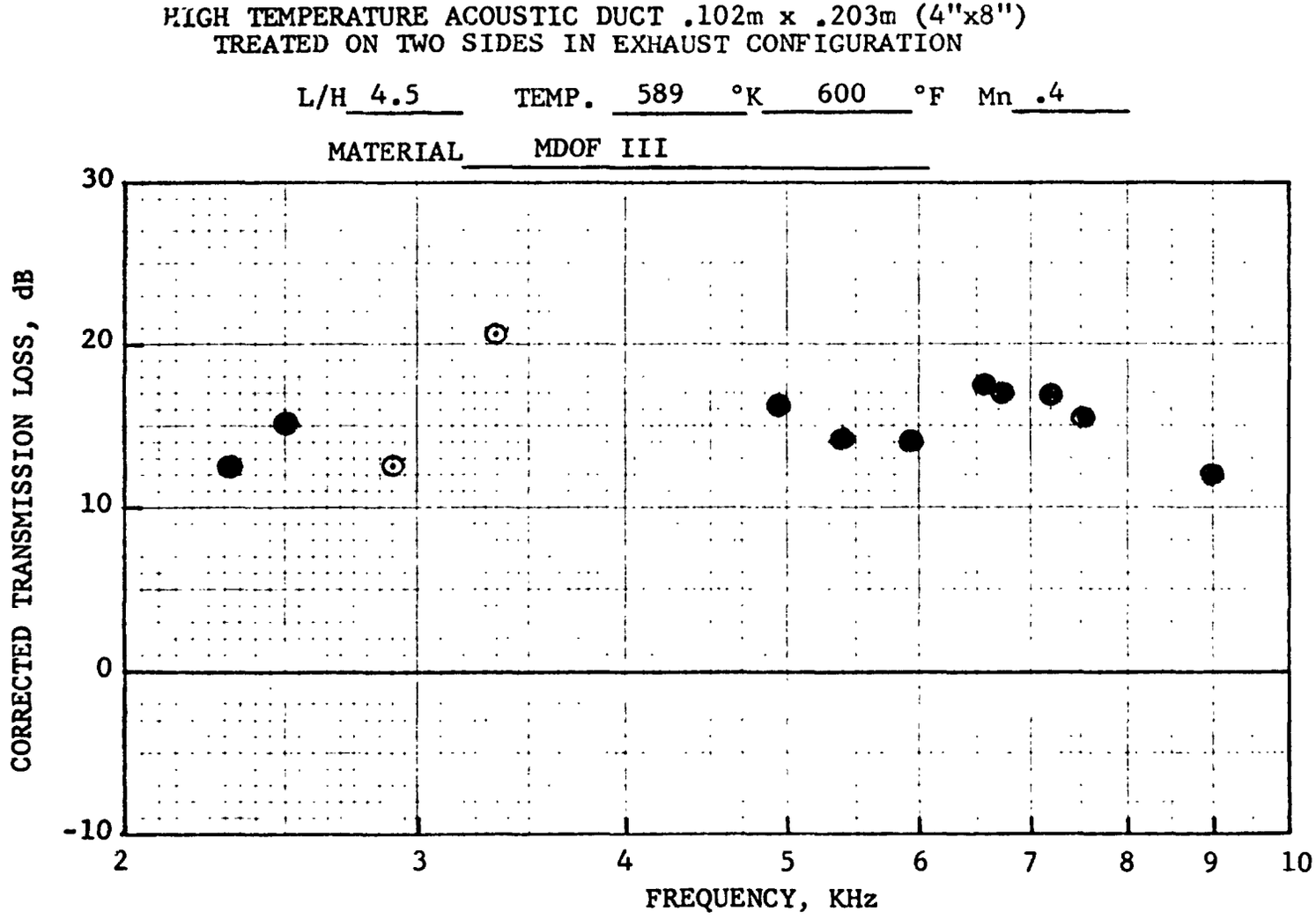

Figure 189. Corrected Transmission Loss Vs. Frequency.

HIGH TEMPERATURE ACOUSTIC DUCT .102m x .203m (4"x8")
TREATED ON TWO SIDES IN EXHAUST CONFIGURATION

L/H 2.25 TEMP. 589 °K 600 °F Mn .21

MATERIAL DOUBLE SANDWICH II

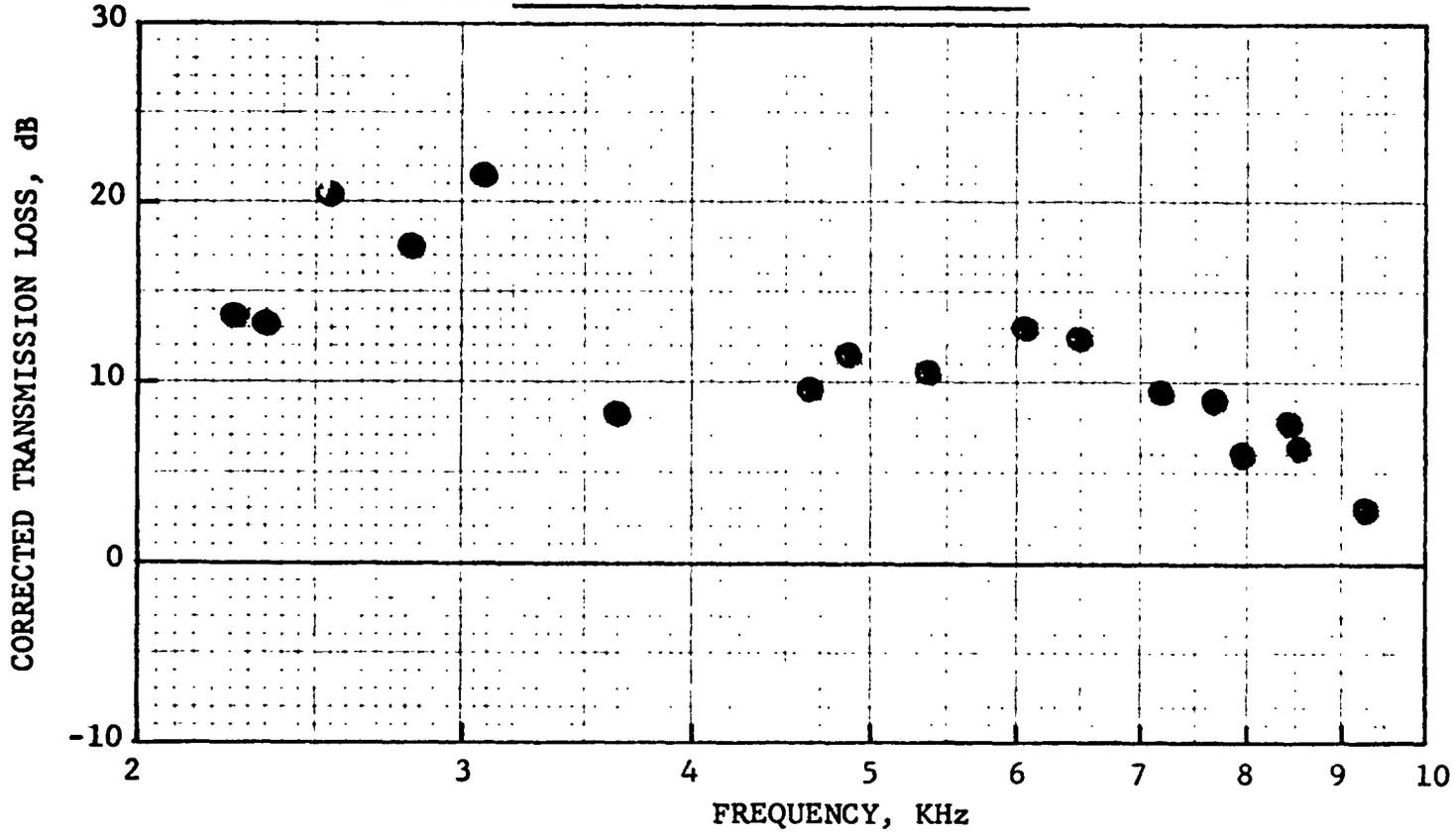

Figure 190. Corrected Transmission Loss Vs. Frequency.

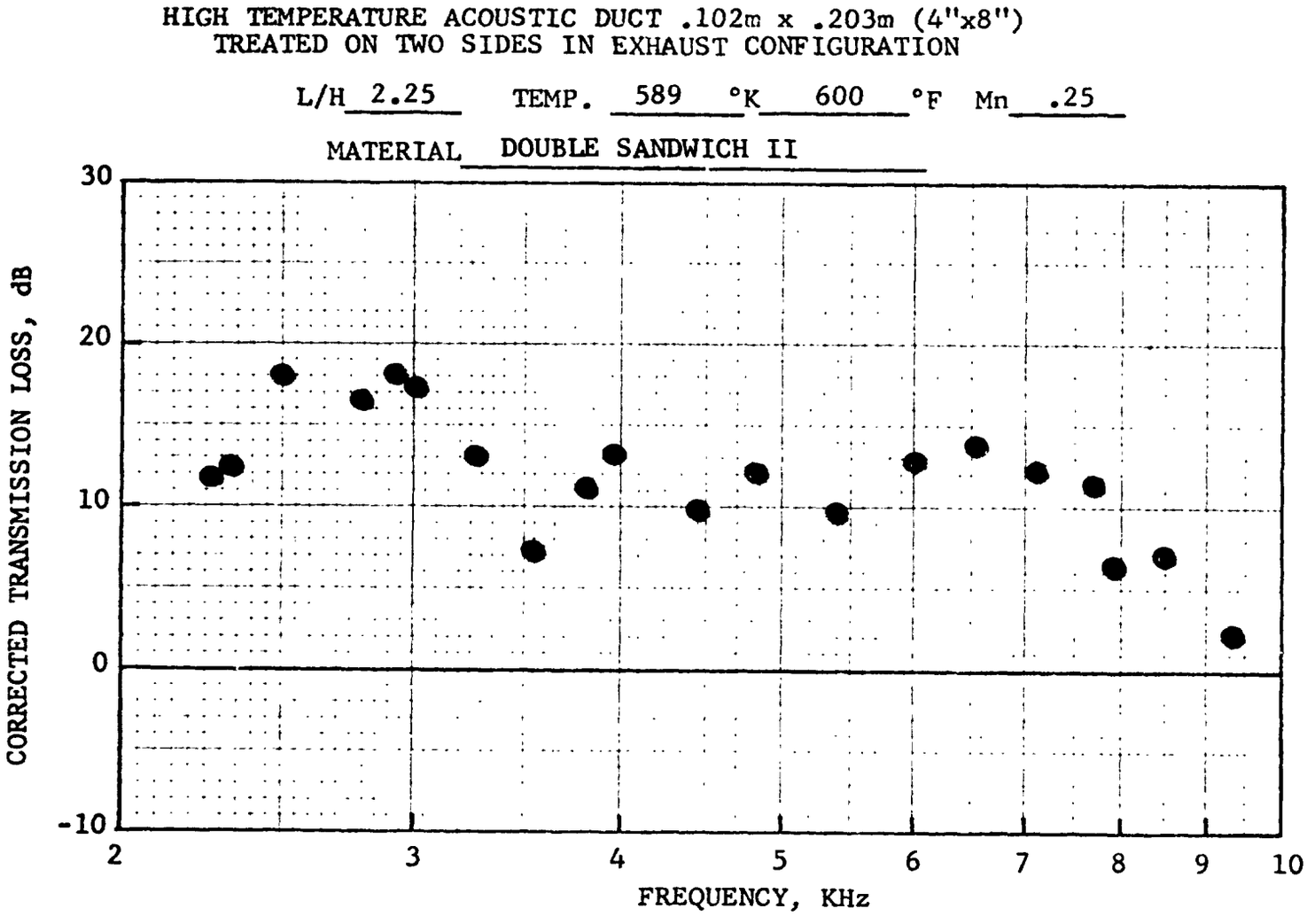

Figure 191. Corrected Transmission Loss Vs. Frequency.

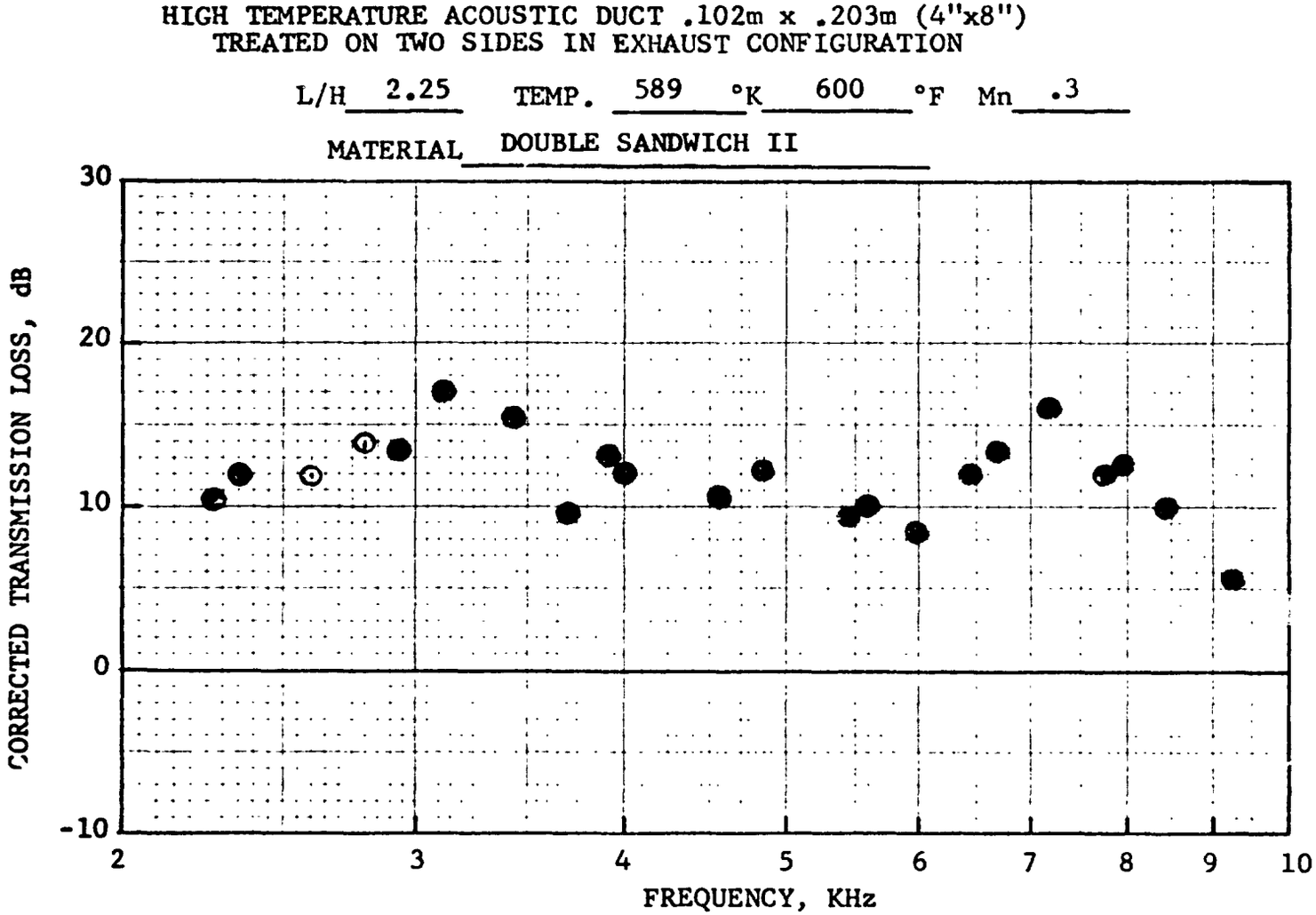

Figure 192. Corrected Transmission Loss Vs. Frequency.

HIGH TEMPERATURE ACOUSTIC DUCT .102m x .203m (4"x8")
TREATED ON TWO SIDES IN EXHAUST CONFIGURATION
L/H 3 TEMP. 658°K 725°F Mn 0.191

MATERIAL DOUBLE SANDWICH II

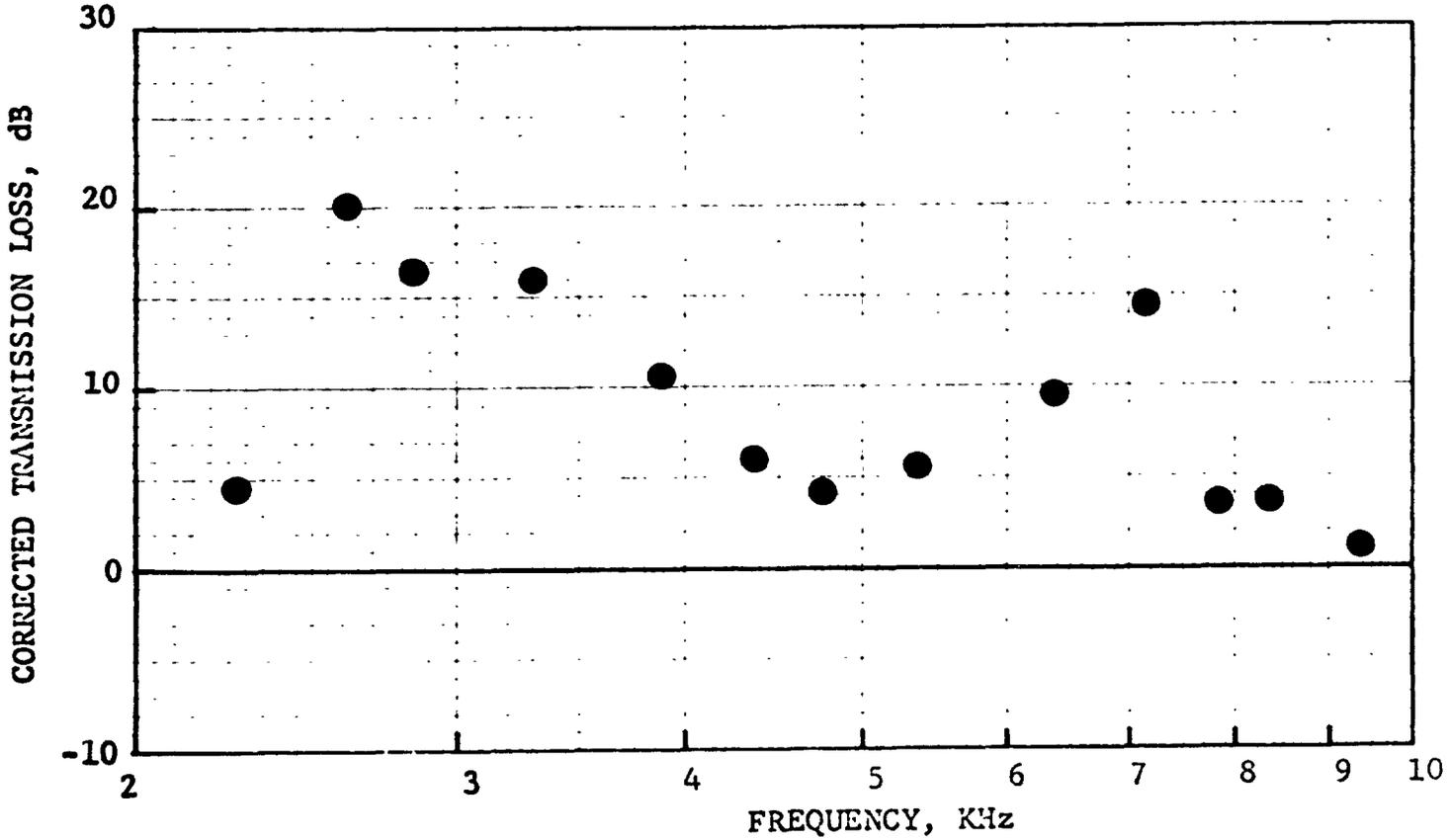

Figure 193. Corrected Transmission Loss Vs. Frequency.

HIGH TEMPERATURE ACOUSTIC DUCT .102m x .203m (4"x8")
TREATED ON TWO SIDES IN EXHAUST CONFIGURATION
L/H 3 TEMP. 658°K 725°F Mn 0.215

MATERIAL DOUBLE SANDWICH II

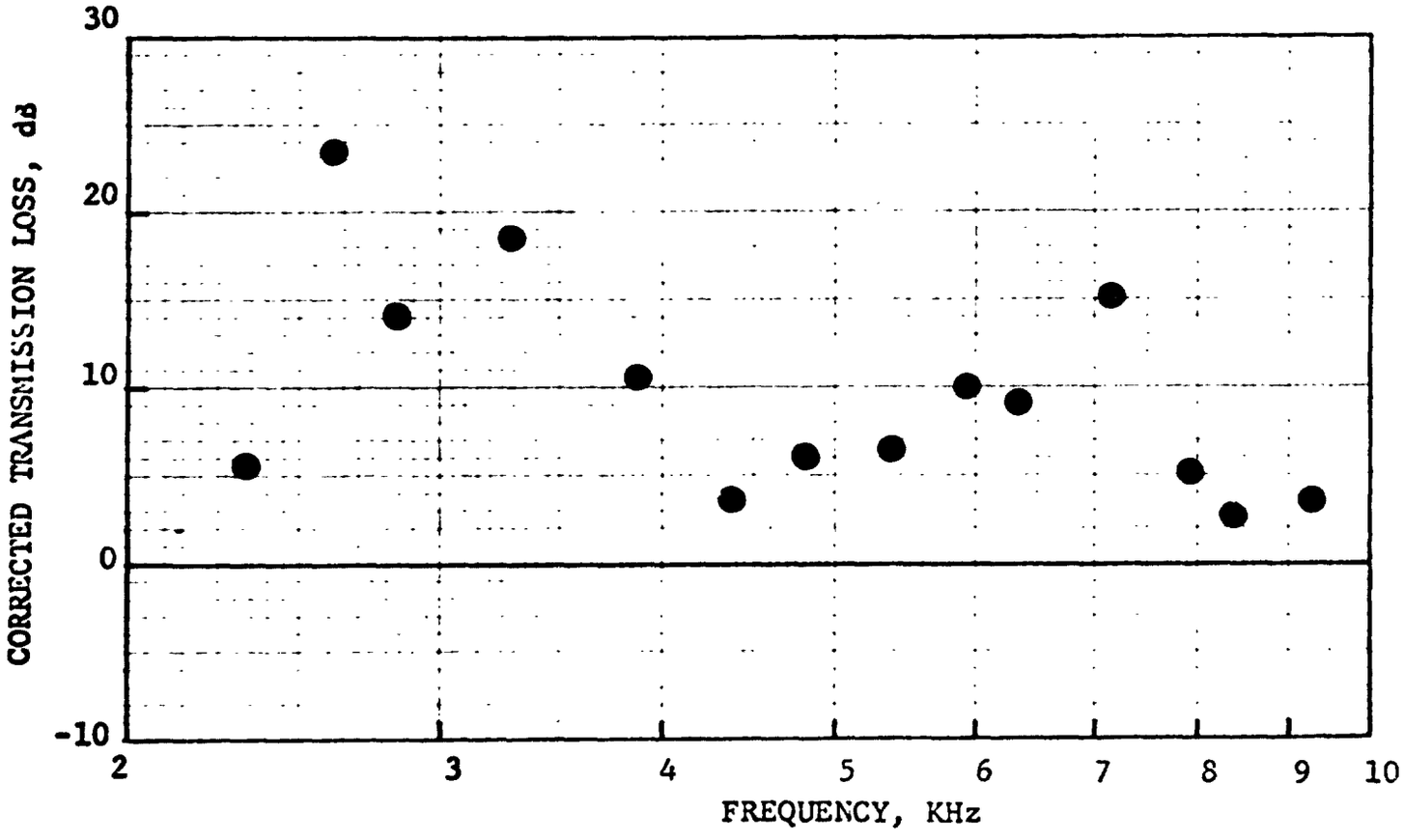

Figure 194. Corrected Transmission Loss Vs. Frequency.

HIGH TEMPERATURE ACOUSTIC DUCT .102m x .203m (4"x8")
TREATED ON TWO SIDES IN EXHAUST CONFIGURATION
L/H 3 TEMP. 658°K 725°F Mn 0.262

MATERIAL DOUBLE SANDWICH II

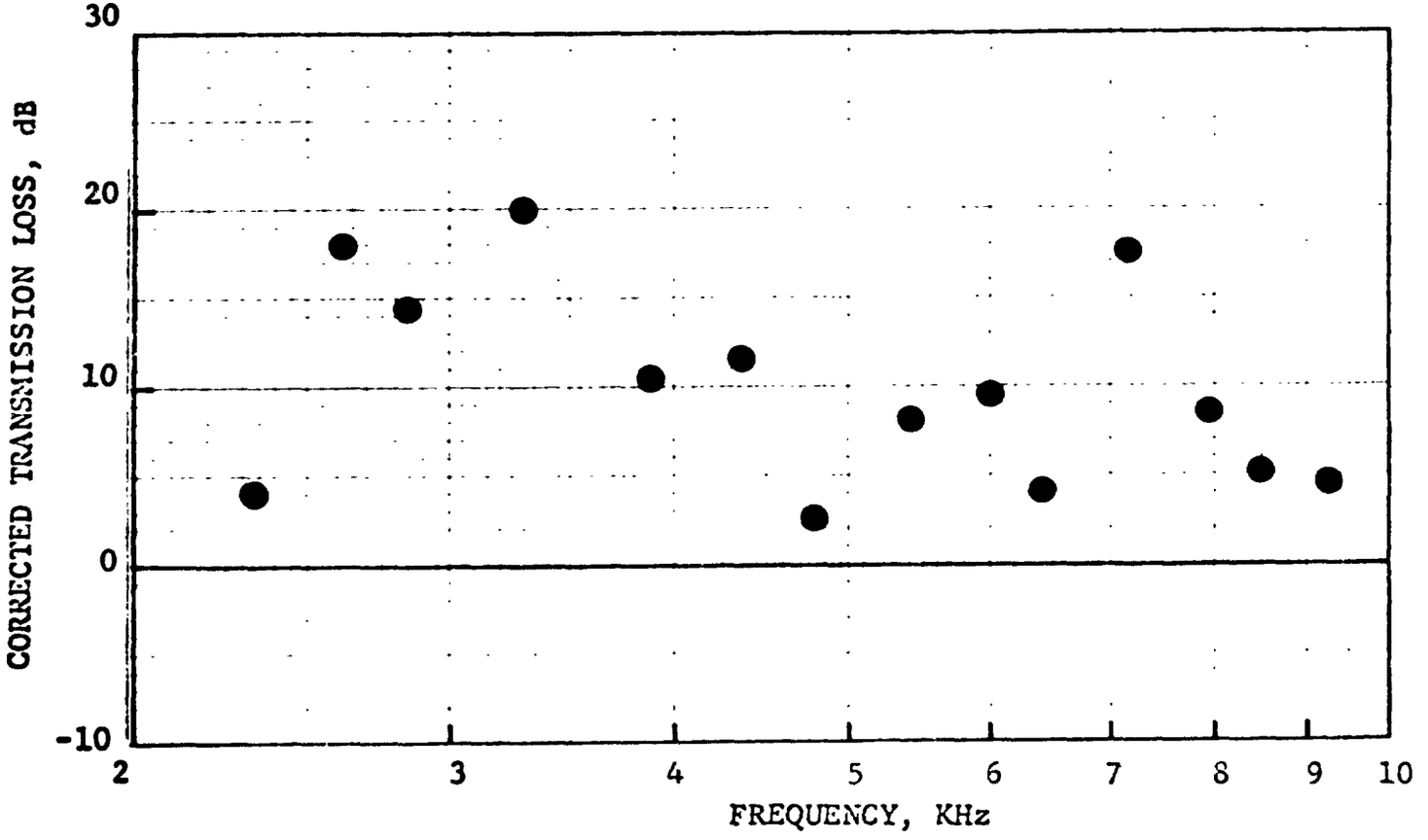

Figure 195. Corrected Transmission Loss Vs. Frequency.

HIGH TEMPERATURE ACOUSTIC DUCT .102m x .203m (4"x8")
TREATED ON TWO SIDES IN EXHAUST CONFIGURATION
L/H 3 TEMP. 783°K 950°F Mn .308

MATERIAL DOUBLE SANDWICH II

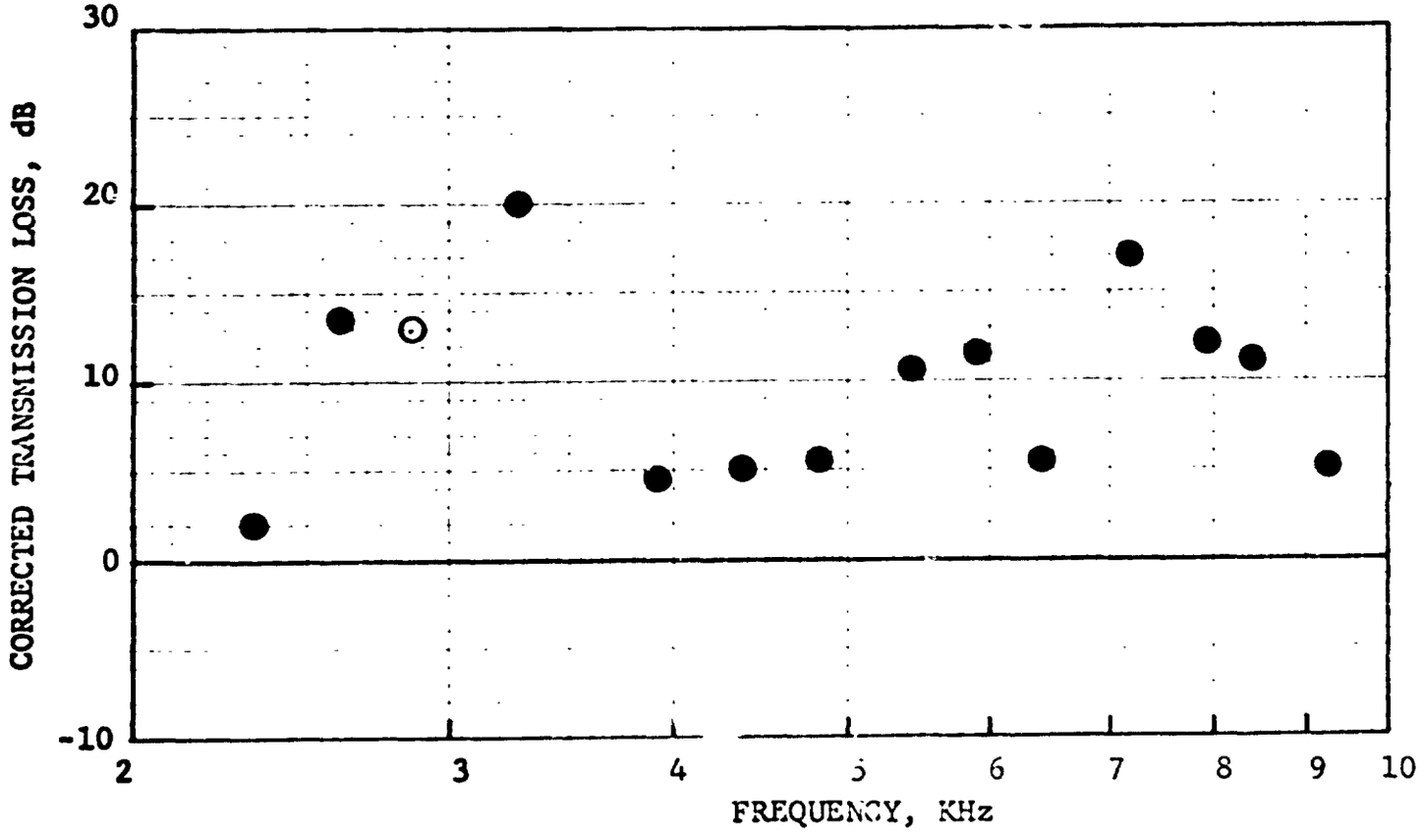

Figure 196. Corrected Transmission Loss Vs. Frequency.

HIGH TEMPERATURE ACOUSTIC DUCT .102m x .203m (4"x8")
TREATED ON TWO SIDES IN EXHAUST CONFIGURATION
L/H 3 TEMP. 783°K 950°F Mn 0.352

MATERIAL DOUBLE SANDWICH II

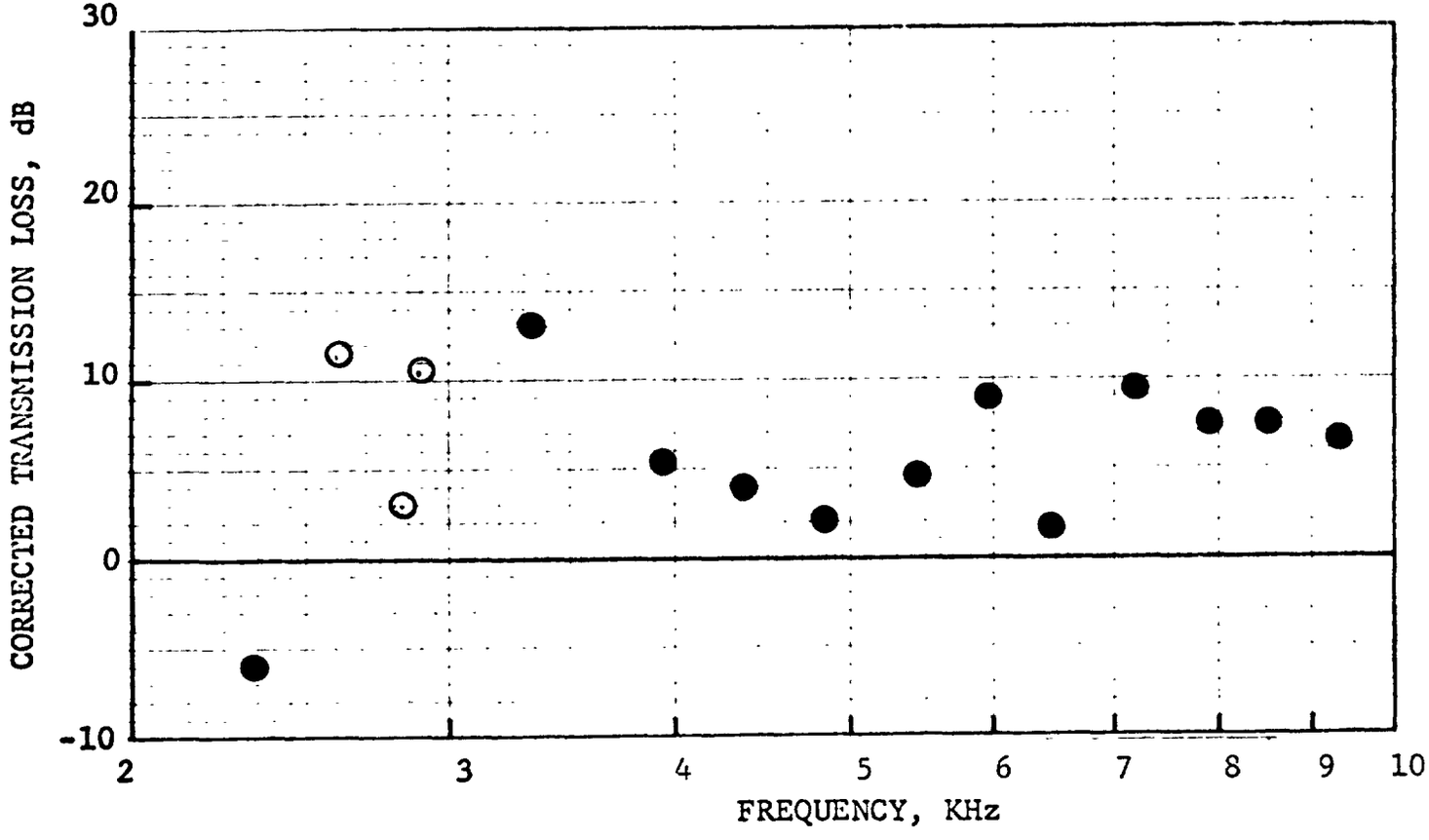

Figure 197. Corrected Transmission Loss Vs. Frequency.

HIGH TEMPERATURE ACOUSTIC DUCT .102m x .203m (4"x8")
TREATED ON TWO SIDES IN EXHAUST CONFIGURATION
L/H 3 TEMP. 783°K 950°F Mn 0.44

MATERIAL DOUBLE SANDWICH II

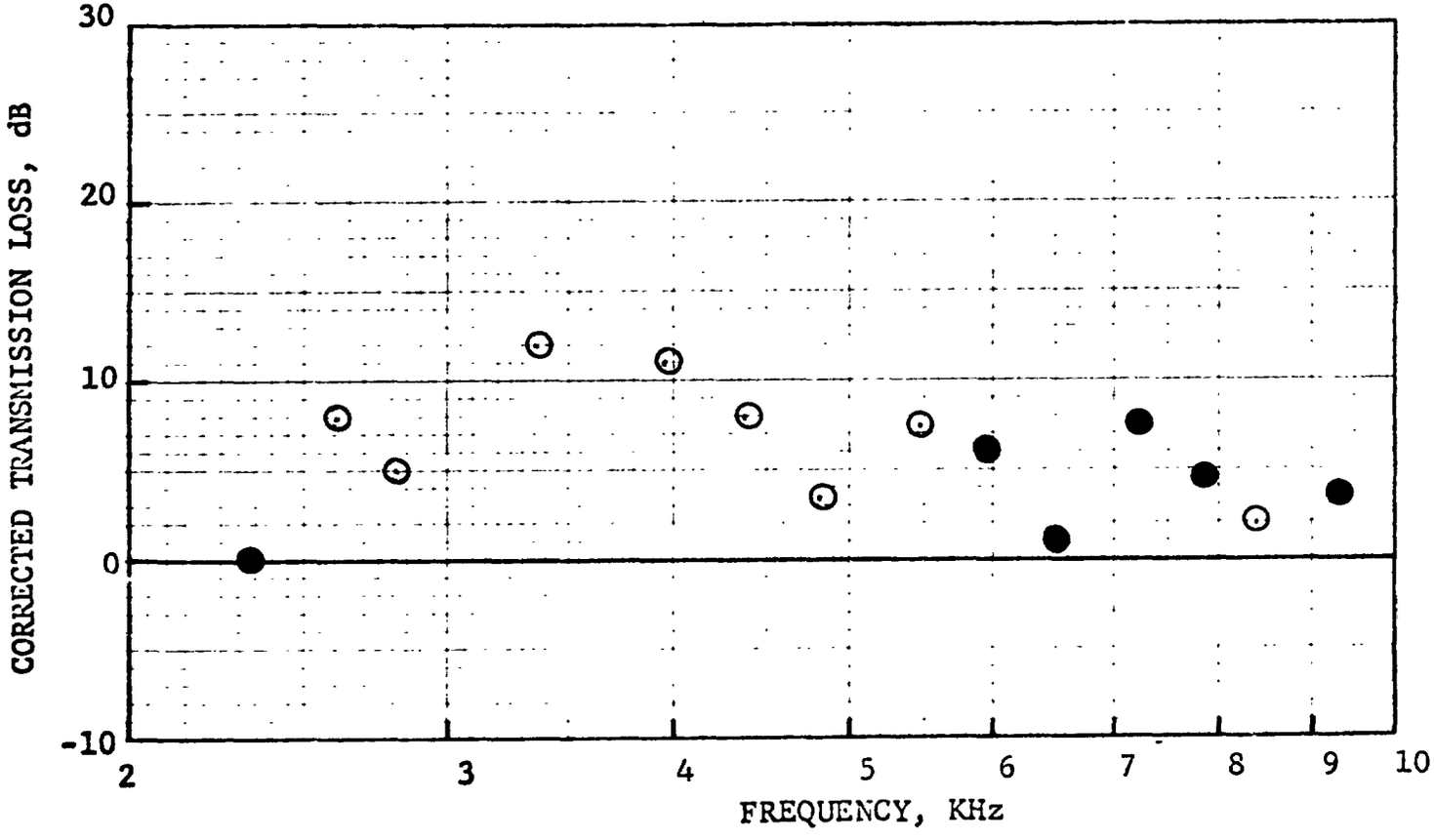

Figure 198. Corrected Transmission Loss Vs. Frequency.

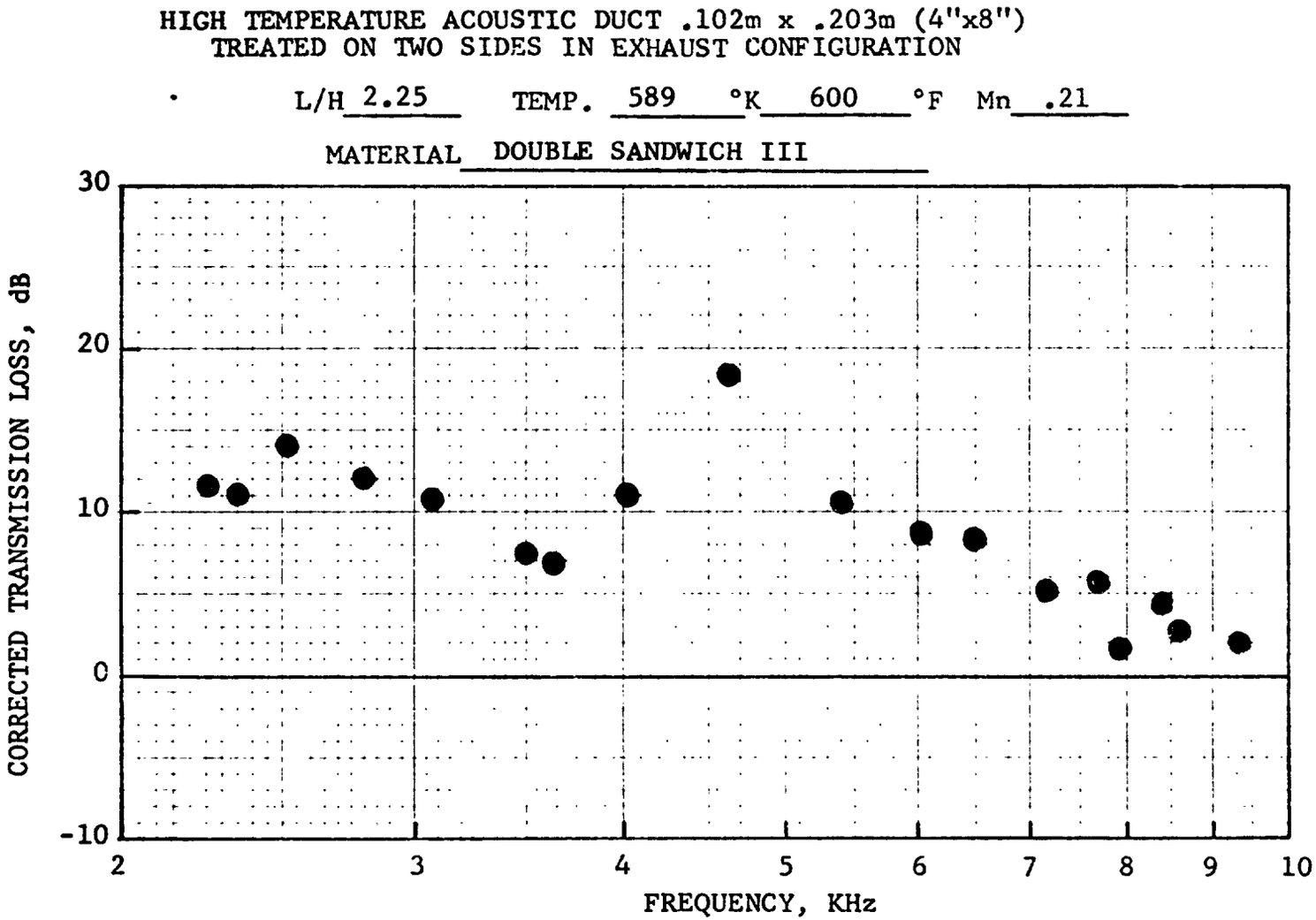

Figure 199. Corrected Transmission Loss Vs. Frequency.

HIGH TEMPERATURE ACOUSTIC DUCT .102m x .203m (4"x8")
TREATED ON TWO SIDES IN EXHAUST CONFIGURATION

L/H 2+25 TEMP. 589 °K 600 °F Mn .25

MATERIAL DOUBLE SANDWICH III

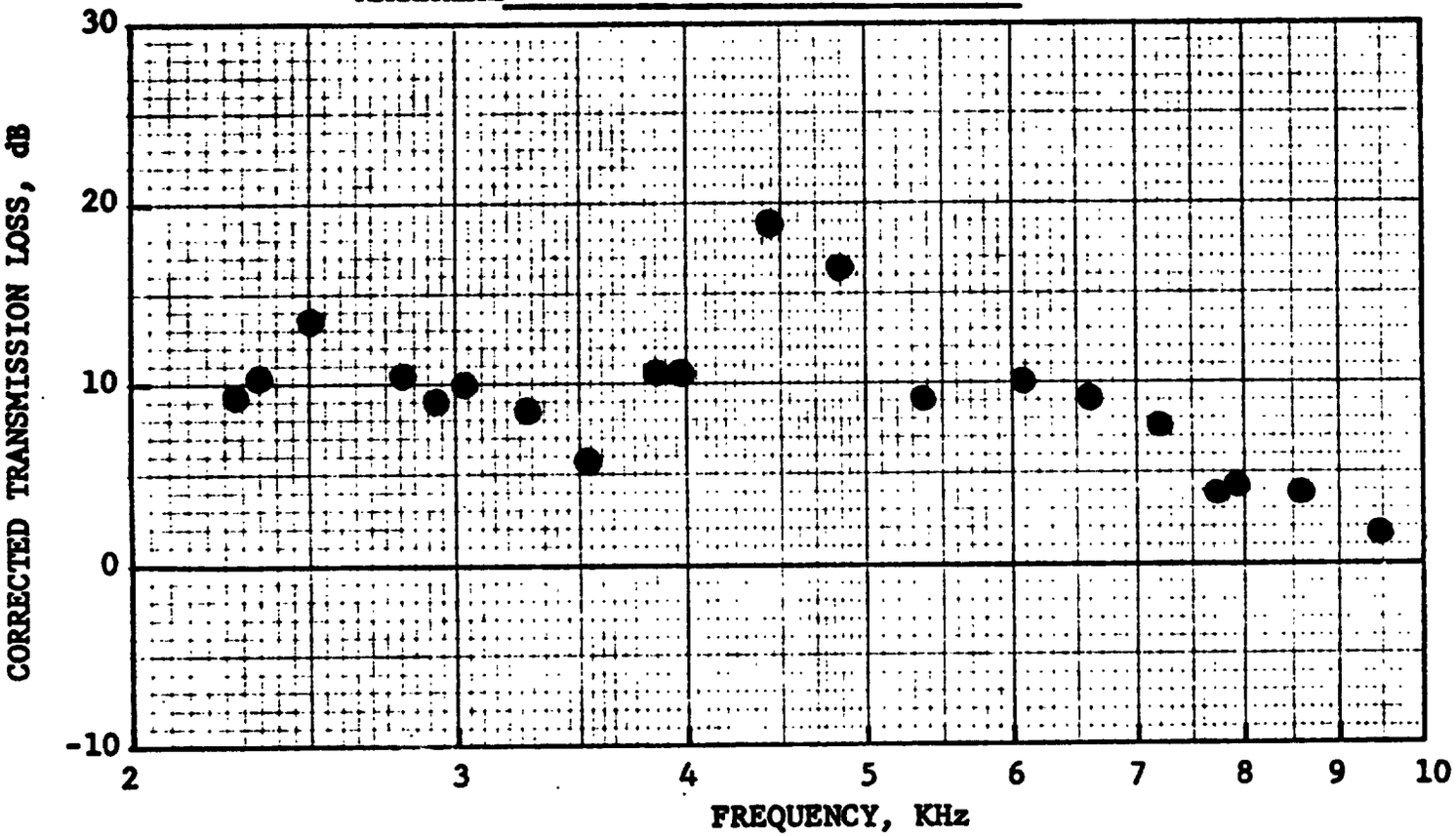

Figure 200. Corrected Transmission Loss Vs. Frequency.

HIGH TEMPERATURE ACOUSTIC DUCT .102m x .203m (4"x8")
TREATED ON TWO SIDES IN EXHAUST CONFIGURATION

L/H 2.25 TEMP. 589 °K 600 °F Mn .3

MATERIAL DOUBLE SANDWICH III

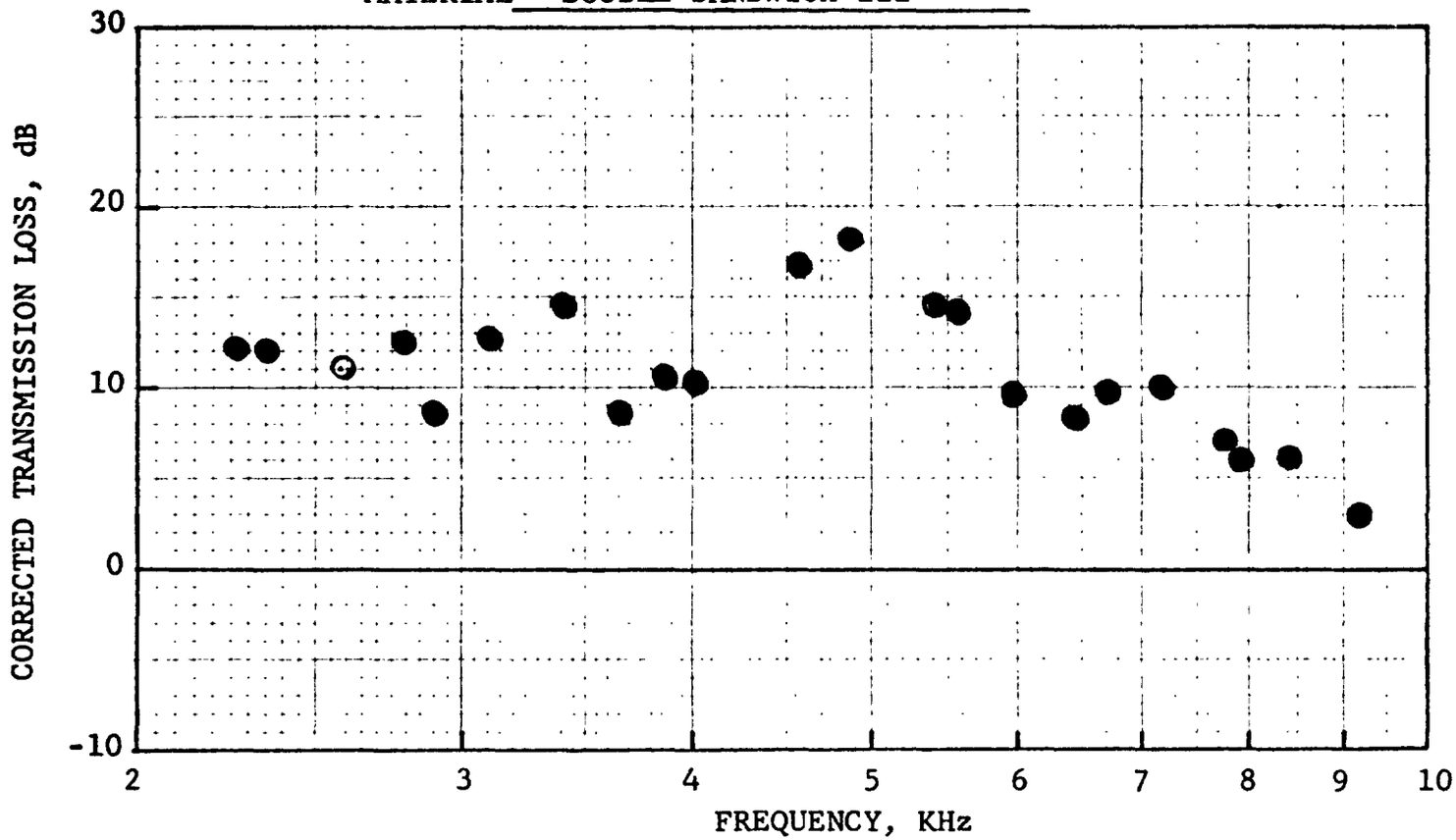

Figure 201. Corrected Transmission Loss Vs. Frequency.

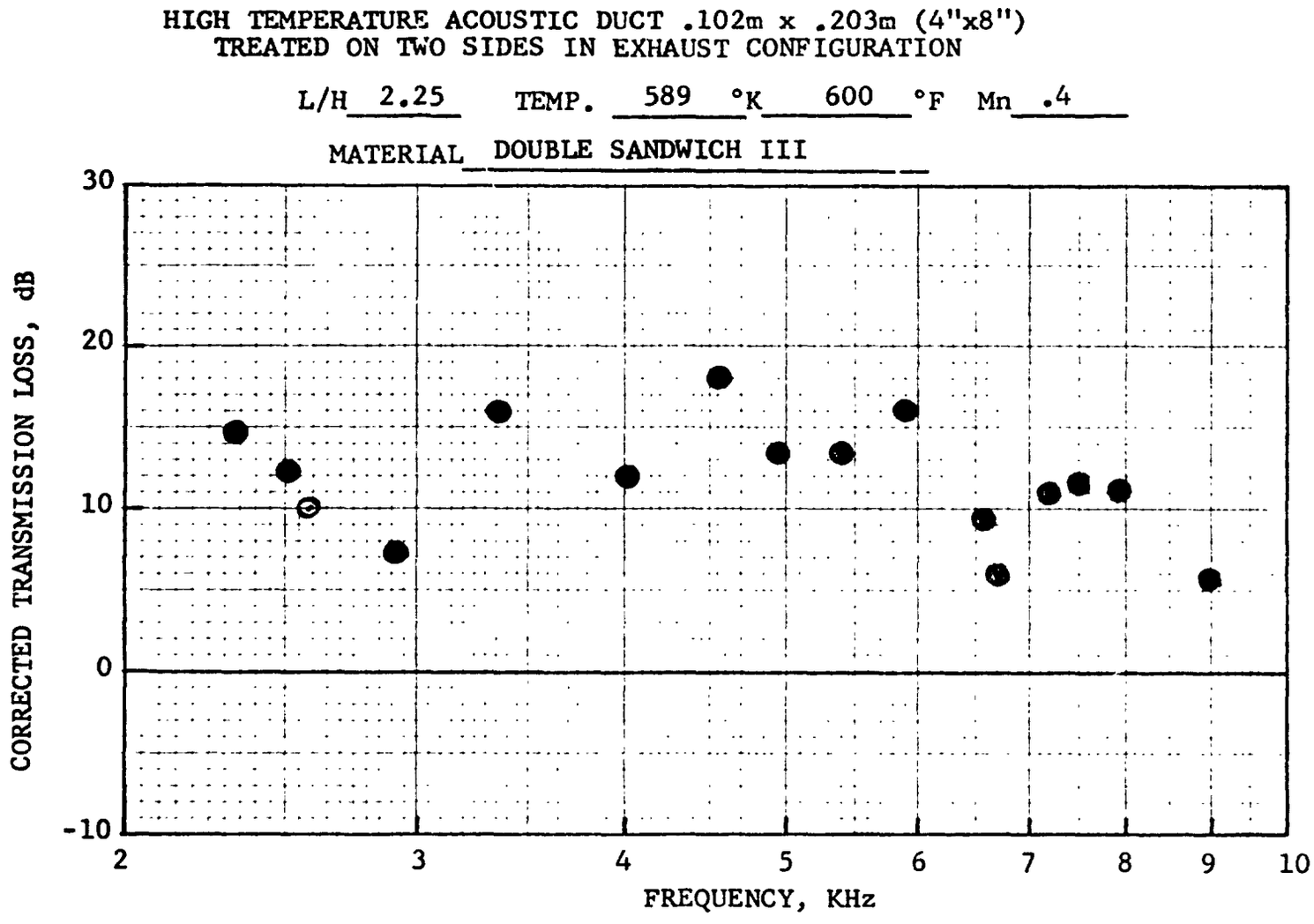

Figure 202. Corrected Transmission Loss Vs. Frequency.

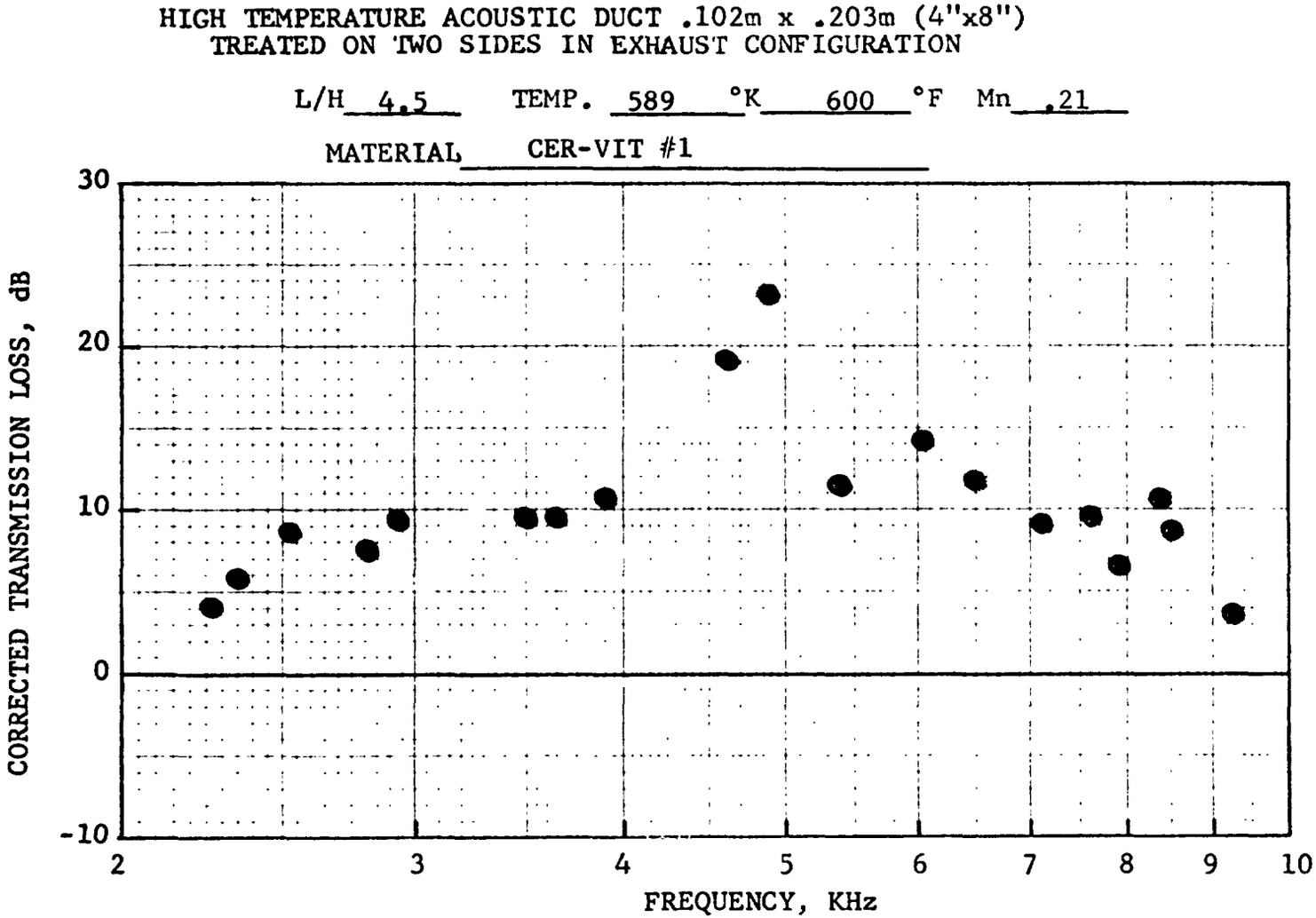

Figure 203. Corrected Transmission Loss Vs. Frequency.

HIGH TEMPERATURE ACOUSTIC DUCT .102m x .203m (4"x8")
TREATED ON TWO SIDES IN EXHAUST CONFIGURATION

L/H 4.5 TEMP. 589 °K 600 °F Mn .25

MATERIAL CER-VIT #1

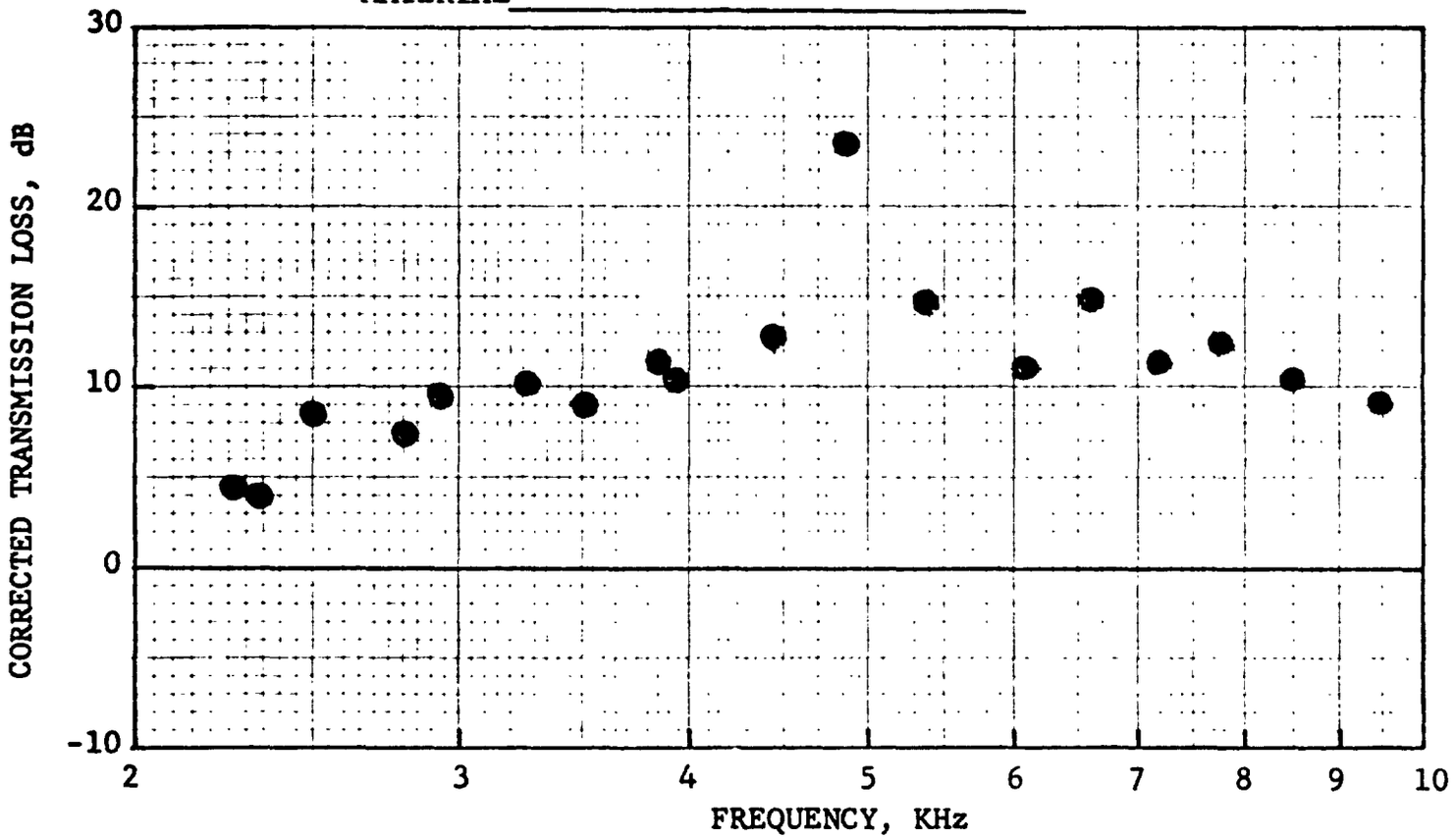

Figure 204. Corrected Transmission Loss Vs. Frequency.

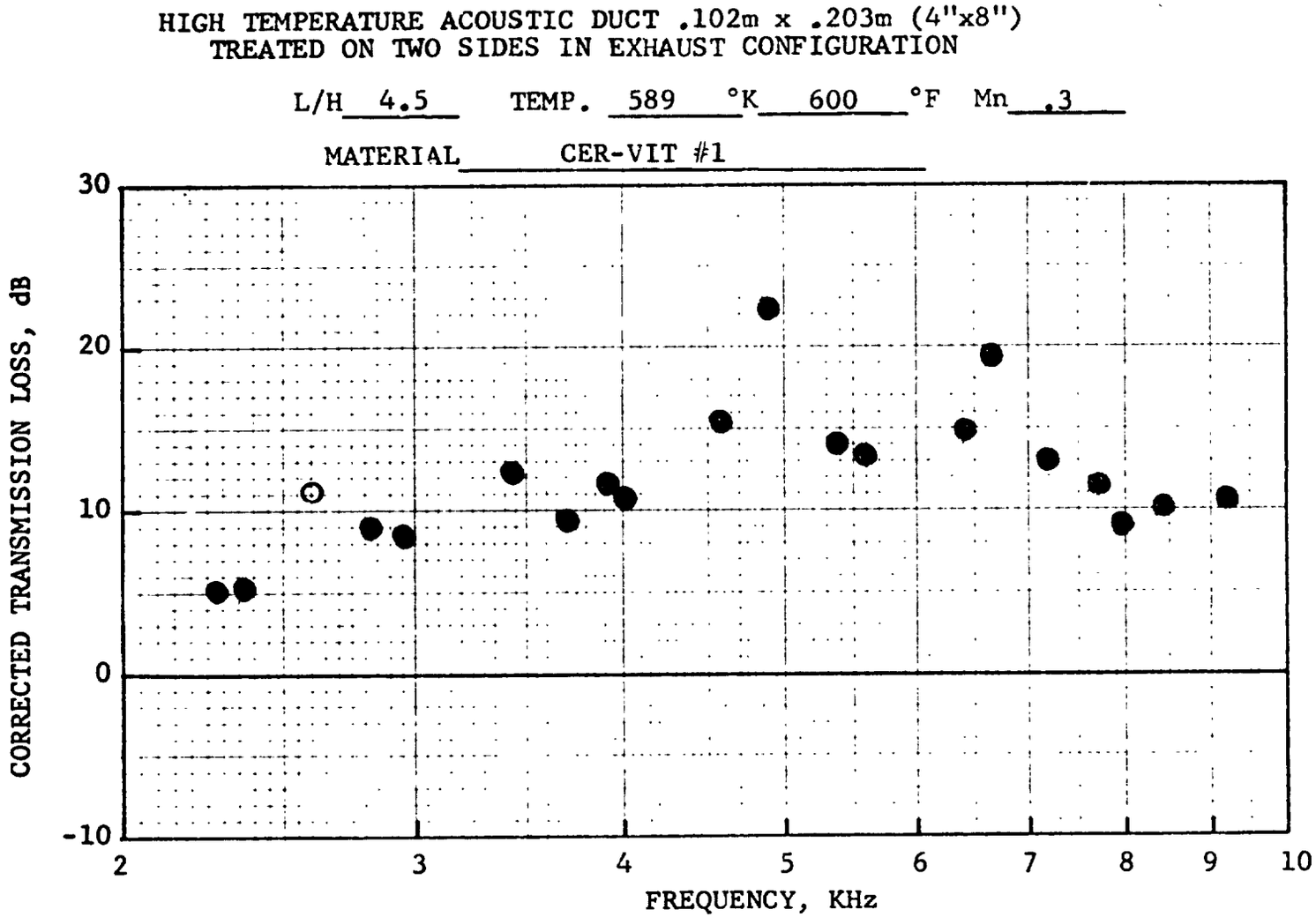

Figure 205. Corrected Transmission Loss Vs. Frequency.

HIGH TEMPERATURE ACOUSTIC DUCT .102m x .203m (4"x8")
TREATED ON TWO SIDES IN EXHAUST CONFIGURATION

L/H 4.5 TEMP. 589 °K 600 °F Mn .4

MATERIAL CER-VIT #1

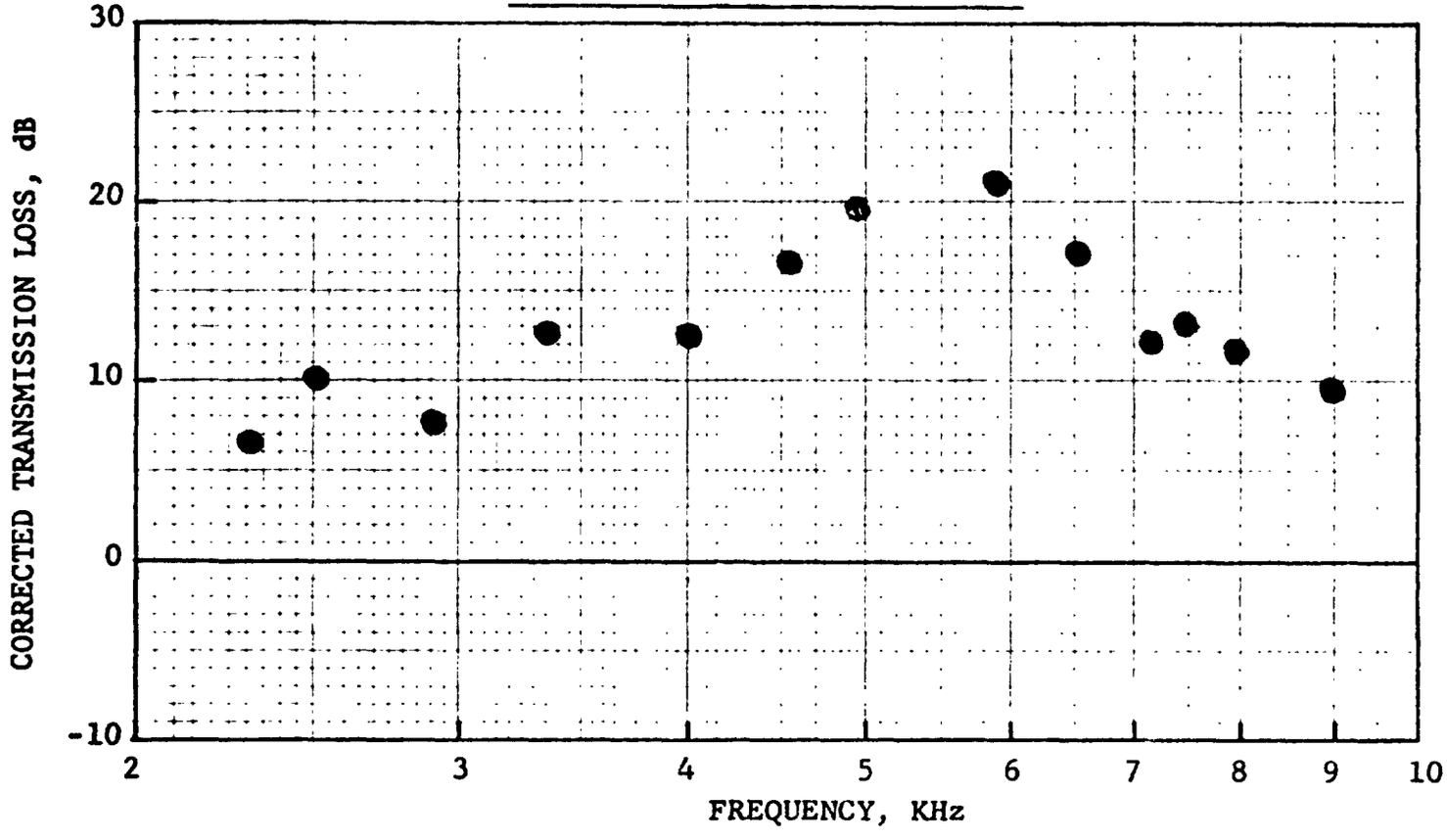

Figure 206. Corrected Transmission Loss Vs. Frequency.

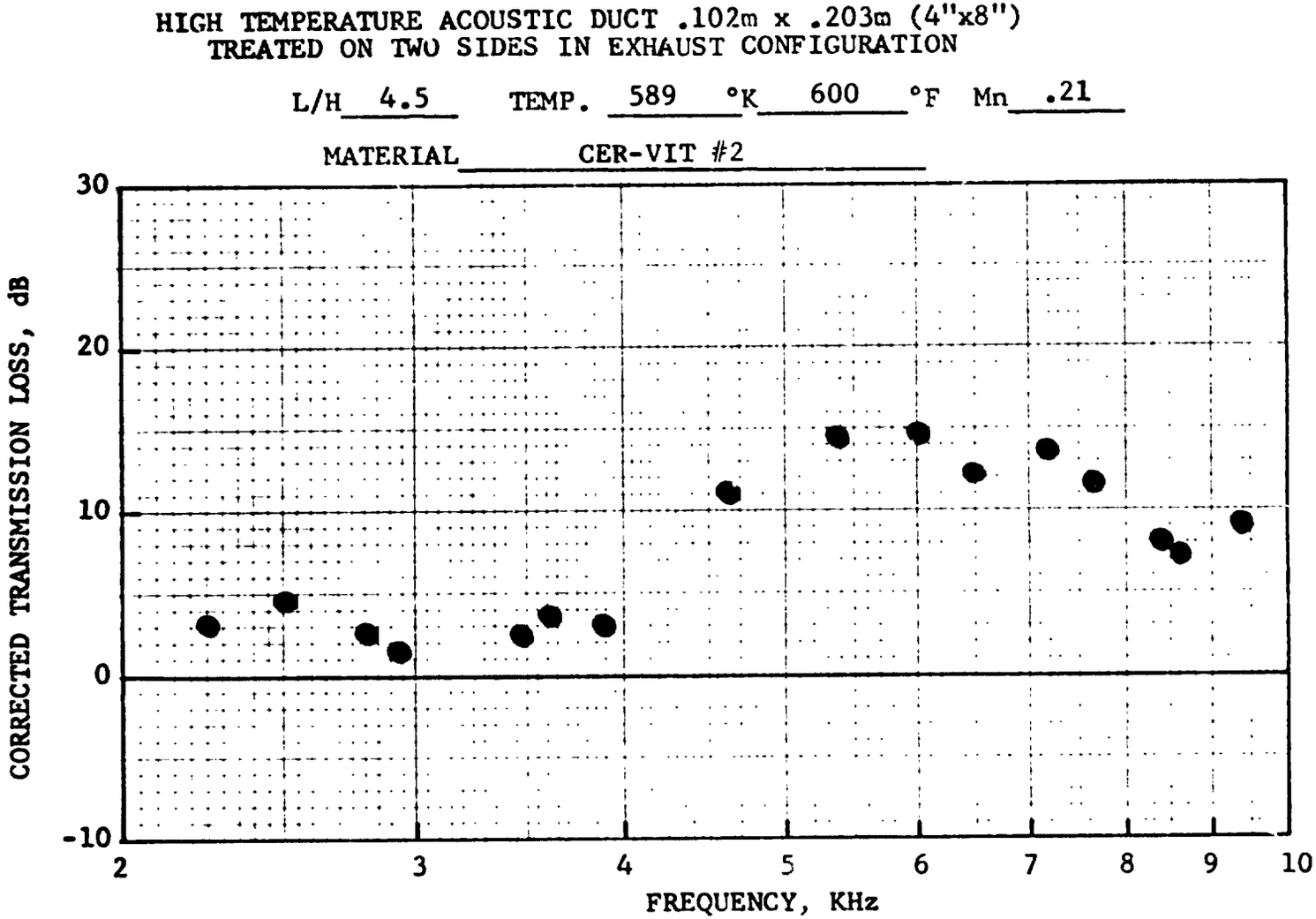

Figure 207. Corrected Transmission Loss Vs. Frequency.

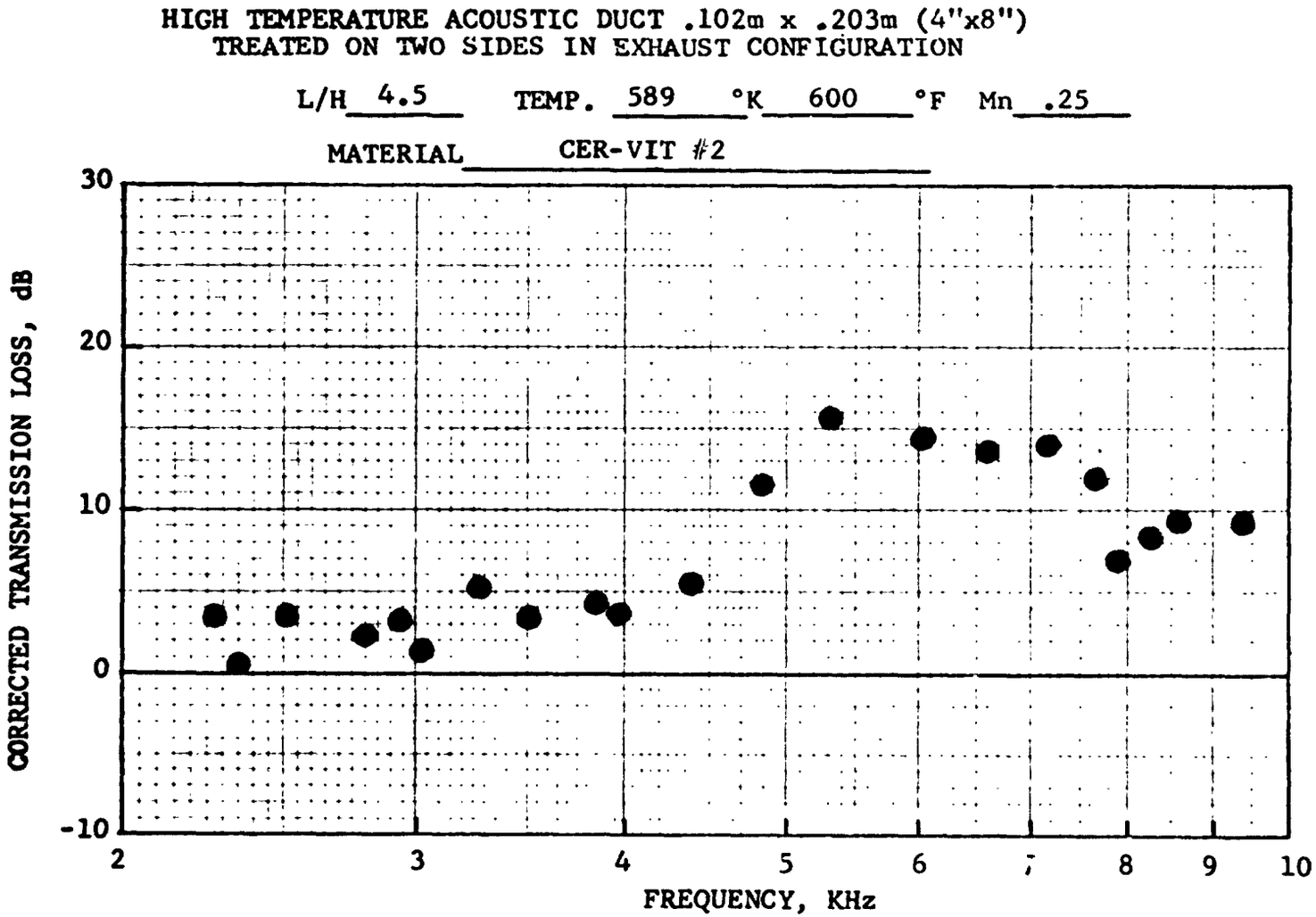

Figure 208. Corrected Transmission Loss Vs. Frequency.

HIGH TEMPERATURE ACOUSTIC DUCT .102m x .203m (4"x8")
TREATED ON TWO SIDES IN EXHAUST CONFIGURATION

L/H 4.5 TEMP. 589 °K 600 °F Mn .3

MATERIAL CER-VIT #2

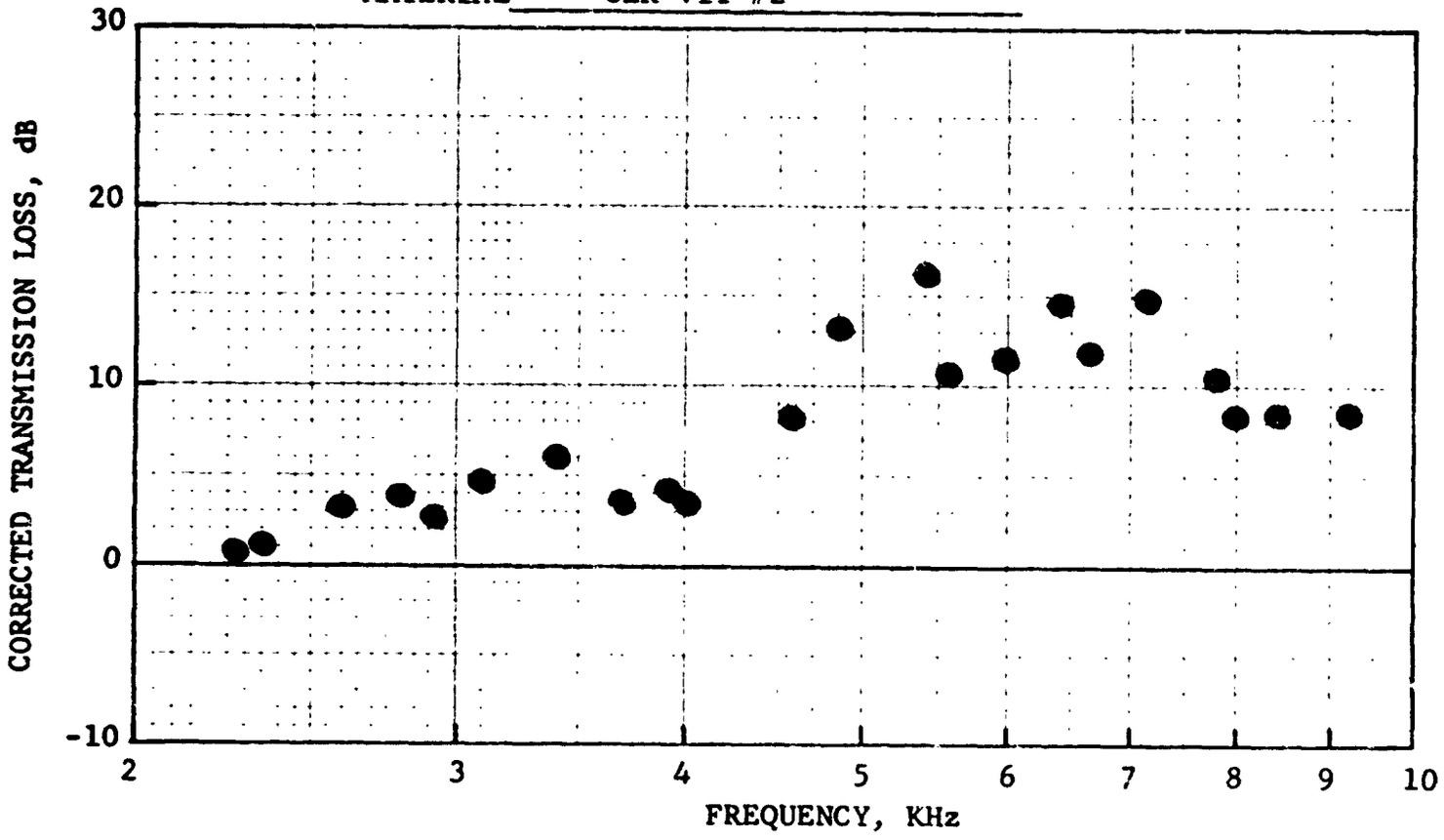

Figure 209. Corrected Transmission Loss Vs. Frequency.

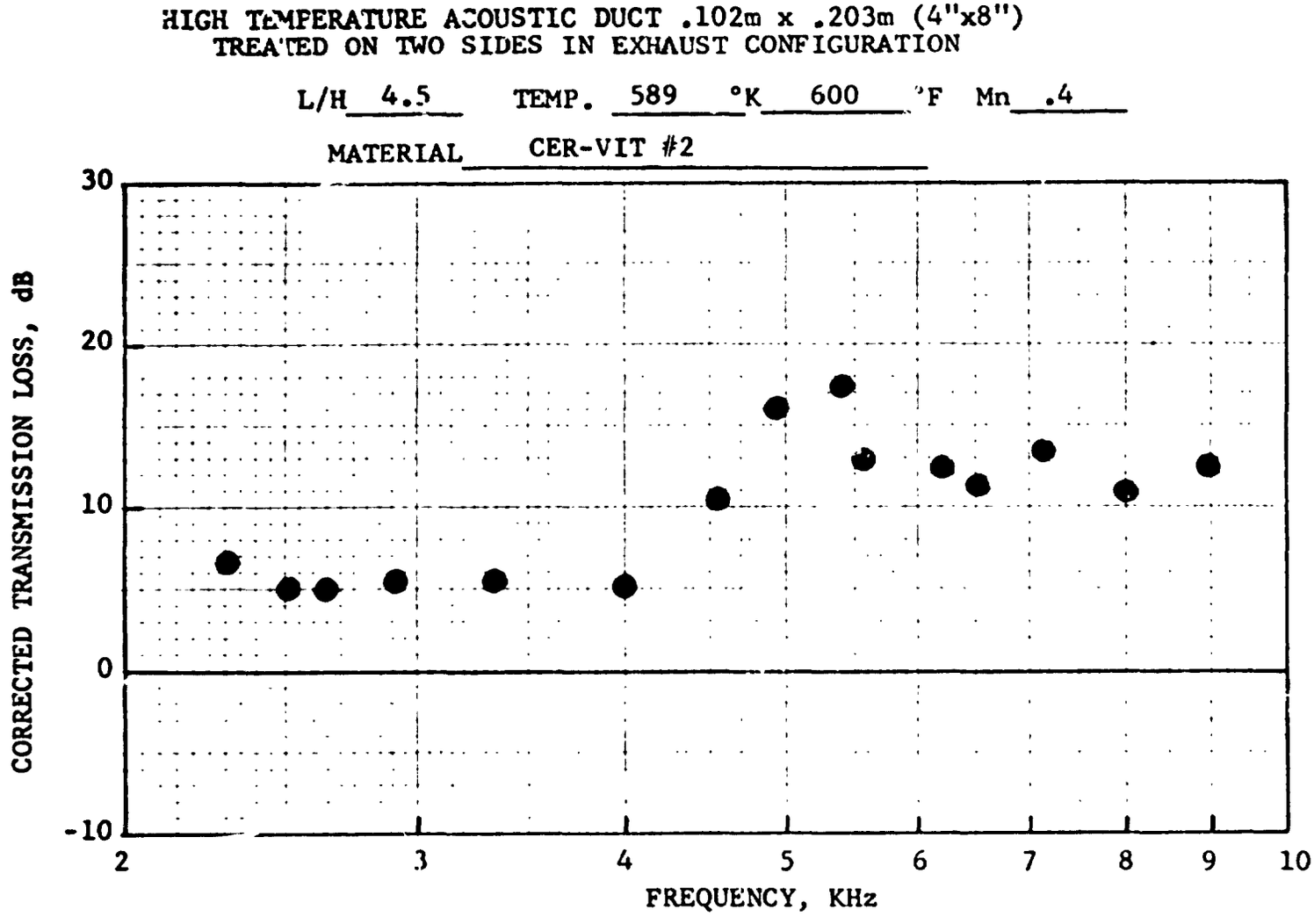

Figure 210. Corrected Transmission Loss Vs. Frequency.

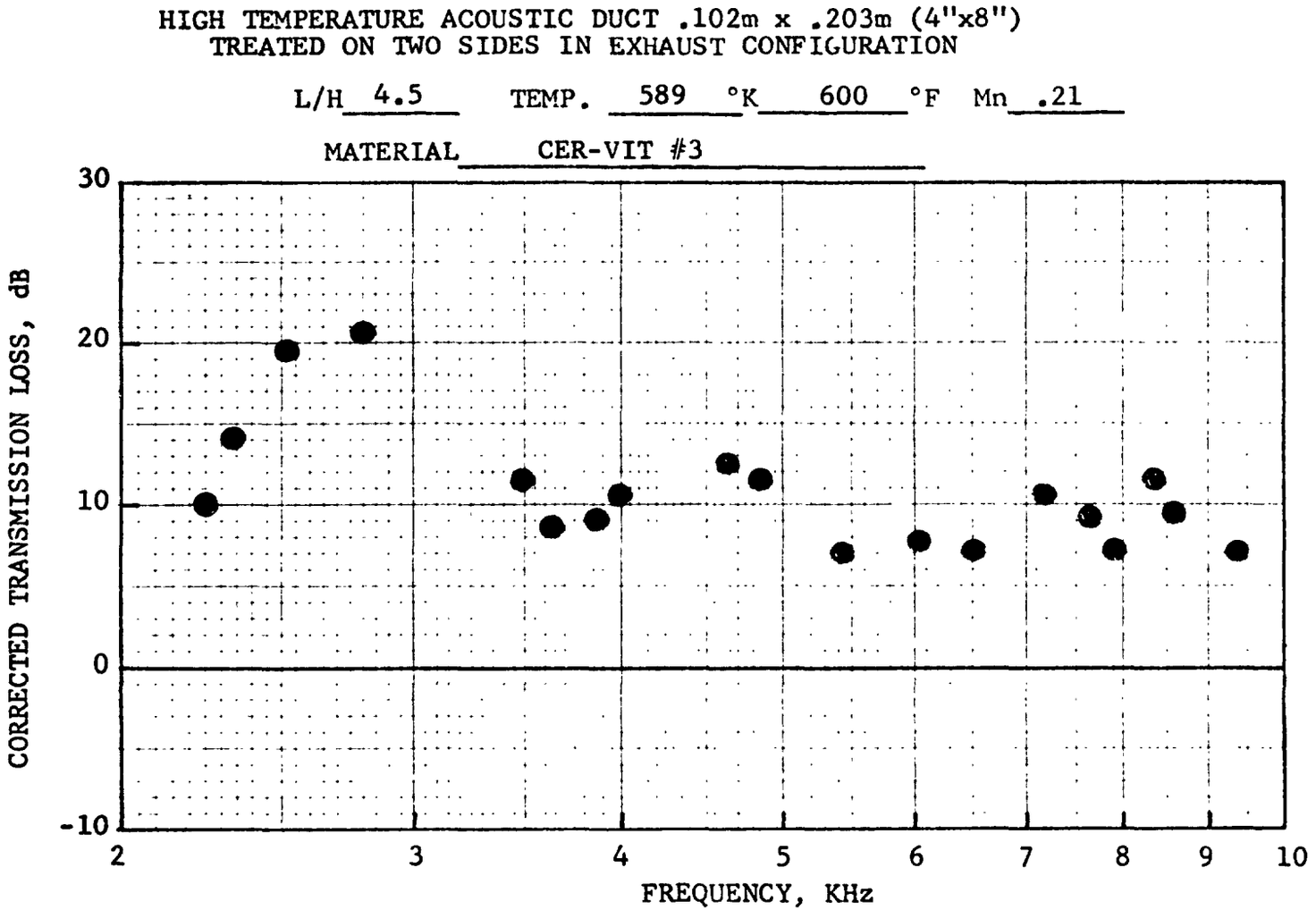

Figure 211. Corrected Transmission Loss Vs. Frequency.

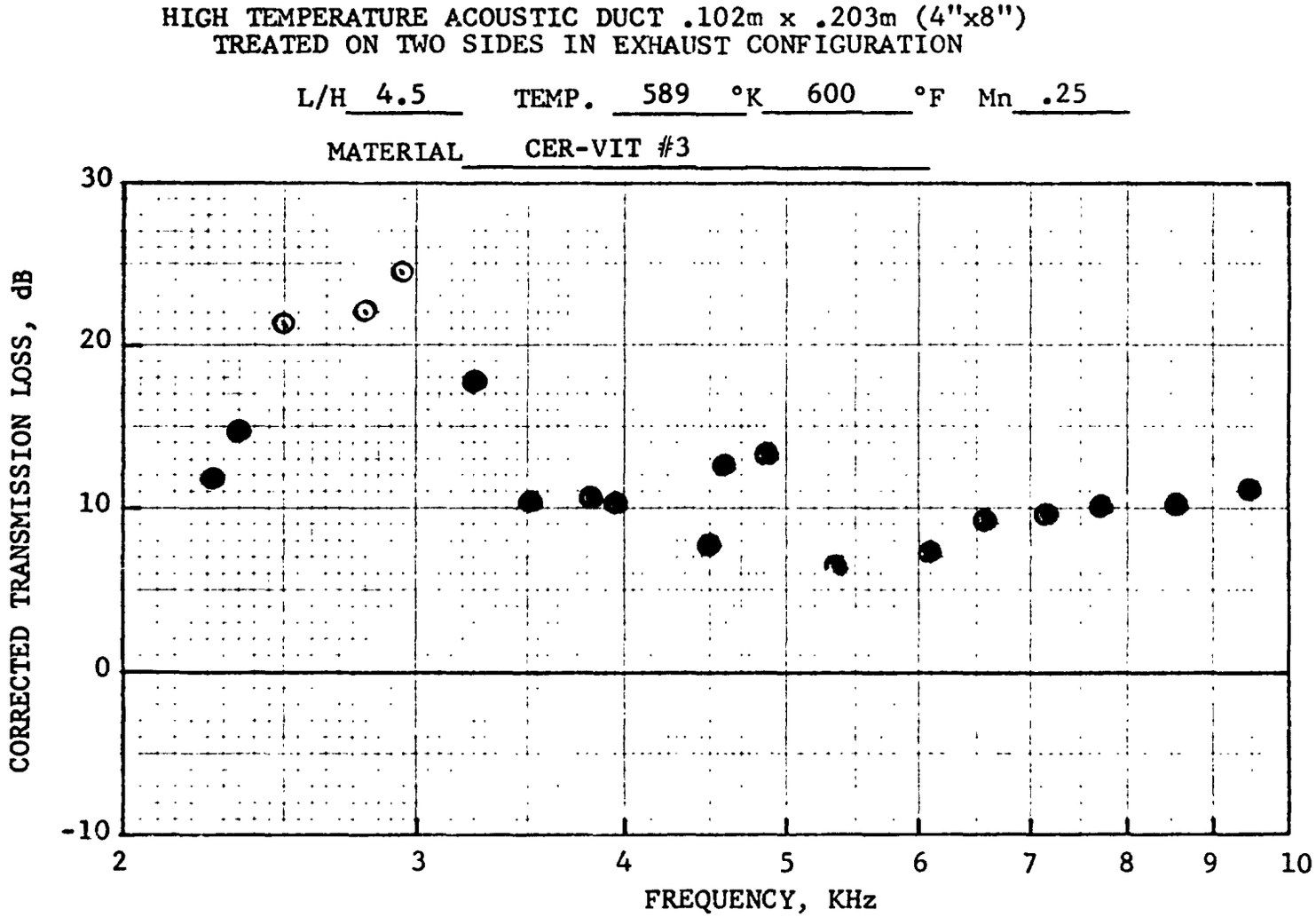

Figure 212. Corrected Transmission Loss Vs. Frequency.

HIGH TEMPERATURE ACOUSTIC DUCT .102m x .203m (4"x8")
TREATED ON TWO SIDES IN EXHAUST CONFIGURATION

L/H 4.5 TEMP. 589 °K 600 °F Mn .3

MATERIAL CER-VIT #3

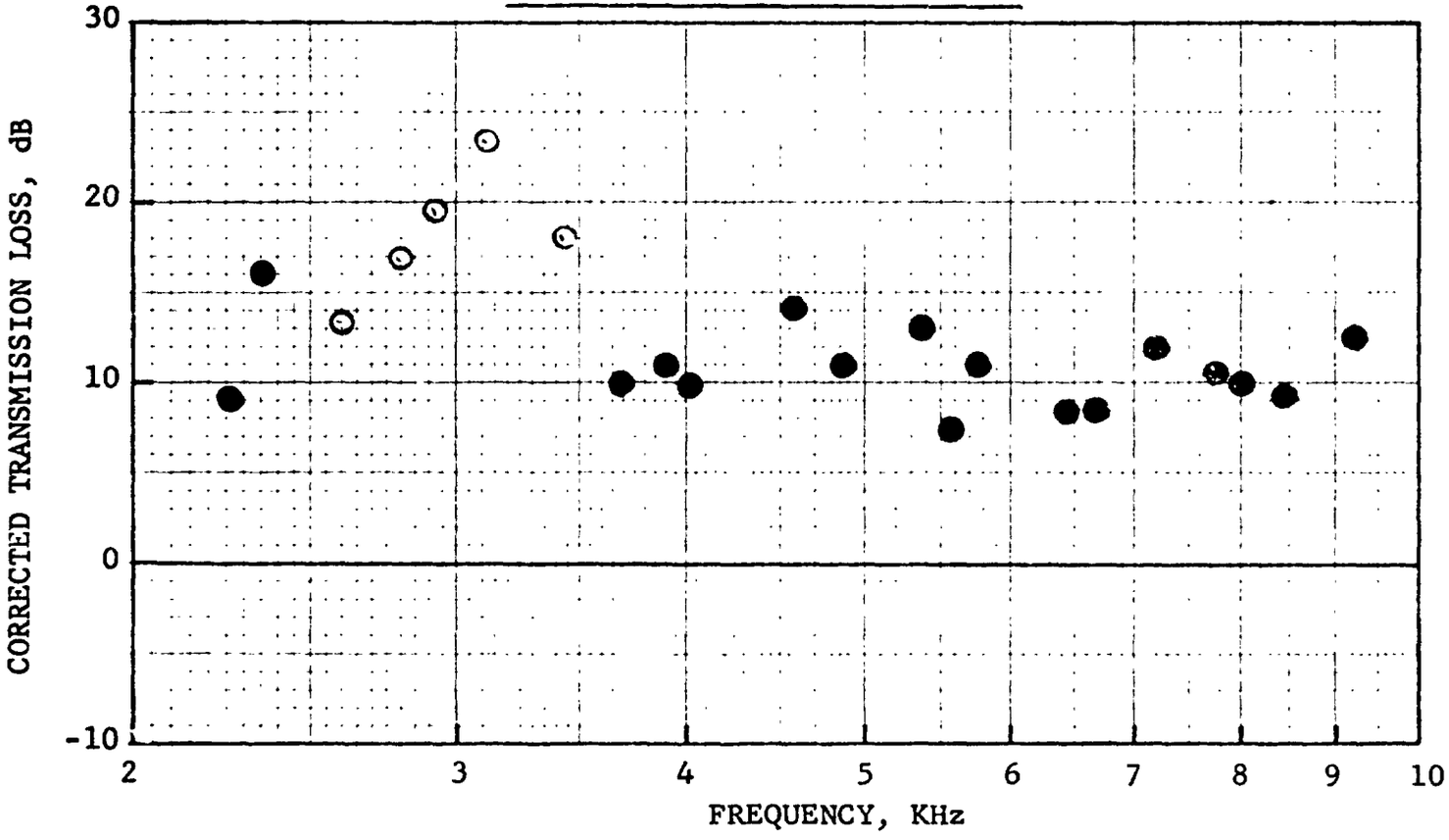

Figure 213. Corrected Transmission Loss Vs. Frequency.

HIGH TEMPERATURE ACOUSTIC DUCT .102m x .203m (4"x8")
TREATED ON TWO SIDES IN EXHAUST CONFIGURATION

L/H 4.5 TEMP. 589 °K 600 °F Mn .4

MATERIAL CER-VIT #3

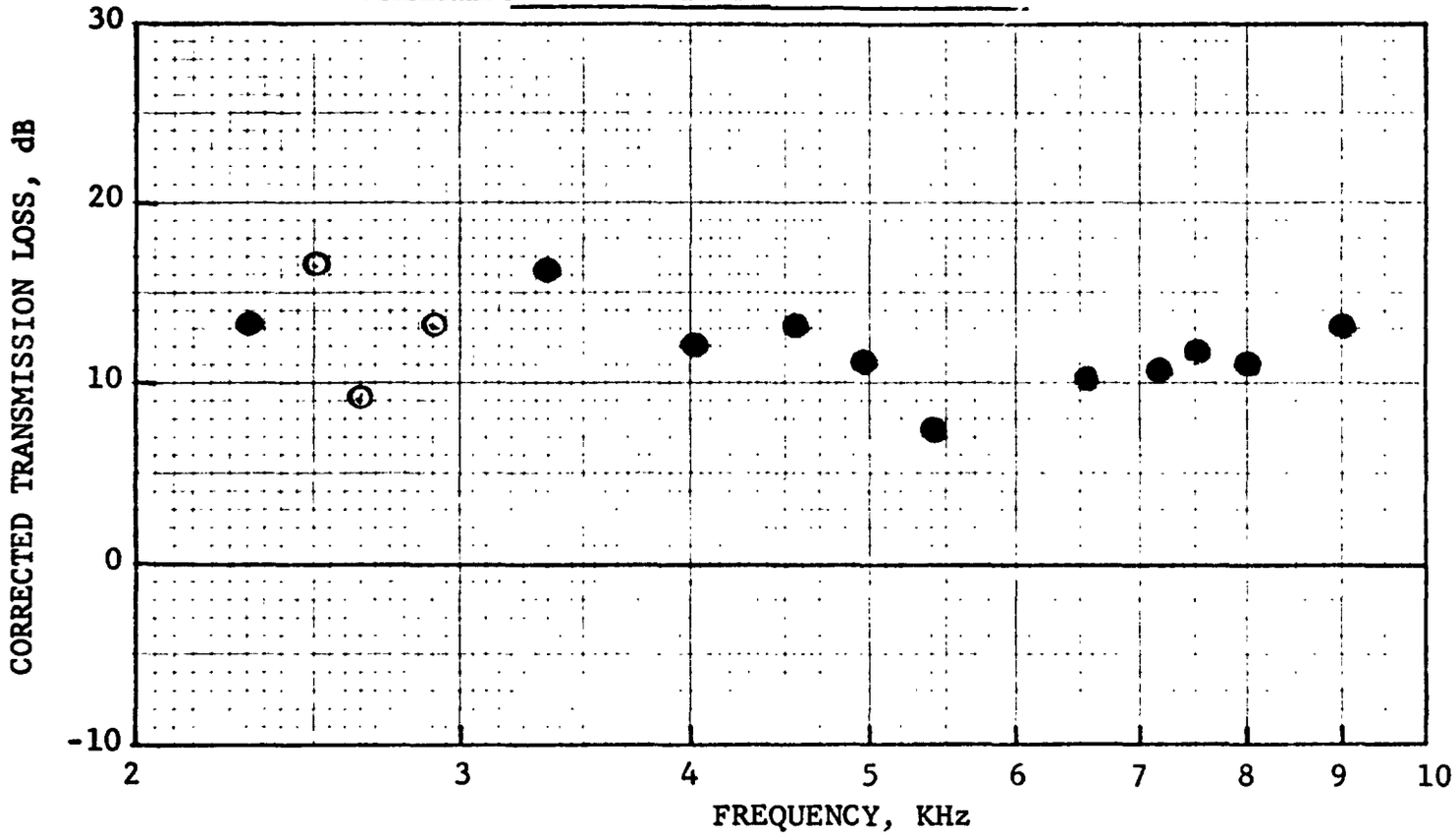

Figure 214. Corrected Transmission Loss Vs. Frequency.

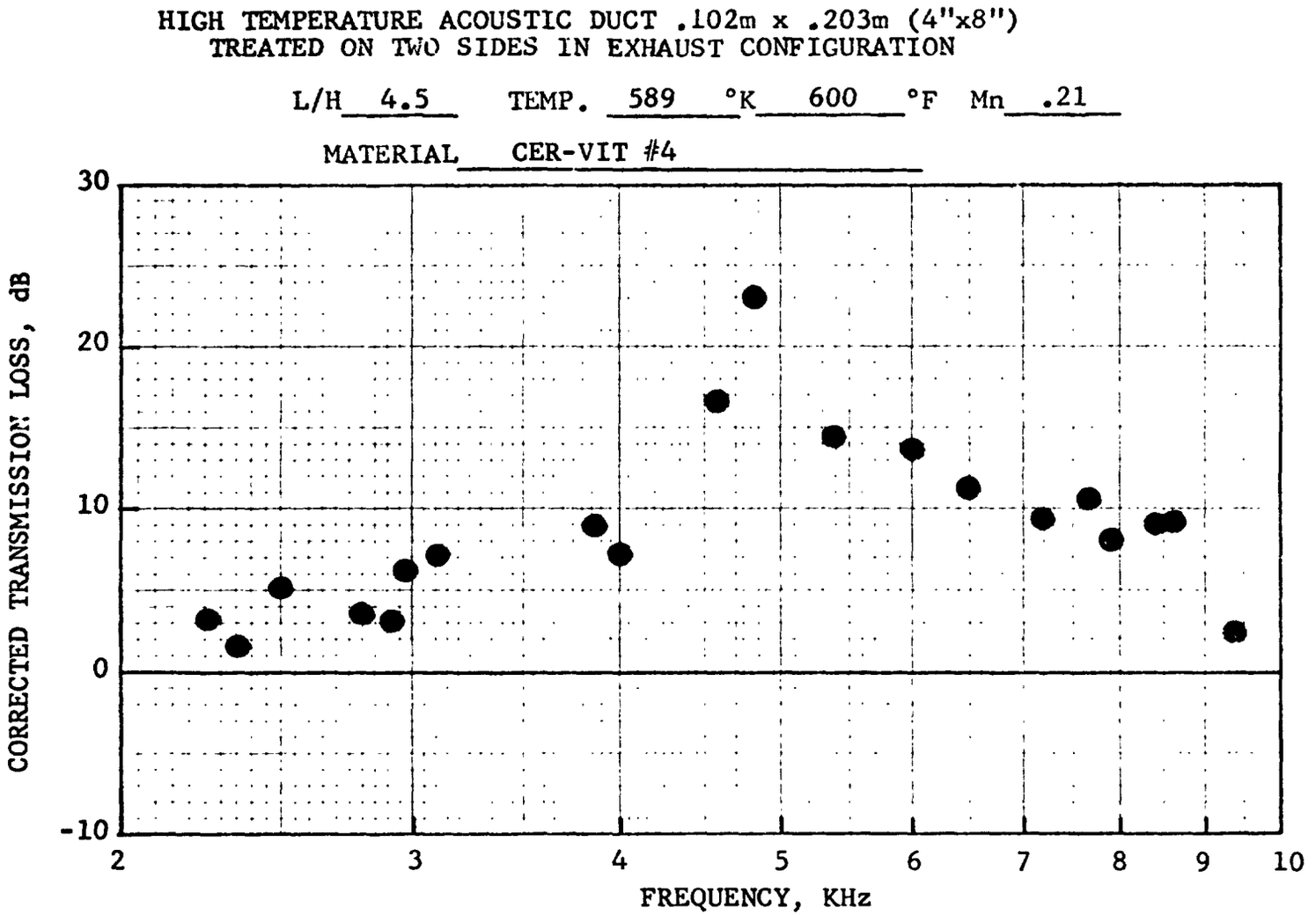

Figure 215. Corrected Transmission Loss Vs. Frequency.

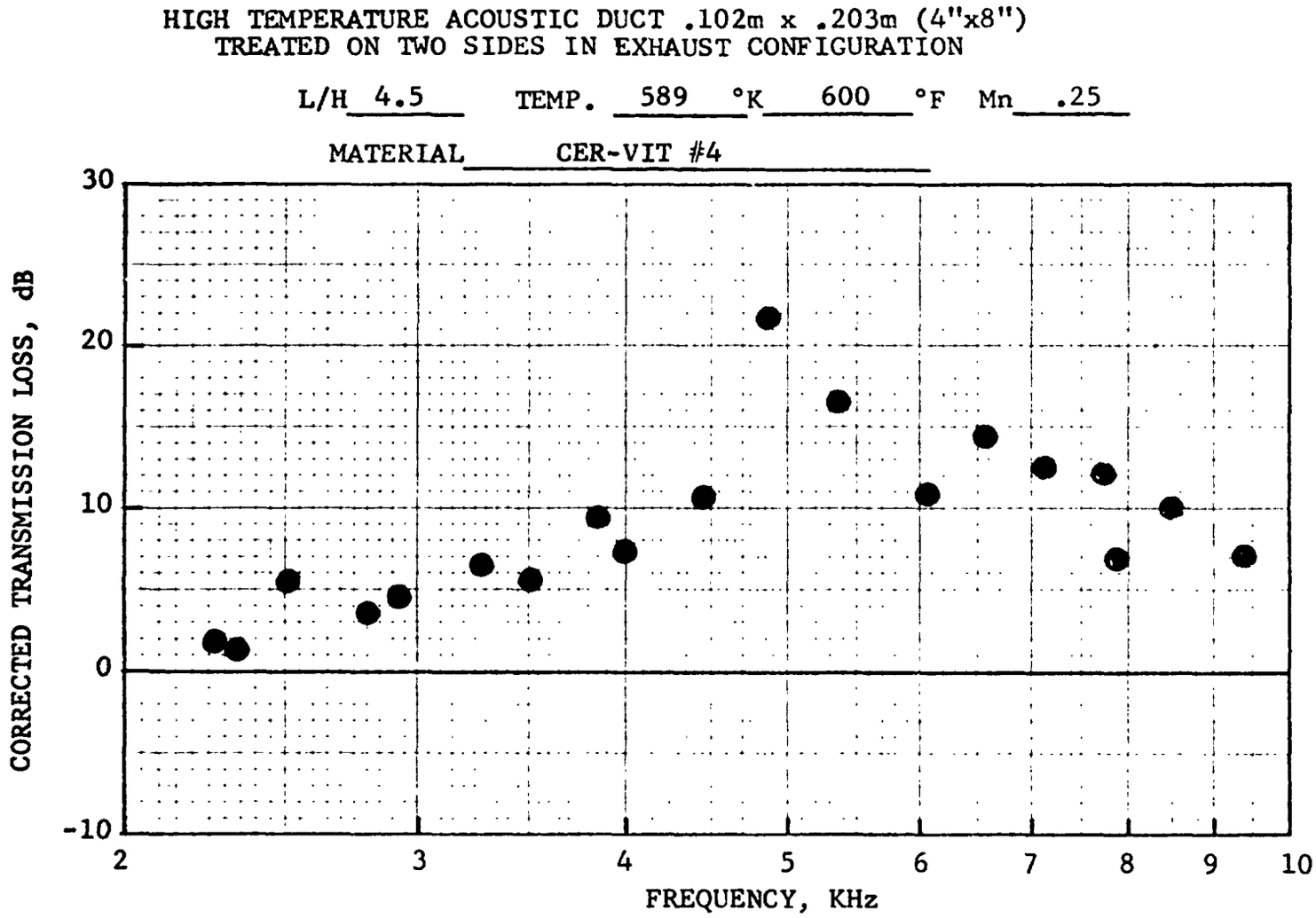

Figure 216. Corrected Transmission Loss Vs. Frequency.

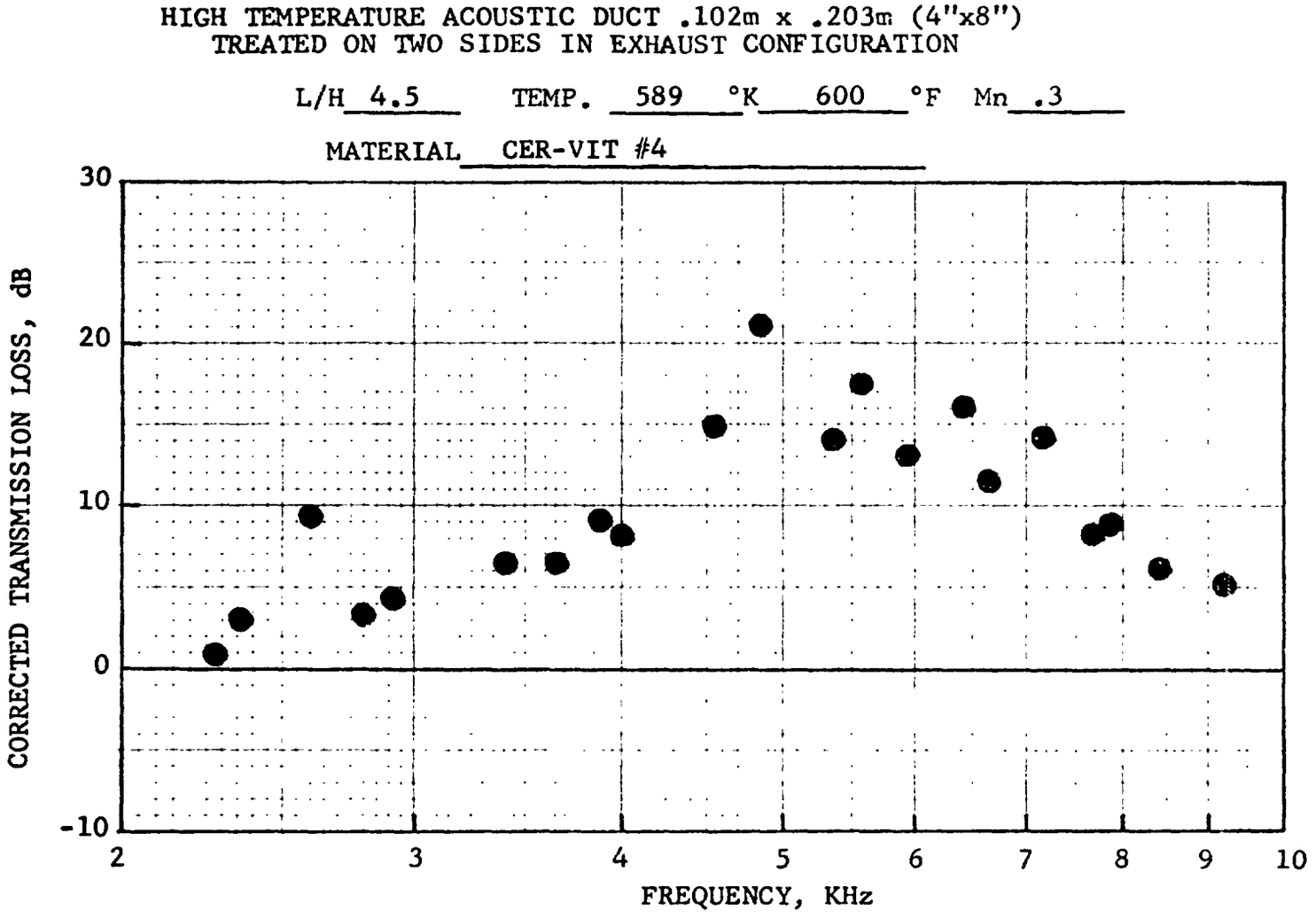

Figure 217. Corrected Transmission Loss Vs. Frequency.

HIGH TEMPERATURE ACOUSTIC DUCT .102m x .203m (4"x8")
TREATED ON TWO SIDES IN EXHAUST CONFIGURATION

L/H 4.5 TEMP. 589 °K 600 °F Mn .4

MATERIAL CER-VIT #4

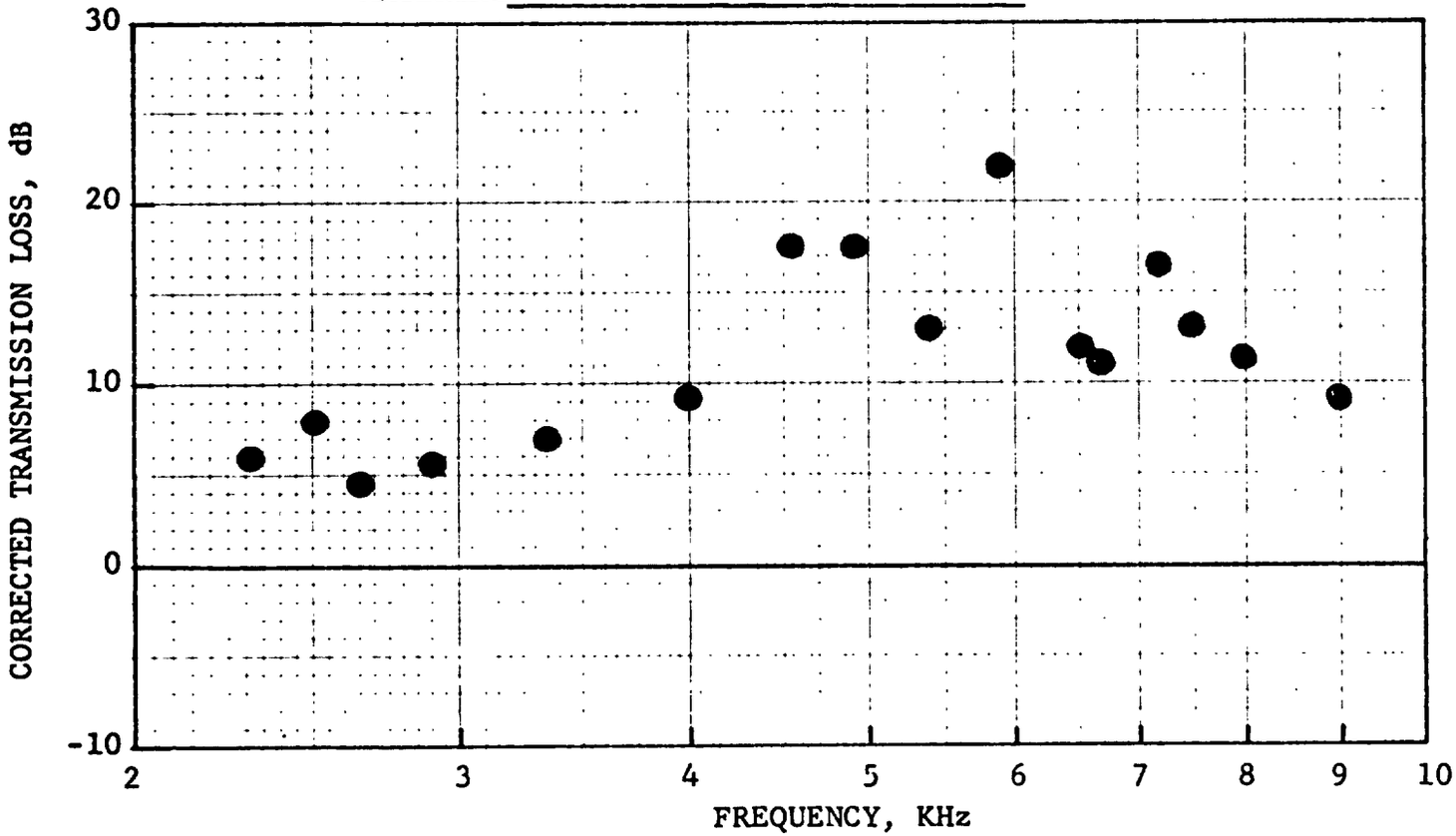

Figure 218. Corrected Transmission Loss Vs. Frequency.

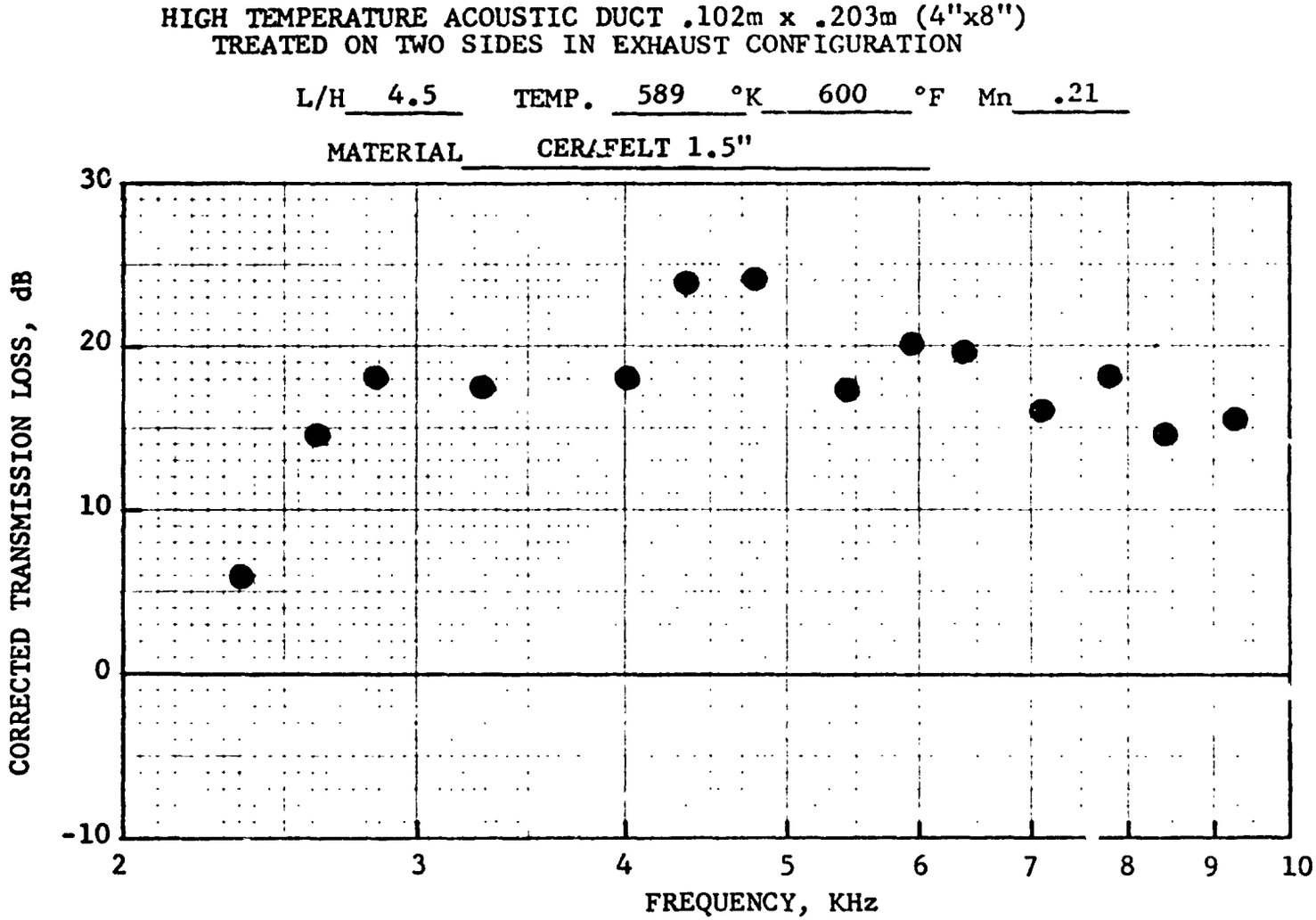

Figure 219. Corrected Transmission Loss Vs. Frequency.

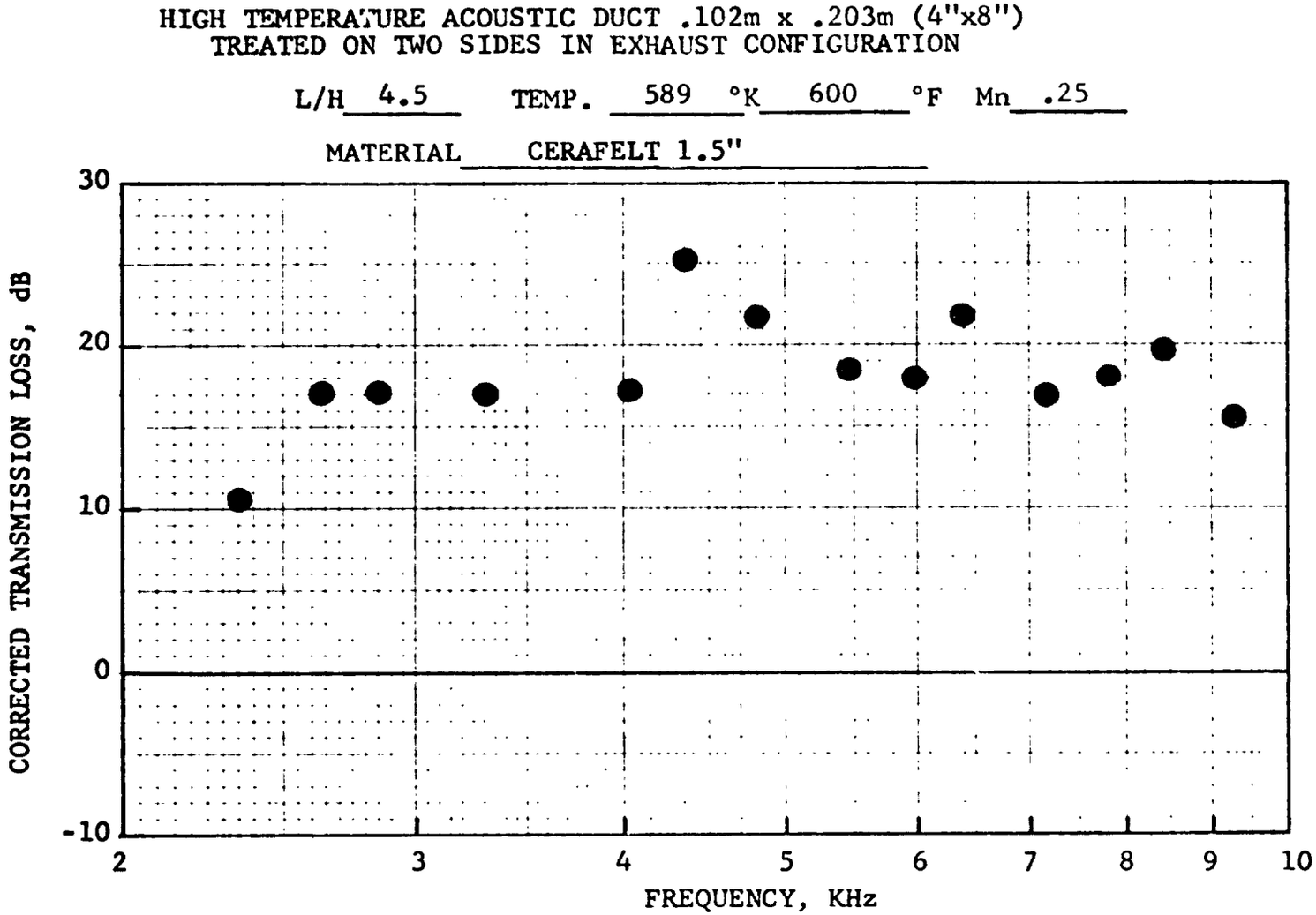

Figure 220. Corrected Transmission Loss Vs. Frequency.

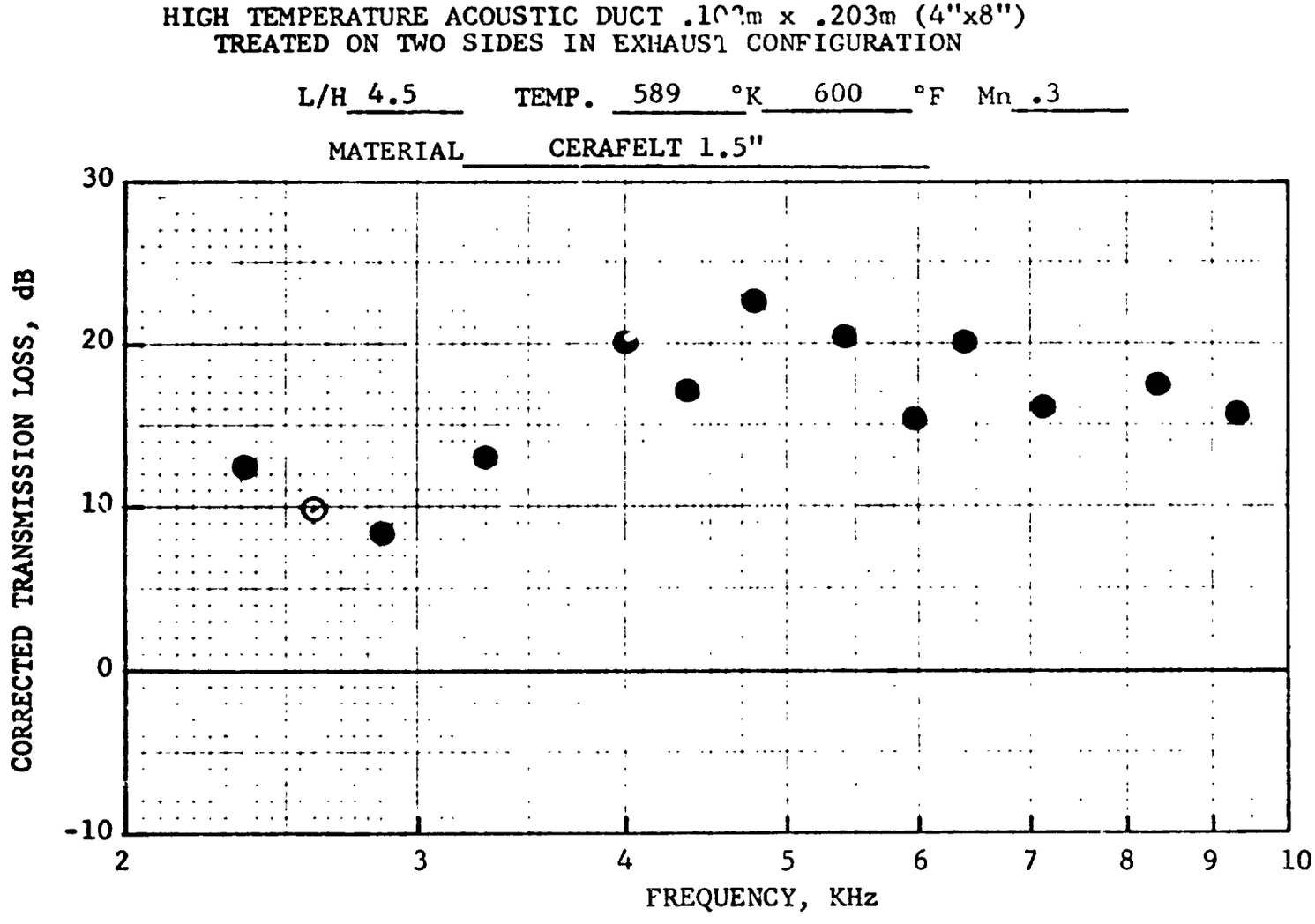

Figure 221. Corrected Transmission Loss Vs. Frequency.

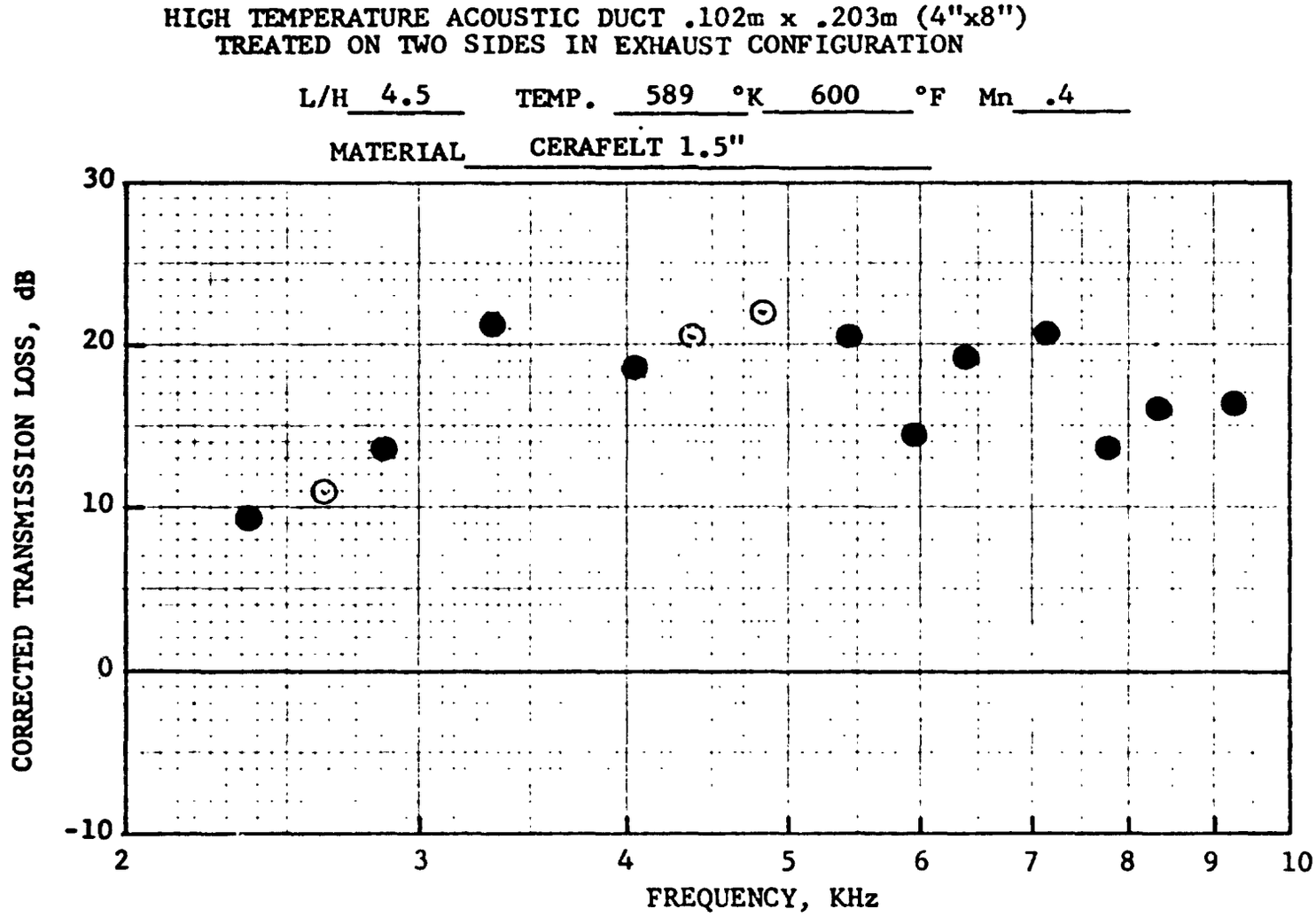

Figure 222. Corrected Transmission Loss Vs. Frequency.

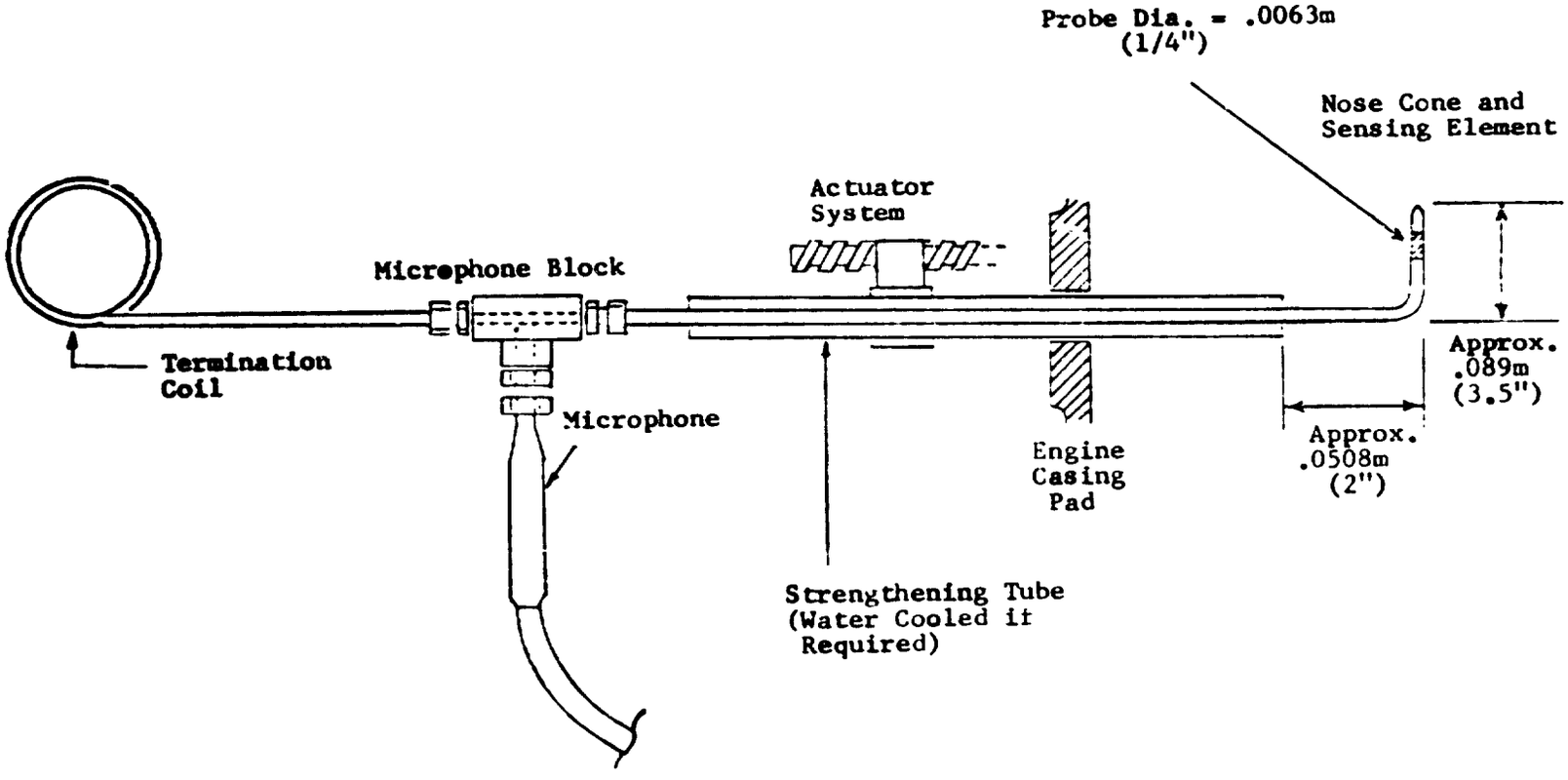

Figure 223. Schematic of Acoustic Probe System.

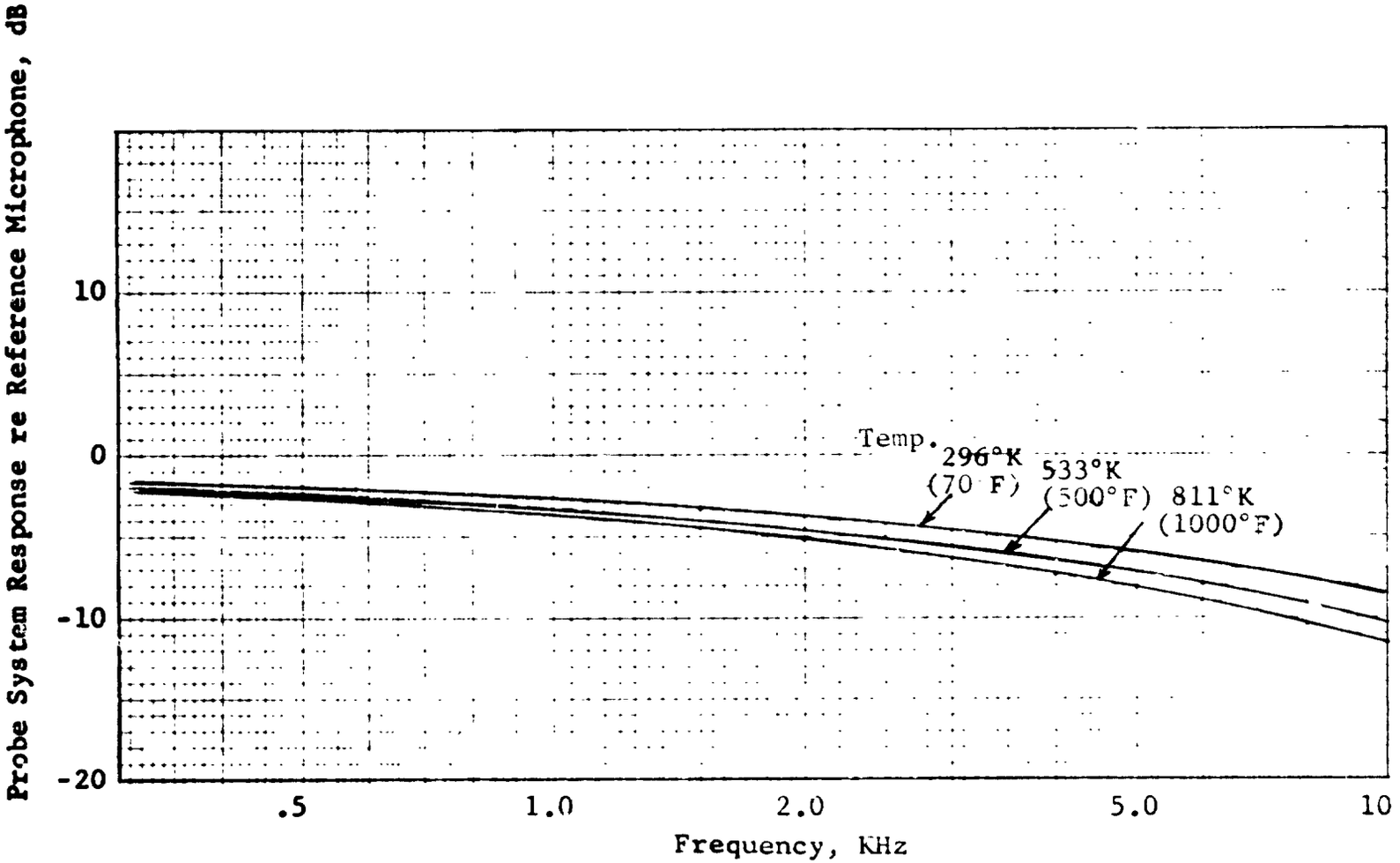

Figure 224. Theoretical Probe Viscous Loss Vs. Frequency for Several Probe Internal Temperatures, Probe Length = 0.762 m (30").

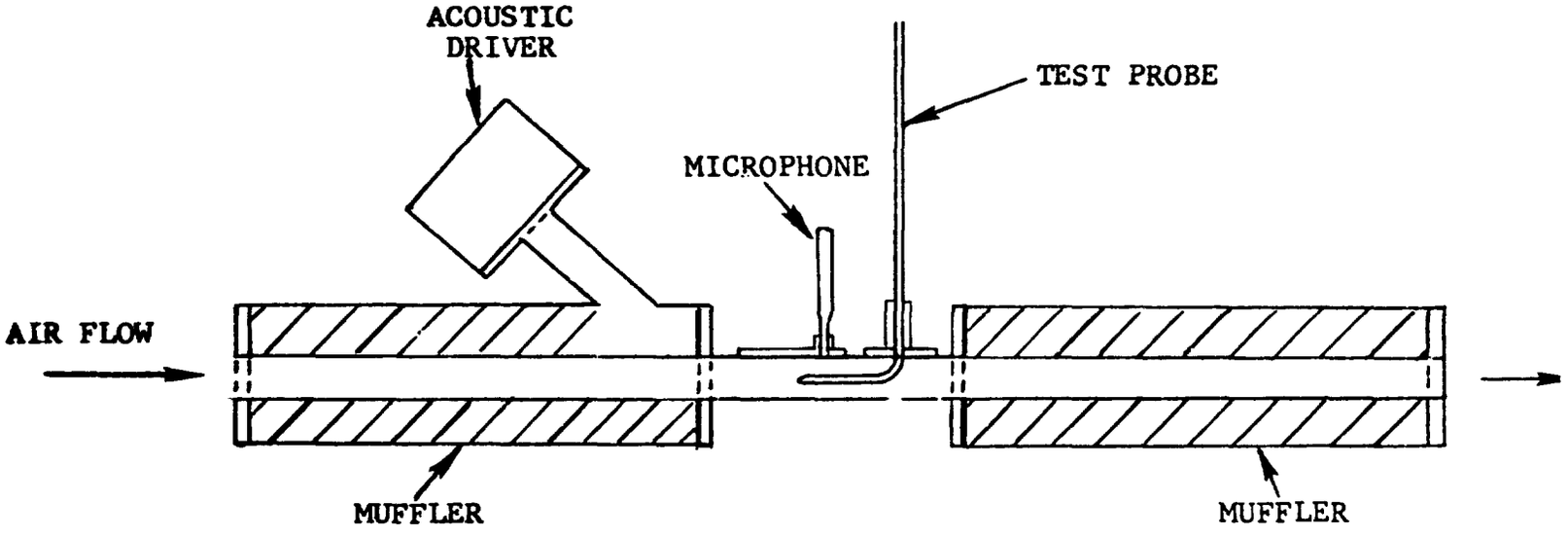

Figure 225. Air Flow Acoustic Probe Calibration Facility.

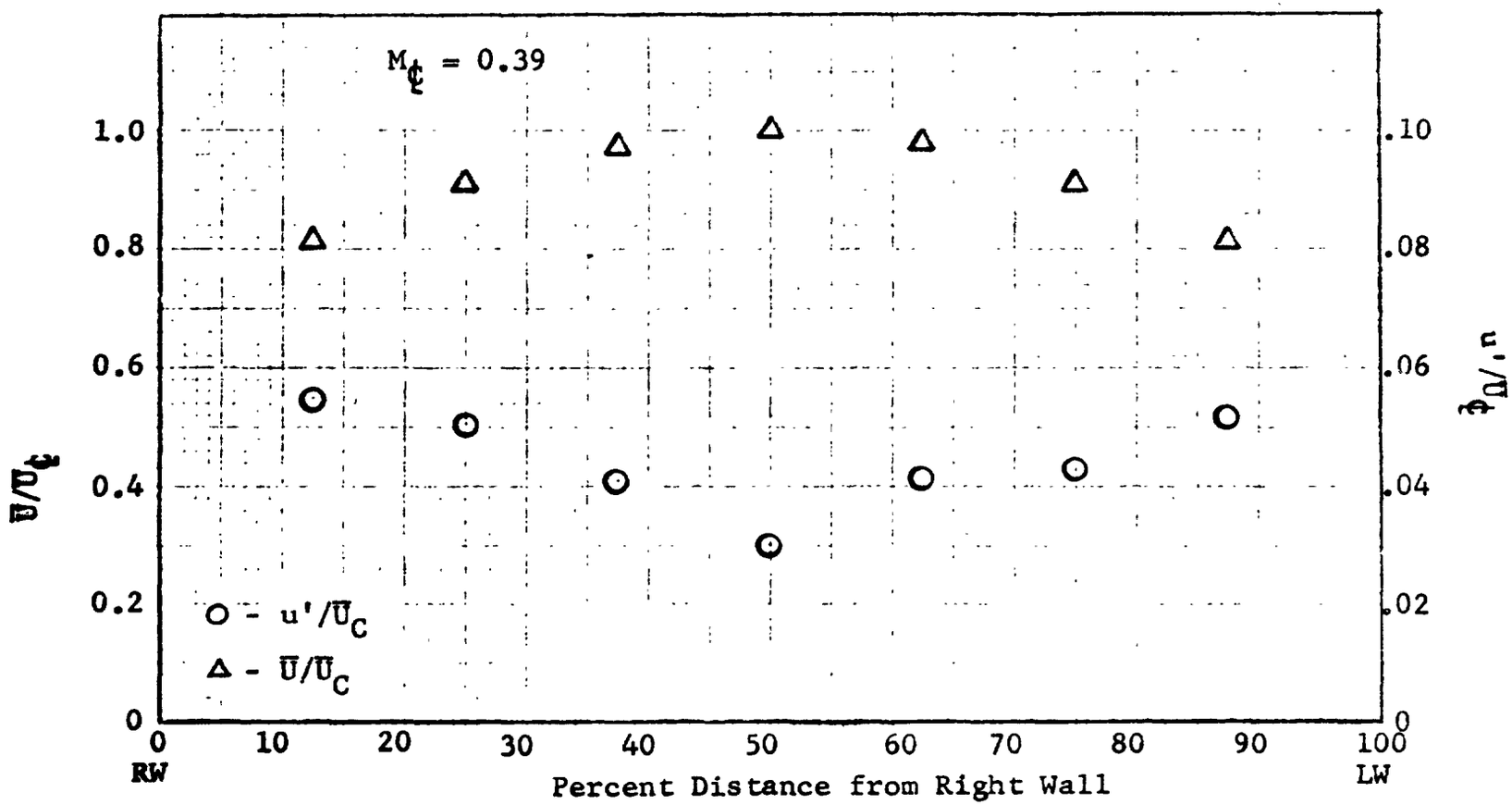

Figure 226. Velocity Profile and Turbulence Intensity in the Test Section, M = 0.39.

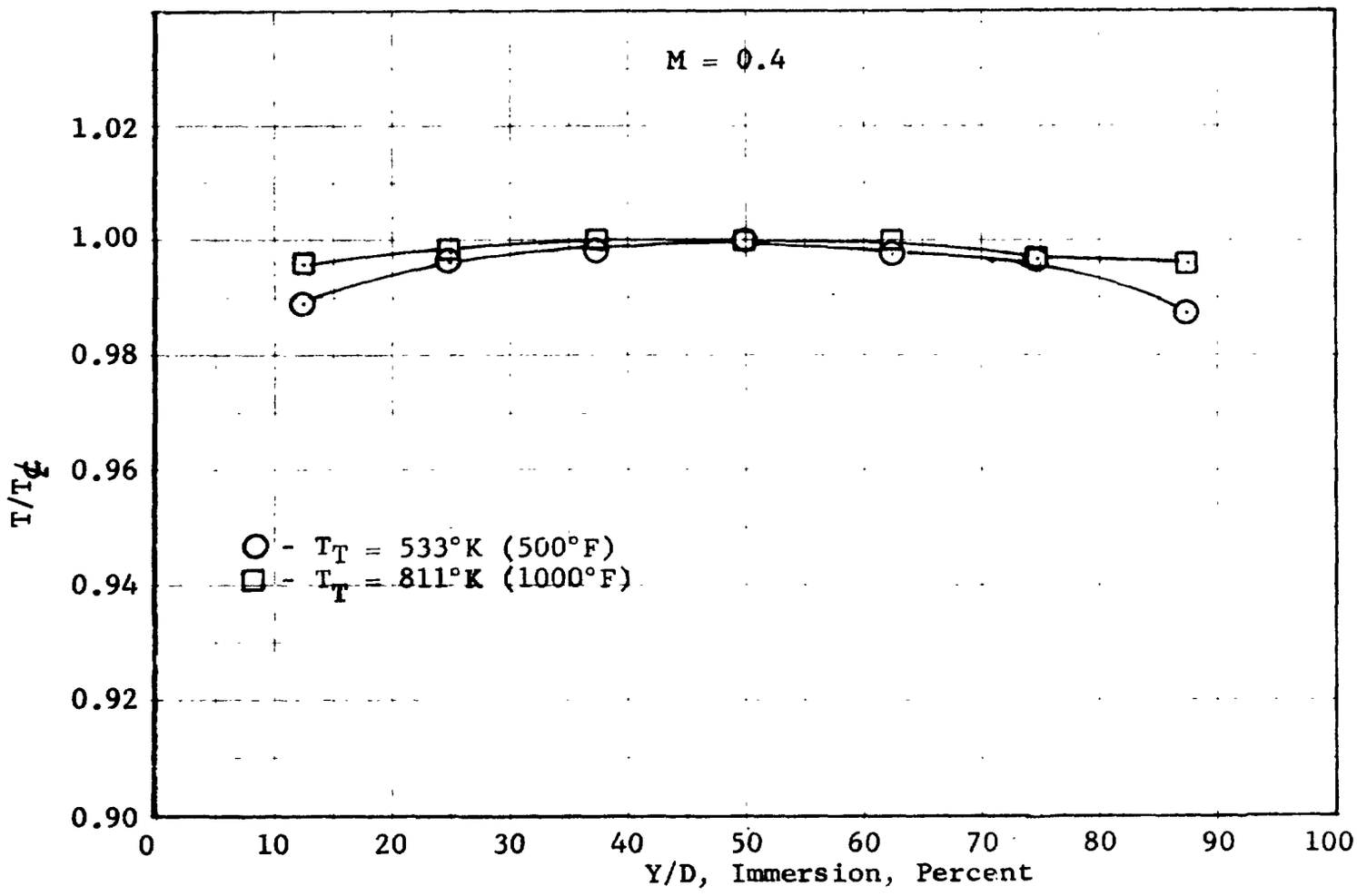

Figure 227. Normalized Temperature Profile in Test Section.

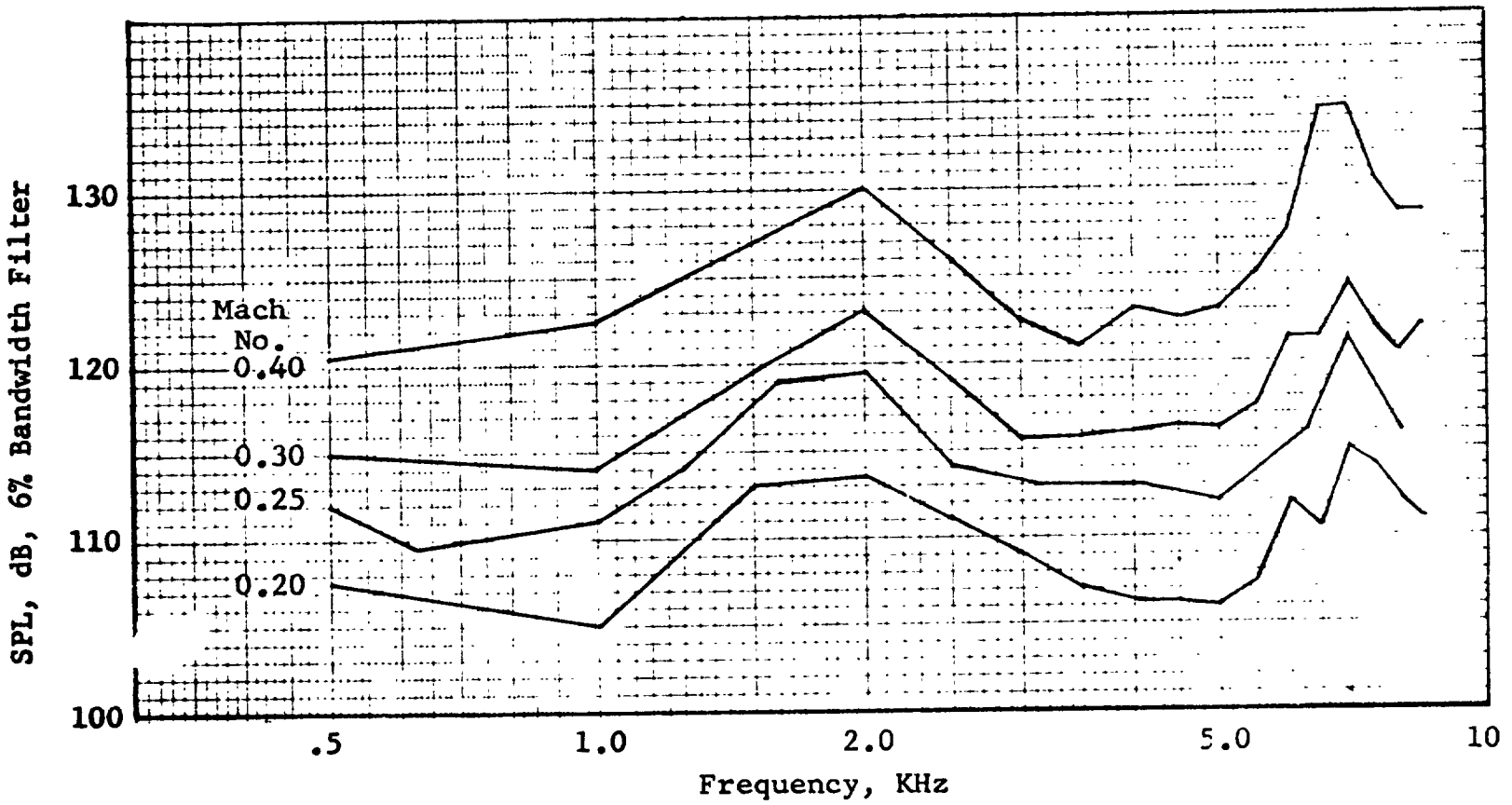

Figure 228. Air Noise in Test Section with Acoustic Probe Present Temperature = 289° K (60° F).

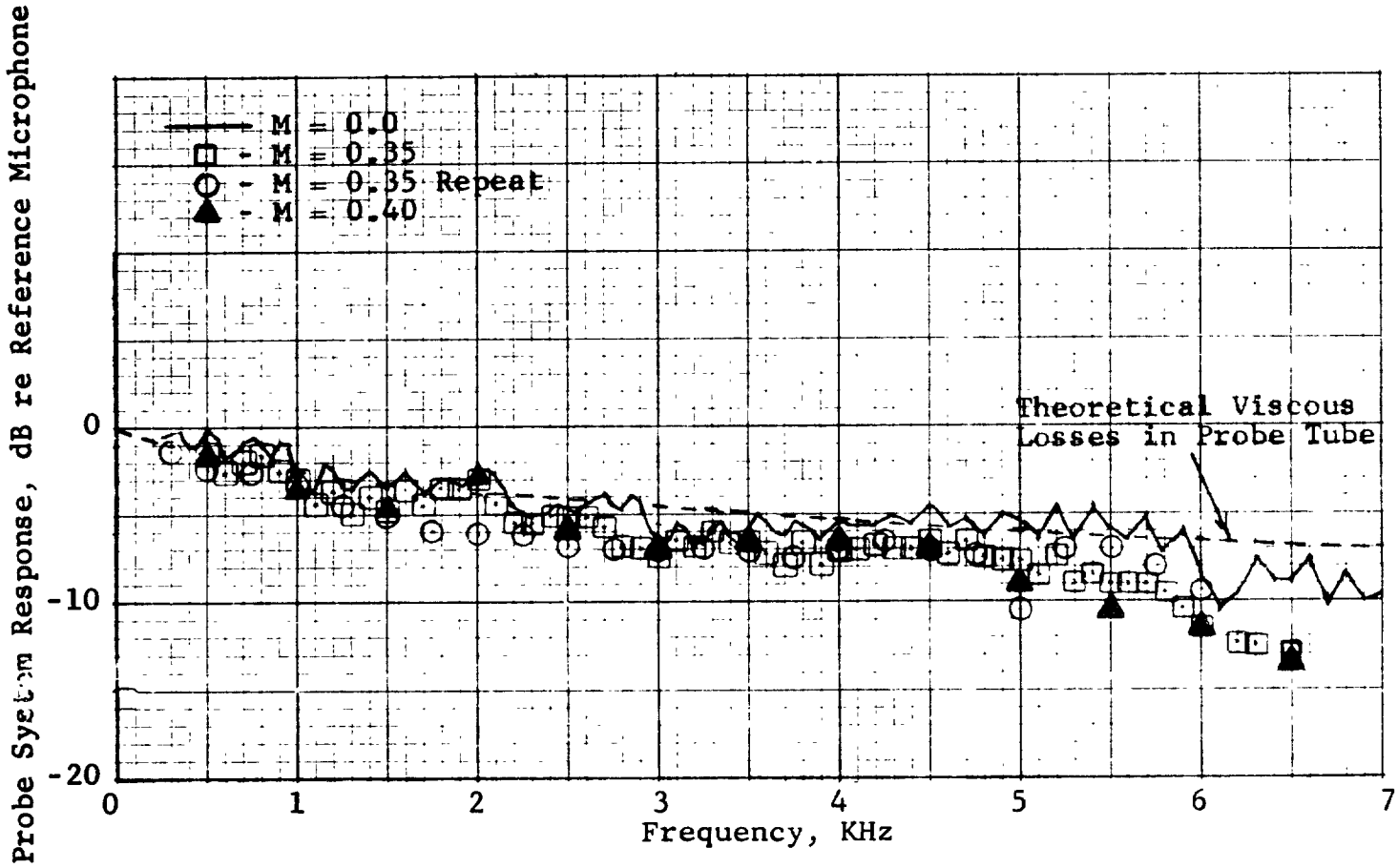

Figure 229. Acoustic Probe Calibration, 30 inch (76.2 cm) Probe with and without Air Flow at 289° K (60° F).

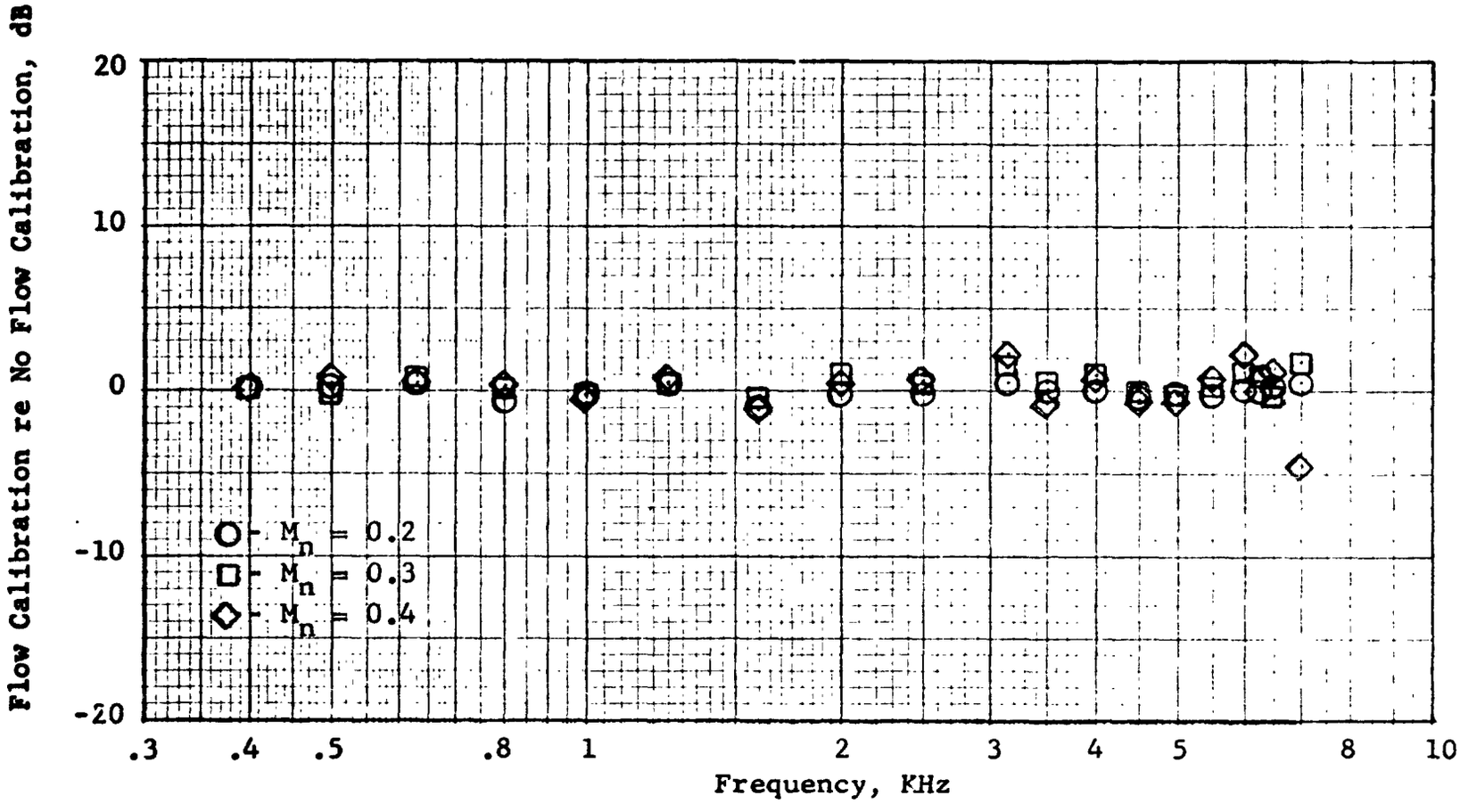

Figure 230. Change in Probe Calibration Due to Air Flow.

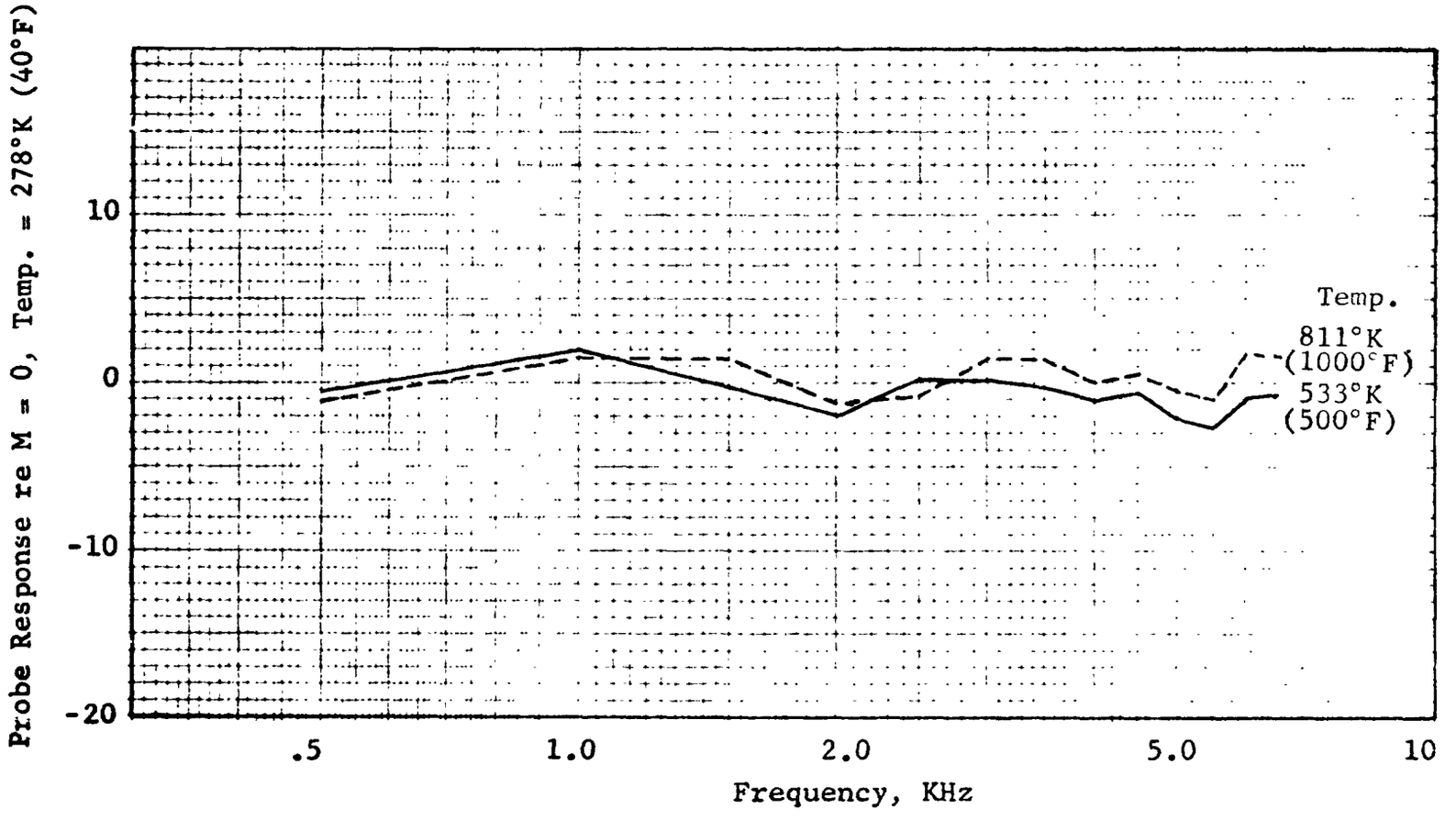

Figure 231. **Probe Response at High Temperatures and M = 0.4 Relative to Temperature = 278° K (40° F) and M = 0.**

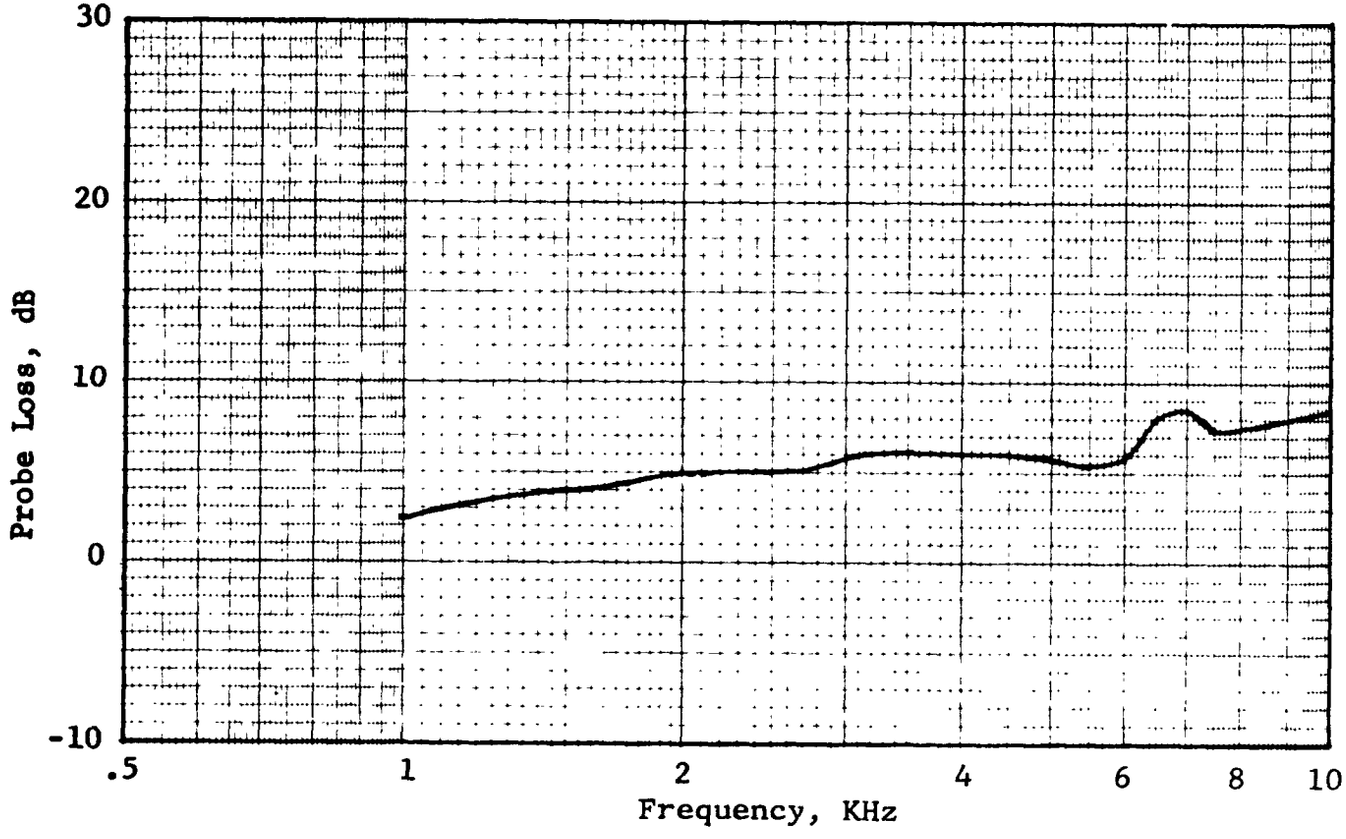

Figure 232. Engine A and C Turbine Loss Correction (1.0 Meter Probe).

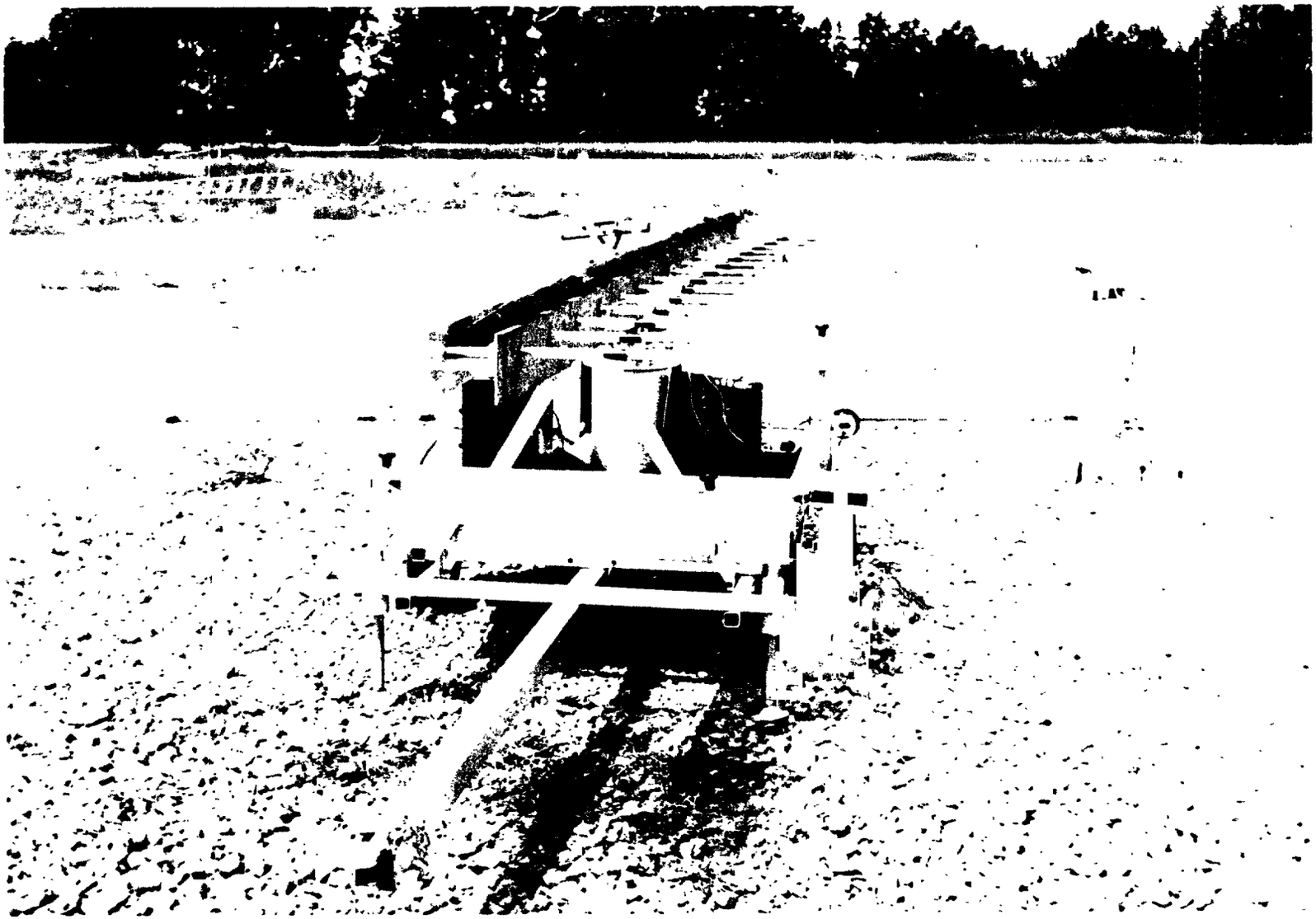

Figure 233. Directional Broadside Acoustic Array.

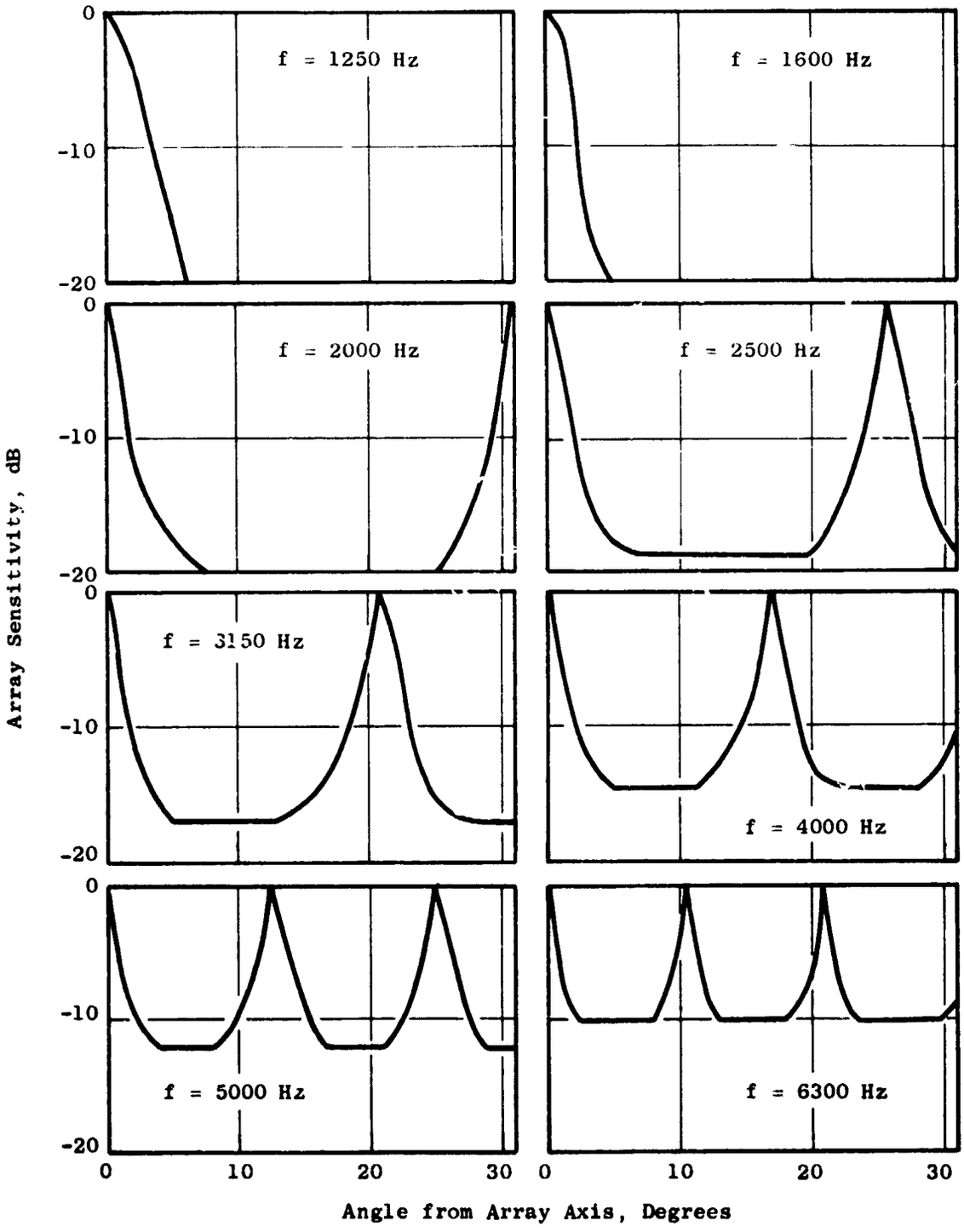

Figure 234. Beam Patterns of Directional Acoustic Array.

NOMENCLATURE LIST

B & K	Bruel and Kjaer Precision Instruments
BPF	Blade Passing Frequency
Broadband Noise	1/3-Octave Band SPL minus pure tone component
CTL	Corrected Transmission Loss, dB
dB	Decibel, re 0.0002 dynes/cm^2
g	Acceleration of Gravity
H/λ_o	Duct Height/Wavelength of Sound in Stationary Medium
Hz	Hertz (cycles per second)
L/H	Length to Duct Height Ratio
LPT	Low Pressure Turbine
M	Duct Mach Number
N_{f_c}	Fan Speed, corrected to standard day
MDOF	Multiple-Degree-of-Freedom
P_o	Ambient Pressure
PNL	Perceived Noise Level; at calculated annoyance weighted sound level, PNdB
Porosity (σ)	Percent Open Area (perforated face plate)
PWL	Power Level; re 10^{-13} watts
QEP	Quiet Engine Program
R	Universal Gas Constant
rpm	Revolutions Per Minute
SDOF	Single-Degree-of-Freedom
Standard Day	288° K (59° F) Temperature and 70% Relative Humidity
SPL	Sound Pressure Level; a level of sound pressure that occurs in a specified frequency range at any instant of time

NOMENCLATURE LIST - Concluded

T_o	Ambient Dry Bulb Temperature
ℓ	t + 0.85d
t	Face Plate Thickness
d	Hole Diameter
f	Frequency, Hz
V	Volume
ρ	Medium Density
c	Sonic Velocity
A	Area
γ	Ratio of Specific Heat at Constant Pressure to Specific Heat at Constant Volume $\left(\frac{c_p}{c_v}\right)$
W	Mass Flow